Relativistic Modeling of Multi-Component Astrophysical Jet : MHD flows around Kerr black holes

Loïc Chantry

PSL UNIVERSITÉ PARIS

l'Observatoire de Paris | LUTH

Laboratoire de l'Univers et de ses Théories

THÈSE DE DOCTORAT
DE L'UNIVERSITÉ PSL

Préparée à l'Observatoire de Paris

Relativistic Jets: Meridional self-similar model for MHD flows around Kerr black holes

Soutenue par
Loïc CHANTRY
Le 23/11/2017

Ecole doctorale n° 127
Ecole Doctorale Astronomie et Astrophysique d'Ile de France

Spécialité
Astrophysique

Composition du jury :

Eric, GOURGOULHON Directeur de recherche, Observatoire de Paris	*Président*
Ioannis, CONTOPOULOS Directeur de recherche, Academy of Athens	*Rapporteur*
Amir, LEVINSON Professeur, Tel Aviv University	*Rapporteur*
Nektarios, VLAHAKIS Professeur, Kapodistrian University of Athens	*Examinateur*
Alexandre, MARCOWITH Professeur, Université de Montpellier	*Examinateur*
Christophe, SAUTY Professeur, Laboratoire Univers et Théorie	*Directeur de thèse*
Véronique, CAYATTE Professeur, Laboratoire Univers et Théorie	*Directeur de thèse*

Résumé

Jets relativistes : Modélisation des écoulements magnétisé dans l'environnement des trous noirs de Kerr utilisant des méthodes auto-similaires

Les jets sont des phénomènes d'éjection collimatée de plasma magnétisé. Ces phénomènes liés à l'accrétion d'un disque sur un objet central, sont relativement répandus dans l'univers : les environnements des étoiles jeunes (objets Herbig-Haro, étoiles T Tauri), des binaires X, des sursauts gamma et les noyeaux actifs de galaxies... Les jets extra-galactiques sont issus des trous noirs super-massifs au centre de galaxies telles que les quasars ou les radiogalaxies. Ils sont caractérisés par leur taille, leur puissance et la vitesse du plasma.

Les jets extragalactiques sont étudiés dans de ce travail de thèse, même si les outils et méthodes développés peuvent être utilisés pour les binaires X et les microquasars. Nous poserons en particulier les questions des mécanismes de lancement, d'accélération et de collimation de ces écoulements. Nous traiterons également de la source énergétique à l'origine de l'écoulement qui peut atteindre une puissance de l'ordre de $10^{47}\mathrm{erg.s}^{-1}$.

Le liens avec l'accrétion, la proximité de la base des jets avec le trou noir central, les vitesses d'écoulement observées dans certains jets, montrent que le traitement de ces questions doit inclure les effet de la relativité générale. Nous étudierons donc des solutions de la décomposition $3{+}1$ des équations de la magnéto-hydrodynamique en métrique de Kerr. Nous nous appliquerons au développement d'un modèle d'écoulement meridional-auto-similaire avec un traitement consistant du cylindre de lumière. Ce modèle pouvant s'appliquer à la fois au jet et à l'accrétion. Nous explorons les mécanismes d'accélération et de collimation des solutions produites. Nous calculerons des solutions de l'écoulement entrant dans l'horizon et de l'écoulement sortant à l'infini incluant des termes d'injection de paires. Le rôle du mécanisme de création de paires et des processus d'extraction de l'énergie du trou noir sera exploré.

Mots clés : Jets relativistes - magnétohydrodynamique en relativité général - auto-similarité - jets extra-galactique - physique des trous noirs

Abstract

Relativistic Jets: Meridional self-similar model for MHD flows around Kerr black holes

Jets are collimated ejection phenomena of magnetized plasma. These phenomena related to the accretion of a disk on a central object, are relatively common in the universe: the environment of young stars (Herbig-Haro Objects, T Tauri stars...), X-ray binaries, Gamma-ray-bursts, and active galactic nuclei... Extragalactic jets come from super-massive black holes in the center of galaxies such as quasars or radiogalaxies. They are characterized by their size, their power and speed of the plasma.

Extragalactic jets will be the subject of studies in this thesis work, although the tools and methods developed can be used for X-ray binaries and microquasars. In particular, we will ask questions about the mechanisms of launching, accelerating and collimating these flows, but also about the energy source at the origin of the flow that can reach a power in the order of $10^{47}\mathrm{erg.s}^{-1}$.

The links with the accretion, the proximity of the jet base to the central black hole, flow velocities observed in some jets, show that the treatment of these issues must include the effects of general relativity. We will therefore study solutions of the $3{+}1$ decomposition of magneto-hydrodynamic equations in Kerr metric. We will apply ourselves the development of a meridional self-similar magnetized flow model with a consistent treatment of the light cylinder effect. This model can be applied to both spine jet and inflow onto the black hole. We explore the mechanisms of acceleration and collimation of the obtained solutions. We will calculate solutions of the incoming flow on the horizon and the outgoing flow reaching infinity including injection terms. The role of the pair creation mechanism and the processes of extracting energy from the black hole are explored.

Keywords : Relativistic jets - general relativistic magnetohydrodynamics - auto-similarity - extragalactic jets - black hole physics

$$\tau = \frac{\epsilon}{1 + \Omega} \longrightarrow 0$$

Peut être une raison d'espérer?...

Remerciements

Je tiens tout premièrement à remercier mes directeurs de thèse Veronique Cayatte et Christophe Sauty qui m'ont dirigé et accompagné durant cette thèse. C'est à l'aide d'une constante discussion scientifique avec eux qu'a put se forger les lignes, les hypothèses générales et l'interpretation des résultats de ce travail. Je les remercie tous deux pour ces heures à débattre du choix d'une notation, de la pertinence d'une hypothèse. Je tiens également à les remercier pour l'encadrements dont ils on fait preuve et qui m'a permis d'apprendre à hierarchisé les priorités lors d'un travaille de recherche. Je leurs adresse ici tout ma gratitude, ainsi qu'a Eric Gourghoulhon qui fut souvent m'a permis de répondre à des interrogations plus spécifique à la relativité général. Je pense également a Annie, Omur et Nathalie avec qui nous partagions parfois les cafés de 16h ainsi qu'a toute l'aides qu'elle nous apportèrent constamment concernant les taches administratives à effectuer.

Je souhaite également remercier Mr Levinson et Mr Contopoulos d'avoir accepté d'être les rapporteurs de mon jury, ainsi que pour la pertinence de leurs remarques et leurs questions concernant mon travail. Celles-ci l'ont indiscutablement amélioré. Je tiens également à remercier Mr Gourgoulhon pour avoir accepteé la présidence, ainsi que ceux qui furent mes rapporteurs Mr. Marcowith et M. Vlahakis.

Mes pensées vont également à Nektarios et à Kanaris qui nous on accueilli si gentiment lors de nos voyages à Athènes. Ces voyages furent toujours l'occasion autant de discussion stimulante à propos des jets relativistes que de la découverte d'un peuple rebelle et courageux dont la culture est à la fois si proche et si éloigné de la notre. Ces échanges m'ont permis de développé une affinité particulière avec ce pays et m'a permis de prendre conscience de certaines problèmes contemporains.

Je tiens également à remercier Mr Joly, mon professeur de physique de première, celui qui, par ses méthodes pédagogiques, m'a engagé sur les voies de la recherches et m'a transmis une passion certaine pour les sciences physiques.

Bien évidement tout ceci n'aura été possible sans le soutient constant et chaleureux de mes parents, de ma famille, de mes amis. Tout d'abords je remercie mes parents Nathalie et Luc et mes frères Alexandre et Simon pour le soutiens et l'aide qu'ils m'apportent a propos de certains problèmes du quotidien. Je souhaite dire à Alexandre toute l'admiration que j'ai pour lui, pour son parcours, son engagement, son courage et pour les épreuves qu'il dépasse sans broncher. Je veux également remercier le reste de ma famille qui furent nombreux lors de ma soutenance, je ne peut tous les nommer ici. C'est en pensant à eux et à ce que je leurs dois que mon courage et mon entrain n'a pas faiblit durant ces trois années.

Concernant mes amis une attention toute particulière va à Tina pour son travail de corrections des fautes d'Anglais du manuscript, travail aussi titanesque que la tailles de jets de M87 et qui fit perdre de nombreux cheveux sur sa tête ainsi que celles de mes encadrants. Je tiens à remercier mes amis du Nord, Bastien, Colas, Felix et Yannick qui après des années dispersé dans le monde on sut garder les liens d'amité aussi fort que durant les années d'écoles préparatoire ou ils furent scellé. Même chose concernant Léo, Michel-Andrès et Simon qui m'ont accompagné au quotidien durants ces 3 ans et dont les discussions concernant nos lectures communes m'ont permis de penser un peu à autre chose qu'au développements de mes recherches et ainsi a trouver une forme d'équilibre me permettant de poursuivre mon travail.

Contents

List of figures

List of Tables

List of symbol

Physical Constant	
$\mathscr{G} = 6,674 \times 10^{-8} \mathrm{cm}^3.\mathrm{g}^{-1}.\mathrm{s}^{-2}$	Gravitational constant
$c = 2,997 \times 10^{10} \mathrm{cm}.\mathrm{s}^{-1}$	Speed of light in vacuum
$k_\mathrm{B} = 1,380 \times 10^{-16}\,\mathrm{g}.\mathrm{cm}^2.\mathrm{s}^{-2}.\mathrm{K}^{-1}$	Boltzmann constant
$\sigma_\mathrm{T} = 6.65 \times 10^{25} \mathrm{cm}^2$	Thomson cross section

Geometry of space time and foliation	
$\mathscr{M}$	Spacetime
$\mathbf{g}$	Spacetime metrics on $\mathscr{M}$
$\mathscr{T}_\mathrm{P}(\mathscr{M})$	Tangent space to $\mathscr{M}$ on P
∇	Covariant derivative on $(\mathscr{M}, \mathbf{g})$
$\Gamma^\sigma_{\mu\nu}$	Christoffel symbols
Σ	Space manifold $\subset \mathscr{M}$
$\mathbf{n}$	Normal to Σ
$\boldsymbol{\gamma}$	Spatial metrics on Σ
$\mathbf{p}$	Orthogonal projector on Σ
$\mathbf{D}$	Covariant derivative on $(\Sigma, \boldsymbol{\gamma})$
$\mathbf{K}$	Second fondamental form
h	Lapse function
$h_r, h_\theta, h_\phi = \varpi$	Line element for Kerr metrics
$\boldsymbol{\beta}$	Shift of coordinate vector
ω	Shift of coordinate pulsation
$\mathbf{a}$	Fiducial observer acceleration
$\boldsymbol{\eta}$	Stationarity Killing vector
$\boldsymbol{\xi}$	Axi-symetry Killing vector
$\mathscr{H}$	Horizon null hypersurface
$\mathbf{e}_i$	Natural basis of $\mathscr{T}(\Sigma)$
$\boldsymbol{\epsilon}_i$	Orthonormal basis of $\mathscr{T}(\Sigma)$
Ω	Four speed hyperboloid manifold $\subset \mathscr{T}(\mathscr{M})$
$\mathscr{C}_+$	Future light cone $\subset \mathscr{T}(\mathscr{M})$
μ	space phase of particles
$\boldsymbol{\epsilon}$	Volum form on $\mathscr{M}$
$\boldsymbol{\omega}$	Volum form on Ω or $\mathscr{C}_+$
$\boldsymbol{\mu}$	Volume form of space phase

Physical quantity	
$\mathscr{J}$	Angular momentum of the Black-Hole
$\mathrm{M}_{\mathscr{H}}$	Angular momentum of the Black-Hole
r_s	Schwarzschild radius
a	Rotation of black hole parameter
$\mathbf{u}$	Generic four speed
$f, f_+, f_-, f_r, f_\Upsilon$	Distribution function of particles
$\mathrm{I}+, \mathrm{I}_-, \mathrm{I}_r$	Collision integrals or scattering operator
$\mathbf{T}, \mathbf{T}_{\mathrm{fl}}, \mathbf{T}_{rm\mathrm{EM}}$	Energy momentum tensor, for fluid, electromagnetic field
k_{N}, k_m	Number, mass Injection rate per unit of volume in fluid reference frame
$\mathbf{k}$	Force due to collision between fluid species
$\mathbf{F}$	Electro-magnetic tensor
$\mathbf{E}$	Electric field measured by fiducial observer
Ω	Isorotation function
$\mathbf{B}$	Magnetic field measured by fiducial observer
A	Magnetic flux
$\mathbf{j}$	Electric four-currant
I	Electric intensity
ρ_e	Electric density measured by fiducial observer
$\mathbf{J}$	Electric currant measured by fiducial observer
$\mathbf{s}$	Entropy flux density
T	Temperature
ξc^2	Specific enthalpy
e	Internal energy
ρ_0	mass density un the fluid reference frame
$\mathbf{V}$	Fluid velocity measured by fiducial observer
γ	Lorentz factor
Ψ_{A}	Mass flux par unit of magnetic flux
L	Total specific angular momentum
$\mathscr{E}$	Total specific energy
$\mathrm{M}_{\mathrm{Alf}}$	Alfvén Mach number
σ	Magnetization parameter

Model quantity	
$\mathrm{P}_\star$	Intersection between axis an Alfvén surface
$r_\star$	Radius of Alfvén surface
$\star$	Evaluation on $\mathrm{P}_\star$
M^2	Alfvén Mach number on the axis
G^2	Dimensionless cylindrical radius
F	Expansion factor
$\mathit{\Pi}$	Dimensionless axis pressure
R	Dimensionless radius
λ	Dimensionless rate of angular momentum flux per unit of magnetic flux
κ	Deviation from pressure sphericity
δ	Logarithmic derivation of Ψ_{A}^2 on polar axis
ν	Ratio between escape velocity and $\mathrm{V}_\star$
l	Dimensionless with $r_\star$ spin of the black hole
μ	Dimensionless Schwarzschild radius
e_1	Logarithmic variation of energy
ϵ	Magnetic collimation efficiency

Astrophysical units and quantity	
$M_{\odot} = 1,988 \times 10^{33} g$	Solar mass
$T_b = 5 \times 10^{10} - 5 \times 10^{12} K$	Brightness temperature of M87 source
$L = 2,7 \times 10^{42} erg.s?1$	Bolometric luminosity of M87 source
$B_{10r_s} = 1 - 15G$	Magnetic field at $10r_s$ for M87 source
$M_{\mathscr{H}} = (6,6 \pm 0.4) \times 10^9 M_{\odot}$	Mass of supermassive black hole of M87

Chapter 1

Introduction

Contents

Extra-galactic jets are astrophysical phenomena of collimated magnetized relativistic plasma outflows traveling through space in the two opposite directions. The bipolar outflows are always associated to accretion disks. The accretion around a central super-massive black hole seems to be the cause of the launching of relativistic jets. These jets are also present in accreting X-ray binary systems, Gamma Ray Bursts (GRBs) and micro-quasars. Many types of high energy astrophysical sources can be explored in order to explain the jet formation and evolution, the mechanisms of acceleration and collimation of plasma outflows and the power involved in them. Indeed, these powerful phenomena involve high energy particles physics, fluid mechanics, magnetohydrodynamics, turbulence and shocks in flows, non-equilibrium thermodynamics, general relativity, and numerical simulation,... In short, they are still relatively poorly understood phenomena and are a very active field of current astrophysical researches.

In this introduction, we do not pretend to make a complete state of the art regarding observations of extragalactic jets and accretion disks around black holes. Thus, we present a summary of observations that give some jet properties and an order of magnitude of the quantities we need to model the jet launching and propagation into the inter-galactic medium. Here we restrict our presentation to jets in blazars and radiosources. Our model has application to microquasars or GRB but the range of spatial, temporal and luminosity scales is different.

Object	a_* (Iron)
IRAS13224-3809	> 0.99
Mrk110	> 0.99
NGC4051	> 0.99
1H0707-495	> 0.98
RBS1124	> 0.98
NGC3783	> 0.98
NGC1365	$0.97^{+0.01}_{-0.04}$
Swift J0501-3239	> 0.96
PDS456	> 0.96
Ark564	$0.96^{+0.01}_{-0.06}$
3C120	> 0.95
Mrk79	> 0.95
MCG-6-30-15	$0.91^{+0.06}_{-0.07}$
TonS180	$0.91^{+0.02}_{-0.09}$
1H0419-577	> 0.88
IRAS00521-7054	> 0.84
Mrk335	$0.83^{+0.10}_{-0.13}$
Ark120	$0.81^{+0.10}_{-0.18}$
Swift J2127+5654	$0.6^{+0.2}_{-0.2}$
Mrk841	> 0.56
Fairall9	$0.52^{+0.19}_{-0.15}$

Table 1.1 – Table of measures of a for some Active Galaxy Nuclei (AGN) given by (Credits : Bambi [2018]). References for each source are presented in the mentioned paper.

We now get some measurements of supermassive black hole spin. However measurement of the spin parameter a of supermassive black holes is currently an issue in astrophysical observations. Different techniques have been explored. A technique consists in analyzing the Kα iron line. Bambi [2013] presents the results obtained for nearby extragalactic jets (see Tab.1.1). These super-massive black holes exhibit spin between 0.56 (forMrk841) to quasi maximally rotating black hole (e.g. Mrk110). To derive the spin it is necessary to model the disk and the shape of the corona. This kind of technique also allows Choudhury et al. [2018] to test general relativity in strong fields, using Johansen metric, which deviates from Kerr metric. They apply this method to Mrk 335 and without deviation to general relativity, they find a value between 0.9 et 0.97. Which is quite a high value of spin compared to the one mentioned in Tab.(1.1), (Parker et al. [2014]). Another technique was used by Gou et al. [2014] to measure the spin of the black hole of Cygnus X-1 binary.

Nevertheless these methods are model dependent for the accretion disk. Such kind of methods and others technics are efficient for measuring black hole spin in X-ray binaries. X-ray binaries or microquasars may be less suitable for steady-state modeling because the variability of accretion has short time scales between hours and months.

Let us also mention the very important detection of gravitational waves (Abbott et al. [2016]) resulting from a fusion of two black holes, and whose pattern gives us a strong indication on the masses, spins of the initial and final black holes. However, this technique does not allow to measure the spin of black holes that do not emit or only faint gravitational waves.

It is now recognized that jets from AGN are made of several components. It seems that outflow has at least two components, a surrounding disk wind and a spine jet the source of which is subject to discussion. Indeed, the spine jet plasma may come from the accreting material or from the black hole corona. But also pairs may be created by highly energetic photons emitted from the disk.

To explain the peculiar emission of BL Lac objects, Ghisellini et al. [2005] proposed a transversally structured jet model with two components. This two-component transverse structure was also used by Sikora et al. [2016] to explain blazar emission. Sikora et al. [2016] develop such a stratification model for the emission of strong-line blazars. It has also be done by Gaur et al. [2017] to study the energy distribution of non thermal particles in the blazar PKS 2155-304.

Fabian and Rees [1995]; Henri and Pelletier [1991]; Sol et al. [1989] studied theoretically the two component models. Henri and Pelletier [1991] explore the idea of a relativistic central jet composed of electron positron pairs and surrounded by classical Magneto-Hydrodynamic (MHD)

wind. Dynamical interactions between components are also explored. For example Gracia et al. [2009] explain the collimation of the spine jet by the presence of an efficiently collimated outer-disk wind component. Hervet et al. [2017] show the role of shock reflection in relativistic transverse stratified jets, for formation and motion of knots.

Numerical simulations including Special Relativistic Magneto-Hydrodynamic (SRMHD) or General Relativistic Magneto-Hydrodynamic (GRMHD) have also been performed to model the jet formation and study their two components structuration. Millas et al. [2017] explored, using the AMR-VAC simulation code, the role of toroidal velocity and magnetic field in the stability of two-component jets. Many simulations after the ones of McKinney and Blandford [2009] exhibit Poynting flux force-free spine jets. From numerical simulations, McKinney et al. [2012] and Tchekhovskoy et al. [2011] have also derived a scaling law from between accretion rate and magnetic flux threading the black hole horizon. In Zamaninasab et al. [2014] the authors justify this scaling law from observations and analysis.

The ejection process, in particular in the spine jet, is deeply linked to the accretion process on the central object. It is therefore essential to study the accretion on the central object to see how it can influence the jet. The standard accretion-ejection models include accretion models dominated by advection. These accretion models are applied to the internal part of the disks, except for very high accretion efficiency, (see Narayan and Yi [1994]). The study of accreting flows is also motivated by rotational energy transfer from the black hole to external medium. The Penrose process (Penrose [1969]) and the Blandford&Znajek process (Blandford and Znajek [1977]) are suspected to play an important role regarding the power observed in jets.

Nevertheless, to evaluate them properly, it is necessary to solve the GRMHD equations up to the horizon of the black hole. These process are not fully explained. At some time a controversy debate occurred about the the "Meissner effect". Komissarov and McKinney [2007] took part in this debate, showing that solutions of electro-magnetic fields are different in vacuum electrodynamics and in MHDs. The authors conclude that the black hole horizon "Meissner effect" does not hold for highly conductive magnetospheres. Nathanail and Contopoulos [2014] also get the same conclusion about "Meissner effect". They calculate solution that extract of black hole rotational energy via Poynting flux. They solve force free solutions of Graad-Shafranov equation for a Kerr magnetosphere. Their solutions are calculated for three different geometries (to infinite) and high values of black hole spin. They smoothly cross the inner and outer light cylinders. Komissarov [2009] also discusses the difference between both processes and the interpretation of Blandford&Znajek one. The pure Penrose process, because of the small number of particle fissions in the ergosphere that satisfy the process conditions, seems almost inefficient. (Bardeen et al. [1972], Wald [1974]). However, Wagh et al. [1985] proved that the electromagnetic field may supply the required energy to push particles into negative energy orbits. This allows to obtain Penrose type extraction. The energetic interaction between the black hole rotational energy and the ideal steady-state MHD fields have been studied by Takahashi et al. [1990] and Hirotani et al. [1992]. The coupling between the fluid field and the electromagnetic field allows an effective Penrose process. Numerical simulations also seem to show that the extraction process plays an important role in jet formation. In most of the simulations (Komissarov 2005, McKinney 2006), the extraction is dominated by the Poynting flux.

The central part of AGNs is possibly filled with high-energy photons from the disk. These photons can be at the origin of a mechanism for creating pairs (electron-positron, see Rees [1984]). It can explain part of the core material of the jet. In fact, this mechanism, witch loading material on magnetic field lines, can (a) fill the environment of the black hole (b) feed an accretion into the black hole (inflow) and (c) launch a spine jet (outflow) on the same fieldline. The works of Globus and Levinson [2013] and Globus and Levinson [2014] explore the importance of this phenomena for final jet energy composition. Indeed for a magnetic field-line passing through the horizon, in this treatment the energy flux inside the jet comes from the pair energy injection and

energy flux extraction from the black hole.

The study of a magnetized plasma can be done using a microscopic description (Boltzmann's equation, Vlasov's equation...) or a mesoscopic description - MHD - which can be derived from the microscopic description. The MHD description will be favored in this work. The microphysics description will serve to us for deriving source terms due to fluid species interaction.

Research on plasma flow is done in two directions,

- Numerical simulations
  They allow to study the evolution over time of a given field configuration. The ambition to test more complex physical effects and situations motivate the improvement of the digital power and efficiency of algorithms.

- The resolution of steady-state MHD equations.
  It has been chosen here. It consists to solve a partial differential equation system of mixed elliptic-hyperbolic type. The resolution of this system is very complex because of the singular points in the equations whose position can only be determined during the calculations. That is why we will look for a subset of solutions of these equations.

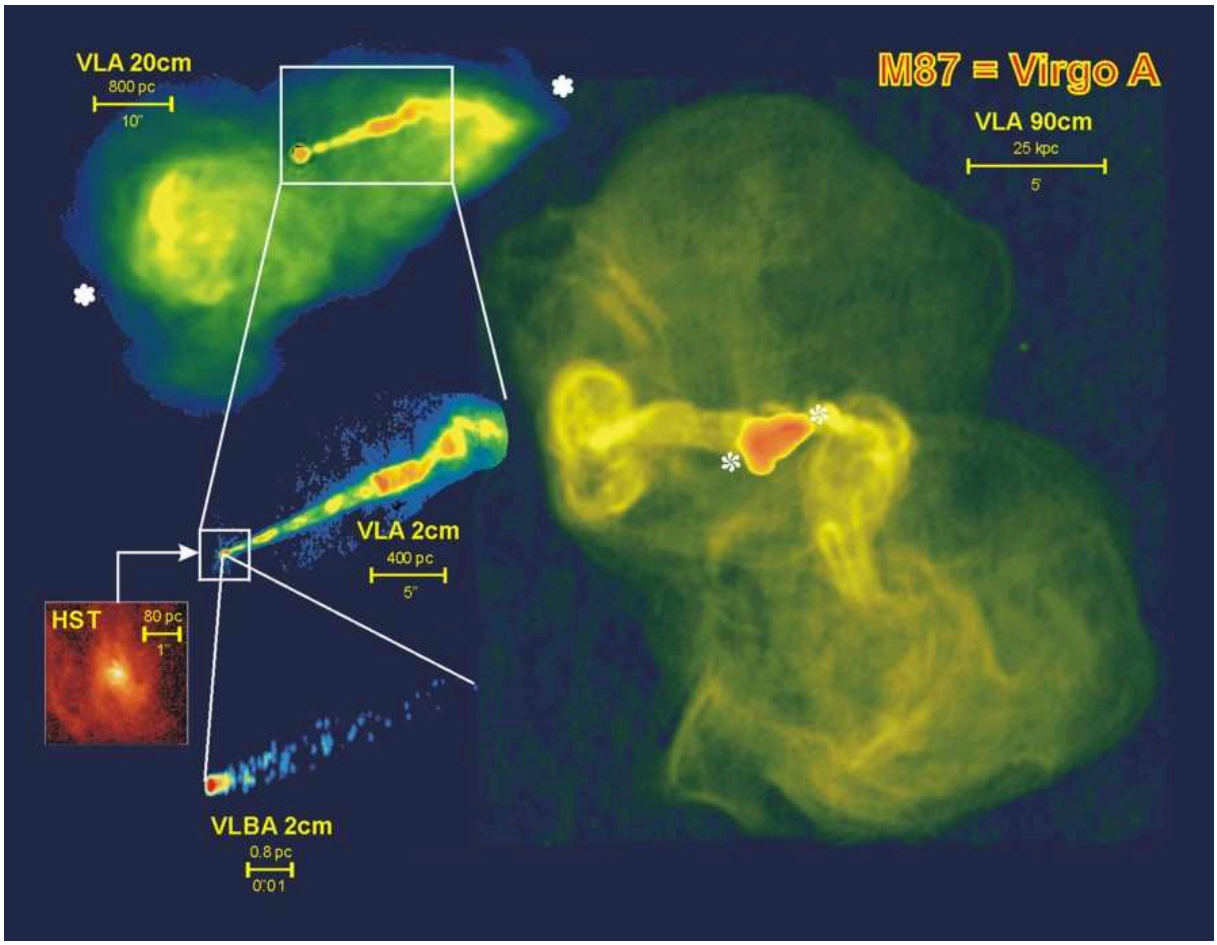

Figure 1.1 – Radio images of the galaxy M87 at different scales (Credits : Image courtesy of NRAO/AUI)

It seems reasonable to add the axi-symmetry assumption. Indeed, jets from AGN such as M87 seem relatively stable and axisymmetric on a spatial scale of few hundred parsec (see $400pc$ Figs.1.1). The quantities of our problem now depend on only 2 variables x^1, x^2. The auto-similarity hypothese consists in choosing for the fundamental functions of the problem $f(x^1, x^2)$

a form of the type : $f(x^1, x^2) = \mathrm{F}(x^1, f_{i=1...}(x^2))$. Where $\mathrm{F}(x^1, f_{i=1...})$ is given explicitly and the $f_i(x^2)$ are unknown real functions. If the F functions are correctly chosen then, injecting them into the equations of the MHD allows a decoupling of the variables. Thus we obtain an ordinary numerically integrable differential system of the $f_i(x^2)$ functions. In such a treatment, the variable x^1 is called the auto-similarity variable.

More concretely about the MHD, there are two main classes of self-similar models.

- Radial self-similarity : which is adapted to disk wind. For the non-relativistic flow, Li [1995] shows how to connect the wind of solutions to the disk characteristics. While Ferreira [1997] constructs solutions for magnetically driven outflow from Keplerian disks. Vlahakis et al. [2000] build self-similar solutions that cross all critical points. Then Vlahakis and Königl [2003a,b] extend these models for relativistic flows and study some of the solutions. Nevertheless the radial self-similar solution cannot by construction, applied to the polar axis. That's one of the reasons this kind of solutions is well adapted for disk-winds.
- Meridional self similar solution : this type is most adapted to describe flows close to the rotational axis. Tsinganos and Trussoni [1991] began to build the meridional self-similar model for MHD flows. Then Sauty and Tsinganos [1994] exposed two classes of solutions and a criterion which allows to characterize these flows. Then Meliani et al. [2006] extended a meridional self-similar model for magnetized flow around Schwarzschild black hole. And Globus et al. [2014] extended it to the magnetized flows around Kerr black hole.

The purpose of this work is to construct solutions from the accretion on the horizon of the black hole and the collimated ejection up to infinity. This allows us to ask ourself the question of acceleration and collimation of the spine jet. We want to explore the amount of energy in the jet coming from the rotational energy of the black hole and the amount coming from the loading term (pairs creation mechanism).

In order to build these solutions, we will start with a presentation of the theoretical foundations of the model. First of all, we will present properties of the 3+1 formalism in Ch.(2). Then we will derive in Ch.(3) the equations of the MHD for a magnetized fluid filled by the pair creation mechanism from statistical physics in curved space-time. Finally, we will derive the main results concerning the General Relativistic Axi-symmetric Stationary Ideal Magneto-Hydrodynamic (GRASIMHD) with source terms. The source terms are necessary to build complete solutions outside the hypothesis of a rarefied flow and are presented in Ch.(4).

The way to find solutions for the considered equations will be done using an extension of the meridionnal self-similar model in Kerr metric built by Globus et al. [2014]. We present the construction of this model in Ch.(5). Then we develop the numerical method used to solve the equations of the models in Ch.(6).

In the Ch.(7), we will present the main characteristics of the ouflow solutions generated by our model. These solutions could be used to describe the flow of magnetized plasma from the spine jets. Finally we in Ch.(8) we explore the use of this meridional self-similar model to build inflow solutions, allowing us to model a magnetized accretion onto the black hole. We have also to quantified the energy exchanges between the rotating black hole and the MHD fields. The articulation of these two types of flow allows us to build complete solutions using source terms. We have to estimate the source term values.

1.1 References

B. P. Abbott, R. Abbott, T. D. Abbott, M. R. Abernathy, and & co Acernese. Observation of gravitational waves from a binary black hole merger. *Phys. Rev. Lett.*, 116:061102, Feb 2016. doi: 10.1103/PhysRevLett.116.061102. URL https://link.aps.org/doi/10.1103/PhysRevLett.116.061102. 2

C. Bambi. Measuring the Kerr spin parameter of a non-Kerr compact object with the continuum-fitting and the iron line methods. jcap, 8:055, August 2013. doi: 10.1088/1475-7516/2013/08/055. 2

Cosimo Bambi. Astrophysical black holes: A compact pedagogical review. *Annalen der Physik*, 530(6):1700430, 2018. doi: 10.1002/andp.201700430. URL https://onlinelibrary.wiley.com/doi/abs/10.1002/andp.201700430. xvii, 2

J. M. Bardeen, W. H. Press, and S. A. Teukolsky. Rotating Black Holes: Locally Nonrotating Frames, Energy Extraction, and Scalar Synchrotron Radiation. apj, 178:347–370, December 1972. doi: 10.1086/151796. 3

R. D. Blandford and R. L. Znajek. Electromagnetic extraction of energy from Kerr black holes. mnras, 179:433–456, May 1977. doi: 10.1093/mnras/179.3.433. 3

K. Choudhury, S. Nampalliwar, A. B. Abdikamalov, D. Ayzenberg, C. Bambi, T. Dauser, and J. A. Garcia. Testing the Kerr metric with X-ray Reflection Spectroscopy of Mrk 335 Suzaku data. *ArXiv e-prints*, September 2018. 2

A. C. Fabian and M. J. Rees. The accretion luminosity of a massive black hole in an elliptical galaxy. mnras, 277:L55–L58, November 1995. doi: 10.1093/mnras/277.1.L55. 2

J. Ferreira. Magnetically-driven jets from Keplerian accretion discs. aap, 319:340–359, March 1997. 5

Haritma Gaur, Liang Chen, R. Misra, S. Sahayanathan, M. F. Gu, P. Kushwaha, and G. C. Dewangan. The hard x-ray emission of the blazar pks 2155?304. *The Astrophysical Journal*, 850(2):209, 2017. URL http://stacks.iop.org/0004-637X/850/i=2/a=209. 2

G. Ghisellini, F. Tavecchio, and M. Chiaberge. Structured jets in TeV BL Lac objects and radiogalaxies. Implications for the observed properties. aap, 432:401–410, March 2005. doi: 10.1051/0004-6361:20041404. 2

N. Globus and A. Levinson. Loaded magnetohydrodynamic flows in Kerr spacetime. prd, 88(8):084046, October 2013. doi: 10.1103/PhysRevD.88.084046. 3

N. Globus and A. Levinson. Jet Formation in GRBs: A Semi-analytic Model of MHD Flow in Kerr Geometry with Realistic Plasma Injection. apj, 796:26, November 2014. doi: 10.1088/0004-637X/796/1/26. 3

N. Globus, C. Sauty, V. Cayatte, and L. M. Celnikier. Magnetic collimation of meridional-self-similar general relativistic MHD flows. prd, 89(12):124015, June 2014. doi: 10.1103/PhysRevD.89.124015. 5

L. Gou, J. E. McClintock, R. A. Remillard, J. F. Steiner, M. J. Reid, J. A. Orosz, R. Narayan, M. Hanke, and J. García. Confirmation via the Continuum-fitting Method that the Spin of the Black Hole in Cygnus X-1 Is Extreme. apj, 790:29, July 2014. doi: 10.1088/0004-637X/790/1/29. 2

J. Gracia, N. Vlahakis, I. Agudo, K. Tsinganos, and S. V. Bogovalov. Synthetic Synchrotron Emission Maps from MHD Models for the Jet of M87. apj, 695:503–510, April 2009. doi: 10.1088/0004-637X/695/1/503. 3

G. Henri and G. Pelletier. Relativistic electron-positron beam formation in the framework of the two-flow model for active galactic nuclei. apjl, 383:L7–L10, December 1991. doi: 10.1086/186228. 2

O. Hervet, Z. Meliani, A. Zech, C. Boisson, V. Cayatte, C. Sauty, and H. Sol. Shocks in relativistic transverse stratified jets. A new paradigm for radio-loud AGN. aap, 606:A103, October 2017. doi: 10.1051/0004-6361/201730745. 3

K. Hirotani, M. Takahashi, S.-Y. Nitta, and A. Tomimatsu. Accretion in a Kerr black hole magnetosphere - Energy and angular momentum transport between the magnetic field and the matter. apj, 386:455–463, February 1992. doi: 10.1086/171031. 3

S. S. Komissarov. Observations of the Blandford-Znajek process and the magnetohydrodynamic Penrose process in computer simulations of black hole magnetospheres. mnras, 359:801–808, May 2005. doi: 10.1111/j.1365-2966.2005.08974.x. 3

S. S. Komissarov. Blandford-Znajek Mechanism versus Penrose Process. *Journal of Korean Physical Society*, 54:2503, June 2009. doi: 10.3938/jkps.54.2503. 3

S. S. Komissarov and J. C. McKinney. The 'Meissner effect' and the Blandford-Znajek mechanism in conductive black hole magnetospheres. mnras, 377:L49–L53, May 2007. doi: 10.1111/j.1745-3933.2007.00301.x. 3

Z.-Y. Li. Magnetohydrodynamic disk-wind connection: Self-similar solutions. apj, 444:848–860, May 1995. doi: 10.1086/175657. 5

J. C. McKinney. General relativistic magnetohydrodynamic simulations of the jet formation and large-scale propagation from black hole accretion systems. mnras, 368:1561–1582, June 2006. doi: 10.1111/j.1365-2966.2006.10256.x. 3

Jonathan C. McKinney and Roger D. Blandford. Stability of relativistic jets from rotating, accreting black holes via fully three-dimensional magnetohydrodynamic simulations. mnras, 394:L126–L130, March 2009. doi: 10.1111/j.1745-3933.2009.00625.x. 3

Jonathan C. McKinney, Alexander Tchekhovskoy, and Roger D. Blandford. General relativistic magnetohydrodynamic simulations of magnetically choked accretion flows around black holes. *Monthly Notices of the Royal Astronomical Society*, 423(4):3083–3117, 2012. doi: 10.1111/j.1365-2966.2012.21074.x. URL http://dx.doi.org/10.1111/j.1365-2966.2012.21074.x. 3

Z. Meliani, C. Sauty, N. Vlahakis, K. Tsinganos, and E. Trussoni. Nonradial and nonpolytropic astrophysical outflows. VIII. A GRMHD generalization for relativistic jets. aap, 447:797–812, March 2006. doi: 10.1051/0004-6361:20053915. 5

D. Millas, R. Keppens, and Z. Meliani. Rotation and toroidal magnetic field effects on the stability of two-component jets. mnras, 470:592–605, September 2017. doi: 10.1093/mnras/stx1288. 3

Ramesh Narayan and Insu Yi. Advection-dominated Accretion: A Self-similar Solution. apj, 428:L13, June 1994. doi: 10.1086/187381. 3

A. Nathanail and I. Contopoulos. Black Hole Magnetospheres. apj, 788:186, June 2014. doi: 10.1088/0004-637X/788/2/186. 3

M. L. Parker, D. R. Wilkins, A. C. Fabian, D. Grupe, T. Dauser, G. Matt, F. A. Harrison, L. Brenneman, S. E. Boggs, F. E. Christensen, W. W. Craig, L. C. Gallo, C. J. Hailey, E. Kara, S. Komossa, A. Marinucci, J. M. Miller, G. Risaliti, D. Stern, D. J. Walton, and W. W. Zhang. The NuSTAR spectrum of Mrk 335: extreme relativistic effects within two gravitational radii of the event horizon? mnras, 443:1723–1732, September 2014. doi: 10.1093/mnras/stu1246. 2

R. Penrose. Gravitational Collapse: the Role of General Relativity. *Nuovo Cimento Rivista Serie*, 1, 1969. 3

M. J. Rees. Black Hole Models for Active Galactic Nuclei. araa, 22:471–506, 1984. doi: 10.1146/annurev.aa.22.090184.002351. 3

C. Sauty and K. Tsinganos. Nonradial and nonpolytropic astrophysical outflows III. A criterion for the transition from jets to winds. aap, 287:893–926, July 1994. 5

Marek Sikora, Mieszko Rutkowski, and Mitchell C. Begelman. A spine-sheath model for strong-line blazars. mnras, 457:1352–1358, April 2016. doi: 10.1093/mnras/stw107. 2

H. Sol, G. Pelletier, and E. Asseo. Two-flow model for extragalactic radio jets. mnras, 237: 411–429, March 1989. doi: 10.1093/mnras/237.2.411. 2

M. Takahashi, S. Nitta, Y. Tatematsu, and A. Tomimatsu. Magnetohydrodynamic flows in Kerr geometry - Energy extraction from black holes. apj, 363:206–217, November 1990. doi: 10.1086/169331. 3

Alexander Tchekhovskoy, Ramesh Narayan, and Jonathan C. McKinney. Efficient generation of jets from magnetically arrested accretion on a rapidly spinning black hole. *Monthly Notices of the Royal Astronomical Society: Letters*, 418(1):L79–L83, 2011. doi: 10.1111/j.1745-3933.2011.01147.x. URL http://dx.doi.org/10.1111/j.1745-3933.2011.01147.x. 3

K. Tsinganos and E. Trussoni. Analytical studies of collimated winds. II - Topologies of 2-D helicoidal MHD solutions. aap, 249:156–172, September 1991. 5

N. Vlahakis and A. Königl. Relativistic Magnetohydrodynamics with Application to Gamma-Ray Burst Outflows. I. Theory and Semianalytic Trans-Alfvénic Solutions. apj, 596:1080–1103, October 2003a. doi: 10.1086/378226. 5

N. Vlahakis and A. Königl. Relativistic Magnetohydrodynamics with Application to Gamma-Ray Burst Outflows. II. Semianalytic Super-Alfvénic Solutions. apj, 596:1104–1112, October 2003b. doi: 10.1086/378227. 5

N. Vlahakis, K. Tsinganos, C. Sauty, and E. Trussoni. A disc-wind model with correct crossing of all magnetohydrodynamic critical surfaces. mnras, 318:417–428, October 2000. doi: 10.1046/j.1365-8711.2000.03703.x. 5

S. M. Wagh, S. V. Dhurandhar, and N. Dadhich. Revival of the Penrose process for astrophysical applications. apj, 290:12–14, March 1985. doi: 10.1086/162952. 3

R. M. Wald. Energy Limits on the Penrose Process. apj, 191:231–234, July 1974. doi: 10.1086/152959. 3

M. Zamaninasab, E. Clausen-Brown, T. Savolainen, and A. Tchekhovskoy. Dynamically important magnetic fields near accreting supermassive black holes. nat, 510:126–128, June 2014. doi: 10.1038/nature13399. 3

Chapter 2

3+1 Methods

Contents

The 3+1 formalism is an approach to general relativity using the notion of foliation of four dimensional spacetime varieties ($\mathscr{M}$) with three dimensional imbedded sub-varieties (Σ_t). These sub-varieties must be "similar" to space. Such that, the general spacetime induces a Riemannian metric. In others words the induced metric is a definite positive bilinear form. This formalism makes possible to systematically rewrite the equations of general relativity in a convenient form. This form is similar to the equations of classical mechanics even if it incorporates relativistic effects. In this formulation the physical meaning of the equations of general relativity appears more clearly. The 3+1 decomposition of Einstein's equations also gives a new perspective on general relativity, the so-called chrono-geometric interpretation of general relativity [Wheeler, 1964], i.e. the evolution over time of the geometry of three dimensional manifold representing space.

The 3+1 formalism also allows us to introduce an observer and a particular frame in which the different physical quantities related to magneto-hydrodynamics are measured. Indeed some quantities as the electric and the magnetic fields have a meaning only in a considered reference frame. This is an important requirement to give a physical meaning to the field we study.

Historically, the development of these methods started at the beginning of last century with the work of Darmois, Lichnerowicz [1939] and Choquet-Bruhat and Geroch [1969]. These last two authors were the first to prove the unicity of the solution to Cauchy's problem arising from the 3+1 decomposition of Einstein's equations. After the Second World War, the 3+1 formalism received great interest because it serves as a basis to the work on Hamiltonian formulation of general relativity, the same way as the chrono-dynamic formulation in general relativity did, (see Arnowitt et al. [2008]). Later on this formalism became one of the essential tools of numerical relativity.

This chapter is not an exhaustive treatment of the 3+1 decomposition methods. It is a summary of useful results and definitions used further down for calculations. This chapter is inspired from the work done by Gourgoulhon [2007]. We shall first study the geometry of the submerged submanifold. Then we shall see how to reconstruct the geometry of full time space from the foliation. Finally we shall express the the Kerr's spacetime foliation and calculate the useful remaining associated quantities.

2.1 Geometry of imbedded hypersurfaces in spacetime

Before introducing the foliation of spacetime, let us give some general results on imbedded submanifolds. These results are valid for any type of submanifold or spacetime, independently of the fact that the considered spacetime is a solution or not of Einstein's equations. Moreover these results can be applied to the black hole horizon, which is a submanifold and is not directly issued from a 3+1 foliation. These results constitute the first step to establishe the tools useful for the 3+1 decomposition of the covariant equations.

2.2 Framework and notations

Let us call $\mathscr{M}$ a smooth spacetime manifold and $\mathbf{g}$ a Lorentzian metric on $\mathscr{M}$ with a signature $(-;+;+;+)$. Here we consider only time orientable spacetime manifold $\mathscr{M}$. This means that a continuous construction of future-directed and past-directed for non-spacelike vectors can be made over the entire manifold.

We note ∇ the covariant derivative associated to $\mathbf{g}$. $\forall \mathrm{P} \in \mathscr{M}$, we also note $\mathscr{T}_{\mathrm{P}}(\mathscr{M})$ the tangent

space of $\mathscr{M}$ around point P. This is a 4-dimensional vectorial space. We call $\mathscr{T}_{\mathrm{P}}^{\star}(\mathscr{M})$ its four dimensional dual space. It contains the ordinary one form. In order to simplify our notations, except in case of ambiguity, we use the same notation for the dual of the tangent space, the tensorial product of the tangent space with itself and the tangent space itself.

We adopt the following convention for the tensor indices. Greek letters run for 4 dimensions, $\{0,1,2,3\}$. We use as far as possible the first letter of the greek alphabet for uncontracted indices such as α,β,γ and other letters such as μ,ν for contracted indices. Latin letters are used for the 3 dimensions, $1,2,3$.

If (x^{α}) is a mapping of $\mathscr{M}$ then we note $\mathbf{e}_{\alpha}$ the natural basis associated to this mapping. We also note $\Gamma^{\alpha}_{\beta\gamma}$ the Christoffel symbols, which are associated to this system of coordinates and the covariant derivative ∇.

We also note $\mathbf{u}\cdot\mathbf{v}=\mathbf{g}(\mathbf{u},\mathbf{v})$ the scalar product, $\oplus$ the direct sum of the vectorial space and $\otimes$ the tensor product.

2.2.1 Hypersurfaces

A hypersurface of $\mathscr{M}$ is a subset of $\mathscr{M}$, which is a three dimensional submanifold.

Definition

The first method, the immersion method to define a hypersurface, consists in using a none zero volume part of $\hat{\Sigma}\subset\mathbb{R}^3$ to construct a parameterized subset of $\mathscr{M}$. Let call it $\Sigma\subset\mathscr{M}$ if there is a $\mathscr{C}^1$-diffeomorphism $\Phi:\hat{\Sigma}\to\Sigma$. Then Σ is a three-dimensional imbedded manifold.

The second method is submersion. It consists by using a sufficiently smooth scalar function $t:\mathscr{M}\to\mathbb{R}$, such that we can define a three-dimensional imbedded manifold using $\Sigma=\{\mathrm{M}\in\mathscr{M}\mid t(\mathrm{M})=0\}$. This definition works only if $\nabla t\neq 0$.

We recall that the tangent space in $\mathrm{P}\in\Sigma$ is generated by all tangent vectors of all $\mathscr{C}^1$ curves passing through P. Because the set of $\mathscr{C}^1$ curves of Σ passing through P is contained into the set of $\mathscr{C}^1$ curves of $\mathscr{M}$, it implies that $\mathscr{T}_{\mathrm{P}}(\Sigma)\subset\mathscr{T}_{\mathrm{P}}(\mathscr{M})$. Note that $\forall\mathbf{dx}\in\mathscr{T}_{\mathrm{P}}(\Sigma)$. We get $\nabla t\cdot\mathbf{dx}=dt$, which is null because of the definition of Σ. Thus we have $\mathscr{T}_{\mathrm{P}}(\Sigma)\subset(\mathbb{R}\nabla t)^{\perp}$.

Normal unit vector

Using the definition of submersion, the hypersurface Σ can be locally of 3 different types,

- A spatial hypersurface if the normal is a time vector $\mathbf{g}(\nabla t,\nabla t)<0$,
- A null surface if the normal is a null vector $\mathbf{g}(\nabla t,\nabla t)=0$
- A Lorentzian surface if the normal is a spatial vector $\mathbf{g}(\nabla t,\nabla t)>0$

In the following, we concentrate our interest on the case of spatial or null hypersurfaces. In the case of spatial or Lorentzian hypersurfaces, let us define the **normal unit vector n**,

$$\mathbf{n}=-\frac{\nabla t}{\sqrt{|\,\mathbf{g}(\nabla t,\nabla t)\,|}}=-hc\nabla t, \tag{2.1}$$

which defines the direction perpendicular to the 3 dimensional hypersurfaces Σ. In the case of a null hypersurface, we call ℓ the normal vector. In this case ℓ is orthogonal and also tangent to Σ. The minus sign is chosen such that the normal vector is oriented towards the future.

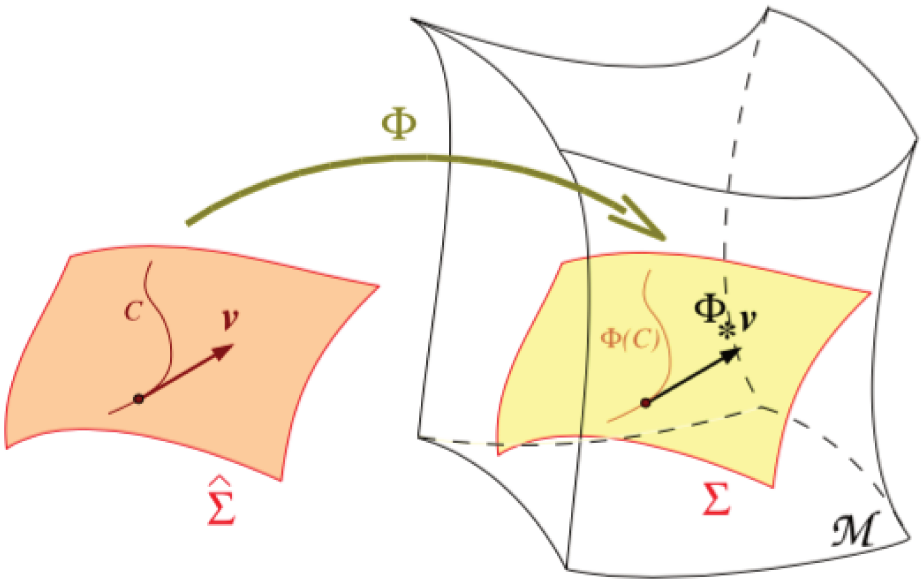

Figure 2.1 – The construction of hypersurface tangent space (Credits : Gourgoulhon [2007])

Induced metric

If Σ is a spatial hypersurface, the normal unit vector is a time vector. It means that for each point $\mathrm{P} \in \Sigma$, the projector on $\mathcal{T}_{\mathrm{P}}(\Sigma)$, which is normal to $\mathbf{n}$, can be expressed as,

$$\begin{array}{rccc} \mathbf{p} & : & \mathcal{T}_{\mathrm{P}}(\mathcal{M}) & \to & \mathcal{T}_{\mathrm{P}}(\Sigma) \\ & & \mathbf{v} & \mapsto & \mathbf{v} + (\mathbf{v}\cdot\mathbf{n})\mathbf{n} \end{array} \tag{2.2}$$

The induced metric $\boldsymbol{\gamma}$ on Σ is also called **the first fundamental form**. It corresponds to the usual metric, for each vector field of $\mathcal{T}(\Sigma)$. To extend its definition to all vectors of $\mathcal{T}(\mathcal{M})$, we use the projector in the argument of the usual metric. After some calculations we get,

$$\boxed{\boldsymbol{\gamma} = \mathbf{g}(\mathbf{p}(.), \mathbf{p}(.)) = \mathbf{g} + \mathbf{n} \otimes \mathbf{n}}. \tag{2.3}$$

We can easily show that this induced metric $\boldsymbol{\gamma}$ is defined, positive and thus its signature is $(+;+;+)$, which justifies calling it spatial hypersurface metric.

In case of a null hypersurface, it is a bit more complex. Indeed, we can always choose for all $\mathrm{P} \in \Sigma$ an orthonormal basis $\boldsymbol{\epsilon}_\alpha$, where $\boldsymbol{\epsilon}_0$ is the time vector. Note that $\boldsymbol{\epsilon}_1$ is chosen such that the decomposition of the normal can be written $\boldsymbol{\ell} = \mathrm{C}(\boldsymbol{\epsilon}_0 + \boldsymbol{\epsilon}_1)/\sqrt{2}$. Introducing $\mathbf{k} = (\boldsymbol{\epsilon}_0 - \boldsymbol{\epsilon}_1)/\mathrm{C}\sqrt{2}$, you get two null vector $\boldsymbol{\ell}$ and $\mathbf{k}$ satisfying $\boldsymbol{\ell}\cdot\mathbf{k} = -1$. Thus, it is easy to see that the operator defined by

$$\begin{array}{rccc} \boldsymbol{\pi} & : & \mathcal{T}_{\mathrm{P}}(\mathcal{M}) & \to & \mathcal{T}_{\mathrm{P}}(\Sigma) \\ & & \mathbf{v} & \mapsto & \mathbf{v} + (\mathbf{v}\cdot\boldsymbol{\ell})\mathbf{k} \end{array}, \tag{2.4}$$

is the projector on $\mathcal{T}_{\mathrm{P}}(\Sigma)$, perpendicular to $\boldsymbol{\ell}$. Thus we get for the induced metric,

$$\boxed{\mathbf{q} = \mathbf{g}(\boldsymbol{\pi}(.), \boldsymbol{\pi}(.)) = \mathbf{g} + \mathbf{k} \otimes \boldsymbol{\ell} + \boldsymbol{\ell} \otimes \mathbf{k}}. \tag{2.5}$$

We also show that this induced metric $\mathbf{q}$ is degenerate. Its signature is $(0;+;+)$. In the following of this chapter we only consider spatial hypersurfaces.

Decomposition of tangent space

Because $\forall \mathrm{P} \in \Sigma$, $\mathcal{T}_{\mathrm{P}}(\Sigma)$ is a vector space of dimension 3, and because $\mathcal{T}_{\mathrm{P}}(\Sigma) \subset \mathrm{Vect}(\nabla t)^{\perp}$, it is easy to show that,

$$\boxed{\mathcal{T}_{\mathrm{P}}(\mathcal{M}) = \mathcal{T}_{\mathrm{P}}(\Sigma) \overset{\perp}{\bigoplus} \mathbb{R}\mathbf{n}}, \tag{2.6}$$

It implies that we can decompose all tensors in different component kinds, function of the "size" of the considered tensor. For instance,

1. the rest mass density ρ_0, which has no decomposition,
2. the four electric-current $\mathbf{j} = -\rho_e c\mathbf{n} + \mathbf{J}$, with $\mathbf{J}$ is the "three dimensional electric-current, more explanations will be given on the physical meaning of this decomposition on Sec.(4.1.3).
3. the energy-impulsion tensor, which can be rewritten, $\mathbf{T} = e\mathbf{n}\otimes\mathbf{n} + \mathbf{p}\otimes\mathbf{n} + \mathbf{n}\otimes\mathbf{p} + \mathbf{S}$, where $\mathbf{S} \in \mathscr{T}(\Sigma)^2$ is its spatial component and $\mathbf{p} \in \mathscr{T}(\Sigma)$ its temporal one.

To obtain the spatial part of any tensor, it is enough to project each order on $\mathscr{T}_{\mathrm{P}}(\Sigma)$,

$$(\mathbf{p}^{\star}\mathbf{M})^{\alpha_1,\ldots,\alpha_p}_{\beta_1,\ldots,\beta_q} = p^{\alpha_1}_{\nu_1}\ldots p^{\alpha_p}_{\nu_p} p^{\mu_1}_{\beta_1}\ldots p^{\mu_q}_{\beta_q} \mathrm{M}^{\nu_1,\ldots,\nu_p}_{\mu_1,\ldots,\mu_q}. \tag{2.7}$$

2.2.2 Curvature of manifolds

We introduce here how to calculate the derivative on a submanifold. In order to re-write the equations, such as the continuity or the Euler equation in a form similar to the classical ones, an important step is to link four dimensional-covariant derivatives ∇ to an object, which plays the role of ordinary gradient. We show that usual "derivatives" are composed of an internal "derivative", which contains the variation where the submanifold is considered by itself and an extrinsic "derivative", which contains the curvature of the imbedded submanifold.

Intrisic curvature

Note that Σ is also a manifold, qualified as a spatial manifold, with $\boldsymbol{\gamma}$ as induced metric. We know that there is a unique, torsion-free connection, entirely determined by the induced metric $\boldsymbol{\gamma}$ and its partial derivatives. We will note this connection D. By definition $\mathrm{D}\boldsymbol{\gamma} = 0$. This connection allows us to define the intrinsic curvature, the Σ-Riemann tensor ${}^{\Sigma}\mathbf{R}$ also called **intrinsic curvature** of $(\Sigma, \boldsymbol{\gamma})$. Note that $\forall \mathbf{v} \in \mathscr{T}(\Sigma)$,

$$(\mathrm{D}_\alpha \mathrm{D}_\beta - \mathrm{D}_\beta \mathrm{D}_\alpha) v^\gamma = {}^{\Sigma}\mathrm{R}^{\gamma}_{\sigma\alpha\beta} v^\sigma. \tag{2.8}$$

We can use the usual formula (Eq.A.5) of the Riemann tensor with the Christoffel symbols. However, here we need to be careful and use the Christoffel symbols associated with the induced metric. D plays the role of the ordinary 3-dimensional gradient of the non-relativistic form of the equations. Thus all the spatial usual operators are defined as functions of D (see An.B.2). The expression of this affine connection is intrinsically linked to the geometry of the "space" submanifold.

Using the concept of foliation, we see that to reconstruct the entire knowledge on the geometry of our spacetime, it is sufficient to know the intrinsic curvature of the submanifold of the foliation and the way its submanifold is bent in spacetime.

Extrinsic curvature

The form of general relativity equations makes appear the global connection ∇ associated to the metric $\mathbf{g}$ on $\mathscr{M}$. This connection contains D, the Σ affine connection associated to the metric $\boldsymbol{\gamma}$ and also the term coming from the variation "along" $\mathbf{n}$ of any tensor on $\mathscr{M}$. These terms may contain some of the components along Σ. We call it the **extrinsic curvature**. It is due to the projection along Σ of the variation of $\mathbf{n}$. So we define what we call the **second fundamental form**,

$$\begin{array}{rccc} \mathbf{K} & : & \mathscr{T}_{\mathrm{P}}(\mathscr{M}) \times \mathscr{T}_{\mathrm{P}}(\mathscr{M}) & \to & \mathbb{R} \\ & & (\mathbf{u}, \mathbf{v}) & \mapsto & -\mathbf{p}(\mathbf{u}) \cdot \nabla_{\mathbf{p}(\mathbf{v})}\mathbf{n} \end{array}, \tag{2.9}$$

To have a good idea about the meaning of the intrinsic and the extrinsic curvatures, it is useful to give some examples using some surface imbedded in the three dimensional flat space.

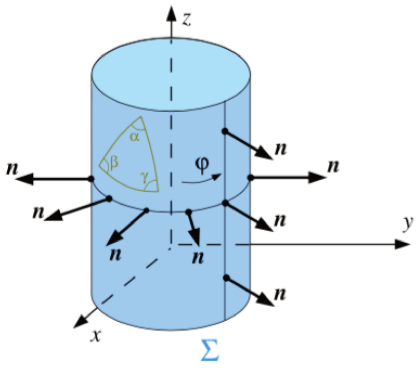

Figure 2.2 – Intrinsic and Extrinsic curvature on the usual two-dimensionnal submanifold cylinders (Credits : Gourgoulhon [2007])

About the usual cylinder, since this surface can be made from a "rolled" plane, it is intuitive to see that the intrinsic curvature is null. Indeed it is easy to see that the induced metric on the cylinder is the usual metric of the plane, which implies that the intrinsic curvature is the same as the planar manifold. Thus the cylinder have null intrinsic curvature. While the extrinsic curvature clearly gets a non-zero component in the direction $\phi\phi$. Indeed the perpendicular direction rotates around the z-axis as one moves along the ϕ-direction. It implies that some of the components along ϕ of $\nabla_\phi \mathbf{n}$ are not zero.

Let us now define the helicoid. The non diagonal component K_{ij} with $i \neq j$ of the extrinsic curvature measures the torsion of the submanifold. Thus the submanifold defines an helicoidal surface of revolution along the z-axis. The perpendicular direction rotates in the ϕ-direction, as one moves along the z-direction. It gives a component $K_{z\phi}$.

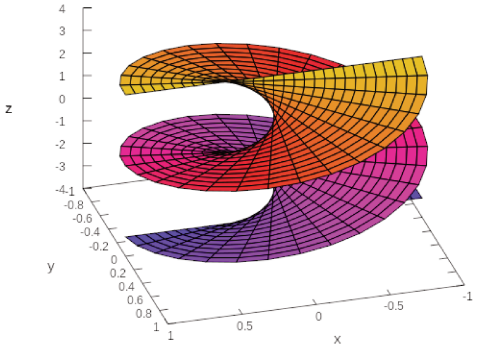

Figure 2.3 – Intrinsic and Extrinsic curvature on the usual two-dimensionnal submanifold Helicoid (Credits : Wikipedia)

The intrinsic curvature is null because the helicoid is a ruled surface, even if the induced metric is not flat.

The extrinsic curvature is a symmetric tensor, thus,

$$
\begin{aligned}
\forall (\mathbf{u},\mathbf{v}) \in \mathcal{T}(\Sigma) \qquad \mathbf{K}(\mathbf{u},\mathbf{v}) &= -\mathbf{u}\cdot\nabla_{\mathbf{v}}\mathbf{n} \\
&= -u^\alpha v^\beta \left[\nabla_\beta (h\partial_\alpha t)\right] \\
&= -\left[\underbrace{u^\alpha v^\beta (\partial_\beta h)(\partial_\alpha t)}_{=0} + h u^\alpha v^\beta \left(\partial_\beta(\partial_\alpha t) - \Gamma^\mu_{\beta\alpha}\partial_\mu t\right)\right] \\
&= -u^\alpha v^\beta \left[(\partial_\alpha h)(\partial_\beta t) + h\left(\partial_\alpha(\partial_\beta t) - \Gamma^\mu_{\alpha\beta}\partial_\mu t\right)\right] \\
&= -u^\alpha v^\beta \left[(\partial_\alpha h)(\partial_\beta t) + h\nabla_\alpha(\partial_\beta t)\right] = -u^\alpha v^\beta \left[\nabla_\alpha\left(h\partial_\beta t\right)\right] \\
&= \mathbf{K}(\mathbf{v},\mathbf{u}).
\end{aligned}
$$

■

In the above demonstration from line 3 to 4, we used the Schwarz property and the symmetry of the Christoffel symbols associated to ∇ and also the fact that $(\mathbf{u},\mathbf{v}) \in \mathcal{T}(\Sigma) \subset (\mathbb{R}\mathbf{n})^\perp$.

To relate the four dimensional covariant derivative ∇ to the the spatial covariant derivative D, the first step is to link the covariant derivative of the orthogonal $\nabla\mathbf{n}$ with the second fundamental

form $\mathbf{K}$.

$$\begin{aligned}\forall(\mathbf{u},\mathbf{v})\in\mathscr{T}(\mathscr{M}) \qquad \mathbf{K}(\mathbf{u},\mathbf{v}) &= -[\mathbf{u}+(\mathbf{u}\cdot\mathbf{n})\mathbf{n}]\cdot[\nabla_{\mathbf{v}}\mathbf{n}+(\mathbf{v}\cdot\mathbf{n})\nabla_{\mathbf{n}}\mathbf{n}] \\ &= -\mathbf{u}\cdot\nabla_{\mathbf{v}}\mathbf{n}-(\mathbf{n}\cdot\mathbf{v})(\nabla_{\mathbf{n}}\mathbf{n}\cdot\mathbf{u})-(\mathbf{n}\cdot\mathbf{u})\underbrace{(\mathbf{n}\cdot\nabla_{\mathbf{v}}\mathbf{n})}_{0}-(\mathbf{n}\cdot\mathbf{u})(\mathbf{n}\cdot\mathbf{v})\underbrace{\mathbf{n}\cdot\nabla_{\mathbf{n}}\mathbf{n}}_{0},\end{aligned}$$

which leads to

$$\boxed{\nabla_\beta n_\alpha = -\mathrm{K}_{\alpha\beta}-a_\alpha n_\beta}, \tag{2.10}$$

where $\mathbf{a}=\nabla_{\mathbf{n}}\mathbf{n}$. We show later that $\mathbf{a}$ represents the acceleration of a specific observer.

2.2.3 Link between connections

Let us show that D, the Levi-Civita connection associated to the metric $\boldsymbol{\gamma}$, is the spatial part of the usual four dimensional Levi-Civita connection ∇, for any tensor of $\mathscr{T}(\Sigma)$,

$$\boxed{\mathbf{DT}\hat{=}\mathbf{p}^\star\nabla\mathbf{T}}. \tag{2.11}$$

For any vector $(\mathbf{u},\mathbf{v})\in\mathscr{T}(\Sigma)$, this definition gives,

$$\begin{aligned}(\mathbf{D_u v})^\alpha &= p^\sigma_\mu p^\nu_\sigma p^\alpha_\lambda u^\mu\nabla_\nu v^\lambda \\ &= p^\nu_\mu u^\mu p^\alpha_\lambda\nabla_\nu v^\lambda \\ &= u^\nu p^\alpha_\lambda\nabla_\nu v^\lambda \\ &= (\nabla_{\mathbf{u}}\mathbf{v})^\alpha + u^\nu n_\lambda\nabla_\nu v^\lambda n^\alpha \\ &= (\nabla_{\mathbf{u}}\mathbf{v})^\alpha - (\mathbf{v}\cdot\nabla_{\mathbf{u}}\mathbf{n})n^\alpha.\end{aligned}$$

Since $(\mathbf{u},\mathbf{v})\in\mathscr{T}(\Sigma)$, we can rewrite this equation as,

$$\boxed{\mathbf{D_u v}=\nabla_{\mathbf{u}}\mathbf{v}+\mathbf{K}(\mathbf{u},\mathbf{v})\mathbf{n}}. \tag{2.12}$$

Let us show that this definition (eq.2.11) is satisfactory. There is a unique Levi-Civita connection on a Riemann manifold. Then to proove that D is the Levi-Civita connexion on Σ we only need to show that this expression (eq.2.11) satisfies the property of a torsion-free connection. Using (eq.2.7) $\forall(\mathbf{u},\mathbf{v},\mathbf{w})\in\mathscr{T}(\Sigma)$ and $\forall f\in\mathscr{C}^\infty$, the following results are obtained,

- Belonging
  Using (eq.2.7) $\mathbf{DT}=\mathbf{p}^\star\nabla\mathbf{T}\in\mathscr{T}(\Sigma)$
- Linearity
  $\mathbf{D}_{f\mathbf{u}+\mathbf{w}}\mathbf{v}=\mathbf{p}^\star\left[\nabla_{f\mathbf{u}+\mathbf{w}}\mathbf{v}\right]=\mathbf{p}^\star\left[f\nabla_{\mathbf{u}}\mathbf{v}+\nabla_{\mathbf{w}}\mathbf{v}\right]=f\mathbf{p}^\star\left[\nabla_{\mathbf{u}}\mathbf{v}\right]+\mathbf{p}^\star\left[\nabla_{\mathbf{w}}\mathbf{v}\right]=f\mathbf{D_u v}+\mathbf{D_w v}$
- Leibniz' rule
  $\mathbf{D_u}\left(f\mathbf{v}\right)=\mathbf{p}^\star\left[\nabla_{\mathbf{u}}\left(f\mathbf{v}\right)\right]=\mathbf{p}^\star\left[(\nabla_{\mathbf{u}}f)\mathbf{v}+f\nabla_{\mathbf{u}}\mathbf{v}\right]=\mathbf{p}^\star\left[(\nabla_{\mathbf{u}}f)\mathbf{v}\right]+\mathbf{p}^\star\left[f\nabla_{\mathbf{u}}\mathbf{v}\right]=(\mathbf{D_u}f)\mathbf{v}+f\mathbf{D_u v}$
- Differential of a scalar
  $\mathbf{D_u}f=\mathbf{p}^\star\left[\nabla_{\mathbf{u}}f\right]=p^\alpha_\mu p^\lambda_\alpha u^\mu\nabla_\lambda f=p^\lambda_\mu u^\mu\partial_\lambda f=u^\lambda\partial_\lambda f=df(\mathbf{u}$
- Existence of symmetric Christoffel symbols
  Using (eq.2.12), we get, $\mathrm{D}_\alpha v^\beta=\partial_\alpha v^\beta+(I^\beta_{\alpha\lambda}+\mathrm{K}_{\alpha\lambda}n^\beta)v^\lambda$. Note that $\left\{{\beta\atop\alpha\gamma}\right\}=I^\beta_{\alpha\gamma}+\mathrm{K}_{\alpha\gamma}n^\beta$ are the Christoffel symbols associated to D. Since $\mathbf{K}$ is symetric, $\left\{{\beta\atop\alpha\gamma}\right\}$ are symmetric too.
- Covariant derivative of associated metric
  Using (eq.2.3) $\mathbf{D}\boldsymbol{\gamma}=\mathbf{p}^\star\left[\nabla(\mathbf{g}+\mathbf{n}\otimes\mathbf{n})\right]=\mathbf{p}^\star\left[\nabla\mathbf{n}\otimes\mathbf{n}+\mathbf{n}\otimes\nabla\mathbf{n}\right]=\left[\nabla\mathbf{n}\otimes\mathbf{p}(\mathbf{n})+\mathbf{p}(\mathbf{n})\otimes\nabla\mathbf{n}\right]=0$

■

So, $\mathbf{D}$ is the **only torsion-free connection** associated with the induced metric $\boldsymbol{\gamma}$.

2.3 Foliation of spacetime

Now we build a foliation of the spacetime. The foliation is composed of a family of spatial hypersurfaces $(\Sigma_t)_{t\in\mathbb{R}}$, which covers our spacetime $\mathscr{M}$. In the previous section, we discussed about the geometry of a hypersurface imbedded in our spacetime $(\mathscr{M},\mathbf{g})$. All the results and decompositions can only be done for points, which belong to this hypersurface Σ. Thus with the foliation, because the family of hypersurfaces covers our spacetime, we shall extend the results of the last section to all points of our spacetime. This construction implies the existence of an observer occupying the entire spacetime because of the spatiality of the foliation. Indeed the universe lines of these observers are the lines moving orthogonally to the foliation. Thus our observers are defined by the choice of spacetime foliation.

By foliation or slicing, we mean the existence of a scalar smooth function $\hat{t}:\mathscr{M}\to\mathbb{R}$, which generates a family of hypersurfaces $\Sigma_t=\{\mathrm{M}\in\mathscr{M}\mid\hat{t}(\mathrm{M})=t\}$ covering our spacetime, such that we have $\mathscr{M}=\bigcup_{t\in\mathbb{R}}\Sigma_t$. These hypersurfaces need to verify $\Sigma_t\cap\Sigma_{t'}=\varnothing$ for $t\neq t'$.

2.3.1 Lapse function

As before, we can define the normal vector $\mathbf{n}$, except that now this vector can be defined in the whole spacetime. It is a unit vector, directed towards the future. This vector field gives the four velocity of a specific observer that we call **Fiducial observer** (Fiducials Observers (FIDO)). This observer is also called Zero Angular Momentum Observer (ZAMO), in the case of stationary and axisymmetric spacetime. The function h, which appears in Eq. 2.1, is now defined on the whole spacetime and called the **lapse function**. Indeed, if we define the **normal evolution vector** $\mathbf{m}=h\mathbf{n}$, we can easily show that,

$$\nabla t\cdot\mathbf{m}=-\mathbf{n}^2=1\qquad\Rightarrow\qquad\nabla_{\mathbf{m}}ct=1\qquad\Rightarrow\qquad\boxed{c\delta t=\nabla_{c\delta t\mathbf{m}}ct}\,, \tag{2.13}$$

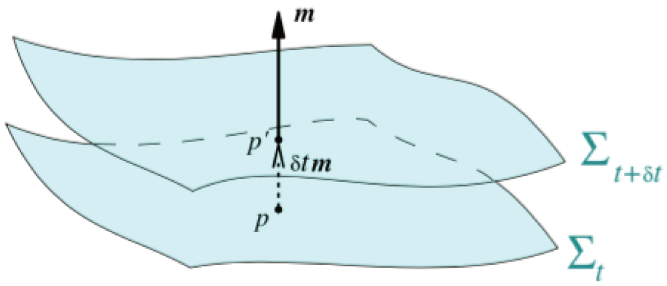

Figure 2.4 – The normal elementary evolution displacement. (Credits : Gourgoulhon [2007])

This is easily interpreted. If you make an elementary displacement $c\delta t\mathbf{m}$ in spacetime $\mathscr{M}$ the scalar function t varies of an infinitely small quantity δt. Thus, we easily build $\Sigma_{t+\delta t}$ from an elementary displacement $c\delta t\mathbf{m}$ of each point of Σ_t.

The proper time $\delta\tau$ spent by the FIDO for the same displacement is the magnitude of this displacement divided by the speed of light.

$$\boxed{\delta\tau_{\mathrm{FIDO}}=h\delta t}\,, \tag{2.14}$$

which justifies the name given to the function h, because it links the evolution of "time coordinate" to the proper time of the FIDO observer.

2.3.2 Shift vector

Let us choose a system of coordinates of $\mathscr{M}$ such that the scalar function t plays the role of time coordinate. We note the coordinates $(x^0, x^1, x^2, x^2) = (ct, x^1, x^2, x^2)$. This kind of coordinate system is known to be adapted to the foliation. As a coordinate system, we have the usual relation $\boldsymbol{\partial}_\alpha \cdot \nabla x^\beta = \delta^\alpha_\beta$, which allows us to find the component along $\mathbf{n}$ of 3+1 decomposition of $\boldsymbol{\partial}_0$,

$$\boxed{\frac{1}{c}\boldsymbol{\partial}_t = h\mathbf{n} + \boldsymbol{\beta}}. \tag{2.15}$$

We note the spatial part of this decomposition $\boldsymbol{\beta}$ the **shift vector**. Indeed, for an elementary displacement $c\delta t\mathbf{m}$, we get,

$$x^i(\mathrm{P} + c\delta t\mathbf{m}) = x^i(\mathrm{P} + \delta t\boldsymbol{\partial}_t - \boldsymbol{\beta}c\delta t) = x^i(\mathrm{P} + \delta t\boldsymbol{\partial}_t) - \beta^i c\delta t = x^i(\mathrm{P}) - \beta^i c\delta t, \tag{2.16}$$

The definition of the natural basis is, $\boldsymbol{\partial}_\alpha = \boldsymbol{\partial}_\alpha \mathrm{M}|_{x^{\mu\neq\alpha}=\mathrm{cst}}$ for $\mu \neq \alpha$. It implies that $x^i(\mathrm{P} + \delta t\boldsymbol{\partial}_t) = x^i(\mathrm{P})$. Thus the coordinate of the FIDO shift of a quantity is $-\beta^i c\delta t$ during the universal time delay δt. This justifies the denomination **shift vector** for $\boldsymbol{\beta}$.

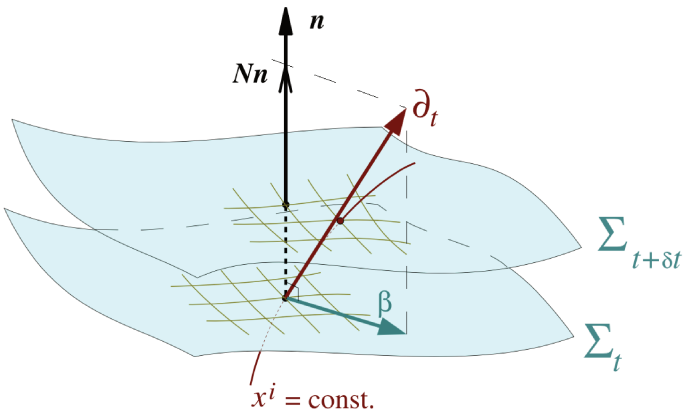

Figure 2.5 – The shift of coordinates between two sheets of space. (Credits : Gourgoulhon [2007])

Let us calculate the covariant derivative of $\mathbf{m}$. We obtain,

$$\nabla\mathbf{m} = -h\mathbf{K} - \mathbf{D}h \otimes \mathbf{n} + \mathbf{n} \otimes \mathbf{D}h - \nabla_{\mathbf{n}} h\mathbf{n} \otimes \mathbf{n}, \tag{2.17}$$

2.3.3 3+1 decomposition of the metric

By definition the metric element is $g_{\alpha\beta} = \boldsymbol{\partial}_\alpha \cdot \boldsymbol{\partial}_\beta$. Using Eq. (2.15) we can calculate the metric and the inverse function of the metric as a function a of the lapse function h, shift vector $\boldsymbol{\beta}$ and inverse function of the spatial metric $\boldsymbol{\gamma}^{-1}$,

$$\mathbf{g} = \begin{bmatrix} -c^2h^2 + \boldsymbol{\beta}^2 & \boldsymbol{\beta} \\ \boldsymbol{\beta} & \boldsymbol{\gamma} \end{bmatrix} \qquad \mathbf{g}^{-1} = \frac{1}{c^2h^2}\begin{bmatrix} -1 & \boldsymbol{\beta} \\ \boldsymbol{\beta} & c^2h^2\boldsymbol{\gamma}^{-1} - \boldsymbol{\beta} \otimes \boldsymbol{\beta} \end{bmatrix} \tag{2.18}$$

Note that the nature of the vector field $\boldsymbol{\partial}_t$ depends of the respective size of h^2 and $\boldsymbol{\beta}^2$,

- If $\boldsymbol{\beta}^2 \leq h^2$ then $\boldsymbol{\partial}_t$ is time-like
- If $\boldsymbol{\beta}^2 = h^2$ then $\boldsymbol{\partial}_t$ is null
- If $\boldsymbol{\beta}^2 \geq h^2$ then $\boldsymbol{\partial}_t$ is spatial

In this last case, we have a super-luminal shift. For example, this situation can appear in the environment of the ergosphere of a rotating black hole (ergo-region), described by the Kerr metric. A rapid calculation of the determinant of metric gives,

$$-\det\mathbf{g} = h^2 \det\boldsymbol{\gamma} \tag{2.19}$$

Calculating the spatial metric determinant is useful to derive the integrals on this space-like hypersurface. This decomposition leads to another expression of the line element, using adapted coordinates,

$$ds^2 = -h^2c^2dt^2 + \gamma_{ij}\left(dx^i + \beta^i c dt\right)\left(dx^j + \beta^j c dt\right) \tag{2.20}$$

2.3.4 Acceleration of FIDO

The acceleration of the FIDO is,

$$\mathbf{a} = \nabla_{\mathbf{n}}\mathbf{n}, \tag{2.21}$$

which justifies the notation choosen earlier. After some algebra, we get,

$$\begin{aligned} a_\alpha &= n^\mu \nabla_\mu n_\alpha \\ &= -n^\mu \nabla_\mu (h\partial t) \\ &= -n^\mu \nabla_\mu h \nabla_\alpha t - h n^\mu \nabla_\mu \partial_\alpha t \\ &= n^\mu \nabla_\mu \ln h n_\alpha + h n^\mu \nabla_\alpha \frac{n_\mu}{h} \\ &= n_\alpha n^\mu \nabla_\mu \ln h + \nabla_\alpha \ln h \\ &= p^\mu_\alpha \nabla_\mu \ln h, \end{aligned}$$

where we used the Schwarz' property and $\mathbf{n}^2 = -1$. So we finally get,

$$\boxed{\mathbf{a} = \mathbf{D}\ln h} \tag{2.22}$$

This acceleration corresponds to the force acting on the FIDO to stay on its universe line. An interesting result, using the expression of the acceleration of the FIDO, is the link between the spacetime and the spatial divergence for a spatial vector. For $\mathbf{v} \in \mathscr{T}(\Sigma)$, using the definition Eq.(2.11) and the Eq.(2.22), few lines of calculation lead to the useful result,

$$\boxed{\nabla \cdot \mathbf{v} = \frac{\mathbf{D}\cdot(h\mathbf{v})}{h}} \tag{2.23}$$

This result is also related to Eq.(2.19), because of the divergence expression on a manifold, Eq. (A.4). From the divergence of $\mathbf{n}$, using the decomposition, Eq.(2.15) and Eq.(2.23) for the shift $\boldsymbol{\beta}$, and Eq.(A.4) for ∂_t, we get a link between the trace of the extrinsic curvature, the divergence of the shift vector and the volum element of space,

$$\mathbf{D}\cdot\boldsymbol{\beta} - h\mathrm{K} = \frac{1}{c}\frac{\partial \ln\gamma}{\partial t} \tag{2.24}$$

2.4 A foliation of Kerr spacetime

In the case spacetime contains a rotating black hole and different kinds of stress-energy tensor, the spacetime geometry is close to the Kerr spacetime. The case, which we are interested in, is the case where we have a set of particles embedded into an electro-magnetic field in the close environment of a rotating black hole. The order of perturbation h_{SG} to the Kerr metric $\mathbf{g} = \mathbf{g}_{\mathrm{K}} + \mathbf{h}_{\mathrm{SG}}$ coming from the self-gravitation of the particles and the electromagnetic field has to be proportional to the compactness of the physical system,

$$h_{\mathrm{SG}} \approx \frac{8\pi\mathscr{G}}{c^4}\left(\frac{\mathrm{E}}{\mathrm{L}}\right), \tag{2.25}$$

where E is approximately the energy and L the typical size of mass and electromagnetic field distribution. If $h_{\mathrm{SG}} \ll \| g_{\mathrm{K}} - g_{\mathrm{Minsk}} \|$, where g_{Minsk} is the Minkowski metric, we can neglect the self-gravitation of the second component, which is valid when compactness of the magnetized flow $\Xi_{\mathrm{MHD}} \sim \frac{8\pi\mathscr{G}}{c^4}\left(\frac{\mathrm{E}}{\mathrm{L}}\right)_{\mathrm{MHD}} \ll 1$ (the compactness of Kerr Hole is between 0.5 and 1 by definition). Thus we can study the evolution of the particles and of the electro-magnetic field fixing the geometry to the Kerr metric and neglecting the self-gravitation of these fields. This is the assumption made in the following chapters. So it is useful to calculate the different quantities associated to the foliation of the Kerr geometry.

2.4.1 Kerr metric

A Kerr manifold is a spacetime manifold describing an isolated rotating black hole. This geometry is axi-symmetric and stationary. There is two Killing vectors fields, one $\boldsymbol{\eta}$ for the stationarity and another one $\boldsymbol{\xi}$ for axi-symmetry. The metric can be expressed in the Boyer-Lindquist coordinates (t, r, θ, ϕ),

$$ds^2 = -\left(1 - \frac{r_s r}{\rho^2}\right)c^2 dt^2 - \frac{r_s^2 r c a}{\rho^2}\sin^2\theta dt d\phi + \frac{\rho^2}{\Delta}dr^2 + \rho^2 d\theta^2 + \frac{\Sigma^2}{\rho^2}\sin^2\theta d\phi^2, \tag{2.26}$$

with,

$$\Delta = r^2 + \frac{r_s^2 a^2}{4} - r_s r, \tag{2.27}$$

$$\rho^2 = r^2 + \frac{r_s^2 a^2}{4}\cos^2\theta, \tag{2.28}$$

$$\Sigma^2 = \left(r^2 + \frac{r_s^2 a^2}{4}\right)^2 - \frac{r_s^2 a^2}{4}\Delta\sin^2\theta. \tag{2.29}$$

We note the rotation parameter $a = \dfrac{\mathscr{J} c}{\mathscr{G}\mathrm{M}_{\mathscr{H}}^2} \in [-1;1]$ and $r_s = \dfrac{2\mathscr{G}\mathrm{M}_{\mathscr{H}}}{c^2}$ the Schwarzschild radius. In these coordinates, we get $\boldsymbol{\eta} = \partial_t$ and $\boldsymbol{\xi} = \partial_\phi$. It implies that all geometrical quantities are independent of t and ϕ.

We note $\mathscr{J}$ the angular momentum of the massive central object and $\mathrm{M}_{\mathscr{H}}$ its mass.

This spacetime contains four notable sub manifolds. The first one is the **hole singularity**, which corresponds to $\rho = 0$ ($r = 0$ and $\theta = \pi/2$). It is the unique real singularity of the Kerr geometry. A geometrical analysis shows that this submanifold is a ring of radius $\frac{r_s a}{2}$ included in the equatorial plane.

The next two submanifolds are three dimensional imbedded manifolds, the **outer event horizon** and the **inner event horizon** defined by the equation $\Delta = 0$. It leads to the two solutions $\mathscr{H}_- = \left\{\mathrm{M} \in \mathscr{M} \mid r(\mathrm{M}) = r_- = \frac{r_s}{2}\left(1 - \sqrt{1-a^2}\right)\right\}$ and $\mathscr{H}_+ = \left\{\mathrm{M} \in \mathscr{M} \mid r(\mathrm{M}) = r_+ = \frac{r_s}{2}\left(1 + \sqrt{1-a^2}\right)\right\}$. These two hypersurfaces are null. Contrary to intuition, another geometrical analysis shows that for $t = \mathrm{cst}$, these surfaces are not spheres. They are some kind of ellipsoids flattened at the poles. This comes from the fact that the Boyer-Lindquist radius coordinate does not coincide with the spherical radius. We can show that surfaces can only be crossed in one direction. In our study, only the outer event horizon appears because we will be interested in the field outside of the outer event horizon . We call it the **event horizon** $\mathscr{H}_{\mathrm{K}}$ for the sake of simplicity.

The last part is also a three dimensional imbedded manifold defined by $\mathscr{E}_{\mathrm{K}} = \left\{\mathrm{M} \in \mathscr{M} \mid \mathbf{g}(\boldsymbol{\eta}, \boldsymbol{\eta}) = 0 \right.$ $\left. \Rightarrow r(\mathrm{M}) = \frac{r_s}{2}\left(1 + \sqrt{1 - a^2\cos^2\theta}\right)\right\}$ called the **ergosphere**. The region between the event horizon and the ergosphere is called the **ergoregion**. In this region, the Killing time vector $\boldsymbol{\eta}$ is a space-like or a null vector. It implies some interesting properties about the energy circulation, see Sec. (4.3.3).

We will be only interested in the fields which fill spacetime outside of the external horizon. Using Boyer-Lindquist coordinates to solve equations which makes the crossing the horizon difficult.

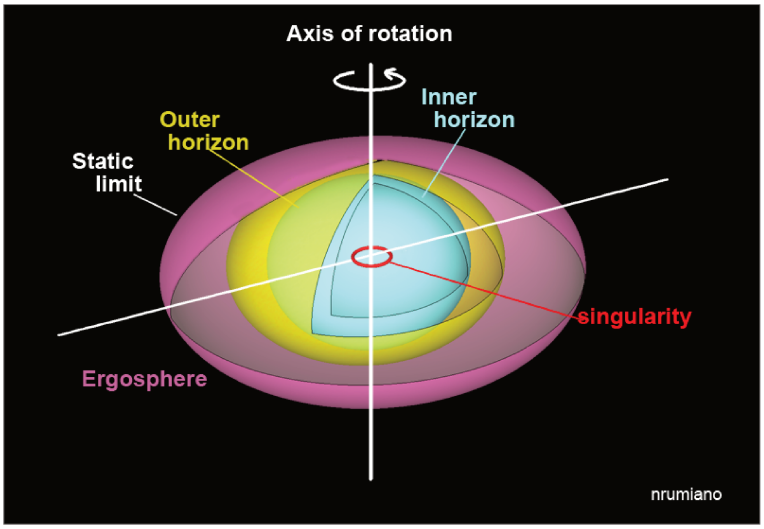

Figure 2.6 – Different Kerr remarkable geometrical structure (Credits : Wikipedia)

2.4.2 Choice of foliation system

We choose the time Boyer-Lindquist coordinate t to construct the foliation of our Kerr spacetime. It gives, using Eq. (2.20), a new expression for the Kerr metric,

$$ds^2 = -h^2c^2dt^2 + h_r^2dr^2 + h_\theta^2d\theta^2 + h_\phi^2\left(d\phi + \beta^\phi c dt\right)^2, \tag{2.30}$$

where,

$$h_r = \frac{\rho}{\sqrt{\Delta}}, \qquad h_\theta = \rho, \qquad h_\phi = \varpi = \frac{\Sigma}{\rho}\sin\theta. \tag{2.31}$$

ϖ can be interpreted as the cylindrical radius. For the lapse function,

$$h = \sqrt{1 - \frac{r_s r}{\rho^2} + \beta^\phi\beta_\phi} = \frac{\rho}{\Sigma}\sqrt{\Delta}. \tag{2.32}$$

and the shift vector,

$$\boldsymbol{\beta} = \beta^\phi\boldsymbol{\partial}_\phi, \qquad \beta^\phi = -\frac{\omega}{c}, \qquad \beta_\phi = -\frac{\omega}{c}\varpi^2, \quad . \tag{2.33}$$

We note ω the shift pulsation,

$$\omega = \frac{car_s r}{\Sigma^2}. \tag{2.34}$$

This foliation has the advantage of being immediately accessible even if, unfortunately, the space hypersurface $\Sigma_t = \Sigma$ contains a coordinate-singularity on the horizon. The spatial hypersurfaces do not evolve and are axi-symmetric. We also introduce the spatial orthonormal base $\boldsymbol{\epsilon}_{i=1,2,3}$, which is decomposed in the natural base $\mathbf{e}_{i=1,2,3}$ associated to the adapted Boyer-Lindquist coordinates $\forall i = 1,2,3 \quad \mathbf{e}_i = h_i\boldsymbol{\epsilon}_i$. We note $\mathrm{V}^{\hat{i}} = \mathrm{V}_{\hat{i}}$ the component in the orthonormal base, such we have $\mathbf{V} = \mathrm{V}^{\hat{i}}\boldsymbol{\epsilon}_i$. We summary here the relations of the transformation between the orthonormal and the natural basis,

$$\begin{aligned} \mathbf{e}_i &= h_i\boldsymbol{\epsilon}_i \\ \mathrm{V}_i &= h_i^2\mathrm{V}^i = h_i\mathrm{V}^{\hat{i}} \end{aligned} \tag{2.35}$$

The four speed of the ZAMO observer is decomposed along the two killing vectors,

$$h\mathbf{n} = \boldsymbol{\eta} + \frac{\omega}{c}\boldsymbol{\xi} \tag{2.36}$$

2.4.3 Expression of the extrinsic curvature

We calculate the trace of the extrinsic curvature, using stationarity, axi-symmetry and Eq.(2.15),

$$\mathrm{K} = -\nabla_\mu n^\mu = -\frac{1}{\sqrt{g}}\partial_\mu(\sqrt{g}n^\mu) = -\frac{1}{\sqrt{g}}\left(\partial_t(\sqrt{g}\frac{1}{h}) - \partial_\phi(\sqrt{g}\frac{\beta^\phi}{h})\right) = 0. \tag{2.37}$$

It is a bit more complex to calculate the extrinsic curvature. Using the expression of the inverse metric function Eq.(2.18), we get,

$$\begin{aligned}
\mathrm{K}_{ij} &= -\nabla_j n_i - n_j\partial_i \ln h \\
&= \partial_j(h\delta^0_i) + \Gamma^\alpha_{ij} n_\alpha + \delta^0_j\partial_i h \\
&= -h\Gamma^0_{ij} \\
&= -\frac{h}{2}g^{0\alpha}\left(\partial_i g_{j\alpha} + \partial_j g_{i\alpha} - \partial_\alpha g_{ij}\right) \\
&= -\frac{h}{2}g^{0\alpha}\left(\partial_i g_{j\alpha} + \partial_j g_{i\alpha}\right) \\
&= \frac{1}{2h}\left[\left(\partial_i g_{j0} + \partial_j g_{i0}\right) - \beta^\phi\left(\partial_i g_{j\phi} + \partial_j g_{i\phi}\right)\right].
\end{aligned}$$

So if i and j are different from ϕ we have $\mathrm{K}_{ij} = 0$.
Using the symmetry of $\mathbf{K}$, we have only to calculate $\mathrm{K}_{\phi j}$,

$$\begin{aligned}
\mathrm{K}_{\phi j} &= \frac{1}{2h}\left[\partial_j g_{\phi 0} - \beta^\phi\partial_j g_{\phi\phi}\right] \\
&= \frac{1}{2h}\left[\partial_j\beta_\phi - \beta^\phi\partial_\phi h^2_\phi\right] \\
&= -\frac{\omega^2}{2hc}\partial_j\omega \\
&= -\frac{1}{2hc}\left(\boldsymbol{\xi}\cdot\boldsymbol{\xi}\right)\left(\nabla\omega\cdot\mathbf{e}_j\right)
\end{aligned}$$

Then, using the fact that $\mathbf{D}\omega = \nabla\omega$ we can write,

$$\mathbf{K} = -\frac{1}{2hc}\left[\mathbf{D}\omega\otimes\boldsymbol{\xi} + \boldsymbol{\xi}\otimes\mathbf{D}\omega\right] \tag{2.38}$$

2.4.4 Spatial operators in Boyer-Lindquist coordinates

Many calculations of non-relativistic field theories, such as fluid mechanics or electromagnetism, are based on the use of spatial operators. This use comes from the fact that these operators have useful properties for the derivation of the equations. The definition of these operators can be extended here on the "spatial" manifold Σ of the Kerr spacetime. We give the expression of these operators under the assumption of axisymmetry of the field on which they act.

Expression of Spatial operators in Boyer-Lindquist coordinates

First of all, we express these operators using the Boyer Lindquist-coordinates. The gradient vector $\mathbf{D}$ in the ZAMO orthogonal base ($\boldsymbol{\epsilon}_i = \frac{1}{h_i}\mathbf{e}_i$) is,

$$\mathbf{D} = \sum_{i=1}^{3}\frac{\vec{\epsilon_i}}{h_i}\partial_i \tag{2.39}$$

The divergence of a vector $\mathbf{V} = \mathrm{V}^{\hat{i}}\boldsymbol{\epsilon}_i$ is,

$$\mathbf{D}\cdot\mathbf{V} = \frac{1}{h_r h_\theta\varpi}\left[\partial_r(h_\theta\varpi\mathrm{V}^{\hat{r}}) + \partial_\theta(h_r\varpi\mathrm{V}^{\hat{\theta}})\right] \tag{2.40}$$

For the scalar Laplace operator, we get,

$$\begin{aligned} \mathrm{D}^2\mathrm{A} &= \mathbf{D}\cdot\mathbf{D}\mathrm{A} \\ &= \frac{1}{h_r h_\theta \varpi}\left[\partial_r\left(\frac{h_\theta \varpi}{h_r}\partial_r \mathrm{A}\right)+\partial_\theta\left(\frac{h_r \varpi}{h_\theta}\partial_\theta \mathrm{A}\right)\right] \end{aligned}$$

The curl operator (eq.B.28) on a vector $\mathbf{V}$ is given as,

$$\mathbf{D}\times\mathbf{V} = \begin{bmatrix} \frac{1}{h_\theta \varpi}\partial_\theta(\varpi \mathrm{V}^{\hat{\phi}}) \\ -\frac{1}{h_r \varpi}\partial_r(\varpi \mathrm{V}^{\hat{\phi}}) \\ \frac{1}{h_r h_\theta}\left(\partial_r(h_\theta \mathrm{V}^{\hat{\theta}})-\partial_\theta(h_r \mathrm{V}^{\hat{r}})\right) \end{bmatrix} \tag{2.41}$$

To obtain the advection term we use (eq.B.2), and after some calculations, we get for the poloidal components of the advection term,

$$[(\mathbf{V}\cdot\mathbf{D})\mathbf{V}]_{\mathrm{p}} = \begin{bmatrix} \frac{\mathrm{V}^{\hat{r}}}{h_r}\partial_r \mathrm{V}^{\hat{r}} + \frac{\mathrm{V}^{\hat{\theta}}}{h_\theta}\partial_\theta \mathrm{V}^{\hat{r}} + \frac{\mathrm{V}^{\hat{r}}\mathrm{V}^{\hat{\theta}}}{h_\theta}\partial_\theta \ln(h_r) - \frac{(\mathrm{V}^{\hat{\theta}})^2}{h_r}\partial_r \ln(h_\theta) - \frac{(\mathrm{V}^{\hat{\phi}})^2}{h_r}\partial_r \ln(h_\phi) \\ \frac{\mathrm{V}^{\hat{r}}}{h_r}\partial_r \mathrm{V}^{\hat{\theta}} + \frac{\mathrm{V}^{\hat{\theta}}}{h_\theta}\partial_\theta \mathrm{V}^{\hat{\theta}} + \frac{\mathrm{V}^{\hat{r}}\mathrm{V}^{\hat{\theta}}}{h_r}\partial_r \ln(h_\theta) - \frac{(\mathrm{V}^{\hat{r}})^2}{h_\theta}\partial_\theta \ln(h_r) - \frac{(\mathrm{V}^{\hat{\phi}})^2}{h_\theta}\partial_\theta \ln(h_\phi) \end{bmatrix} \tag{2.42}$$

It can be useful to get the non-symmetric advection term,

$$[(\mathbf{B}\cdot\mathbf{D})\mathbf{C}] = \begin{bmatrix} \frac{\mathrm{B}^{\hat{r}}}{h_r}\partial_r \mathrm{C}^{\hat{r}} + \frac{\mathrm{B}^{\hat{\theta}}}{h_\theta}\partial_\theta \mathrm{C}^{\hat{r}} + \frac{\mathrm{B}^{\hat{r}}\mathrm{C}^{\hat{\theta}}}{h_\theta}\partial_\theta \ln(h_r) - \frac{\mathrm{B}^{\hat{\theta}}\mathrm{C}^{\hat{\theta}}}{h_r}\partial_r \ln(h_\theta) - \frac{\mathrm{B}^{\hat{\phi}}\mathrm{C}^{\hat{\phi}}}{h_r}\partial_r \ln(h_\phi) \\ \frac{\mathrm{B}^{\hat{r}}}{h_r}\partial_r \mathrm{C}^{\hat{\theta}} + \frac{\mathrm{B}^{\hat{\theta}}}{h_\theta}\partial_\theta \mathrm{C}^{\hat{\theta}} + \frac{\mathrm{C}^{\hat{r}}\mathrm{B}^{\hat{\theta}}}{h_r}\partial_r \ln(h_\theta) - \frac{\mathrm{B}^{\hat{r}}\mathrm{C}^{\hat{r}}}{h_\theta}\partial_\theta \ln(h_r) - \frac{\mathrm{B}^{\hat{\phi}}\mathrm{C}^{\hat{\phi}}}{h_\theta}\partial_\theta \ln(h_\phi) \\ \frac{\mathrm{B}^{\hat{r}}}{h_r}\partial_r \mathrm{C}^{\hat{\phi}} + \frac{\mathrm{B}^{\hat{\theta}}}{h_\theta}\partial_\theta \mathrm{C}^{\hat{\phi}} + \frac{\mathrm{C}^{\hat{r}}\mathrm{B}^{\hat{\phi}}}{h_r}\partial_r \ln(h_\phi) + \frac{\mathrm{C}^{\hat{\theta}}\mathrm{B}^{\hat{\phi}}}{h_\theta}\partial_r \ln(h_\phi) \end{bmatrix} \tag{2.43}$$

Cylindrical Coordinates

To plot a scalar or a vector field, it is useful to introduce cylindrical coordinates. The first intuitive proposition for the cylindrical radius is to choose $\varpi(r,\theta)$, because $2\pi\varpi$ represents the length of the circle defined in Σ, with r and θ constant. Nevertheless, this definition is not satisfactory for different reasons. First, the function $\varpi^2(r,\theta)$ is a rational function of radius and latitude, and if we choose $z = r\cos\theta$ for the vertical coordinate, the inversion of the system of equations to obtain r and θ as functions of ϖ and z leads to solving a 8th degree polynomial equation. Doing it for each point is numerically possible but increases dramatically the computing time. Further more the proposition $z = r\cos\theta$ is not justified by geometrical arguments.

Then another point of view consists in choosing a line of constant radius $r = \mathrm{Cst}$ in the poloidal plane. The line element of this line is,

$$\mathrm{d}l^2 = \left(r^2 + \frac{r_s^2 a^2}{4}\right)\mathrm{d}\theta^2 \tag{2.44}$$

This line element $\mathrm{d}l^2$ corresponds to the line element of an ellipse. Its semi-minor axis is aligned with the symmetry axis and its value is r. The semi-major axis, $\sqrt{r^2 + \frac{r_s^2 a^2}{4}}r$, is contained in the equatorial plane. Then we can introduce the usual parametrization of this ellipse,

$$\begin{cases} z_{\mathrm{cyl}} = r\cos\theta \\ r_{\mathrm{cyl}} = \sqrt{r^2 + \frac{r_s^2 a^2}{4}}\sin\theta \end{cases} \iff \begin{cases} r = \sqrt{z_{\mathrm{cyl}}^2 + r_{\mathrm{cyl}}^2 - \frac{a^2 r_s^2}{4}}\sqrt{\frac{1+\sqrt{1+\frac{z_{\mathrm{cyl}}^2 r_s^2}{\left(z_{\mathrm{cyl}}^2 + r_{\mathrm{cyl}}^2 - \frac{a^2 r_s^2}{4}\right)^2}}}{2}} \\ \tan\theta = \frac{1}{\sqrt{1+\frac{r_s^2 a^2}{4r^2(z_{\mathrm{cyl}}, r_{\mathrm{cyl}})}}}\frac{r_{\mathrm{cyl}}}{z_{\mathrm{cyl}}} \end{cases} \tag{2.45}$$

This parameterization is used to define the cylindrical coordinates. They are more practical than the use of ϖ^2. Indeed these are analytically invertible. Nevertheless these coordinates do not correspond to any obvious physical distances contrary to ϖ^2. Note that for small latitudes we have $r_{\mathrm{cyl}} \equiv \varpi$.

2.5 Conclusion

The system of equations (eqs.B.9, B.22, B.24) is derived in details in the Appendix (B.1). It gives the so called chrono-geometric point of view of general relativity. In this point of view, space is a non-euclidian manifold in which the geometry evolves as function of a stress tensor, a momentum density flux and energy density measured by a specific observer called ZAMO.

In this point of view, stress energy tensors play the role of a source term. They are the quantities that govern the evolution of the geometry. Nevertheless this system needs to be coupled to some specific physical constrains, some specific form of the stress energy tensor, to add an equation which governs the evolution of the stress-energy tensor. Indeed, for a set of particles inside an electromagnetic field, we need to add equations which control the evolution of the distributions function of each species and the Maxwell's equations. This point of view is developped in Chapter (3). In the case of a perfect ideal gas in an electro-magnetic field, the evolution of these quantities is given by the continuity equation, the conservation of the stress-energy tensor, the equation of state and Maxwell's equations. This point of view is exposed in Chapter (4).

Thus, putting all these equations together gives a complete description of a self-gravitating stress-energy tensor. This really general case can be useful for describing very compact objects such as a neutron star or a binary compact system. In the following we neglect self-gravitating formulation.

The object of our study, inter-galactic spin jets, can be described via a kinetic plasma of magnetized relativistic electron-positron or hadronic particles or via a magnetized ionized fluid of electron-positron or hadron-electron pairs. In this case, the approach is simplified, because as in Sec.(2.4) we neglect the self-gravitation of the particles and the electromagnetic field which is in the vicinity of the black hole. Thus we choose a Kerr metric for our spacetime. The evolution of the different fields, which compose our system around the blach hole, will be the object of the two next chapters. The tools developed here are useful to write the General Relativistic Magneto-Hydrodynamic (GRMHD) in Kerr metric in a form similar to the classical one. This formulation of GRMHD equations constitutes the base of our model.

2.6 References

Richard Arnowitt, Stanley Deser, and Charles W. Misner. Republication of: The dynamics of general relativity. *General Relativity and Gravitation*, 40(9):1997–2027, Sep 2008. ISSN 1572-9532. doi: 10.1007/s10714-008-0661-1. URL https://doi.org/10.1007/s10714-008-0661-1. 10

Y. Choquet-Bruhat and R. Geroch. Global aspects of the Cauchy problem in general relativity. *Communications in Mathematical Physics*, 14:329–335, December 1969. doi: 10.1007/BF01645389. 10

G. Darmois. Les equations de la gravitation einsteinienne. *Memorial des Sciences Mathématiques 25, Gauthier-Villars, Paris*, 1927. 10

E. Gourgoulhon. 3+1 Formalism and Bases of Numerical Relativity. *ArXiv General Relativity and Quantum Cosmology e-prints*, March 2007. xi, 10, 12, 14, 16, 17

A. Lichnerowicz. Sur certains problemes globaux relatifs au systeme des equations d?Einstein. *Hermann, Paris, Actual. Sci. Ind. 833*, 1939. 10

J.A. Wheeler. *Geometrodynamics and the issue of the final state, in Relativity*. August 1964. 10

Chapter 3

Statistical physics in curved spacetime & Relativistic thermodynamics

Contents

Some material component of the relativistic spine-jet is likely to be composed of electron-positron pairs extracting energy from the black hole. This plasma is produced via a pair creation mechanism from highly energetic photons or neutrinos from the disk. In function of the emission of the accretion disk (neutrinos for Gamma Ray Burst (GRB), photons for Active Galaxy Nuclei (AGN) disk) the source of pair plasma is the annihilation of neutrinos or photons (see. McKinney [2005b], McKinney [2005a]). The effect on pair plasma injection by neutrino annihilation for GRB is studied in various publications (e.g. Birkl et al. [2007], Globus and Levinson [2014], Zalamea and Beloborodov [2011]). The fluid has several components, which can interact with each other. If there is a mechanism of pair creation, then the fluid components do not conserve their particle number. Thus in ideal, axi-symmetric and stationary MHD, the mass flux along the stream line is not conserved. Indeed the line can be mass loaded or unloaded in function of the evolution of the processes of creation/annihilation. Because of this process, the flow on these lines can be in both directions. The plasma is flowing down on a part of the line which is linked to the black hole (inflow). On the other part, the plasma flows away (outflow). If such lines are connected to the horizon of the black hole, then the exchange of energy between the rotational energy of the black hole and the Magneto-Hydrodynamic (MHD) field via Penrose and/or Blandford-Znajek processes can play an important role in powering the outflow. Indeed we show that the MHD flow of energy far away from the event horizon of the black hole is composed to the energy given by the black hole and the energy brought into this flow by the loading of pairs (Sec.4.3.3).

First, we must introduce how the pair creation reacts on the flow. In order to correctly analyze and calculate the particle creation rate, the volume forces, the energy and momentum supplied, resulting from the mechanism of creating pairs , it is necessary to start from relativistic statistical mechanics. Once we get Boltzmann's equation, we derive the magneto-hydrodynamic equations of the plasma of pairs, including the effect of the creation/annihilation mechanism. This theoretical work gives the opportunity to formally introduce the phenomena of thermal agitation and internal energy which appear in the following chapters to be essential for understanding the phenomena.

3.1 From relativistic Boltzmann system of equation to the General Relativistic Magneto-Hydrodynamic (GRMHD) description of plasma

This section is based on Marle [1969a], Marle [1969b], Droz-Vincent [1968] and Hakim [2011] works. They study the specific case of a fluid composed of three species, with a mechanism of pair creation. As in the previous section, we consider a spacetime $(\mathscr{M},\mathbf{g})$, which can be foliated by a set of hypersurfaces $\mathscr{M} = \bigcup_{t\in\mathbb{R}} \Sigma_t$, such as $\mathscr{T}_{\mathrm{P}}(\mathscr{M}) = \mathscr{T}_{\mathrm{P}}(\Sigma) \overset{\perp}{\bigoplus} \mathbb{R}\mathbf{n}$.

3.1.1 Particles content

We consider that this spacetime contains a set of particles of three species. A set of indistinguishable, massive m_+, positively charged $+q$ particles $\{q_{+,i}\}_{i=1\ldots \mathrm{N}_+}$, another set of indistinguishable, massive m_-, negatively charged $-q$ particles $\{q_{-,j}\}_{j=1\ldots \mathrm{N}_-}$, and another set of indistinguishable neutral particles r. A pair of charged particles is produced or annihilated via a mechanism we can

write as follows,

$$2r \rightleftharpoons e_+ + e_- \tag{3.1}$$

Practically, the positive and negative species are electrons and hadrons (hadronic model) or electrons and positrons (leptonic model). Leptonic pairs are produced by highly energetic photons (non massive particles) or neutrinos (massive particles). We also introduced in this spacetime two four-force fields $\boldsymbol{\mathcal{F}}_+$ and $\boldsymbol{\mathcal{F}}_-$ which act on charged particles. We note $\mathbf{p}_{+,i} = m_+ c\mathbf{u}_{+,i}$, $\mathbf{p}_{-,j} = m_- c\mathbf{u}_{-,j}$ and $\mathbf{p}_{r,l}$ the four-momentum of the i-th positively particles, the j-th negatively charged particles and the l-th neutral particles. In all cases, the charged particles are massive such that $\mathbf{p}_{+,i} = m_+ c\mathbf{u}_{+,i}$ and $\mathbf{p}_{-,j} = m_- c\mathbf{u}_{-,j}$ are future oriented time vectors. If the neutral particles are massive (non-massive) then $\mathbf{p}_{r,l}$ is a future oriented time (null vector, respectively). Thus the equations of motion for each particle are,

$$\begin{cases} \nabla_{\mathbf{u}_{+,\mathrm{i}}} \mathbf{p}_{+,\mathrm{i}} = \boldsymbol{\mathcal{F}}_+ \left(x^{\mu}_{+,\mathrm{i}}, \mathbf{p}_{+,\mathrm{i}} \right) \\ \nabla_{\mathbf{u}_{-,\mathrm{j}}} \mathbf{p}_{-,\mathrm{j}} = \boldsymbol{\mathcal{F}}_- \left(x^{\mu}_{-,\mathrm{j}}, \mathbf{p}_{-,\mathrm{j}} \right) \\ \nabla_{\mathbf{p}_{\mathrm{r,l}}} \mathbf{p}_{\mathrm{r,l}} = 0 \end{cases} , \tag{3.2}$$

which are valid $\forall(\mathrm{i},\mathrm{j},\mathrm{l})$. In practice, the force field is the Lorentz force (electric and magnetic forces) due to the presence of an electro-magnetic-field $\boldsymbol{\mathcal{F}}_+ \left(x^{\mu}_{+,i}, \mathbf{u}_{+,i} \right) = \mathbf{F}\left(., q\mathbf{u}_{-,j}\right)$ and $\boldsymbol{\mathcal{F}}_- \left(x^{\mu}_{-,j}, \mathbf{u}_{-,j} \right) = \mathbf{F}\left(., -q\mathbf{u}_{-,j}\right)$. $\mathbf{F}$ is a second order fully anti-symmetric electro-magnetic tensor.

$$\begin{cases} m_+ c \dfrac{du^{\alpha}_{+,\mathrm{i}}}{ds_{+,\mathrm{i}}} = \dfrac{m_+ \gamma_{+,\mathrm{i}}}{h} \dfrac{du^{\alpha}_{+,\mathrm{i}}}{dt} = & -m_+ \Gamma^{\alpha}_{\mu\nu} u^{\mu}_{+,\mathrm{i}} u^{\nu}_{+,\mathrm{i}} + \dfrac{q}{c} \mathrm{F}^{\alpha}_{\mu} u^{\mu}_{+,\mathrm{i}} \\ m_- \dfrac{du^{\alpha}_{-,\mathrm{j}}}{ds_{-,\mathrm{j}}} = \dfrac{m_- \gamma_{-,\mathrm{j}}}{h} \dfrac{du^{\alpha}_{-,\mathrm{j}}}{dt} = & -m_- \Gamma^{\alpha}_{\mu\nu} u^{\mu}_{-,\mathrm{j}} u^{\nu}_{-,\mathrm{j}} - \dfrac{q}{c} \mathrm{F}^{\alpha}_{\mu} u^{\mu}_{-,\mathrm{j}} \\ \dfrac{dk^{\alpha}_{\mathrm{r,l}}}{d\lambda_{\mathrm{r,j}}} = & -\Gamma^{\alpha}_{\mu\nu} k^{\mu}_{-,\mathrm{j}} k^{\nu}_{-,\mathrm{j}} \end{cases} \tag{3.3}$$

Note that $\gamma_{+,i} = -\mathbf{n}\cdot\mathbf{u}_{+,i}$ ($\gamma_{-,j} = -\mathbf{n}\cdot\mathbf{u}_{-,j}$) is the Lorentz factor of the positively charged particles (negatively charged respectively) seen by the Fiducials Observers (FIDO). The electro-magnetic tensor field $\mathrm{F}_{\alpha\beta}$, which appears here, is a solution of the covariant Maxwell's equations where the source term is composed by the "discrete" four current associated to the motion of each particule individually as in Sec.(3.1.3, 3.1.7).

3.1.2 Phase space properties

For a particle of a determined massive species (non massive species), if we do not care about the evolution of its spin, its state is entirely determined by the information of its position ($\mathrm{M} \in \mathscr{M}$), and its four-speed $\mathbf{u}$ for a massive particle (the quadri-impulsion vector $\mathbf{k}$ for non massive particle respectively).

Phase space geometry of massive particles

The position in phase space of a massive particle is composed of its position in spacetime and its four velocity $(\mathrm{M}, \mathbf{u}) \in \mathscr{M} \times \mathscr{T}_{\mathrm{M}}(\mathscr{M}) = \mathscr{P}_8$. Nevertheless, the four velocity $\mathbf{u}$ verifies $\mathbf{u}^2 = -1$ and $u^t \geq 0$ (because four velocities are future oriented), so the four velocity of the particles in M is embedded inside a sub-manifold $\Omega_f \subset \mathscr{T}_{\mathrm{M}}(\mathscr{M})$. The sub-manifold Ω_f imbedded in $\mathscr{T}_{\mathrm{M}}(\mathscr{M})$, is the future map of the hyperboloid defined by $\mathbf{u}^2 = -1 \Longleftrightarrow \mathbf{u} \in \Omega_{f+p} = \Omega_f \cup \Omega_p$. The past map is denoted Ω_p. For the sake of simplicity from here on, the future map Ω_f is noted Ω and called **four speed hyperboloid**. Because the tangent space is flat, note that the four speed hyperboloid sub-manifold Ω plunged in the tangent space $\mathscr{T}_{\mathrm{M}}(\mathscr{M})$ is fully determined by the metric tensor $\mathbf{g}_{\mathrm{M}}$

with the choice of a basis of this tangent spacetime. We can choose an orthogonal base or the natural basis adapted to the coordinate system which maps our spacetime.

The four speed hyperboloid sub-manifold Ω is plunged in the tangent space $\mathcal{T}_{\mathrm{M}}(\mathcal{M})$, which is a flat Minkowskian space. Then the geometry of this four speed hyperboloid, as well as the geometry of the future light cone are independent of the localisation in spacetime. Only the description of this object, using the natural basis, which is a basis of $\mathcal{T}_{\mathrm{M}}(\mathcal{M})$, depends on the considered $\mathrm{P} \in \mathcal{M}$ point in spacetime. We proove it in the following paragraph.

Using the natural basis of spacetime as base of our tangent space, a point on this sub-manifold is characterized by the three "spatial" components of the four speed u^j. These three spatial components can be chosen as coordinates for this sub-manifold. Indeed following Debbasch and van Leeuwen [2009a], for the further expansion in the model, it is very useful to calculate the contravariant u^0 and covariant u_0 components of the four speeds as function of u^j and the metric tensor at the point M only. Using the definition of the future sheet of the hyperboloid we get,

$$\begin{cases} u^0 = & -\dfrac{1}{g_{00}}\left[g_{0i}\,u^i + \sqrt{\left(g_{0i}\,u^i\right)^2 - g_{00}\left(1 + g_{ij}\,u^i\,u^j\right)}\right] \\ u_0 = & \sqrt{\left(g_{0i}\,u^i\right)^2 - g_{00}\left(1 + g_{ij}\,u^i\,u^j\right)} \end{cases} \tag{3.4}$$

Thus the three "spatial" components of the four speed constitute a coordinate system to the future sheet of the hyperboloid Ω. A point of $\mathcal{M} \times \Omega \,\hat{=}\, \mu$ describes the state of a particle. We call **phase space** this μ space. It is a 7-dimensional manifold. A point of this variety is noted using a tilde over a upper index coordinate, $z^{\tilde{\mu}} = (x^\alpha, u^j)$. We introduce $(\mathbf{e}_\mu)$ the natural basis of the spacetime, which depends on the position in spacetime, and $(\mathbf{o}_i)$ the natural basis of the four-speed hyperboloid associated with the u^i coordinate. The $(\mathbf{o}_i)$ basis depends on the position on the four-speed hyperboloid, but also on the point in spacetime. The coordinate u^i corresponds to the spatial component of the four-speed in the natural basis. Then the natural basis of μ phase space associated to the coordinates $z^{\tilde{\mu}}$ depends on the position in spacetime. We note $(\mathbf{m}_{\tilde{\mu}}) = (\mathbf{e}_\mu, \mathbf{o}_i)$ its natural basis. Following the path, which leads to Eq. (3.4), we also obtain the derivative in phase space coordinates $z^{\tilde{\mu}}$ of the time covariant component u_0 of the four speed. These results are used to achieve properly some of the following calculations,

$$\begin{cases} \dfrac{\partial u_0}{\partial x^\mu} = \dfrac{\partial g_{0\nu}}{\partial x^\mu}\,u^\nu - \dfrac{g_{00}}{2u_0}\dfrac{\partial g_{\sigma\nu}}{\partial x^\mu}\,u^\sigma\,u^\nu \\ \dfrac{\partial u^0}{\partial x^\mu} = -\dfrac{1}{2u_0}\dfrac{\partial g_{\sigma\nu}}{\partial x^\mu}\,u^\sigma\,u^\nu \end{cases} \quad \text{and} \quad \begin{cases} \dfrac{\partial u_0}{\partial u^j} = \dfrac{g_{0j}\,u_0 - g_{00}\,u_j}{u_0} \\ \dfrac{\partial u^0}{\partial u^j} = -\dfrac{u_j}{u_0} \end{cases} \tag{3.5}$$

Metric of massive particles phase space

If we use u^α as the coordinates of $\mathcal{T}_{\mathrm{M}}(\mathcal{M})$, the metric is $\mathbf{g}_{\mathrm{M}}$. The hyperboloid is locally defined by the submersion $f : u^\alpha \longrightarrow g_{\mathrm{M}}(\mathbf{u},\mathbf{u}) = g_{\mu\nu}u^\mu u^\nu$. Then the normal vector of Ω is $\partial_\alpha f(\mathbf{u})\,\mathbf{du}^\alpha = 2u_\alpha \mathbf{du}^\alpha = 2\mathbf{u} = 2\mathbf{n}_\Omega$. It is fully determined by the u^i component. This is obviously a future time oriented vector and so Ω is a spatial sub-manifold. Therefore the induced metric of Ω is $\mathbf{g}_\Omega = \mathbf{g}_{\mathrm{M}} + \mathbf{u}\otimes\mathbf{u}$. It will be used for the construction of the metric of the phase space μ.

If we use u^α as coordinates of $\mathcal{T}_{\mathrm{M}}(\mathcal{M})$ associated to the natural basis $\mathbf{e}_\alpha$, the metric coefficients are $\mathbf{g}_{\mathrm{M}} = g_{\alpha\beta}(\mathrm{M})\,\mathbf{dx}^\alpha \otimes \mathbf{dx}^\beta$. These coefficients depend on the point M in spacetime. Nevertheless it is an artifact coming from the description of $\mathcal{T}_{\mathrm{M}}(\mathcal{M})$ choosing $\mathbf{e}_\alpha$ as a basis. In fact, the tangent space is a flat space. If we choose an orthonormal base or an orthonormal system of coordinates to described it, then the components of the metric tensor in this basis are the usual Minkowskian ones.

Once we have the induced metric of Ω, we get the metric of the phase space μ,

$$\mathbf{G} = \begin{bmatrix} \mathbf{g} & \mathbf{0} \\ \mathbf{0} & \mathbf{g}_\Omega \end{bmatrix}. \tag{3.6}$$

The zero terms came from the construction of the phase space μ. Remark that the metric of phase space is fully determined by the given spacetime metric. In fact, if we choose an orthonormal system of coordinates to describe $\mathcal{T}_{\mathrm{M}}(\mathcal{M})$, then $\mathbf{g}_{\Omega}$ only depends on the position on the future sheet of the hyperboloid Ω.

Volume form of phase space for massive particles

To integrate properly the tensor fields on spacetime, on the the four speed hyperboloid or again on the phase space, we need to determine the volume form of each of these spaces. For spacetime, the volum form, is written from Levi-Civita tensor, in any system of coordinates,

$$\boldsymbol{\epsilon} = \sqrt{-g}\mathbf{dx}^0 \wedge \mathbf{dx}^1 \wedge \mathbf{dx}^2 \wedge \mathbf{dx}^3, \tag{3.7}$$

where g is the determinant of the matrix composed of the covariant components $g_{\alpha,\beta} = \mathbf{g}(\mathbf{e}_\alpha, \mathbf{e}_\beta)$ in the natural basis associated to the x^α coordinates of $\mathcal{M}$.

For the four speed hyperboloid, we note $\boldsymbol{\varpi}$ the volume form of $\mathcal{T}_{\mathrm{M}}(\mathcal{M})$ and $\boldsymbol{\omega}$ the volume form of Ω. Since $\mathbf{n}_{\Omega}$ is the normal timelike future oriented unit vector of Ω as a plunged sub-variety in $\mathcal{T}_{\mathrm{M}}(\mathcal{M})$, we have $\boldsymbol{\varpi} = -\mathbf{n}_{\Omega} \wedge \boldsymbol{\omega}$.

Writing separately the components along $\mathbf{e}_0$ for the four velocity, we can use Eq. (3.4) to express $\mathbf{u}(u^i) = u^i\mathbf{e}_i + u^0(u^i)\mathbf{e}_0$ the four velocity in function of u^i only. When u^i goes in whole $\mathbb{R}^3$ space then $\mathbf{u}(u^i)$ spans the whole futur sheet of the hyperboloid Ω. Then as for any manifold, the volumic element of Ω can be written as $\boldsymbol{\omega} = \sqrt{\det(g_{\Omega})}\mathbf{du}^1 \wedge \mathbf{du}^2 \wedge \mathbf{du}^3$. g_{Ω} is the determinant of the metric composed of the covariant components $g_{\Omega ij} = \mathbf{g}_{\Omega}(\mathbf{o}_i, \mathbf{o}_j)$, with $(\mathbf{o}_i)$ the natural basis of Ω associated to the u^i coordinates.

Using u^μ as coordinates of $\mathcal{T}_{\mathrm{M}}(\mathcal{M})$, the volume form can be written as $\boldsymbol{\varpi} = \sqrt{g_{\mathrm{M}}}\mathbf{du}^0 \wedge \mathbf{du}^1 \wedge \mathbf{du}^2 \wedge \mathbf{du}^3$, where $\sqrt{g_{\mathrm{M}}}$ is the determinant of the matrix of covariant components $g_{\alpha\beta} = \mathbf{g}(\mathbf{e}_i, \mathbf{e}_j)$. As a matter of fact, the natural basis associated to the use of u^μ coordinates is the natural basis of spacetime $\mathbf{e}_\alpha$ associated to x^μ coordinates.

Using $\mathbf{n}_{\Omega} = \mathbf{u} = u_k\mathbf{du}^k$, we finally show that $-u_0\sqrt{\det(g_{\Omega})} = \sqrt{-\det(g_{\mathrm{M}})}$. Thus we find the volume form of the four speed hyperboloid is,

$$\boldsymbol{\omega} = -\frac{\sqrt{-g_{\mathrm{M}}}}{u_0}\mathbf{du}^1 \wedge \mathbf{du}^2 \wedge \mathbf{du}^3 \tag{3.8}$$

Another way to write this expression consists to remark that the tangent space is flat and its expression is valid for each base of the tangent space. We choose an orthonormal base $\mathbf{f}_\mu$ of $\mathcal{T}_{\mathrm{M}}(\mathcal{M})$ and note f^μ the coordinates in this base, where $\sqrt{-g_{\mathrm{M}}} = 1$, adapted to some time vector defining the first vector $\mathbf{f}_0$ of the base. Then we can now introduce a spherical change of coordinates,

$$\begin{cases} f^0 = -f_0 = \cosh\psi \\ f^1 = f_1 = \sinh\psi\sin\theta\cos\phi \\ f^2 = f_2 = \sinh\psi\sin\theta\sin\phi \\ f^1 = f_3 = \sinh\psi\cos\theta \end{cases}, \tag{3.9}$$

We get a well adapted system of coordinates of the hyperboloid and find the volum form in this coordinate system.

$$\boldsymbol{\omega} = \sinh^2\psi\sin\theta\mathbf{d}\psi \wedge \mathbf{d}\theta \wedge \mathbf{d}\phi \tag{3.10}$$

In the following we note $\delta^3 u$ the integrand. It is independent of the coordinate system used to described the hyperboloid. $\delta^3 u = -\frac{\sqrt{-g_{\mathrm{M}}}}{u_0}d^3u$ for the coordinate system u^i issued from the natural basis or equivalently from $\delta^3 u = \sinh^2\psi\sin\theta d\psi d\theta d\phi$. From here, it is trivial to get the phase space volumic element,

$$\boldsymbol{\mu} = -\boldsymbol{\epsilon} \wedge \boldsymbol{\omega} = \frac{\det(g)}{u_0}\mathbf{dx}^0 \wedge \mathbf{dx}^1 \wedge \mathbf{dx}^2 \wedge \mathbf{dx}^3 \wedge \mathbf{du}^1 \wedge \mathbf{du}^2 \wedge \mathbf{du}^3 \tag{3.11}$$

So the determinant of $\mathbf{G}$ is, $\sqrt{\det \mathrm{G}} = \frac{\det(g)}{u_0}$.

Phase space geometry of non-massive particles

In case of non massive particles, the four-impulsion vector $\mathbf{k}$, which is tangent to the trajectory of the non massive particles, is a future oriented null vector. This peculiarity brings some difficulty to carry out the following calculations correctly. So the four-impulsion of a non massive particle in $\mathrm{M} \in \mathscr{M}$ is included in a well know hypersurface $\mathbf{k} \in \mathscr{C}_+ \subset \mathscr{T}_{\mathrm{M}}(\mathscr{M})$ **the future light cone**. Like the previous sub-manifold Ω the following relation shows that the future light cone is described by the spatial component of $\mathbf{k}$,

$$\begin{cases} k^0 = & -\frac{1}{g_{00}}\left[g_{0i}k^i + \sqrt{\left(g_{0i}k^i\right)^2 - g_{00}g_{ij}k^i k^j}\right] \\ k_0 = & \sqrt{\left(g_{0i}k^i\right)^2 - g_{00}g_{ij}k^i k^j} \end{cases}. \tag{3.12}$$

After some calculations, we show that the normal vector to $\mathscr{C}_+$ is $\mathbf{k}$. Thus the future cone is a null hypersurface. Therefore, it brings the peculiar property that the normal is included in its own tangent space $\mathbf{k} \in \mathscr{T}_{\mathbf{k}}(\mathscr{C}_+)$. The relation Eq.3.5 is also valid on the future light cone,

$$\begin{cases} \frac{\partial k_0}{\partial x^\mu} = \frac{\partial g_{0\nu}}{\partial x^\mu}k^\nu - \frac{g_{00}}{2k_0}\frac{\partial g_{\sigma\nu}}{\partial x^\mu}k^\sigma k^\nu \\ \frac{\partial k^0}{\partial x^\mu} = -\frac{1}{2k_0}\frac{\partial g_{\sigma\nu}}{\partial x^\mu}k^\sigma k^\nu \end{cases} \quad \text{and} \quad \begin{cases} \frac{\partial k_0}{\partial k^j} = \frac{g_{0j}k_0 - g_{00}k_j}{k_0} \\ \frac{\partial k^0}{\partial k^j} = -\frac{k_j}{k_0} \end{cases}. \tag{3.13}$$

If we use a spatial foliation of the spacetime, we can make a 3+1 decomposition of the four impulsion $\mathbf{k} = \frac{\mathrm{E}}{c}(\mathbf{n} + \mathbf{s})$, where $\mathbf{s}$ is a spatial unit vector and E the energy of this non massive particle. It allows us to define **the ingoing null vector** $\boldsymbol{\ell} = \frac{c}{\mathrm{E}}(\mathbf{n} - \mathbf{s})$. By construction the four momentum $\mathbf{k}$ and the ingoing null vector verifies $\boldsymbol{\ell}^2 = \mathbf{k}^2 = 0$ and $\boldsymbol{\ell} \cdot \mathbf{k} = -1$. Using it and Eq.(2.5), we can show that the induced metric $\mathbf{q}$ on the light cone is degenerate.

$$\mathbf{q} = \mathbf{g}(\boldsymbol{\pi}(.), \boldsymbol{\pi}(.)) = \mathbf{g} + \mathbf{k} \otimes \boldsymbol{\ell} + \boldsymbol{\ell} \otimes \mathbf{k} \tag{3.14}$$

Like all metric of a null sub-manifold, this metric is degenerate. We call the phase space of non-massive particles $\mu = \mathscr{M} \times \mathscr{C}_+$.

Volume form of non-massive particles phase space

The same kind of development can be made to calculate the volume element of the future light cone.

$$\boldsymbol{\omega} = -\frac{\sqrt{-g_{\mathrm{M}}}}{k_0}\mathbf{dk}^1 \wedge \mathbf{dk}^2 \wedge \mathbf{dk}^3 \tag{3.15}$$

As in Eq. (3.10), it is possible to find an adapted coordinate system of the future oriented cone. Expressing coordinates of $\mathbf{k}$ in any orthonormal directed oriented basis of the tangent space, we use the following system of coordinates,

$$\begin{cases} f^0 = -f_0 = l \\ f^1 = f_1 = l\sin\theta\cos\phi \\ f^2 = f_2 = l\sin\theta\sin\phi \\ f^1 = f_3 = l\cos\theta \end{cases}, \tag{3.16}$$

we find an similar expression,

$$\boldsymbol{\omega} = l\sin\theta \mathbf{d}l \wedge \mathbf{d}\theta \wedge \mathbf{d}\phi. \tag{3.17}$$

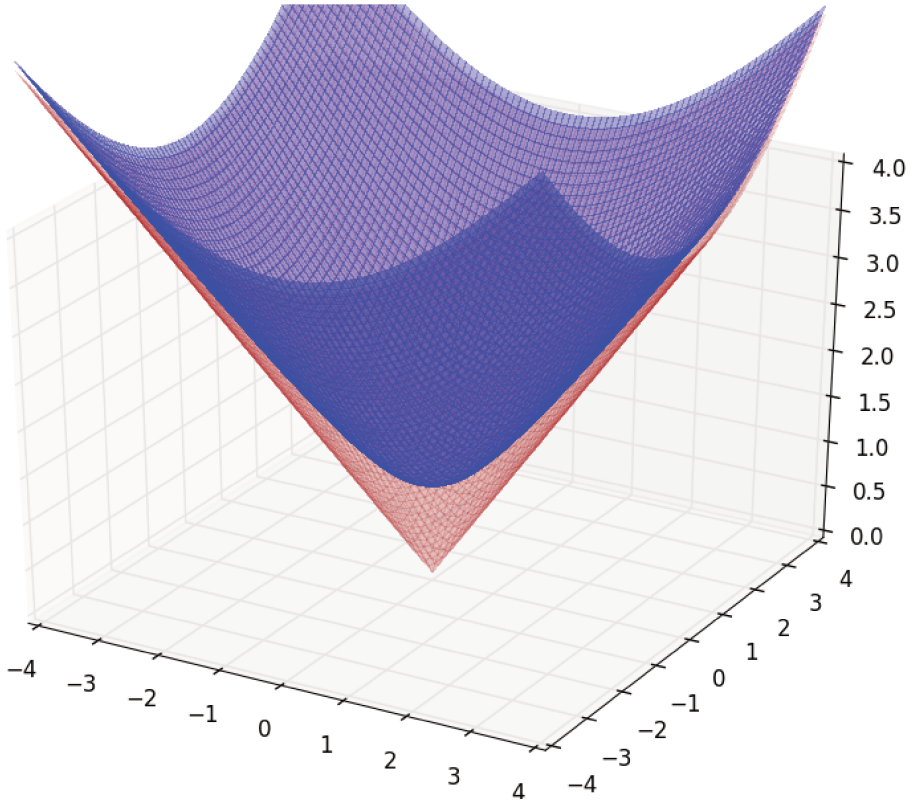

Figure 3.1 – Plot of the hyperboloid sub-manifold (blue) for massive particles and future cone (red) for non-massive particles. It represents the geometry where momentum is embedded

3.1.3 Conservation of volume form along motion

If we consider that particles having a charge q, are plunged in a global electro-magnetic field, the evolution of the state (x^α, u^j) of the particles is determined from the four velocity and Eq.(3.3),

$$\begin{cases} \dfrac{dx^\alpha}{ds} = & u^\alpha \\ \dfrac{du^j}{ds} = & -\Gamma^j_{\mu\nu}u^\mu u^\nu + \dfrac{q}{m}\mathrm{F}^{j\mu}u_\mu + \mathrm{C}^j \end{cases} \iff \frac{dz^{\tilde{\mu}}}{ds} = \underbrace{\mathrm{X}^{\tilde{\mu}}\left(z^{\tilde{\nu}}\right) + \mathrm{Y}^{\tilde{\mu}}\left(z^{\tilde{\nu}}\right)}_{\mathrm{Z}^{\tilde{\mu}}\left(z^{\tilde{\nu}}\right)} + \mathrm{C}^{\tilde{\mu}}\left(z^{\tilde{\nu}}\right), \quad (3.18)$$

where $\mathrm{X}^{\tilde{\mu}} = \left(u^\alpha, -\Gamma^j_{\mu\nu}u^\mu u^\nu\right)$.

It corresponds to a geodesic evolution of the state of particles in phase space, and $\mathrm{Y}^{\tilde{\mu}} = \left(0^\alpha, \frac{q}{m}\mathrm{F}^{j\mu}u_\mu\right)$ to an electromagnetic acceleration. $\mathrm{C}^{\tilde{\mu}}$ represents the term due to collisions or interactions with others species of particles. The electromagnetic forces here, contrary to those in Eq.(3.3), are divided in two parts. The first part $\mathrm{Y}^{\tilde{\mu}}$ contains only the "average" electromagnetic forces, that is to say the forces due to the average electromagnetic field and the average current. More precisions are given in Sec. (3.1.7). A useful lemma exposed in Marle [1969a] is that the Lie derivative of the volume form $\boldsymbol{\mu}$ along the collisionless evolution in phase space is null, i.e.,

$$\boxed{\mathscr{L}_{\mathbf{Z}}\boldsymbol{\mu} = 0}. \quad (3.19)$$

This property means that for a set of particles, which forms an infinitesimal volume in the phase space, if these particles evolve following Eq.(3.18) where we neglect the collision term, the volume of this set remains constant. This property is also valid for each kind of motion having a Hamiltonian (see.Debbasch and van Leeuwen [2009b]). To show this property, let use the property of linearity of the Lie derivative Eq.(A.9 & eq.A.10),

$$\mathscr{L}_{\mathbf{Z}}\boldsymbol{\mu} = \mathbf{Z}\cdot\overbrace{\mathbf{d}\left(\boldsymbol{\epsilon}\wedge\boldsymbol{\omega}\right)}^{8-\text{form}\Rightarrow 0} + \mathbf{d}\left(\mathbf{Z}\cdot\boldsymbol{\mu}\right) = \frac{1}{\sqrt{\det \mathrm{G}}}\frac{\partial}{\partial z^{\tilde{\mu}}}\left(\sqrt{\det \mathrm{G}}\mathrm{Z}^{\tilde{\mu}}\right)\boldsymbol{\mu}.$$

For the geodesic evolution, using Eqs.3.18& 3.5), the anti-symmetry of $\mathbf{F}$ and the property (A.3), we get,

$$\begin{aligned}\frac{1}{\sqrt{\det G}}\frac{\partial}{\partial z^{\tilde{\mu}}}\left(\sqrt{\det G}X^{\tilde{\mu}}\right) &= \frac{u_0}{g}\left[\frac{\partial}{\partial x^\mu}\left(\frac{g u^\mu}{u_0}\right) - g\Gamma^i_{\mu\nu}\frac{\partial}{\partial u^i}\left(\frac{u^\mu u^\nu}{u_0}\right)\right] \\ &= \underbrace{\frac{\partial u^\mu}{\partial x^\mu}}_{a} + \underbrace{u^\mu\frac{\partial}{\partial x^\mu}\ln\left(\frac{g}{u_0}\right)}_{b} + \underbrace{\Gamma^i_{\mu\nu}u^\mu u^\nu\frac{\partial}{\partial u^i}\ln u_0}_{c} - \underbrace{\Gamma^i_{\mu\nu}\frac{\partial}{\partial u^i}\left(u^\mu u^\nu\right)}_{d} \\ \Longrightarrow \qquad & \mathscr{L}_{\mathbf{X}}\boldsymbol{\mu} = 0. \end{aligned} \tag{3.20}$$

Details of the calculations are given in Sec. (C.1). For the evolution due to electro-magnetic forces, we also get,

$$\mathscr{L}_{\mathbf{Y}}\boldsymbol{\mu} = -\frac{q u_0}{m}\frac{\partial}{\partial u^i}\left(\frac{\mathrm{F}^i_\mu u^\mu}{u_0}\right)\boldsymbol{\mu} = 0$$

Thus we have demonstrated Eq. (3.19). All the results of this chapter are valid for all kinds of particles, whatever their charge. For the rest of the section, we call $\mu_+ = \mathscr{M}\times\Omega_+$, $\mu_- = \mathscr{M}\times\Omega_-$, and $\mu_r = \mathscr{M}\times\Omega_r$ the phase space of the positive, negative or neutral particles, respectively.

3.1.4 Relativistic distribution function

Using the results of Sec.(C.2), for a set of N particles, evolving in our spacetime following Eq. (3.18), we can introduce the **world line distribution function** defined as,

$$\boxed{\mathrm{R}\left(z^{\tilde{\nu}}\right) \hat{=} \int_{s\in\mathbb{R}} \mathrm{d}s \sum_{i=1}^{\mathrm{N}} \delta^{(7)}\left(z^{\tilde{\mu}} - z_i^{\tilde{\mu}}(s)\right)}. \tag{3.21}$$

If the particles are not distinguishable, the function R, defined on the phase space, contains the entire information on the line of universe of this set of particles and their distribution in the phase space. We note $\sigma_t = \Sigma_t \times \Omega$ a foliation of phase space associated with a foliation of spacetime. Le us write Eq.(C.4) for the set of particles,

$$\boxed{\mathrm{N} = \int_{\sigma_t}\left[\mathrm{R}\left(z^{\tilde{\nu}}\right)\frac{\mathbf{dz}}{\mathrm{d}s}\left(z^{\tilde{\nu}}\right)\right]\cdot\mathbf{N}\delta^6\sigma}. \tag{3.22}$$

Even if the world line distribution function contains a lot of information on this system, this function is not useful because it is not smooth. So to obtain the usual **distribution function**, one needs to build some mean value of the world line distribution function in order to smooth R.

$$\boxed{f(\mathrm{M},\mathbf{u}) \hat{=} \left\langle \mathrm{R}(\mathrm{M},\mathbf{u}) \right\rangle}. \tag{3.23}$$

We assume that the previous results Eq.(3.22) on the world line distribution function is valid for the distribution function.

$$\mathrm{N} = \int_{\sigma_t}\left[f\left(z^{\tilde{\nu}}\right)\frac{\mathbf{dz}}{\mathrm{d}s}\left(z^{\tilde{\nu}}\right)\right]\cdot\mathbf{N}\delta^6\sigma. \tag{3.24}$$

The vector field $f\left(z^{\tilde{\nu}}\right)\frac{\mathbf{dz}}{\mathrm{d}s}\left(z^{\tilde{\nu}}\right)$ can be considered as the 7-number current of particles in phase space. This is valid for any spatial foliation of $\mathscr{M}$, which implies that the 7-number current field inside the integral of the phase space is conserved on μ manifold. Using the expression of the divergence on the phase space manifold we get,

$$\boxed{\hat{\mathscr{L}}[f] = \frac{u_0}{g}\frac{\partial}{\partial z^{\tilde{\mu}}}\left(\frac{g}{u_0}\frac{dz^{\tilde{\mu}}}{ds}\left(z^{\tilde{\nu}}\right) f\left(z^{\tilde{\nu}}\right)\right) = 0}. \tag{3.25}$$

This is the so called **Liouville equation** for the distribution function, where $\hat{\mathscr{L}}$ is the **Liouville operator**. This should not be confused with the Lie derivative. When particles which are created or annihilated, collide, the null right hand side of this equation needs to be replaced by the collision term and the rate of creation of particles minus the rate of annihilation per unit volume in the phase space. This term is specified in Sec. (3.1.6).

The averaging used to build the distribution function is still a problem concerning the invariance of the function f, (see Debbasch et al. [2001] for more details on the subject). It is important to write the number of particles inside an infinitesimal element of phase space. Let us define the elementary volume on the spatial hypersurface Σ_t around a point $x \in \Sigma_t$,

$$\delta^3\mathcal{V}_{t,x} = \left\{ x \in \Sigma_t \quad | \quad \forall i \in [1,2,3] \quad x^i(x) \in \left[x^i; x^i + dx^i \right] \right\} \subset \Sigma_t, \tag{3.26}$$

and an infinitesimal part of the hyperboloid of four-speed around the speed $u \in \Omega_{t,x}$,

$$\delta^3\Omega_{t,x,u} = \left\{ u \in \Omega_{t,x} \quad | \quad \forall i \in [1,2,3] \quad u^i(u) \in \left[u^i; u^i + du^i \right] \right\} \subset \Omega. \tag{3.27}$$

Finally, we note $\delta^6\sigma_{t,x,u} = \delta^3\mathcal{V}_{t,x} \times \delta^3\Omega_u \subset \mu$. To get the number of particles inside $\delta^6\sigma_{t,x,u}$ we need to start from the integral, Eq.3.22, but only on the infinitesimal elements of the hypersurface $\delta^6\sigma_{t,x,u}$, using $\delta^6\sigma = -\frac{g}{hu_0} d^3x d^3u$ and $\frac{\mathbf{dz}}{\mathrm{ds}} \cdot \mathbf{N} = -hu^0$. After some calculations, we get,

$$\boxed{\delta^6 \mathrm{N}\left[\delta^3\mathcal{V}_{t,x}, \delta^3\Omega_{t,x,u}\right] = \int_{\delta^6\sigma_{t,x,u}} f(\mathrm{M}, \mathbf{u}) \frac{g u^0}{u_0} d^3x d^3u}. \tag{3.28}$$

Another quantity, which is useful to introduce, is $\mathbf{J}$ the number four-current also call Feynman current,

$$\mathbf{J} \hat{=} \int_{\mathbf{u}^i \in \mathbb{R}^3} f(\mathrm{M}, \mathbf{u}) \mathbf{u} \frac{\sqrt{-g}}{u_0} \mathrm{du}^1 \mathrm{du}^2 \mathrm{du}^3 \quad . \tag{3.29}$$

This quantity allows us to define in the rest frame the fluid particle number density and the four speed associated to the fluid,

$$\begin{cases} n_0 \hat{=} -\sqrt{-\mathbf{J} \cdot \mathbf{J}} \\ \mathbf{u}_{\mathrm{fl}} \hat{=} \dfrac{\mathbf{J}}{n_0} \end{cases} \tag{3.30}$$

3.1.5 Boltzmann's equations system

Let us consider a system with different species. We note the distribution functions of charged particles, for the positive, the negative and the neutral particles $f_+ : \mu_+ \longrightarrow \mathbb{R}_+$, $f_- : \mu_- \longrightarrow \mathbb{R}_+$ and $f_r : \mu_r \longrightarrow \mathbb{R}_+$, respectively. These species are plunged in a curved spacetime and an electromagnetic field, such that the particles evolve following Eq.(3.18).

From Eq.(3.25), replacing $dz^{\tilde{\mu}}/ds$ using Eq. (3.18), we treat separately $\mathrm{Z}^{\tilde{\mu}}$, which stays on the left hand side and $\mathrm{C}^{\tilde{\mu}}$, which contains the collision effect and is moving on the right hand side. Using volume conservation in phase space Eq.(3.19), the left hand side can be simplified. Thus the system of equations, which governs the different distribution functions becomes,

$$\boxed{\begin{cases} u^\mu \dfrac{\partial f_+}{\partial x^\mu} - \Gamma^i_{\nu\sigma} u^\nu u^\sigma \dfrac{\partial f_+}{\partial u^i} + \dfrac{q}{mc} \mathrm{F}^i_\nu u^\nu \dfrac{\partial f_+}{\partial u^i} & = \mathrm{I}_+ \\ u^\mu \dfrac{\partial f_-}{\partial x^\mu} - \Gamma^i_{\nu\sigma} u^\nu u^\sigma \dfrac{\partial f_-}{\partial u^i} - \dfrac{qc}{m} \mathrm{F}^i_\nu u^\nu \dfrac{\partial f_-}{\partial u^i} & = \mathrm{I}_- \\ u^\mu \dfrac{\partial f_r}{\partial x^\mu} - \Gamma^i_{\nu\sigma} u^\nu u^\sigma \dfrac{\partial f_r}{\partial u^i} & = \mathrm{I}_r \end{cases}}. \tag{3.31}$$

These equations are called **Boltzmann's equations system**. It can be adapted for a more general configuration of species mixing. On the right hand side we get some source terms due to collision and creation or annihilation of pairs, which will be calculated in details in the next section. The left hand side contains the effect of gravity and average electromagnetic Lorentz force.

3.1.6 Collision terms

Regarding the model develloped here, this section is the most important part of this chapter. Indeed, the collision term is the groundwork of the calculations allowing us to link microphysics and dynamical processes of the flow. Indeed, we see that these terms can take into account Compton and inverse Compton processes. It can also take into account, how the creation and annihilation of pairs play a role on the distribution functions of each species.

First, we see that elastic or unelastic particle collisions are characterized by a unit spatial vector which characterizes a reflection symmetry. The set of collisions is described by making this vector crossing the unity sphere of the sub-space where it belongs. Second, based on Chernikov [1963], we see how to calculate these terms. A collision probability function needs to be introduced. This function, related to the notion of effective cross-section, is not calculated here. It contains the micro-physical characteristics of each process.

In order to consider collisions, we assume the following hypotheses,

- First, we consider only collisions with two particles.
- Second, we consider that the collision time (clean particle time) is infinitely short compared to the characteristic time of motion created by mean fields. Thus collisions are considered as punctual and instantaneous.
- Third, elastic collisions concern collisions in which the species before and after the collision are identical.
- Fourth, inelastic collisions concern collisions in which the species before and after the collision are not the same.

The second hypothesis on the punctuality of the collisions may be a problem for collisions between charged particles. However, we assume that the density of the gas is sufficiently low to ensure the validity of this assumption.

Elastic collisions

In the case of an elastic collision, at $\mathrm{M} \in \mathscr{M}$ where the collision occurs, the two particles of four-momentum $\mathbf{p}$ and $\mathbf{q}$ before the collision become $\mathbf{p}'$ and $\mathbf{q}'$ after it. The conservation of momenum during the collision implies that $\mathbf{p}+\mathbf{q}=\mathbf{p}'+\mathbf{q}'$. The elasticity implies that the deviation of four momentum $\mathbf{p}-\mathbf{p}'$ and $\mathbf{q}-\mathbf{q}'$ is a spatial vector. Writing the conservation of the four momentum, $\mathbf{p}-\mathbf{p}'=-(\mathbf{q}-\mathbf{q}')$. It proves that the deviation vectors are aligned. We deduce the existence of a vector $\mathbf{n}$ such as,

$$\begin{cases} \mathbf{p}' = \mathbf{p} - 2\left(\mathbf{p}\cdot\mathbf{n}\right)\mathbf{n} \\ \mathbf{q}' = \mathbf{q} - 2\left(\mathbf{q}\cdot\mathbf{n}\right)\mathbf{n} \end{cases} \tag{3.32}$$

Elasticity induces that $\mathbf{n}$ is proportional to a difference between the two four-momentum of particles of the same mass. Thus $\mathbf{n}$ is a spatial vector, which is perpendicular to the total momentum of the two particles.

$$\begin{cases} \left(\mathbf{p}+\mathbf{q}\right)\cdot\mathbf{n} = \left(\mathbf{p}'+\mathbf{q}'\right)\cdot\mathbf{n} = 0 \\ \mathbf{n}^2 = 1 \end{cases} \tag{3.33}$$

Eqs. (3.32) indicates that a collision is characterized by a reflexion symmetry with respect to the hyperplane orthogonal to $\mathbf{n}$ in $\mathscr{T}_{\mathrm{M}}(\mathscr{M})$. In the following we called this hyperplane $\mathbf{n}^{\perp}$. This hyperplane is fully characterized by the spatial unit vector $\mathbf{n}$ orthogonal to $\mathbf{p}+\mathbf{q}$. Thus, $\mathbf{n}$ describes the 2-sphere unit $\mathscr{S}_{\mathbf{p}+\mathbf{q}^{\perp}} \subset \mathbf{p}+\mathbf{q}^{\perp} \subset \mathscr{T}_{\mathrm{M}}(\mathscr{M})$ plunged in the sub-space orthogonal to $\mathbf{p}+\mathbf{q}$. Normalizing the vector $\mathbf{p}+\mathbf{q}$ we get the four speeds of the reference frame of center of

mass, then $\mathbf{n}$ is a vector of the "space" seen by an observer of the center of mass reference frame. We describe all the possible elastic collisions for a given value of $\mathbf{p}+\mathbf{q}$. It means that, when $\mathbf{n}$ scans the sphere $\mathscr{S}_{\mathbf{p}+\mathbf{q}^{\perp}}$, Eqs.(3.32) give us all possible p' and q' values of an elastic collision. The property of reflexion symmetry allows us to write,

$$\begin{cases} \mathbf{p} = \mathbf{p}' - 2\left(\mathbf{p}'\cdot\mathbf{n}\right)\mathbf{n} \\ \mathbf{q} = \mathbf{q}' - 2\left(\mathbf{q}'\cdot\mathbf{n}\right)\mathbf{n} \end{cases} \tag{3.34}$$

We can remark that this transformation, described by a spatial unit vector $\mathbf{n}$, is also valid for collisions of particles, either massive or not.

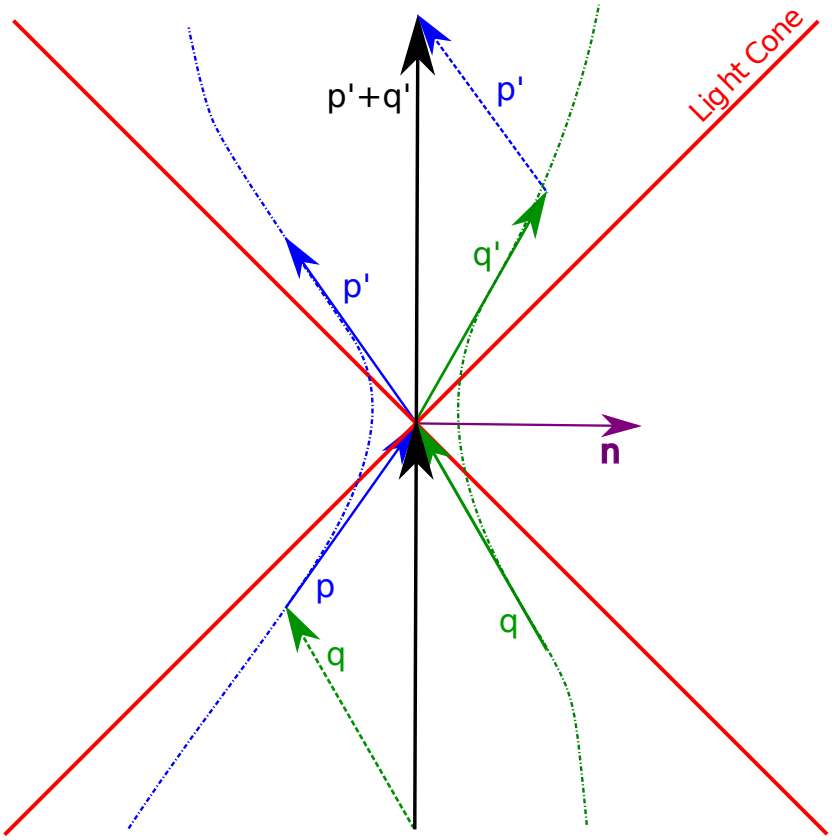

Figure 3.2 – Display of elastic collision of two massive particles, in the plane defined by the four-velocity in the barycentric frame $\mathbf{p}+\mathbf{q}$ and the vector $\mathbf{n}$ of the collision. The dotted lines correspond to some possible real trajectory of the particles.

The Fig.3.2 displays the elastic collision of two massive particles. The dotted line corresponds to some possible real possible trajectories. Nevertheless the assumption of punctual and instantaneous treatment of collision implies that the considered trajectory is the one which follows the line along four-velocity vector.

Inelastic collisions

For an inelastic collision we need to proceed in two steps. Considering that the collision starts with particles of proper masses m_p and m_q to produce particles of masses $m_{p'}$ and $m_{q'}$. Like before the four-momentum is conserved, so we get $\mathbf{p}+\mathbf{q}=\mathbf{p}'+\mathbf{q}'$. Let us suppose we get a couple $(\mathbf{p}'_0,\mathbf{q}'_0)$ resulting from the collision of the two four-momenta $\mathbf{p}'_0$, corresponding to a mass of $m_{p'}$, and $\mathbf{q}'_0$, corresponding to a mass of $m_{q'}$, all the couples $(\mathbf{p}',\mathbf{q}')$ verify,

$$\begin{cases} \mathbf{p}' = \mathbf{p}'_0 - 2\left(\mathbf{p}'_0\cdot\mathbf{n}\right)\mathbf{n} \\ \mathbf{q}' = \mathbf{q}'_0 - 2\left(\mathbf{q}'_0\cdot\mathbf{n}\right)\mathbf{n} \end{cases}, \tag{3.35}$$

where the vector $\mathbf{n}$ follows the condition,

$$\begin{cases} (\mathbf{p}'+\mathbf{q}')\cdot\mathbf{n} = (\mathbf{p}'_0+\mathbf{q}'_0)\cdot\mathbf{n} = 0 \\ \mathbf{n}^2 = 1 \end{cases} \tag{3.36}$$

We look for an inelastic transformation $(\mathbf{p},\mathbf{q} \underset{\text{unelastic}}{\rightarrow} \mathbf{p}'_0,\mathbf{q}'_0)$, which combined to all elastic transformations $(\mathbf{p}'_0,\mathbf{q}'_0 \underset{\text{elastic},\mathbf{n}}{\rightarrow} \mathbf{p}',\mathbf{q}')$ describes all inelastic collisions. Indeed, the composition of an inelastic collision $(m_p, m_q \rightarrow m'_p, m'_q)$ with an elastic collision Eq. (3.32) is another inelastic collision $(m_p, m_q \rightarrow m'_p, m'_q)$.

Finally, we need to find the couple $(\mathbf{p}'_0,\mathbf{q}'_0)$. The idea is to search for this couple in the plane generated by $(\mathbf{p},\mathbf{q})$. If we note $\mathbf{P}_{\mathbf{p}+\mathbf{q}}$ the operator of projection perpendicular to $(\mathbf{p}+\mathbf{q})$, this plan is also generated by $(\mathbf{p}+\mathbf{q},\mathbf{P}_{\mathbf{p}+\mathbf{q}}(\mathbf{p}))$ or $(\mathbf{p}+\mathbf{q},\mathbf{P}_{\mathbf{p}+\mathbf{q}}(\mathbf{q}))$. Thus we can seek the scalars (α,β), such that,

$$\begin{cases} \mathbf{p}'_0 = \alpha(\mathbf{p}+\mathbf{q}) + \beta\mathbf{P}_{\mathbf{p}+\mathbf{q}}(\mathbf{p}) \\ \mathbf{q}'_0 = (1-\alpha)(\mathbf{p}+\mathbf{q}) + \beta\mathbf{P}_{\mathbf{p}+\mathbf{q}}(\mathbf{q}) \end{cases} \tag{3.37}$$

To obtain the resulting masses (m'_p, m'_q) from the initial masses (m_p, m_q) before the collision, we take the square of each equation, and get after some calculations,

$$\begin{cases} \alpha = \dfrac{1}{2}\left(1 + \dfrac{m^2_{p'} - m^2_{q'}}{\lambda^2}\right) \\ \lambda^2 = -(\mathbf{p}+\mathbf{q})^2 \\ \beta^2 = \dfrac{\left[-\lambda^2 + (m_{p'} - m_{q'})^2\right]\left[-\lambda^2 + (m_{p'} + m_{q'})^2\right]}{\left[-\lambda^2 + (m_p - m_q)^2\right]\left[-\lambda^2 + (m_p + m_q)^2\right]} \end{cases} . \tag{3.38}$$

Using the fact that the scalar product of two four-velocities is less than -1, we deduce that $-\lambda^2 + (m_p + m_q)^2 \leq 0$, using a second inequality we also get $-\lambda^2 + (m_p - m_q)^2 \leq 0$. These two inequalities are also valid for $m_{p'}$ and $m_{q'}$. Thus β^2 exists because each term is negative, which implies that the fraction in the last equation (3.38) is positive.

Because the tangent space is a flat space, the volume element associated to $\mathscr{S}_{\mathbf{p}+\mathbf{q}^\perp}$ is the usual element of volume $(\sin^2\theta d\theta d\phi)$ of the sphere independently of the collision center in the momentum frame $\mathbf{p}+\mathbf{q}$. The axis defining θ,ϕ is any couple orthogonal axis of the sphere $\mathscr{S}_{\mathbf{p}+\mathbf{q}^\perp}$.

Decomposition of collision terms

The collision term of Boltzmann's equations system Eq.(3.31) is the balance of particles of each species, which leave and enter (in-out) some fluid volume in the phase space due to collision or pair creation-annihilation. This term is calculated in Chernikov [1963] and Marle [1969a]. Each part can be decomposed in different terms, which represent the collision between 2 different species,

$$\begin{cases} \mathrm{I}_+ = \mathrm{I}^{++}_{++} + \mathrm{I}^{+-}_{+-} + \mathrm{I}^{+r}_{+r} + \mathrm{I}^{2r}_{+-} \\ \mathrm{I}_- = \mathrm{I}^{-+}_{-+} + \mathrm{I}^{--}_{--} + \mathrm{I}^{-r}_{-r} + \mathrm{I}^{2r}_{-+} \\ \mathrm{I}_r = \mathrm{I}^{rr}_{rr} + \mathrm{I}^{r+}_{r+} + \mathrm{I}^{r-}_{r-} + \mathrm{I}^{2r}_{2r} + \mathrm{I}^{+-}_{2r} + \mathrm{I}^{-+}_{2r} \end{cases} \tag{3.39}$$

Thus the term I^{+-}_{+-} represents the rate of elastic collision between electron and positron. The terms $\mathrm{I}^{++}_{++}, \mathrm{I}^{+-}_{+-}, \mathrm{I}^{+r}_{+r}, \mathrm{I}^{--}_{--}, \mathrm{I}^{-r}_{-r}, \mathrm{I}^{2r}_{2r}$ constitute the elastic collision rates and $\mathrm{I}^{2r}_{+-}, \mathrm{I}^{+-}_{2r}$ the inelastic ones. The terms $\mathrm{I}^{++}_{++}, \mathrm{I}^{+-}_{+-}, \mathrm{I}^{--}_{--}$ are the elastic collisions between electrons and positrons. If the neutral species is photon, we may have radiative transfer, especially Compton and inverse-Compton processes. The effect of those physical processes on the evolution of the distribution is determined by $\mathrm{I}^{-\gamma}_{-\gamma}$ and $\mathrm{I}^{+\gamma}_{+\gamma}$. The terms I^{2r}_{+-} and I^{2r}_{-+}) contain the effect of the creation of positrons and electrons, respectively. Therefore I^{+-}_{2r} contains the effect of the annihilation of pairs on the

neutral component. Chernikov [1963] was the first to derive explicitly these expressions assuming collisions.

$$\mathrm{I}^{+-}_{+-}(\mathrm{M},\mathbf{u}) = \int_{\frac{\mathbf{q}}{m_e}\in\Omega}\int_{\mathbf{n}\in\mathscr{S}_{\mathbf{p}+\mathbf{q}^\perp}} \left\{ f_+(\mathbf{u}')\, f_-\left(\frac{\mathbf{q}'}{m_e}\right) - f_+(\mathbf{u})\, f_-\left(\frac{\mathbf{q}}{m_e}\right)\right\} \mathrm{A}^{+-}_{+-}(m_e\mathbf{u},\mathbf{q},\mathbf{n}) \sin^2\theta_{\mathbf{n}}\, d\theta_{\mathbf{n}}\, d\phi_{\mathbf{n}} \tag{3.40}$$

$$\times \frac{\sqrt{-g}}{m_e^2 q_0}\, dq^1 dq^2 dq^3 \tag{3.41}$$

The differential cross section terms $\mathrm{A}^{+-}_{+-}(m_e\mathbf{u},\mathbf{q},\mathbf{n})$ are proportional to the probability of collision characterized by the vector $\mathbf{n}$ between a positron of momentum $m_e\mathbf{u}$ and an electron of momentum $\mathbf{p}$. The other collision terms have the same form as in Eq.(3.41), except that the differential cross section is different. The differential cross section terms must verify the following properties,

- A^{kl}_{ij} is a positive function.
- It respects the symmetry $\mathrm{A}^{kl}_{ij}(\mathbf{p},\mathbf{q},\mathbf{n}) = \mathrm{A}^{lk}_{ij}(\mathbf{p},\mathbf{q},\mathbf{n}) = \mathrm{A}^{kl}_{ji}(\mathbf{q},\mathbf{p},\mathbf{n})$, which means that the probability of collisions $(\mathbf{p},\mathbf{q} \underset{\mathbf{n}}{\rightarrow} \mathbf{p}',\mathbf{q}')$ is equal to the probability of the collision $(\mathbf{p},\mathbf{q} \underset{\mathbf{n}}{\rightarrow} \mathbf{q}',\mathbf{p}')$ and is also equal to the probability of $(\mathbf{q},\mathbf{p} \underset{\mathbf{n}}{\rightarrow} \mathbf{p}',\mathbf{q}')$.
- There is an equal probability of the inverse process, $\mathrm{A}^{kl}_{ij}(\mathbf{p},\mathbf{q},\mathbf{n})\,\delta^3 q = \mathrm{A}^{kl}_{ij}(\mathbf{p}',\mathbf{q}',\mathbf{n}')\,\delta^3 q'$.

These properties of symmetry are important for future developments. This differential cross section term contains all the essential elements of physics of the collisions. In order to understand the role of the creation of pairs, we need to calculate the $\mathrm{I}^{2\gamma}_{+-}$ and $\mathrm{I}^{+-}_{2\gamma}$ terms. The calculation of these differential cross-sections involves the standard particle model and will not be discussed here. You can find details in Berestetskii et al. [1982].

3.1.7 Maxwell's equations

We show here how to properly integrate Maxwell's equations in order to link the distribution function to the electromagnetic field. Generally speaking, the evolution of the electro-magnetic anti-symmetric tensor $\mathbf{F}$ is given by the **Maxwell's equations** in Gaussian Unit (GU) that we can write in its covariant form,

$$\boxed{\begin{cases} \nabla\cdot\mathbf{F} = & \dfrac{4\pi}{c}\mathbf{j} \\ \nabla\cdot\star\mathbf{F} = & 0 \end{cases}}, \tag{3.42}$$

where $\star\mathbf{F}$ is the Hodge dual Eq.(A.16). The source term is due to the circulation of charges in spacetime. Indeed $\mathbf{j}$ is the charged four-current vector. About the current, two definitions appear, the discrete one or the continuous one,

$$\begin{cases} \mathbf{j}_{\mathrm{D}} = q\int\left[\sum_{i=1}^{\mathrm{N}_+}\delta^4\left(\mathrm{M}-\mathrm{M}_{+,i}(s)\right)\frac{dx^\mu_{+,i}}{ds}(s) - \sum_{j=1}^{\mathrm{N}_-}\delta^4\left(\mathrm{M}-\mathrm{M}_{-,j}(s)\right)\frac{dx^\mu_{-,j}}{ds}(s)\right] ds = q\int_{\mathbf{u}^i\in\mathbb{R}^3}\left(\mathrm{R}_+(\mathrm{M},\mathbf{u})-\mathrm{R}_-(\mathrm{M},\mathbf{u})\right)\mathbf{u}\frac{\sqrt{-g}}{u_0}\mathrm{du}^1\mathrm{du}^2 \\ \mathbf{j}_{\mathrm{C}} = q\left(\mathbf{J}_+ - \mathbf{J}_-\right) = q\int_{\mathbf{u}^i\in\mathbb{R}^3}\left(f_+(\mathrm{M},\mathbf{u}) - f_-(\mathrm{M},\mathbf{u})\right)\mathbf{u}\frac{\sqrt{-g}}{u_0}\mathrm{du}^1\mathrm{du}^2\mathrm{du}^3 \end{cases} \tag{3.43}$$

The first expression of the current treats the source as a discrete function linked to the world-line distribution function. In this case, the electromagnetic field solution of Maxwell's equations is the sum of the contribution of each particle. The problem of this solution is that it includes all singularities of the field in the environment of particles. The second expression considers the

source as a continuous field linked to the distribution function. Here, the solution of Maxwell's equations gives us a continuous average field. If we remember the discussion in the beginning of Sec. 3.1.3, the electromagnetic field, which appears in the Boltzmann system is the averaged one. Thus in the following, except if we mention it, the charge current refers to the continuous field. Note that $\mathbf{J}$ is the four-current number also called Feynman's current mentioned in Eq. (3.29).

3.1.8 GRMHD equations system and coupling terms between species

Compiling all informations introduced in this chapter, we are now building in this section the equations of the positron-electron fluid motion according to the effects and the mechanism of pair annihilation/creation and elastic interaction between species. To calculate the rate of apparition of pairs, one needs to integrate the Boltzmann equation on all possible velocities. The divergence of the energy momentum tensor of each species is given by the integration on the velocity space Ω of the first order momentum equation of the Boltzmann system. The terms due to the interactions (Compton, Inverse Compton, pair creation or annihilation) between photons and electron-positron fluid is integrated in many astrophysical system studies concerning high energy phenomena. Fargion and Salis [1998] study the effect of elastic processes (Compton, Inverse Compton) on the emission spectrum.

The use of this kind of term are really important in astrophysics. Especially for highly energetics flow, GRB, AGN... Let mention the discussion about pairs creation rate in the environnement of black hole magnetosphere for AGN jets. The work of (Levinson and Rieger [2011]) argue that in the best condition for the accretion disk the pair formation rate via annihilation of photons could be always too low to get the Goldreich-Julian density (for steady and ideal magneto-hydrodynamics) of pairs. In region where injection is too low ideal MHD break down and a gap is formed and Hirotani and Pu [2016] propose a model of steady gap. These models are subject to recent study as the work of Ford et al. [2017] which study the condition in such solution to have an efficient Blandford-Znajek. Nevertheless the work of Levinson and Segev [2017] argue that solutions of these models exists only under restrictive conditions which could not apply to concrete astrophysical system, they conclude that the assumption of steady flow could not hold in the magnetosphere of the black hole. The study of such a solution needs a bi-fluid+radiative treatment in order to include the terms of interaction between photons and electon-positron fluid, and the effect of annihilation or creation processes, Compton/inverse Compton type processes, and synchrotron emission. Birkl et al. [2007] and Zalamea and Beloborodov [2011] have examined the pair production mechanism via neutrino source in the environnement of accreting black hole magnetosphere.

Maxwell-Enskog transfer equation

Following Chernikov [1963] and Marle [1969a], to get the equation of motion of each component of the fluid, it is useful to obtain what we call a transfer equation. We introduce the **tensorial observable** determined by the state of the particles, $\forall (k,l) \in \mathbb{N}^2$

$$\begin{array}{rccc} \mathbf{t} \ : & \mu = \mathscr{M} \times \Omega & \rightarrow & \mathscr{T}(\mathrm{M})^k \otimes \mathscr{T}^\star(\mathrm{M})^l \\ & \left(x^\mu, u^i\right) & \mapsto & \mathbf{t}\left(x^\mu, u^i\right) \end{array}, \tag{3.44}$$

This observable can be the mass $\mathbf{t} = m$, the momentum $\mathbf{t} = m\mathbf{u}$ or the energy of the particles measured by a specific observer $\mathbf{t} = mc^2 \mathbf{u}\cdot\mathbf{v}$, where $\mathbf{v}$ is the four velocity of the observer. From this tensorial observable, we can build its spacetime **observable flux-density**,

$$\bar{t}^{\gamma,\alpha_1,\ldots,\alpha_k}_{\beta_1,\ldots,\beta_l} = \int_{u^i\in\mathbb{R}^3} u^\gamma t^{\alpha_1,\ldots,\alpha_k}_{\beta_1,\ldots,\beta_l}\left(x^\mu, u^i\right) f\left(x^\mu, u^i\right)\left(\frac{-\sqrt{-g}}{u_0}\right) d^3u, \tag{3.45}$$

which is a $(k+1,l)$ usual tensor. The **observable density** per unit volume measured by a specific observer is simply $\bar{t}^{\alpha_1,\ldots,\alpha_k}_{\beta_1,\ldots,\beta_l} = \bar{t}^{\gamma,\alpha_1,\ldots,\alpha_k}_{\beta_1,\ldots,\beta_l} v_\gamma$, where $\mathbf{v}$ is the four velocity of the observer. Using

Boltzmann's equation Eq.(3.31), we can calculate the divergence of the observable flux-density,

$$\boxed{\frac{1}{\sqrt{-g}}\frac{\partial}{\partial x^{\mu}}\left(\sqrt{-g}\,\bar{t}^{\mu\alpha_1,\ldots,\alpha_k}_{\beta_1,\ldots,\beta_l}\right)=\int_{u^i\in\mathbb{R}^3}\frac{-\sqrt{-g}}{u_0}\left\{\mathrm{I}\left(x^{\mu},u^i\right)t^{\alpha_1,\ldots,\alpha_k}_{\beta_1,\ldots,\beta_l}\left(x^{\mu},u^i\right)+f\left(x^{\mu},u^i\right)\hat{\mathscr{L}}\left[t^{\alpha_1,\ldots,\alpha_k}_{\beta_1,\ldots,\beta_l}\right]\right\}d^3u}. \tag{3.46}$$

This equation is the relativistic analogous of **Maxwell-Enskog transfer equation**. Details of the demonstration are proposed in Appendix (C.3). This equation is valid for each species of the different fluid components. The application of this equation on mass (or on unity) gives the continuity equation of each component. For the momentum, it gives the conservation of the energy-momentum tensor of each component of the fluid. The derivation of these equations is the object of the next subsections.

Particle number conservation

If we take as tensorial observable the scalar function, which is 1 everywhere on the phase space, the density flux associated with this observable is the quantity already introduced called 4-current number Eq.(3.29). The application of the transfer equation gives the particle number conservation of each species.

$$\boxed{\begin{cases}\nabla\cdot\mathbf{J}_{+}=q_{+}=k_{\mathrm{N}}\\ \nabla\cdot\mathbf{J}_{-}=q_{-}=k_{\mathrm{N}}\\ \nabla\cdot\mathbf{J}_{\gamma}=q_{\gamma}=-2k_{\mathrm{N}}\end{cases}}. \tag{3.47}$$

The source term is,

$$\begin{aligned}k_{\mathrm{N}}=\int_{\frac{\mathbf{p}}{m_e}\in\Omega}\int_{\frac{\mathbf{q}}{m_e}\in\Omega}\int_{\mathbf{n}\in\mathscr{S}_{\mathbf{p}+\mathbf{q}^{\perp}}}&\left\{f_r\left(\frac{\mathbf{p}'}{m_e}\right)f_r\left(\frac{\mathbf{q}'}{m_e}\right)-f_{+}\left(\frac{\mathbf{p}'}{m_e}\right)f_{-}\left(\frac{\mathbf{q}}{m_e}\right)\right\}\\ &\mathrm{A}^{2r}_{-+}\left(\mathbf{p},\mathbf{q},\mathbf{n}\right)\sin^2\theta_{\mathbf{n}}d\theta_{\mathbf{n}}d\phi_{\mathbf{n}}\times\delta^3p\times\delta^3q\end{aligned} \tag{3.48}$$

In fact the symmetry of the differential cross section and the property of elastic collisions Eq.(3.34) imply that each contribution from the elastic collision is null. This is developed in details in Appendix (C.4). If we combine the electrons and the positrons together, we get the fluid of pairs separately from the fluid of photons. The four current of the fluid of pairs is simply the sum of the electron component and the positron component $\mathbf{J}=\mathbf{J}_{-}+\mathbf{J}_{+}$. Its divergence is,

$$\boxed{\nabla\cdot\mathbf{J}=2k_{\mathrm{N}}}. \tag{3.49}$$

This equation can be simply interpreted. The pair creation mechanism gives the amount of loading or unloading of pairs. k_{N} corresponds to the rate of pair creation in the fluid frame. Then $2k_{\mathrm{N}}$ corresponds to the rate of apparition of the particles, electrons or positron. Thus to estimate this rate and to see how it affects the continuity equation, the fundamental quantities to estimate are the differential cross sections of pairs creation $\mathrm{A}^{2\gamma}_{-+}\left(\mathbf{p},\mathbf{q},\mathbf{n}\right)$.

Conservation of momentum

If we take as tensorial observable the momentum of the particles, by definition, the momentum flux density of each component corresponds to the fluid contribution of each fluid component to the energy-momentum tensor,

$$\boxed{\mathbf{T}_{\mathrm{FL}}=mc^2\int_{u^i\in\mathbb{R}^3}\delta^3u\left[\mathbf{u}\otimes\mathbf{u}\,f\left(x^{\mu},u^i\right)\right]}. \tag{3.50}$$

m is the mass of the particles of the considered component.

Applying the transfer equation to each species, we get,

$$\boxed{\begin{aligned}\nabla\cdot\mathbf{T}_{\mathrm{FL},+}+\mathbf{F}\left(\frac{\mathbf{j}_+}{c},.\right)&=\mathbf{k}_{\rightarrow e_+}\\ \nabla\cdot\mathbf{T}_{\mathrm{FL},-}+\mathbf{F}\left(\frac{\mathbf{j}_-}{c},.\right)&=\mathbf{k}_{\rightarrow e_-}\\ \nabla\cdot\mathbf{T}_{\mathrm{FL},r}&=\mathbf{k}_{\rightarrow r}\end{aligned}}. \tag{3.51}$$

The details of the proof are given in Appendix (C.5). $\mathbf{j}_+$ or $\mathbf{j}_-$, is the charge current due to positrons or electrons, respectively. Each component may be decomposed into,

$$\begin{aligned}\mathbf{k}_{\rightarrow e_+}&=\mathbf{k}_{e_-\rightarrow e_+}+\mathbf{k}_{r\rightarrow e_+}+\mathbf{k}_{\rightarrow e_+}^{2r\rightleftharpoons e_++e_-}\\ \mathbf{k}_{\rightarrow e_-}&=\mathbf{k}_{e_+\rightarrow e_-}+\mathbf{k}_{r\rightarrow e_-}+\mathbf{k}_{\rightarrow e_-}^{2r\rightleftharpoons e_++e_-}\\ \mathbf{k}_{\rightarrow r}&=\mathbf{k}_{e_+\rightarrow r}+\mathbf{k}_{e_-\rightarrow r}+\mathbf{k}_{\rightarrow r}^{2r\rightleftharpoons e_++e_-}\end{aligned}. \tag{3.52}$$

It is possible to show that no force appears due to collisions between particles of the same species (internal forces to the fluid component). For interactions between different species, the explicit expression of the terms implies some equality between these terms. More fundamentally this is a consequence of the action/reaction principle. The action of an electron on a positron is the back reaction of the force of a positron on an electron $\mathbf{k}_{e_-\rightarrow e_+}+\mathbf{k}_{e_+\rightarrow e_-}=\mathbf{0}$. It is the same for elastic interactions between positrons or electrons and the neutral component $\mathbf{k}_{r\rightarrow e_+}+\mathbf{k}_{e_+\rightarrow r}=\mathbf{0}$ ($\mathbf{k}_{r\rightarrow e_-}+\mathbf{k}_{e_-\rightarrow r}=\mathbf{0}$). The last interaction concerns the creation of pairs. We get $\mathbf{k}_{\rightarrow e_+}^{2r\rightleftharpoons e_+e_-}+\mathbf{k}_{\rightarrow e_-}^{2r\rightleftharpoons e_+e_-}=-\mathbf{k}_{\rightarrow r}^{2r\rightleftharpoons e_+e_-}$. The action-reaction between components implies that the total stress energy tensor is conserved,

$$\nabla\cdot\left(\mathbf{T}_{\mathrm{FL},+}+\mathbf{T}_{\mathrm{FL},-}+\mathbf{T}_{\mathrm{FL},r}+\mathbf{T}_{\mathrm{EM}}\right)=\mathbf{0}. \tag{3.53}$$

Indeed, we have used here the well know result that $\mathbf{F}\left(\mathbf{j},.\right)=\nabla\cdot\mathbf{T}_{\mathrm{EM}}$. Yet, the object of our work is to study the effect on pair fluid of the pair injection mechanism. So as in the last section, we need to consider the fluid of pairs. Introducing $\mathbf{k}_{r\rightarrow e_+e_-}^{\mathrm{Elastic}}=\mathbf{k}_{r\rightarrow e_+}+\mathbf{k}_{r\rightarrow e_-}$, the force of elastic collisions between pairs and neutrals is $\mathbf{k}_{\rightarrow e_+e_-}^{2r\rightleftharpoons e_++e_-}=\mathbf{k}_{(2r\rightleftharpoons e_++e_-)\rightarrow e_+}+\mathbf{k}_{(2r\rightleftharpoons e_++e_-)\rightarrow e_-}$. This is the force on pairs due to the creation of pairs and $\mathbf{T}_{\mathrm{FL}}=\mathbf{T}_{\mathrm{FL},+}+\mathbf{T}_{\mathrm{FL},-}$ is the energy momentum tensor of pair plasma fluid. We get,

$$\boxed{\nabla\cdot\mathbf{T}_{\mathrm{FL}}+\mathbf{F}\left(\frac{\mathbf{j}}{c},.\right)=\mathbf{k}_{r\rightarrow e_+e_-}^{\mathrm{Elastic}}+\mathbf{k}_{\rightarrow e_+e_-}^{2r\rightleftharpoons e_+e_-}\qquad\Longleftrightarrow\qquad\nabla\cdot\mathbf{T}_{\mathrm{MHD}}=\mathbf{k}_{r\rightarrow e_+e_-}^{\mathrm{Elastic}}+\mathbf{k}_{\rightarrow e_+e_-}^{2r\rightleftharpoons e_+e_-}}. \tag{3.54}$$

where $\mathbf{T}_{\mathrm{MHD}}=\mathbf{T}_{\mathrm{FL}}+\mathbf{T}_{\mathrm{EM}}$ with for the electro-magnetic energy momentum tensor,

$$\boxed{\mathrm{T}_{\mathrm{EM}}^{\alpha\beta}=\frac{1}{4\pi}\left[\mathrm{F}^{\alpha}{}_{\mu}\mathrm{F}^{\mu\beta}-\frac{\mathrm{F}^{\mu\nu}\mathrm{F}_{\mu\nu}}{4}g^{\alpha\beta}\right]}. \tag{3.55}$$

Thus there are two processes applying forces on pairs.

First, there is the elastic collision with neutrals, which is the force due to Compton/Inverse – Compton effect on the fluid when the neutral component is composed of photons.

$$\begin{aligned}\mathbf{k}_{r\rightarrow e_+e_-}^{\mathrm{Elastic}}=\int_{\frac{\mathbf{p}}{m_e}\in\Omega}\int_{\frac{\mathbf{q}}{m_e}\in\Omega}\int_{\mathbf{n}\in\mathscr{S}_{\mathbf{p}+\mathbf{q}^\perp}}\mathbf{p}\Bigg[&\left\{f_+\left(\frac{\mathbf{p}'}{m_e}\right)f_r\left(\frac{\mathbf{q}'}{m_e}\right)-f_+\left(\frac{\mathbf{p}'}{m_e}\right)f_r\left(\frac{\mathbf{q}}{m_e}\right)\right\}\mathrm{A}_{+r}^{+r}\left(\mathbf{p},\mathbf{q},\mathbf{n}\right)\\ &+\left\{f_-\left(\frac{\mathbf{p}'}{m_e}\right)f_r\left(\frac{\mathbf{q}'}{m_e}\right)-f_-\left(\frac{\mathbf{p}'}{m_e}\right)f_r\left(\frac{\mathbf{q}}{m_e}\right)\right\}\mathrm{A}_{+r}^{+r}\left(\mathbf{p},\mathbf{q},\mathbf{n}\right)\Bigg]\sin^2\theta_{\mathbf{n}}d\theta_{\mathbf{n}}d\phi_{\mathbf{n}}\times\delta^3p\times\delta^3q\end{aligned}, \tag{3.56}$$

Second, there is the force on the pairs by the creation/annihilation mechanism,

$$\begin{aligned}\mathbf{k}_{\rightarrow e_+e_-}^{2r\rightleftharpoons e_+e_-}=\int_{\frac{\mathbf{p}}{m_e}\in\Omega}\int_{\frac{\mathbf{q}}{m_e}\in\Omega}\int_{\mathbf{n}\in\mathscr{S}_{\mathbf{p}+\mathbf{q}^\perp}}&\left(\mathbf{p}+\mathbf{q}\right)\left\{f_r\left(\mathbf{p}'\right)f_r\left(\mathbf{q}'\right)-f_+\left(\frac{\mathbf{p}}{m_e}\right)f_-\left(\frac{\mathbf{q}}{m_e}\right)\right\}\mathrm{A}_{+-}^{2r}\left(\mathbf{p},\mathbf{q},\mathbf{n}\right)\\ &\sin^2\theta_{\mathbf{n}}d\theta_{\mathbf{n}}d\phi_{\mathbf{n}}\times\delta^3p\times\delta^3q\end{aligned}, \tag{3.57}$$

3.1.9 H Theorem

Using for the i-th species $t = -k_{\mathrm{B}}\left[\ln\left(f_i\right)\right) - 1\right]$ in the equation of transfer Eq.(3.46), we get,

$$\nabla \cdot \mathbf{s}_i = -k_{\mathrm{B}} \int_{u^j \in \mathbb{R}^3} \delta^3 u \ln\left(f_i\left(x^{\mu}, u^i\right)\right) \mathrm{I}_i\left(x^{\mu}, u^i\right) \tag{3.58}$$

Precisions on the derivation are given in Appendix C.6). The entropy flux density of $i-$th species $\mathbf{s}_i$ is defined as,

$$\mathbf{s}_i = -k_{\mathrm{B}} \int_{u^j \in \mathbb{R}^3} \delta^3 u\, \mathbf{u} \left[\ln\left(f\left(x^{\mu}, u^i\right)\right) - 1\right] f\left(x^{\mu}, u^i\right) \tag{3.59}$$

Using the symmetry of the differential cross section and changing of variables in the collision integral, the total enthalpy flux density $\mathbf{s} = \mathbf{s}_+ + \mathbf{s}_- + \mathbf{s}_r$ verifies,

$$\nabla \cdot \mathbf{s} = s_{c\,++}^{\;++} + s_{c\,--}^{\;--} + s_{c\,2r}^{\;2r} + s_{c\,+-}^{\;+-} + s_{c\,+-}^{\;2r}, \tag{3.60}$$

where,

$$\begin{cases} s_{c\,++}^{\;++} = \dfrac{k_{\mathrm{B}}}{4} \displaystyle\int_{\frac{\mathbf{p}}{m_e} \in \Omega} \int_{\frac{\mathbf{q}}{m_e} \in \Omega} \int_{\mathbf{n} \in \mathscr{S}_{\mathbf{p}+\mathbf{q}^{\perp}}} \ln\left(\dfrac{f_+(\mathbf{p}) f_+(\mathbf{q})}{f_+(\mathbf{p}') f_+(\mathbf{q}')}\right) \left[f_+(\mathbf{p}') f_+(\mathbf{q}') - f_+(\mathbf{p}) f_+(\mathbf{q})\right] \mathrm{A}_{++}^{++}(\mathbf{p}, \mathbf{q}, \mathbf{n})\, \delta^2 n \times \delta^3 p \times \delta^3 q \\ s_{c\,--}^{\;--} = \dfrac{k_{\mathrm{B}}}{4} \displaystyle\int_{\frac{\mathbf{p}}{m_e} \in \Omega} \int_{\frac{\mathbf{q}}{m_e} \in \Omega} \int_{\mathbf{n} \in \mathscr{S}_{\mathbf{p}+\mathbf{q}^{\perp}}} \ln\left(\dfrac{f_-(\mathbf{p}) f_-(\mathbf{q})}{f_-(\mathbf{p}') f_-(\mathbf{q}')}\right) \left[f_-(\mathbf{p}') f_-(\mathbf{q}') - f_-(\mathbf{p}) f_-(\mathbf{q})\right] \mathrm{A}_{--}^{--}(\mathbf{p}, \mathbf{q}, \mathbf{n})\, \delta^2 n \times \delta^3 p \times \delta^3 q \\ s_{c\,-+}^{\;-+} = \dfrac{k_{\mathrm{B}}}{4} \displaystyle\int_{\frac{\mathbf{p}}{m_e} \in \Omega} \int_{\frac{\mathbf{q}}{m_e} \in \Omega} \int_{\mathbf{n} \in \mathscr{S}_{\mathbf{p}+\mathbf{q}^{\perp}}} \ln\left(\dfrac{f_-(\mathbf{p}) f_+(\mathbf{q})}{f_-(\mathbf{p}') f_+(\mathbf{q}')}\right) \left[f_-(\mathbf{p}') f_+(\mathbf{q}') - f_-(\mathbf{p}) f_+(\mathbf{q})\right] \mathrm{A}_{-+}^{-+}(\mathbf{p}, \mathbf{q}, \mathbf{n})\, \delta^2 n \times \delta^3 p \times \delta^3 q \\ s_{c\,rr}^{\;-+} = \dfrac{k_{\mathrm{B}}}{4} \displaystyle\int_{\frac{\mathbf{p}}{m_e} \in \Omega} \int_{\frac{\mathbf{q}}{m_e} \in \Omega} \int_{\mathbf{n} \in \mathscr{S}_{\mathbf{p}+\mathbf{q}^{\perp}}} \ln\left(\dfrac{f_r(\mathbf{p}) f_r(\mathbf{q})}{f_-(\mathbf{p}') f_+(\mathbf{q}')}\right) \left[f_r(\mathbf{p}') f_r(\mathbf{q}') - f_-(\mathbf{p}) f_+(\mathbf{q})\right] \mathrm{A}_{-+}^{rr}(\mathbf{p}, \mathbf{q}, \mathbf{n})\, \delta^2 n \times \delta^3 p \times \delta^3 q \end{cases} \tag{3.61}$$

Because the distribution function and the differential cross section are positive functions and also because the function $x \longrightarrow \ln x\,(x-1)$ is positive for all positive reals, we deduce that all terms are positive terms. We get the so-called **H theorem**, which is equivalent to the second principle of thermodynamics,

$$\boxed{\nabla \cdot \mathbf{s} \geq 0} \tag{3.62}$$

3.1.10 Notion of thermodynamics equilibrium

We assume that the positron component and the electron component are in thermodynamical equilibrium if we have $s_{c\,++}^{\;++} = 0$ and $s_{c\,--}^{\;--} = 0$, respectively. The positron and electron are in equilibrium means $s_{c\,+-}^{\;+-} = 0$. The neutral component and the positron (electron) gas are in equilibrium only if $s_{+r}^{+r} = 0$ ($s_{-r}^{-r} = 0$, respectively). The pair creation-annihilation transformation is in thermodynamical equilibrium if $s_{c\,+-}^{\;2r} = 0$. The thermodynamical equilibrium implies that the distribution function is a **Maxwell distribution**.

If we impose thermodynamical equilibrium between massive species of index $i + j \rightleftharpoons k + l$, it is possible to prove (see Appendix C.7) that,

$$\begin{array}{l} i + j \rightleftharpoons k + l \\ \text{in equilibrium} \end{array} \quad \Leftrightarrow \quad \begin{cases} \left.\begin{array}{ll} \forall \mathrm{M}(x^{\mu}) \in \mathscr{M} & \exists \mathrm{T} \in \mathbb{R} \quad \text{and} \quad \mathbf{u}_{fl} \in \mathscr{T}_{\mathrm{M}}(\mathscr{M}) \\ \exists a_i, a_j, a_k, a_l \in \mathbb{R} & \text{such that } a_i a_j = a_k a_l \end{array}\right\} \begin{array}{l} \text{wich depends of the} \\ \text{position on spacetime} \end{array} \\ f_i\left(x^{\mu}, u^i\right) = a_i\left(x^{\mu}\right) \exp\left(\beta_i \mathbf{u}_{fl} \cdot \mathbf{u}\right) \qquad f_j\left(x^{\mu}, u^i\right) = a_j\left(x^{\mu}\right) \exp\left(\beta_j \mathbf{u}_{fl} \cdot \mathbf{u}\right) \\ f_k\left(x^{\mu}, u^i\right) = a_k\left(x^{\mu}\right) \exp\left(\beta_k \mathbf{u}_{fl} \cdot \mathbf{u}\right) \qquad f_l\left(x^{\mu}, u^i\right) = a_l\left(x^{\mu}\right) \exp\left(\beta_l \mathbf{u}_{fl} \cdot \mathbf{u}\right) \end{cases}, \tag{3.63}$$

where $\beta_i = \frac{m_i c^2}{k_{\mathrm{B}} \mathrm{T}}$ for massive particles. This factor defines the temperature of the equilibrium. The four vector $\mathbf{u}_{fl}$ is the four velocity of the fluid, thus it is a unit time vector. The scalars

a_i, a_j, a_k, a_l are linked to the number of particles per unit volume in the fluid referential frame for each species.

$$\frac{n}{a} = \frac{\partial Z}{\partial \beta} \quad \Rightarrow \quad Z(\beta) = -\int_{u^i \in \mathbb{R}^3} \delta^3 u \exp\left[\beta \mathbf{u}_{fl} \cdot \mathbf{u}\right] \tag{3.64}$$

For photons, this expression is not convenient because it does not follow Planck's law for a black body. Thus, to treat properly the gas of photons, an analysis based on quantum mechanics is required.

3.2 Pair plasma gas in thermodynamical equilibrium

To have an idea of the behavior of the pair plasma, we look at the consequences of the gas equilibrium. We derive an expression of the Feynman current, the energy-momentum tensor and the entropy flux density. This gives us a way to get an expression of the pairs production rate and of the recoiling forces due to pair production.

3.2.1 Synge-Jüttner distribution function

First of all, we consider that the gas of pairs is in thermodynamical equilibrium, which implies that each of its component is in equilibrium. Thus the distribution function is,

$$\begin{cases} f_+\left(x^\mu, u^i\right) = n_+(x^\mu) \dfrac{\exp\left[\beta_+ \mathbf{u}_{fl} \cdot \mathbf{u}\right]}{\dfrac{\partial Z}{\partial \beta}(\beta_+)} \\ f_-\left(x^\mu, u^i\right) = n_-(x^\mu) \dfrac{\exp\left[\beta_- \mathbf{u}_{fl} \cdot \mathbf{u}\right]}{\dfrac{\partial Z}{\partial \beta}(\beta_-)} \end{cases}, \tag{3.65}$$

where $\beta_+ = \frac{m_+ c^2}{k_B T}$ and $\beta_- = \frac{m_- c^2}{k_b T}$, n_+ and n_- is the density in the fluid rest frame, of four-speed $\mathbf{u}_{fl}$. The unique temperature T expresses that the two components are in equilibrium together. Using adapted orthonormal basis in tangent spacetime Eq.(3.10) gives,

$$\boxed{Z(\beta) = -\frac{4\pi K_1(\beta)}{\beta} = -\int_{u^i \in \mathbb{R}^3} \delta^3 u \exp\left[\beta \mathbf{u}_{fl} \cdot \mathbf{u}\right]}. \tag{3.66}$$

$(K_n)_{n\in\mathbb{N}}$ is a modified Bessel function of the second kind, which significant properties are described in Appendix.(A.5). In this notation, the number four current is,

$$\left.\begin{array}{l} \mathbf{J}_+ = n_+ \mathbf{u}_{fl} \\ \mathbf{J}_- = n_- \mathbf{u}_{fl} \end{array}\right\} \quad \Rightarrow \quad \begin{array}{l} \rho_0 \mathbf{u}_{fl} = m_+ \mathbf{J}_+ + m_- \mathbf{J}_- \\ \text{where} \quad \rho_0 = m_+ n_+ + m_- n_- \end{array}. \tag{3.67}$$

We introduce here the mass flux density $\rho_0 \mathbf{u}_{fl}$ of the two fluid components.

3.2.2 Energy momentum tensor

Using the definition, Eq.3.50, and the expression of the distribution function Eq.(3.65) and introducing $\mathbf{b} = \beta \mathbf{u}_{fl}$, we find,

$$\begin{cases} T^{\alpha\beta}_{+,fl} = -m_+ c^2 n_+ \left[\dfrac{\dfrac{\partial}{\partial b^\alpha_+}\left(\dfrac{\partial Z}{\partial b^\beta_+}\right)}{\dfrac{\partial Z}{\partial \beta_+}}\right] \\ T^{\alpha\beta}_{-,fl} = -m_+ c^2 n_- \left[\dfrac{\dfrac{\partial}{\partial b^\alpha_-}\left(\dfrac{\partial Z}{\partial b^\beta_-}\right)}{\dfrac{\partial Z}{\partial \beta_-}}\right] \end{cases}, \tag{3.68}$$

Using Eqs.(C.17,C.18) and Eq. (A.12), we get,

$$\left.\begin{aligned}\mathbf{T}_{+,fl} &= n_+ m_+ c^2 \left[\frac{\mathrm{K}_3(\beta_+)}{\mathrm{K}_2(\beta_+)}\mathbf{u}_{fl}\otimes\mathbf{u}_{fl} + \frac{1}{\beta_+}\mathbf{g}\right]\\ \mathbf{T}_{-,fl} &= n_- m_- c^2 \left[\frac{\mathrm{K}_3(\beta_-)}{\mathrm{K}_2(\beta_-)}\mathbf{u}_{fl}\otimes\mathbf{u}_{fl} + \frac{1}{\beta_-}\mathbf{g}\right]\end{aligned}\right\} \quad\Rightarrow\quad \begin{aligned}&\mathbf{T}_{fl,-+} = \rho_0 \xi c^2 \mathbf{u}_{fl}\otimes\mathbf{u}_{fl} + \mathrm{P}\mathbf{g}\\ &\text{where}\quad \xi = \frac{m_+ n_+ \frac{\mathrm{K}_3(\beta_+)}{\mathrm{K}_2(\beta_+)} + m_- n_- \frac{\mathrm{K}_3(\beta_-)}{\mathrm{K}_2(\beta_-)}}{m_+ n_+ + m_- n_-}\\ &\text{and}\quad \mathrm{P} = (n_+ + n_-)\, k_\mathrm{B}\mathrm{T} = n k_\mathrm{B}\mathrm{T}\end{aligned} \tag{3.69}$$

Then we interpreted ξ as the adimensionate specific enthalpy of the pairs plasma fluid. Then the internal energy at equilibrium of positron (electron) component is $1+\frac{e_+(\beta_+)}{c^2} = \frac{\mathrm{K}_3(\beta_+)}{\mathrm{K}_2(\beta_+)} - \frac{1}{\beta_+}$ ($1+\frac{e_-(\beta_-)}{c^2} = \frac{\mathrm{K}_3(\beta_-)}{\mathrm{K}_2(\beta_-)} - \frac{1}{\beta_-}$). P is the pressure of the pair fluid.

3.2.3 Specific entropy

For the entropy flux density, a quick calculation using the same method as for the energy momentum tensor leads to,

$$\begin{aligned}\mathbf{s}_{+-} &= s_+\mathbf{J}_+ + s_-\mathbf{J}_-\\ &= (n_+ s_+ + n_- s_-)\,\mathbf{u}_{fl} = n s \mathbf{u}_{fl}\end{aligned} \quad \text{where} \quad \left\{\begin{aligned}s_+ &= k_\mathrm{B}\left[\beta_+ \frac{\mathrm{K}_3(\beta_+)}{\mathrm{K}_2(\beta_+)} + \ln\left(\frac{4\pi \mathrm{K}_2(\beta_+)}{n_+\beta_+}\right)\right]\\ s_- &= k_\mathrm{B}\left[\beta_- \frac{\mathrm{K}_3(\beta_-)}{\mathrm{K}_2(\beta_-)} + \ln\left(\frac{4\pi \mathrm{K}_2(\beta_-)}{n_-\beta_-}\right)\right]\end{aligned}\right. . \tag{3.70}$$

If there are no third species, there cannot be creation of pairs then $k_\mathrm{N} = 0$ and thus $\nabla\cdot n\mathbf{u}_{fl} = 0$. In this case, the H-theorem Eq.(3.62) becomes $\nabla_{\mathbf{u}_{fl}} s \geq 0$, which means that the specific entropy should increase along the fluid world line.

3.2.4 First principle

If we have a fluid particle of a single gas component in thermodynamical equilibrium, Eqs. (3.70, 3.69) lead to the link between the differential forms,

$$d\xi = \frac{d\mathrm{P}}{\rho_0 c^2} + \frac{\mathrm{T}}{mc^2} ds \tag{3.71}$$

This parallel evolution between these quantities is true for a gas in thermodynamical equilibrium. Indeed, the temperature is properly defined only for such a gas.

3.2.5 Specific internal energy

The specific energy is the energy per unit of mass in the fluid frame. The specific internal energy corresponds to the specific energy of the fluid, where one removes the rest mass energy. To build the density flux of the internal energy, we need to use Eq.(3.45) choosing $t = mc^2(-\mathbf{u}_{fl}\cdot\mathbf{u} - 1)$. From there we can easily show that the specific energy of each species is linked to the fluid referential component of the energy-momentum tensor of the species via $n_+ m_+ c^2\left(1+\frac{e_+}{c^2}\right) = \mathbf{T}_{+,fl}\left(\mathbf{u}_{fl},\mathbf{u}_{fl}\right)$,

$$\left\{\begin{aligned}\frac{e_+}{c^2} &= e(\beta_+) = \frac{\mathrm{K}_1(\beta_+)}{\mathrm{K}_2(\beta_+)} + \frac{3}{\beta_+} - 1\\ \frac{e_-}{c^2} &= e(\beta_-) = \frac{\mathrm{K}_1(\beta_-)}{\mathrm{K}_2(\beta_-)} + \frac{3}{\beta_-} - 1\end{aligned}\right. \quad\Rightarrow\quad e = \frac{n_+ m_+ e_+ + n_- m_- e_-}{n_+ m_+ + n_- m_-} = \xi - 1 - \frac{\mathrm{P}}{\rho_0 c^2} . \tag{3.72}$$

This equation, which links the specific internal energy with the temperature, is called the (Equation of state (EOS)). This EOS ($e = e(\beta)$) is valid for gas in thermodynamical equilibrium and for relativistic and non-relativistic temperature regimes. This form of EOS was first derived by Synge [1957]. Thus we call this equation of states the **Synge** EOS.

3.2.6 Taub-Mathews approximation

For pair fluid in thermodynamical equilibrium, the internal energy of each component follows a Synge's EOS Eq.(3.72). We can study the different regimes of the Synge's EOS with temperature Eq.(3.72). For ultra-relativistic temperatures, $\beta \to 0$ and the non-relativistic temperatures correspond to $\beta \to \infty$. Using the expansion $\frac{K_1(u)}{K_2(u)} \underset{u\to 0}{\sim} \frac{u}{2}$ and $\frac{K_1(u)}{K_2(u)} \underset{u\to\infty}{\sim} 1 - \frac{3}{2u}$ we remark that in the relativistic regime,

$$1 + \frac{e(\beta)}{c^2} - \frac{1}{1 + \frac{e(\beta)}{c^2}} \underset{\beta\to 0}{\sim} \frac{3}{\beta} \tag{3.73}$$

In the non relativistic regime we also have,

$$1 + \frac{e(\beta)}{c^2} - \frac{1}{1 + \frac{e(\beta)}{c^2}} \underset{\beta\to\infty}{\sim} 1 + \frac{3}{2\beta} - \frac{1}{1 + \frac{3}{2\beta}} \underset{\beta\to\infty}{\sim} \frac{3}{\beta} \tag{3.74}$$

Thus Taub and Mathews proposed an approximation to the Synge EOS, which is given by,

$$\boxed{\frac{1}{\beta} = \frac{1}{3}\left(1 + \frac{e(\beta)}{c^2} - \frac{1}{1 + \frac{e(\beta)}{c^2}}\right) = \frac{P}{\rho_0 c^2}}. \tag{3.75}$$

The last equality is valid only for a single component or for fluid with two-components where $m_+ = m_-$. That we can write,

$$\frac{e}{c^2} = \frac{3}{2}\frac{P}{\rho_0 c^2} + \sqrt{1 + \left(\frac{3}{2}\frac{P}{\rho_0 c^2}\right)^2} - 1 \tag{3.76}$$

This law, that we call **Taub-Mathews' approximate equation of state**, follows the behavior of the Synge's equation of state in both relativistic and non relativistic temperature regimes. We can check this on the graph comparing the internal energy using synge Juttner EOS or Taub-Mathews's one in Fig. (3.3) and the graphic drawing the effective polytropic index $d\frac{e}{c^2} = \frac{1}{\Gamma_{\text{eff}}-1} d\frac{P}{\rho_0 c^2}$ in Fig. (3.4).

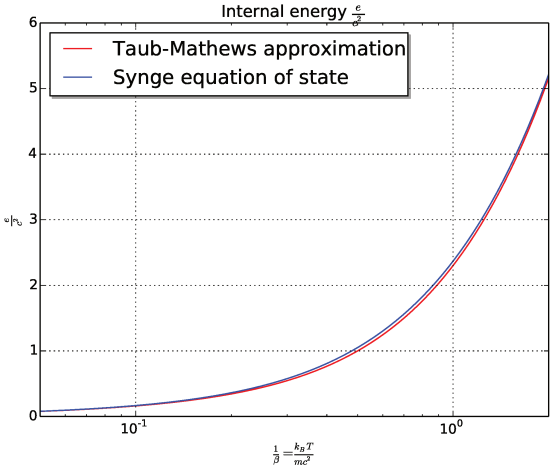

Figure 3.3 – Specific internal energy for Synge equation of state and Taub-Matthews approximate equation of state

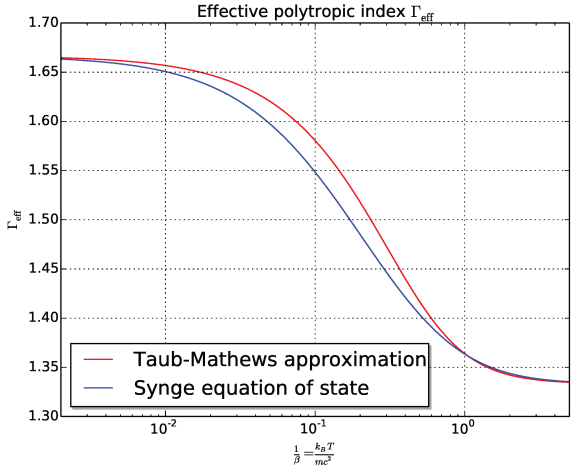

Figure 3.4 – Effective polytropic index for Synge's equation of state and Taub-Matthews' approximate equation of state

The Taub-Mathews' approximation Eq.(3.75) for a specific internal energy of a gas in thermodynamical equilibrium is a good alternative to Synge's equation of state. Indeed this EOS is more practical for analytical and numerical purposes because there is no need to calculate the second

special modified Bessel function. Mignone and McKinney [2007] investigated the difference on numerical simulations between different Γ-law equations of state ($\frac{e}{c^2} = \frac{1}{\Gamma-1}\frac{1}{\beta}$ for non-relativistic and ultra-relativistic Γ polytropic index) and the Taub-Matthews' equation of state for adiabatic flows, using the PLUTO code.

3.2.7 How the mechanism of pair creation acts on the dynamics?

To understand how the mechanism of pair creation acts on the dynamics, an interesting sub case to explore consists on studying a gas composed of three species (electrons, positrons and neutrinos), in which all kind elastic collision is in thermodynamical equilibrium. That is to say all elastic collision between particles of a singles species $e_+e_+ \rightleftharpoons e_+e_+$, $e_-e_- \rightleftharpoons e_-e_-$, $\nu\nu \rightleftharpoons \nu\nu$, $\bar{\nu}\bar{\nu} \rightleftharpoons \bar{\nu}\bar{\nu}$, but also all elastic collision between two different species $e_+e_- \rightleftharpoons e_+e_-$, $e_+\nu \rightleftharpoons e_+\nu$, $e_-\nu \rightleftharpoons e_-\nu$ are supposed to be in thermodynamics equilibrium. Then the distribution function of all species is equals to a Maxwell distribution function with the same temperature and the same fluid four velocity,

$$\begin{cases} f_{e_+}(x^\mu, \mathbf{u}) = a_{e_+}(x^\mu)\exp\left(\beta_e \mathbf{u}_{\rm fl}\cdot\mathbf{u}\right) \\ f_{e_-}(x^\mu, \mathbf{u}) = a_{e_-}(x^\mu)\exp\left(\beta_e \mathbf{u}_{\rm fl}\cdot\mathbf{u}\right) \\ f_{\nu}(x^\mu, \mathbf{u}) = a_{\nu}(x^\mu)\exp\left(\beta_\nu \mathbf{u}_{\rm fl}\cdot\mathbf{u}\right) \\ f_{\bar{\nu}}(x^\mu, \mathbf{u}) = a_{\bar{\nu}}(x^\mu)\exp\left(\beta_\nu \mathbf{u}_{\rm fl}\cdot\mathbf{u}\right) \end{cases} \tag{3.77}$$

with $\beta_e = \frac{m_e c^2}{k_{\rm B}T}$ and $\beta_\nu = \frac{_\nu c^2}{k_{\rm B}T}$. Nevertheless we do not make assumption of equilibrium for inelastic reaction $\nu\bar{\nu} \rightleftharpoons e_+e_-$, then a priori we do not have $a_{e_+}a_{e_-} \neq a_\nu a_{\bar{\nu}}$. In this case, we are able to calculate the direction and the evolution of the amplitude of the creation rate and the forces due to the creation/annihilation of pairs $\nu\bar{\nu} \rightleftharpoons e_+e_-$. Then the number of particles creation/annihilation rate $k_{\rm N}$ and the force $\mathbf{k}^{2\nu\rightleftharpoons e_+e_-}_{\rightarrow e_+e_-}$ due to the creation/annihilation mechanism are given by

$$\begin{cases} k_{\rm N} = \left[a_\nu a_{\bar{\nu}} - a_{e_+}a_{e_-}\right] {\rm F}^{2\nu\rightleftharpoons e_+e_-}_{\rightarrow e_+e_-}(\beta) \\ \mathbf{k}^{2\nu\rightleftharpoons e_+e_-}_{\rightarrow e_+e_-} = -\left[a_\nu a_{\bar{\nu}} - a_{e_+}a_{e_-}\right]\dfrac{\partial {\rm F}^{2r\rightleftharpoons e_+e_-}_{\rightarrow e_+e_-}}{\partial\beta}(\beta)\,\mathbf{u}_{\rm FL} \end{cases} \quad \text{where} \quad {\rm F}^{2\nu\rightleftharpoons e_+e_-}_{\rightarrow e_+e_-}({\rm T}) = \int_{\frac{\mathbf{p}}{m_e}\in\Omega}\int_{\frac{\mathbf{q}}{m_e}\in\Omega}\int_{\mathbf{n}} {\rm A}^{2\nu}_{+-}(\mathbf{p},\mathbf{q},\mathbf{n}) \exp\left[\frac{\beta}{m_e}\mathbf{u}_{\rm FL}\cdot(\mathbf{p}+\mathbf{q})\right]\sin^2\theta_{\mathbf{n}}\, d\theta_{\mathbf{n}} d\phi_{\mathbf{n}} \times \delta^3 p \times \delta^3 q \,, \tag{3.78}$$

where $\beta = \frac{m_e c^2}{k_{\rm B}T}$ and ${\rm F}^{2\nu\rightleftharpoons e_+e_-}_{\rightarrow e_+e_-}(\beta)$ is a positive and decreasing scalar function of β. Then the pair creation rate increases with temperature. The function ${\rm F}^{2\nu\rightleftharpoons e_+e_-}_{\rightarrow e_+e_-}(\beta)$ is characteristic of the differential cross section of this mechanism. The creation/annihilation rate is a function of the sign $[a_\nu a_{\bar{\nu}} - a_+a_-]$. If $a_\nu a_{\bar{\nu}} \geq a_+a_-$, the pair creation rate is bigger than the annihilation rate and if $a_\nu a_{\bar{\nu}} \leq a_+a_-$, pairs annihilation rate is bigger than creation rate. The equilibrium of this mechanism is reach when,

$$\left.\frac{n_\nu n_{\bar{\nu}}}{n_+ n_-}\right|_{\rm eq} = \left(\frac{{\rm K}_2(\beta_\nu)}{{\rm K}_2(\beta)}\frac{m_e}{m_\nu}\right)^2, \tag{3.79}$$

where $\beta_\nu = \frac{m_\nu c^2}{k_{\rm B}T}$. Because of the very low mass of the neutrinos, this equilibrium constant means that the process is efficient for a very high density of neutrinos in comparison to the density of pairs. In fact, due to modified Bessel fonction property we have $n_\nu n_{\bar{\nu}}/n_{e_+}n_{e_-} \longrightarrow (m_e/m_\nu) \sim (1/4.8\times10^{-3})^6 \sim 7.3\times10^{13}$ for highly relativistic temperature. The equilibrium fraction Fig.(3.5) decrease with the temperature which means that this is more easy to produce pairs for relativistic temperature. In this case the pair production rate is positive and the four-force exerted on the pair fluid is oriented in the direction of the four velocity of the fluid. In fact the neutrinos, which are the source of pairs, transfer their momentum to the pair fluid. The momentum of neutrino fluid is oriented along $\mathbf{u}_{fl}$. It is the same for the forces.

In a more general case, let us consider, that neutrinos are in thermodynamic equilibrium. And the pairs are in thermodynamic equilibrium, without imposing balance of elastic collisions between

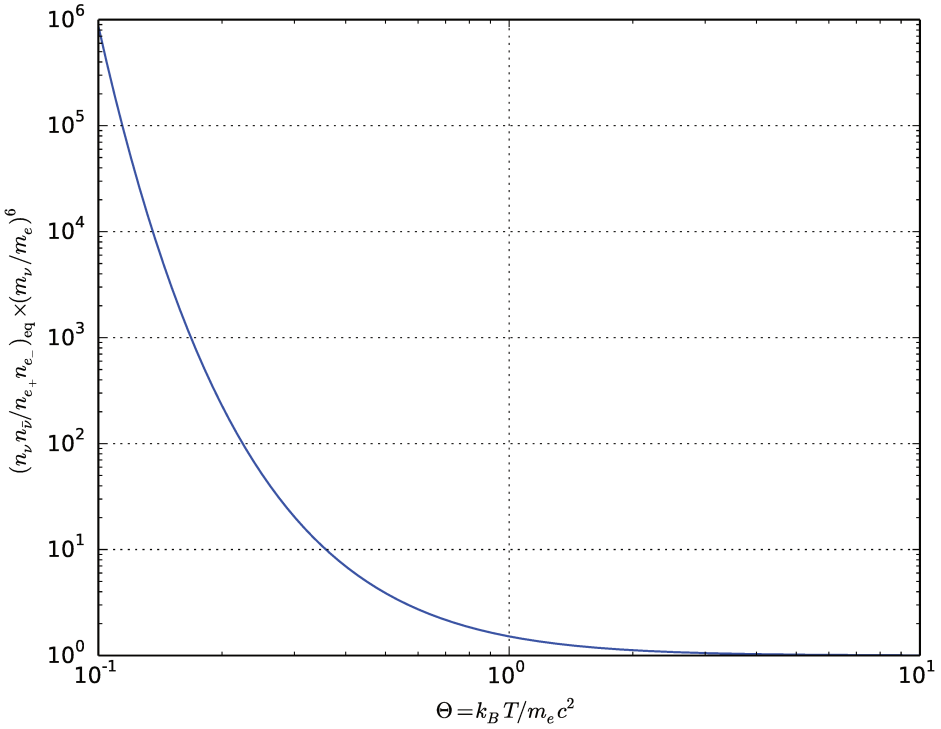

Figure 3.5 – Value of $\frac{n_\nu n_{\bar{\nu}}}{n_{e_+} n_{e_-}}$ when creation and annihilation of electron positron pairs from neutrino and anti-neutrino reach equilibrium for different value of temperature Θ

neutrinos and the pairs. Then we obtain a temperature $\mathrm{T}_{\mathrm{pairs}}$ and a four velocity $\mathbf{u}_{\mathrm{pairs}}$ for the pairs and a temperature T_ν and a four velocity $\mathbf{u}_\nu$ for the neutrinos. Reasonably the four-force due to the creation of pairs must be inside the 2D plane $\mathrm{Span}\left(\mathbf{u}_{\mathrm{pairs}}, \mathbf{u}_\nu\right)$.

3.3 Heated fluid

A lot of astrophysical phenomena, as the acceleration of the solar wind, can be explained only if we consider that there is a source of heating. In this section, we explore different ways to treat this heating in the relativistic regime. First, we briefly summarize the treatment of heating by conduction. Then we explore how to treat a fluid containing an additional source of internal energy.

3.3.1 Conductive heating

We change notation replacing $\mathbf{u}_{fl}$ by $\mathbf{u}$. The treatment of conduction in general relativity has been discussed at length since the first proposition of Eckart [1940]. Indeed this treatment of conduction changed the nature of the equations of hydrodynamics, allowing waves to propagate at super luminous velocities, which is physically problematic with respect to the causality principle. Landau and Lifshitz [1958] also proposed a model but it suffers the same kind of problem as Eckart's model. Marle [1969b] solved Krook's equation near equilibrium (Boltzmann's equation with a collision term replaced by a relaxation term). Using Chapman-Enskog expansion, he ended up to a model close to Eckart's one. After Carter [1988] proposed the so-called regular solution to this problem.

We expose here Eckart's formulation. Its formulation consists to introducing the heat flux $\mathbf{q}$

to write the mass flux density flux $\mathbf{P}$ and the energy momentum tensor $\mathbf{T}$ of the fluid as,

$$\begin{cases} \mathbf{T} = \rho_0 \xi c^2 \mathbf{u}\otimes\mathbf{u} + \mathbf{q}\otimes\mathbf{u} + \mathbf{u}\otimes\mathbf{q} + \mathrm{P}\mathbf{g} \\ \mathbf{P} = \rho_0 \mathbf{u} \end{cases} \qquad \xi = 1 + \frac{e}{c^2} + \frac{\mathrm{P}}{\rho_0 c^2} \quad \text{with}$$

$$\Downarrow \qquad \text{where} \qquad de = -\mathrm{P}d\frac{1}{\rho_0} + \mathrm{T}ds \quad ,$$

$$\begin{cases} \nabla\cdot\mathbf{T} = \mathbf{0} \\ \nabla\cdot\mathbf{P} = 0 \end{cases} \qquad \mathbf{q} = -\kappa\mathrm{T}^2\left(\mathbf{g}+\mathbf{u}\otimes\mathbf{u}\right)\cdot\left[\nabla\mathrm{T} + \frac{1}{\mathrm{T}}\mathbf{a}\right] \tag{3.80}$$

where $\mathbf{a} = \nabla_{\mathbf{u}}\mathbf{u}$ and s are the specific entropies. The constant κ is the scalar conductivity of the fluid. Marle [1969b], gives a value of this conductivity as a function of the temperature T, the rest frame mass density ρ_0 and the relaxation time of the distribution function. The expression of $\mathbf{q}$ is the simplest expression leading in any case to an increase of the entropy.

3.3.2 Isotropic non-equilibrium distribution function

In our model, we consider a plasma with no heat flux. Here the "internal" energy and the pressure contain some additional terms for which the nature is not explored here. However, it should be noted that these terms could incorporate effects due to turbulence or the installation of stationary MHD waves in the plasma.

In general, we can build a distribution function for the two-component fluid, $(m_+ + m_-)\, f_{+-} = m_+ f_+ + m_- f_-$. Indeed f allows us to easily define the mass 4-current of the fluid, noting $m = m_+ + m_-$). Using equations similar to Eqs. (3.30) and (3.50), we obtain,

$$\begin{cases} \rho_0 \mathbf{u}_{\mathrm{fl}} = m\displaystyle\int_{\mathbf{u}\in\Omega} \delta^3 u\, \mathbf{u} f\left(\mathrm{M},\mathbf{u}\right) \\ \mathbf{T}_{\mathrm{FL}} = mc^2 \displaystyle\int_{u^i\in\mathbb{R}^3} \delta^3 u \left[\mathbf{u}\otimes\mathbf{u}\, f\left(x^\mu,\mathbf{u}\right)\right] \end{cases} . \tag{3.81}$$

We assume that the distribution function is out of equilibrium. This kind of hypothesis is justified for non-collisional plasmas. We also assume that in the frame of the fluid, which is unambiguously defined as soon as there is a distribution function, the velocity in the fluid reference frame and we have $\gamma\left(\mathrm{V}/c\right) = \left(1-\mathrm{V}^2/c^2\right)^{-1/2}$). Using these notations, the isotropy of the distribution function in the fluid reference frame is mathematically written as $f\left(x^\mu,\mathbf{u}\right) = f\left(x^\mu,\mathrm{V}\right)$. This assumption is verified for Synge's distribution function. This is a reasonable assumption even if the anisotropy could exist due to the magnetic field or due to the particular direction of curvature (Riemman tensor) in spacetime. Using this assumption, the mass flux and the energy momentum tensor of the multi-component fluid can be put in the form,

$$\begin{cases} \mathbf{P} = \rho_0 \mathbf{u}_{\mathrm{fl}} \\ \mathbf{T} = \rho_0 \xi c^2 \mathbf{u}_{\mathrm{fl}}\otimes\mathbf{u}_{\mathrm{fl}} + \mathrm{P}\mathbf{g} \end{cases} , \tag{3.82}$$

where we have,

$$\begin{aligned} \rho_0 &= m\int_{\mathbf{u}\in\Omega} \delta^3 u\, \gamma f\left(\mathrm{M},\mathrm{V}\right) \\ \xi &= 1 + \frac{e}{c^2} + \frac{\mathrm{P}}{\rho_0 c^2} \quad \text{with} \quad 1 + \frac{e}{c^2} = \frac{\int_{\mathbf{u}\in\Omega}\delta^3 u\,\gamma^2 f\left(\mathrm{M},\mathrm{V}\right)}{\int_{\mathbf{u}\in\Omega}\delta^3 u\,\gamma f\left(\mathrm{M},\mathrm{V}\right)} \\ \mathrm{P} &= \frac{m}{3}\int_{\mathbf{u}\in\Omega}\delta^3 u\,\gamma^2\mathrm{V}^2 f\left(\mathrm{M},\mathrm{V}\right) = \frac{4\pi m}{3}\int_{\mathrm{V}\in\mathbb{R}} d\mathrm{V}\mathrm{V}^4\gamma^2 f\left(\mathrm{M},\mathrm{V}\right) \end{aligned} . \tag{3.83}$$

Let us consider the difference between our distribution function f and the Synge function $f_{\mathrm{eq}}(\beta_{\mathrm{eff}}, n_0, \mathbf{u}_{\mathrm{fl}}, \mathbf{u})$ for any temperature $\frac{1}{\beta_{\mathrm{eff}}} = \Theta_{\mathrm{eff}} = \frac{k_{\mathrm{B}}\mathrm{T}_{\mathrm{eff}}}{mc^2}$, but with the same density and the same

fluid four speed. We note $f = f_{\rm eq} + \delta f$. In this case we have different relations,

$$\begin{aligned}
&\rho_0 = m\int_{\mathbf{u}\in\Omega}\delta^3 u\,\gamma\left(f_{\rm eq}\left(\beta_{\rm eff}, n_0, \mathbf{u}_{\rm fl}, \mathbf{u}\right) + \delta f\left(\mathrm{M},\mathrm{V}\right)\right) = \rho_0 + m\int_{\mathbf{u}\in\Omega}\delta^3 u\,\gamma\,\delta f\left(\mathrm{M},\mathrm{V}\right) \;\Rightarrow\; \int_{\mathbf{u}\in\Omega}\delta^3 u\,\gamma\,\delta f\left(\mathrm{M},\mathrm{V}\right) = \delta\rho_0 = 0\\
&\mathrm{P} = \frac{m}{3}\int_{\mathbf{u}\in\Omega}\delta^3 u\,\gamma^2\mathrm{V}^2\left(f_{\rm eq}\left(\beta_{\rm eff}, n_0, \mathbf{u}_{\rm fl}, \mathbf{u}\right) + \delta f\left(\mathrm{M},\mathrm{V}\right)\right) = \mathrm{P}_{\rm eff} + \delta\mathrm{P} \quad \text{with} \quad \Theta \hat{=} \frac{\mathrm{P}}{\rho_0 c^2} = \Theta_{\rm eff} + \delta\Theta\\
&\text{and} \quad \Theta_{\rm eff} = \frac{1}{\beta_{\rm eff}} = \frac{k_{\rm B}\mathrm{T}_{\rm eff}}{mc^2} \quad \text{also} \quad 1 + \frac{e}{c^2} = 1 + \frac{e_{\rm eq} + \delta e}{c^2} \quad \text{with} \quad \frac{\delta e}{c^2} = \frac{\int_{\mathbf{u}\in\Omega}\delta^3 u\,\gamma^2\,\delta f\left(\mathrm{M},\mathrm{V}\right)}{\int_{\mathbf{u}\in\Omega}\delta^3 u\,\gamma f\left(\mathrm{M},\mathrm{V}\right)}
\end{aligned} \tag{3.84}$$

The temperature $\beta_{\rm eff}$ can be chosen in order to contain the whole pressure $\mathrm{P} = \mathrm{P}_{\rm eff}$, then $\Theta = \Theta_{\rm eff}$. And this will be the case of our first analysis. Then the deviation from the Synge gas only appears as a supplement of internal energy. In the following, we call this choice **pure additional internal energy out of thermodynamic equilibrium**. The characteristic function $e_{\rm eq}$ of the Synge gas Eq.(3.72) follows the first principle of thermodynamics,

$$de_{\rm eq} = -\mathrm{P}_{\rm eff} d\frac{1}{\rho_0} + \mathrm{T}\,ds_{\rm eq} \tag{3.85}$$

Where $s_{\rm eq}$ is given in Eq.(3.70). You have $\Theta_{\rm eff} = \frac{\mathrm{P}_{\rm eff}}{\rho_0 c^2} = \frac{k_{\rm B}\mathrm{T}_{\rm eff}}{mc^2}$, which is valid with the definition using the Synge-Jüttner distribution. Few lines of derivation give the well-know result called Joule's law, $e_{\rm eq} = e_{\rm eq}\left(\Theta_{\rm eff}\right)$. In fact we interpret $e_{\rm eq}$ and $\mathrm{P}_{\rm eff}$ (or $\Theta_{\rm eff}$) as equilibrium internal energy of effective thermal temperature. The δe and $\delta\mathrm{P}$ (or $\delta\Theta$) are modeling the effects of turbulence or MHD waves on the flow. Recombining the first principle Eq.(3.85) with the projection along the flow of momentum-energy conservation Eq.(3.54), and using ideality of the flow ($\mathbf{F}(\mathbf{u},.) = 0$), we obtain,

$$-\mathrm{T}\nabla_{\mathbf{u}} s = \nabla_{\mathbf{u}}\delta e + \delta\mathrm{P}\nabla_{\mathbf{u}}\left(\frac{1}{\rho_0}\right) + \frac{\mathbf{u}_{\rm fl}\cdot\mathbf{k} + \xi c^2 k_m}{\rho_0 c^2} \tag{3.86}$$

with $k_m = k_{\rm N}(m_+ + m_-)$ and $\mathbf{k} = \mathbf{k}^{\rm Elastic}_{r\to e_+e_-} + \mathbf{k}^{2r\rightleftharpoons e_+e_-}_{\to e_+e_-}$. We see that these additional pressure and additional internal energy can heat the flow, but also act for the loading of pairs.

Polytropic extra-internal energy

Consider a fluid with a given Joule's law $e_{\rm K} = e_{\rm K}\left(\mathrm{T}\right)$. If we make the extra assumption of no extra-pressure $\delta\mathrm{P} = 0$, having a polytropic law with constant index Γ, which links the pressure and the rest mass density $\mathrm{P} \propto \rho_0^{\Gamma}$, we find that,

$$d\frac{\delta e}{c^2} = \frac{\mathrm{T}}{c^2} ds = \frac{\Gamma - \Gamma_{\rm eff}(\mathrm{T})}{\left(\Gamma_{\rm eff}(\mathrm{T}) - 1\right)\left(\Gamma - 1\right)} d\frac{\mathrm{P}}{\rho_0 c^2} \tag{3.87}$$

with an effective polytropic index define by $de_{\rm eq} = \frac{1}{\Gamma_{\rm eff}(\mathrm{T})-1} d\frac{k_{\rm B}\mathrm{T}}{m} = \frac{c^2}{\Gamma_{\rm eff}(\mathrm{T})-1} d\frac{\mathrm{P}}{\rho_0 c^2}$. The gas has an adiabatic evolution only if $\Gamma = \Gamma_{\rm eff}(\mathrm{T})$ (Γ-law equation of state). It is not expected for a gas where the temperature present strong variations. A mono-atomic polytropic gas may have an adiabatic evolution only in both the non-relativistic (and $\Gamma = 5/3$) and the ultra-relativistics ($\Gamma = 4/3$) limits.

Other ways can be explored for retrieving the pressure in function of density rest mass for a relativistic temperature. By example for a Taub-Matthews EOS, Meliani et al. [2004] calculated the pressure $\mathrm{P} = \mathrm{P}(\rho_0)$ (eq.15 in their paper) for a mono-atomic gas and the assumption of polytropic internal energy (in our notation $\frac{e}{c^2}\left(2 + \frac{e}{c^2}\right) \propto \rho_0^{\Gamma-1}$ with a constant value of Γ).

3.3.3 Use of relativistic κ-distribution function

The distribution function of plasma with highly energetic particles, for example in planetary magnetospheres, usually have the characteristics of a pronounced high energy tail. One way to model distribution functions with high energy tail is to use κ-distribution functions. The κ-distribution functions were introduce in the domain of astrophysics by Chateau and Meyer-Vernet [1991] but also more precisely to model the solar wind Scudder [1992]. They are also used in planetary environments, see Meyer-Vernet [2001]. Even if there is some difficulties in the normalization, extension of the κ-function to relativistic temperatures was proposed by Xiao [2006]. The main idea of the κ-distribution function, is to have a family of distribution function $s(f_\kappa)_{\kappa\in[3,+\infty]}$ characterized by a pseudo-temperature β_κ, a four-speed of the fluid $\mathbf{u}_{\rm fl}$ and a density in the rest frame ρ_0, such that if $\kappa \to +\infty$ the distribution function reaches the Synge-Jüttner one. We follow Xiao [2006] without the anisotropy for the dependance in velocity of the relativistic κ-distribution function. From the useful expression of volume element Eq.(3.10) and Eq.(3.84) for the value of the normalization function, we get

$$\begin{aligned} f_\kappa\left(\beta_\kappa, n_0, \mathbf{u}_{\rm fl}, \mathbf{u}\right) &= \frac{n_0}{z_\kappa\left(\beta_\kappa\right)} \frac{1}{\left(1+\frac{\beta_\kappa}{\kappa}\left(\mathbf{u}_{\rm fl}\cdot\mathbf{u}+1\right)\right)^{\kappa+1}} \\ \text{with} \quad z_\kappa\left(\beta_\kappa\right) &= 4\pi \int_{\Psi\in\mathbb{R}_+} d\Psi \frac{\sinh^2\Psi\cosh\Psi}{\left(1+\frac{\beta_\kappa}{\kappa}\left(\cosh\Psi-1\right)\right)^{\kappa+1}} \end{aligned} \tag{3.88}$$

The normalization function, $z_\kappa\left(\beta_\kappa\right)$ is different from the normalization function proposed by Xiao [2006] in their paper (eq.25). Indeed, the definition of the fluid rest frame in relativistic statistical physics is linked to the notion of Feynmann's four-current Eq.(3.30), which is the first moment of the four-speed. For classical temperatures (non-relativistic velocity of particles in fluid rest frame) $\mathbf{u} \approx \left(\mathbf{u}_{\rm fl} + \frac{\mathbf{v}}{c}\right)$, then $\mathbf{u}\cdot\mathbf{u}_{\rm fl} \approx -1$ which justifies the classical normalization. Yet, for relativistic temperatures, we need to choose $n_0 = \int \delta^3 u\gamma f$ and not $n_0 = \int \delta^3 u f$, which justifies the expression in Eq.(3.88). Fundamentally the difference comes from the fact that the number density of particles n is not a frame independent quantity, because of the volume contraction. Indeed, the number density measured by an observer of four speed $\mathbf{v}$ is $n = -\mathbf{v}\cdot\mathbf{J}$. Then the definition of Feynmann's four-current replaces the classical definition of normalization.

Then, from Eq. (3.84), using a gas with pure additional internal energy out of thermodynamical equilibrium, we can calculate the extra energy δe_κ as a function of $\Theta_{\rm eff} = \Theta = \frac{\rm P}{\rho_0 c^2}$. This extra energy reaches zero, where $\kappa \to +\infty$. This is logical because the distribution function reaches the Synge-Jüttner one. If $\kappa \to 3$, and for fixed value of β_κ the internal energy reaches ∞, nevertheless the effective temperature $\Theta_{\rm eff} = {\rm P}/\rho_0 c^2 = \Theta_{\rm eff}(\kappa, \beta_\kappa)$ also reaches infinity. Then the equilibrium energy for effective temperature $e_{\rm eq}\left(\Theta_{\rm eff}\right) \to +\infty$ reaches infinity. And we have an undifferentiated limit. Nevertheless numerical calculation seems indicate that this extra energy reaches $\frac{\delta e}{c^2} \to +1$. Thus for each given value of $\Theta_{\rm eff}$ and $0 \leq \delta e_\kappa / c^2 \leq 1$, we have an adapted value of κ.

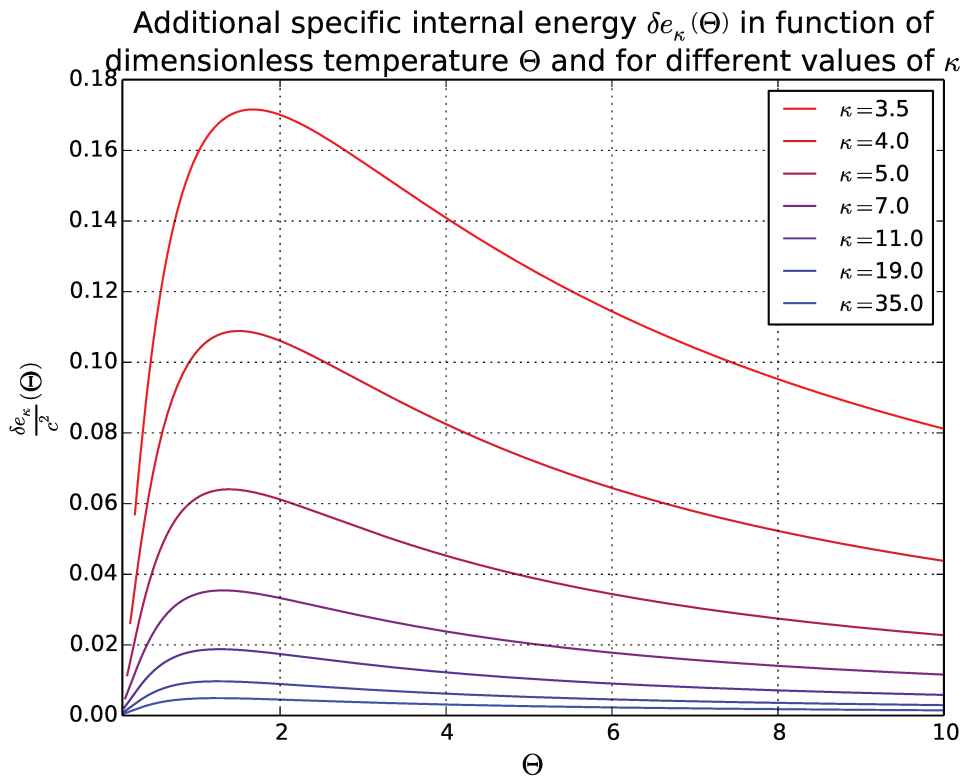

Figure 3.6 – Additional specific internal energy δe_κ for pure additional internal energy out of thermodynamic equilibrium κ-gas as a function of temperature and for different values of κ.

3.4 Conclusion

A statistical approach allows us to calculate how micro-physics interactions, elastic collisions or creation/annihilation, act on the dynamics of the fluid. We apply a relativistic treatment from the beginning to the end. We derive the modification of the usual fluid equations, which comes from the interaction between different species. Nevertheless, to be complete, we need to add to the process a more rigorous derivation of the differential cross section (Berestetskii et al. [1982]). Another approach could be, as in Levinson and Segev [2017] and Ford et al. [2017] to introduce some model for these differential cross section terms.

We treat the case of thermodynamical equilibrium. We derive the expression of a several thermodynamical quantities, especially the internal energy as function of temperature, Synge's EOS and its approximation by Taub and Matthews.

We also see how a plasma, out of thermodynamical equilibrium, but with an isotropic distribution of speed in the rest frame, could be considered as a gas with an extra internal energy in comparison to the gas in thermodynamical equilibrium, with the same effective temperature. We treat in details the case of gas for which the distribution function is a relativistic κ distribution function.

In the following chapters, we use the results of these two chapters to derive the main results on loaded/unloaded axi-symmetric, stationary ideal MHD flows.

3.5 References

V.B. Berestetskii, L.D. Landau, E.M. Lifshitz, L.P. Pitaevskii, and J.B. Sykes. *Quantum Electrodynamics*. Course of theoretical physics. Elsevier Science, 1982. ISBN 9780750633710. URL https://books.google.fr/books?id=URL5NKX8vbAC. 37, 50

R. Birkl, M. A. Aloy, H.-T. Janka, and E. Müller. Neutrino pair annihilation near accreting, stellar-mass black holes. aap, 463:51–67, February 2007. doi: 10.1051/0004-6361:20066293. 26, 38

B. Carter. Conductivity with Causality in Relativistic Hydrodynamics - the Regular Solution to Eckart's Problem. In B. R. Iyer, C. V. Vishveshwara, J. V. Narlikar, and A. K. Kembhavi, editors, *Highlights in Gravitation and Cosmology*, page 58, January 1988. 46

Y. F. Chateau and N. Meyer-Vernet. Electrostatic noise in non-Maxwellian plasmas - Generic properties and 'kappa' distributions. jgr, 96:5825–5836, April 1991. doi: 10.1029/90JA02565. 49

N.A. Chernikov. Relativistic Gas in Gravitational Field. *Acta Physica Poloica*, 24(5), 1 1963. 34, 36, 37, 38

F. Debbasch and W. A. van Leeuwen. General relativistic Boltzmann equation, I: Covariant treatment. *Physica A Statistical Mechanics and its Applications*, 388:1079–1104, April 2009a. doi: 10.1016/j.physa.2008.12.023. 28

F. Debbasch and W. A. van Leeuwen. General relativistic Boltzmann equation, II: Manifestly covariant treatment. *Physica A Statistical Mechanics and its Applications*, 388:1818–1834, May 2009b. doi: 10.1016/j.physa.2009.01.009. 31

F. Debbasch, J. P. Rivet, and W. A. van Leeuwen. Invariance of the relativistic one-particle distribution function. *Physica A Statistical Mechanics and its Applications*, 301:181–195, December 2001. doi: 10.1016/S0378-4371(01)00359-4. 33

Rémi Droz-Vincent, Ph.; Hakim. Collective motions of the relativistic gravitational gas. *Annales de l'I.H.P. Physique théorique*, (1):17–33, 1968. 26

C. Eckart. The Thermodynamics of Irreversible Process. III Relativistic theroy of the simple fluid. Physical Review, 58:919–924, September 1940. 46

D. Fargion and A. Salis. METHODOLOGICAL NOTES: Inverse Compton scattering off black body radiation in high energy physics and gamma (MeV-TeV) astrophysics. *Physics Uspekhi*, 41:823–829, August 1998. doi: 10.1070/PU1998v041n08ABEH000432. 38

A. L. Ford, B. D. Keenan, and M. V. Medvedev. Electron-Positron Cascade in Magnetospheres of Spinning Black Holes. *ArXiv e-prints*, June 2017. 38, 50

N. Globus and A. Levinson. Jet Formation in GRBs: A Semi-analytic Model of MHD Flow in Kerr Geometry with Realistic Plasma Injection. apj, 796:26, November 2014. doi: 10.1088/0004-637X/796/1/26. 26

R. J. Hakim. *Introduction to Relativistic Statistical Mechanics: Classical and Quantum*. World Scientific Publishing Co, 2011. doi: 10.1142/7881. 26

K. Hirotani and H.-Y. Pu. Energetic Gamma Radiation from Rapidly Rotating Black Holes. apj, 818:50, February 2016. doi: 10.3847/0004-637X/818/1/50. 38

Landau and Lifshitz. *Fluid Mechanics*. U.S.S.R. Academie of Science, 1958. 46

Amir Levinson and Frank Rieger. Variable tev emission as a manifestation of jet formation in m87? *The Astrophysical Journal*, 730(2):123, 2011. URL http://stacks.iop.org/0004-637X/730/i=2/a=123. 38

Amir Levinson and Noam Segev. Existence of steady gap solutions in rotating black hole magnetospheres. *Phys. Rev. D*, 96:123006, Dec 2017. doi: 10.1103/PhysRevD.96.123006. URL https://link.aps.org/doi/10.1103/PhysRevD.96.123006. 38, 50

C. Marle. Sur l'établissement des équations de l'hydrodynamique des fluides relativistes dissipatifs. i. - l'équation de boltzmann relativiste. *Annales de l'I.H.P. Physique théorique*, (1):67–126, 1969a. 26, 31, 36, 38

C. Marle. Sur l'établissement des équations de l'hydrodynamique des fluides relativistes dissipatifs. ii. - méthodes de résolution approchée de l'équation de boltzmann relativiste. *Annales de l'I.H.P. Physique théorique*, (2):127–194, 1969b. 26, 46, 47

J. C. McKinney. Jet Formation in Black Hole Accretion Systems I: Theoretical Unification Model. *ArXiv Astrophysics e-prints*, June 2005a. 26

J. C. McKinney. Jet Formation in Black Hole Accretion Systems II: Numerical Models. *ArXiv Astrophysics e-prints*, June 2005b. 26

Z. Meliani, C. Sauty, K. Tsinganos, and N. Vlahakis. Relativistic Parker winds with variable effective polytropic index. aap, 425:773–781, October 2004. doi: 10.1051/0004-6361:20035653. 48

N. Meyer-Vernet. Large scale structure of planetary environments: the importance of not being Maxwellian. planss, 49:247–260, March 2001. doi: 10.1016/S0032-0633(00)00146-X. 49

A. Mignone and J. C. McKinney. Equation of state in relativistic magnetohydrodynamics: variable versus constant adiabatic index. mnras, 378:1118–1130, July 2007. doi: 10.1111/j.1365-2966.2007.11849.x. 45

J. D. Scudder. On the causes of temperature change in inhomogeneous low-density astrophysical plasmas. apj, 398:299–318, October 1992. doi: 10.1086/171858. 49

J. L. Synge. *The Relativistic Gas*. North-Holland Publishing Company, 1957. 43

F. Xiao. Modelling energetic particles by a relativistic kappa-loss-cone distribution function in plasmas. *Plasma Physics and Controlled Fusion*, 48:203–213, February 2006. doi: 10.1088/0741-3335/48/2/003. 49

I. Zalamea and A. M. Beloborodov. Neutrino heating near hyper-accreting black holes. mnras, 410:2302–2308, February 2011. doi: 10.1111/j.1365-2966.2010.17600.x. 26, 38

Chapter 4

Magneto-Hydrodynamics in curved spacetime

Contents

This chapter describes the general results concerning Magneto-Hydrodynamic (MHD) with equations including loading terms in curved spacetime, the General Relativistic Magneto-Hydrodynamic (GRMHD). Indeed to take into account the effect of the creation/annihilation of pairs on a MHD flow, we saw on the last chapter Ch.(3), that it is possible to modify in adding some source terms in the continuity equation Eq.(3.49) and in the conservation of energy momentum equation Eq.(3.54). We also gave an explicit value of these source terms as a function of the different differential cross sections of interaction Eq.(3.48, 3.56, 3.78). In the following we seek to extract general results on flow regardless of the form and values of the source terms even if they are included as an unknown functions. These general results form the theoretical basis for the construction of the MHD flow model close to a Kerr black hole. The construction of this model is explained in the following chapter.

The effect of pair creation mechanism or Compton/inverse Compton mechanism is studied in the dynamics of magnetized astrophysical flows. Globus and Levinson [2013] built an inflow/outflow model for a radial geometry of the flow and Pu et al. [2015] for a parabolic geometry. In their work Globus and Levinson [2014] implement a split monopole model of flows incorporate realistic and volumic plasma injection around Kerr black hole. The recent works of Levinson and Segev [2017] and Ford et al. [2017] study the steady gap solution for black hole magnetosphere including the rate of pair creation and the role of Compton/Inverse Compton forces.

First, we derive the 3+1 form of the MHD equations in any spacetime framework before writing these equations in Kerr geometry. We continue with the search of the motion integrals of General Relativistic Axi-symmetric Stationary Ideal Magneto-Hydrodynamic (GRASIMHD) flow, which are the main assumptions of the flow described by the solution of our model. Then we discuss briefly about the Grad-Shafranov approach of this problem. Finally, we calculate the quantities such as the mass, angular momentum and the energy exchanged at the level of the event horizon between the Kerr black hole and the MHD fields.

4.1 3+1 Decomposition of GRMHD

The goal of this section is to use the main results from Ch.(2) to perform a 3+1 decomposition of the covariant expression of magneto-hydrodynamics. We consider a foliated spacetime ($\mathscr{M} = \bigcup_{t\in\mathbb{R}} \Sigma_t, \mathbf{g}$) with a space sub-manifold Σ_t. We choose a coordinate system adapted to this foliation. Our spacetime is filled with an electromagnetic field and an injected fluid.

4.1.1 Covariant form

As we mentioned before, the GRMHD equations can be derivated in their covariant form from a statistical approach. The electromagnetic tensor evolves with the covariant Maxwell's system of equations in Gaussian Unit (GU) Eq.(3.42), that we write here,

$$\boxed{\begin{cases} \nabla\cdot\mathbf{F} = & \dfrac{4\pi}{c}\mathbf{j} \\ \nabla\cdot\star\mathbf{F} = & 0 \end{cases}} \tag{4.1}$$

Note that the creation of plasma does not perturb the usual Maxwell's equations. We suppose that the plasma pair has an infinite conductivity such that the electromagnetic field adapts itself continuoulsy in order to always cancel the electric field in the fluid frame. This condition is called **ideality condition**.

$$\mathbf{F}(\mathbf{u},.) = 0 \tag{4.2}$$

The second expression is already the 3+1 form of ideality condition. For the mass four-current and the fluid energy momentum tensor, we choose the form given in Sec.(3.3.2). The fluid is loaded in spacetime via some source terms Eq.(3.47). Thus we have the covariant form of continuity equation,

$$\boxed{\nabla\cdot\left(\rho_0\mathbf{u}\right)=k_m}. \tag{4.3}$$

where $k_m=(m_+ + m_-)\,k_{\rm N}$ is given by Eq. (3.48). For the equation of motion the loading induces some extra terms (see Eq.3.54), and we get,

$$\boxed{\nabla\cdot\mathbf{T}_{\rm FL}+\mathbf{F}\left(\frac{\mathbf{j}}{c},.\right)=\mathbf{k}}. \tag{4.4}$$

The force due to the injected plasma $\mathbf{k}=\mathbf{k}^{\rm Elastic}_{r\to e_+e_-}+\mathbf{k}^{2r\rightleftharpoons e_+e_-}_{\to e_+e_-}$ is expressed via Eqs. (3.56, 3.78). Eqs. (4.1, 4.3, 4.4) constitute the GRMHD system of equations in a covariant form describing the flow of loaded/unloaded plasma. The goal here is to use 3+1 formalism to write these equations in a more adapted form.

4.1.2 Kinematics

Let us consider the motion of a fluid element, $t\to \mathrm{M}(t)\in\mathscr{M}$. Its four velocity is denoted $\mathbf{u}=\frac{\mathbf{dM}}{ds}$, where $ds=cd\tau_0$ is the arclength of its trajectory in spacetime, which is proportional to the proper time of the fluid element. Now we consider the displacement of the element when it starts to some point $\mathrm{P}\in\Sigma_t$ to reach the point $\mathrm{Q}\in\Sigma_{t+dt}$. We have $\mathbf{dM}=\mathbf{PQ}$.

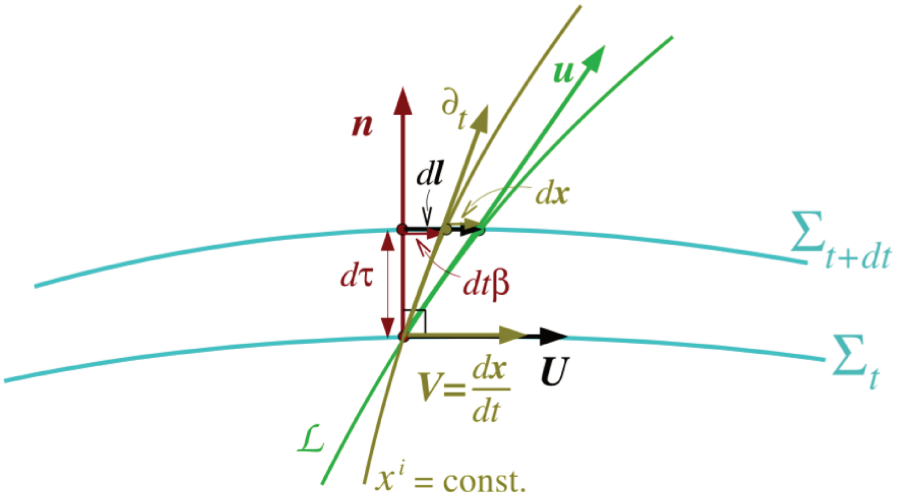

Figure 4.1 – Representation of the decomposition of the four speed (Credits , Gourgoulhon [2007]). The notations used are Gourgoulhon ones. Here $\mathbf{U}$ is the Fiducials Observers (FIDO) velocity, and $\mathbf{V}$ the coordinate velocity.

Following Fig. (4.1), we decompose the variation of position $\mathbf{PQ}$ using the 3+1 procedure $\mathbf{PQ}=\mathbf{PQ}'+\mathbf{Q}'\mathbf{Q}$. Then $\mathbf{PQ}'=cd\tau_{\rm FIDO}\mathbf{n}=chdt\mathbf{n}$, where $d\tau_{\rm FIDO}$ is the proper time of the FIDO observer. We used Eq. (2.14). Note that $\mathbf{Q}'\mathbf{Q}=\mathbf{d}\ell$ is the spatial displacement measured by the FIDO. If we introduce γ the Lorentz factor which links the proper time $d\tau_{\rm FIDO}$ of the FIDO to the proper time of the fluid frame $d\tau_{\rm FL}$, we have $d\tau_{\rm FIDO}=\gamma d\tau_{\rm FL}$. Then the four speed of the fluid is,

$$\boxed{\mathbf{u}=\gamma\left(\mathbf{n}+\frac{\mathbf{V}}{c}\right)\quad\text{where}\quad\mathbf{V}=\frac{\mathbf{d}\ell}{d\tau_{\rm FIDO}}\qquad\text{and}\qquad d\tau_{\rm FIDO}=\gamma d\tau_{\rm FL}} \tag{4.5}$$

$\mathbf{V}$ is the velocity measured by the FIDO. We call it **FIDO velocity**. After some calculations we get,

$$\boxed{\gamma = -\mathbf{n}\cdot\mathbf{u} = \frac{1}{\sqrt{1-\frac{\mathbf{V}^2}{c^2}}}} \tag{4.6}$$

The definition of the shift of coordinates Eq.(2.16) implies that $\mathbf{d\ell} = \mathbf{dx} + \boldsymbol{\beta} dt$, where $\mathbf{dx}$ corresponds to the coordinate variation of the fluid element. Thus we can introduce $\mathbf{W} = \frac{\mathbf{dx}}{dt}$ the velocity in terms of the variation of the coordinates, that we call **coordinate velocity**. Using the lapse function Eq.(2.14), the coordinate velocity is link to the FIDO velocity via

$$h\mathbf{V} = \mathbf{W} + \boldsymbol{\beta} \tag{4.7}$$

Thus, using Eq.(2.15) we can write,

$$\mathbf{u} = \gamma\left(\mathbf{n} + \frac{\mathbf{V}}{c}\right) = \frac{\gamma}{hc}\left(\partial_t + \mathbf{W}c\right) \tag{4.8}$$

These different definitions of the velocities are important for the physical understanding of the following section.

4.1.3 3+1 Decomposition of Maxwell's equations

The electric (magnetic) field measured by the FIDO is $\mathbf{E} = \mathbf{F}(.,\mathbf{n})$ ($\mathbf{B} = \star\mathbf{F}(\mathbf{n},.)$, respectively) by definition of the electromagnetic tensor. Let us introduce the 2-form $\mathbf{G} = \mathbf{F} - \mathbf{n}\wedge\mathbf{E}$, which is identically null along $\mathbf{n}$. Then the information of $\mathbf{G}$ on $\mathscr{T}(\mathscr{M})$, is entirely determined by the value of $\mathbf{G}$ on $\mathbf{n}^\perp = \mathscr{T}(\Sigma)$. $\mathbf{G}|_{\mathbf{n}^\perp}$ is a 2-form on a 3 dimensional space. Because $\mathbf{n}^\perp$ is a three dimensional space, then $\mathbf{G}|_{\mathbf{n}^\perp}$ has at least one real eigenvalue. However, $\mathbf{G}|_{\mathbf{n}^\perp}$ is antisymmetric thus the real eigenvalue is null, which is equivalent to say that there is a non null vector $\mathbf{B}$ in the kernel of $\mathbf{G}|_{\mathbf{n}^\perp}$. Then, as before, the information of $\mathbf{G}|_{\mathbf{n}^\perp}$ is equivalent to the information of $\mathbf{G}|_{(\mathbb{R}\mathbf{n}\oplus\mathbb{R}\mathbf{B})^\perp}$. Thus since $\mathbf{G}|_{(\mathbb{R}\mathbf{n}\oplus\mathbb{R}\mathbf{B})^\perp}$ is a 2-form of dimension 2 on a space of dimension 2, $\mathbf{G}|_{(\mathbb{R}\mathbf{n}\oplus\mathbb{R}\mathbf{B})^\perp}$ is proportional to the Levi-Civita (determinant) form on this space. If one chooses $\mathbf{B}$ properly, then $\mathbf{G}|_{(\mathbb{R}\mathbf{n}\oplus\mathbb{R}\mathbf{B})^\perp} =^2 \boldsymbol{\epsilon}(.,.) =^4 \boldsymbol{\epsilon}(\mathbf{n},\mathbf{B}.,.)$. Thus we have,

$$\begin{cases} \mathbf{F} = \mathbf{n}\wedge\mathbf{E} +^4 \boldsymbol{\epsilon}(\mathbf{n},\mathbf{B},.,.) \\ \star\mathbf{F} = -\mathbf{n}\wedge\mathbf{E} +^4 \boldsymbol{\epsilon}(\mathbf{n},\mathbf{E},.,.) \end{cases}. \tag{4.9}$$

As a matter of fact, the 4-speed, the source term of the Maxwell's equations, the four-current charge, can be decomposed as,

$$\mathbf{j} = \rho_e c\mathbf{n} + \mathbf{J} \tag{4.10}$$

where ρ_e is the charge density per unit volume measured by the FIDO and $\mathbf{J}$ the charge current measured by the FIDO. Thus for an elementary surface $\mathbf{dS} \in \mathscr{T}(\Sigma)$, in the FIDO, one measures a charge $\delta^3 Q = \mathbf{J}\cdot\mathbf{dS}d\tau$, which crosses the surface during its proper time $d\tau$. After some calculations , the details are given in Appendix (D.1.1), we get,

$$\boxed{\begin{array}{ll} \mathbf{D}\cdot\mathbf{B} = 0 & \mathbf{D}\cdot\mathbf{E} = 4\pi\rho_e \\ \mathbf{D}\times(h\mathbf{E}) = h\mathbf{K}\mathbf{E} - \left(\frac{1}{c}\frac{\partial}{\partial t} - \mathscr{L}_{\boldsymbol{\beta}}\right)\mathbf{B} & \mathbf{D}\times(h\mathbf{B}) = \frac{4\pi h}{c}\mathbf{J} - h\mathbf{K}\mathbf{E} + \left(\frac{1}{c}\frac{\partial}{\partial t} - \mathscr{L}_{\boldsymbol{\beta}}\right)\mathbf{E} \end{array}} \tag{4.11}$$

This system corresponds to **Maxwell's equations in 3+1 form** expressed in GU. The additional term proportional to the Lie derivative of the electric or the magnetic field along the shift is the term, which compensates the coordinates shift. Indeed, $\frac{1}{c}\frac{\partial}{\partial t} - \mathscr{L}_{\boldsymbol{\beta}} = \mathscr{L}_{\mathbf{m}}$. Thus this term is some kind of time coordinate derivative in the FIDO frame. Also remark the presence of the lapse function in the rotational equation. This system is reduced to the usual one when the mass and the angular momentum of the black hole reach zero.

The ideality condition became,

$$\mathbf{E} + \frac{\mathbf{V}\times\mathbf{B}}{c} = \mathbf{0} \tag{4.12}$$

4.1.4 The 3+1 form of continuity equation

For the continuity equation, we get,

$$\boxed{\frac{\partial \rho_0 \gamma}{\partial t} - c\boldsymbol{\beta}\cdot\mathbf{D}\rho_0\gamma - \rho_0 c\gamma \mathrm{K} + \mathbf{D}\cdot\left(\rho_0\gamma h\mathbf{V}\right) = hck_m} \tag{4.13}$$

Details of the calculations are given in Appendix (D.1.2). In comparison to the non-relativistic expression, the first thing to remark is that we replace the rest frame density by the FIDO density $\rho_0\gamma$. The velocity term is the FIDO velocity, measured in the time-coordinate $h\mathbf{V}$. The term $c\boldsymbol{\beta}\cdot\mathbf{D}\rho_0\gamma$ compensates the effect of the shift of coordinates in order to get a time coordinate derivative but in the FIDO frame. The term $-\rho_0 c\gamma\mathrm{K}$ compensate the effect of expansion of volume seen by the FIDO's (indeed $\mathrm{K} = -\nabla\cdot\mathbf{n}$).

4.1.5 Spatial part of stress energy tensor conservation

To get the details of the derivation see Appendix.(D.1.3).

$$\boxed{\frac{\rho_0\gamma c}{h}\mathscr{L}_{\mathbf{m}}\gamma\xi\mathbf{V} + \rho_0\gamma\left(\mathbf{V}\cdot\mathbf{D}\right)\gamma\xi\mathbf{V} = -\mathbf{D}\mathrm{P} - \rho_0\gamma^2\xi c^2\mathbf{D}\ln h + \mathbf{p}\left(\mathbf{k}\right) - \gamma\xi k_m c\mathbf{V} + \rho_e\mathbf{E} + \frac{\mathbf{J}\times\mathbf{B}}{c}} \tag{4.14}$$

Note that in this expression the term $\mathscr{L}_{\mathbf{m}}\gamma\xi\mathbf{V}$ is calculated for the linear form $\gamma\xi\mathrm{V}_\alpha$. Because of the property of Lie derivative Eq.(B.8), this term is included in $\mathscr{T}\left(\Sigma_t\right)$. This term also contains the frame dragging forces, that we express in more details in the Kerr geometry. First of all in comparison to the classical model, we remark that in the term of "acceleration" (left-hand side of the equation), the accelerated quantity is not the velocity of the fluid but $\gamma\xi\mathbf{V}$. This implies that a fluid with more specific enthalpy or with FIDO velocity closest to c, is more difficult to accelerate. We also observe the usual gradient of pressure $-\mathbf{D}\mathrm{P}$, and the gravitational forces $-\rho_0\gamma^2\xi c^2\mathbf{D}\ln h$. We also have the electrical forces $\rho_e\mathbf{E}$ and the Lorentz force $\frac{\mathbf{J}\times\mathbf{B}}{c}$. The term $\mathbf{p}\left(\mathbf{k}\right) - \gamma\xi k_m c\mathbf{V}$, where $\mathbf{p}$ is the projector normal to $\mathbf{n}$ Eq.(2.2) is the recoiling forces due to the loading of plasma.

4.1.6 Evolution of internal energy along the flow

Using Eq.(4.12), the projection of Eq.(4.4) along the four speed gives,

$$\boxed{\nabla_{\mathbf{u}}\mathrm{P} = \rho_0 c^2\nabla_{\mathbf{u}}\xi + \mathbf{u}\cdot\mathbf{k} + \xi c^2 k_m} \tag{4.15}$$

As in Sec.(3.3.2), we note that the loaded term can heat the flow.

4.1.7 Axisymmetric GRMHD in Kerr metric

We know that that, in Kerr metric the FIDO observer associated to Boyer-Lindquist coordinates has a motion with no angular momentum, which justifies the denomination that we use in the denomination Zero Angular Momentum Observer (ZAMO). Using the result of Sec.(2.4), we are able to quickly obtain the system,

$$\begin{cases}
\mathbf{D}\cdot\mathbf{B} = 0 \quad \mathrm{Maxwell-Flux} & \mathbf{D}\times\left(h\mathbf{E}\right) = -\dfrac{1}{c}\dfrac{\partial}{\partial t}\mathbf{B} + \left(\mathbf{B}\cdot\mathbf{D}\dfrac{\omega}{c}\right)\varpi\boldsymbol{\epsilon}_\phi \quad \mathrm{Maxwell-Faraday} \\
\mathbf{D}\cdot\mathbf{E} = 4\pi\rho_e \quad \mathrm{Maxwell-Gauss} & \mathbf{D}\times\left(h\mathbf{B}\right) = \dfrac{4\pi h}{c}\mathbf{J} + \dfrac{1}{c}\dfrac{\partial}{\partial t}\mathbf{E} - \left(\mathbf{E}\cdot\mathbf{D}\dfrac{\omega}{c}\right)\varpi\boldsymbol{\epsilon}_\phi \quad \mathrm{Maxwell-Ampere} \\
\mathbf{E} + \dfrac{\mathbf{V}\times\mathbf{B}}{c} = \mathbf{0} \quad \mathrm{Ideality} & \dfrac{\partial\rho_0\gamma}{\partial t} + \mathbf{D}\cdot\left(\rho_0\gamma h\mathbf{V}\right) = hck_m \quad \mathrm{Continuity} \\
\dfrac{\rho_0\gamma}{h}\dfrac{\partial\gamma\xi\mathbf{V}}{\partial t} + \rho_0\gamma\left(\mathbf{V}\cdot\mathbf{D}\right)\gamma\xi\mathbf{V} = -\mathbf{D}\mathrm{P} - \rho_0\gamma^2\xi c^2\left[\mathbf{D}\ln h + \dfrac{\varpi\omega\mathrm{V}^{\hat{\phi}}}{hc^2}\mathbf{D}\ln\omega\right] + \rho_e\mathbf{E} + \dfrac{\mathbf{J}\times\mathbf{B}}{c} + \mathbf{p}\left(\mathbf{k}\right) - \gamma\xi k_m c\mathbf{V} \quad \mathrm{Euler} \\
\dfrac{\gamma}{c}\left(\partial_t + \mathbf{V}_\mathrm{p}\cdot\mathbf{D}\right)\mathrm{P} = \rho_0 c\gamma\left(\partial_t + \mathbf{V}_\mathrm{p}\cdot\mathbf{D}\right)\xi + \mathbf{u}\cdot\mathbf{k} + \xi c^2 k_m \quad \text{First principle along the flow}
\end{cases} \tag{4.16}$$

In the Maxwell's system of equations the shift of coordinate add ssome terms which take into account the gradient of shift pulsation $\mathbf{D}\omega$ along field (magnetic for Maxwell-Faraday, electric field for Maxwell-Ampere). This differential rotation is the differentiation of the toroidal coordinate of the Zero Angular Momentum Observer (ZAMO). This term is due to the nature of the Lie derivative of vector field. By axisymmetry the variation of the electric field along the shift is null, but the variation of the shift along the electric field is non-null. Such kind of explanation applies to Maxwell-Ampere.

In the decomposition of the term proportional to $\mathscr{L}_{\mathbf{m}}\gamma\xi\mathbf{V}$ of Euler equation, we get a term from the differential rotation of the coordinate system. We call this term the frame-dragging force $-\rho_0\gamma^2\xi c^2\frac{\varpi\omega V^{\hat{\phi}}}{hc^2}\mathbf{D}\ln\omega$. The frame-dragging effect can act as a repulsive (attractive) force as a function of the sign of toroidal velocity. This term is repulsive for $V^{\hat{\phi}}\geq 0$ and attractive for $V^{\hat{\phi}}\leq 0$. A quick comparison of gravity forces leads to a non-negligible frame dragging force for relativistic toroidal speed and for radius below $\frac{r}{r_{\mathrm{H}}}\approx\frac{3a\sin\theta}{1+\sqrt{1-a^2}}$. Thus this force will play a non-negligible role especially for inflows with an extreme spin $a\approx 0.8-1$, and should not be neglected in the construction of the model. The frame dragging force may be interpret as a Coriolis forces coming from the relative rotation.

4.2 General results on General Relativistic Axi-symmetric Stationary Ideal Magneto-Hydrodynamic (GRASIMHD) in Kerr geometry

The aim of this section is to derive the general results on GRASIMHD in Kerr geometry. We use here the convention introduced in Sec.(2.4.1). First we discuss briefly about the coupled system of equations of GRASIMHD in Kerr geometry. Then we will derive the motion-integral.

4.2.1 Expression of GRASIMHD

Apply stationarity on ideal, axisymmetry GRMHD in Kerr metric means removing all derivative ∂_t terms in Eq.(4.16). We quickly obtain,

$$\begin{cases}
\mathbf{D}\cdot\mathbf{B}_{\mathrm{p}}=0 \quad \mathrm{Maxwell-Flux} & \mathbf{D}\times(h\mathbf{E})=\left(\mathbf{B}_{\mathrm{p}}\cdot\mathbf{D}\dfrac{\omega}{c}\right)\varpi\boldsymbol{\epsilon}_{\phi} \quad \mathrm{Maxwell-Faraday}\\
\mathbf{D}\cdot\mathbf{E}=4\pi\rho_e \quad \mathrm{Maxwell-Gauss} & \mathbf{D}\times(h\mathbf{B})=\dfrac{4\pi h}{c}\mathbf{J}-\left(\mathbf{E}\cdot\mathbf{D}\dfrac{\omega}{c}\right)\varpi\boldsymbol{\epsilon}_{\phi} \quad \mathrm{Maxwell-Ampere}\\
\mathbf{E}+\dfrac{\mathbf{V}\times\mathbf{B}}{c}=\mathbf{0} \quad \mathrm{Ideality} & \mathbf{D}\cdot\left(\rho_0\gamma h\mathbf{V}_{\mathrm{p}}\right)=hck_m \quad \mathrm{Continuity}\\
\rho_0\gamma\left(\mathbf{V}\cdot\mathbf{D}\right)\gamma\xi\mathbf{V}=-\mathbf{D}\mathrm{P}-\rho_0\gamma^2\xi c^2\left[\mathbf{D}\ln h+\dfrac{\varpi\omega V^{\hat{\phi}}}{hc^2}\mathbf{D}\ln\omega\right]+\rho_e\mathbf{E}+\dfrac{\mathbf{J}\times\mathbf{B}}{c}+\mathbf{p}\left(\mathbf{k}\right)-\gamma\xi k_m c\mathbf{V} \quad \mathrm{Euler}\\
\mathbf{V}_{\mathrm{p}}\cdot\mathbf{D}\mathrm{P}=\rho_0c^2\mathbf{V}_{\mathrm{p}}\cdot\mathbf{D}\xi+c\dfrac{\mathbf{u}\cdot\mathbf{k}+\xi c^2k_m}{\gamma} \quad \mathrm{First\ principle\ along\ the\ flow}
\end{cases} \tag{4.17}$$

4.2.2 Motion integrals

The GRASIMHD equations system can be partially integrated to get several field/streamline integrals (Beskin [2010]). Motion integrals are important functions of GRASIMHD flows. Physically these integrals concern the general properties of the flow and some of them express "extensive" quantities. We shall also see later on that, in the case of a plasma considered as a ideal gas which reaches thermodynamic equilibrium and without loading of material, these motion integrals can be written as combination of each other. So we will choose one of these integrals to be the "master

potential" and then express all the others integrals in function of it. Knowing the dependence of the motion integrals with the "master potential", its "master potential" value and its spatial derivative on the critical surface are sufficient to completely solve the equations of GRASIMHD.

Magnetic Flux

First of all the Maxwell-Flux equation Eq.(4.17) coupled with axisymmetry, implies the existence of a potential vector $\mathbf{A}$ for the poloidal magnetic field $\mathbf{B}_\mathrm{p} = \mathbf{D}\times(\mathbf{A})$. Let us decompose the potential vector $\mathbf{A} \hat{=} \mathbf{A}_\mathrm{p} + \frac{\mathrm{A}}{\varpi}\boldsymbol{\epsilon}_\phi$, using the expression of the rotational differential operator Eq.(2.41), $\mathbf{D}\times\mathbf{A}_\mathrm{p}$ is a toroidal field, thus $\mathbf{D}\times\mathbf{A}_\mathrm{p} = \mathbf{0}$. So using Eq.(B.30) but also Eq.(2.41) to prove that $\mathbf{D}\times\frac{\boldsymbol{\epsilon}_\phi}{\varpi} = 0$ we finally obtain,

$$\boxed{\mathbf{B}_\mathrm{p} = \mathbf{D}\times\left(\frac{\mathrm{A}}{\varpi}\boldsymbol{\epsilon}_\phi\right) = \frac{\mathbf{D}\mathrm{A}\times\boldsymbol{\epsilon}_\phi}{\varpi}}, \tag{4.18}$$

Using the theorem of Kelvin-Stokes Eq.(B.33) on a circle $\mathscr{C}(r,\theta) = \{\mathrm{M}\in\Sigma \mid r(\mathrm{M}) = r \text{ and } \theta(\mathrm{M}) = \theta\}$, and calling $\mathscr{S}$ an axisymmetric surface such that $\mathscr{C} = \partial\mathscr{S}$, we obtain,

$$\iint_\mathscr{S}\mathbf{B}\cdot\mathbf{dS} = \iint_\mathscr{S}\mathbf{B}_\mathrm{p}\cdot\mathbf{dS} = \int_\mathscr{C}\mathbf{A}\cdot\mathbf{d}\boldsymbol{\ell} = \int\mathbf{A}\cdot\mathbf{e}_\phi d\phi = \int_0^{2\pi}\frac{\mathrm{A}}{\varpi}\boldsymbol{\epsilon}_\phi\varpi\cdot\boldsymbol{\epsilon}_\phi d\phi = 2\pi\mathrm{A} \quad , \tag{4.19}$$

where the passage of the first to the second equality is justified by the axisymmetry of $\mathscr{S}$. For the second to the third equality we used the Kelvin-Stokes theorem Eq.(B.33). Then A is the magnetic flux inside the circle $\mathscr{C}(r,\theta)$. Because of Eq.(4.19), the axi-symmetry and the symmetry $\theta\leftrightarrow\pi-\theta$, the magnetic flux function is a symmetric and π-periodic function of θ, which cancels out on the axis. Then we can decompose the magnetic flux,

$$\mathrm{A} = \sum_{n=1}^{\infty} a_n(r)\sin^{2n}\theta\,. \tag{4.20}$$

Current

The current $\mathbf{J}$ is the electric current, seen by the ZAMO. Then if we took an elementary surface $\mathbf{dS}$ plunged in Σ, $\mathbf{J}\cdot\mathbf{dS}d\tau = \delta^3\mathrm{Q}$ is the amount of charges that the ZAMO sees crossing the elementary surface $\mathbf{dS}$ during the ZAMO proper time $d\tau$. Using the lapse function to link this proper time to the universal time coordinate Eq.(2.14), we obtain $h\mathbf{J}\cdot\mathbf{dS}dt = \delta^3\mathrm{Q}$. This justifies that the charges, which cross the $\mathscr{C}$ circle during a step dt of coordinate time are,

$$\mathrm{I} = \frac{d\mathrm{Q}}{dt} = \iint_\mathscr{S} h\mathbf{J}\cdot\mathbf{dS}\,. \tag{4.21}$$

Using Maxwell-Ampere Eq.(4.17) and the theorem of Kelvin-Stokes Eq.(B.33) leads to,

$$\mathrm{I} = \frac{c}{4\pi}\iint_\mathscr{S}\mathbf{D}\times(h\mathbf{B})\cdot\mathbf{dS} = \frac{c}{4\pi}\int_\mathscr{C} h\mathrm{B}^{\hat{\phi}}\varpi d\phi = \frac{h\mathrm{B}^{\hat{\phi}}\varpi c}{2}\,, \tag{4.22}$$

It allows us to express the magnetic field as a function of the magnetic flux A and the current intensity I,

$$\mathbf{B} = \frac{\mathbf{D}\mathrm{A}\times\boldsymbol{\epsilon}_\phi}{\varpi} + \frac{2\mathrm{I}}{h\varpi c}\boldsymbol{\epsilon}_\phi\,. \tag{4.23}$$

Isorotation law & Mass flux

Let us write the Maxwell-Faraday equation Eq.(4.17). Using Eq.(4.18), the permutativity property of the mixed product given by Eq.(B.27) and the relation which gives the rotational of scalar times a vector Eq.(B.30), we are able to write $\left(\mathbf{B}_\mathrm{p}\cdot\mathbf{D}\frac{\omega}{c}\right)\varpi\boldsymbol{\epsilon}_\phi = \mathbf{D}\times\left(\frac{\omega}{c}\mathbf{D}\mathrm{A}\right)$. This implies $\mathbf{D}\times\left(h\mathbf{E} - \frac{\omega}{c}\mathbf{D}\mathrm{A}\right) = 0$. Then there exists a scalar field, the electric potential Φ, such that

$$h\mathbf{E} = \frac{\omega}{c}\mathbf{D}\mathrm{A} - \mathbf{D}\Phi\,. \tag{4.24}$$

Then there is no toroidal electric field. Introducing the family of surface $\mathscr{T}_{\rm A} = \{{\rm M} \in \Sigma \,|\, {\rm A}({\rm M}) = {\rm A}\}$ that we call flux tubes. These surfaces are axisymmetric. Then Eq.(4.23) of the magnetic field shows that $\mathbf{B}$ is tangent to these surfaces, $\mathbf{B}\cdot\mathbf{D}{\rm A} = 0$. With the ideality condition Eq.(4.17), and the nonexistence of toroidal electric field imply that $\mathbf{V}\times\mathbf{B}\cdot\boldsymbol{\epsilon}_\phi = 0$. Using the permutativity of mixed product Eq.(B.27) and Eq.(4.18), we obtain $\mathbf{V}\cdot\mathbf{D}{\rm A} = 0$, which is equivalent to say that $\mathbf{V}$ is tangent to the flux tube. Then the field line of $\mathbf{V}$ and $\mathbf{B}$ are included on the flux tube $\mathscr{T}_{\rm A}$. Using Eq.(4.24) and multiplying the ideality condition given in Eq.(4.17) by $\times\mathbf{D}{\rm A}$, we prove that $\mathbf{D}\Phi\times\mathbf{D}{\rm A} \propto \mathbf{D}{\rm A}\times(\mathbf{B}\times\mathbf{V}) = \mathbf{B}(\mathbf{V}\cdot\mathbf{D}{\rm A}) - \mathbf{B}(\mathbf{V}\cdot\mathbf{D}{\rm A}) = 0$. Then $\mathbf{D}\Phi \parallel \mathbf{D}{\rm A}$, which is equivalent to say that $\Phi = \Phi({\rm A})$ (See Appendix.A.1)). Then introducing the **isorotation function** $\Omega({\rm A}) = c\frac{d\Phi}{d{\rm A}}$, we get,

$$\boxed{\mathbf{E} = -\frac{\Omega-\omega}{hc}\mathbf{D}{\rm A} \qquad \text{with} \qquad \Omega({\rm A}) \hat{=} c\frac{d\Phi}{d{\rm A}}}\,. \tag{4.25}$$

Reminding that $\mathbf{V}$ and $\mathbf{B}$ are tangent to the flux tube $\mathscr{T}_{\rm A} = \{{\rm M} \in \Sigma \,|\, {\rm A}({\rm M}) = {\rm A}\}$, the poloidal velocity is proportional to the magnetic field. It exists a function Ψ_A such that,

$$\boxed{\Psi_A\mathbf{B}_{\rm p} = 4\pi\rho_0\gamma h\mathbf{V}_{\rm p} \qquad \Rightarrow \qquad \mathbf{B}_{\rm p}\cdot\mathbf{D}\Psi_A = 4\pi hck_m}\,. \tag{4.26}$$

The function Ψ_A is linked to the mass flux function. As for the current of charge $\rho_0\gamma\mathbf{V}$ is the current of mass measured by the ZAMO. Then $\delta^3 m = \rho_0\gamma\mathbf{V}\cdot\mathbf{dS}d\tau$ is the mass which crosses $\mathbf{dS}$ measured by the ZAMO during a ZAMO proper time $d\tau$. Then for a coordinate lapse of time dt we have $\delta^3 m = \rho_0 h\gamma\mathbf{V}\cdot\mathbf{dS}dt$. It implies,

$$\dot{\rm M} = \iint_{\mathscr{S}} \rho_0 h\gamma\mathbf{V}_{\rm p}\cdot\mathbf{dS} = \iint_{\mathscr{S}} \frac{\Psi_A}{4\pi}\frac{\mathbf{D}{\rm A}\times\boldsymbol{\epsilon}_\phi}{\varpi}\cdot\mathbf{dS}\,, \tag{4.27}$$

To finish the calculation, let us introduce the curvilinear poloidal coordinate along a flux tube $\ell({\rm R},\theta)$. Then, except for a particular case or a particular point, $({\rm A},\ell,\phi)$ is a coordinate system. Because ℓ is a curvilinear length, we have $\|\,\mathbf{D}{\rm A}\,\|\,\boldsymbol{\partial}_\ell = \mathbf{D}{\rm A}\times\boldsymbol{\epsilon}_\phi$. This system of coordinates is adapted to the case we are studying. Using this coordinate system we write Eq.(4.26) getting the different equalities,

$$\begin{aligned}
&\mathbf{B}_{\rm p}\cdot\mathbf{D}\Psi_A = {\rm B_p}\left.\frac{\partial\Psi_A}{\partial\ell}\right|_{\rm A=cst} \qquad \Rightarrow \qquad \Psi_{\rm A}({\rm A},\ell) = \Psi_{\rm A}({\rm A},0) + \int_0^\ell \left.\frac{4\pi hck_m}{\|\,\mathbf{B}_{\rm p}\,\|}\right|_{\rm A=cst} d\ell \\
&\Rightarrow \Psi({\rm A},\ell) \hat{=} \int_0^{\rm A} \Psi_A({\rm A},\ell)\,|_{\ell=\rm cst}\, d{\rm A} = \int_0^{\rm A}\Psi_A({\rm A},0)\,d{\rm A} + \int_0^{\rm A}\int_0^\ell \frac{4\pi hck_m}{\|\,\mathbf{B}_{\rm p}\,\|}d\ell d{\rm A} \\
&\Rightarrow \Psi_A\mathbf{D}{\rm A} = \mathbf{D}\Psi - \left(\int_0^{\rm A}\left.\frac{4\pi hck_m}{\|\,\mathbf{B}_{\rm p}\,\|}\right|_{\ell=\rm cst} d{\rm A}\right)\mathbf{D}\ell
\end{aligned} \tag{4.28}$$

In Eq.(4.27), we are free to choose $\mathscr{S}$ as long as it is axisymmetric and its boundaries are $\mathscr{C}$. If we choose $\mathscr{S}(r,\theta) = \{{\rm M}\in\Sigma \,|\, \ell = \ell(r,\theta) \quad \text{and} \quad {\rm A} \le {\rm A}(r,\theta)\}$. Then let us replace the last equality of Eq.(4.28) in Eq.(4.27). The second term proportional to $\mathbf{D}\ell$ disappears in the integral, because the choice of $\mathscr{S}$ implies $\mathbf{dS}\propto\mathbf{D}\ell$ and then $(\mathbf{D}\ell\times\boldsymbol{\epsilon}_\phi)\cdot\mathbf{dS} = 0$. Using it for all functions f such as, $\frac{\mathbf{D}f\times\boldsymbol{\epsilon}_\phi}{\varpi} = \mathbf{D}\times\left(\frac{f}{\varpi}\boldsymbol{\epsilon}_\phi\right)$ similarly to the current function and applying the theorem of Kelvin-Stokes Eq.(B.33), we get,

$$\boxed{\begin{aligned}
\dot{\rm M} &= \frac{\Psi}{2} = \frac{1}{2}\left[\int_0^{\rm A}\Psi_A({\rm A},0)\,d{\rm A} + \int_0^{\rm A}\int_0^\ell \frac{4\pi hck_m}{\|\,\mathbf{B}_{\rm p}\,\|}d\ell d{\rm A}\right] \\
\frac{d\dot{\rm M}}{d{\rm A}}d{\rm A} &= \frac{1}{2}\left[\Psi_{\rm A}({\rm A},0) + \int_0^\ell \left.\frac{4\pi hck_m}{\|\,\mathbf{B}_{\rm p}\,\|}\right|_{\rm A=cst} d\ell\right] d{\rm A}
\end{aligned}} \tag{4.29}$$

The factor 2, is well adapted because $\dot{\rm M}$ is the mass flux for one hemisphere. The total mass flux is $2\dot{\rm M}$. The second term in the right hand side of the equation represents the mass flux

between two flux tubes, $\mathcal{T}_{\rm A}$ and $\mathcal{T}_{\rm A+dA}$. We see here that the mass flux is composed of the mass-flux at the base of the flow, plus the mass flux injected in the system by the loading term. The mass flux is conserved for non loaded flow ($k_m = 0$), and in this case $\Psi_A = \Psi_A({\rm A})$.

After injection in the ideality condition of the expression of the electric field Eq.(4.25) and the expression of poloidal velocity Eq.(4.27), we obtain the Isorotation frequency as a function of toroidal velocity and magnetic field.

$$\Omega = \omega + \frac{h}{\varpi}\left[{\rm V}^{\hat{\phi}} - \frac{\Psi_A {\rm B}^{\hat{\phi}}}{4\pi\rho_0 h\gamma}\right] \qquad \Rightarrow \qquad x = \frac{\varpi\,(\Omega-\omega)}{hc} = \frac{{\rm V}^{\hat{\phi}}}{c} - \frac{\Psi_A {\rm B}^{\hat{\phi}}}{4\pi\rho_0 h\gamma c} = \frac{{\rm V}^{\hat{\phi}}}{c} - \frac{{\rm V_p}}{c}\frac{{\rm B}^{\hat{\phi}}}{{\rm B_p}} \tag{4.30}$$

Here we introduce the physical quantity x, the cylindrical radius in unit of the light cylinder radius. The light cylinder surface is defined for $x^2 = 1$ where $x = \frac{{\rm V}^{\hat{\phi}}}{c} - \frac{{\rm V_p}}{c}\frac{{\rm B}^{\hat{\phi}}}{{\rm B_p}}$. When the flow crosses the light cylinder with $x \geq 1$, the toroidal magnetic field must be negative and sufficiently strong because toroidal velocity stays lower than the speed of light. One of the two following conditions must be fulfilled, either we have $|\,{\rm B}^{\hat{\phi}}\,| \gg {\rm B_p}$ or ${\rm V_p} \gg |\,{\rm V}^{\hat{\phi}}\,|$ or both. Outside this surface, the flow does not necessarily have a relativistic rotational velocity, but it is sufficient to have a large magnetic screw pitch $|\,{\rm B}^{\hat{\phi}}\,| \gg {\rm B_p}$ and quite relativistic poloidal velocity. The expression of Ω allows us to express a link between the velocity field $\mathbf{V}$ and the magnetic field $\mathbf{B}$,

$$\frac{\mathbf{V}}{c} = \frac{\Psi_A}{4\pi\rho_0 h\gamma c}\mathbf{B} + x\boldsymbol{\epsilon}_\phi \tag{4.31}$$

This expression allows us to interpret x as the difference of rotation between magnetic and velocity field lines.

Specific Angular momentum

We recall that $\boldsymbol{\xi} = \partial_\phi$ is the Killing vector of axisymmetry. Following the work of Lasota et al. [2014], we introduce and calculate the Noether angular momentum Flux,

$$\mathbf{M} \hat{=} \mathbf{T}(\boldsymbol{\xi}, .) \qquad \Rightarrow \qquad \nabla\cdot\mathbf{M} = \mathbf{k}\cdot\boldsymbol{\xi} \tag{4.32}$$

where $\mathbf{T} = \mathbf{T}_{\rm FL} + \mathbf{T}_{\rm EM}$ Eq.(3.54, 3.55). The advantage to work with the Noether flux instead of the flux measured by the ZAMO observer is that this flux respects some conservation equations. Using the axisymmetry and the stationarity of the flow, the conservation equation Eq.(4.32) can be written as,

$$\mathbf{D}\cdot\left(h\mathbf{M}_{\rm p}\right) = h\mathbf{k}\cdot\boldsymbol{\xi} \tag{4.33}$$

Then using Eqs.(3.55, 3.82) for the energy momentum tensor, and for electromagnetic tensor the 3+1 decomposition Eq.(4.9), the 3+1 decomposition of four velocity Eq.(4.5), and the definition of the mass flux per unit of magnetic flux Eq.(4.26), we obtain for the poloidal Noether Angular momentum flux,

$$\boxed{h\mathbf{M}_{\rm p} = \rho_0 h\gamma {\rm L}\mathbf{V}_{\rm p} = \frac{\Psi_A {\rm L}}{4\pi}\mathbf{B}_{\rm p} \qquad \text{with} \qquad {\rm L} \hat{=} \varpi\left(\gamma\xi {\rm V}^{\hat{\phi}} - \frac{h{\rm B}^{\hat{\phi}}}{\Psi_A}\right)} \tag{4.34}$$

We define here the function L, which is the total specific angular momentum. Indeed $\mathbf{M}_{\rm p}$ is the Angular momentum Noether flux. If $\rho_0\gamma h\mathbf{V}_{\rm p}$ is the mass flux, we can consider L as a specific angular momentum. This total specific angular momentum is composed of the specific angular momentum of the fluid and of the specific angular momentum of the electro-magnetic field. $\Psi_A {\rm L}$ is the angular momentum flux per unit of magnetic flux. The evolution along the flow of the angular momentum flux per unit of magnetic flux is calculated using the conservation of

the Noether Angular momentum flux Eq.(4.33). Combine the expression of this flux Eq.(4.34) and the Maxwell-Flux equation Eq.(4.17), we get,

$$\boxed{\mathbf{B}_{\rm p}\cdot\mathbf{D}\left(\Psi_A{\rm L}\right)=4\pi h\mathbf{k}\cdot\boldsymbol{\xi}} \tag{4.35}$$

Then as for the mass flux, we interpret $\Psi_A{\rm L}$ as the angular momentum flux per unit of magnetic flux. We derive a result for the angular momentum flux equivalent to Eq.(4.29) for the mass flux,

$$\boxed{\frac{d\dot{\rm J}_{\rm tot}}{d{\rm A}}=\Psi_A{\rm L}=\Psi_A{\rm L}\left({\rm A},\ell=0\right)+\int_0^{\ell}\left.\frac{4\pi h\mathbf{k}\cdot\boldsymbol{\xi}}{||\,\mathbf{B}_{\rm p}\,||}\right|_{\rm A=cst}d\ell} \tag{4.36}$$

Then the angular momentum flux between two flux tubes at some altitude is composed of the angular momentum flux at the base of the tube plus the angular momentum flux brought by the loading term $4\pi h\mathbf{k}\cdot\boldsymbol{\xi}$. The angular momentum flux per unit of magnetic flux is also conserved along the tube of magnetic flux for flow without plasma injection $k_m=\mathbf{k}=0$.

Specific Total Energy , Bernoulli Integrals

Following the same logic as for the angular momentum, we can introduce the Noether energy flux. Indeed, let us remind that $\boldsymbol{\eta}=\frac{1}{c}\partial_t$ is the Killing vector of stationarity. Then we can define and calculate the Noether energy flux,

$$\mathbf{P}\hat{=}-\mathbf{T}\left(\boldsymbol{\eta},.\right)\qquad\Rightarrow\qquad\nabla\cdot\mathbf{P}=-\mathbf{k}\cdot\boldsymbol{\eta}\qquad\Rightarrow\qquad\mathbf{D}\cdot\left(h\mathbf{P}_{\rm p}\right)=-h\mathbf{k}\cdot\boldsymbol{\eta} \tag{4.37}$$

where the last implication comes from the stationarity and axisymmetry assumptions. If the stress-energy tensor satisfies what we call the dominant energy condition. Which can be formulated as follows $\forall\mathbf{x}\in\mathscr{C}_+(\mathscr{M})$ a future oriented vector $-\mathbf{T}(\mathbf{x},.)$ is a future oriented vector. Then everywhere outside the ergosphere, $\mathbf{P}$ is a future oriented vector. Now using the different equations Eqs.(3.55, 3.82, 4.9, 4.5, 4.26, 2.33, 2.15, 4.25, 4.18) we obtain,

$$\boxed{h\mathbf{P}_{\rm p}=\rho_0\gamma h\mathscr{E}\mathbf{V}_{\rm p}=\frac{\Psi_A\mathscr{E}}{4\pi c}\mathbf{B}_{\rm p}\qquad\text{with}\qquad\mathscr{E}\hat{=}h\gamma\xi c^2+\gamma\xi\varpi\omega{\rm V}^{\hat{\phi}}-\frac{h\varpi\Omega}{\Psi_A}{\rm B}^{\hat{\phi}}} \tag{4.38}$$

We define here the function $\mathscr{E}$, which is the total specific energy. Indeed $\mathbf{P}_{\rm p}$ is the covariant Noether energy flux. Eq.(4.37) allows us to interpret $h\mathbf{P}_{\rm p}$ as the ZAMO Noether energy flux. Then if $\rho_0\gamma h\mathbf{V}_{\rm p}$ is the mass flux, we can consider $\mathscr{E}$ as some kind of total Noether specific energy. This total Noether specific energy is composed of the specific energy of the fluid and the specific energy of the electro-magnetic field. The specific energy of the fluid contains the gravitational potential, the kinetics energy, the enthalpy energy and the frame dragging energy. $\Psi_A\mathscr{E}$ is the total Noether energy flux per unit of magnetic flux. The evolution along the flow of the Noether energy flux per unit of magnetic flux is calculated using the conservation of the Noether Angular momentum Flux Eq.(4.37), the expression of this flux with E Eq.(4.38) and the Maxwell-Flux equation Eq.(4.17),

$$\boxed{\mathbf{B}_{\rm p}\cdot\mathbf{D}\Psi_A\mathscr{E}=-4\pi hc\mathbf{k}\cdot\boldsymbol{\eta}} \tag{4.39}$$

As before for the mass flux and for the angular momentum flux, we can derive an equivalent result to Eq.(4.29) for this energy flux.

$$\boxed{\frac{d\dot{\mathscr{E}}_{\rm tot}}{d{\rm A}}=\Psi_A\mathscr{E}=\Psi_A\mathscr{E}\left({\rm A},\ell=0\right)-\int_0^{\ell}\left.\frac{4\pi hc\mathbf{k}\cdot\boldsymbol{\eta}}{||\,\mathbf{B}_{\rm p}\,||}\right|_{\rm A=cst}d\ell} \tag{4.40}$$

$\Psi_A\mathscr{E}$ is the Noether energy flux per unit of magnetic flux. The Noether energy flux between two flux tubes is composed of the Noether energy flux at the base of the tube plus the Noether energy flux brought by the loading term $4\pi h\mathbf{k}\cdot\boldsymbol{\xi}$. The Noether energy flux per unit of magnetic flux is also

conserved along the tube of magnetic flux for non-loaded flow. The definition of Noether energy flux is practical for calculation because this quantity is attached to some conservation relation Eq.(4.37), but this flux does not correspond to any energy flux measured by an observer except at infinity. In particular it is the case in the ergoregion where the nature of $\boldsymbol{\eta}$ is not time like and so is not even proportional to some four velocity. Indeed the energy-flux measured by an observer of four-speed $\mathbf{v}$ is $-\mathbf{T}(\mathbf{v},.)$. Thus it will be interesting to introduce the energy flux measured by the ZAMO as $-\mathbf{T}(\mathbf{n},.)$. Then calculating its poloidal part, we obtain $\frac{\Psi_A}{4\pi hc}(\mathscr{E}-\mathrm{L}\omega)\mathbf{B}_\mathrm{p}$. Thus we can interpret $\frac{\mathscr{E}-\mathrm{L}\omega}{h}$ as the specific energy measured in the ZAMO frame,

$$\frac{\mathscr{E}-\mathrm{L}\omega}{h}=\gamma\xi c^2-\frac{\varpi(\Omega-\omega)}{\Psi_A}\mathrm{B}^{\hat{\phi}} \tag{4.41}$$

Alfvénic Mach Number

One of the fundamental function of magnetized flow is called **the Alfvén Mach number**. This number is the ratio of the poloidal velocity with the velocity of Alfvén waves. We use, in the rest of the document, the poloidal Mach number given by,

$$\boxed{\mathrm{M}_\mathrm{Alf}^2\hat{=}h^2\frac{\mathrm{V}_\mathrm{p}^2}{\mathrm{V}_\mathrm{A,p}^2}=\frac{\xi\Psi_A^2}{4\pi\rho_0}}. \tag{4.42}$$

Following Breitmoser and Camenzind [2000] we introduce here for practical reasons the lapse function in the definition. Indeed $h\mathrm{V}_\mathrm{p}$ is the velocity of fluid measured by the ZAMO in term of coordinate time $h\mathbf{V}_\mathrm{p}=\frac{d\mathbf{M}}{dt}$, where $d\mathrm{M}$ is measured in the ZAMO frame. We define here the Alfvénic poloidal velocity by,

$$\mathrm{V}_\mathrm{A,p}^2=\frac{\mathrm{B}_\mathrm{p}^2}{4\pi\rho_0\xi\gamma^2} \tag{4.43}$$

Expression of the enthalpy and the toroidal fields

Using this definition of the Mach number M_Alf, Eq.(4.42), the system of first integrals including the isorotation frequency Ω Eq.(4.30), the specific angular momentum L, Eq.(4.34) and the specific energy $\mathscr{E}$, Eq.(4.38), can be inversed to express some important quantities of the flow,

$$\boxed{\begin{cases}-\dfrac{2\mathrm{I}(\Omega-\omega)}{\Psi_A c}=-\dfrac{h\varpi(\Omega-\omega)\mathrm{B}^{\hat{\phi}}}{\Psi_A}=(\mathscr{E}-\mathrm{L}\omega)\dfrac{h^2\left(x^2-x_\mathrm{MR}^2\right)}{\mathrm{M}_\mathrm{Alf}^2-h^2\left(1-x^2\right)}=(\mathscr{E}-\mathrm{L}\omega)\dfrac{\mathscr{N}_\mathrm{I}}{\mathscr{D}},\\ h\gamma\xi\dfrac{\mathrm{V}^{\hat{\phi}}}{c}=\dfrac{(\mathscr{E}-\mathrm{L}\omega)}{c^2x}\dfrac{\mathrm{M}_\mathrm{Alf}^2x_\mathrm{MR}^2-(1-x_\mathrm{MR}^2)h^2x^2}{\mathrm{M}_\mathrm{Alf}^2-h^2\left(1-x^2\right)}=\dfrac{(\mathscr{E}-\mathrm{L}\omega)}{c^2x}\dfrac{\mathscr{N}_\mathrm{V}}{\mathscr{D}},\\ \gamma h\xi c^2=(\mathscr{E}-\mathrm{L}\omega)\dfrac{\mathrm{M}_\mathrm{Alf}^2-h^2(1-x_\mathrm{MR}^2)}{\mathrm{M}_\mathrm{Alf}^2-h^2\left(1-x^2\right)}=(\mathscr{E}-\mathrm{L}\omega)\dfrac{\mathscr{N}_\mathscr{E}}{\mathscr{D}},\end{cases}} \tag{4.44}$$

where, we used the following definition,

$$x_\mathrm{MR}^2=\frac{\mathrm{L}(\Omega-\omega)}{\mathscr{E}-\mathrm{L}\omega}. \tag{4.45}$$

x_MR^2 measures the fraction of magnetic rotator energy $\mathrm{L}(\Omega-\omega)$ divided by the specific energy in the ZAMO frame. This new parameter x_MR, conversely to the previous one x_A defined in Meliani et al. [2006], is not any more a constant along a field line, since ω is not an integral of the motion. These quantities have the same denominator, which makes appear a singular surface.

$$\Sigma_\mathrm{A}\hat{=}\left\{\mathrm{M}\in\Sigma\,|\,\mathscr{D}=\mathrm{M}_\mathrm{Alf}^2-h^2\left(1-x^2\right)=0\right\} \tag{4.46}$$

We call this surface the **Alfvén surface**. Therefore all quantities need to be regular at the Alfvén surface crossing. The conditions of regularity of the quantities $\mathrm{B}^{\hat{\phi}}$, $h\gamma\xi\frac{\mathrm{V}^{\hat{\phi}}}{c}$ and $\gamma h\xi$ imply that the numerator of the equations also cancel out each other. Furthermore, the numerator of the current I and the numerator of $h\gamma\xi\frac{\mathrm{V}^{\hat{\phi}}}{c}$ are linear functions of the denominator $\mathscr{D}$ and the numerator of $h\gamma\xi$. Indeed $\mathscr{N}_{\mathrm{I}} = \mathscr{D} - \mathscr{N}_{\mathscr{E}}$ and $\mathscr{N}_{\mathrm{V}} = \left(\frac{\mathrm{M}^2_{\mathrm{Alf}}}{h^2} + x^2\right)\mathscr{N}_{\mathscr{E}} - \frac{\mathrm{M}^2_{\mathrm{Alf}}}{h^2}\mathscr{D}$, the regularity of $h\gamma\xi$ implies the regularity of the two others. Then the condition of regularity implies that for each point on the Alfvén surface,

$$\mathrm{M} \in \Sigma_{\mathrm{A}} \quad \Rightarrow \quad \begin{cases} \mathscr{D} = \mathrm{M}^2_{\mathrm{Alf}} - h^2\left(1 - x^2\right) = 0 \\ \mathscr{N}_{\mathscr{E}} = \mathrm{M}^2_{\mathrm{Alf}} - h^2(1 - x^2_{\mathrm{MR}}) = 0 \end{cases} . \tag{4.47}$$

4.2.3 The volumic poloidal forces

We present here different ways to decompose and re-organize the forces, which act on the GRMHD flow. First of all, we see the decomposition of the forces, which is used to draw the forces applying on the fluid in the solution of the model. This decomposition is really adapted for a dynamical analysis of the flow. Then we give a mathematically "simple" decomposition, which is the basis of the Grad-Shafranov approach of the problem.

Decomposition used in the model

Les us start from the Euler equation. The variation of angular momentum along a field line, Eq.(4.35), is equivalent to the toroidal component of the Euler equation. Putting the advection term on the forces side in order to analyze the dynamics from the fluid frame point of view, we get,

$$\mathscr{F}_{\mathrm{A}} + \mathscr{F}_{\mathrm{G}} + \mathscr{F}_{\mathrm{LT}} + \mathscr{F}_{\mathrm{P}} + \mathscr{F}_{\mathrm{E}} + \mathscr{F}_{\mathrm{M}} + \mathscr{F}_{\mathrm{L}} = \mathbf{0} \tag{4.48}$$

where the $\mathscr{F}_i$ term are the poloidal forces. We have,

$$\begin{aligned}
&\mathscr{F}_{\mathrm{A}} = -\rho_0\gamma\left(\mathbf{V}\cdot\mathbf{D}\right)\gamma\xi\mathbf{V}\,|_{\mathrm{p}}\,, && \text{Advection force}\\
&\mathscr{F}_{\mathrm{G}} = -\rho_0\xi\gamma^2c^2\mathbf{D}\ln h\,, && \text{Gravitational force}\\
&\mathscr{F}_{\mathrm{LT}} = -\rho_0\xi\gamma^2\frac{\varpi\omega\mathrm{V}^{\hat{\phi}}}{h}\mathbf{D}\ln\omega\,, && \text{Lense}-\text{Thirring force}\\
&\mathscr{F}_{\mathrm{E}} = \rho_e\mathbf{E} = \frac{\mathbf{D}\cdot\mathbf{E}}{4\pi}\mathbf{E}\,, && \text{Electric force}\\
&\mathscr{F}_{\mathrm{M}} = \frac{\mathbf{J}\times\mathbf{B}}{c} = \frac{[\mathbf{D}\times(h\mathbf{B})]\times\mathbf{B}}{4\pi h} + \frac{\mathbf{E}\cdot\mathbf{D}\omega}{4\pi ch}\mathbf{D}\mathrm{A}\,, && \text{Magnetic force}\\
&\mathscr{F}_{\mathrm{M}} = -\mathbf{D}\mathrm{P}\,, && \text{Pressure force}\\
&\mathscr{F}_{\mathrm{L}} = \mathbf{p}\,(\mathbf{k}) - \gamma\xi k_m c\mathbf{V}\,, && \text{Loading force}
\end{aligned} \tag{4.49}$$

where we directly used Maxwell-Gauss an Maxwell-Ampere equations to replace the charge density and the current of charges measured by the ZAMO. The loading force is composed by a force due to the interaction with the source (Creation/Annihilation + Compton/Inverse Compton) $\mathbf{p}\,(\mathbf{k})$ and a force due to the change of volumic mass of the fluid $\gamma\xi k_m c\mathbf{V}$. The study of forces will be restricted to the analysis of poloidal forces. The poloidal advection may be decomposed in one term coming from the poloidal velocity and one term coming from the toroidal velocity,

$$\mathscr{F}_{\mathrm{A}} = -\rho_0\gamma\left(\mathbf{V}\cdot\mathbf{D}\right)\gamma\xi\mathbf{V} = \mathscr{F}_{\mathrm{A_p}} + \mathscr{F}_{\mathrm{A}_\phi} \quad \Rightarrow \quad \begin{cases} \mathscr{F}_{\mathrm{A}_\phi} = \rho_0\xi\gamma^2{\mathrm{V}^{\hat{\phi}}}^2\mathbf{D}\ln\varpi & \text{Centrifugal forces} \\ \mathscr{F}_{\mathrm{A_p}} = -\rho_0\gamma\left(\mathbf{V}_{\mathrm{p}}\cdot\mathbf{D}\right)\gamma\xi\mathbf{V}_{\mathrm{p}} & \text{Poloidal velocity advection force} \end{cases} \tag{4.50}$$

The term $\mathscr{F}_{\mathrm{A}_\phi}$ is simply the centrifugal force. The term coming from the poloidal velocity advection force can also be decomposed. Indeed using Leibniz rule on the derivation of $\xi\times\gamma\mathbf{V}_{\mathrm{p}}$, we also decompose the poloidal velocity advection force into two components,

$$\mathscr{F}_{\mathrm{A_p}} = -\rho_0 \gamma \left(\mathbf{V}_\mathrm{p}\cdot\mathbf{D}\right)\gamma\xi\mathbf{V}_\mathrm{p} = \mathscr{F}_\xi + \mathscr{F}_{\mathrm{AP}} \qquad \Rightarrow \qquad \begin{cases} \mathscr{F}_\xi = \gamma^2 \dfrac{\mathrm{V}_\mathrm{p}^2}{c^2}\mathscr{F}_{\mathrm{P}\parallel} + \gamma\left(\mathbf{u}\cdot\mathbf{k} + \xi c^2 k_m\right)\dfrac{\mathbf{V}_\mathrm{p}}{c} & \text{enthalpy force} \\ \mathscr{F}_{\mathrm{A_p}} = -\rho_0\xi\gamma\left(\mathbf{V}_\mathrm{p}\cdot\mathbf{D}\right)\gamma\mathbf{V}_\mathrm{p} & \text{Poloidal acceleration force} \end{cases} \tag{4.51}$$

where we note $\mathscr{F}_{\mathrm{P}\parallel} = -\left(\mathbf{e}_\parallel\cdot\mathbf{D}\mathrm{P}\right)\mathbf{e}_\parallel$, with $\mathbf{e}_\parallel = \mathbf{B}_\mathrm{p}/\mathrm{B}_\mathrm{p}$ is the unit spatial vector parallel to the flow in the poloidal plane. The first term, that we call enthalpy force, is due to the variation of enthalpy along line. This term can be written as a function of the pressure force along the line using the projection of first principle along the flow. The second term is simply the poloidal acceleration which is the acceleration for a motion in poloidal plane. This term can be traditionally decomposed in its part along the line (pure acceleration), and a "tension" term due to the curvature of the poloidal field line. But we shall not use this decomposition in the presentation of the results.

The second force to be decomposed is the poloidal magnetic force. Separating the magnetic field into its poloidal and toroidal parts, we get,

$$\mathscr{F}_\mathrm{M} = \frac{\left[\mathbf{D}\times\left(h\mathbf{B}_\mathrm{p}\right)\right]\times\mathbf{B}_\mathrm{p}}{4\pi h} + \frac{\left[\mathbf{D}\times\left(h\mathrm{B}^{\hat\phi}\boldsymbol{\epsilon}_\phi\right)\right]\times\mathrm{B}^{\hat\phi}\boldsymbol{\epsilon}_\phi}{4\pi h} + \frac{\mathbf{E}_\mathrm{p}\cdot\mathbf{D}\omega}{4\pi c h}\mathbf{D}\mathrm{A} = \mathscr{F}_{\mathrm{M},\mathrm{B_p}} + \mathscr{F}_{\mathrm{M},\mathrm{B}^{\hat\phi}} + \mathscr{F}_{\mathrm{M},\omega} \tag{4.52}$$

Knowing the expression of the curl operator, Eq.(2.41), the mixed terms are both either zero or along $\boldsymbol{\epsilon}_\phi$. Now using the Leibniz operation Eq.(B.30) on the gradient of a scalar product, we decompose the vector product of a field with the curl operator of the same field. Thus for the poloidal magnetic force,

$$\begin{aligned} \mathscr{F}_{\mathrm{M},\mathrm{B_p}} &= \frac{1}{4\pi h^2}\left[h\left(\mathbf{B}_\mathrm{p}\cdot\mathbf{D}\right)h\mathbf{B}_\mathrm{p} - \mathbf{D}\frac{h^2\mathbf{B}_\mathrm{p}^2}{2}\right] \\ &= \frac{1}{4\pi h^2}\left[h^2\mathbf{B}_\mathrm{p}^2\left(\mathbf{e}_\parallel\cdot\mathbf{D}\right)\mathbf{e}_\parallel - \left\{\mathbf{D}\frac{h^2\mathbf{B}_\mathrm{p}^2}{2} - \left(\mathbf{e}_\parallel\cdot\mathbf{D}\frac{h^2\mathbf{B}_\mathrm{p}^2}{2}\right)\right\}\right] \end{aligned} \qquad \Rightarrow \qquad \begin{cases} \mathscr{F}_{\mathrm{M,T},\mathrm{B_p}} = \dfrac{\mathbf{B}_\mathrm{p}^2}{4\pi}\dfrac{\mathbf{e}_\perp}{\mathscr{R}_\mathrm{p}} \\ \mathscr{F}_{\mathrm{M,P},\mathrm{B_p}} = -\dfrac{1}{8\pi h^2}\mathbf{D}_\perp h^2\mathbf{B}_\mathrm{p}^2 \end{cases} \tag{4.53}$$

The curvature radius appears using the usual relation $\left(\mathbf{e}_\parallel\cdot\mathbf{D}\right)\mathbf{e}_\parallel = \frac{\mathbf{e}_\perp}{\mathscr{R}_\mathrm{p}}$. The first term is called the magnetic poloidal tension. This force acts on the flow and pushes the poloidal fieldlines to straighten up, i.e. to reduce their curvature $\frac{1}{\mathscr{R}_\mathrm{p}}$,, or in an equivalent way to flatten them, i.e. to increase their radius of curvature $\mathscr{R}_\mathrm{p}$. This force is proportional to the curvature of the line and its orientation is directed towards the inside of the field line. The second term is the poloidal pressure. The orthogonal operator is defined by $\mathbf{D}_\perp f \hat{=} \left(\mathbf{e}_\perp\cdot\mathbf{D}f\right)\mathbf{e}_\perp$. Then this force is orthogonal to the poloidal fieldline. This force pushes to distribute the poloidal magnetic pressure, so it tends to open the lines when there is an "over-density" of magnetic fieldlines (which is equivalent to a magnetic field locally relatively strong), and to close them when there is an under-density (which is equivalent to a magnetic field locally relatively weak). For the toroidal magnetic force, we obtain,

$$\begin{aligned} \mathscr{F}_{\mathrm{M},\mathrm{B}^{\hat\phi}} &= \frac{1}{4\pi h^2}\left[h\mathrm{B}^{\hat\phi}\left(\boldsymbol{\epsilon}_\phi\cdot\mathbf{D}\right)h\mathrm{B}^{\hat\phi}\boldsymbol{\epsilon}_\phi - \mathbf{D}\frac{h^2\mathrm{B}^{\hat\phi 2}}{2}\right] \\ &= -\frac{\mathrm{B}^{\hat\phi 2}}{4\pi}\mathbf{D}\ln\varpi - \frac{1}{8\pi h^2}\mathbf{D}h^2\mathrm{B}^{\hat\phi 2} \end{aligned} \qquad \Rightarrow \qquad \begin{cases} \mathscr{F}_{\mathrm{M,T},\mathrm{B}^{\hat\phi}} = -\dfrac{\mathrm{B}^{\hat\phi 2}}{4\pi}\mathbf{D}\ln\varpi \\ \mathscr{F}_{\mathrm{M,P},\mathrm{B}^{\hat\phi}} = -\dfrac{1}{8\pi h^2}\mathbf{D}h^2\mathrm{B}^{\hat\phi 2} \end{cases} \tag{4.54}$$

In the toroidal decomposition, we use the axisymmetry and the expression of the advection term Eq.(2.42) to show that $\left(\boldsymbol{\epsilon}_\phi\cdot\mathbf{D}\right)\boldsymbol{\epsilon}_\phi = -\mathbf{D}\ln\varpi$. The first term is called toroidal magnetic magnetic tension. Its effect is to collimate the magnetic tube flux when $\mathrm{B}^{\hat\phi}$ is strong. This force is decreasing when the toroidal field decreases. The second term is the toroidal magnetic pressure.

Decomposition-reorganization, prelude for Grad-Shafranov

The derivation of the Grad-Shafranov equation is relatively difficult. To prepare and avoid fastidious development, it is useful to present a way to decompose forces adapted to this issue. Let us start with the advection forces. The centrifugal force keeps the same expression as in Eq.(4.50), but we do not proceed to the same decomposition as in Eq.(4.51) for the poloidal velocity advection force. Indeed we try here to decompose-recompose the maximum of force terms in order to make the transversal terms appear. A clever derivation presented in (An.D.2.1) leads to the decomposition,

$$\mathscr{F}_{\rm A} = \mathscr{F}_{\rm A_p1} + \mathscr{F}_{\rm A_p2} + \mathscr{F}_{\rm A_{\hat\phi}} + \xi\gamma c k_m \mathbf{V}_{\rm p} \qquad \text{with} \qquad \left\{ \begin{array}{l} 4\pi\mathscr{F}_{\rm A_p11} = -\dfrac{1}{2h^2{\rm M}_{\rm Alf}^2}\mathbf{D}\left(\dfrac{{\rm M}_{\rm Alf}^4\mathbf{D}{\rm A}^2}{\varpi^2}\right) \\ 4\pi\mathscr{F}_{\rm A_p12} = \dfrac{{\rm M}_{\rm Alf}^2\mathbf{D}{\rm A}^2}{\varpi^2h^2}\mathbf{D}\ln h \\ 4\pi\mathscr{F}_{\rm A_p2} = \left[\mathbf{D}\cdot\left(\dfrac{{\rm M}_{\rm Alf}^2\mathbf{D}{\rm A}}{h\varpi^2}\right)\right]\dfrac{\mathbf{D}{\rm A}}{h} \\ 4\pi\mathscr{F}_{\rm A_{\hat\phi}} = \dfrac{\Psi_A^2(\mathscr{E}-{\rm L}\omega)^2}{{\rm M}_{\rm Alf}^2c^2h^2}\left(\dfrac{\mathscr{N}_{\rm V}}{x\mathscr{D}}\right)^2\mathbf{D}\ln\varpi \end{array} \right. \tag{4.55}$$

The term proportional to $k_m\mathbf{V}_{\rm p}$ is simplified by the second term of the advection velocity forces. A similar calculation presented in Appendix.(D.2.1) leads for the magnetic force,

$$\mathscr{F}_{\rm M} = \mathscr{F}_{\rm M_{\hat\phi}} + \mathscr{F}_{\rm M_p} + \mathscr{F}_{\rm M,\omega} \qquad \text{with} \qquad \left\{ \begin{array}{l} 4\pi\mathscr{F}_{\rm M_{\hat\phi}} = -\dfrac{2}{h^2c^2\varpi^2}\mathbf{D}{\rm I}^2 \\ 4\pi\mathscr{F}_{\rm M_p} = \left[\mathbf{D}\cdot\left(\dfrac{h\mathbf{D}{\rm A}}{\varpi^2}\right)\right]\dfrac{\mathbf{D}{\rm A}}{h} \\ 4\pi\mathscr{F}_{\rm M,\omega} = -\dfrac{(\Omega-\omega)}{h^2c^2}(\mathbf{D}{\rm A}\cdot\mathbf{D}\omega)\,\mathbf{D}{\rm A} \end{array} \right. \tag{4.56}$$

Then for the electrical force (see details of calculation in Appendix.(D.2.1)

$$4\pi\mathscr{F}_{\rm E} = \left[\mathbf{D}\cdot\left(\frac{hx^2\mathbf{D}{\rm A}}{\varpi^2}\right) - \frac{\Omega-\omega}{hc^2}\frac{d\Omega}{d{\rm A}}\right]\frac{\mathbf{D}{\rm A}}{h} - 4\pi\mathscr{F}_{\rm M,\omega} \tag{4.57}$$

For the gravity force we get,

$$4\pi\mathscr{F}_{\rm G} = -\frac{\Psi_A^2(\mathscr{E}-{\rm L}\omega)^2}{{\rm M}_{\rm Alf}^2c^2h^2}\left(\frac{\mathscr{N}_{\mathscr{E}}}{\mathscr{D}}\right)^2\mathbf{D}\ln h \tag{4.58}$$

And the Lense-thirring force,

$$4\pi\mathscr{F}_{\rm LT} = -\frac{\Psi_A^2(\mathscr{E}-{\rm L}\omega)^2\varpi\omega}{{\rm M}_{\rm Alf}^2c^3h^3x}\left(\frac{\mathscr{N}_{\mathscr{E}}\mathscr{N}_{\rm V}}{\mathscr{D}^2}\right)\mathbf{D}\ln\omega \tag{4.59}$$

Then it is useful to write the energy integrals Eq.(4.44), using the expression of the Lorentz factor, γ Eq.(4.6). Expressing $1/\gamma^2$, as a function of poloidal and toroidal velocities, and multiplying both side of equation per $h^2\gamma^2\xi^2$ combined with Eq.(4.44) and Eq.(4.18, 4.26), we obtain,

$$\boxed{-\frac{{\rm M}_{\rm Alf}^4\,||\,\mathbf{D}{\rm A}\,||^2}{\varpi^2} = \Psi_A^2h^2\xi^2c^2 + \frac{\Psi_A^2(\mathscr{E}-{\rm L}\omega)^2}{c^2}\frac{\mathscr{N}_{\rm V}^2-x^2\mathscr{N}_{\mathscr{E}}^2}{x^2\mathscr{D}^2}} \tag{4.60}$$

This equation is sometimes called the wind equation. It gives the evolution of the Alfvénic Mach number with the first integrals, magnetic flux and enthalpy in the flow. This equation is not a differential equation in ${\rm M}_{\rm Alf}^2$. This is the primitive of Euler-equation along the flow. So this equation is a first order term in Alfenic Mach number. These decomposition and the use of

equation Eq.(4.60) allow us to make some simplifications, which bring in the recomposition of the forces to the poloidal plane equation,

$$\left[\mathbf{D}\cdot\left(\frac{\mathscr{D}\mathbf{D}\mathrm{A}}{h\varpi^2}\right)\right]\frac{\mathbf{D}\mathrm{A}}{h}-\frac{1}{2h^2\mathrm{M}_{\mathrm{Alf}}^2}\mathbf{D}\left(\frac{\mathrm{M}_{\mathrm{Alf}}^4\mathbf{D}\mathrm{A}^2}{\varpi^2}\right)-\frac{2}{h^2c^2\varpi^2}\mathbf{D}\mathrm{I}^2-4\pi\mathbf{D}\mathrm{P}-\frac{\Omega-\omega}{h^2c^2}\frac{d\Omega}{d\mathrm{A}}\mathbf{D}\mathrm{A}+4\pi\mathbf{k}_{\mathrm{p}}$$
$$-4\pi\rho_0\xi c^2\left(1+\left(\frac{\gamma\mathrm{V}^{\hat{\phi}}}{c}\right)^2\right)\mathbf{D}\ln h-\frac{\Psi_A^2(\mathscr{E}-\mathrm{L}\omega)^2\varpi\omega}{\mathrm{M}_{\mathrm{Alf}}^2c^3h^3x}\left(\frac{\mathscr{N}_{\mathscr{E}}\mathscr{N}_{\mathrm{V}}}{\mathscr{D}^2}\right)\mathbf{D}\ln\omega+\frac{\Psi_A^2(\mathscr{E}-\mathrm{L}\omega)^2}{\mathrm{M}_{\mathrm{Alf}}^2c^2h^2}\left(\frac{\mathscr{N}_{\mathrm{V}}}{x\mathscr{D}}\right)^2\mathbf{D}\ln\varpi=\mathbf{0} \tag{4.61}$$

The first term is a second differential non-linear order term in the magnetic flux. The presence of the $\mathscr{D}$ inside of the derivation shows again the importance of this term for the property and the regime of the flow. Indeed the first term can be interpreted as the term which opens or closes the flux tube (some kind of global transversal inertia of the tube). Eq.(4.60) must be used to calculate and decompose the second term. The third term is coming from the effect of the toroidal magnetic field. The fifth term is linked to the effect of electrical field on the tube geometry. The seventh term is composed by the gravitational terms and some term from advection. We also use Eq.(4.60) to obtain the term in parenthesis. The two last terms are the Lense-thirring and centrifugal forces.

4.2.4 Grad-Shafranov approach

The Grad-Shafranov approach consists to use all given first integrals in order to resume the study of GRASIMHD magnetized flow in a simultaneous resolution of the motion along the flow Eq.(4.60) and a resolution of the motion orthogonally to the flow from Eq.(4.61). These equations gives the topology of the poloidal flow.

This approach can be done only for magnetized flows which satisfy specific properties. Grad-Shafranov approach concern ideal gaz in thermodynamics equilibrium, no heating, and no ideal conduction. This kind of approach was introduced in the case of force free magnetized gases by Grad and Rubin [1958] and Shafranov [1966], which worked on plasmas in Tokamak. This approach was imported in the domain of astrophysical flows by Okamoto [1974, 1975] and Heinemann and Olbert [1978]. The derivation in the case of Schwarzchild metric was done by Mobarry and Lovelace [1986]. For Kerr metric, the equation was obtained by the work of Nitta et al. [1991] and Beskin and Par'ev [1993]. This is the approach we expose here. The more general Grad-Shafranov equation concerns the case of a fluid in any axisymmetric and stationary space-time. The first to obtain such an equation were Ioka and Sasaki [2003]. Let us also mention the fully covariant derivation done by Gourgoulhon et al. [2011]. This approach may also be used for analytical work on magnetospheres in the free-force context as it has been done by Nathanail and Contopoulos [2014].

Transverse equation for a plasma out of equilibrium and with loaded terms

We need to find an equation which is characteristic to the transversal evolution of the flow. Started from Eq.(4.61), we need to work on the non-transversal term (not $\propto \mathbf{D}\mathrm{A}$). The second term of Eq.(4.61) is proportional to the gradient of a quantity expressed in Eq.(4.60). The third term of Eq.(4.61) is the gradient of I^2 expressed in Eq.(4.44). These two quantities inside the gradient of the first end the third term of Eq.(4.61) are function of $\mathrm{M}_{\mathrm{Alf}}^2, \xi, h, \varpi, \omega, \Psi_A, \Omega, \Psi_A\mathrm{L}$ and $\Psi_A\mathscr{E}$. Then we decompose these terms (see the details in Appendix.D.2.2) and reorganize them with the other terms.

Finally we get the transverse equation out of equilibrium and with the injection terms $k_m, \mathbf{k}$,

$$\frac{1}{h}\left[\mathbf{D}\cdot\left(\frac{\mathscr{D}\mathbf{D}\mathrm{A}}{h\varpi^2}\right)\right]-\left[\frac{\Psi_A\xi\varpi}{hc}\frac{\Psi_A(\mathscr{E}-\mathrm{L}\omega)}{\mathrm{M}^2_{\mathrm{Alf}}}\frac{\mathscr{N}_{\mathrm{I}}}{x\mathscr{D}}+\frac{\Omega-\omega}{h^2c^2}\mathbf{D}\mathrm{A}^2\right]\frac{d\Omega}{d\mathrm{A}}+\frac{\Psi_A\xi^2c^2}{\mathrm{M}^2_{\mathrm{Alf}}}\frac{\mathbf{D}\Psi_A\cdot\mathbf{D}\mathrm{A}}{\mathbf{D}\mathrm{A}^2}$$
$$+\frac{\Psi_A(\mathscr{E}-\mathrm{L}\omega)}{c\mathrm{M}^2_{\mathrm{Alf}}\varpi}\left[\frac{\varpi\omega}{hc}\frac{\mathscr{N}_{\mathscr{E}}}{\mathscr{D}}+\frac{\mathscr{N}_{\mathrm{V}}}{x\mathscr{D}}\right]\frac{\mathbf{D}\Psi_A\mathrm{L}\cdot\mathbf{D}\mathrm{A}}{\mathbf{D}\mathrm{A}^2}+\frac{\Psi_A(\mathscr{E}-\mathrm{L}\omega)}{\mathrm{M}^2_{\mathrm{Alf}}h^2}\frac{\mathscr{N}_{\mathscr{E}}}{\mathscr{D}}\frac{\mathbf{D}\Psi_A\mathscr{E}\cdot\mathbf{D}\mathrm{A}}{\mathbf{D}\mathrm{A}^2}+\frac{4\pi}{\mathbf{D}\mathrm{A}^2}\left\{\left(\rho_0\xi c^2\mathbf{D}\xi-\mathbf{D}\mathrm{P}+\mathbf{k}_{\mathrm{p}}\right)\cdot\mathbf{D}\mathrm{A}\right\} \tag{4.62}$$

Critical surface of Grad Shafranov formulation

To achieve and complete the Grad-Shafranov formulation of GRASIMHD, we need to do additional assumptions. Choose a case without loading term ($k_m=\mathbf{k}=0$) and with a plasma which reaches everywhere its thermodynamical equilibrium. Let us remove also the heating terms. In this case several simplifications appear. First of all, first integrals are now constants of motion along the flow, and thus, are function of the magnetic flux $\Psi_A=\Psi_A(\mathrm{A})$, $\mathrm{L}=\mathrm{L}(\mathrm{A})$ and $\mathscr{E}=\mathscr{E}(\mathrm{A})$. The plasma is in thermodynamical equilibrium, thus we can use the first principle Eq.(3.71). This principle associated with the last equation of Eq.(4.17) implies that the specific entropy is also a constant of motion,

$$\mathbf{V}_{\mathrm{p}}\cdot\mathbf{D}s=0 \qquad \Rightarrow \qquad s=s(\mathrm{A}) \tag{4.63}$$

Thus the entropy is a function of magnetic flux A. There is an adiabatic evolution along field line. The transverse equation Eq.(4.62) can be simplified and we get,

$$\begin{aligned}&\frac{1}{h}\left[\mathbf{D}\cdot\left(\frac{\mathscr{D}\mathbf{D}\mathrm{A}}{h\varpi^2}\right)\right]-\left[\frac{\Psi_A\xi\varpi}{hc}\frac{\Psi_A(\mathscr{E}-\mathrm{L}\omega)}{\mathrm{M}^2_{\mathrm{Alf}}}\frac{\mathscr{N}_{\mathrm{I}}}{x\mathscr{D}}+\frac{\Omega-\omega}{h^2c^2}\mathbf{D}\mathrm{A}^2\right]\frac{d\Omega}{d\mathrm{A}}+\frac{\Psi_A\xi^2c^2}{\mathrm{M}^2_{\mathrm{Alf}}}\frac{d\Psi_A}{d\mathrm{A}}\\&+\frac{\Psi_A(\mathscr{E}-\mathrm{L}\omega)}{c\mathrm{M}^2_{\mathrm{Alf}}\varpi}\left[\frac{\varpi\omega}{hc}\frac{\mathscr{N}_{\mathscr{E}}}{\mathscr{D}}+\frac{\mathscr{N}_{\mathrm{V}}}{x\mathscr{D}}\right]\frac{d\Psi_A\mathrm{L}}{d\mathrm{A}}+\frac{\Psi_A(\mathscr{E}-\mathrm{L}\omega)}{\mathrm{M}^2_{\mathrm{Alf}}h^2}\frac{\mathscr{N}_{\mathscr{E}}}{\mathscr{D}}\frac{d\Psi_A\mathscr{E}}{d\mathrm{A}}+4\pi\frac{\Theta}{k_{\mathrm{B}}}\frac{ds}{d\mathrm{A}}\end{aligned}\quad . \tag{4.64}$$

The thermodynamic equilibrium implies that the main thermodynamical quantities of the plasma are those of Synge-Jüttner's gas Sec.(3.2). And these quantities obey to the first principle Eq.(3.71). Using that Synge-Jüttner's gas is an ideal gas ($\frac{\mathrm{P}}{\rho_0c^2}=\Theta=\frac{k_{\mathrm{B}}\mathrm{T}}{mc^2}$) and the first principle, we prove (Joule's law) that $\xi=\xi(\mathrm{T})$. Then the first principle can be written as,

$$\rho_0c^2d\xi=\xi\frac{c_s^2}{c^2}\left(d\rho_0c^2+\frac{\Theta}{k_{\mathrm{B}}}ds\right) \qquad \text{with} \qquad \frac{c_s^2}{c^2}=\frac{1}{\xi}\left.\frac{\partial\mathrm{P}}{\partial\rho_0c^2}\right|_{s=\mathrm{C}st}=\frac{\dot{\xi}\Theta}{\xi\left(\xi-1\right)}\,, \tag{4.65}$$

where $\dot{\xi}=\frac{d\xi}{d\Theta}$. We can use Eqs.(A.13, A.12) to calculate the sound speed. The last equation implies that $\xi=\xi(s,\mathrm{T})$. Let us differentiate the Alfvén Mach number Eq.(4.42) and replace the term proportional to $d\rho c^2$ with Eq.(4.65). We obtain,

$$\frac{d\xi}{\xi}=\frac{c_s^2/c^2}{1-c_s^2/c^2}\left(\frac{d\Psi_A^2}{\Psi_A^2}-\frac{d\mathrm{M}^2_{\mathrm{Alf}}}{\mathrm{M}^2_{\mathrm{Alf}}}+\frac{\Theta}{k_{\mathrm{B}}}ds\right). \tag{4.66}$$

Thus the specific dimensionless enthalpy $\xi=\xi(s,\mathrm{M}^2_{\mathrm{Alf}},\Psi_A^2)=\xi(\mathrm{A},\mathrm{M}^2_{\mathrm{Alf}})$. With the same kind of arguments, we can also write $\Theta=\Theta(\mathrm{A},\mathrm{M}^2_{\mathrm{Alf}})$. Then Eq.(4.64, 4.60) are sufficient to solve the GRASIMHD system. The nature of the transverse equation is determined by the coefficients of the highest degree in magnetic flux derivatives. The transverse equation is a second order differential equation in the magnetic flux. Then the next step is to get away the dependence in the gradient of $\mathrm{M}^2_{\mathrm{Alf}}$ in the first term of Eq.(4.64). The gradient of Alfvén Mach number $\mathbf{D}\mathrm{M}^2_{\mathrm{Alf}}$ contain the second order derivative of magnetic flux, and appears in the following equation,

$$\frac{1}{h}\left[\mathbf{D}\cdot\left(\frac{\mathscr{D}\mathbf{D}\mathrm{A}}{h\varpi^2}\right)\right]=\frac{\mathscr{D}}{h^2\varpi^2}\left[\Delta\mathrm{A}+\frac{\mathbf{D}\mathrm{A}\cdot\mathbf{D}\mathrm{M}^2_{\mathrm{Alf}}}{\mathscr{D}}\right]+... \tag{4.67}$$

Where the ..., means all the terms which do not have a second order spatial derivative term in magnetic flux. To calculate the second term, let us use Eq.(4.60) to express explicitly $\mathbf{D}\mathrm{A}^2$ as a function of $\mathrm{M}^2_{\mathrm{Alf}}, \xi, h, \varpi, \omega, \Psi_A, \Omega, \Psi_A \mathrm{L}$ and $\Psi_A \mathscr{E}$. We write the gradient of this relation, using Eq.(4.66) to avoid the term in $\mathbf{D}\xi$,

$$\begin{aligned}(\mathbf{D}\mathrm{A}\cdot\mathbf{D})\,\mathbf{D}\mathrm{A} = \frac{\mathscr{D}_{\mathrm{SF}}}{\mathscr{D}}\mathbf{D}\mathrm{M}^2_{\mathrm{Alf}} + \mathscr{D}_h \mathbf{D}h^2 + \mathscr{D}_\varpi \mathbf{D}\varpi^2 + \mathscr{D}_\omega \mathbf{D}\omega \\ + \mathscr{D}_{\Psi_A}\mathbf{D}\Psi_A + \mathscr{D}_{\Psi_A \mathrm{L}}\mathbf{D}\Psi_A \mathrm{L} + \mathscr{D}_{\Psi_A \mathscr{E}}\mathbf{D}\Psi_A \mathscr{E} + \mathscr{D}_s \mathbf{D}s\,,\end{aligned} \tag{4.68}$$

were,

$$\mathscr{D}_{\mathrm{SF}} = -\frac{\mathbf{D}\mathrm{A}^2}{\mathrm{M}^2_{\mathrm{Alf}}}\left[\mathscr{D} - \frac{h^2 \mathrm{B}^{\hat{\phi}^2}}{\mathrm{B}^2_{\mathrm{p}}} - \frac{c^2\mathscr{D}}{\gamma^2 \mathrm{V}^2_{\mathrm{p}}}\frac{c_s^2/c^2}{1-c_s^2/c^2}\right] = -\frac{\mathbf{D}\mathrm{A}^2}{\gamma^2\mathbf{V}^4_{\mathrm{p}}}\left[\gamma^2\mathbf{V}^4_{\mathrm{p}} - \mathbf{V}^2_{\mathrm{p}}\left(\gamma_s^2 c_s^2 + \gamma^2(\mathrm{V}^2_{\mathrm{A}} - \mathrm{V}^2_{\mathrm{E}})\right) + \gamma_s^2 \mathrm{V}_s^2\left(\mathrm{V}^2_{\mathrm{A,p}} - \mathrm{V}^2_{\mathrm{E}}\right)\right] \tag{4.69}$$

The details of the calculation of $\mathscr{D}_{\mathrm{SF}}$ term are given in Appendix.(D.2.2). Following Mobarry and Lovelace [1986], we introduce $\mathrm{V}^2_{\mathrm{A}} = \mathrm{V}^2_{\mathrm{A,p}} + \mathrm{V}^2_{\mathrm{A},\phi}$ the Alfvén velocity, where $\mathrm{V}^2_{\mathrm{A},\phi} = \mathrm{V}^2_{\mathrm{A,p}}\frac{\mathrm{B}^{\hat{\phi}^2}}{\mathbf{B}^2_{\mathrm{p}}}$ is the toroidal Alfvén velocity. We also introduce $\gamma_s^2 = \frac{1}{1-c_s^2/c^2}$ and the Alfvén-like velocity $\mathrm{V}^2_{\mathrm{E}} = x^2\mathrm{V}^2_{\mathrm{A,p}}$. Using Eq.(4.43), it is simpler to introduce $\mathrm{U}^2_{\mathrm{A}} = \gamma^2(\mathrm{V}^2_{\mathrm{A}} - \mathrm{V}^2_{\mathrm{E}}) = \frac{\mathrm{B}^2 - \mathrm{E}^2}{4\pi\rho_0\xi c^2}$, and $\mathrm{U}^2_{\mathrm{A,p}} = \frac{\mathrm{B}^2_{\mathrm{p}} - \mathrm{E}^2}{4\pi\rho_0\xi c^2}$, including $\mathrm{U}_s^2 = \gamma_s^2 c_s^2$. We get,

$$\boxed{\mathscr{D}_{\mathrm{SF}} = -\frac{\mathbf{D}\mathrm{A}^2}{\gamma^4\mathbf{V}^4_{\mathrm{p}}}\left[\gamma^4\mathbf{V}^4_{\mathrm{p}} - \gamma^2\mathbf{V}^2_{\mathrm{p}}\left(\mathrm{U}_s^2 + \mathrm{U}^2_{\mathrm{A}}\right) + \mathrm{U}_s^2\mathrm{U}^2_{\mathrm{A,p}}\right]} \tag{4.70}$$

The roots of this polynomial equation Eq.(4.70) define the slow and fast magneto-sonic velocities.

$$\begin{cases}\gamma^2\mathrm{V}^2_{\mathrm{SM}} = \left(\mathrm{U}_s^2 + \mathrm{U}^2_{\mathrm{A}} - \sqrt{(\mathrm{U}_s^2 + \mathrm{U}^2_{\mathrm{A}})^2 - 4\mathrm{U}_s^2\mathrm{U}^2_{\mathrm{A,p}}}\right)/2 & \mathrm{Slow-Magneto-Sonic} \\ \gamma^2\mathrm{V}^2_{\mathrm{FM}} = \left(\mathrm{U}_s^2 + \mathrm{U}^2_{\mathrm{A}} + \sqrt{(\mathrm{U}_s^2 + \mathrm{U}^2_{\mathrm{A}})^2 - 4\mathrm{U}_s^2\mathrm{U}^2_{\mathrm{A,p}}}\right)/2 & \mathrm{Fast-Magneto-Sonic}\end{cases} \tag{4.71}$$

Using Eq.(4.68) to calculate the second order term derivative term of magnetic flux we get,

$$\begin{aligned}\frac{1}{h}\left[\mathbf{D}\cdot\left(\frac{\mathscr{D}\mathbf{D}\mathrm{A}}{h\varpi^2}\right)\right] &= \frac{\mathscr{D}}{h^2\varpi^2}\left[\Delta\mathrm{A} + \frac{\mathbf{D}\mathrm{A}\cdot\{(\mathbf{D}\mathrm{A}\cdot\mathbf{D})\,\mathbf{D}\mathrm{A}\}}{\mathscr{D}_{\mathrm{SF}}}\right] + \ldots \\ &= \frac{1}{h_r^2}\left(1 + \frac{\mathrm{DA}^{\hat{r}^2}}{\mathscr{D}_{\mathrm{SF}}}\right)\frac{\partial^2\mathrm{A}}{\partial r^2} + \frac{1}{h_r h_\theta}\frac{2\mathrm{DA}^{\hat{r}}\mathrm{DA}^{\hat{\theta}}}{\mathscr{D}_{\mathrm{SF}}}\frac{\partial^2\mathrm{A}}{\partial\theta\partial r} + \frac{1}{h_\theta^2}\left(1 + \frac{\mathrm{DA}^{\hat{\theta}^2}}{\mathscr{D}_{\mathrm{SF}}}\right)\frac{\partial^2\mathrm{A}}{\partial\theta^2} + \ldots\end{aligned}\,. \tag{4.72}$$

Then we see that the slow-magneto-sonic and fast-magneto-sonic are singular points of this equation. Nevertheless this analysis do not leads to conclude to the fact that these singular surface are equivalent to the fast-magnetosonic separatrix surface which is linked to causal connections of the flow. Indeed Bogovalov [1994] shows that in addition to $\mathscr{D}_{\mathrm{SF}}$ there is an additional singular surface called modified fast-magnetosonic surface, which corresponds to the fast-magnetosonic separatrix surface. The determinant of Eq.(4.72) is given as,

$$\Delta_{\mathrm{GS}} = \frac{4\left(\mathrm{U}_s^2 + \mathrm{U}^2_{\mathrm{A}}\right)}{h_r^2 h_\theta^2}\left[\frac{\gamma^2\mathrm{V}^2_{\mathrm{p}} - \mathrm{U}_c^2}{\gamma^4\mathbf{V}^4_{\mathrm{p}} - \gamma^2\mathbf{V}^2_{\mathrm{p}}\left(\mathrm{U}_s^2 + \mathrm{U}^2_{\mathrm{A}}\right) + \mathrm{U}_s^2\mathrm{U}^2_{\mathrm{A,p}}}\right], \tag{4.73}$$

where we introduce the cusp-velocity $\mathrm{U}_c^2 = \mathrm{U}_s^2\mathrm{U}^2_{\mathrm{A,p}}/\left(\mathrm{U}_s^2 + \mathrm{U}^2_{\mathrm{A}}\right)$. The region is hyperbolic for $\Delta_{\mathrm{GS}} \geq 0$ and elliptic for $\Delta_{\mathrm{GS}} \leq 0$. Then for $\gamma^2\mathrm{V}^2_{\mathrm{p}} \leq \max(\mathrm{U}^2_{\mathrm{SM}}, \mathrm{U}_c^2)$ you are in an elliptic regime, for $\gamma^2\mathrm{V}^2_{\mathrm{p}} \geq \max(\mathrm{U}^2_{\mathrm{FM}}, \mathrm{U}_c^2)$ you are in an hyperbolic region.

Following Beskin and Par'ev [1993], we notice that when we move toward the horizon, the first integrals need to be continuous, then from Eq.(4.22) we have $\mathrm{B}^{\hat{\phi}} \sim 1/h$ associated to the

relation Eq.(4.34). It implies that $\gamma\xi V^{\Phi}$ remains finite. Thus Eq.(4.38) involves that $\gamma\xi \sim 1/h$ near the black hole. The proper density ρ_0, the pressure P, the specific dimensionnless enthalpy ξ have a meaning in the fluid reference-frame. They must remain continuous as they cross the black hole horizon and we need to have $\gamma V_p \longrightarrow \infty$. Then the flow is super-fast magneto sonic, near the horizon. It implies that any disturbance can move up along the flow from a given surface, the super-fast magnetosonic surface.

It is also interresting to note, that on the horizon, the electric field is directed only towards θ and the poloidal magnetic field is aligned with the radial vector. Using the fact that the mass flux also remains finite, the Alfvén Mach number also needs to remain finite. Combining Eq.(4.60) with Eqs.(4.44, 4.25) and the expression of gradient, leads to $hE^{\hat{\theta}} = hB^{\hat{\phi}}$ on the black hole horizon.

4.3 Flux on the horizon of event for a Kerr black hole

Since the work of Penrose and Floyd [1971], we know that a rotating black hole could exchange its rotational energy with its environment. Blandford and Znajek [1977] generalize the idea of Penrose by studying the interaction between a Kerr hole with an electro-magnetic field. Extraction processes became a potential source of energy (even there is no general agreement) to explain the phenomenal power of relativistic jets ejected from stellar massive black holes of binary systems or an accreting super massive black holes. Lasota et al. [2014] generalization allows us to consider a most general interactions and especially the case of a full GRASIMHD.

The Blandford&Znajek mechanism is still subject to much debates and discussions. We mention here the discussion induced by the discovery of Meisner effect related to the vacuum electro-dynamics around a Kerr black hole. Indeed, the discussion appears since Wald [1974] calculated the exact solution of Maxwell's equations vacuum for a magnetic field which tends to be uniform and aligned with its rotation axis at infinity. He observed a decrease followed by a total disappearing of the magnetic flux, which crosses the black hole when the spin reaches its maximum value. Bicak and Janis [1985] remark the same kind of phenomena for axi-symetric steady state vacuum solutions. Nevertheless the development of GRMHD simulation do not show this phenomena. Komissarov and McKinney [2007] explain that this phenomena hold for vacuum electrodynamics but not for GRMHD. Indeed they show that, for a sufficiently high conduction medium around the black hole, especially for ideal plasma, this phenomena does not appear.

Let us introduce $(\mathscr{M}, \mathbf{g})$ a spacetime with two Killing vectors, one for stationarity, $\boldsymbol{\eta}$, the other for axisymmetry, $\boldsymbol{\xi}$. We do the extra-assumption that our spacetime is circular (Se definition in Appendix.(A.7)). It is the presence of an ergoregion (a region in contact with the horizon of the black hole where $\boldsymbol{\eta}$ is space-like) which is the essential property allowing the extraction of the rotational energy from the rotating black hole.

In this section we briefly summary the basis of Penrose's process and the notion of ergosphere in this process. Then we detail the general conditions for energy extraction from black holes. Finally we apply this to the interaction between a Kerr black hole and the GRASIMHD fields.

4.3.1 Penrose process

The Penrose process was theorized by Penrose and Floyd [1971] to extract rotational energy from a rotating black hole. The process is quite simple. A test-particle (1) coming from infinity enters in the ergoregion then splits (event $P \in \mathscr{M}$) into two particles. One of the pieces (2) escapes from the black hole, the other ($\star$) fall into the horizon without getting out. The motion of each of

these particles (test particles) is a geodesic motion. The conservation of impulsion during the splitting implies that on the P splitting event, in the tangent space $\mathscr{T}_{\mathrm{P}}(\mathscr{M})$, we have,

$$m_1\mathbf{u}_1 = m_2\mathbf{u}_2 + m_\star\mathbf{u}_\star \tag{4.74}$$

The property of killing vector implies that for a geodesic motion of four speed $\mathbf{u}$ we have $\nabla_{\mathbf{u}}(\mathbf{u}\cdot\boldsymbol{\eta}) = 0$. Then if we note $\mathscr{L}$ the geodesic considered world line, we have $\mathbf{u}\cdot\boldsymbol{\eta}\,|_{\mathscr{L}} = \mathrm{C}st$. If we note $\mathscr{L}_1$, $\mathscr{L}_2$ and $\mathscr{L}_\star$ the world lines of the test particles (1), (2) and ($\star$). The world line $\mathscr{L}_1$ starts from infinity and reaches the point P. Therefore $\mathscr{L}_2$ starts from P and reaches the infinity. Then $m_1c^2\mathbf{u}_1\cdot\boldsymbol{\eta}\,|_{\mathscr{L}_1} = m_1c^2\mathbf{u}_1\cdot\boldsymbol{\eta}\,|_{\mathrm{P}} = m_1c^2\mathbf{u}_1\cdot\boldsymbol{\eta}\,|_{\infty} = m_1c^2\mathbf{u}_1\cdot\mathbf{n}\,|_{\infty} = -\mathrm{E}_1$ and $m_2c^2\mathbf{u}_2\cdot\boldsymbol{\eta}\,|_{\mathscr{L}_2} = m_2c^2\mathbf{u}_2\cdot\boldsymbol{\eta}\,|_{\mathrm{P}} = m_2c^2\mathbf{u}_2\cdot\boldsymbol{\eta}\,|_{\infty} = m_2c^2\mathbf{u}_2\cdot\mathbf{n}\,|_{\infty} = -\mathrm{E}_2$. Relation Eq.(4.74) implies that the difference of energy is $\mathrm{E}_2 - \mathrm{E}_1 = m_\star c^2\mathbf{u}_\star\cdot\boldsymbol{\eta}\,|_{\mathscr{L}_\star}$. The world line $\mathscr{L}_\star$ is included inside the ergoregion. On this line, $\boldsymbol{\eta}$ is a space-like four vector and it is possible for some configuration to extract energy from the black hole. In order to extract energy we simply need to have $-\Delta\mathrm{E}_{\mathscr{H}} = \mathrm{E}_2 - \mathrm{E}_1 = m_\star c^2\mathbf{u}_\star\cdot\boldsymbol{\eta}\,|_{\mathscr{L}_\star} \geq 0$. Note that if the ($\star$) particle leaves the ergoregion in a part of its world line then the extraction is not possible. Indeed outside of the ergoregion $\boldsymbol{\eta}$ is time like and future oriented like the four speed, which implies $\boldsymbol{\eta}\cdot\mathbf{u}_\star \leq 0$.

We also have an other killing vector $\boldsymbol{\xi}$ associated to axi-symmetry. Then, for a geodesic motion, we have $\mathrm{J} = mc\mathbf{u}\cdot\boldsymbol{\xi}\,|_{\mathscr{L}} = \mathrm{C}st$. We could interpret J as the angular momentum of the geodesic motion. Thus for the variation of the black hole angular momentum, we have $-\Delta\mathrm{J}_{\mathscr{H}} = \mathrm{J}_2 - \mathrm{J}_1 = -m_\star c\boldsymbol{\xi}\cdot\mathbf{u}_\star$. For circular spacetime we show that we can choose a system of coordinates adapted to circularity. The ZAMO four speed is given by Eq.(A.19). The energy measured by the ZAMO observer is always positive. Then $-m_\star c^2\mathbf{u}_\star\cdot\mathbf{n} \geq 0$ on the world line $\mathscr{L}_\star$. This condition implies,

$$\boxed{\omega_{\mathscr{H}}\Delta\mathrm{J}_{\mathscr{H}} \leq \Delta\mathrm{E}_{\mathscr{H}}}\,. \tag{4.75}$$

where $\omega_{\mathscr{H}}$ is the maximal value of the function ω. This maximum value is reached on the horizon. The last relation implies that, during a Penrose process, negative angular momentum absorption is a necessary condition to have extraction of rotational energy.

4.3.2 General calculus of the extraction for any stress-energy tensor field

This subsection is strongly inspired from the work of Lasota et al. [2014]. As before, let us consider an axi-symmetric ($\boldsymbol{\xi} = \boldsymbol{\partial}_t$) and stationary ($\boldsymbol{\eta} = \boldsymbol{\partial}_\phi$) spacetime $(\mathscr{M}, \mathbf{g})$, which contains a black-hole. So there is an horizon $\mathscr{H}$ which is a null hypersurface. The coordinate system is chosen to avoid any singularity on the horizon. We use a foliation $\mathscr{M} = \bigcup_{t\in\mathbb{R}} \Sigma_t$. We call $\mathscr{S}_t = \mathscr{H}\cap\Sigma_t$, which is a two dimensional closed surface into the three dimensional Σ_t manifold. Note $\mathbf{s}$ the normal to $\mathscr{S}_t$ considered as an hypersurface of Σ. Let us introduce $\boldsymbol{\ell}$ defined on $\mathscr{H}$ to be the normal vector to $\mathscr{H}$. Because $\mathscr{H}$ is a null hypersurface, $\boldsymbol{\ell}$ is a null vector and $\boldsymbol{\ell}\in\mathscr{T}(\mathscr{H})$. Let us choose to normalize $\boldsymbol{\ell}$ such that its 3+1 decomposition is $\boldsymbol{\ell} = hc\mathbf{n} + \mathbf{b}$, with $\mathbf{b}\in\mathscr{T}(\Sigma)$. Then $\forall\mathbf{v}\in\mathscr{T}(\mathscr{S}_t)\subset\mathscr{T}(\mathscr{H})$ $\boldsymbol{\ell}\cdot\mathbf{v} = 0$, we also have $\forall\mathbf{v}\in\mathscr{T}(\mathscr{S}_t)\subset\mathscr{T}(\Sigma)$ $\mathbf{n}\cdot\mathbf{v} = 0$. This implies that $\forall\mathbf{v}\in\mathscr{T}(\mathscr{S}_t)$ $\mathbf{b}\cdot\mathbf{v} = 0$ then $\mathbf{b}\in\mathscr{S}_\sqcup$ and $\mathbf{b}\in\mathscr{T}(\Sigma)$, and $\boldsymbol{\ell} = hc(\mathbf{n}+\mathbf{s})$. We introduce $\mathbf{k} = \frac{1}{2hc}(\mathbf{n}-\mathbf{s})$, which is a null vector normal to $\mathscr{S}_t$ verifying $\mathbf{k}\cdot\boldsymbol{\ell} = -1$. Then we could use Eqs.(2.4, 2.5) to calculate the projection on $\mathscr{H}$ and the induced metric on $\mathscr{H}$.

$$\begin{cases} \mathbf{v} \longrightarrow \mathbf{v} + (\boldsymbol{\ell}\cdot\mathbf{v})\mathbf{k} & \text{Orthogonal projector on } \mathscr{H} \\ \mathbf{q} = \mathbf{g} + \mathbf{k}\otimes\boldsymbol{\ell} + \boldsymbol{\ell}\otimes\mathbf{k} = \mathbf{g} + \mathbf{n}\otimes\mathbf{n} - \mathbf{s}\otimes\mathbf{s} & \text{Induced metric on } \mathscr{H} \end{cases} \tag{4.76}$$

We note that the degenerate metric $\mathbf{q}$ on $\mathscr{H}$ is also identically equal to the induced metric on $\mathscr{S}_t$. It is possible to show (rigidity theorem) that the tangent $\boldsymbol{\ell}$ to the horizon $\mathscr{H}$ vector field can be decomposed as,

$$\boldsymbol{\ell} \propto \boldsymbol{\eta} + \frac{\omega}{c}\boldsymbol{\xi}, \tag{4.77}$$

with $\frac{\omega}{c} = -\frac{\boldsymbol{\xi}\cdot\boldsymbol{\eta}}{\boldsymbol{\xi}\cdot\boldsymbol{\xi}}$ constant on $\mathscr{H}$. We consider a stress-energy tensor field $\mathbf{T}$ that fills the environment of the black hole horizon. We suppose that this tensor obeys to a minimal physical condition, the **null energy condition**, at the event horizon,

$$\mathbf{T}(\ell,\ell)\,|_{\mathscr{H}} \geq 0 \tag{4.78}$$

This condition is the weakest version of **the weak energy condition**, which requires that the density of energy measured by any observer is always positive. This condition replace, in the general case, the role taken by the ZAMO observer $\mathbf{n}$ in the Penrose process to get an equivalent version of Eq.(4.75).

Let us introduce the Noether angular momentum flux Eq.(4.32) and energy flux Eq.(4.37). At present, we do not suppose that these two fluxes obey to any symmetry property. We also took the case with no loading term $\mathbf{k} = 0$. Then we took any volume of spacetime $\mathscr{V}_t \subset \Sigma$ which is in contact with the horizon. Thus the boundary is composed of $\partial\mathscr{V}_t = \Delta\mathscr{S}_t \cup \sigma_{\text{ext}}$ where $\Delta\mathscr{S}_t$ is a part of $\mathscr{S}_t$ and σ_{ext} is a two dimensional sub-manifold, which is restricted to be outside of the horizon. Then we introduce $\mathscr{U} = \bigcup_{t\in[t,t+\Delta t]} \mathscr{V}_t$. Thus we have $\partial\mathscr{U} = \mathscr{V}_{t+dt} \cup \mathscr{V}_t \cup \left(\bigcup_{t\in[t,t+\Delta t]} \Delta\mathscr{S}_t\right) \cup \left(\bigcup_{t\in[t,t+\Delta t]} \sigma_{\text{ext}}\right)$. Let us integrate Eq.(4.32) and Eq.(4.37) on $\mathscr{U}$ and applying the Stokes theorem Eq.(A.11) using Eq.(A.9), we obtain,

$$\begin{cases} \mathrm{E}_{t+\Delta t} - \mathrm{E}_t + \Delta^2\mathrm{E}_{\text{ext}} - \Delta^2\mathrm{E}_{\mathscr{H}} = 0 \\ \mathrm{J}_{t+\Delta t} - \mathrm{J}_t + \Delta^2\mathrm{J}_{\text{ext}} - \Delta^2\mathrm{J}_{\mathscr{H}} = 0 \end{cases}, \tag{4.79}$$

where

$$\begin{cases} \mathrm{E}_t = \displaystyle\int_{\mathscr{V}_t} (\mathbf{P}\cdot\mathbf{n})\sqrt{\gamma}\,\mathrm{d}x^1\mathrm{d}x^3\mathrm{d}x^3 \\ \Delta^2\mathrm{E}_{\text{ext}} = \displaystyle\int_t^{t+\Delta t}\left(\int_{\sigma_{\text{ext}}} h\mathbf{P}\cdot\mathbf{dS}\right)c\,\mathrm{d}t \\ \Delta^2\mathrm{E}_{\mathscr{H}} = -\displaystyle\int_t^{t+\Delta t}\left(\int_{\Delta\mathscr{S}_t} \mathbf{P}\cdot\ell\, d^2q\right)c\,\mathrm{d}t \end{cases}. \tag{4.80}$$

Similar expressions are valid for the angular momentum replacing $\mathbf{M}$ instead of $\mathbf{P}$. The details of this calculus are given in Appendix.(D.3). (x^1, x^2, x^3) is a coordinate system of Σ, $\mathbf{dS}$ is the surface vector of Σ_{ext} and d^2q is the surface element of $\mathscr{S}_t$. We interpret $\Delta^2\mathrm{E}_{\mathscr{H}}$ as an energy flux flowing out of the hole, using the fact that far from the horizon of the black hole the Noether energy flux $\mathbf{P}$ is also the energy flux measured by the ZAMO. Assuming stationarity, we have $\mathrm{E}_t = \mathrm{E}_{t+\Delta t}$ and $\mathrm{J}_t = \mathrm{J}_{t+\Delta t}$. The surface σ_{ext} is chosen as the surface build by the flow of $h\mathbf{P}$ which starts from the line $\partial\Delta\mathscr{S}_t$. Supposing that the line flow of $\mathbf{P}$ started from $\partial\Delta\mathscr{S}_t$ reaches infinity, as in Fig.(4.2).

Then we have,

$$\Delta^2\mathrm{E}_{\mathscr{H}} = \Delta^2\mathrm{E}_{\text{ext}} = \int_{\sigma_\infty} h\mathbf{P}\cdot\mathbf{dS}c\Delta t \tag{4.81}$$

The surface σ_∞ can be chosen as far as we want. We interpret the integrals in Eq.(4.81) as an energy flux which crosses σ_∞ during Δt. It allows us to interpret $\Delta^2\mathrm{E}_{\mathscr{H}}$ as the flux of energy which crosses the part of horizon $\Delta\mathscr{S}_t$ during the period of time dt. The same kind of analysis and work could be done for angular momentum flux. In a similar way, we prove that $\Delta^2\mathrm{J}_{\mathscr{H}}$ is the flux of angular momentum, which crosses the horizon of the black hole during the amount of time dt.

Let us take the null energy condition, Eq.(4.78), we immediately find,

$$\boxed{\omega_{\mathscr{H}}\Delta^2\mathrm{J}_{\mathscr{H}} \leq \Delta^2\mathrm{E}_{\mathscr{H}}} \tag{4.82}$$

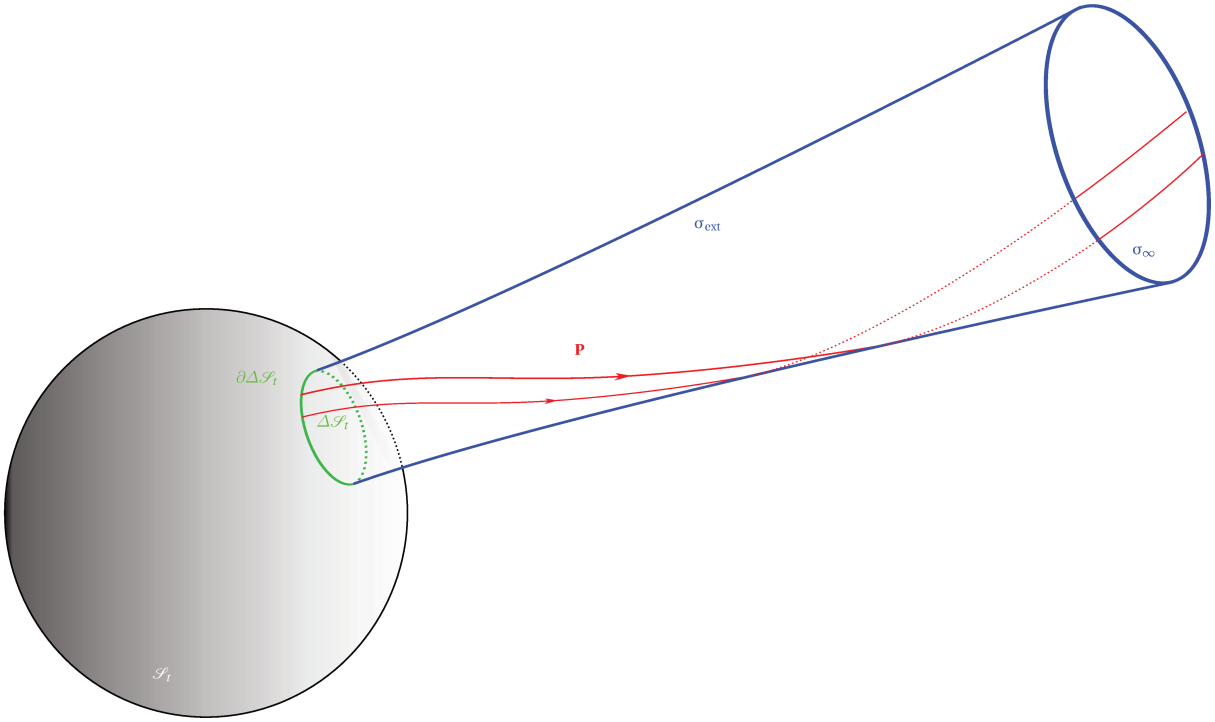

Figure 4.2 – Representation of the different surfaces of integration. In black is a spatial surface of horizon of the hole $\mathscr{S}$, in green the surface element $\Delta\mathscr{S}$, in blue the choose of σ_{ext} which is based on the flow of $\mathbf{P}$ (red lines)

Then as announced before, the same inequality as during a Penrose process holds between the variation of energy and the variation of angular momentum of a black hole. Again, to have extraction of energy of the black hole $\Delta^2 \mathrm{E}_{\mathscr{H}} \leq 0$, we need to have $\Delta^2 \mathrm{J}_{\mathscr{H}} \leq 0$, then a process of extraction may appear only when the black hole absorbs negative angular momentum.

4.3.3 Extraction via GRASIMHD field in Kerr metric

Now let discuss the special case of the interaction with a loaded GRASIMHD field. In this case, the stress energy tensor can be decomposed in three part $\mathbf{T} = \mathbf{T}_{\mathrm{FL}} + \mathbf{T}_{\mathrm{EM}} + \mathbf{T}_{\mathrm{k}} = \mathbf{T}_{\mathrm{MHD}} + \mathbf{T}_{\mathrm{k}}$, where $\mathbf{T}_{\mathrm{k}}$ represents the stress energy tensor of the source of pairs (photons or neutrinos or others particles). Then the Noether fluxes are also composed of their MHD part and their source part ($\mathbf{M} = \mathbf{M}_{\mathrm{MHD}} + \mathbf{M}_{\mathrm{k}}$ and $\mathbf{P} = \mathbf{P}_{\mathrm{MHD}} + \mathbf{P}_{\mathrm{k}}$).

An another conserved quantity is the Feynmann mass 4-current given as $\mathbf{F} = \mathbf{F}_{\mathrm{FL}} + \mathbf{F}_{\mathrm{k}} = \rho_0 \mathbf{u} + \mathbf{F}_{\mathrm{k}}$. This quantity verifies,

$$\nabla \cdot \mathbf{F} = 0 \quad \Longrightarrow \quad \mathbf{D} \cdot \left(h \mathbf{F}_{\mathrm{p}} \right) = 0 \tag{4.83}$$

The GRASIMHD parts of the fluxes are given by,

$$\begin{cases} m_e h \mathbf{F}_{\mathrm{FL,p}} = \dfrac{\Psi_A}{4\pi c} \nabla \times \left(\dfrac{\mathrm{A}}{\varpi} \mathbf{e}_{\hat{\phi}} \right) \\ h \mathbf{M}_{\mathrm{MHD,p}} = \dfrac{\Psi_A \mathrm{L}}{4\pi} \nabla \times \left(\dfrac{\mathrm{A}}{\varpi} \mathbf{e}_{\hat{\phi}} \right) \\ h \mathbf{P}_{\mathrm{MHD,p}} = \dfrac{\Psi_A \mathscr{E}}{4\pi c} \nabla \times \left(\dfrac{\mathrm{A}}{\varpi} \mathbf{e}_{\hat{\phi}} \right) \end{cases} \tag{4.84}$$

It is necessary to pay attention to the flux coming from GRASIMHD. We choose for $\Delta\mathscr{S}$ the part of $\mathscr{S}$ where the magnetic flux is between A and $\mathrm{A} + d\mathrm{A}$. The Eq.(4.84) implies immediately that the surface σ_{ext}, which is built by the flow of the conserved flux, Eq.(4.84), is simply the

magnetic flux tube that we stop at a certain radius $r_{\rm ext}$. Thus the expression of Eq.(4.81) and its analogous with the angular momentum and mass flux become,

$$\begin{cases} \left.\dfrac{\Delta^2 \mathrm{M}_{\mathscr{H}}}{\Delta t}\right|_{\rm MHD} = -\Psi_A\,(\mathrm{A}, r_{\rm ext})\,d\mathrm{A} \\ \left.\dfrac{d^2 \mathrm{J}_{\mathscr{H}}}{dt}\right|_{\rm MHD} = -\Psi_A \mathrm{L}\,(\mathrm{A}, r_{\rm ext})\,d\mathrm{A} \\ \left.\dfrac{d^2 \mathrm{E}_{\mathscr{H}}}{dt}\right|_{\rm MHD} = -\Psi_A \mathscr{E}\,(\mathrm{A}, r_{\rm ext})\,d\mathrm{A} \end{cases} \tag{4.85}$$

We calculate here the contribution of GRASIMHD field between A and $\mathrm{A}+d\mathrm{A}$ to the evolution of the black hole. In fact Carter [2010] showed (Chapter 8 of Carter [2010]) that only the two last equations of Eq.(4.85), contribute to the evolution of the black hole parameters. He correctly deduced that the mass parameter of the black hole is linked to the Noether energy flux and the angular momentum parameter to the Noether angular momentum flux. The first equation is linked to the conservation of the number of particles. A Kerr black hole is characterized by two parameters its mass and its angular momentum. The way the black hole evolves with the exchange of particles allows us to introduce the chemical potential of the black hole, its entropy and some effective temperature. To know the total evolution of the black hole we need to add the contribution of the source term. In the following we make the assumption, that this source term becomes null in the environment of the horizon, i.e. for a radius $r_{\mathscr{H}} \leq r_{\rm ext} \leq r_k$. Then the evolution of the hole is entirely determined by the value of Ψ_A, $\Psi_A \mathrm{L}$ and $\Psi_A \mathscr{E}$ for radius in the range $r_{\mathscr{H}} \leq r_{\rm ext} \leq r_k$.

Thus, we get three time scales, which correspond to the evolution of the black hole parameter. About the energy, it is useful to decompose the energy flux in its different physical contributions,

$$\Phi_{\mathscr{E}} = \Psi_A \mathscr{E} = \Psi_A \gamma \xi h c^2 \left(1 + \frac{\varpi \omega \mathrm{V}^{\hat{\phi}}}{hc^2}\right) - h \varpi \Omega \mathrm{B}^{\hat{\phi}} = \Phi_{\rm FL} + \Phi_{\rm EM} \tag{4.86}$$

The first term is the fluid energy flux $\Phi_{\rm FL}$ and corresponds to the Noether energy flux. the Noether Poynting flux $\Phi_{\rm EM}$ corresponds to electromagnetic energy flux. Note that the perfect fluid contribution $\Phi_{\rm FL}$ can be written as,

$$\Phi_{\rm FL} = -\Psi_A \xi c^2 \left(\mathbf{u} \cdot \boldsymbol{\eta}\right) \tag{4.87}$$

Eqs.(4.85) are valid, for each value of $r_{\rm ext} > r_{\mathscr{H}}$ and also valid in the limit of $r_{\rm ext} \to r_{\mathscr{H}}$. So it is useful to calculate this decomposition on the black hole horizon,

$$\begin{cases} \Phi_{\rm M}\big|_{\mathscr{H}} = -\dfrac{\mathrm{M}^2_{\rm Alf}\big|_{\mathscr{H}}}{\mathrm{M}^2_{\rm Alf}\big|_{\mathscr{H}} + \varpi^2_{\mathscr{H}} (\Omega - \omega_{\mathscr{H}})^2 / c^2} \left(\Psi_A \mathrm{L} \omega_{\mathscr{H}} - \Psi_A \mathscr{E}\right) \\ \Phi_{\rm LT}\big|_{\mathscr{H}} = \Psi_A \mathscr{L} \omega_h + \dfrac{\varpi^2_{\mathscr{H}} \omega_{\mathscr{H}} (\Omega - \omega_{\mathscr{H}}) / c^2}{\mathrm{M}^2_{\rm Alf}\big|_{\mathscr{H}} + \varpi^2_{\mathscr{H}} (\Omega - \omega_{\mathscr{H}})^2 / c^2} \left(\Psi_A \mathrm{L} \omega_{\mathscr{H}} - \Psi_A \mathscr{E}\right) \\ \Phi_{\rm EM}\big|_{\mathscr{H}} = \dfrac{\varpi^2_{\mathscr{H}} \Omega (\omega_{\mathscr{H}} - \Omega) / c^2}{\mathrm{M}^2_{\rm Alf}\big|_{\mathscr{H}} + \varpi^2_{\mathscr{H}} (\Omega - \omega_{\mathscr{H}})^2 / c^2} \left(\Psi_A \mathrm{L} \omega_{\mathscr{H}} - \Psi_A \mathscr{E}\right) \end{cases} \tag{4.88}$$

We claim that the electromagnetic extraction process is active when $\Phi_{\rm EM} > 0$. Fluide energy flux can be decomposed, in the internal energy flow $\Phi_{\rm M}$ and the Lense-Thirring flux $\Phi_{\rm LT}$. Lense-Thirring flux sign depends on the sign of $\mathrm{V}^{\hat{\phi}}$. We claim that the ideal fluid extraction process is active when $\Phi_{\rm PF} = \Phi_{\rm M} + \Phi_{\rm LT} > 0$. The definition of a black hole implies that sufficiently close the horizon the mass flux becomes negative $\Psi_A \leq 0$. The null energy condition at the event horizon is equivalent to,

$$\Psi_A \mathscr{E} \leq \Psi_A \mathscr{L} \omega_{\mathscr{H}} \tag{4.89}$$

There is a generalized extraction between A and $\mathrm{A}+d\mathrm{A}$, if $0 \leq \Psi_A \mathscr{E} \leq \Psi_A \mathscr{L} \omega_{\mathscr{H}}$. The Eq.(4.88) combined with the null energy condition Eq.(4.89) implie that the electromagnetic extraction process is active if $0 \leq \Omega \leq \omega_{\mathscr{H}}$. The null energy condition Eq.(4.89) associated with Eq.(4.88) imply that the internal energy flow inside the horizon of black hole. This energy flux increases the mass of the black hole.

Eq.(4.87) implies that for an inflow ($\Psi_A \leq 0$) outside of the ergosphere (reminding that outside of the ergosphere $\boldsymbol{\eta}$ is a timelike vector thus $\boldsymbol{\eta}\cdot\mathbf{u} \geq 0$) we have $\Phi_{\mathrm{PF}} \leq 0$. Thus in the hydrodynamical case ($\Phi_{\mathrm{EM}} = 0$, $\Phi_{\mathscr{E}} = \Phi_{\mathrm{FL}} = \mathrm{Cst}$ along a poloidal fieldline flow), to get active fluide extraction process we need to have the pairs creation inside of the ergosphere. Indeed, let us consider a magnetic flux line $\mathrm{A} = \mathrm{cst}$. This line starts from the horizon $r = r_{\mathscr{H}}$ and crosses the ergosphere radius $r = r_{\mathrm{erg}}(\mathrm{A})$ and the point where we start to produce pairs $r = r_k(\mathrm{A})$ Fig.(4.3). In the hydrodynamical case, for $r \leq r_k$, we have $\Phi_{\mathrm{M}}(\mathrm{A}, r_{\mathscr{H}} \leq r \leq r_k(\mathrm{A})) = \mathrm{Cst}$, then if $r_{\mathrm{erg}}(\mathrm{A}) \leq r_k(\mathrm{A})$ we know it for $r_{\mathrm{erg}}(\mathrm{A}) \leq r \leq r_k(\mathrm{A})$. Then we have $\Phi_{\mathrm{M}}(r_{\mathscr{H}}(\mathrm{A})) = \Phi_{\mathrm{M}}(r(\mathrm{A})) \leq 0$. See Fig.(4.3). This is equivalent to the Penrose process for splitting particles inside the ergosphere. In the MHD case, you can have extraction via a process of fluid extraction and have pairs creation only outside of the ergosphere because we can have exchange between the ideal fluid energy flux and the Poynting flux. Thus, in this case, the Poynting flux increases as we move outward of the ergosphere while the perfect fluid flux became positive inside the ergosphere, being negative outside the ergosphere. Then it seems less restrictive to have a global extraction in the GRASIMHD case than in the pure hydrodynamical one.

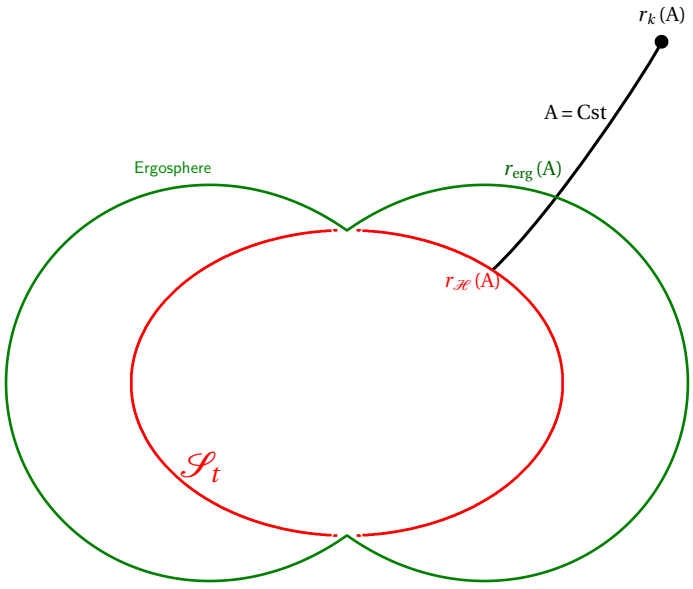

Figure 4.3 – Representation of flow line configuration with stagnation radius outside of the ergosphere. For a pure fluid interaction, because $r_{\mathrm{erg}}(\mathrm{A}) \leq r_k(\mathrm{A})$ no extraction can be achieved. The ergosphere and the horizon are represented for a maximally rotating black hole respectively in green and red. The black line represents a poloidal field line.

Using eqs.(4.26, 4.35, 4.39), if we consider a line which starts at some point on the horizon

and reaches infinity, then we get,

$$\begin{cases} \Psi_A^{\rm out}({\rm A}) = -\dfrac{d^2{\rm M}_{\mathscr{H}}}{dtd{\rm A}}(\theta_{\mathscr{H}}({\rm A})) + \displaystyle\int_{r_{\mathscr{H}}}^{\infty} \left.\frac{4\pi chk_m}{{\rm B}^{\hat{r}}}\right|_{\rm A=Cst} dr \\ (\Psi_A{\rm L})^{\rm out}({\rm A}) = -\dfrac{d^2{\rm J}_{\mathscr{H}}}{dtd{\rm A}}(\theta_{\mathscr{H}}({\rm A})) + \displaystyle\int_{r_{\mathscr{H}}}^{\infty} \left.\frac{4\pi h\boldsymbol{\xi}\cdot\mathbf{k}}{{\rm B}^{\hat{r}}}\right|_{\rm A=Cst} dr \\ (\Psi_A\mathscr{E})^{\rm out}({\rm A}) = -\dfrac{d^2{\rm E}_{\mathscr{H}}}{dtd{\rm A}}(\theta_{\mathscr{H}}({\rm A})) - \displaystyle\int_{r_{\mathscr{H}}}^{\infty} \left.\frac{4\pi ch\boldsymbol{\eta}\cdot\mathbf{k}}{{\rm B}^{\hat{r}}}\right|_{\rm A=Cst} dr \end{cases} \tag{4.90}$$

This can be simply interpreted. The energy and the angular momentum following this line is composed of the angular momentum and the energy fluxes of the black hole plus the contribution of the loading term (pair creation mechanism, by example photons in the mechanism $\gamma+\gamma \rightleftharpoons e_+ + e_-$). One of the issue to understand the power of magnetized jets launched from a supermassive black hole is to quantify both terms.

4.4 Conclusion

Using the 3+1 method, we saw how the loading terms (k_m and $\mathbf{k}$) change the general equation of GRASIMHD Eq.(4.17). Maxwell's equations stay identical. Then the usual electromagnetic integrals, the magnetic flux, and the isorotation remain the same as usual. They are function of each others. Nevertheless the source term acts as a load of mass-flux, Eq.(4.26), of angular momentum flux, Eq.(4.35), and of energy flux, Eq.(4.39). The material source of the pair transfer, its number, its angular momentum and its energy to the GRASIMHD fields.

We also see different way to decompose/recompose the forces which appear in Euler equation. This decomposition-recomposition help us to understand the role of each forces in the flow, or to obtain the Grad-Shafranov equation. The analysis of this equation allows us to determine the singular surface of GRASIMHD, linked to some regime of the flow velocity. It introduces 3 specific velocities for which the system is singular, the slow-magneto-sonic velocity, the Alfvén velocity, the fast-magneto-sonic velocity. These velocities also correspond to the velocity of wave propagation in the GRMHD fields.

The last part gives us the different exchanges of flux between the GRASIMHD field and the black hole, and then the evolution of the black hole parameters. The extraction of energy may concern different processes; it could be dominated by electromagnetic processes or by an ideal fluid process. This analysis also gives the interesting result, that for a line which links the horizon of the hole to the infinity, the angular momentum flux (the energy flux) at infinity is composed of the angular momentum (respectively energy) extracted from the hole, plus the contribution brought by the loading term (e.g. the source of pair, for pair creation/annihilation mechanism). Then the goal is to quantify these two terms. This can be done solving the GRASIMHD equations from the black hole horizon to infinity. This is the object of the following chapter.

4.5 References

V. S. Beskin. *MHD Flows in Compact Astrophysical Objects*. 2010. doi: 10.1007/978-3-642-01290-7. 58

V. S. Beskin and V. I. Par'ev. METHODOLOGICAL NOTES: Axially symmetric steady-state flows in the vicinity of a Kerr black hole and the nature of the activity of galactic nuclei. *Physics Uspekhi*, 36:529–539, June 1993. doi: 10.1070/PU1993v036n06ABEH002165. 67, 69

J. Bicak and V. Janis. Magnetic fluxes across black holes. mnras, 212:899–915, February 1985. doi: 10.1093/mnras/212.4.899. 70

R. D. Blandford and R. L. Znajek. Electromagnetic extraction of energy from Kerr black holes. mnras, 179:433–456, May 1977. doi: 10.1093/mnras/179.3.433. 70

S. V. Bogovalov. On the Theory of Magnetohydrodynamic Winds from a Magnetosphere of Axisymmetric Rotators. mnras, 270:721, October 1994. doi: 10.1093/mnras/270.4.721. 69

E. Breitmoser and M. Camenzind. Collimated outflows of rapidly rotating young stellar objects. Wind equation, GSS equation and collimation. aap, 361:207–225, September 2000. 63

B. Carter. Republication of: Black hole equilibrium states Part II. General theory of stationary black hole states. *General Relativity and Gravitation*, 42:653–744, March 2010. doi: 10.1007/s10714-009-0920-9. 74

A. L. Ford, B. D. Keenan, and M. V. Medvedev. Electron-Positron Cascade in Magnetospheres of Spinning Black Holes. *ArXiv e-prints*, June 2017. 54

N. Globus and A. Levinson. Loaded magnetohydrodynamic flows in Kerr spacetime. prd, 88(8):084046, October 2013. doi: 10.1103/PhysRevD.88.084046. 54

N. Globus and A. Levinson. Jet Formation in GRBs: A Semi-analytic Model of MHD Flow in Kerr Geometry with Realistic Plasma Injection. Apj, 796:26, November 2014. doi: 10.1088/0004-637X/796/1/26. 54

E. Gourgoulhon. 3+1 Formalism and Bases of Numerical Relativity. *ArXiv General Relativity and Quantum Cosmology e-prints*, March 2007. xi, 55

E. Gourgoulhon, C. Markakis, K. Uryū, and Y. Eriguchi. Magnetohydrodynamics in stationary and axisymmetric spacetimes: A fully covariant approach. prd, 83(10):104007, May 2011. doi: 10.1103/PhysRevD.83.104007. 67

Harold Grad and Hanan Rubin. Hydromagnetic equilibria and force-free fields. *Journal of Nuclear Energy (1954)*, 7(3-4):284–285, 1958. 67

M. Heinemann and S. Olbert. Axisymmetric ideal MHD stellar wind flow. jgr, 83:2457–2460, June 1978. doi: 10.1029/JA083iA06p02457. 67

Kunihito Ioka and Misao Sasaki. Grad-shafranov equation in noncircular stationary axisymmetric spacetimes. *Phys. Rev. D*, 67:124026, Jun 2003. doi: 10.1103/PhysRevD.67.124026. URL https://link.aps.org/doi/10.1103/PhysRevD.67.124026. 67

S. S. Komissarov and J. C. McKinney. The 'Meissner effect' and the Blandford-Znajek mechanism in conductive black hole magnetospheres. mnras, 377:L49–L53, May 2007. doi: 10.1111/j.1745-3933.2007.00301.x. 70

J.-P. Lasota, E. Gourgoulhon, M. Abramowicz, A. Tchekhovskoy, and R. Narayan. Extracting black-hole rotational energy: The generalized Penrose process. prd, 89(2):024041, January 2014. doi: 10.1103/PhysRevD.89.024041. 61, 70, 71

Amir Levinson and Noam Segev. Existence of steady gap solutions in rotating black hole magnetospheres. *Phys. Rev. D*, 96:123006, Dec 2017. doi: 10.1103/PhysRevD.96.123006. URL https://link.aps.org/doi/10.1103/PhysRevD.96.123006. 54

Z. Meliani, C. Sauty, N. Vlahakis, K. Tsinganos, and E. Trussoni. Nonradial and nonpolytropic astrophysical outflows. VIII. A GRMHD generalization for relativistic jets. aap, 447:797–812, March 2006. doi: 10.1051/0004-6361:20053915. 63

C. M. Mobarry and R. V. E. Lovelace. Magnetohydrodynamic flows in Schwarzschild geometry. apj, 309:455–466, October 1986. doi: 10.1086/164617. 67, 69

A. Nathanail and I. Contopoulos. Black Hole Magnetospheres. apj, 788:186, June 2014. doi: 10.1088/0004-637X/788/2/186. 67

Shin-ya Nitta, Masaaki Takahashi, and Akira Tomimatsu. Effects of magnetohydrodynamic accretion flows on global structure of a kerr black-hole magnetosphere. *Phys. Rev. D*, 44:2295–2305, Oct 1991. doi: 10.1103/PhysRevD.44.2295. URL https://link.aps.org/doi/10.1103/PhysRevD.44.2295. 67

I. Okamoto. Force-free pulsar magnetosphere - I. The steady, axisymmetric theory for the charge-separated plasma. mnras, 167:457–474, June 1974. doi: 10.1093/mnras/167.3.457. 67

I. Okamoto. Force-free pulsar magnetosphere. II - The steady, axisymmetric theory for a normal plasma. mnras, 170:81–93, January 1975. doi: 10.1093/mnras/170.1.81. 67

R. Penrose and R. M. Floyd. Extraction of rotational energy from a black hole. *Nature Physical Science*, 229(6):177–179, Feb 1971. ISSN 2058-1106. doi: 10.1038/physci229177a0. URL https://doi.org/10.1038/physci229177a0. 70

Hung-Yi Pu, Masanori Nakamura, Kouichi Hirotani, Yosuke Mizuno, Kinwah Wu, and Keiichi Asada. Steady general relativistic magnetohydrodynamic inflow/outflow solution along large-scale magnetic fields that thread a rotating black hole. *The Astrophysical Journal*, 801(1):56, 2015. URL http://stacks.iop.org/0004-637X/801/i=1/a=56. 54

V. D. Shafranov. Plasma Equilibrium in a Magnetic Field. *Reviews of Plasma Physics*, 2:103, 1966. 67

R. M. Wald. Black hole in a uniform magnetic field. prd, 10:1680–1685, September 1974. doi: 10.1103/PhysRevD.10.1680. 70

Chapter 5

Meridional self-similar model

Contents

The model we propose is an extension in Kerr geometry of previous meridional self-similar models for ideal axi-symmetric and stationary MHD flows. It generalizes and solves the difficulty of the treatment of the light cylinder effect compared to previous models from Meliani et al. [2006a] and Globus et al. [2014]. Indeed, this effect appears in a Special Relativity (SR) treatment of Axi-symmetric Stationary Ideal Magneto-Hydrodynamic (ASIMHD) and is modified by a General Relativity (GR) treatment. When a fluid element crosses the light cylinder, the isorotational "velocity" measured by the Zero Angular Momentum Observer (ZAMO) reaches the speed of light. The light cylinder is also the surface where the electric field is equal in magnitude to the magnetic poloidal field. The isorotational "velocity" does not correspond to a fluid velocity but to the rotational velocity associated with the electric potential per unit of magnetic flux (isorotation Ferraro's law).

There is no physical problem for a fluid line to cross this surface. This effect of the light cylinder leads to a change for the critical Alfvénic surface. Thus including this effect in the model makes incompatible the assumptions of a radial Mach Alfvénic number and a spherical Alfvénic critical surface. This contradiction was previously solved by choosing to construct an analytical solution in area where the light cylinder effect is negligible. In order to take into account this effect, one of the two above assumptions has to be released. We choose to keep the sphericity of the critical surface while we let Mach number to follow a given form. This new formulation results in a model that can describe the flow in areas where the light cylinder effect is not negligible, particularly outside the light cylinder. As in the previous self-similar model the fast-magnetosonic surface could coincide with the Alfvénic surface.

In the second section of this chapter, we present the construction of our meridional self-similar model published in Chantry et al. [2018]. Parts which are extracted from the publication are indicated by a grey band in the left margin. Note that in the article the notation ∇ is reserved for the covariant derivative on the space surface of the Kerr metric foliation proposed in sec.2.4.1. Thus ∇ corresponds to the Kerr geometry analogous to the flat gradient. Then, in the third section, we present with some details the derivation of the equations, especially the expression and the decomposition of each force component. Finally in the fourth section we present the way to obtain and discuss the differential equation system of the model.

5.1 Construction of the meridional self-similar model

We choose to use our article Chantry et al. [2018] published in the A&A newspaper to present the model. The following will therefore be the first three sections of the article

5.1.1 Steady axisymmetric relativistic MHD outflows

Kerr metric

The first step in building self-similar solutions in relativistic flows is to define the metric. In fact the central massive black hole dominates the gravitational field in the near regions and determines completely the metric field. Thus, in Kerr metric, the geodesics are defined as follows.

$$ds^2 = -\left(1-\frac{r_s r}{\rho^2}\right)c^2dt^2 - \frac{2r_s r c a}{\rho^2}\sin^2\theta\, dt\, d\phi + \frac{\rho^2}{\Delta}dr^2 + \rho^2 d\theta^2 + \frac{\Sigma^2}{\rho^2}\sin^2\theta\, d\phi^2 \quad (5.1)$$

We have the usual notations of the elements,

$$\Delta = r^2 + a^2 - r_s r, \tag{5.2}$$
$$\rho^2 = r^2 + a^2 \cos^2\theta, \tag{5.3}$$
$$\Sigma^2 = (r^2 + a^2)^2 - a^2 \Delta \sin^2\theta, \tag{5.4}$$

where $a = \frac{\mathcal{J}}{\mathcal{M}c}$ and $r_s = \frac{2\mathcal{G}\mathcal{M}}{c^2}$.

We note that $\mathcal{J}$ is the angular momentum of the massive central object, $\mathcal{M}$ is its mass, h is the lapse function, ω is the angular velocity of zero angular momentum observers (ZAMO) and we use a for the length-scale related to the angular momentum of the black hole (Kerr scale). We can define the dimensionless spin of the black hole $a_{\rm H}$ in units of the gravitational radius $r_s/2$ such that, $a_{\rm H} = 2a/r_s$. Furthermore, $\boldsymbol{\beta}$ is the shift vector.

The lapse function h, the angular velocity ω of zero angular momentum observers (ZAMO) and the shift vector coordinates can be written as,

$$h = \left(1 - \frac{r_s r}{\rho^2} + \beta^\phi \beta_\phi\right)^{1/2} = \frac{\rho}{\Sigma}\sqrt{\Delta}, \tag{5.5}$$
$$\omega = \frac{a c r_s r}{\Sigma^2}, \quad \beta_\phi = -\frac{\omega}{c}\varpi^2, \quad \beta^\phi = -\frac{\omega}{c}, \tag{5.6}$$

with $\varpi = \frac{\Sigma}{\rho}\sin\theta$. The corresponding line elements for the Kerr metric are given in Appendix.A of Chantry et al. [2018].

Maxwell's equations

The next step is to define the electromagnetic field in this metric. Using covariant derivatives, we can write Maxwell's equations in Kerr space, assuming stationarity and axisymmetry,

$$\nabla \cdot \mathbf{E} = 4\pi\rho_e, \tag{5.7}$$
$$\nabla \cdot \mathbf{B} = 0, \tag{5.8}$$
$$\nabla \times (h\mathbf{E}) = \left(\mathbf{B} \cdot \nabla \frac{\omega}{c}\right)\varpi \boldsymbol{\epsilon}_\phi, \tag{5.9}$$
$$\nabla \times (h\mathbf{B}) = \frac{4\pi h}{c}\mathbf{J} - \left(\mathbf{E} \cdot \nabla \frac{\omega}{c}\right)\varpi \boldsymbol{\epsilon}_\phi, \tag{5.10}$$

where $(\vec{\epsilon_i})_{i=1\ldots3}$ is the space orthonormal basis. We note that all quantities in the above equations are given in the ZAMO frame. We can split all vector fields in a poloidal component in the meridional plane and a toroidal one along the azimuthal direction. The poloidal magnetic field $\vec{\mathrm{B}_{\rm p}}$ can be expressed in terms of the magnetic flux function A,

$$\mathbf{B}_{\rm p} = \nabla \times \left(\frac{\mathrm{A}}{\varpi}\boldsymbol{\epsilon}_\phi\right), \tag{5.11}$$

and using Faraday's law, we get the electric field,

$$\nabla \times \left(h\mathbf{E} - \frac{\omega}{c}\nabla \mathrm{A}\right) = 0. \tag{5.12}$$

We can introduce the electric potential, Φ, but the electric field $\vec{\mathrm{E}}$ is not directly proportional to the gradient of the electric potential,

$$h\mathbf{E} = \frac{\omega}{c}\nabla \mathrm{A} - \nabla\Phi. \tag{5.13}$$

The condition of ideal MHD for infinite electrical conductivity leads to

$$\mathbf{E} + \frac{\mathbf{V}\times\mathbf{B}}{c} = 0\,. \tag{5.14}$$

We note that ∇ is the covariant derivative on a space hypersurface; see Appendix.B of Chantry et al. [2018] for the expression of its coordinates.

Equations of motion

In the Kerr metric, the 3+1 formalism gives the equation for mass conservation, the Euler equation, and the energy conservation, respectively,

$$\nabla\cdot(\rho_0\gamma h\mathbf{V}) = 0\,, \tag{5.15}$$

$$\rho_0\gamma\,(\mathbf{V}\cdot\nabla)\left(\gamma\xi\mathbf{V}\right) + \rho_0\xi\gamma^2\left[c^2\nabla\ln h + \frac{\varpi\omega V^{\hat{\phi}}}{h}\nabla\ln\omega\right] + \nabla P = \rho_e\mathbf{E} + \frac{\mathbf{J}\times\mathbf{B}}{c}\,, \tag{5.16}$$

$$\gamma^2\rho_0\xi c\left[\mathbf{V}\cdot\nabla\ln(\gamma\xi h) + \frac{\omega\varpi V^{\hat{\phi}}}{hc^2}\mathbf{V}\cdot\nabla\ln\omega\right] = \frac{\mathbf{J}\cdot\mathbf{E}}{c}\,. \tag{5.17}$$

Here $V^{\hat{\phi}}$ is the toroidal component of the bulk flow speed as seen by the ZAMO. The factor γ is the bulk Lorentz factor, ρ_0 is the mass density, and ξc^2 the specific enthalpy measured in the comoving frame of the outflow, that contains kinetic enthalpy of perfect relativistic gas ξ_K and some heating term Q/c^2.

$$\xi = \xi_K + \frac{Q}{c^2}\,. \tag{5.18}$$

For the kinetic enthalpy we use the Taub-Matthews approximation of ideal fluid equation of state; for more details see Taub [1948], Meliani et al. [2004] and Mignone et al. [2005].

$$\xi_K = \frac{5}{2}\left(\frac{P}{\rho_0 c^2}\right) + \sqrt{1+\left(\frac{3P}{2\rho_0 c^2}\right)^2}\,. \tag{5.19}$$

The energy conservation has been derived in the frame of the ZAMO and equivalently the first law of thermodynamics can be obtained by projecting the conservation of the energy-momentum tensor along the fluid 4-velocity but in the comoving frame. Assuming infinite conductivity, the contribution of the electromagnetic field is null and only the thermal energy affects the variation of the enthalpy of the fluid, giving,

$$\rho_0\left(\nabla_p\cdot\nabla\right)(\xi c^2) = \left(\nabla_p\cdot\nabla\right)P\,. \tag{5.20}$$

Constants of motion

Under the assumptions of steadiness and axisymmetry, the magnetohydrodynamic equations in general relativity can be partially integrated to yield several field/streamline constants (Beskin 2010). We already deduced those constants including the magnetic field with the same formalism in Cayatte et al. [2014]. Here we present the derivation of the equations, following the notations of Tsinganos 1982, in order to compare with previous self-similar models, for example, Meliani et al. [2006b] and give the choice of the first integrals.

Steady and axisymmetric flows are characterized by a function A that defines the geometry of the magnetic flux surfaces. In the poloidal plane, field lines are lines of constant

magnetic flux A and first integrals will be functions of A, among which the mass flux Ψ. The poloidal velocity can be expressed in terms of Ψ,

$$4\pi\rho_0\gamma h\mathbf{V}_\mathrm{p} = \nabla\times\left(\frac{\Psi}{\varpi}\boldsymbol{\epsilon}_\phi\right). \tag{5.21}$$

The frozen-in condition for ideal MHD flows, gives, in the toroidal direction, combined with Eq. (5.11),

$$4\pi\rho_0\gamma h\mathbf{V}_\mathrm{p} = \Psi_\mathrm{A}\mathbf{B}_\mathrm{p},$$

where $\Psi_\mathrm{A}\equiv \mathrm{d}\Psi/\mathrm{dA}$ is the magnetic to mass flux ratio.

The poloidal components of the law of flux freezing (Eq. 5.14) give in turn the isorotation law,

$$\Omega-\omega = \frac{h\mathrm{V}^{\hat\phi}}{\varpi}-\frac{\Psi_\mathrm{A}\mathrm{B}^{\hat\phi}}{4\pi\rho_0\gamma\varpi}, \tag{5.22}$$

where $\Omega(\mathrm{A})\equiv c\mathrm{d}\Phi/\mathrm{dA}$, which is the isorotation frequency, constant along each magnetic flux tube.

By integrating the Euler equation in the toroidal direction, we get the conservation of the angular momentum flux L(A),

$$\mathrm{L} = \varpi\left(\gamma\xi\mathrm{V}^{\hat\phi}-\frac{h\mathrm{B}^{\hat\phi}}{\Psi_\mathrm{A}}\right). \tag{5.23}$$

The last equation to integrate is the energy conservation. In other words, we may take the Euler equation projected along the time axis of the 3+1 decomposition, and integrate it under the hypothesis of steadiness,

$$\mathscr{E}-\mathrm{L}\omega = \gamma\xi hc^2-\frac{h\varpi(\Omega-\omega)}{\Psi_\mathrm{A}}\mathrm{B}^{\hat\phi}. \tag{5.24}$$

Toroidal fields

Using the three last integrals of motion, we may express the toroidal components of the velocity and the magnetic fields and the enthalpy density as functions of these first integrals and the poloidal components. Using the standard procedure of inversion we get

$$\varpi\frac{h\mathrm{B}^{\hat\phi}}{\Psi_\mathrm{A}} = \frac{\mathrm{L}\left[h^2c^2+\varpi^2\omega(\Omega-\omega)\right]-\mathscr{E}\varpi^2(\Omega-\omega)}{\left(\mathrm{M}_\mathrm{Alf}^2-h^2\right)c^2+\varpi^2(\Omega-\omega)^2}, \tag{5.25}$$

$$\varpi\gamma\xi\mathrm{V}^{\hat\phi} = \frac{\mathrm{M}_\mathrm{Alf}^2\mathrm{L}c^2-(\mathscr{E}-\mathrm{L}\Omega)\varpi^2(\Omega-\omega)}{\left(\mathrm{M}_\mathrm{Alf}^2-h^2\right)c^2+\varpi^2(\Omega-\omega)^2}, \tag{5.26}$$

$$\gamma h\xi = \frac{\mathrm{M}_\mathrm{Alf}^2(\mathscr{E}-\mathrm{L}\omega)-h^2(\mathscr{E}-\mathrm{L}\Omega)}{\left(\mathrm{M}_\mathrm{Alf}^2-h^2\right)c^2+\varpi^2(\Omega-\omega)^2}, \tag{5.27}$$

where we have defined the poloidal Alfvén Mach number,

$$\mathrm{M}_\mathrm{Alf}^2 = h^2\frac{{\mathrm{V}_\mathrm{p}}^2}{\mathrm{V}_\mathrm{Alf}^2} = \frac{4\pi h^2\rho_0\xi\gamma^2{\mathrm{V}_\mathrm{p}}^2}{{\mathrm{B}_\mathrm{p}}^2} = \frac{\xi{\Psi_\mathrm{A}}^2}{4\pi\rho_0}. \tag{5.28}$$

This definition of the poloidal Alfvén Mach number is consistent with the definition used by Meliani et al. [2006b] and includes the lapse function. This is also the definition taken by Breitmoser and Camenzind [2000] because the velocity, $h\mathrm{V}_\mathrm{p}$, calculated with the universal time is continuous across the event horizon.

The numerator and denominator of Eq. (5.25) are zero at the Alfvén transition surface, if the following two equations are satisfied,

$$\mathrm{M}^2_{\mathrm{Alf}}\big|_{\mathrm{a}} = h^2_{\mathrm{a}}\left[1 - \frac{\varpi^2_{\mathrm{a}}(\Omega-\omega_{\mathrm{a}})^2}{h^2_{\mathrm{a}}c^2}\right], \tag{5.29}$$

$$\frac{\varpi^2_{\mathrm{a}}(\Omega-\omega_{\mathrm{a}})^2}{h^2_{\mathrm{a}}c^2} = \frac{\mathrm{L}(\Omega-\omega_{\mathrm{a}})}{(\mathscr{E}-\mathrm{L}\omega_{\mathrm{a}})}. \tag{5.30}$$

The denominators of Eqs. (5.26) and (5.27) are identical to the one of Eq. (5.25) and there numerators are a linear combination of Eqs. (5.29) and(5.30). Hence, the numerators and the denominators of Eqs. (5.26) and (5.27) are also zero at the Alfvén transition surface.

We can reformulate the above equations by changing variables. We rescale the cylindrical radius with $ch/(\Omega-\omega)$ leading to the dimensionless cylindrical radius x and introduce the parameter x_{MR},

$$x = \frac{\varpi(\Omega-\omega)}{hc}, \quad x^2_{\mathrm{MR}} = \frac{\mathrm{L}(\Omega-\omega)}{(\mathscr{E}-\mathrm{L}\omega)}. \tag{5.31}$$

Hence we can write,

$$\mathrm{B}^{\hat{\phi}} = \frac{-(\mathscr{E}-\mathrm{L}\omega)\Psi_{\mathrm{A}}}{cx}\,\frac{x^2-x^2_{\mathrm{MR}}}{\mathrm{M}^2_{\mathrm{Alf}}-h^2\left(1-x^2\right)}, \tag{5.32}$$

$$h\gamma\xi\frac{\mathrm{V}^{\hat{\phi}}}{c} = \frac{(\mathscr{E}-\mathrm{L}\omega)}{c^2x}\,\frac{\mathrm{M}^2_{\mathrm{Alf}}x^2_{\mathrm{MR}}-(1-x^2_{\mathrm{MR}})h^2x^2}{\mathrm{M}^2_{\mathrm{Alf}}-h^2\left(1-x^2\right)}, \tag{5.33}$$

$$\gamma h\xi = \frac{(\mathscr{E}-\mathrm{L}\omega)}{c^2}\,\frac{\mathrm{M}^2_{\mathrm{Alf}}-h^2(1-x^2_{\mathrm{MR}})}{\mathrm{M}^2_{\mathrm{Alf}}-h^2\left(1-x^2\right)}. \tag{5.34}$$

The second condition, Eq. (5.30), at the Alfvén transition surface becomes, keeping the first one unchanged,

$$x^2\big|_{\mathrm{a}} = x^2_{\mathrm{MR}}\big|_{\mathrm{a}}. \tag{5.35}$$

In Kerr metric, the parameter x^2_{MR} is an extension of x^2_{A} defined by Meliani et al. [2006b]. It measures the amount of energy carried by the electromagnetic field. This is the energy flux of the magnetic rotator (**MR**) divided by the total energy flux of the outflow in the co-rotating frame, $\mathscr{E}-\mathrm{L}\omega$. This new parameter x_{MR}, conversely to the previous x_{A}, is not any more constant along a field line, since ω is not an integral of the motion.

5.1.2 Model equations

Angular expansion

The MHD equations and the metric constitute a coupled set of highly nonlinear equations that cannot be solved analytically. The approach followed so far for Newtonian flows has been to look for solutions with separable variables in the frame of self-similarity. However, this technic cannot be applied in the frame of general relativity due to the complexity of the metric even for the simpler cases of a Schwarzschild or a Kerr metric. Instead, we may model the jet close to its symmetry axis, that is, to describe the spine jet, by expanding all variables with $\sin\theta$ to second order.

Along the polar axis where ϖ and θ go to zero, we may define the spherical Alfvén radius to be the distance $r_\star$ from the center where the Alfvén transition surface condition, $\mathrm{M}^2_{\mathrm{Alf},,=0} = h^2_\star$, applies. The subscript $\star$ denotes the value of a physical quantity at the Alfvén

transition surface, along the polar axis. We shall use this location to write all our quantities in dimensionless form. Thus, the dimensionless spherical radius is

$$\mathrm{R} = \frac{r}{r_\star}. \tag{5.36}$$

At $\mathrm{R}=1$, the velocity is $\mathrm{V}_\star$, the magnetic field $\mathrm{B}_\star$, the density $\rho_\star$, the enthalpy $\xi_\star$ and the lapse function $h_\star$. Because of the Alfvén transition along the polar axis, we have,

$$\mathrm{B}_\star^2 = 4\pi {\gamma_\star}^2 \rho_\star \xi_\star {\mathrm{V}_\star}^2. \tag{5.37}$$

Thus the dimensionless magnetic flux function α is defined as,

$$\alpha = \frac{2}{{r_\star}^2 \mathrm{B}_\star} \mathrm{A}. \tag{5.38}$$

Moreover we can expand to the second order the metric of the system in dimensionless form using the characteristic dimensions of the system defined in the previous Section. This introduces the two following new parameters,

$$\mu = \frac{r_s}{r_\star}, \qquad l = \frac{a}{r_\star} = \frac{\mathscr{J}}{\mathscr{M} c r_\star} \Rightarrow \frac{2a}{r_\star} = \frac{2l}{\mu}, \tag{5.39}$$

which are respectively the Schwarzschild radius in units of the Alfvén radius and the dimensionless black hole spin.

Another dimensionless parameter is needed to describe the gravitational potential, as in the classical model. This parameter ν represents the escape speed at the Alfvén point along the polar axis in units of $\mathrm{V}_\star$. Then, the value of $\mathrm{V}_\star$ is fixed by the following condition,

$$\nu = \frac{\mathrm{V}_{esc,\star}}{\mathrm{V}_\star} = \sqrt{\frac{2\mathscr{G}\mathscr{M}}{r_\star \mathrm{V}_\star^2}} \quad \Rightarrow \quad \mathrm{V}_\star^2 = \frac{\mu}{\nu^2} c^2. \tag{5.40}$$

Thus, to second order in $\sin\theta$ the ZAMO angular velocity and the lapse function are written as,

$$\omega = \frac{l c \mu \mathrm{R}}{r_\star (\mathrm{R}^2 + l^2)^2} \left(1 + \frac{l^2 {h_z}^2}{\mathrm{R}^2 + l^2} \sin^2\theta\right) \tag{5.41}$$

$$h = \sqrt{1 - \frac{\mu \mathrm{R}}{\mathrm{R}^2 + l^2}} \left(1 - \frac{\mu l^2 \mathrm{R}}{2(\mathrm{R}^2 + l^2)^2} \sin^2\theta\right). \tag{5.42}$$

In order to simplify our notation, we define the lapse function along the polar axis,

$$h_z(\mathrm{R}) = h(\mathrm{R}, \theta = 0) = \sqrt{1 - \frac{\mu \mathrm{R}}{\mathrm{R}^2 + l^2}}, \tag{5.43}$$

and the polar shift of the metric,

$$\omega_z(\mathrm{R}) = \omega(\mathrm{R}, \theta = 0) = \frac{l c \mu \mathrm{R}}{r_\star (\mathrm{R}^2 + l^2)^2}. \tag{5.44}$$

See sec. 2.4.1 (Appendix A in the paper) for details.

It will be useful to introduce the dimensionless polar shift function (see also Eq. 5.59),

$$\overline{\omega}_z(\mathrm{R}) = \frac{\omega_z r_\star}{\mathrm{V}_\star h_\star} = \frac{l \sqrt{\mu} \nu \mathrm{R}}{h_\star (\mathrm{R}^2 + l^2)^2}. \tag{5.45}$$

We also expand the magnetic flux function to second order in $\sin\theta$. The magnetic flux is an even function which is zero along the polar axis due to axisymmetry and because of the symmetry around the equatorial plane. Thus all odd orders are zero and the first nonvanishing even order is the second order in colatitude. If we keep the lowest order in the expansion we get

$$\alpha(R,\theta) = f(R)\sin^2\theta, \tag{5.46}$$

where f is the inverse of the classical expansion factor for solar coronal holes (see Tsinganos and Sauty 1992). This expansion, similarly to the classical self similar model of Sauty and Tsinganos [1994], is equivalent to a hypothesis of separation of the variables in the magnetic flux function.

Thus from Eq. (5.50), the cylindrical radius can also be seen as an expansion in the magnetic flux. This is physically more meaningful as the magnetic flux is constant on a given mass flux tube. Moreover, several free integrals depend solely on this magnetic flux.We define the dimensionless cylindrical radius G in units of the polar Alfvén radius as,

$$G(R) = \sqrt{\frac{R^2 + l^2}{f(R)}}. \tag{5.47}$$

The cylindrical radius can be written in the various following forms,

$$\varpi^2 \quad = r_\star^2(R^2 + l^2)\sin^2\theta \quad = {r_\star}^2 G^2 \alpha = G^2 \varpi_a^2. \tag{5.48}$$

We can also write the metric as an expansion in α (see also Appendix 2.4.1 (Appendix A in the paper)),

$$\omega \quad = \quad \frac{lc\mu R}{r_\star(R^2 + l^2)^2}\left(1 + \frac{l^2 {h_z}^2 G^2}{(R^2 + l^2)^2}\alpha\right), \tag{5.49}$$

$$h \quad = \quad \sqrt{1 - \frac{\mu R}{R^2 + l^2}}\left(1 - \frac{\mu l^2 R G^2}{2(R^2 + l^2)^3}\alpha\right). \tag{5.50}$$

Of course we can always reverse our point of view and go back to the expansion in θ. This would be the case if we wanted to use the steady analytical solution as initial conditions for numerical simulations.

We can parametrize the geometry of the flux tubes with the logarithm derivative of f denoted F,

$$F = \frac{d\ln f}{d\ln R} = 2\left(\frac{R^2}{R^2 + l^2} - \frac{d\ln G}{d\ln R}\right). \tag{5.51}$$

The angle χ of the magnetic poloidal field line with the radial direction (see Sauty et al. 1999) is given in our metric by,

$$\tan\chi = \frac{\sqrt{R^2 + l^2 - \mu R}}{2R} F \tan\theta. \tag{5.52}$$

Choice of the Alfvén surface and pressure

We can expand all physical quantities to the first order in α. Thus the Alfvén number is given by,

$$M_{Alf} = M(R)\left(1 + M_1(R)\alpha\right). \tag{5.53}$$

Contrary to previous self-similar models, the Alfvén number cannot be spherically symmetric because of the presence of the cylindrical radius in units of the "light cylinder" x, in the numerator and the denominator of Eqs. (5.32),(5.33), and (5.34). This is induced by the regularity conditions, Eqs (5.29) and (5.30), and the sphericity of the Alfvén surface. The

surface $x = 1$ is the so-called outer "light cylinder". Of course this surface may not be exactly cylindrical if x depends also on α, which may be the case for instance close to the black hole where ω has a strong dependence on α or if Ω is not constant with α. Therefore, this is rather a light surface, but for the sake of simplicity we refer to it as a "light cylinder" in the rest of the text.

Similarly, the pressure can be expanded to first order,

$$P(R,\alpha) = P_0 + \frac{{\gamma_\star}^2 \rho_{0\star} \xi_\star {V_\star}^2}{2} \Pi(R)\,(1 + K(R)\alpha)\,, \tag{5.54}$$

where P_0 is a constant.
In order to simplify and as a first step, we assume for both equations that the radial dependence of the nonpolar component of the Alfvén number and the pressure are simply constant, $M_1(R) = m_1 = \text{cst}$, $K(R) = \kappa = \text{cst}$. Thus,

$$M_{\text{Alf}} = M(R)\,(1 + m_1\alpha)\,. \tag{5.55}$$

We note that we have $m_1 = 0$ in previous models; see Meliani et al. [2006b] and Globus et al. [2014].

Choice of the free integrals

Free integrals are also expanded to the first order in the magnetic flux. The mass to magnetic flux ratio is similar to the one in the classical case, expanded as,

$${\Psi_A}^2(\alpha) = \frac{4\pi\rho_{0\star} h_\star^2}{\xi_\star}(1 + \delta\alpha)\,. \tag{5.56}$$

where δ is a free parameter describing the deviations from spherical symmetry of the ratio number density/enthalpy as in Meliani et al. [2006b] and not of the density itself, conversely to Sauty and Tsinganos [1994].

The total angular momentum loss flux density is given by

$$\vec{J} = \gamma\rho_0 L h \vec{\nabla}_p = \frac{L\Psi_A}{4\pi}\vec{B}_p\,. \tag{5.57}$$

Thus it is natural to expand the quantity $L\Psi_A$ rather than L itself. $L\Psi_A$ is also the poloidal current density along the polar axis and writes as

$$L\Psi_A = \lambda h_\star B_\star r_\star \alpha\,. \tag{5.58}$$

The isorotation law can be expanded to first order as well as the total energy,

$$\Omega = \Omega_\star(1 + w_1\alpha)\,, \tag{5.59}$$

and

$$\mathscr{E} = \mathscr{E}_\star(1 + e_1\alpha)\,, \tag{5.60}$$

where we see from Eq. (5.24) that $\mathscr{E}_\star = h_\star\gamma_\star\xi_\star c^2$.

Although we have some freedom with the choice of w_1 and e_1, we could choose $e_1 = 0$ and $w_1 = -\delta/2$ to restrict ourselves to the values of the previous models, in particular in Schwarzschild metric; see Meliani et al. [2006b] and Meliani et al. [2010]. In fact, the isorotation function Ω does not need to be expanded beyond the zeroth-order term because Ω always appears multiplied by another quantity as in $(\Omega - \omega)\varpi$ or $L\Omega$. Thus, the value

of w_1 is free and does not affect the solution. Conversely, the value of e_1 affects the whole dynamics and we shall study the effects of its variation in a future publication. We already discussed the fact that taking a weak dependence of Ω on α has the advantage of minimizing the variation of the "light cylinder" near the base of the jet. Thus for the sake of simplicity, we shall study here the case where $e_1 = 0$ and $w_1 = 0$.

Constraints on the Alfvén Mach number, the isorotation law, and the angular momentum flux

The value of m_1 is, in fact, determined by the prescription to cross the Alfvén transition surface. In order for the denominator in Eqs.5.25, 5.26, and 5.27 to vanish at the Alfvénic transition, the two following relations given in Eqs.5.29 and 5.30 must be fulfilled. They can be expanded to first order. For the first regularity condition we get,

$$\mathrm{M_{Alf}}|_a = h_\star(1 + m_1\alpha) \text{ with } m_1 = -\frac{\mu}{2}\left(\frac{\lambda^2}{\nu^2} + \frac{l^2}{(1+l^2)^3}\right). \tag{5.61}$$

The first term in the right part of Eq.5.61 is due to the "light cylinder", and the second one to the nonsphericity of the gravitational field in Kerr metric. m_1 is negligible whenever the rotational speed $\lambda V_\star$ is sub-relativistic and either the μ parameter or the angular momentum of the black hole are negligible too. Since $m_1 < 0$, there is a limiting field line where we have $\mathrm{M_{Alf}} = 0$ since the magnetic flux increases going out from the polar axis.

To apply the second regularity condition we use the numerator of Eq. 5.25 and we get to the first order in α,

$$\Omega_\star - \omega_\star = \frac{\lambda V_\star h_\star}{r_\star}. \tag{5.62}$$

Thus we can write

$$\varpi(\Omega - \omega) \quad = \quad \mathrm{G(R)}\sqrt{\alpha}\lambda V_\star h_\star \Lambda(\mathrm{R}), \tag{5.63}$$

where,

$$\Lambda(\mathrm{R}) \quad = \quad \left[1 + \frac{\sqrt{\mu}\nu l}{\lambda h_*}\left(\frac{1}{(1+l^2)^2} - \frac{\mathrm{R}}{(\mathrm{R}^2+l^2)^2}\right)\right]. \tag{5.64}$$

The regularity conditions on the Alfvén surface fixes the value of m_1. Thus the critical Alfvén surface is a sphere, as in previous meridional self-similar models. We warn, however, that the Alfvén transition surface is a **generalized** or **modified** Alfvén surface as it takes into account the modification by the "light cylinder" .

Simultaneously, surfaces of constant Poloidal Alfvén Mach Number, $\mathrm{M_{Alf}}$=const. (see Eq.(5.55))are not spherical surfaces, conversely to the one defined by Meliani et al. [2006b]. Two effects modify it; first the "light cylinder" effect, which was neglected in Meliani et al. [2006b] and Globus et al. [2014], and second the frame-dragging effect (Lense-Thirring).

Expansion of the velocity and magnetic fields

The model is obtained using an expansion to the second order for $\sin\theta$ in the Euler equation. Due to axisymmetry, first-order terms are zero along r and ϕ while the antisymmetry along θ gives the zeroth and second orders as null along the colatitude.

Then, for the poloidal velocity field, this gives

$$\begin{aligned} V^{\hat{r}} &= \frac{V_\star M^2}{h_\star^2 G^2}\left\{1+\sin^2\theta\left[\frac{1}{2}\left(\frac{l^2 h_z^2}{R^2+l^2}-1\right)\right.\right. \\ &+ \left.\left.\frac{R^2+l^2}{G^2}\left(\frac{\lambda^2\mu}{\nu^2}\left(\frac{\Lambda^2 N_B}{D}+\frac{\overline{\omega}_z}{\lambda}\right)-e_1-\frac{\delta}{2}+2m_1\right)\right]\right\} \\ V^{\hat{\theta}} &= -\frac{V_\star h_z M^2\sqrt{R^2+l^2}F}{2h_\star^2 R G^2}\sin\theta. \end{aligned} \tag{5.65}$$

And for the poloidal magnetic field, we get

$$B^{\hat{r}} = \frac{B_\star}{G^2}\left[1+\frac{1}{2}\left(\frac{l^2 h_z^2}{R^2+l^2}-1\right)\sin^2\theta\right] \tag{5.66}$$

$$B^{\hat{\theta}} = -\frac{B_\star h_z F\sqrt{R^2+l^2}}{2G^2 R}\sin\theta. \tag{5.67}$$

Now from Eqs.(5.25) and (5.26), we can calculate to the first order in $\sin\theta$ the toroidal components of fields

$$V^{\hat{\Phi}} = -\frac{\lambda V_\star h_z \Lambda N_V}{h_\star G^2 D}\sqrt{R^2+l^2}\sin\theta, \tag{5.68}$$

$$B^{\hat{\Phi}} = -\frac{\lambda B_\star h_\star \Lambda N_B\sqrt{R^2+l^2}}{h_z D G^2}\sin\theta, \tag{5.69}$$

where the functions N_V, N_B , and D have been generalized,

$$N_V = \frac{M^2}{h_*^2\Lambda}-G^2 \tag{5.70}$$

$$N_B = \frac{h_z^2}{h_*^2\Lambda}-G^2 \tag{5.71}$$

$$D = \frac{h_z^2-M^2}{h_*^2}. \tag{5.72}$$

Expansion of the enthalpy, densities, and electric field

We used Eq. (5.27) to deduce the enthalpy,

$$\gamma h\xi c^2 = \gamma_\star h_\star \xi_\star c^2\left[1+\alpha\left(e_1-\frac{\lambda^2\mu}{\nu^2}\left(\frac{\Lambda^2 N_B}{D}+\frac{\overline{\omega}_z}{\lambda}\right)\right)\right], \tag{5.73}$$

and the mass density is given by

$$\begin{aligned} \gamma^2\rho_0\xi = \gamma_\star^2\rho_{0\star}\xi_\star\frac{h_\star^4}{h_z^2 M^2}\left[1+\sin\theta^2\left\{\frac{\mu l^2 R}{(R^2+l^2)^2}\right.\right. \\ \left.\left.+\frac{R^2+l^2}{G^2}\left(2e_1-2m_1+\delta-\frac{2\lambda^2\mu}{\nu^2}\left(\frac{\Lambda^2 N_B}{D}+\frac{\overline{\omega}_z}{\lambda}\right)\right)\right\}\right]. \end{aligned} \tag{5.74}$$

In GRMHD, we also need the expressions of the electric field and the charge density. The electric field is a second-order term for the radial component and a first-order term for

the θ-component,

$$E^{\hat{r}} = -\frac{\lambda V_\star h_\star B_\star}{2c}\frac{(R^2+l^2)F\Lambda}{RG^2}\sin^2\theta \tag{5.75}$$

$$E^{\hat{\theta}} = -\frac{\lambda V_\star h_\star B_\star}{c}\frac{\Lambda\sqrt{R^2+l^2}}{h_z G^2}\sin\theta\,. \tag{5.76}$$

Using Maxwell-Gauss Eq. 5.7, we calculate the charge density from the divergence of the above electric field, to zeroth order only,

$$\rho_e = -\frac{\lambda V_\star B_\star h_\star}{2\pi r_\star c}\frac{\Lambda}{h_z G^2}\,. \tag{5.77}$$

With all these quantities we are able to expand the Euler equation. The radial component is expanded to the second order and the colatitude component to the first order. From the expansion of poloidal components in the Euler equation (Eq. 5.16) and using Eq. (5.51), we can reverse the system to get the equations of the model (see sec. 5.3 for details (Appendix C in the paper)).

"Light cylinder"

The rescaling value $ch/(\Omega-\omega)$ for the cylindrical radius used in Eqs. (5.32 - 5.34) has been defined by Meliani et al. [2006b] as the "light cylinder". It is a surface of revolution $\Sigma_{\rm LC}$ where,

$$x^2 = \frac{\varpi^2(\Omega-\omega)^2}{h^2c^2} = 1\,. \tag{5.78}$$

On the "light cylinder", the electric field $|\,\mathbf{E}\,|$ is equal to the poloidal component of the magnetic field $|\,\mathbf{B}_{\rm p}\,|$. In the present publication, $\Sigma_{\rm LC}$ designed the external "light cylinder", that is, $x=+1$, though, strictly speaking, this is not a cylinder as explained earlier, but a surface of revolution. This external "light cylinder" is outside the Alfvén surface since the denominator of Eqs. (5.32 - 5.34) is equal to M^2_{Alf} on the "light cylinder", is negative before crossing the Alfvén transition surface, and is positive after crossing it. At large distance in the jet, the lapse function h goes to unity and $\Omega-\omega$ tends to Ω, which is assumed constant in our model. Thus, $\Sigma_{\rm LC}$ is located on a constant cylindrical radius along the z axis, becoming a real cylinder.

From the iso-rotation law, we get,

$$\frac{V^{\hat{\phi}}}{c} = x + \frac{\Psi_A B^{\hat{\phi}}}{4\pi\rho_0\gamma hc} = x + \frac{V_{\rm p}}{c}\frac{B^{\hat{\phi}}}{B_{\rm p}}\,. \tag{5.79}$$

As in special relativity, the second term of Eq. 5.79 cannot be neglected in the vicinity of the "light cylinder". The sign of $B^{\hat{\phi}}$ is such that $V^{\hat{\phi}}$ always remains less than the speed of light (Vlahakis 2015). Moreover after crossing the "light cylinder" one of the two following conditions must be fulfilled. Either, we have $|\,B^{\hat{\phi}}\,| \gg B_{\rm p}$ or $V_{\rm p} \gg V^{\hat{\phi}}$, or both.

The term x was neglected in the equation of the previous relativistic meridional-self-similar models, Globus et al. [2014]; Meliani et al. [2006b]. Hence, these models could not produce jets crossing the "light cylinder". Conversely, in this model this quantity is taken into account. We assume an expansion in $\sin(\theta)$ of this quantity.

Contrary to the two previous models we can choose the dependence of the isorotation frequency with the magnetic flux (see discussion on Eq. 5.59) and this choice will not affect the solution. Thus, if Ω does not depend strongly on the magnetic flux A, even at

the base of the jet, the ratio $h/(\Omega-\omega)$ will be nearly constant. The reason for this is that ϖ is larger than the Alfvén radius, which is at least a few times the Schwarzschild radius. As a consequence, the departure of $\Sigma_{\rm LC}$ from a real cylinder is unnoticeable.

Domain of validity

The equations of the model are the result of an inversion of the expanded conservation equations. Therefore, it will be useful to quantify the relative error of the expansion we made in order to properly analyze our results and to obtain the domain of validity of these results. To have an idea of the domain of validity, we quantify the rest in the expansion of the momentum equation, for each force $\mathbf{F}^i(\mathrm{R},\sin\theta)$,

$$\mathbf{F}^i(\mathrm{R},\sin\theta)=\mathbf{F}^i_0(\mathrm{R})+\mathbf{F}^i_1(\mathrm{R})\sin\theta+\mathbf{F}^i_2(\mathrm{R})\sin^2\theta+\mathbf{R}^i(\mathrm{R},\sin\theta)\sin^3\theta\,, \tag{5.80}$$

where $\mathbf{F}$ is one of the following forces, gravitational, centrifugal, inertial, electric or magnetic pressure, and so on. We define a new function in order to map the relative error,

$$\mathbf{R}^i(\mathrm{R},\sin\theta)\underset{\theta\to 0}{\sim}\mathbf{g}^i(\mathrm{R})\,. \tag{5.81}$$

For example, in the case of the electric force, in Schwarzschild metric, we get, assuming solid rotation $(w_1=0)$,

$$\begin{aligned}|\,\mathbf{R}_{\mathrm{E}l}(\mathrm{R},\sin\theta)\,|=\frac{\mathrm{B}_\star^2}{4\pi r_\star}\frac{\lambda^2 h_\star^2\mu}{\nu^2}\frac{\mathrm{R}}{h_z^2\mathrm{G}^4}\left(\frac{\mathrm{F}^2h_z^2}{2}+\frac{\mathrm{F}h_z^2}{2}-3+\frac{d\mathrm{F}}{d\mathrm{R}}\right)\\ \times\sqrt{1+\sin^2\theta\left(\frac{\mathrm{F}^2h_z^2}{4}-1\right)}\,.\end{aligned} \tag{5.82}$$

The relative error on the electric force which tends to zero in the asymptotic regime of cylindrical jets is defined as

$$\mathrm{err}=\frac{|\,\mathbf{R}^{\mathrm{E}l}(\mathrm{R},\sin\theta)\sin^3\theta\,|}{|\,\mathbf{F}^{\mathrm{E}l}(\mathrm{R},\sin\theta)\,|}\,. \tag{5.83}$$

Even at the base of the jet this error can be reduced, as can be seen in Fig. 5.1 for the solution in Kerr metric presented in Sect. 7.2 when the co-latitude is less than 30 degrees.

To get an estimate of the error in the expanded forces, we should add all relative error terms or take the largest one. This gives an estimate of the domain of validity of the solutions for a given set of parameters. We postpone the full error analysis for a future paper.

The magnetic collimation efficiency, ϵ

By writing the first law of thermodynamics in the frame of the fluid along streamlines of an axisymmetric flow, we can construct a constant of the motion, as in the classical case. The first law of thermodynamics reduces to the adiabatic law if the heating is included in some effective enthalpy (see Eq. 5.20). Thus (ξc^2) is an effective specific enthalpy, like for polytropic flows where the enthalpy also hides the heating (cf. Sauty and Tsinganos 1994) but generalized for relativistic outflows (see Eq. 5.18).Using Eq. (5.28), we can rewrite the first law of thermodynamics in the following form,

$$\xi\Psi_{\mathrm{A}}^2c^2\left.\frac{d\xi}{d\mathrm{R}}\right|_{\alpha=cst}=4\pi\mathrm{M}_{\mathrm{A}lf}^2\left.\frac{d\mathrm{P}}{d\mathrm{R}}\right|_{\alpha=cst}\,. \tag{5.84}$$

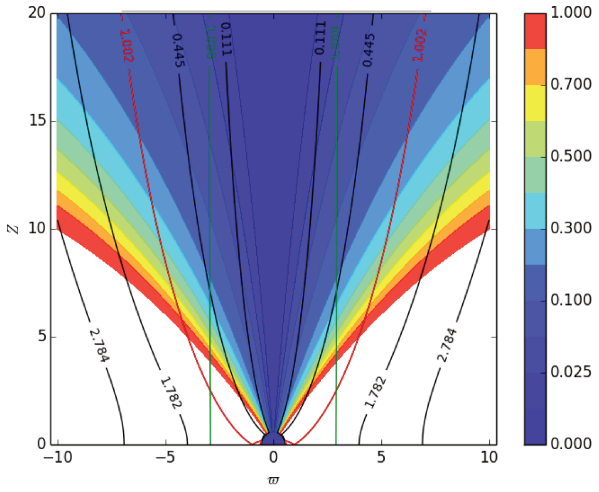

Figure 5.1 – Relative error on the electric force for a recollimating oscillating solution in Kerr metric (**K1**, see Sect. 7.2). Colored isocontours correspond to the relative error in the electric force. Field lines anchored into the black hole magnetosphere and in the accretion disk are plotted in black solid lines. The limiting field line between the inner jet coming from black hole corona and the outflow outgoing from the accretion disk is plotted in red. The "light cylinder" is indicated by a green solid line. The cylindrical radius and the distance above the equatorial plane are in units of Schwarzschild radius.

As the magnetic-to-mass-flux ratio and the total energy flux are constant along each streamline, this is equivalent to

$$\left.\frac{d(\Psi_{\rm A}^2\xi^2c^2)}{d{\rm R}}\right|_{\alpha=cst} = 8\pi {\rm M}_{Alf}^2 \left.\frac{d{\rm P}}{d{\rm R}}\right|_{\alpha=cst}. \tag{5.85}$$

We note that $\Psi_{\rm A}\xi c^2$ is proportional to the thermal energy. If we write

$$\Psi_{\rm A}^2\xi^2c^2 = [\Psi_{\rm A}^2\xi^2c^2]_0({\rm R}) + \alpha[\Psi_{\rm A}^2\xi^2c^2]_1({\rm R}), \tag{5.86}$$

and using the expressions of the pressure and the Mach number, we get an equation of the form

$$\frac{d[\Psi_{\rm A}^2\xi^2c^2]_0}{d{\rm R}} + \alpha\frac{d[\Psi_{\rm A}^2\xi^2c^2]_1}{d{\rm R}} = {\rm B}_\star^2{\rm M}^2\frac{d\Pi}{d{\rm R}}\left[1+(\kappa+2m_1)\alpha\right]. \tag{5.87}$$

We see, as in the classical case, that the second term of the pressure is proportional to the first one such that,

$$\frac{d[\Psi_{\rm A}^2\xi^2c^2]_1}{d{\rm R}} - (\kappa+2m_1)\frac{d[\Psi_{\rm A}^2\xi^2c^2]_0}{d{\rm R}} = 0. \tag{5.88}$$

We deduce from the previous equation that the quantity ϵ , which is defined by

$$\epsilon({\rm R}){\rm B}_\star^2 = [\Psi_{\rm A}^2\xi^2c^2]_1 - (\kappa+2m_1)[\Psi_{\rm A}^2\xi^2c^2]_0 = {\rm cst.}, \tag{5.89}$$

is a dimensionless constant for all the field lines. To give explicitly $[\Psi_{\rm A}^2\xi^2c^2]_0$ and $[\Psi_{\rm A}^2\xi^2c^2]_1$, it may be useful to write

$$\Psi_{\rm A}^2\xi^2c^2 = \Psi_{\rm A}^2\frac{(h\gamma\xi c)^2}{h^2}\left(1-\frac{({\rm V}^{\hat\phi})^2}{c^2}\right) - \frac{{\rm M}_{Alf}^4{\rm B}_{\rm p}^2}{h^2}.$$

Finally the calculation leads to

$$\begin{aligned}\epsilon &= \frac{\mathrm{M}^4}{h_z^2 h_*^4 \mathrm{G}^2(\mathrm{R}^2+l^2)}\left[\frac{h_z^2\mathrm{F}^2(\mathrm{R}^2+l^2)}{4\mathrm{R}^2}-\frac{\mathrm{R}^2}{(\mathrm{R}^2+l^2)}\right.\\ &- \left.(\kappa-2m_1)\frac{(\mathrm{R}^2+l^2)}{\mathrm{G}^2}\right]-\frac{\nu^2(2e_1-2m_1+\delta-\kappa)\mathrm{R}}{h_z^2(\mathrm{R}^2+l^2)}\\ &- \frac{\nu^2 l^2\mathrm{R}\mathrm{G}^2}{h_z^2(\mathrm{R}^2+l^2)^3}+\frac{2\lambda^2}{h_z^2}\left(\frac{\Lambda^2\mathrm{N_B}}{\mathrm{D}}+\frac{\overline{\omega}_z}{\lambda}\right)+\lambda^2\left(\frac{\Lambda\mathrm{N_V}}{h_*\mathrm{G}\mathrm{D}}\right)^2.\end{aligned} \tag{5.90}$$

This equation is similar to Eq. (71) in Meliani et al. [2006b] and can be interpreted the same way. The parameter ϵ measures the efficiency of the magnetic rotator to collimate the flow. At the outflow base, ϵ is the relative difference of the transverse variation of internal energy that is simply the exchange of work done by the macroscopic forces. As this is perpendicular to the flow axis, this means that ϵ really measures the transverse force which collimates the flow and mainly its magnetic component.

We note that the quantity $-2m_1$ appears twice in Eq. (5.90). First, it is associated with κ, having a similar effect to the nonspherically symmetric pressure in the term which is given as a factor of M^4. Second, it is associated with $2e_1$ in the term corresponding to the excess or the deficit of the gravitational energy not compensated by the thermal driving at the base of the jet.

To conclude we can also derive the magnetic collimation efficiency in a different form; after some calculations, we can write

$$\begin{aligned}\epsilon &= -\frac{\nu^2 h_\star^4}{\mu\gamma_z^2 h_z^2}\frac{\partial}{\partial\alpha}\ln\left(\frac{\mathrm{P}-\mathrm{P}_0}{\rho_0\xi}\right)\Big|_{\alpha=0}\\ &= h_\star^2\frac{\nu^2}{\mu}\left(1-\frac{\mu}{\nu^2}\right)\frac{\xi_z^2}{\xi_\star^2}\left(\frac{\partial}{\partial\alpha}\ln(\rho_0\xi)\Big|_{\alpha=0}-\kappa\right).\end{aligned} \tag{5.91}$$

This new relation brings a link between the total enthalpy on the axis and its logarithmic variation with α. In particular, the sign of ϵ seems to connect the balance between logarithmic variation of total enthalpy per unit of volume and the meridional increase of the pressure. The factor indicates that $|\epsilon|$ probably tends to decrease for solutions which reach ultra-relativistic speed.

5.2 Expansion of the forces

To finish our model, we expand to second order in colatitude each forces of Eqs.(5.16). More precisely we use the decomposition given in Sec.(4.2.3). We introduce the generic expansion of each force,

$$\mathscr{F} = -\frac{\mathrm{B}_\star^2}{4\pi r_\star}\left[\frac{1}{2\mathrm{G}^2}\left(\mathscr{X}+\theta^2\mathscr{Y}\right)\boldsymbol{\epsilon}_r+\frac{\sqrt{\mathrm{X}_+}}{\mathrm{G}^4}\mathscr{Z}\theta\boldsymbol{\epsilon}_\theta\right]+\mathscr{O}\left(\theta^3\right) \tag{5.92}$$

where $\mathrm{X}_+ = \mathrm{R}^2+l^2$ and $\mathrm{X}_- = \mathrm{R}^2-l^2$.

5.2.1 Magnetic Forces

Let us start with the magnetic forces. For the magnetic poloidal pressure, we get,

$$\begin{cases}\mathscr{X}_{\mathrm{M,P,B}_p} = 0\\ \mathscr{Y}_{\mathrm{M,P,B}_p} = \dfrac{h_z\mathrm{F}}{\mathrm{R}\mathrm{G}^2}\left[\dfrac{3h_z^2\mathrm{F}^2\mathrm{X}_+}{4\mathrm{R}^2}+h_z^2\mathrm{F}\left(\dfrac{\mu\mathrm{X}_-}{4h_z^2\mathrm{R}\mathrm{X}_+}-1\right)-\dfrac{\mathrm{R}^2}{\mathrm{X}_+}-\dfrac{2\mu l^2\mathrm{R}}{\mathrm{X}_+^2}\right]\\ \mathscr{Z}_{\mathrm{M,P,B}_p} = \dfrac{1}{\mathrm{X}_+}\left[\dfrac{3h_z^2\mathrm{F}^2\mathrm{X}_+}{4\mathrm{R}^2}+h_z^2\mathrm{F}\left(\dfrac{\mu\mathrm{X}_-}{4h_z^2\mathrm{R}\mathrm{X}_+}-1\right)-\dfrac{\mathrm{R}^2}{\mathrm{X}_+}-\dfrac{2\mu l^2\mathrm{R}}{\mathrm{X}_+^2}\right]\end{cases} \tag{5.93}$$

For the magnetic toroidal pressure,

$$\begin{cases} \mathscr{X}_{\mathrm{M,P,B_\phi}} = 0 \\ \mathscr{Y}_{\mathrm{M,P,B_\phi}} = \dfrac{2\lambda^2 h_\star^2 \Lambda \mathrm{N_B X_+}}{h_z \mathrm{D G^2}} \left[\dfrac{\Lambda \mathrm{N_B}}{h_\star^2 \mathrm{D^2}} \dfrac{d\mathrm{M^2}}{d\mathrm{R}} + \dfrac{\Lambda \mathrm{N_B}}{\mathrm{DR}} \left(\mathrm{F} - \dfrac{\mathrm{R^2}}{\mathrm{X_+}} \right) + \dfrac{\mathrm{G^2}}{\mathrm{D}} \left(\dfrac{\sqrt{\mu}\nu l}{\lambda h_\star} \dfrac{l^2 - 3\mathrm{R^2}}{\mathrm{X_+^3}} + \dfrac{\Lambda}{\mathrm{R}} \left(\mathrm{F} - \dfrac{2\mathrm{R^2}}{\mathrm{X_+}} \right) \right) - \dfrac{\mu \Lambda \mathrm{N_V X_-}}{h_\star^2 \mathrm{D^2 X_+^2}} \right] \\ \mathscr{Z}_{\mathrm{M,P,B_\phi}} = \dfrac{\lambda^2 h_\star^2 \Lambda^2 \mathrm{N_B^2}}{h_z^2 \mathrm{D^2}} \end{cases} \tag{5.94}$$

For magnetic poloidal tension,

$$\begin{cases} \mathscr{X}_{\mathrm{M,T,B}_p} = 0 \\ \mathscr{Y}_{\mathrm{M,T,B}_p} = -\dfrac{h_z \mathrm{F}}{\mathrm{RG^2}} \left[-\dfrac{h_z^2 \mathrm{X_+}}{2\mathrm{R}} \dfrac{d\mathrm{F}}{d\mathrm{R}} + \dfrac{h_z^2 \mathrm{F^2 X_+}}{4\mathrm{R^2}} - \dfrac{h_z^2 \mathrm{F X_-}}{2\mathrm{R^2}} - \dfrac{\mu \mathrm{F X_-}}{\mathrm{R X_+}} + \dfrac{l^2}{\mathrm{X_+}} \right] \\ \mathscr{Z}_{\mathrm{M,T,B}_p} = \dfrac{1}{\mathrm{X_+}} \left[\dfrac{h_z^2 \mathrm{X_+}}{2\mathrm{R}} \dfrac{d\mathrm{F}}{d\mathrm{R}} - \dfrac{h_z^2 \mathrm{F^2 X_+}}{4\mathrm{R^2}} + h_z^2 \mathrm{F} \left(\dfrac{\mathrm{X_-}}{2\mathrm{R^2}} + \dfrac{\mu \mathrm{X_-}}{4 h_z^2 \mathrm{R X_+}} \right) - \dfrac{l^2}{\mathrm{X_+}} \right] \end{cases} \tag{5.95}$$

And finally, for the toroidal tension,

$$\begin{cases} \mathscr{X}_{\mathrm{M,T,B_\phi}} = 0 \\ \mathscr{Y}_{\mathrm{M,T,B_\phi}} = \dfrac{2\lambda^2 h_\star^2 \Lambda^2 \mathrm{N_B^2 R}}{h_z \mathrm{D^2 G^2}} \\ \mathscr{Z}_{\mathrm{M,T,B_\phi}} = \dfrac{\lambda^2 h_\star^2 \Lambda^2 \mathrm{N_B^2}}{h_z^2 \mathrm{D^2}} \end{cases} \tag{5.96}$$

For the global magnetic force, we obtain,

$$\begin{cases} \mathscr{X}_{\mathrm{M}} = 0 \\ \mathscr{Y}_{\mathrm{M}} = -\dfrac{h_z \mathrm{F}}{\mathrm{RG^2}} \left[-\dfrac{h_z^2 \mathrm{X_+}}{2\mathrm{R}} \dfrac{d\mathrm{F}}{d\mathrm{R}} + 1 + \dfrac{2l^2 \mu \mathrm{R}}{\mathrm{X_+^2}} - \dfrac{\mu \mathrm{F X_-}}{2\mathrm{R X_+}} + \dfrac{h_z^2 \mathrm{X_+ F(1-F)}}{2\mathrm{R^2}} \right] \\ \qquad + \dfrac{2\lambda^2 h_\star^2 \Lambda \mathrm{N_B X_+}}{h_z \mathrm{D G^2}} \left[\dfrac{\Lambda \mathrm{N_B}}{h_\star^2 \mathrm{D^2}} \dfrac{d\mathrm{M^2}}{d\mathrm{R}} + \dfrac{\Lambda \mathrm{N_B F}}{\mathrm{DR}} + \dfrac{\mathrm{G^2}}{\mathrm{D}} \left(\dfrac{\sqrt{\mu}\nu l}{\lambda h_\star} \dfrac{l^2 - 3\mathrm{R^2}}{\mathrm{X_+^3}} + \dfrac{\Lambda}{\mathrm{R}} \left(\mathrm{F} - \dfrac{2\mathrm{R^2}}{\mathrm{X_+}} \right) \right) - \dfrac{\mu \Lambda \mathrm{N_V X_-}}{h_\star^2 \mathrm{D^2 X_+^2}} \right] \\ \mathscr{Z}_{\mathrm{M}} = \dfrac{h_z^2}{2\mathrm{R}} \dfrac{d\mathrm{F}}{d\mathrm{R}} + \dfrac{h_z^2 \mathrm{F(F-1)}}{2\mathrm{R^2}} + \dfrac{\mu \mathrm{F X_-}}{2\mathrm{R X_+^2}} + \dfrac{1}{\mathrm{X_+}} \left(1 - \dfrac{2\mu \mathrm{R} l^2}{\mathrm{X_+^2}} \right) + \dfrac{2\lambda^2 h_\star^2 \Lambda^2 \mathrm{N_B^2}}{h_z^2 \mathrm{D^2}} \end{cases} \tag{5.97}$$

5.2.2 Electrical Force

For the electrical force, we obtain,

$$\begin{cases} \mathscr{X}_{\mathrm{E}} = 0 \\ \mathscr{Y}_{\mathrm{E}} = -\dfrac{2\lambda^2 \mu}{\nu^2} \dfrac{h_\star^2 \Lambda^2 \mathrm{F X_+}}{h_z \mathrm{RG^2}} \\ \mathscr{Z}_{\mathrm{E}} = -\dfrac{2\lambda^2 \mu}{\nu^2} \dfrac{h_\star^2 \Lambda^2}{h_z^2} \end{cases} \tag{5.98}$$

5.2.3 Advection forces

The expand of poloidal advection force gives,

$$\begin{cases} \mathscr{X}_{\mathrm{A}_p} = \dfrac{2}{h_z \mathrm{G}^2}\dfrac{d\mathrm{M}^2}{d\mathrm{R}} + \dfrac{2\mathrm{M}^2}{h_z \mathrm{G}^2 \mathrm{R}}\left(\mathrm{F} - \dfrac{2\mathrm{R}^2}{\mathrm{X}_+} - \dfrac{\mu \mathrm{R}\mathrm{X}_-}{2h_z^2 \mathrm{X}_+^2}\right) \\ \mathscr{Y}_{\mathrm{A}_p} = -\dfrac{2}{h_z \mathrm{G}^2}\left(1 - \dfrac{3l^2}{2\mathrm{X}_+} - \dfrac{2m_1 \mathrm{X}_+}{\mathrm{G}^2}\right)\dfrac{d\mathrm{M}^2}{d\mathrm{R}} - \dfrac{\mathrm{M}^2}{h_z^2 \mathrm{R}\mathrm{G}^2}\left[\dfrac{\mathrm{F}^2 h_z^2}{2} - \mathrm{F} + \dfrac{2\mathrm{R}^2 l^2}{\mathrm{X}_+^2} + 2\left(\mathrm{F} - \dfrac{2\mathrm{R}^2}{\mathrm{X}_+} - \dfrac{\mu \mathrm{R}\mathrm{X}_-}{2h_z^2 \mathrm{X}_+^2}\right)\left(1 - \dfrac{3l^2}{2\mathrm{X}_+} - \dfrac{2m_1 \mathrm{X}_+}{\mathrm{G}^2}\right)\right] \\ \mathscr{Z}_{\mathrm{A}_p} = -\dfrac{1}{2\mathrm{R}}\dfrac{d(\mathrm{M}^2\mathrm{F})}{d\mathrm{R}} + \dfrac{\mathrm{M}^2 l^2}{h_z^2 \mathrm{X}_+^2} - \dfrac{\mathrm{M}^2 \mathrm{F}(\mathrm{F}-2)}{4\mathrm{R}^2} \end{cases} \tag{5.99}$$

For the centrifugal advection forces, we get,

$$\begin{cases} \mathscr{X}_{\mathrm{A}_\phi} = 0 \\ \mathscr{Y}_{\mathrm{A}_\phi} = -\dfrac{2\lambda^2 h_\star^2 \Lambda^2 \mathrm{N}_\mathrm{V}^2 h_z \mathrm{R}}{\mathrm{G}^2 \mathrm{D}^2 \mathrm{M}^2} \\ \mathscr{Z}_{\mathrm{A}_\phi} = -\dfrac{\lambda^2 h_\star^2 \Lambda^2 \mathrm{N}_\mathrm{V}^2}{\mathrm{M}^2 \mathrm{D}^2} \end{cases} \tag{5.100}$$

5.2.4 Gravitational Force

For the gravitational force, we obtain,

$$\begin{cases} \mathscr{X}_\mathrm{G} = \dfrac{\nu^2 h_\star^4 \mathrm{G}^2 \mathrm{X}_-}{h_z^3 \mathrm{M}^2 \mathrm{X}_+^2} \\ \mathscr{Y}_\mathrm{G} = \dfrac{\nu^2 h_\star^4 \mathrm{G}^2}{h_z^3 \mathrm{M}^2 \mathrm{X}_+^2}\left[\dfrac{\mu l^2 \mathrm{R}}{\mathrm{X}_+^2} + \dfrac{\mathrm{X}_+}{\mathrm{G}^2}\left\{2e_1 - 2m_1 + \delta - \dfrac{2\lambda^2 \mu}{\nu^2}\left(\dfrac{\Lambda^2 \mathrm{N}_\mathrm{B}}{\mathrm{D}} + \dfrac{\omega_z}{\lambda}\right)\right\} + \dfrac{l^2}{2\mathrm{X}_+}\left(1 + 2h_z^2 \dfrac{3\mathrm{R}^2 - l^2}{\mathrm{X}_-}\right)\right] \\ \mathscr{Z}_\mathrm{G} = -\dfrac{\nu^2 l^2 h_\star^4 \mathrm{R}\mathrm{G}^4}{h_z^2 \mathrm{M}^2 \mathrm{X}_+^3} \end{cases} \tag{5.101}$$

5.2.5 Lense-Thirring Force

For the Lense-Thirring force, we obtain,

$$\begin{cases} \mathscr{X}_\mathrm{LT} = 0 \\ \mathscr{Y}_\mathrm{LT} = \dfrac{2\lambda l \nu \sqrt{\mu} \Lambda \mathrm{N}_\mathrm{V} h_\star^3}{\mathrm{D} h_z \mathrm{M}^2}\dfrac{\left(3\mathrm{R}^2 - l^2\right)}{\mathrm{X}_+^2} \\ \mathscr{Z}_\mathrm{LT} = 0 \end{cases} \tag{5.102}$$

5.2.6 Pressure Force

For the pressure force, we obtain,

$$\begin{cases} \mathscr{X}_\mathrm{P} = h_z \mathrm{G}^2 \dfrac{d\Pi}{d\mathrm{R}} \\ \mathscr{Y}_\mathrm{P} = \left(\kappa h_z \mathrm{X}_+ + \dfrac{l^2 h_z \mathrm{G}^2}{2\mathrm{X}_+}\right)\dfrac{d\Pi}{d\mathrm{R}} + \dfrac{\kappa \Pi \mathrm{F} h_z \mathrm{X}_+}{\mathrm{R}} \\ \mathscr{Z}_\mathrm{P} = \kappa \Pi \mathrm{G}^2 \end{cases} \tag{5.103}$$

5.3 Differential equation system

Let us add the different contributions of each force, we get at the end

$$\begin{cases} \mathscr{X} = \mathscr{X}_{\rm M} + \mathscr{X}_{\rm E} + \mathscr{X}_{{\rm A}_p} + \mathscr{X}_{{\rm A}_\phi} + \mathscr{X}_{\rm G} + \mathscr{X}_{\rm LT} + \mathscr{X}_{\rm P} \\ \mathscr{Y} = \mathscr{Y}_{\rm M} + \mathscr{Y}_{\rm E} + \mathscr{Y}_{{\rm A}_p} + \mathscr{Y}_{{\rm A}_\phi} + \mathscr{Y}_{\rm G} + \mathscr{Y}_{\rm LT} + \mathscr{Y}_{\rm P} \\ \mathscr{Z} = \mathscr{Z}_{\rm M} + \mathscr{Z}_{\rm E} + \mathscr{Z}_{{\rm A}_p} + \mathscr{Z}_{{\rm A}_\phi} + \mathscr{Z}_{\rm G} + \mathscr{Z}_{\rm LT} + \mathscr{Z}_{\rm P} \end{cases} \tag{5.104}$$

Each function $\mathscr{X} = \mathscr{X}({\rm R})$, $\mathscr{Y} = \mathscr{Y}({\rm R})$ and $\mathscr{Z} = \mathscr{Z}({\rm R})$ is function of radius only. Then, because of the unicity of the expansion we have $\mathscr{X} = 0$, $\mathscr{Y} = 0$ and $\mathscr{Z} = 0$. Note that in the expression of these three terms, we could put together the terms proportional to the derivative, we get,

$$\begin{cases} \mathscr{X} = \mathscr{X}^{{\rm M}^2} \dfrac{d{\rm M}^2}{d{\rm R}} + \mathscr{X}^{\rm F} \dfrac{d{\rm F}}{d{\rm R}} + \mathscr{X}^{\Pi} \dfrac{d\Pi}{d{\rm R}} + \mathscr{X}^0 \\ \mathscr{Y} = \mathscr{Y}^{{\rm M}^2} \dfrac{d{\rm M}^2}{d{\rm R}} + \mathscr{Y}^{\rm F} \dfrac{d{\rm F}}{d{\rm R}} + \mathscr{Y}^{\Pi} \dfrac{d\Pi}{d{\rm R}} + \mathscr{Y}^0 \\ \mathscr{Z} = \mathscr{Z}^{{\rm M}^2} \dfrac{d{\rm M}^2}{d{\rm R}} + \mathscr{Z}^{\rm F} \dfrac{d{\rm F}}{d{\rm R}} + \mathscr{Z}^{\Pi} \dfrac{d\Pi}{d{\rm R}} + \mathscr{Z}^0 \end{cases} \tag{5.105}$$

Then we can write our system of first order differential equations in the form

$$\begin{bmatrix} \mathscr{X}^{{\rm M}^2} & \mathscr{X}^{\rm F} & \mathscr{X}^{\Pi} \\ \mathscr{Y}^{{\rm M}^2} & \mathscr{Y}^{\rm F} & \mathscr{Y}^{\Pi} \\ \mathscr{Z}^{{\rm M}^2} & \mathscr{Z}^{\rm F} & \mathscr{Z}^{\Pi} \end{bmatrix} \frac{d}{d{\rm R}} \begin{bmatrix} {\rm M}^2 \\ {\rm F} \\ \Pi \end{bmatrix} = - \begin{bmatrix} \mathscr{X}^0 \\ \mathscr{Y}^0 \\ \mathscr{Z}^0 \end{bmatrix} \tag{5.106}$$

The final ordinary differential equations of our model can be written as,

$$\boxed{ {\rm R} \frac{d}{d{\rm R}} \begin{pmatrix} {\rm M}^2 \\ {\rm G}^2 \\ {\rm F} \\ \Pi \end{pmatrix} = \begin{pmatrix} \dfrac{\mathscr{N}_{{\rm M}^2}}{\mathscr{D}({\rm M}^2,{\rm G}^2,{\rm F},\Pi,{\rm R})} \\ {\rm G}^2 \left(\dfrac{2{\rm R}^2}{{\rm R}^2 + l^2} - {\rm F} \right) \\ \dfrac{\mathscr{N}_{\rm F}}{\mathscr{D}({\rm M}^2,{\rm G}^2,{\rm F},\Pi,{\rm R})} \\ \dfrac{\mathscr{N}_{\Pi}}{\mathscr{D}({\rm M}^2,{\rm G}^2,{\rm F},\Pi,{\rm R})} \end{pmatrix} } , \tag{5.107}$$

where,

$$\boxed{ \mathscr{D}(m^2,{\rm G}^2,{\rm F},{\rm R}) \;=\; \frac{h_*^2}{\rm R} \left[-{\rm D} \left(1 + (\kappa - 2m_1) \frac{{\rm R}^2 + l^2}{{\rm G}^2} - \frac{l^2}{{\rm X}_+} \right) + \frac{\lambda^2 \Lambda^2 {\rm N}_{\rm B}^2 {\rm X}_+}{{\rm D}^2} + \frac{h_z^4 {\rm F}^2 {\rm X}_+}{4 h_*^2 {\rm R}^2} \right] } , \tag{5.108}$$

This function $\mathscr{D}$ is a possible singular point of our system Eqs.(5.107). $\mathscr{D}$ is not the 1-D equivalent of the singular value obtain from Grad-Shafranov Eq.(4.69). This singular point seems to be related (or close) to the modified slow-magneto-sonic transition as it as been inferred by Tsinganos et al. [1996]. They gave more details and discussion about singular points of meridional self-similar model. $\mathscr{N}_{\rm F}, \mathscr{N}_{{\rm M}^2}$ are function of ${\rm R}, {\rm M}^2, {\rm G}^2, {\rm F}, \Pi$ and the seven parameters introduced in the model $\lambda, \kappa, \delta, \nu, l, \mu, e_1$. Note that this system is of order one in the function which characterizes the speed ${\rm M}^2$ and of second order in the function ${\rm G}^2$ which characterizes the geometry. The system of Eq.(5.107) is a generalization including the light cylinder and the variation of the energy of Bernoulli with magnetic flux around a rotating Kerr black hole of the work of, Meliani et al. [2006b] near a Schwarzchild black hole and Globus et al. [2014] for Kerr blach hole and with a light cylinder pushed toward infinity. With this generalized model we can recover solutions for a Kerr black hole neglecting the light cylinder effect ($m_1 \to 0$) and variation of energy integral, effect ($e_1 \to 0$) and the same for Schwarzschild case studied by Meliani et al. [2006b] ($l, m_1, e_1 \to 0$).

The terms $\mathscr{N}_{\rm F}$ and $\mathscr{N}_{{\rm M}^2}$ are given as,

$$
\begin{aligned}
\mathcal{N}_{\mathrm{F}} &= \frac{\mathrm{F}\mathrm{M}^2}{h_*^2}\left[\frac{\mathrm{F}}{2}\left(\frac{h_z^2\mathrm{F}}{2}-1\right)+\left(\frac{\mathrm{F}}{2}-1\right)\left(1+(\kappa-2m_1)\frac{\mathrm{X}_+}{\mathrm{G}^2}-\frac{l^2}{\mathrm{X}_+}+\frac{\lambda^2\Lambda^2\mathrm{N}_\mathrm{B}^2\mathrm{X}_+}{\mathrm{D}^3}\right)\right]\\
&+ \frac{\mathrm{R}^2h_z^2}{\mathrm{X}_+h_*^2}\left[\frac{\mathrm{X}_+}{\mathrm{R}^2}\mathrm{F}(\mathrm{F}-1)-\frac{2}{h_z^2}-\frac{4\lambda^2\mu h_*^2\Lambda^2\mathrm{X}_+}{\nu^2h_z^4}-\frac{4l^2\mu\mathrm{R}}{h_z^2\mathrm{X}_+^2}\right]\left[1+(\kappa-2m_1)\frac{\mathrm{X}_+}{\mathrm{G}^2}-\frac{l^2}{\mathrm{X}_+}-\frac{\lambda^2\Lambda^2\mathrm{N}_\mathrm{B}^2\mathrm{X}_+}{\mathrm{D}^3}-\frac{h_z^2\mathrm{F}^2\mathrm{X}_+}{4\mathrm{R}^2}\right]\\
&+ \left(\frac{2\kappa\Pi\mathrm{G}^2\mathrm{R}^2}{h_*^2}+\frac{\mu\mathrm{F}\mathrm{R}\mathrm{X}_-}{h_*^2\mathrm{X}_+^2}\right)\left[1+(\kappa-2m_1)\frac{\mathrm{X}_+}{\mathrm{G}^2}-\frac{l^2}{\mathrm{X}_+}-\frac{\lambda^2\Lambda^2\mathrm{N}_\mathrm{B}^2\mathrm{X}_+}{\mathrm{D}^3}-\frac{h_z^2\mathrm{F}^2\mathrm{X}_+}{4\mathrm{R}^2}\right]\\
&+ \frac{\nu^2h_*^2\mathrm{F}\mathrm{G}^2\mathrm{R}}{2h_z^2\mathrm{M}^2}\frac{\mathrm{X}_-}{\mathrm{X}_+}(\kappa-2e_1+2m_1-\delta)-\frac{\mu\mathrm{F}\mathrm{M}^2\mathrm{R}\mathrm{X}_-}{2h_*^2h_z^2\mathrm{X}_+^2}\left[1+(\kappa-2m_1)\frac{\mathrm{X}_+}{\mathrm{G}^2}-\frac{l^2}{\mathrm{X}_+}\right]\\
&+ \frac{\lambda^2\mu\Lambda^2\mathrm{N}_\mathrm{B}\mathrm{N}_\mathrm{V}\mathrm{F}\mathrm{R}}{h_*^2\mathrm{D}^3}\frac{\mathrm{X}_-}{\mathrm{X}_+}-\frac{\lambda^2\Lambda\mathrm{N}_\mathrm{B}h_z^2\mathrm{F}\mathrm{X}_+}{h_*^2\mathrm{D}^2}\left(\mathrm{F}-\frac{2\mathrm{R}^2}{\mathrm{X}_+}\right)+\frac{\lambda^2\mu h_*^2\mathrm{F}\mathrm{G}^2}{h_z^2\mathrm{M}^2}\frac{\mathrm{R}\mathrm{X}_-}{\mathrm{X}_+}\left(\frac{\Lambda^2\mathrm{N}_\mathrm{B}}{\mathrm{D}}+\frac{\bar{\omega}_z}{\lambda}\right) \qquad (5.109)\\
&+ \frac{4\lambda^2\Lambda^2\mathrm{R}^2}{h_z^2}\left(\frac{\mathrm{N}_\mathrm{B}^2}{\mathrm{D}^2}-\frac{h_z^2}{2\mathrm{M}^2}\frac{\mathrm{N}_\mathrm{V}^2}{\mathrm{D}^2}\right)\left[1+(\kappa-2m_1)\frac{\mathrm{X}_+}{\mathrm{G}^2}-\frac{l^2}{\mathrm{X}_+}-\frac{\lambda^2\Lambda^2\mathrm{N}_\mathrm{B}^2\mathrm{X}_+}{\mathrm{D}^3}-\frac{h_z^2\mathrm{F}}{2}\right]\\
&+ \lambda\sqrt{\mu}\nu l h_*\frac{\Lambda\mathrm{G}^2\mathrm{F}\mathrm{R}}{\mathrm{D}}\frac{(3\mathrm{R}^2-l^2)}{\mathrm{X}_+^2}\left(\frac{\mathrm{N}_\mathrm{B}}{h_*^2\mathrm{D}}-\frac{\mathrm{N}_\mathrm{V}}{\mathrm{M}^2}\right)\\
&- \frac{2\nu^2l^2h_*^2\mathrm{G}^4}{h_z^2\mathrm{M}^2}\frac{\mathrm{R}^3}{\mathrm{X}_+^3}\left[1-\frac{l^2}{\mathrm{X}_+}+(\kappa-2m_1)\frac{\mathrm{X}_+}{\mathrm{G}^2}-\frac{\lambda^2\Lambda^2\mathrm{N}_\mathrm{B}^2\mathrm{X}_+}{\mathrm{D}^3}+\left(\frac{\mathrm{X}_-}{4\mathrm{R}^2}+\frac{h_z^2}{2}\right)\mathrm{F}\right]\\
&+ \frac{2\mathrm{M}^2l^2\mathrm{R}^2}{h_*^2h_z^2\mathrm{X}_+^2}\left[1+(\kappa-2m_1)\frac{\mathrm{X}_+}{\mathrm{G}^2}-\frac{l^2}{\mathrm{X}_+}-\frac{\lambda^2\Lambda^2\mathrm{N}_\mathrm{B}^2\mathrm{X}_+}{\mathrm{D}^3}+\frac{h_z^2\mathrm{F}\mathrm{X}_+}{\mathrm{R}^2}\left(\frac{3\mathrm{R}^2}{2\mathrm{X}_+}+(\kappa-2m_1)\frac{\mathrm{X}_+}{\mathrm{G}^2}\right)\right],
\end{aligned}
$$

And

$$
\begin{aligned}
\mathcal{N}_{\mathrm{M}^2} &= \frac{\mathrm{M}^4}{4h_*^2}\left[-h_z^2\mathrm{F}^2+2\mathrm{F}-\frac{4\mathrm{R}^2l^2}{\mathrm{X}_+^2}-4\left(\mathrm{F}-2\frac{\mathrm{R}^2}{\mathrm{X}_+}\right)\left(1+(\kappa-2m_1)\frac{\mathrm{X}_+}{\mathrm{G}^2}-\frac{l^2}{\mathrm{X}_+}\right)\right]\\
&+ \frac{h_z^2\mathrm{M}^2}{h_*^2}\left[\frac{h_z^2\mathrm{X}_+\mathrm{F}^3}{8\mathrm{R}^2}+\frac{h_z^2\mathrm{F}^2}{4}\left(1+\frac{\mu\mathrm{X}_-}{h_z^2\mathrm{R}\mathrm{X}_+}\right)+(\kappa-2m_1)\frac{\mathrm{X}_+\mathrm{F}}{\mathrm{G}^2}-\mathrm{F}\frac{\lambda^2\mu}{\nu^2}\mathrm{X}_+\Lambda^2\frac{h_*^2}{h_z^2}-2\frac{\mathrm{R}^2}{\mathrm{X}_+}-(\kappa-2m_1)\frac{2\mathrm{R}^2}{\mathrm{G}^2}+\frac{3\mathrm{R}^2l^2}{\mathrm{X}_+^2}-\frac{\mathrm{F}l^2}{\mathrm{X}_+}\left(\frac{3}{2}-h_z^2\right)\right]\\
&+ \frac{\nu^2h_*^4\mathrm{D}\mathrm{R}\mathrm{G}^2}{2h_z^2\mathrm{M}^2}\frac{\mathrm{X}_-}{\mathrm{X}_+}(\kappa-\delta+2m_1-2e_1)+\kappa\frac{\mathrm{X}_+}{2}\frac{h_z^2}{h_*^2}\mathrm{F}\Pi\mathrm{G}^2\mathrm{M}^2-\frac{\mathrm{D}\mathrm{M}^2\mu\mathrm{R}\mathrm{X}_-}{2h_z^2\mathrm{X}_+^2}\left[1+(\kappa-2m_1)\frac{\mathrm{X}_+}{\mathrm{G}^2}-\frac{l^2}{\mathrm{X}_+}\right]+\frac{\lambda^2\mu\mathrm{R}\Lambda^2\mathrm{N}_\mathrm{B}\mathrm{N}_\mathrm{V}}{\mathrm{D}^2}\frac{\mathrm{X}_-}{\mathrm{X}_+}\\
&+ \lambda^2\Lambda^2\mathrm{X}_+\left(\frac{\mathrm{N}_\mathrm{B}^2}{\mathrm{D}^2}-\frac{h_z^2}{2\mathrm{M}^2}\frac{\mathrm{N}_\mathrm{V}^2}{\mathrm{D}^2}\right)\left(2\mathrm{M}^2\frac{\mathrm{R}^2}{\mathrm{X}_+}+h_z^2(\mathrm{F}-2\frac{\mathrm{R}^2}{\mathrm{X}_+})\right)-\frac{\lambda^2\Lambda\mathrm{N}_\mathrm{B}h_z^2\mathrm{X}_+}{\mathrm{D}}\left(\mathrm{F}-2\frac{\mathrm{R}^2}{\mathrm{X}_+}\right)+\frac{\lambda^2\mu h_*^4\mathrm{R}\mathrm{G}^2}{h_z^2\mathrm{M}^2}\frac{\mathrm{X}_-}{\mathrm{X}_+}\left(\Lambda^2\mathrm{N}_\mathrm{B}+\frac{\mathrm{D}r_*\omega_z}{\lambda\mathrm{V}_*h_*}\right)\\
&- \frac{l^2\nu^2\mathrm{R}\mathrm{G}^4h_*^2}{2\mathrm{M}^2\mathrm{X}_+^3}\left[h_*^2\mathrm{D}\left(3\mathrm{R}^2-l^2+\frac{\mu\mathrm{R}\mathrm{X}_-}{h_z^2\mathrm{X}_+}\right)+h_z^2\mathrm{F}\mathrm{X}_+\right]+\lambda\sqrt{\mu}\nu l h_*\mathrm{R}\mathrm{G}^2\Lambda\frac{l^2-3\mathrm{R}^2}{\mathrm{X}_+^2}\left(\frac{\mathrm{N}_\mathrm{V}h_*^2}{\mathrm{M}^2}-\frac{\mathrm{N}_\mathrm{B}}{\mathrm{D}}\right),
\end{aligned} \qquad (5.110)
$$

$$
\frac{d\Pi}{d\mathrm{R}}=-\frac{2}{h_z^2\mathrm{G}^4}\left[\frac{d}{d\mathrm{R}}\mathrm{M}^2+\frac{\mathrm{M}^2}{\mathrm{R}}\left(\mathrm{F}-\frac{2\mathrm{R}^2}{\mathrm{R}^2+l^2}\right)\right]-\frac{1}{h_z^4\mathrm{M}^2}\frac{\mathrm{R}^2-l^2}{(\mathrm{R}^2+l^2)^2}\left(\nu^2h_*^4-\frac{\mu\mathrm{M}^4}{\mathrm{G}^4}\right)\ , \qquad (5.111)
$$

We see that our system of Eqs.(5.107) has two singular points. One of them corresponds to the cancellation of D (Alfvén point) and the other to the cancellation of $\mathscr{D}$.

5.4 Conclusion

We have presented here a way, from the General Relativistic Axi-symmetric Stationary Ideal Magneto-Hydrodynamic (GRASIMHD) system of partial differential equations, which allow to derive a ordinary differential system of first order equations, Eq.(5.107), under certain assumptions. This type of differential equations allows to compute solution faster than integrating directly the GRASIMHD partial differential system.

This system of equations allow us to describe the GRASIMHD field in the proximity of the Kerr black hole axis. This system is characterized by seven parameters $\lambda, \kappa, \delta, \mu, \nu, l, e_1$. The first one μ and l are link to the gravitational field and the Alfvén surface. The parameter μ is directly the relative value of Schwarzschild radius (Mass of the black hole) with the Alfvén surface. The second one is link to dimensionless spin parameter $l = 2a/\mu$ of the black hole. The next parameter ν (once choose μ) fix the value of launched speed $\nu = c\sqrt{\mu}/\mathrm{V}_\star$. This parameter is negative for inflow and positive for outflow. The λ parameter is the dimensionless ratio of angular momentum flux per unit of magnetic flux $\lambda = \frac{r_\star}{2h_\star}\frac{\Psi_{\mathrm{AL}}}{\mathrm{A}}$. The next two ones δ and e_1 are the logarithmic variation rate of mass flux $\delta = 2\frac{d\ln\Psi_{\mathrm{A}}}{d\alpha}$ and Bernoulli energy $e_1 = 2\frac{d\ln\mathscr{E}}{d\alpha}$ with magnetic flux. The last parameter κ is the variation of pressure with the magnetic flux, $\kappa = \frac{\partial \ln \mathrm{P} - \mathrm{P}_0}{d\alpha}$.

We shall see in the next chapter, Ch.(6), that an entire solution is characterized by these seven parameters and the initial value of $\Pi = \Pi_\star$, that we could constrain for outflow solution Sec.(6.3).

The model takes into account the second order term in latitude coming from the light cylinder radius x. It implies a non spherical Mach Alfvén number, in order to keep the assumption of spherical Alfvén surface.

For this model we generalize the expression of the magnetic collimation parameter ϵ Eq.(5.90). This expression can be written, Eq.(5.92), in order to have a thermodynamical interpretation of this quantity.

5.5 References

V. S. Beskin. *MHD Flows in Compact Astrophysical Objects*. 2010. doi: 10.1007/978-3-642-01290-7. 82

E. Breitmoser and M. Camenzind. Collimated outflows of rapidly rotating young stellar objects. Wind equation, GSS equation and collimation. aap, 361:207–225, September 2000. 83

V. Cayatte, N. Vlahakis, T. Matsakos, J. J. G. Lima, K. Tsinganos, and C. Sauty. Counter-rotation in Relativistic Magnetohydrodynamic Jets. apjl, 788:L19, June 2014. doi: 10.1088/2041-8205/788/1/L19. 82

L. Chantry, V. Cayatte, C. Sauty, N. Vlahakis, and K. Tsinganos. Nonradial and nonpolytropic astrophysical outflows. X. Relativistic MHD rotating spine jets in Kerr metric. aap, 612:A63, April 2018. doi: 10.1051/0004-6361/201731793. 80, 81, 82

N. Globus, C. Sauty, V. Cayatte, and L. M. Celnikier. Magnetic collimation of meridional-self-similar general relativistic MHD flows. prd, 89(12):124015, June 2014. doi: 10.1103/PhysRevD.89.124015. 80, 87, 88, 90, 96

Z. Meliani, C. Sauty, K. Tsinganos, and N. Vlahakis. Relativistic Parker winds with variable effective polytropic index. aap, 425:773–781, October 2004. doi: 10.1051/0004-6361:20035653. 82

Z. Meliani, C. Sauty, N. Vlahakis, K. Tsinganos, and E. Trussoni. Nonradial and nonpolytropic astrophysical outflows. VIII. A GRMHD generalization for relativistic jets. aap, 447:797–812, March 2006a. doi: 10.1051/0004-6361:20053915. 80

Z. Meliani, C. Sauty, N. Vlahakis, K. Tsinganos, and E. Trussoni. Nonradial and nonpolytropic astrophysical outflows. VIII. A GRMHD generalization for relativistic jets. aap, 447:797–812, March 2006b. doi: 10.1051/0004-6361:20053915. 82, 83, 84, 87, 88, 90, 93, 96

Z. Meliani, C. Sauty, K. Tsinganos, E. Trussoni, and V. Cayatte. Relativistic spine jets from Schwarzschild black holes. Application to AGN radio-loud sources. aap, 521:A67, October 2010. doi: 10.1051/0004-6361/200912920. 87

A. Mignone, T. Plewa, and G. Bodo. The Piecewise Parabolic Method for Multidimensional Relativistic Fluid Dynamics. apjs, 160:199–219, September 2005. doi: 10.1086/430905. 82

C. Sauty and K. Tsinganos. Nonradial and nonpolytropic astrophysical outflows III. A criterion for the transition from jets to winds. aap, 287:893–926, July 1994. 86, 87, 91

C. Sauty, K. Tsinganos, and E. Trussoni. Nonradial and nonpolytropic astrophysical outflows. IV. Magnetic or thermal collimation of winds into jets? aap, 348:327–349, August 1999. 86

A. H. Taub. Relativistic rankine-hugoniot equations. Phys. Rev., 74:328–334, Aug 1948. doi: 10.1103/PhysRev.74.328. URL https://link.aps.org/doi/10.1103/PhysRev.74.328. 82

K. Tsinganos and C. Sauty. Nonradial and nonpolytropic astrophysical outflows. I - Hydrodynamic solutions with flaring streamlines. aap, 255:405–419, February 1992. 86

K. Tsinganos, C. Sauty, G. Surlantzis, E. Trussoni, and J. Contopoulos. On the relation of limiting characteristics to critical surfaces in magnetohydrodynamic flows. mnras, 283:811–820, December 1996. doi: 10.1093/mnras/283.3.811. 96

K. C. Tsinganos. Magnetohydrodynamic equilibrium. II - General integrals of the equations with one ignorable coordinate. apj, 252:775–790, January 1982. doi: 10.1086/159600. 82

Nektarios Vlahakis. Theory of Relativistic Jets. In Ioannis Contopoulos, Denise Gabuzda, and Nikolaos Kylafis, editors, *The Formation and Disruption of Black Hole Jets*, volume 414, page 177, January 2015. doi: 10.1007/978-3-319-10356-3_7. 90

Chapter 6

Numerical integration and methods

Contents

6.1 Introduction

The goal of this section is to present the mathematical and numerical resolution of the system Eq.(5.107). First of all, we present the main characteristics of the solutions for Eqs.(5.107) and the numerical way used to obtain them. We also discuss the nature of singular points of Eq.(5.107) and the numerical strategy used to cross them. Then we show how to use the last degree of freedom for an outflow solution characterized by the seven parameters $(\lambda, \kappa, \delta, \nu, \mu, l, e_1)$ to obtain solutions which obey to specific constraints at infinity. Finally, we explain how we seek solutions with physical characteristics.

6.2 Resolution of the system

The system of Eqs.(5.107) has two singular points. The Alfvén point is found for $\mathrm{D} = 0$, which means that flow reaches the Alfvén speed, and the slow-magneto-sonic point for $\mathscr{D} = 0$. We seek the solutions of the system, which cross these singular points. First of all we present the general architecture of the code. Then we dicuss the regularity condition required on the Alfvén point. Finally we will see how we automatize the crossing of the slow-magneto-sonic point.

6.2.1 General architecture of code

To integrate the system of differential equations Eq.(5.107), I build a Fortran 90 code. The architecture of the code is built around a main programm jet_thetkerr .f90 which receives the information via the file jet_thetkerr .in. This file contains the parameters for integration, the parameters of the solution and the type of solution we want to calculate. With these informations the main program calls one of the six principal subroutines defined in dmin.f90 depending on the solution type.

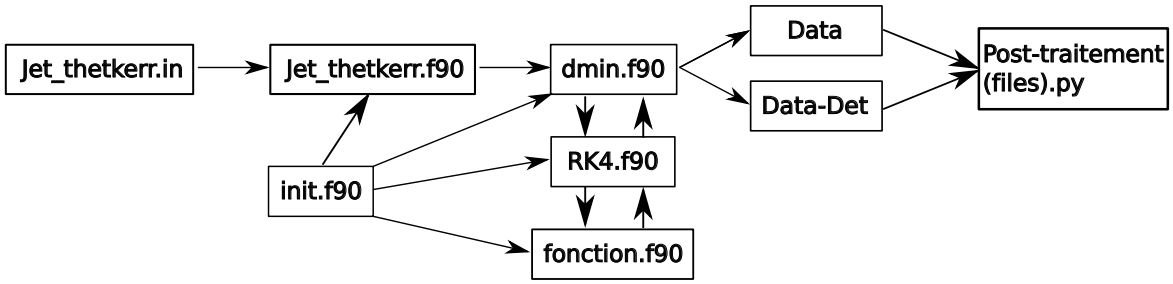

Figure 6.1 – Schema of code architecture.

The first subroutine calculates an inflow solution, the second one an outflow solution. The third and the fourth calculate respectevely a cylindrical or conical outflow solution in which we minimize $\Pi_\star$ Sec.(6.3). The fifth subroutine calculates one hundred sub-afvenic branches for different value of p, Sec.(6.2.3). This is useful when there is a problem in the automatic search of the slow-magneto-sonic point crossing. The two last ones (one for inflow and one for outflow) concern the evolution of a solution under constraints, see Sec.(6.4). These subroutine call a Runge-Kutta of the order 4 integrator defined in RK4.f90. Eqs.(5.107) of the system we integrate are defined in fonction .f90. One program init .f90 contains some important values such as the precision of the number used in the rest of the program or the value of π. Once the calculus has been done in the subroutine, the program writes the result in a file .dat in the directory Data−Det or Data. Then a post treatment using different python .py codes allows us to calculate and to draw the different graphics needed to understand and represent the solution.

6.2.2 Regularity on the Alfvén point

The solution crosses the singular Alfvén point if the functions, which appear in Eqs.(5.107), remain continuous at the crossing of the singularity. The assumption on the sphericity of Alfvén surface, implies that the Alfvén point is located for $\mathrm{R}=1$. The construction of the model, especially the definition and the assumption on the Alfvén surface, insures that $\mathrm{M}^2 \underset{\mathrm{R}\to 1}{\to} h_\star^2$ and using the definition of $\mathrm{B}_\star$, we get $\mathrm{G}^2 \underset{\mathrm{R}\to 1}{\to} 1$.

The regularity condition of the system Eq.(5.32) implies that the ratio remains finite, $\frac{\mathrm{N_B}}{\mathrm{D}} \underset{\mathrm{R}\to 1}{\to} \tau$. Then using Eqs.(5.70, 5.71, 5.72), we have $\frac{\mathrm{N_V}}{\mathrm{D}} \underset{\mathrm{R}\to 1}{\to} \tau - 1$. It implies that $\mathscr{N}_{\mathrm{M}^2}$ remains regular at the Alfvén radius $\mathrm{R}=1$. Using Eq.(5.111), it also implies that $\mathscr{N}_{\mathit{\Pi}}$ remains finite. It also implies that the the slope $p \hat{=} \left.\frac{d\mathrm{M}^2}{d\mathrm{R}}\right|_{\mathrm{R}=1}$ remains finite. F is defined everywhere, then $\left.\frac{d\mathrm{G}^2}{d\mathrm{R}}\right|_{\mathrm{R}=1} = \frac{2}{1+l^2} - \mathrm{F}_\star$. Thus, we can use l'Hôpital's rule to link τ, p and $\mathrm{F}_\star$.

$$\tau = \left.\frac{\mathrm{N_B}}{\mathrm{D}}\right|_* = \frac{\left.\frac{d\mathrm{N_B}}{d\mathrm{R}}\right|_*}{\left.\frac{d\mathrm{D}}{d\mathrm{R}}\right|_*} = \frac{h_*^2\left(\frac{2}{1+l^2} - \mathrm{F}_*\right) - \frac{\mu(1-l^2)}{(1+l^2)^2} - \frac{h_* l\sqrt{\mu}\nu}{\lambda}\frac{l^2-3}{(1+l^2)^3}}{p - \frac{\mu(1-l^2)}{(1+l^2)^2}}, \tag{6.1}$$

About Alfvén radius, we still have the case of the singularity that appears in $\mathscr{N}_{\mathrm{F}}$. Indeed, near the Alfvén point we have $\mathscr{N}_{\mathrm{F}} \sim \frac{\mathscr{P}(\tau,\mathrm{F}_\star,\mathit{\Pi}_\star)}{\mathrm{D}}$. In order, that the slope of the expansion factor F remains finite, the condition required on the value of $\tau, \mathrm{F}_\star, \mathit{\Pi}_\star$ is $\mathscr{P}(\tau,\mathrm{F}_\star,\mathit{\Pi}_\star)=0$, which is equivalent to $\mathscr{N}_{\mathrm{F}}\mathrm{D}|_\star = 0$. Using some algebra, this condition leads to,

$$\mathscr{N}_{\mathrm{F}}\mathrm{D}|_\star = 0 \qquad \Longrightarrow \qquad \mathrm{F}_\star p = 2\mathscr{Z}_\star^0 \tag{6.2}$$

The definition of the slope of M^2, p, implies also that $\mathscr{D}_\star = p\mathscr{N}_{\mathrm{M}^2,\star}$. Nevertheless, this equation is equivalent to a $\mathrm{F}_\star p = 2\mathscr{Z}_\star^0$. Then, using some algebra on $\mathrm{F}_\star p = 2\mathscr{Z}_\star^0(\tau,\mathrm{F}_\star,\mathit{\Pi}_\star)$, and removing the τ dependence using Eq.(6.2), the only condition needed for regularity on the Alfvén point is,

$$\mathscr{A}(p)\mathrm{F}_*^2 + \mathscr{B}(p)\mathrm{F}_* + \mathscr{C}(p,\mathit{\Pi}_*) = 0, \tag{6.3}$$

with

$$\mathscr{A}(p) = \lambda^2 h_*^4 + \frac{h_*^2}{4}\left(p - \frac{\mu(1-l^2)}{(1+l^2)^2}\right)^2 \tag{6.4}$$

$$\mathscr{B}(p) = \left[\frac{1}{2}\left(\frac{\mu(1-l^2)}{(1+l^2)^2} - p\right)^3 - 2\lambda^2 h_*^2\left(p + \frac{2}{1+l^2} - \frac{2\mu(1-l^2)}{(1+l^2)^2} + \frac{l\sqrt{\mu}\nu h_*}{\lambda}\frac{3-l^2}{(1+l^2)^3}\right)\right] \tag{6.5}$$

$$\mathscr{C}(p,\mathit{\Pi}_*) = \lambda^2\left(p + \frac{2h_*^2}{1+l^2} - \frac{2\mu(1-l^2)}{(1+l^2)^2} + \frac{l\sqrt{\mu}\nu h_*}{\lambda}\frac{3-l^2}{(1+l^2)^3}\right)^2 \tag{6.6}$$

$$+ \left(\kappa\mathit{\Pi}_* - \frac{1}{(1+l^2)^2} - \frac{2\lambda^2\mu}{\nu^2} - 2\lambda^2 - \frac{l^2(2\mu+\nu^2)}{(1+l^2)^3}\right)\left(p - \frac{\mu(1-l^2)}{(1+l^2)^2}\right)^2. \tag{6.7}$$

The equation Eq.(6.3) implies that for given values of p and $\mathit{\Pi}_\star$, we get the value of $\mathrm{F}_\star$. The two degrees of freedom on p and $\mathit{\Pi}_\star$, will allow later on for the crossing of the other critical surfaces. The degree of freedom on the slopes of M^2 implies that in the $(\mathrm{R},\mathrm{M}^2)$ plan the Alfvén point is a **star point**.

6.2.3 Crossing the slow-magneto-sonic point

To build the solution, we start the integration near the Alfven point. For outflows, we start the integration in $\mathrm{R} = 1 - d\mathrm{R}$. We know the value of $\mathrm{M}^2, \mathrm{G}^2, \mathrm{F}, \mathit{\Pi}$ on the Alfvén point as a function

of p and $\Pi_\star$. Then, we are able to evaluate the value of these functions at $1-d\mathrm{R}$. We use p to evaluate $\mathrm{M}^2(1-d\mathrm{R}) = h_\star^2 - pd\mathrm{R}$, and $\mathrm{F}_\star$ to evaluate $\mathrm{G}^2(1-d\mathrm{R})$. From Eq.(5.90) we know that the magnetic collimation parameter, ϵ, is constant and it allows to evaluate $\mathrm{F}(1-d\mathrm{R})$. From Eq.(5.111) we can evaluate $\Pi(1-d\mathrm{R})$. Then we start the integration to reach the slow-magneto-sonic point. Depending of the value of p, we determine two kind of branches and a limiting value for p in Fig.(6.2). The first family of branches has positive values for $\mathscr{D}$ everywhere, the second family has negative values for $\mathscr{D}$ on the part where $d\mathrm{R} \leq 0$. For inflow solutions the same analysis is done with $-d\mathrm{R} \leftrightarrow d\mathrm{R}$, the slow magnetosonic point being located above the Alfvén point.

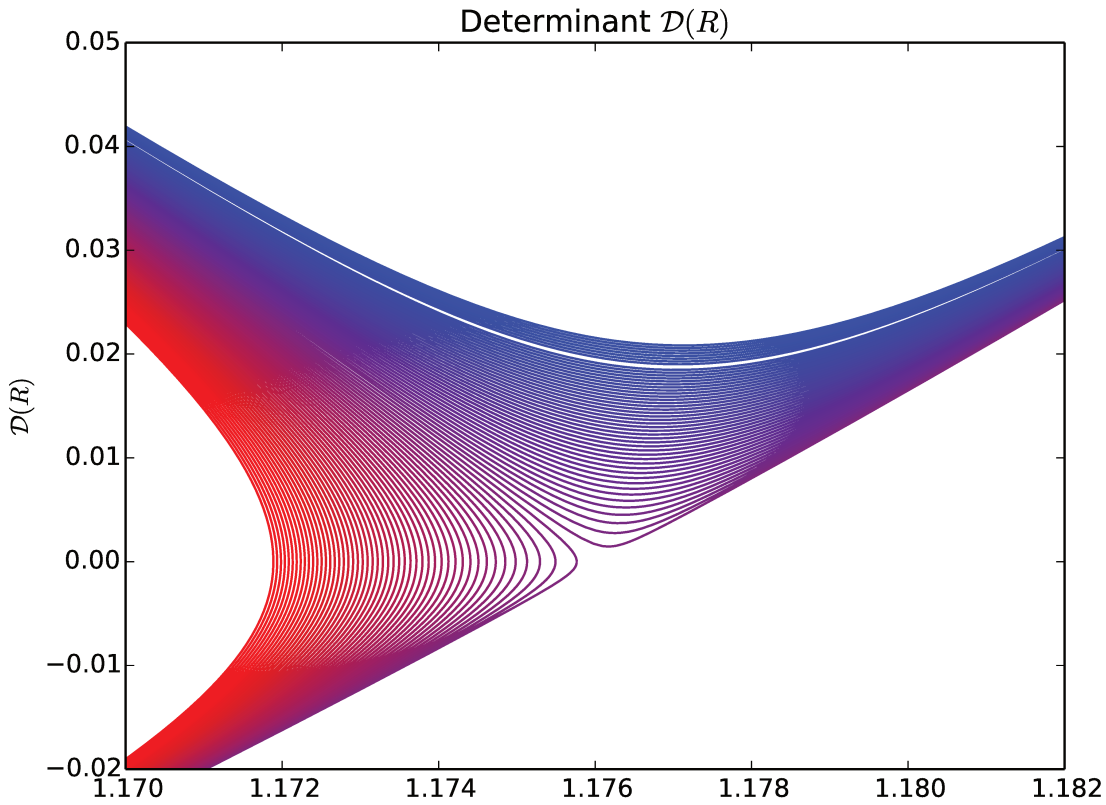

Figure 6.2 – $\mathscr{D}$ in function of R for hundred sub-alfvenic solutions of an inflow with different values of p.

The physical solution, which crosses the slow-magneto-sonic point, is obtained by determining the limiting value of p_{lim} with a sufficient precision. Then we cut the branch near the slow-magneto-sonic point and jump over the critical point, using the slope of the solution just before the bifurcation. Then we finish the rest of the integration to determine the sub-slow-magneto-sonic region solution. The integration stops for a null value of the function M^2.

Two subroutines, one for inflow solutions and one for outflow solutions allow to search automatically the p_{lim} value, using a dichotomous principle. Indeed, we start with two values, p_-, which correspond to one family, and p_+, which corresponds to the other family. We test which family corresponds to the solution with $2p = p_- + p_+$, and then we determine a new value of p_- or p_+. These subroutines also give the value of the function $\mathrm{M}^2, \mathrm{G}^2, \mathrm{F}, \Pi$ for the two final solutions, and the point, which is closer to the bifurcation for these two solutions. Then we build another set of two subroutines, one for inflow solutions and one for outflow solutions, to jump beyond the critical point and restart the integration.

The calculation of an inflow or outflow solution is completed by the integration of the super-

Alfvénic branch. Then, we merge the tables corresponding to the values of M^2, G^2, F, Π for the 3 regimes considered. We get a solution characterized by seven parameters $(\lambda, \kappa, \delta, \nu, \mu, l, e_1)$ and $\Pi_\star$.

6.2.4 The equilibrium at infinity

We aim at determining the asymptotic region of the flow. We can study the forces equilibrium in the asymptotic region, for solutions which are cylindrical or conical. This is equivalent to $G \sim R^0$ for cylindrical solutions and $G \sim R^1$ for conical solutions. We get a transverse equilibrium between electrical, centrifugal, toroidal magnetic and pressure forces. The toroidal magnetic force plays the role of a collimating force, while the electrical and the centrifugal ones are decollimating forces. The pressure term increases the collimation ($\kappa\Pi_\infty \geq 0$ for over-pressurized jets) or decollimates the flow ($\kappa\Pi_\infty \leq 0$ for under pressurized jets). In most cases, the solutions of the model are under-pressurized jets (in which the pressure is lower in the periphery at infinity). Then the transverse force balance of the flow can be written as,

$$\frac{\kappa\Pi_\infty G_\infty^2}{2\lambda^2 \Lambda_\infty^2 h_\star^2} = \frac{\mu}{\nu^2} + \frac{1}{D_\infty^2}\left(\frac{N_{V\infty}^2}{2M_\infty^2} - N_{B\infty}^2\right) \tag{6.8}$$

The left hand-side is characteristic of a term due to transversal pressure. In the right hand side, we have, first the term due to electrical forces, second the centrifugal forces, and eventually the toroidal magnetic force. It seems there is an ambiguity for conical flows ($G^2 \underset{R\to\infty}{\longrightarrow} \infty$) in the left-hand side of the previous equation. However we can show that for conical flows $G^2\Pi \underset{R\to\infty}{\longrightarrow} \text{Cst}$. In the conical case, the first term in parenthesis disappears for conical outflows. A second equation is needed to solve the value (cylindrical) or the behavior (conical) of M^2 and G^2 at infinity. From the value of ϵ Eq.(5.90), we get,

$$\begin{aligned}
\text{for cylindrical solutions} \quad & \frac{\epsilon}{2\lambda^2} = -\frac{M_\infty^4}{h_\star^4 G_\infty^4}\frac{(\kappa - 2m_1)}{2\lambda^2} + \Lambda_\infty^2\left(\left.\frac{N_B}{D}\right|_\infty + \left.\frac{N_V{}^2}{2h_\star^2 G_\infty^2 D^2}\right|_\infty\right) \\
\text{for conical solutions} \quad & \frac{\epsilon}{2\lambda^2} = -\frac{1}{2\lambda^2 h_\star^4}\left.\frac{M^4}{G^4}\right|_\infty\left(\left.(\kappa - 2m_1) + \frac{G^2}{R^2}\right|_\infty\right) - \Lambda_\infty^2 h_\star^2\left.\frac{G^2}{M^2}\right|_\infty
\end{aligned} \tag{6.9}$$

The main difference of the analysis in comparison to the Schwarzschild case is the introduction of the parameter m_1, which takes into account the effect of the light cylinder and the spin of the black hole. m_1 becomes zero in the case of a light cylinder pushed towards infinity and for a non rotating black hole. The second difference is the value $\Lambda_\infty = \Omega_{\text{Kerr}}/\Omega_{\text{Schwarzschild}}$ which contains the deviation due to the black hole spin, for keeping continuity at Alfvén surface.

6.3 Choice of $\Pi_\star$ for outflow solutions

An inflow or an outflow solution is characterized by the value of the parameters and the value of $\Pi_\star$. A generalization of the parametric study presented in Sauty et al. [2002] allows us to determine for outflows, a specific value of $\Pi_{\star,\text{lim}}$, which minimizes the oscillation of the velocity on the axis. This specific value is determined and calculated numerically using two different processes in function of the nature of the outflow. Indeed there are two kinds of outflow depending on the limiting value of F when the radius reaches infinity.

6.3.1 Cylindrical Solutions

For the first kind of outflows, the geometry of the flow becomes asymptotically cylindrical ($F \underset{R\to\infty}{\longrightarrow} 2$) at infinity. The solutions with constant values of λ, κ, δ, ν, ℓ, μ and e_1 and different value of $\Pi_\star$ are divided into two classes separated by a limiting value $\Pi_{\star,\text{lim}}$ which is function of the rest

of the parameters. To describe this two classes, we present an example for this set of parameters,

λ	κ	δ	ν	ℓ	μ	e_1
1	0.2	1.35	0.5	0.049	0.1	0.0001

We show in Figs.(6.3, 6.4) the function $\Pi(\mathrm{R})$ and the factor velocity $\beta(\mathrm{R})$ along the axis. And in Figs.(6.5, 6.6) are plotted $\mathrm{G}^2(\mathrm{R})$ and its derivative for the same set of parameters. These solutions are plotted with different values of $\Pi_\star$ between 0.19 and 0.38.

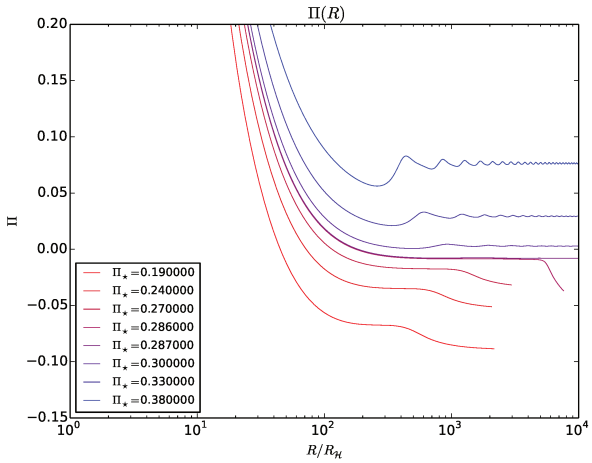

Figure 6.3 – Value of $\Pi(\mathrm{R})$ for different value of $\Pi_\star$

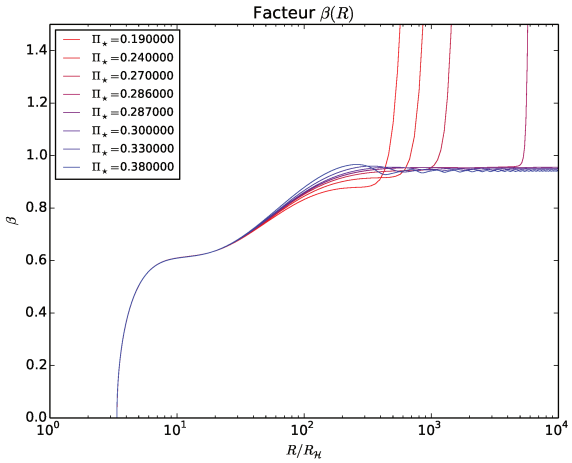

Figure 6.4 – Value of $\beta(\mathrm{R})$ speed on the axis for different value of $\Pi_\star$

We observe different trends when the solution reaches infinity. Indeed for values $\Pi_\star \leq \Pi_{\star,\mathrm{lim}}$, the solution does not get enough pressure to collimate and starts to flare/decollimate Fig.(6.5) at some point. This flaring could lead to a super-luminal motion Fig.(6.4) and thus unphysical solutions. The other solutions, with $\Pi_\star \geq \Pi_{\star,\mathrm{lim}}$, start to recollimate (decrease of G^2) and create oscillations for M^2 and G^2 at some point.

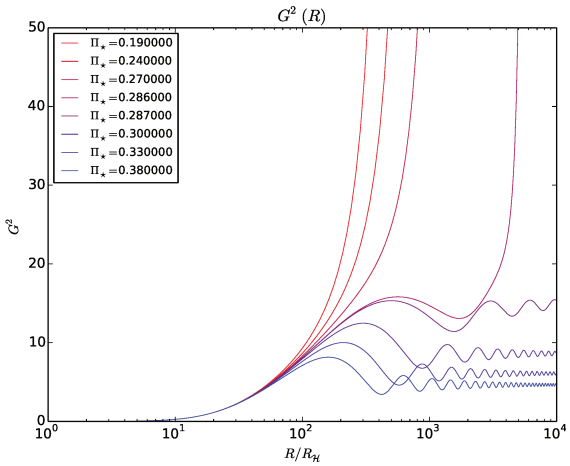

Figure 6.5 – Value of $\mathrm{G}^2(\mathrm{R})$ for different value of $\Pi_\star$

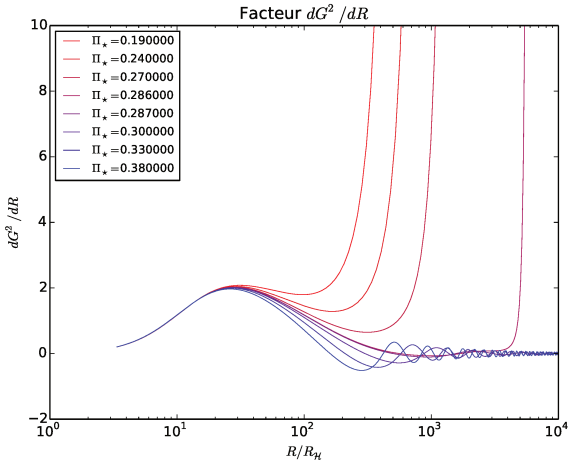

Figure 6.6 – Value of $\frac{d\mathrm{G}^2}{d\mathrm{R}}(\mathrm{R})$ speed on the axis for different value of $\Pi_\star$

The final size of the jet decreases as the value of $\Pi_\star$ increases Fig.(6.5). Indeed, this implies the increase of pressure and collimating work. The value of the final velocity increase with the

increasing of $\Pi_\star$ as a consequence of the decrease of the final size of the jet, Fig.(6.4).

The most physically satisfying solution, even if some solutions with $\Pi_\star \geq \Pi_{\star,\lim}$ are physical, is the solution with $\Pi_\star = \Pi_{\star,\lim}$. This is the solution with no oscillation on the polar velocity curve, even if the curve of G^2 slightly oscillates. We explore the boundaries of the physical solutions in the parameter space, and find a solution in which the maximum velocity is reached in the asymptotic regime.

For a cylindrical solution, we calculate numerically the value of $\Pi_{\star,\lim}$. For that we use a criterion to recognize the solution with $\Pi_\star \leq \Pi_{\star,\lim}$. Such a solution, for a sufficiently large value of the integration boundary, verifies, Fig.(6.6),

$$\Pi_\star \leq \Pi_{\star,\lim} \Longleftrightarrow \quad \begin{cases} & \exists R_{\lim},\ \forall R_{\max} \geq R_{\lim} \\ \dfrac{dG^2}{dR}(R_{\max}) = \underset{R\in[1;R_{\max}]}{\text{Max}} & \left(\dfrac{dG^2}{dR}\right) \end{cases} \tag{6.10}$$

Using this characterization, we build a subroutine to automatize the search for $\Pi_{\star,\lim}(\lambda, \kappa, \delta, \nu, \ell, \mu, e_1)$. A first numerical test is built to find $R_{\lim}$. After that a second test using the equality is numerically applied in order to find $\Pi_{\star,\lim}$ by dichotomy of the two solution families. Finally we get $\Pi_{\star,\lim}$ with a choosen relative error. In the following, unless mentioned by us, any outgoing cylindrical flow solution will be calculated with the approximate value $\Pi_{\star,+}$ of $\Pi_{\star,\lim}$ (in order to avoid the explosion of the factor beta on the axis). So the cylindrical outflow solution is characterized by the seven parameters λ, κ, δ, ν, ℓ, μ and e_1, since the value of $\Pi_{\star,\lim}$ is function of those parameters.

6.3.2 Conical Solution

The same kind of approach is applied for conical solutions with fixed values of λ, κ, δ, ν, ℓ, μ and e_1, and varying $\Pi_\star$. Indeed, there are also two classes of solutions separated by a limiting value of $\Pi_\star = \Pi_{\star,\lim}$. To show this partition, as before, we take an example of eight solutions with, the set of parameters given as, and for different value of $\Pi_\star$ taken between 0.24 and 0.27.

λ	κ	δ	ν	ℓ	μ	e_1
0.0143	1.451	3.14	0.8	0.15	0.40	0

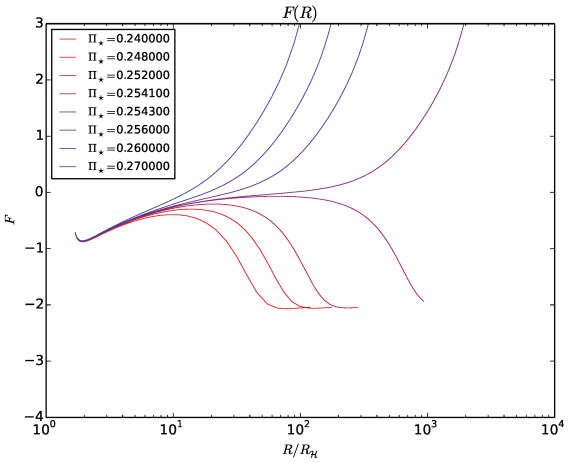

Figure 6.7 – Values of expansion factor $F(R)$ for different value of $\Pi_\star$

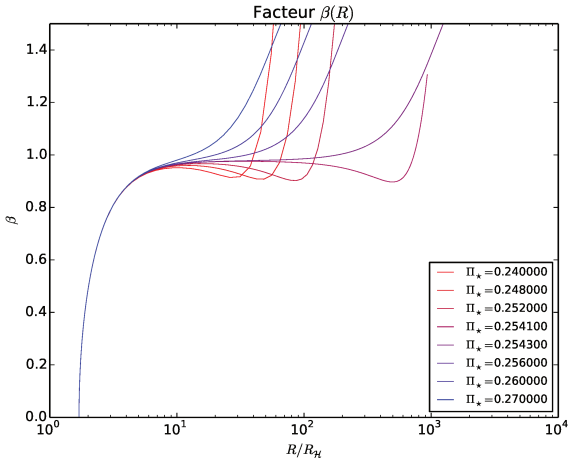

Figure 6.8 – Values of $\beta(R)$ speed on the axis for different value of $\Pi_\star$

In figs.(6.7, 6.8) we observe different asymptotic behaviors. For both families the fieldline reaches some radial regime (we see that for a range of radius around 10 in Fig.(6.7)). Then either it recollimates rather violently or, to the contrary, it opens suddenly, see Fig.(6.9).

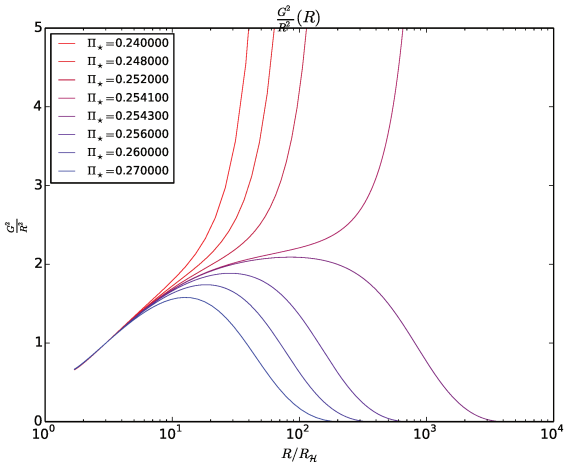

Figure 6.9 – Value of $\frac{G^2}{R^2}(R)$ for different values of $\Pi_\star$

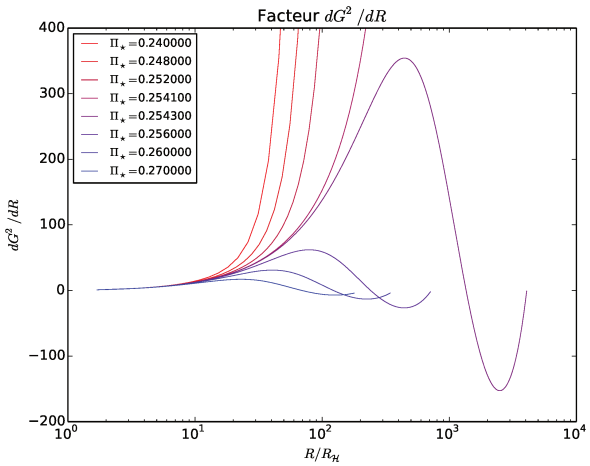

Figure 6.10 – Value of $\frac{dG^2}{dR}(R)$ for different values of $\Pi_\star$

Note that contrary to the cylindrical outflows, for a sufficiently large value of the radius, solutions of both families become unphysical. Nevertheless, the closer the value of $\Pi_\star$ is to the value of $\Pi_{\star,\mathrm{lim}}$, the more physical the solution at large radius remains. Thus, for radial outflow solutions, the choice of $\Pi_\star = \Pi_{\star,\mathrm{lim}}$ is more important because it makes possible to describe solutions with a larger radius. Another point to note is that the limiting value at infinity for Π is zero for the choose of $\Pi_\star = \Pi_{\star,\mathrm{lim}}$

The criteria chosen to numerically distinguish the two kinds of family with a certain error on the value of $\Pi_{\star,\mathrm{lim}}$ relates to the asymptotic behavior of the expansion factor F. Indeed it seems that we have,

$$\Pi_\star \geq \Pi_{\star,\mathrm{lim}} \Longleftrightarrow \quad \begin{cases} \exists \mathrm{R_{lim}},\ \forall \mathrm{R_{max}} \geq \mathrm{R_{lim}} \\ \mathrm{F}(\mathrm{R_{max}}) = \underset{\mathrm{R}\in[1;\mathrm{R_{max}}]}{\mathrm{Max}}\ (\mathrm{F}) \end{cases} \tag{6.11}$$

This test is quite easy to compute numerically. Thus a subroutine was built using this criteria. It starts to check that the limit of integration of the Runge-Kutta 4 is sufficiently large to lead effectively to a good criterion. This condition is a little bit more sensitive than in the case of a cylindrical outflow. So it starts, as before, with a dichotomic process, to approach with a higher precision the value of $\Pi_{\star,\mathrm{lim}}$. In the following, any outgoing conical solution is calculated with the lower approximate value of $\Pi_{\star,\mathrm{lim}}$. So conical outflow solutions are characterized by the seven parameters λ, κ, δ, ν, ℓ, μ and e_1, and the initial value of $\Pi_\star$ taken equals to $\Pi_{\star,\mathrm{lim}}$ estimation.

6.4 Strategies of optimization under constraints

The code is able to calculate outflow and inflow solutions accurately enough depending on the parameters to enter. Then the goal is to choose parameter sets either able to model a source with given observational characteristics (opening angle, temperature, final velocity or Lorentz factor...) or to extract a solution with interesting physical properties (nature of the energy exchange with the black hole...). We expose in the following the processes that we have used in order to effectively explore the parameter space, avoiding the location with non-physical solutions, pathologies or lack of solution for Eq.(5.107). This section will be really useful for obtaining the different kinds of

energy exchange between an inflow solution and the rotational energy of a black hole, See Ch.(8). It is also useful to match inflow and outflow solutions in order to obtain a physically satisfying complete solution from the horizon of the black hole until the infinity, Sec.(8.4).

6.4.1 Search method

Let us consider the case, where we need to obtain a solution with a set of characteristics. Each of these characteristics could be transformed in a real value that we will call in the following the structural value. For example, for outflow solutions it could be the value of final velocity along the axis, the stagnation radius, the opening angle in the case of conical flow, the value of isorotation function, the spin of the hole etc... For inflow solutions we can use the stagnation radius, the isorotation function, the spin of the black hole, the fluid velocity of fluid when it crosses the horizon, the latitude value for the beginning of extraction but also different energy flux, etc...

In the following, we consider that we have $j_{\rm Max}$ ($j_{\rm Max} \leq 7$ for outflows and $j_{\rm Max} \leq 8$ for inflows) structural parameters. We will note them $\left(f_j\right)_{j=1,\dots,j_{\rm Max}}$. For any set of parameters we can obtain the structural parameters of the formula using some arithmetical operations applied to the parameters and the solution functions. Thus all the structural parameters are a function of the parameters of the solution. Thus for inflows we have $f_j = f_j\left(\lambda,\kappa,\delta,\nu,\ell,\mu,e_1,\Pi_\star\right)$. We shall see how to move through the parameter space in order to match the values of these structural parameters.

A solution consists to use a Monte-Carlo program. Nevertheless the automatization of the solution search using a great number of "while" loops, but also the frequency to get unphysical solutions, or no solution makes this kind of program painstaking to use. So we choose to use a more robust approach, which allows to learn about the evolution of structural parameters with solution parameters during the process of searching.

We do the hypothesis that, except in certain areas of the parameter space, the structural parameter functions must be differentiable according to the solution parameters. Thus knowing the order of evolution for these parameters we move step by step in the wanted direction.

In case of discontinuity, we try to quantify them in order to prevent the induced pathology. To give an example, during the calculation of inflow solutions, there is some domain of parameter space for which the solution does not cross the sub-alfvenic point. In this case, the value of p needed to cross the slow-magneto-sonic point implies the lack of reals roots of the polynome of Eq.(6.3). For this kind of solution either we cross the critical Alfvén point and not the slow point, or we cross the critical slow point and not the critical Alfvén point. In all cases, this kind of solution is not physically satisfying in our search. Nevertheless for any solution which does not have this pathology, the value of the determinant of the polynomial Eq.(6.3) depending on $p_{\rm lim}$ gives an indication of how far we are in the parameter space from the discontinuity. The boundary is defined in the solution parameters space by $\mathrm{Det}(p_{\rm lim}) = 0$. So including this determinant in the scalar parameter gives us the possibility to move in the parameter space in order to avoid this discontinuity.

6.4.2 Gradient descent method

If these structural parameters are $\mathscr{C}^1$ function of the solution parameters, it is possible to make an expansion to the first order in the parameter variations. We note $\mathbf{s} = \left(\lambda,\kappa,\delta,\nu,\ell,\mu,e_1,\Pi_\star\right)$ for inflow solution and $\mathbf{s} = \left(\lambda,\kappa,\delta,\nu,\ell,\mu,e_1\right)$ for outflow one the set of parameter. Then we have the usual formula,

$$\forall\, j \in [1, j_{\rm Max}] \quad f_j\left(\mathbf{s}+d\mathbf{s}\right) = f_j\left(\mathbf{s}\right) + \nabla f_j\left(\mathbf{s}\right)\cdot d\mathbf{s} + \mathscr{O}\left(||d\mathbf{s}||^2\right) \tag{6.12}$$

Let us suppose we have a solution such that the values of $f_2...f_{j_{\max}}$ are satisfying and we need to increase the value of f_1. Then it is possible to move in the direction of the projection of $\nabla f_1(\mathbf{s})$ orthogonally to the vectorial sub- parameter space generated by $\mathrm{Span}\left(\nabla f_2,...,\nabla f_{j_{\mathrm{Max}}}\right)$. We note $\mathbf{d}=\mathbf{p}_{j_{\mathrm{Max}}-1}\left(\nabla f_1;\nabla f_2,...,\nabla f_{j_{\mathrm{Max}}}\right)$, where $\mathbf{p}_{j_{\mathrm{Max}}-1}\left(.;\nabla f_2,...,\nabla f_{j_{\mathrm{Max}}}\right)$ the orthogonal projector to $\mathrm{Span}\left(\nabla f_2,...,\nabla f_{j_{\mathrm{Max}}}\right)$. Then choosing $d\mathbf{s}=ds\mathbf{d}$ we have,

$$\begin{aligned} &f_1(\mathbf{s}+d\mathbf{s})=f_1(\mathbf{s})+\nabla f_1(\mathbf{s})\cdot d\mathbf{s}+\mathscr{O}\left(||d\mathbf{s}||^2\right)\\ &\forall j\in[2,j_{\mathrm{Max}}]\;\; f_j(\mathbf{s}+d\mathbf{s})=f_j(\mathbf{s})+\mathscr{O}\left(||d\mathbf{s}||^2\right)\end{aligned} \tag{6.13}$$

Furthermore $\nabla f_1(\mathbf{s})\cdot d\mathbf{s}$ is positive for positive values of ds. Then, for a sufficiently small positive value of ds we obtain $f_1(\mathbf{s}+d\mathbf{s})\geq f_1(\mathbf{s})$. The last difficulty now consists in calculating the orthogonal projection $\mathbf{d}=\mathbf{p}_{j_{\mathrm{Max}}-1}\left(\nabla f_1;\nabla f_2,...,\nabla f_{j_{\mathrm{Max}}}\right)$. To calculate this projector we use a recurrence reasoning, the demonstration by reccurence being presented in Appendix.(E). We obtain,

$$\mathbf{p}_{j-1}\left(\mathbf{u}_1;\mathbf{u}_2,...,\mathbf{u}_j\right)=\mathbf{p}_{j-2}\left(\mathbf{p}_1\left(\mathbf{u}_1;\mathbf{u}_j\right);\mathbf{p}_1\left(\mathbf{u}_2;\mathbf{u}_j\right),...,\mathbf{p}_1\left(\mathbf{u}_{j-1};\mathbf{u}_j\right)\right) \tag{6.14}$$

We have to build a code which calculates the gradient of the structural parameters. Thus the recurrence formula allows us to calculate the direction where to move in order to obtain the wished evolution of these structural parameters. To explain the interest of these calculations we give here an example of a set of outflow solutions, using the tools exposed here. The structural parameters taken into account here are the stagnation radius normalized by the black hole horizon radius $\mathrm{R}_s/\mathrm{R}_{\mathscr{H}}$, the dimensionless black hole spin $a=2l/\mu$, the isorotation frequency per unit of black hole pulsation $\Omega/\omega_{\mathscr{H}}$ and the maximal Lorentz factor of the flow on the axis γ_∞. We use the tools built to calculate solutions with different stagnation radius and with the same spin, the same isorotation frequency and the same maximal Lorentz factor of the flow on the axis. We compute the parameter (up to a precision of 10^{-3}) in the table,

	λ	κ	δ	ν	μ	e_1	$\Pi_{\star,\mathrm{lim}}$	a	$\Omega/\omega_{\mathscr{H}}$	γ_∞	$\mathrm{R}_s/\mathrm{R}_{\mathscr{H}}$
S1	1.171	0.291	1.319	0.600	0.184	-0.063	0.265	0.519	0.502	10.04	1.175
S2	1.170	0.286	1.325	0.613	0.187	-0.049	0.282	0.519	0.502	10.03	1.225
S3	1.169	0.280	1.333	0.627	0.190	-0.037	0.298	0.519	0.502	10.05	1.275
S4	1.169	0.274	1.336	0.641	0.193	-0.027	0.317	0.519	0.502	10.05	1.325
S5	1.170	0.269	1.341	0.655	0.196	-0.016	0.335	0.519	0.502	10.04	1.375
S6	1.173	0.265	1.345	0.668	0.198	-0.004	0.352	0.519	0.502	10.09	1.425
S7	1.177	0.260	1.349	0.681	0.200	0.009	0.370	0.519	0.502	10.05	1.475
S8	1.182	0.257	1.353	0.694	0.202	0.022	0.388	0.519	0.502	10.08	1.525

Table 6.1 – Set of parameters for 8 solutions calculated in order to get different values of stationary radius. We keep constant the final Lorentz factor, isorotation and spin of the black hole.

We remove here the parameter ℓ because it is simply linked to the black hole spin and the value of μ via $a=2\ell/\mu$. We observe here the ability of the model to produce solutions with the same values of spin parameter, isorotation and final velocity. It shows the independence of these structural parameters in the considered area of parameter. Indeed, when a structural parameter is function of others, it means that the generated gradient is not a free vector in the parameter space. In some situations, we observe in part of the parameter space, a gradient "close" to be a linear combination of some other gradients. In this case it is sometimes difficult to move efficiently in the parameter space. Indeed, in this case, using the projection Eq.(6.13), implies to use a direction close to orthogonality with the gradient of the structural parameter we want to evolve keeping the others constant. The table Tab.(6.1) shows the evolution of the parameter $\mathrm{R}_s/\mathrm{R}_{\mathscr{H}}$. Note that the evolution of the parameter is not linear when you move from **S1** up to **S8**. In particular, the parameter λ starts to decrease and then increases. This non linearity reveals

the evolution of the gradient in the parameter space and then a globally linear analysis is not sufficient to describe the evolution of solutions in the parameter space. Thus the displacement in the parameter space from a linear analysis needs to be sufficiently small to give a good evolution behavior.

See on Fig.(6.11), the evolution of the curve of velocity along the axis. We note, for this set of solutions, the evolution of $\beta(R)$ when the stationary radius increases. The "bump" on the speed curve decreases and the initial acceleration also. Indeed as we see in the following chapter Sec.(7.2), the acceleration on the axis being dominated by the pressure force,this force must be stronger to leave the gravitational well as the radius of stationarity approaches the black hole horizon.

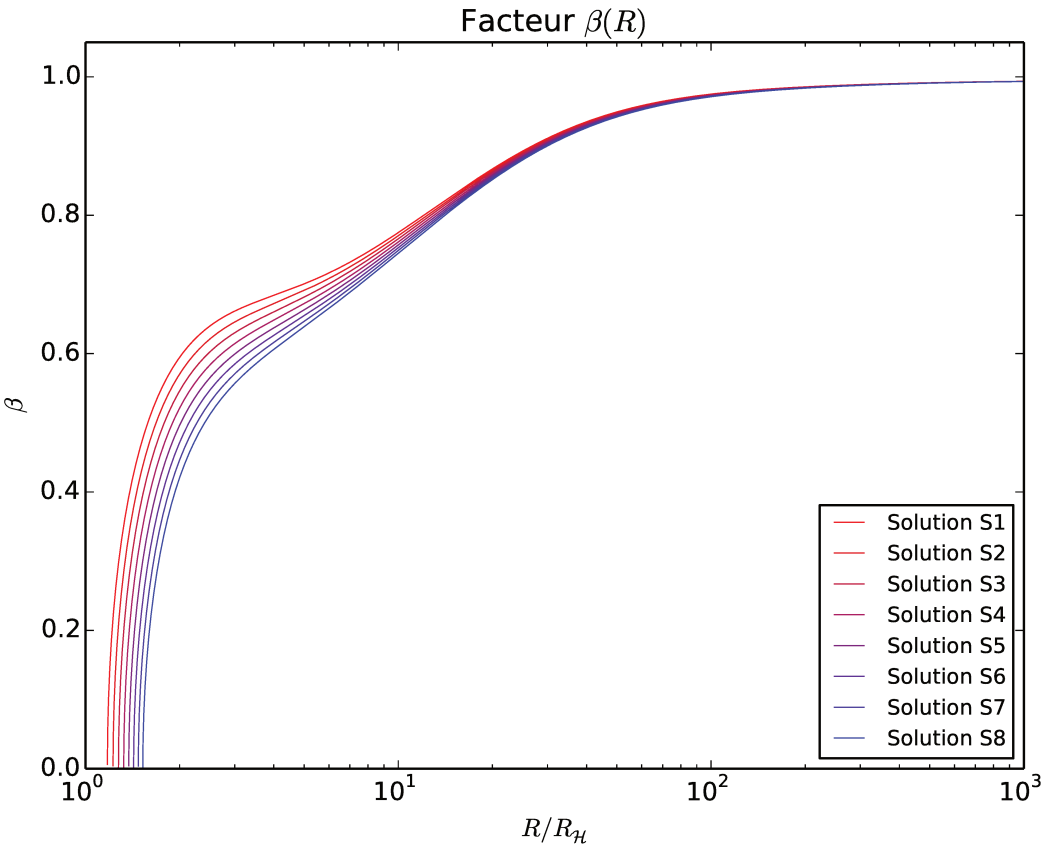

Figure 6.11 – Factor β on the axis for the list of solution S1 to S8

6.5 Conclusion

We saw in this chapter the different tools used to solve numerically and automatically the system of Eqs.(5.107). We find the solution which crosses the different critical points. We also build some sub-routines to seek the adapted value of $\Pi_\star$ for outflow solutions, whatever the asymptotic geometry of them is cylindrical or conical.

Finally we present a subroutine which is useful to explore the parameter space by small steps in order to find solutions with characteristic values of given structural parameters.

All these tools are useful to construct the outflow solutions, Ch.(7), and the inflow solutions, Ch.(8). The Sec.(6.4.2) will be particularly useful in Ch.(8) to find a matching between an outflow

solution and an inflow one.

6.6 References

C. Sauty, E. Trussoni, and K. Tsinganos. Nonradial and nonpolytropic astrophysical outflows. V. Acceleration and collimation of self-similar winds. aap, 389:1068–1085, July 2002. doi: 10.1051/0004-6361:20020684. 105

Chapter 7

Outflow solutions

Contents

7.1 Introduction

This chapter is dedicated to the presentation of outflow solutions. Given the large variety of jets morphologies we want to emphasize the ability of the model to reproduce different kind of outflow. First of all, as in Ch.(5.1), we reproduce here part of Chantry et al. [2018] which presented four outflow solutions. We discuss the effect of deviation to sphericity of Alfvén Mach number m_1 in the acceleration and the collimation of the jet. We present the different solutions, a moderately relativistic collimated solution **K1**, an ultra-relativistic collimated one **K2**, a solution **K3** which may model the M87 source and a conical one **K4**. We also present the effect of the spin of black hole black hole spin l on the solutions. We also show the effect of parameter e_1 on solutions. And finally we present some discussion about matter content and departure from thermodynamical equilibrium.

7.2 Published solutions

Effect of a nonspherical Alfvén number in a Schwarzschild metric

To illustrate our model, we present the following two solutions, which are built in the framework of the Schwarzschild metric. The first one corresponds to a solution of a model presented in Meliani et al. [2006], in which $m_1 = 0$.

The chosen values of the other parameters are $\lambda = 1.0$, $\kappa = 0.2$, $\delta = 1.2$, $\nu = 0.8$, $\ell = 0$, $\mu = 0.1$, $e_1 = 0$. We compare this solution to a solution with the same parameters but by keeping the value of m_1 given by Eq. (5.61), $m_1 = -0.078$. In both solutions, the value of $\Pi_\star$ is the minimum value of the limiting solution. Such solutions have the minimum amplitude of oscillations in the jet.

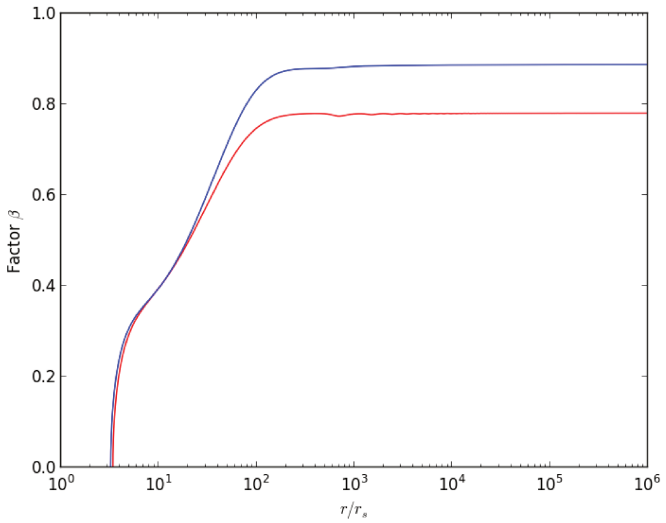

Figure 7.1 – Evolution of the radial velocity along the polar axis for solutions in a Schwarzschild metric, with $m_1 = 0$ (blue) and $m_1 = -0.078$ (red). The second case has a smaller terminal velocity.

In Fig. 7.1 the radial velocity on the polar axis is compared for the two solutions, while field lines in the poloidal plane are plotted in Fig. 7.2. We note that in Eqs. (5.107) and (5.110) and Eqs. (5.107) and (5.109), giving the plasma acceleration and the variation of the expansion factor with the radius R, respectively, there are several terms proportional to the factor $(\kappa - 2m_1)$. As m_1 is always negative, it is evident that $-m_1$ effectively increases the transverse pressure gradient, which is proportional to κ. In other words, the effect of

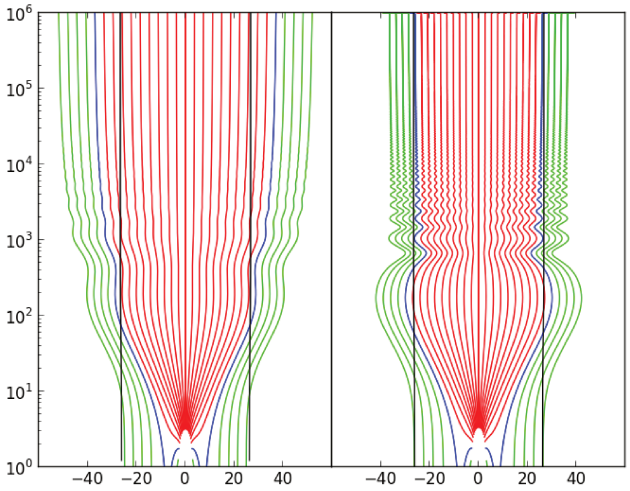

Figure 7.2 – Field lines for a solution in a Schwarzschild metric, with parameters $\lambda = 1.0$, $\kappa = 0.2$, $\delta = 1.2$, $\nu = 0.8$, $\ell = 0$, $\mu = 0.1$, $e_1 = 0$ and $m_1 = 0$ (left) and $m_1 = -0.078$ (right). We note that the case $m_1 = -0.078$ corresponds to a more tightly collimated jet. Lengths are in units of the Schwarzschild radius. The red lines are connected to the magnetosphere of the central object while the green lines are connected to the disk. The separating line is in blue and the light cylinder in black.

$-m_1$ is similar to the effect of κ which enforces collimation for $\kappa > 0$. Hence, taking into account a nonspherical Alfvén number ($m_1 \neq 0$) introduces an extra collimation force which explains why the second solution with a nonzero m_1 is more collimated. Indeed, the width of the jet at infinity over its value at the base, G_∞/G_0, decreases from 13.74 to 9.42, which is similar to an increase of κ and this fact can be checked directly by looking at the poloidal field line's shape shown in Fig. (7.2).

Since more tightly collimated solutions have a smaller super-Alfvénic acceleration, the second solution reaches a lower Lorentz factor asymptotically. Thus, similarly to κ, the introduction of a negative $m_1 \neq 0$ leads to a decrease of the velocity because of the tighter collimation. The higher collimation reduces the pressure gradient along the axis, which in turn decreases the acceleration due to pressure driving on large distances (see Sauty et al. 2004).

Additionally, m_1 appears within the term $(\kappa + 2m_1 - \delta - 2e_1)$ which appears in the plasma acceleration function $\mathcal{N}_{M^2}$ in Eqs. (5.107) and (5.110) and the function $\mathcal{N}_F$ determining the expansion factor F in Eqs. (5.107) and (5.109). The first three terms $(\kappa + 2m_1 - \delta)$ arise from the variation across the field lines of the heat content P/ρ with α, that is, $\partial/\partial\alpha\{[\Pi(R)M^2(R)](1+\kappa\alpha)(1+m_1\alpha)^2/(1+\delta\alpha)\} \simeq [\Pi(R)M^2(R)](\kappa + 2m_1 - \delta)$, while the fourth term e_1 is proportional to the variation of the total energy $\mathscr{E}$ with α. The bigger this term is, the larger the initial acceleration (see Sauty and Tsinganos 1994), because it is linked with the distribution of the heating which opposes gravity to accelerate the outflow. As the weight of the plasma decreases with the latitude, then the pressure gradient increases along the axis resulting in a larger acceleration close to the base, as explained in Tsinganos and Sauty [1992]. This term decreases rapidly as the Alfvén surface is reached. Thus, it is responsible only for the initial acceleration. With the parameter m_1 being negative, the second solution is more accelerated between the base and the Alfvén surface. The velocity of the second solution reaches the velocity of the first one at the Alfvén surface. This effect disappears far from the source.

7.2.1 Solutions in a Kerr metric

In the following, we discuss four different solutions in a Kerr metric to illustrate the present model. A more detailed parametric study is postponed to a following paper. For the purposes of the present paper, we show three cylindrically collimated solutions with high asymptotic Lorentz factor, typical of AGNs and GRBs. Those solutions cross the "light cylinder" and are sorted with increasing magnetic collimation efficiency parameter ϵ. We also exhibit a conical solution crossing the "light cylinder" with high Lorentz factor and strongly negative ϵ, something that was not possible with the previous relativistic meridionally self-similar solutions.

In order to get a Lorentz factor as high as possible in the asymptotic part of the collimated part of the jet, we know from the study of the classical solutions that among all cylindrical solutions, the limiting solutions with the lowest value of $\Pi_\star$ reach the highest terminal velocity. These solutions are the so called limiting solutions in Sauty et al. [2002]. As Π_∞ is negative for the limiting solutions, we have to add a positive P_0 value to the pressure. Of course, it is always possible for those cylindrical solutions to have a higher pressure P_0, but by doing so it also increases the effective temperature, in particular in the asymptotic part. For the same set of parameters, it is also possible to get cylindrical solutions by increasing $\Pi_\star$. However, such solutions usually have a strong initial decollimation associated with a peak in both the Lorentz factor and temperature, while the asymptotic jet is decelerated to lower Lorentz factors and smaller radii, a result that we used to interpret the FRI/FRII dichotomy [cf. Meliani et al. [2010]].

	λ	κ	δ	ν	μ	l
K1	1.0	0.2	2.3	0.9	0.1	0.05
K2	1.0	0.2	1.35	0.46223	0.1	0.05
K3	1.2	0.005	2.3	0.42	0.08	0.024
K4	0.0143	1.451	3.14	0.8	0.41	0.15

Table 7.1 – Set of parameters used for the four selected solutions in the Kerr metric. **K1** is the solution displayed in Figs. 7.3, 7.4, and 7.5 (blue line). Solution **K2** is displayed in Figs. 7.5 (red line) and 7.6, while solution **K3** is displayed in Figs. 7.11 and 7.12. Finally, solution **K4** is shown in Figs. 7.13 and 7.14.

	ϵ	m_1	$\Pi_{\star,lim}$	r_0/r_s
K1	-1.76	-0.062	0.826	5.72
K2	-0.04	-0.234	0.216	1.57
K3	0.55	-0.326	0.189	2.55
K4	-5.84	-0.004	0.255	1.39

Table 7.2 – Output parameters for the four solutions in the Kerr metric. Those parameters result from the integration of the equations.

Solutions **K1** and **K2** have been obtained for maximally rotating black holes, that is, a_H close to 1 ($a \simeq r_s/2$). In solution **K4** the value of a_H has been fixed to 0.73 ($a = 0.73 r_s/2$). We do not expect all black holes to be maximally rotating. For example, in M87, the dimensionless spin should be above 0.65 (i.e., $a > 0.65 r_s/2$), (Li et al. 2009) but not too close to one. Other examples can be found and for **K3** we will use the value $a_\mathrm{H} = 0.6$ ($a = 0.6 r_s/2$) adopted in Mertens et al. [2016] for M87.

A mildly relativistic collimated solution with oscillations (K1)

The collimated solution **K1** corresponds to an over-pressured outflow ($\kappa \geq 0$) in a Kerr metric. As $\epsilon \leq 0$, the collimation of the jet is not fully magnetic but it has a significant contribution by the gas pressure, at least during the phase of strong acceleration up to $\simeq 30 r_s$. In this solution, field lines are strongly oscillating compared to the two previous solutions in the Schwarzschild metric. The outflow undergoes series of strong oscillations connected to the balance between the toroidal magnetic tension and the decollimation forces (centrifugal and electric forces and transverse pressure gradient) of the plasma.

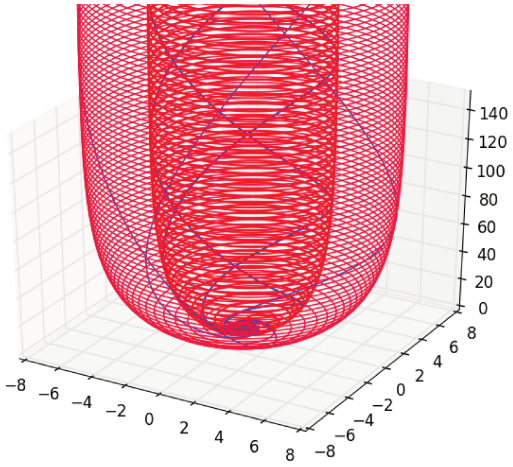

Figure 7.3 – Three-dimensional (3D) representation of the field lines and streamlines for the thermally collimated solution **K1** at the base of the jet and for two flux tubes. The blue lines correspond to streamlines, the red lines to magnetic field lines. The length is in units of the Alfvén radius, that is, ten times the Schwarzschild radius.

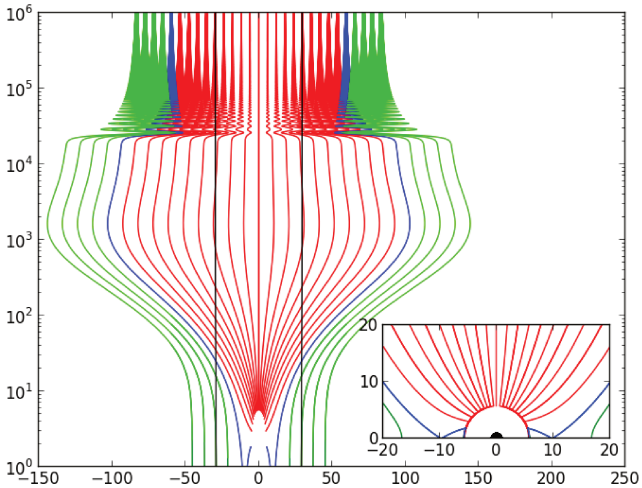

Figure 7.4 – Poloidal field lines and "light cylinder" for the thermally collimated solution **K1**, for $\lambda = 1.0$, $\kappa = 0.2$, $\delta = 2.3$, $\nu = 0.9$, $\mu = 0.1$, $\ell = 0.05$, $e_1 = 0$. The length unit is the Schwarzschild radius.

The significant contribution of the transverse pressure gradient also explains these strong oscillations in the flow, as is also shown in the classical solutions. The parameters of this solution are displayed in the first row **K1** of Table 1 and the output values of m_1 and ϵ in Table 2. We note that $m_1 = -0.062$ is a relatively small value, which clearly indicates that the Alfvén surface is almost spherically symmetric in this case. As a consequence, the light cylinder is relatively far from the jet axis. Most of the central field lines (see the inner 5 to 7 central red lines in Fig. 7.4) remain within the "light cylinder", which means that despite the important role of the magnetic field in the collimation, the jet is pressure or enthalpy driven in the relativistic case. However, unlike in the classical solutions, the electric field is the dominant decollimating force for the lines that cross the "light cylinder". This decollimation and expansion after the Alfvén surface is associated with a strong pressure gradient yielding a strong acceleration of the jet in the super-Alfvénic regime. More details on this will be given in the following solution. The pressure gradient is the gas pressure gradient close to the axis but assisted by the toroidal magnetic pressure outside the "light cylinder". This is similar to superfast flows in radially self-similar models for disk winds (see Vlahakis and Königl 2003a and Vlahakis and Königl 2003b). Moreover, in the relativistic regime the inertia increases faster when the flow is accelerated such that the collimation from the magnetic field is delayed to larger distances.

In Fig. 7.4 we see that the expansion after the Alfvén surface is strong and leads to a late acceleration of the flow. After the large expansion, the jet recollimates smoothly and consequently decelerates slightly because of the compression.

In Fig. 7.3, we clearly see that there is a strong azimuthal magnetic field, although the scale of the Figure tends to exaggerate this phenomenon.

The Lorentz factor γ of this solution reaches a relatively small value around 3.7, typical of less powerful AGN jets like some of the FRI radio-galaxies.

A highly relativistic collimated solution with oscillations (K2)

The solution **K2** is collimated and has an extremely high Lorentz factor, which may be typical of GRBs. This **K2** model corresponds to the values of the parameters given in the second line of Table 1, that is, $\lambda = 1.0$, $\kappa = 0.2$, $\delta = 1.35$, $\nu = 0.46223$, $\ell = 0.5$, $\mu = 0.1$, $e_1 = 0$ and the second line of Table 2 for the output parameters, $m_1 = -0.234$ and $\boldsymbol{\epsilon} = -0.04$.

For this model, the outflow starts very close to the black hole horizon at $r_0 = 1.57\, r_s$, (see Fig. 7.6), and thus at the base of the jet the effects of general relativity play an important role. The final velocity is highly relativistic, as is shown in Fig. 7.5.

The parameter ν of the **K2** solution is accurately adjusted (to the fifth digit), so as to obtain a rather high Lorentz factor (larger than 100). This proves the versatility of the model which handles any magnitude of Lorentz factors. In order to obtain such high Lorentz factors, we must carefully tune the parameter directly linked to gravitation, ν, as mentioned above. The same parameter is also responsible for the thermal acceleration in the classical model (Sauty and Tsinganos 1994).

In Figs. 7.7 and 7.8 we plot the forces along and perpendicular to a field line defined by $\alpha = 0.01\alpha_{\rm lim}$ where $\alpha_{\rm lim}$ is the dimensionless magnetic flux between the inner jet and an external accretion disk wind.

The strong decollimation associated with the slow acceleration enhances the electric force as in the previous solution **K1**. This can be seen in Fig. 7.8. However due to the higher rotation here, more field lines cross the light cylinder, which is very close to the axis, such that the decollimation from the electric field is much stronger in this solution.

The feedback of this strong electric field is to further increase the decollimation beyond the Alfvén surface at large distances. Again, the large expansion increases the pressure and enthalpy gradient as seen in Fig. 7.7. Thus, the pressure force increases, resulting in a very

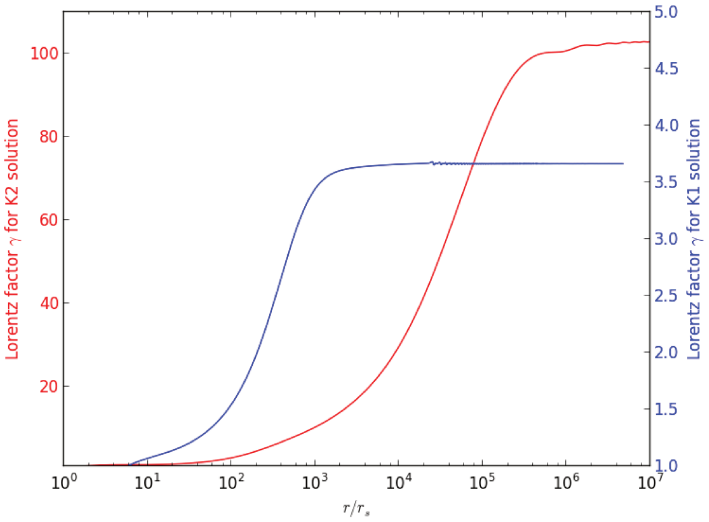

Figure 7.5 – Lorentz factor γ for the **K1** (blue line) and **K2** (red line) solutions. Distances are given in Schwarzschild radius units.

long acceleration phase up to $10^6 r_s$. Thus, the thermal acceleration becomes very efficient and the plasma asymptotically reaches an extremely high Lorentz factor. Indeed, the jet radius increase of this solution is also very high with an expansion factor $G_\infty/G_0 \simeq 1300$, as can be seen in Fig. 7.6.

The value of ϵ is still negative but very close to zero ($\epsilon = -0.04$). As in the classical case, this means the magnetic efficiency to collimate the flow is higher in this model at larges distances. However the decollimating force that ensures the equilibrium is no longer the centrifugal force or the pressure gradient but the electric force on the lines that cross the "light cylinder". This is a specific feature of relativistic jets.

To further analyze the jet acceleration we may calculate the contribution of the different components of the total energy and the conversion of the magnitude of each component to another form along the streamlines. First, we want to obtain a physically acceptable heating term which goes to zero at infinity along the axis of the flow. By defining the enthalpy in Eqs. (5.18) and (5.19) and its analytical expression in our model in Eq. (5.34), we may fix a streamline limiting the zone where the pressure is positive. Once this field line has been chosen, for example, at $\alpha = 0.4\alpha_{\rm lim}$, the dimensionless pressure $P_0/\rho_\star c^2$ can be calculated. In the particular case presented here, we have taken $P_0/\rho_\star c^2 = 4.3 \cdot 10^{-7}$. The pressure P_0 in Eq. (5.54) is chosen such that the gas pressure is equal to zero, when $\Pi(R)$ reaches its minimum value. For some value of α, the term $P_0 = P_0(\alpha) = -[B_\star^2/8\pi]\Pi_{\rm min}(1+\kappa\alpha)$ will be too large to ensure that Q goes to zero at infinity along the axis. Indeed, α can take any value below a maximum $\alpha_{\rm max}$.We can consider that the solution can be valid only in the region wherein the pressure is positive. When α is fixed and $P_0/\rho_\star c^2$ is deduced, we are able to calculate $\xi_\star$. In this particular case, a value $\xi_\star \simeq 78$ is chosen.

Figure 7.9 shows the normalized total energy on the axis $\mathscr{E}/c^2 = h\gamma\xi$, the kinetic component $h\gamma\xi_K$ and the external heating $h\gamma Q/c^2$. We find a decrease of the external heating and a related increase of the kinetic part. Thus, the kinetic enthalpy represents the major component up to $r = 10^2 r_s$.

Figure 7.10 shows the same energetic distribution, but on a streamline with $\alpha = 0.05\alpha_{\rm lim}$. Out of the polar axis, there are extra energetic components, such as the frame-dragging and the Poynting fluxes. Both these energetic contributions are very small on this field line, as compared to the total energy. Hence, the jet is enthalpy-driven from the axis right up to

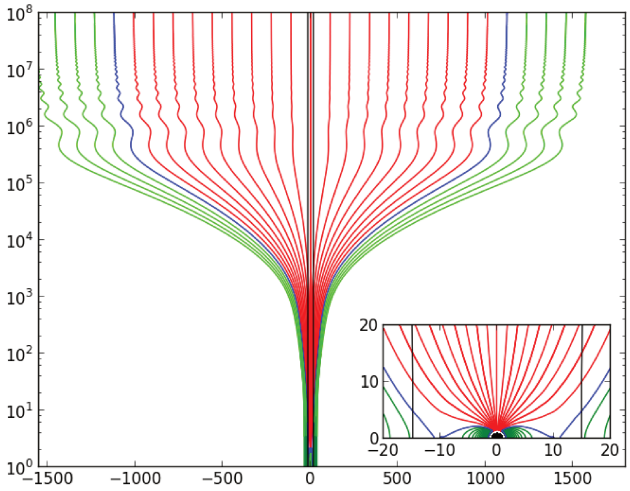

Figure 7.6 – Poloidal field lines and "light cylinder" for the **K2** solution, that is, for $\lambda = 1.0, \kappa = 0.2, \delta = 1.35, \nu = 0.46223, \mu = 0.1, \ell = 0.05, e_1 = 0$. Distances are given in Schwarzschild radius units.

the limiting line. We also note that at the base of the jet, the frame-dragging energy is of the same order as the Poynting flux. Contrary to the energetic distribution along the axis, the external heating constitutes the larger part of energy at infinity. While along the axis a high value of $\gamma_\infty \simeq 100$ is obtained, the Lorentz factor at infinity on this particular line is $\gamma_\infty \simeq 3.6$. Hence, since the acceleration of the plasma and the resulting final flow speed at infinity on this particular field line are small, the external heating is not consumed when accelerating the flow and therefore it is left unused at infinity, contrary to what happens along the axis; Fig. 7.9.

A mildly relativistic collimated solution without oscillations (K3)

From VLBI imaging, Mertens et al. [2016] recovered a detailed two-dimensional velocity field in the jet of M87 at sub-parsec scales. They confirmed the stratification of the flow from the very beginning of the jet and identified a relativistic sheath,that is, an accelerating layer, which is launched from the inner part of the accretion disk at a cylindrical distance of around 5 r_s. Mertens et al. [2016] interpret this outer sheath layer as the internal part of an external disk wind. They also interpret the inner spine jet as a component coming from the internal accretion disk. However, it is not clear that the inner spine necessarily has to be one of the disk wind components. Instead we propose that the inner spine jet originates from the black hole corona and has a higher Lorentz factor. The authors note that this fast inner spine jet cannot be detected in their data because of its lower emissivity compared to that of the sheath layer or because its speed is too high.

We propose here, as an alternative scenario, that the spine beam may originate from the magnetosphere of the black hole, either connected to the black hole itself, as in the Blandford-Znajek-Penrose mechanism, or connected to the inner part of the accretion disk. In the first case, the spine jet would be a leptonic plasma, and in the second it would be a hadronic one. In such a case, we can model the spine jet with our meridionally self-similar solutions. We note that unlike Poynting-flux-dominated models, our model is valid on the jet axis.

The Lorentz factor profile inferred by Mertens et al. [2016] (see their Fig. 19) supposes that the velocity structure observed in the 43 GHz VLBA maps at a deprojected distance of $z \simeq 10 mas \simeq 1300 r_s$ is due to the sheath layer. The Lorentz factor of the sheath has a

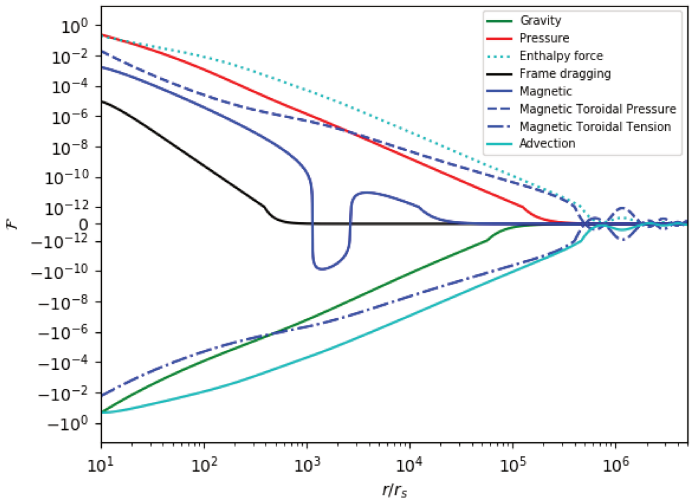

Figure 7.7 – Plot of the longitudinal forces, that is, along the field line, for the **K2** solution, along the line $\alpha = 0.01\alpha_{\rm lim}$. Distances are given in Schwarzschild radius units.

value $\gamma \simeq 2.4$ at $R \simeq 1000 r_s$.

From the curve deduced for the spine jet with an approximated MHD disk wind solution, those authors, following Anderson et al. [2003], model the acceleration and collimation of the flow with a Lorentz factor $\gamma \approx 7$. We propose that it is possible to construct a MHD solution along the lines of the model analysed in this paper, by choosing a positive value of $\epsilon \approx 0.5$ and a similar velocity profile. The solution **K3** presented here has a Lorentz factor $\gamma \simeq 5$ at $R \simeq 1000 r_s$. By appropriately tuning the parameters, we could obtain even higher Lorentz factors from 7 to 10, as is observed at the distance of the knot HST-1, where this velocity is observed in the optical band. However, the spine jet is deboosted relative to the sheath and a precise measurement of its Lorentz factor is difficult.

Solution **K3** with a maximum Lorentz factor on the axis $\gamma \simeq 5.5$ has an asymptotic spine jet radius $G_\infty \simeq 20 r_s$. At this distance from the axis, the Lorentz factor has dropped to a value $\gamma \simeq 2.4$ consistent with the radius and the Lorentz factor at the inner observed distance of the outer sheath jet of Mertens et al. [2016]. Thus, our solution may model the initial spine jet inside the sheath layer. However, to confirm that, we need to use this initial solution in simulations similar to those in Hervet et al. [2017]. The spine jet/sheath jet interaction will probably produce shocks and rarefaction waves that may further accelerate the jet.

Therefore, although we can obtain such a type of collimated solution for different sets of the parameters, we focus here on the specific solution **K3**, where $\lambda = 1.2$, $\kappa = 0.005$, $\delta = 2.3$, $\nu = 0.409$, $\ell = 0.024$ and $\mu = 0.08$. Compared to the other Kerr solutions studied in this paper, λ is higher and κ is very small, leading to a solution with a positive value of the magnetic collimation efficiency, $\epsilon = 0.55$. Another advantage of this solution is the fact that the pressure depends only very weakly on the magnetic flux function, that is, on a particular field line.

Interestingly, in Mertens et al. [2016], the radius of the base of this spine jet is equal to $r_0 = 2.4 r_s$, which is consistent with their model of a disk wind solution, by fixing the jet shape and solving the Bernoulli equation. In our self-similar solution, we have a similar radius for the magnetospheric polar cup, where our jet solution starts. Clearly, this is an alternative scenario.

Moreover, the angular velocity of the field lines anchored in this polar cup above the

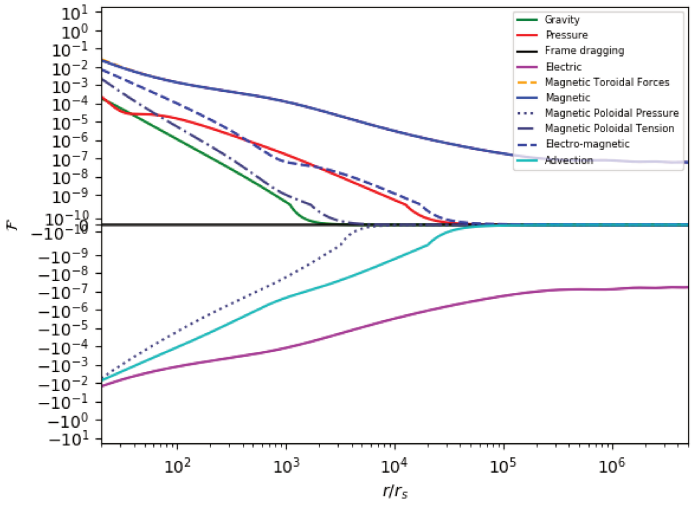

Figure 7.8 – Plot of the transverse forces, that is, perpendicular to the field line, for the **K2** solution, along the line $\alpha = 0.01\alpha_{\rm lim}$. We see that the Lorentz force is collimating and is balanced by the electric force that decollimates. Distances are given in Schwarzschild radius units.

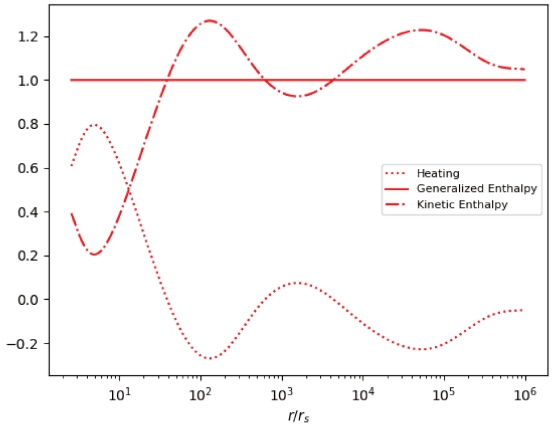

Figure 7.9 – Relative normalized contribution to the total energy of the kinetic enthalpy $h\gamma\xi_k$ and the external heating distribution $h\gamma Q/c^2$ along the axis.

black hole can be calculated from our parameters,

$$\Omega_\star = \frac{c\mu}{r_s}\left[\frac{\sqrt{\mu}\lambda}{\nu}\sqrt{1-\frac{\mu}{(1+l^2)}}+\frac{l\mu}{(1+l^2)^2}\right] \simeq 6.2\times10^{-2}\frac{c}{r_s}. \tag{7.1}$$

By taking the value of the M87 distance and the black hole mass, as in Mertens et al. [2016], we can calculate $\Omega_\star$ in the context of this **K3** solution. This value may directly be compared to the values they deduced in two jet regions from the conservation of total energy and angular momentum fluxes in the approximation of special relativity.

Hence, we find $\Omega_\star \simeq 1.03\times10^{-6}s^{-1}$, a value which is for the spine jet almost the same value as the isorotation frequency of a Keplerian speed at the launching location of the sheath layer. It also corresponds to the initial toroidal velocity of the Blandford and Payne [1982] mechanism.

Our model corresponds to an alternative configuration, because the spine jet may either originate from the Keplerian disk, in which case it would be hadronic, or form via the

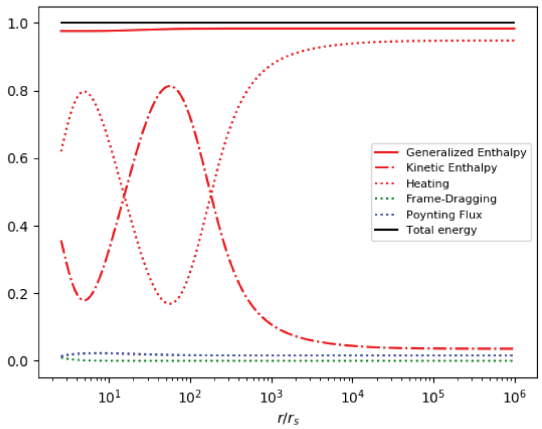

Figure 7.10 – Relative normalized contribution to the total energy of the kinetic enthalpy $h\gamma\xi_k$ and the external heating distribution $h\gamma Q/c^2$ along the streamline $\alpha = 0.05\alpha_{\rm lim}$

generalized Penrose-Blandford-Znajek mechanism. In this second alternative, the jet would be a leptonic beam with an angular frequency proportional to the spin of the central black hole. The Blandford-Znajek mechanism allows us to extract energy from the black hole when $0 \leq \Omega \leq \omega_{\rm BH}$, with a maximum value for $0.5\omega_{\rm BH}$. We note that $\omega_{\rm BH}$ is, by definition, the angular velocity of ZAMO at the location of the outer event horizon and is given by,

$$\omega_{\rm BH} = \frac{a_{\rm H} c}{r_s\left(1+\sqrt{1-a_{\rm H}^2}\right)}, \tag{7.2}$$

where $a_{\rm H}$ is the dimensionless spin of the black hole in units of the gravitational radius $r_s/2$. Indeed simulations of such Poynting-dominated and force-free jets (Tchekhovskoy 2015) have shown that the angular speed of a field line anchored in the magnetosphere is about half the black hole angular speed $\omega_{\rm BH}$. Our value of $\Omega_\star$ is one third of $0.5\omega_{\rm BH}$ (Nathanail and Contopoulos 2014). In order to determine if the spine jet of our solutions originates from a Keplerian disk or from a black hole via a generalized Penrose-Blandford-Znajek mechanism, we need to solve the MHD equations up stream up to the black hole horizon. Moreover, in order to model the full jet of M87, a complete MHD simulation including a disk wind and a spine jet must be developed. Something that should be done in the future.

We note that as is already known, at the interface of the spine jet and the sheath layer, a re-collimation shock may occur, producing compression and rarefaction waves which may accelerate the flow (Hervet et al. 2017). For those reasons we have chosen here to adjust the value of ν to $\nu = 0.42$, in order to get the solution **K3**, with a lower Lorentz factor but suppressing completely the oscillations of the field lines. The value calculated above for $\Omega_\star$ is not changed, but radio emission maps, which are obtained for the M87 jet, will be produced by re-collimation shocks due to the interaction between the fast spine jet and the sheath layer.

As can be seen in Fig. 7.11 for the **K3** model, the Lorentz factor reaches a nearly constant value at the distance of the B structure observed in the 43 GHz VLBA maps and γ is larger than that deduced for the sheath layer by Mertens et al. [2016]. As explained above, the interaction between the sheath layer and the spine jet can induce a bulk flow acceleration. However, as we mention, the Lorentz factor γ is maximum along the axis and decreases with latitude such that at its outer boundary it matches the sheath layer value.

The values of the parameters of the **K3** model are given in the third line of Tables 1 and

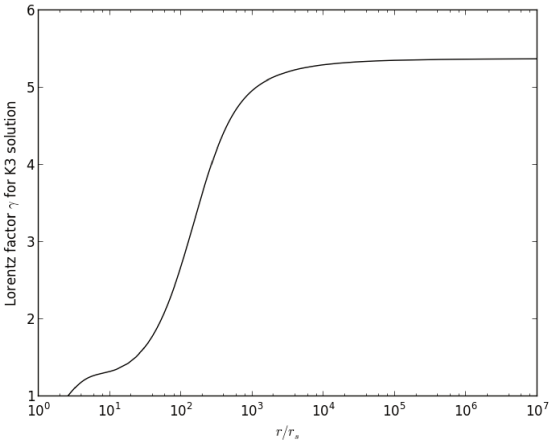

Figure 7.11 – Lorentz factor for the nonoscillating collimated solution **K3**.

2. The radius at the base of this spine jet is equal to $r_0 = 2.55 r_s$ and the magnetic efficiency to collimate the flow is larger compared to the other two Kerr solutions discussed in this paper, as ϵ is now positive, which means that the jet is fully magnetically collimated. The field lines displayed for **K3** in Fig. 7.12 are nearly cylindrical above the equatorial plane, at distances $10^4\ r_s$, with a smooth flaring occurring after the Alfvén surface.

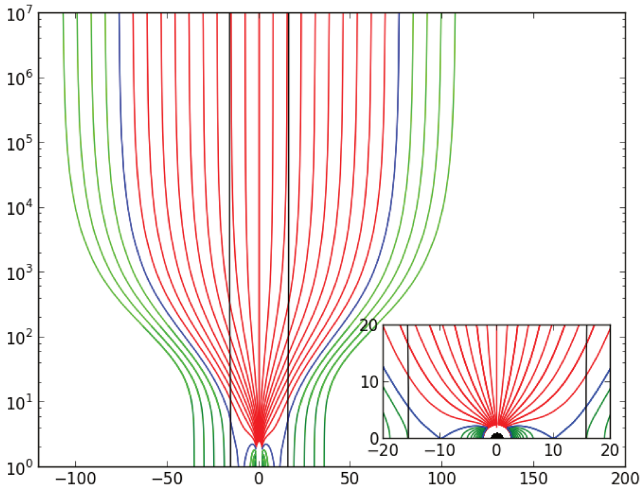

Figure 7.12 – Poloidal field lines and "light cylinder" for the nonoscillating collimated solution **K3**, that is, for $\lambda = 1.2$, $\kappa = 0.005$, $\delta = 2.3$, $\nu = 0.42$, $\mu = 0.08$, $\ell = 0.024$, $e_1 = 0$. Distances are given in Schwarzschild radius units.

Conical solution

The parameters of the conical solution **K4** are given in Tables 1 and 2. Such radial solutions could be useful to describe relativistic noncollimated outflows, such as those seen in association with radio-quiet galaxies, such as Seyfert galaxies. Conical solutions could also be useful to model GRBs, wherein an unstable noncollimated relativistic wind may fragment into small pieces under some instabilities. In such cases, the apparent collimation of the GRB would be due to fragmentation – see Meliani and Keppens [2010]; van Eerten et al.

[2011].

A conical solution is a solution in which the limiting value of F at infinity is 0. In this solution, the spherical part of the Mach number diverges, $\mathrm{M} \to \infty$. The same effect occurs for the cylindrical radius of the flow, G. To obtain this conical solution, we started with the parameters used for modeling the solar wind, as in Sauty et al. [2005]. The magnetic collimation parameter must be strongly negative, $\epsilon/(2\lambda^2) \leq 0$. We adjust the solution to the relativistic case and increase the velocity by taking a larger value for δ. For the radial solution **K4**, the parameters λ and κ are adjusted as well in order to obtain a terminal Lorentz factor larger than 8. Thus, we find a conical solution **K4** for the following set of parameters: $\lambda = 0.0143$, $\kappa = 1.451$, $\delta = 3.14$, $\nu = 0.8$, $\ell = 0.15$, $\mu = 0.41$, $m_1 = -0.004$ and $e_1 = 0$.

For this set of parameters we get a much more negative value for the magnetic collimation efficiency parameter, $\epsilon = -5.68$. The solution quickly reaches the conical regime (see Fig. 7.13), and most of the field lines cross the "light cylinder" plotted as a black solid line. The axial radial velocity profile is plotted in Fig. 7.14. As can be seen, high Lorentz factors are obtained.

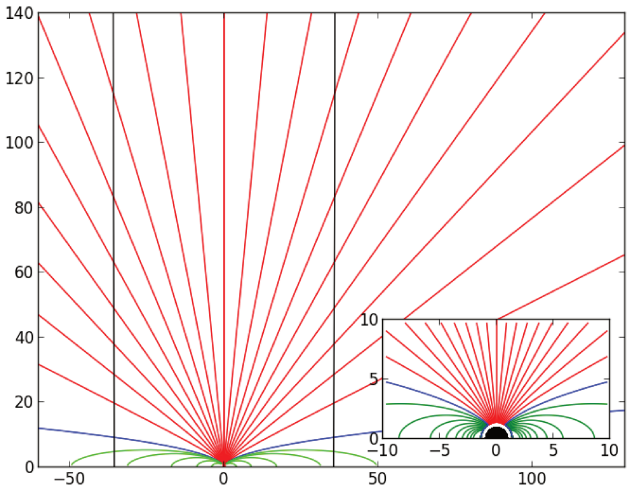

Figure 7.13 – Poloidal field lines and "light cylinder" for the conical solution **K4**, that is, for $\lambda = 0.0143$, $\kappa = 1.451$, $\delta = 3.14$, $\nu = 0.8$, $\mu = 0.41$, $\ell = 0.15$, $e_1 = 0$. Distances are given in Schwarzschild radius units.

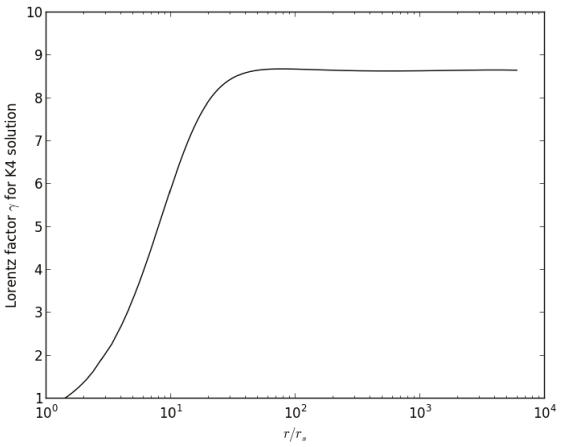

Figure 7.14 – Lorentz factor for the conical solution **K4**. Distances are given in Schwarzschild radius units.

Magnetic collimation efficiency versus black hole spin

As already mentioned, the constant ϵ is a measure of the efficiency of the magnetorotational forces to collimate the flow. We have studied how ϵ relates to the black hole spin $a_{\rm H} = 2l / \mu$, keeping unchanged all the other parameters: $\lambda, \kappa, \delta, \nu,$ and μ.

In Fig. 7.15, we plot ϵ versus the black hole spin $a_{\rm H}$, for several cases studied in the context of our model. First we note that for solutions with parameters similar to the **K3** solution, referred to here as **K3**-type solutions, the value of ϵ is positive, it increases with the black hole spin $a_{\rm H}$ and shows the largest variation in relative magnitude with an absolute total variation equal to 0.05. On the other hand, for **K1**-type and **K4**-type solutions, the values of epsilon are negative. The total variation for **K1**-type solutions is equal to 0.10 and for the **K4**-type solutions is equal to 0.25. We see that ϵ is increasing with the black hole spin $a_{\rm H}$ for **K1**-type and **K3**-type solutions. It also presents a minimum value for **K4** at a black hole spin slightly smaller than $a_{\rm H} = 0$. This means that the magnetic collimation efficiency is lower for counter-rotating black holes in relation to their accretion disk for **K1**-type and **K3**-type solutions and depends weakly on the spin directionfor **K4**-type ones. However, **K4**-type solutions are conical, contrary to all other solutions, which are cylindrically collimated. In all cases ϵ does not vary linearly with the black hole spin $a_{\rm H}$.

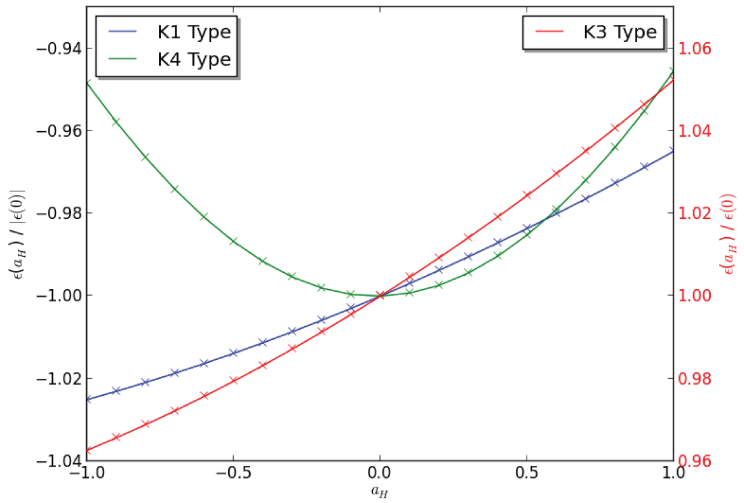

Figure 7.15 – Variation of the magnetic collimation efficiency parameter ϵ vs. the black hole spin parameter $a_{\rm H}$ for **K1**-type, **K3**-type, and **K4**-type solutions. The value of ϵ has been normalized by $|\epsilon(0)|$ when it is negative and by $\epsilon(0)$ when it is positive.

This nonlinear variation of epsilon with the black hole spin $a_{\rm H}$ is explained if we try to derive it at the base of the jet where the Alfvénic number is equal to 0, since some terms of the second order in l cannot be neglected in the following equation.

$$\epsilon = \frac{2\lambda^2}{h_z^2}\left(\frac{\Lambda^2 \mathrm{N_B}}{\mathrm{D}} + \frac{\overline{\omega}_z}{\lambda}\right) + \lambda^2\left(\frac{\Lambda \mathrm{N_V}}{h_* \mathrm{G_0 D}}\right)^2 - \frac{\nu^2(2e_1 - 2m_1 + \delta - \kappa)\mathrm{R_0}}{h_z^2(\mathrm{R_0}^2 + l^2)} - \frac{\nu^2 l^2 \mathrm{R_0 G_0}^2}{h_z^2(\mathrm{R_0}^2 + l^2)^3}. \tag{7.3}$$

An increase in ϵ coincides with a decrease in the maximal Lorentz factor for the collimating Kerr solutions, as we will see for **K1**-type and **K3**-type solutions. This explains

why it was not possible to obtain physical solutions by decreasing l for **K2**-type solutions. For this second Kerr solution, we performed a fine tuning of the parameters to obtain the largest possible Lorentz factor at large distances from the maximally rotating black hole. Then, decreasing l leads automatically to exceed the value of the speed of light, c, for the polar velocity at some distance in the jet. The acceleration phase does not vary for **K1**-type and **K3**-type solutions with l except immediately before $\mathrm{R} = 500$ where the Lorentz factor reaches a plateau. The value of the maximum γ increases when l decreases.

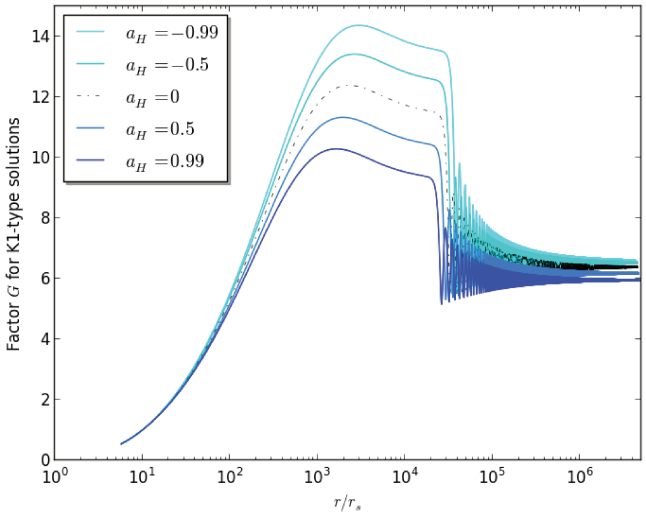

Figure 7.16 – Plot of the cylindrical jet radius normalized to its value at the Alfvén surface, G, for **K1**-type solutions, as a function of the distance along the polar axis, for five different values of the black hole spin a_{H}. The function G is equal to 1 at the Alfvén distance $r = 10 r_s$.

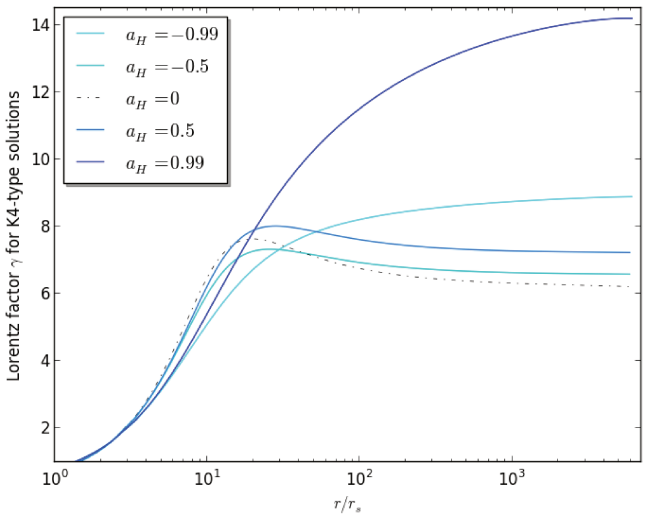

Figure 7.17 – Plot of the Lorentz factor γ for **K4**-type solutions when the black hole spin parameter a_{H} varies between -0.99 and 0.99.

For the two collimated solutions **K1** and **K3**, there is a clear effect of collimation induced by the rotation of the black hole. In Fig. 7.16 we plot for five values of the black hole spin the evolution of the factor G along the jet, that is, i.e., the ratio of the jet cylindrical radius divided by its value at the Alfvén surface. From this plot it can be seen that the maximum

of the radius of the jet is reached at different distances, as the spin varies, and decreases when $a_{\rm H}$ increases. The same trend is observed for the terminal jet radius but the ratio of G_∞/G_0 decreases only by a factor of 0.96 between a nonrotating and a maximally rotating black hole ($a_{\rm H}=0.99$). Hence, the faster the black hole rotates, the smaller the maximal jet radius. This result is expected because for a fast black hole rotation, the magnetic collimation efficiency parameter (ϵ) is higher.

The case of **K3**-type solutions is simple, as the factor G increases with distance until it reaches a constant value. The ratio G_∞/G_0 gives directly the expansion factor which is decreasing when $a_{\rm H}$ increases from -0.99 up to 0.99.

As can be seen from Fig. 7.17, the Lorentz factor maximum follows the opposite trend to ϵ for the conical **K4**-type solutions: the minimum value of ϵ is obtained for $a_{\rm H}\simeq 0$ and for a nonrotating black hole the Lorentz factor curve reaches a maximum before decreasing up to a plateau at large distances. This type of curve is no longer observed when the absolute value of $a_{\rm H}$ goes above some threshold. The increase of the plateau value for the Lorentz factor is much more pronounced for $a_{\rm H}>0$ but can be seen also for negative values of the spin. At a distance of $r=1000r_s$ γ increases from a value of the order of 6 for $a_{\rm H}=0$ up to 14 for $a_{\rm H}=0.99$.

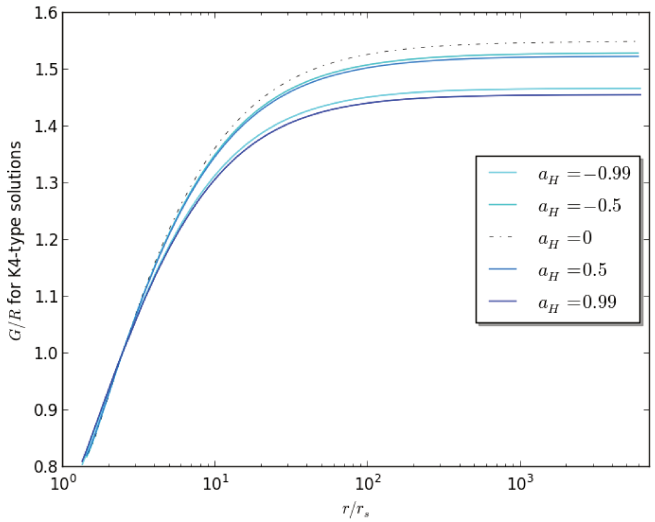

Figure 7.18 – Plot of the ratio of the cylindrical radius to the spherical radius for the conical **K4**-type solutions with a spin parameter $a_{\rm H}$ varying between -0.99 and 0.99 vs. the distance z above the equatorial plane in units of the Schwarzschild radius.

For the conical solutions wherein the asymptotic geometry is fixed, their geometry is less affected. The effect of varying ϵ is different in this case, as compared to this effect for the cylindrically collimated solutions. To analyze the effect of collimation induced by the black hole spin, we plot the ratio of the cylindrical to spherical radius of the field lines for **K4**-type solutions and five different values of the black hole spin. We note that the ratio of the cylindrical to spherical radius of the field lines gives their opening angle with respect to the axis. The field lines start at the base of the jet with an opening angle which increases with the radial distance and expands away from the polar axis more rapidly for higher black hole rotation.The effect is more pronounced for negative spin parameters. At some distances above the equatorial plane ($z\simeq 100r_s$) the opening angle becomes constant as the field lines are finally becoming radial. It is found that for a given ratio of $\alpha/\alpha_{\rm lim}$, where $\alpha_{\rm lim}$ is the last open field line, the asymptotic opening angle is constant for all **K4**-type solutions, regardless of the spin of the black hole.

As seen in Fig. 7.18, the collimation of the jet increases with $|a_{\rm H}|$ which is consistent with the increase of ϵ. We note also that the base of the jet becomes slightly closer to the black hole horizon as $|a_{\rm H}|$ increases.

Globally we see that the total geometry of the solution, and in particular the expansion of the jet radius, is extremely sensitive to the black hole speed.

The magnetic flux and power of the jets

Intuitively, by physical arguments of magnetic flux conservation, it is expected that magnetic fields not only play a dominant role in collimating large-scale AGN jets, but also critically affect the origin of the jets in accretion disks of black hole systems, which are accordingly termed *magnetically arrested disks* (Narayan et al. 2003). Indeed, theoretical modeling concludes that magnetic fields at the base of AGN jets are related to the corresponding accretion rate (Tchekhovskoy and McKinney 2012). Zamaninasab et al. [2014] reported that the measured magnetic flux of the jet and the accretion disk luminosity are tightly correlated over several orders of magnitude for a sample of many radio-loud AGN, concluding thus that the jet-launching region is threaded by a dynamically important magnetic field. The magnetic fields of AGN can be measured either by the effect of a frequency-dependent shift of the VLBI core position (known as the core-shift effect), or by Faraday rotation (e.g., Martí-Vidal et al. 2015, who reported magnetic fields of at least tens of Gauss on scales of the order of several light days - 0.01 parsecs - from the black hole). Furthermore, magnetohydrodynamic simulations in the frame of general relativity allow us to calculate the saturation or equilibrium value for the poloidal magnetic flux $\Phi_{\rm BH}$ threading the black hole (McKinney 2005, Tchekhovskoy et al. 2011, McKinney et al. 2012).

In Zamaninasab et al. [2014] this poloidal flux $\Phi_{\rm BH}$ is calculated as a function of the mass-accretion rate $\dot{\rm M}$ as,

$$\Phi_{\rm BH} \simeq 50\sqrt{\dot{\rm M}c\left(\frac{r_s}{2}\right)^2}. \tag{7.4}$$

We consider that since such a strong magnetic flux can thread the black hole, we can use this formula to link our value of poloidal magnetic field at the Alfvén point $\rm B_\star$ with the mass-accretion rate $\dot{\rm M}$. In our model the magnetic flux from each hemisphere is given by $\Phi_{\rm BH} = \pi\bar{\omega}_a^2 {\rm B}_\star = \pi r_\star^2 {\rm B}_\star \alpha_{\rm lim}$. Then, the magnitude of the magnetic field is calculated from the expression

$${\rm B}_\star \simeq 25 r_s \frac{\sqrt{\dot{\rm M}c}}{\pi r_\star^2 \alpha_{\rm lim}} = 25\mu \frac{\dot{\rm M}^{1/2} c^{1/2}}{\pi r_\star \alpha_{\rm lim}}. \tag{7.5}$$

In order to compare the jet power for the **K2** and **K3** solutions with the one obtained by general relativistic magnetohydrodynamic simulations, we calculate this power in terms of the parameters of our model. Similarly to the way we deduced the angular momentum flux density in Eqs. (5.57) and (5.58), we may calculate the jet+counterjet power by substituting $\Psi_{\rm A}$ from Eq. (5.56) and $\mathscr{E} = \mathscr{E}_\star(1 + e_1\alpha)$ with $\mathscr{E}_\star$ from Eq. (5.60), and with the help of Eq. (5.40), we obtain, in terms of the constants of our model,

$$\begin{aligned} {\rm P_{jet}} &= \int_0^{\rm A_{lim}} \Psi_{\rm A} \mathscr{E}\, d{\rm A} \\ &= \frac{\nu h_\star^2 c}{2\sqrt{\mu}} ({\rm B}_\star r_\star)^2 \int_0^{\alpha_{\rm lim}} (1 + e_1\alpha)\sqrt{1 + \delta\alpha}\, d\alpha. \end{aligned} \tag{7.6}$$

Hence, we finally get

$$\mathrm{P_{jet}} \simeq 625 \frac{\nu\mu^{3/2} h_\star^2}{2\pi^2 \alpha_{\rm lim}^2} \dot{\mathrm{M}} c^2 \int_0^{\alpha_{\rm lim}} (1 + e_1 \alpha) \sqrt{1 + \delta\alpha} d\alpha \,. \tag{7.7}$$

Therefore, for the efficiency $\eta_{\rm jet} \equiv \mathrm{P_{jet}}/\dot{\mathrm{M}}c^2$ for our **K2** model we obtain a value $\eta_{\rm jet} \simeq 0.52$, while for our **K3** model we obtain $\eta_{\rm jet} \simeq 0.40$. On the other hand, McKinney [2005] determined self-consistently the jet power in Blandford-Znajek numerical models and deduced an efficiency $\eta_{\rm jet}$ between 0.01 and 0.1 for ultra-relativistic Poynting-dominated jets with $a_{\rm H}$ larger than 0.8. Later, Tchekhovskoy et al. [2011] and McKinney et al. [2012] increased the magnetic flux which can be pushed near the black hole leading to magnetically arrested accretion and obtained values of the net flow efficiency larger than 1 for rapidly spinning black holes with $a_{\rm H}$ larger than 0.9. Their models that develop a highly non-axisymmetric magnetically choked accretion flow, initially have the poloidal component of the magnetic field dominant and the wind has an efficiency always smaller than that of the jet. We note that the **net** flow efficiency for the jet is equal to $(\mathrm{P_{jet}} - \dot{\mathrm{M}}_{\rm H} c^2)/[\dot{\mathrm{M}}_{\rm H} c^2]_t$ where $\dot{\mathrm{M}}_{\rm H}$ is the black hole mass-accretion rate and $[\dot{\mathrm{M}}_{\rm H} c^2]_t$ is the time-averaged value of accretion power. This black hole mass-accretion rate could be smaller than the mass-accretion rate measured by Zamaninasab et al. [2014]. In fact, they deduced the accretion power by dividing the bolometric luminosity with a radiative efficiency of 0.4. Larger values of the inflow rates $\dot{\mathrm{M}}_{\rm in,i}$ and $\dot{\mathrm{M}}_{\rm in,o}$ have been obtained by McKinney et al. [2012] at radii $5r_s$ and $25r_s$, respectively.Zdziarski et al. [2015] found also that the jet power moderately exceeds the accretion power $\dot{\mathrm{M}}c^2$ for blazars estimating the magnetic flux from the radio-jet core-shift effect and the self-absorbed flux evaluation. However, there is a large scatter around the mean value for blazars $\eta_{\rm jet} \simeq 1.3$ and the jet power for radio galaxies is smaller, especially for M87. Therefore, our estimations of jet power from our **K2** and **K3** solutions with mass loading could perfectly match that for less-efficient blazars and radio galaxies. Moreover, they do not overly depend on the spin parameter $a_{\rm H}$, since $\alpha_{\rm lim}$ keeps a value slightly smaller than 1 when the spin parameter varies for the **K3**-type solutions, even for retrograde black holes.

At this point, we prefer to postpone a further discussion of the jet power, until we have completed our study, which also includes inflow solutions and leads to a spin-energy extraction or addition from the black hole.

7.2.2 Summary and Conclusions

As was pointed already in 1957 by Parker (see also Parker 1963), for the driving of the solar wind and similar enthalpy-driven astrophysical outflows, some energy/momentum addition is required. The original isothermal and polytropic models with a heat conduction, have shown that effectively energy and/or momentum are necessary for producing supersonic/superAlfvénic outflows at large distances, to also meet the respective causality requirements. Quasi-radial wind-type astrophysical outflows with shock transitions (Habbal and Tsinganos 1983) have been applied to explain the appearance of emission knots in galactic (Silvestro et al. 1987) and extragalactic objects (Ferrari et al. 1984, Ferrari et al. 1986), also in the framework of special relativity (Ferrari et al. 1985).

When deviations of the outflow geometry from radial expansion exist and the problem is fully two-dimensional, these outflows can be collimated in the form of jets (Sauty and Tsinganos 1994) mainly by magnetic fields with a suitable external gas pressure distribution. Along these lines, in Vlahakis and Tsinganos [1998], the original Parker model was extended to include general MHD effects, in the context of meridional self-similarity. The present paper takes the extra step of using the framework of a Kerr metric to explore analogous

enthalpy- or generalized pressure-driven outflows from the environment of a rotating black hole.

Specifically, in this paper we present an exact MHD solution for an outflow in a Kerr metric, constructed by using the assumption of self similarity and the mechanism for driving the outflow which is developed in Sauty and Tsinganos [1994]. Additionally, the model is based on a first-order expansion of the governing general relativistic equations in the magnetic flux function around the symmetry axis of the system. It yields four nonlinear and coupled differential equations as a function of the radius, for the Alfvén number, the gas pressure, the expansion function and the radius of the jet. The model depends on seven parameters. Two of them are the meridional increase of the gas pressure and the mass to magnetic flux ratio, κ and δ, respectively. There is also the meridional increase of the total energy with the magnetic flux function, e_1, the poloidal current density flowing along the system axis, λ, the escape speed in units of the Alfvén speed, ν, the Schwarzschild radius in units of the Alfvén radius, μ, and the dimensionless black hole spin l. In addition to those seven parameters, we have to adjust the pressure at the Alfvénic transition. We chose to adjust it such as to minimize the oscillations of the magnitude of the flow speed along the axis and taking the limiting solution. We also fix the magnetic field at the Alfvén transition, $B_\star$, and a uniform pressure constant P_0 to ensure a zero external heating at infinity along the axis where the Lorentz factor is maximum.

The model takes into account the light cylinder effects and the meridional increase of the Alfvén number with the magnetic flux function, m_1. This parameter is deduced from the regularity conditions at the Alfvén transition surface.

The classical energetic criterion for the transition from conical winds to cylindrical jets is generalized in general relativity and it amounts to say that if the total available energy along a nonpolar streamline exceeds the corresponding energy along the axis, then the outflow collimates in a jet.

In the framework of a Kerr metric, we illustrate the model with four different enthalpy-driven solutions wherein the contribution of the Poynting flux is rather small. The first three solutions are cylindrically collimated, while the fourth represents a conical outflow at infinity. The flow collimation is induced by electromagnetic forces. In all four models, relativistic speeds are obtained, while in one of them the Lorentz factor γ obtains ultra-relativistic values. A preliminary application of one of our Kerr solutions (**K3**) was explored to model the spine jet in M87, yielding encouraging results. A more complete modeling for the M87 jet including an external disk-wind component will be explored in another study.

Our analytical solutions of the full general relativistic MHD equations in a Kerr metric may contribute to a better understanding of relativistic AGN jets and are complementary to sophisticated numerical simulations of such jets (e.g., McKinney 2005, Tchekhovskoy et al. 2011, McKinney et al. 2012). In both the analytical and the numerical approach, the outflows are electromagnetically confined. However, while in the above numerical simulations the outflow is driven electromagnetically (e.g., via the Blandford-Znajek mechanism), in the present analytical solutions the outflow from the hot corona surrounding the black hole is enthalpy- or generalized pressure-driven (e.g., via the Sauty-Tsinganos mechanism). Nevertheless, it is interesting to note that the jet powers for the two representative analytical solutions we present in this paper are similar to those determined by the numerical simulations.

The present model can also serve to construct an inflow solution, in order to link it with an outflow solution and the physical creation of leptonic pairs to determine the energy balance of the black hole, via a generalized Penrose process as compared to the Blandford-Znajek mechanism. This undertaking is in progress and will be presented in another publication.

7.3 Magnetization of K2 and K3 solution

Define the levels of magnetization as,

$$\sigma = \frac{h\varpi\Omega B^{\hat{\phi}}}{\Psi_A h\gamma\xi c^2} = \frac{2I\Omega}{\Psi_A h\gamma\xi c^3} = -\frac{\lambda^2\mu}{\nu^2}\frac{\Lambda_\infty \Lambda N_B}{h_z D}\alpha + \mathcal{O}(\alpha^2) \tag{7.8}$$

the ration between Poynting flux ($h\varpi\Omega B^{\hat{\phi}}$ per unit of magnetic flux) and the internal energy flux ($\Psi_A h\gamma\xi c^2$ also per unit of magnetic flux). This quantity measured the importance of toroidal magnetic magnetic field in the fluids dynamics. Neglecting the variation of Lense-Thirring energy flux, the diminution of this ratio along magnetic flux tube means there is a transfer of Poynting flux to Internal energy one. The magnetization is also play a role of collimation, indeed strong magnetization could be characterized by strong electric currant and thus a strong importance of toroidal magnetic field in collimation.

In Millas et al. [2017] the authors study on numerical simulation the role of maximal magnetization, toroidal speed and Lorentz factor of spine-jet for transversal stability of two component jets. The maximal magnetization used in this study is between 0.001 and 0.1. The authors note in their simulation that whatever the central Lorentz factor or the maximum toroidal velocity the increase in magnetization always results in a decrease in Rayleigh-Taylor instability mixing the components and thus stabilizing this two-component solution in order to maintain the central solution with high Lorentz factor.

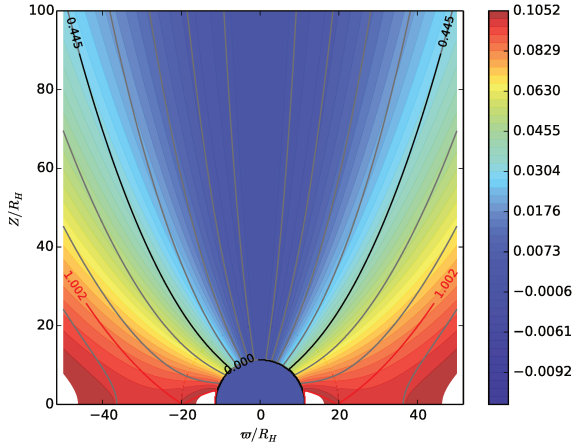

Figure 7.19 – Magnetisation parameter map σ for **K1** solution

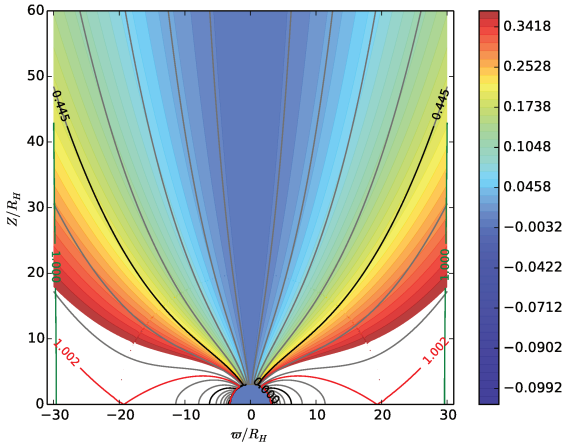

Figure 7.20 – Magnetisation parameter map σ for **K2** solution

The magnetization on the field line with $\alpha \approx 0.5\alpha_{\rm lim}$ start from 0.05 at stagnation radius to reach 0.02 at infinity for **K1** solution. On the same field line this evolution start from 0.17 to reach 0.16 fo **K2** solution. For **K3** solution it start at 0.4 to reach 0.22 and from 0.0045 to 0.0015 for **K4**. We deduce that the solution **K2** and **K3** have higher magnetization than solution **K1** and **K4**. This is understandable from an analytical point of view from Eq.(7.8), indeed the term that mainly determines the transversal evolution of magnetization is $\frac{\lambda^2\mu}{\nu^2}$. This is also characteristic of transversal equilibrium difference between these solution which much more important role given on toroidal magnetic collimation in the solution **K2** and **K3**.

The other term of Eq.(7.8) depending on the radius $\frac{\Lambda N_B}{D}D$ remains around one and determines the evolution of magnetization along the line. In all solution we see a decreasing of magnetization, it means that the toroidal magnetic field contributes to the acceleration of the flow on the non axial field lines where magnetization at the base of the flow is bigger. Nevertheless, for these solutions it remains less important than the acceleration the acceleration due to pressure.

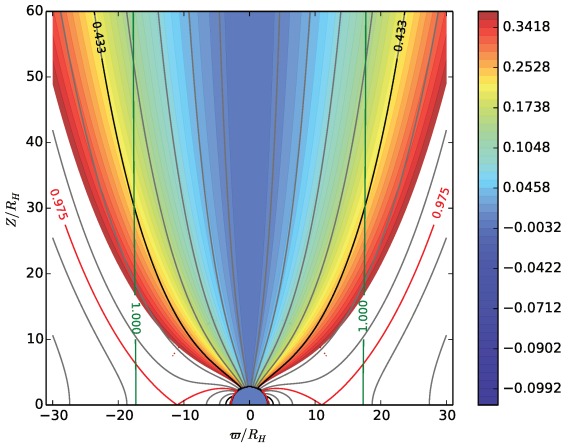

Figure 7.21 – Magnetisation parameter map σ for **K3** solution

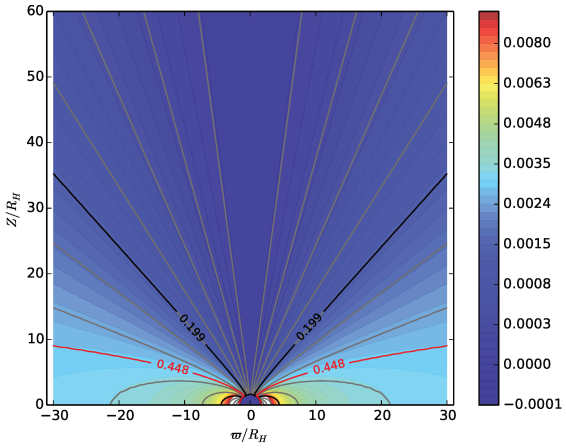

Figure 7.22 – Magnetisation parameter map σ for **K4** solution

7.4 Effect of the variation of energy integral with magnetic flux

We extend our study, by searching how a solution evolves with the parameter e_1. We choose to start a solution with the other parameters given in Table.(7.3).

λ	κ	δ	ν	ℓ	μ
1	0.2	1.35	0.5	0.049	0.1

Table 7.3 – Set of parameters for a solution calculated in order to study the impact of parameter e_1 around this solution

Note that the initial value of $\Pi_\star$ is chosen equal to $\Pi_{\star,\mathrm{lim}}$ (Sec.6.3), with an accuracy of 10^{-7}. We plot on Fig.(7.23) the evolution of the expansion factor G^2 for different values of e_1 from -0.1 to 0.1. We observe that the final value of G^2_∞ increases when e_1 increases. Increasing the variation of $\mathscr{E}$ with α implies an increasing of final expansion of the magnetic field-lines. The evolution with e_1 of the opening angle factor F is represented on Fig.(7.24). It shows the decrease of the frequency and amplitude of the oscillations of the jet.

In Fig.(7.25) we plot the evolution of the proper velocity factor βγ along the polar axis with e_1. The final proper velocity and the stagnation radius increase with e_1. In the last figure, Fig.(7.26), we show the asymptotic transversal profile of the poloidal β_p factor. We observe that in addition to the increase of the velocity on the axis, the increase of e_1 reduces the decrease of β_p in the transverse direction at infinity.

This evolution can be energetically interpreted. Indeed, the transverse distribution of energy available in the poloidal field lines varies with the parameter e_1. Eq.(4.44) implies that the increase of e_1, leads to an increase of $\mathscr{E} - \mathrm{L}\omega$ and thus of all the energetic flux and function which appears in Eq.(4.44) for $\alpha \neq 0$. Thus it explains why the velocity does not decrease as fast in the case of $e_1 \leq 0$ than in the case $e_1 \geq 0$. There is more energy available for kinetic and internal energy in the case $e_1 \geq 0$. This amount of energy increases also the strength of the gravitational forces, Eq.(5.101). It also explains the increase of the stagnation radius with e_1. Indeed, the stationary radius of the flow moves away from the black hole to compensate for the increase in the gravitational forces.

When we look carefully at the functions involved in the system of Eqs.(5.107), we note that the differential system is only a function of $2e_1 + \delta$, and not e_1 and δ separately. Thus the effects

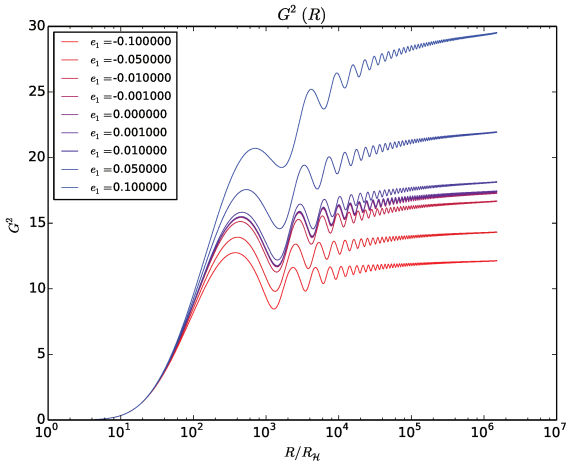

Figure 7.23 – Expansion factor G^2 for different values of e_1

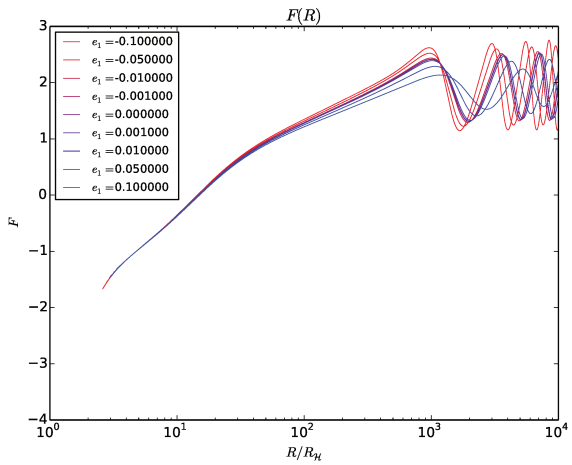

Figure 7.24 – Opening angle factor F for different values of e_1

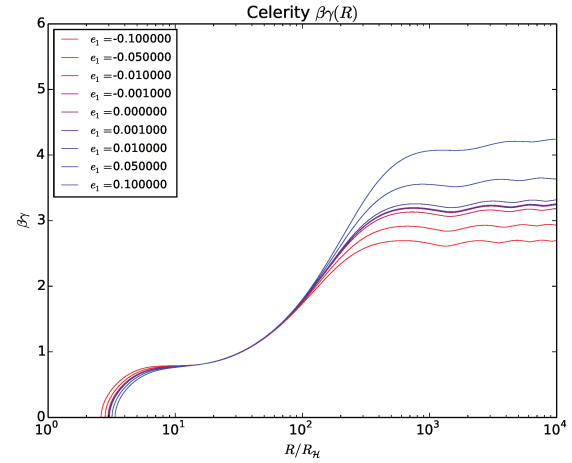

Figure 7.25 – proper velocity $\beta\gamma$ on the axis for different values of e_1

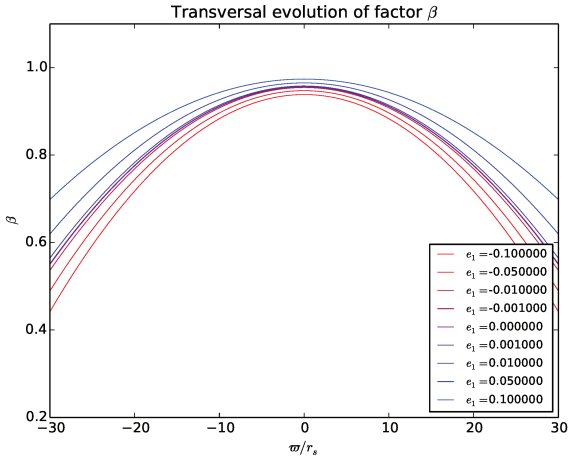

Figure 7.26 – Transversal evolution of β for asymptotic z value and for different values of e_1

of e_1 and $\delta/2$ are the same for the evolution of the functions $\mathrm{M}^2, \mathrm{G}^2, \Pi$. Intuitively, this degeneracy is the expression, in the equations of the model, of the equivalence principle which implies the identity of the inertial mass and the gravitational mass. Thus only $e_1 + \delta/2$, which is the first order variation in α of $\Psi_{\mathrm{A}}\mathscr{E}$ appears in the model equations. If things were that simple, then Grad-Shafranov analysis, Sec.(4.2.4), should also be able to do without Ψ_{A}, which is not the case. This property therefore seems to be related to the construction of the model.

7.5 Observational constraints

It is useful to aplly observationalal constrain to solutions from the model (**K2** and **K3**). We present here a short analysis illustrating the capabilities of the model. This complement the discussion about magnetic flux and jet efficiency, Sec.(7.2). These results must be handled carefully and are subject to discussion. In the following, we discuss the material composition of the jet using the observed brightness temperature given by Homan et al. [2006]. Then we continue the discussion started in Sec.(7.2), using the tools of Sec.(3.3.3), in order to estimate the deviation to the thermodynamical equilibrium.

7.5.1 Matter content from temperature estimation

The basic equations, Eqs.(4.17), used to build our model, are based on the fluid stress-energy tensor, Eq.(3.82, 3.83), of an isotropic non-equilibrium distribution functions. We consider a fluid composed of leptons (electron/positron) and protons, such that the distribution function of species is an isotropic non-equilibrium distribution function with the same fluid 4-speed. Then each species could be represented by an equilibrium distribution function as in Eq.(3.84), with an effective temperature $\mathrm{T}_{\mathrm{eff},i}$. We choose these temperatures in order to have for each species $\delta \mathrm{P}_i = 0$. Then we obtain,

$$\mathrm{P} = \mathrm{P}_l + \mathrm{P}_h = k_{\mathrm{B}} \left(n_l \mathrm{T}_{\mathrm{eff},l} + n_p \mathrm{T}_{\mathrm{eff},p} \right) . \tag{7.9}$$

We make the reasonable assumption that the effective leptonic temperature and the proton temperature are of the same order of magnitude (same order of magnitude of the thermal agitation energy for each species) $\mathrm{T}_l \simeq \mathrm{T}_p \simeq \mathrm{T}$. In this case, it is possible to calculate leptonic fraction,

$$y_l = \frac{n_l}{n_l + n_p} = \frac{m_p - \frac{k_{\mathrm{B}}\mathrm{T}}{\Theta c^2}}{m_p - m_l} , \tag{7.10}$$

where $\Theta = \mathrm{P}/\rho_0 c^2$ is the dimensionless model temperature. It is the pressure-related quantity that accelerates the flow in the model solutions. To give an order of magnitude of this fraction we consider that the effective temperature could be at the same order of the brightness temperature $\mathrm{T} \simeq \mathrm{T}_b$, we are able to give an order of magnitude of this leptonic fraction. The observed brightness temperatures mentioned in Homan et al. [2006] for a large sample of AGN are around $\mathrm{T}_b \sim 2.10^{11} - 5.10^{11}\mathrm{K}$. In Kim et al. [2016] the brightness temperature measured for the source M87, Mrk421 and NGC1052 for different wavelengths and on different locations in the range $\mathrm{T}_b \sim 5.10^{10} - 5.10^{12}\mathrm{K}$.

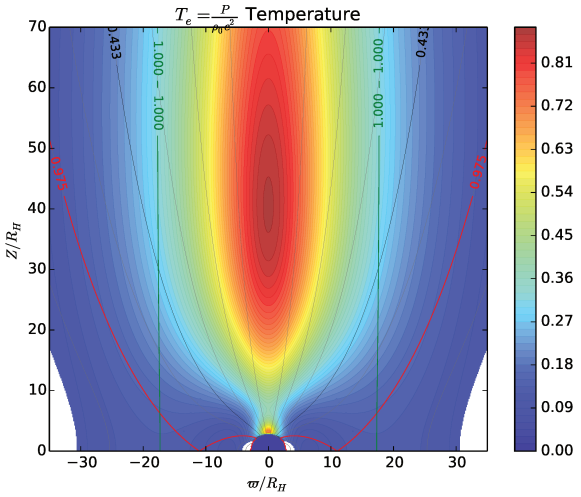

Figure 7.27 – Values of dimensionless model temperature for **K3** solution

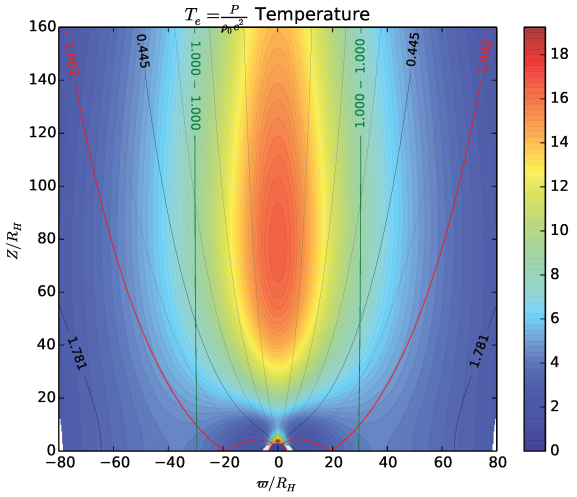

Figure 7.28 – Values of dimensionless model temperature for **K2** solution

On Fig.(7.27, 7.28), the dimensionless model temperature $\Theta = \mathrm{P}/\rho_0 c^2$ of the **K2** solution during the jet acceleration phase are between $5-15$ and between $0.5-1$ for **K3** solution. Keeping the values of brightness temperature mentioned by Homan et al. [2006], we obtain a leptonic fraction $y_l \sim 0.995 - 0.9995$ for **K2** during the jet acceleration phase and $y_l \sim 0.945 - 0.98$ for **K3**. So it seems that these two solutions are mostly composed of leptons. For the same mass density of matter and the same temperature, a leptonic gas has more pressure, which is necessary for its acceleration along the axis.

Nevertheless, this analysis is done with the extra-assumption of an identical effective temperature of the two species equals to brightness temperature and that the two fluids have the same

velocity. The implicit assumption in Eq.(7.9) saying that the model pressure has is of thermal origin can also be discussed. The thermal pressure entering in Eq.(7.9) could be a fraction of the total pressure P, which allows to accelerate the flow. It would decrease the thermal Θ values in Eq.(7.10) and thus increase the value of the proton fraction. Furthermore, the temperature presents variations inside the jet, which are the same order of the observed brightness temperature. Thus there is good reasons to think that the fraction of the species could also evolve across the jet. This species evolution could allow a continuity between a spine jet which matter source is the pair creation and a disk wind. On Fig.(7.27, 7.28) the temperature decreases from the axis up to the border of the jet.

7.5.2 Cooling time scale

In the previous subsection we see that if the brightness temperature is a good estimation for the effective temperature, then the leptonic fraction $y_l \sim 1$ which means that the medium is mostly composed of highly temperature electron positron pair. In such environment the leptons loss their energy via Syncrotron and Inverse Compton emission. In the fluid reference frame, the mean value of energy for an electron (positron) is $m_e c^2 < \gamma >= m_e(c^2 + e)$ (where e is the specific energy mention in Eq.(3.84)). This single electron (positron) in presence of a magnetic field or radiation radiated away a power estimated to,

$$\mathrm{P}_r = \frac{4}{3}\sigma_\mathrm{T} c < \gamma^2\beta^2 > u \tag{7.11}$$

where $\sigma_\mathrm{T} \simeq 6.65\times10^2 5\mathrm{cm}^2$ is the Thomson cross section, and u could be the magnetic field energy density $u_\mathrm{B} = \mathrm{B}^2/8\pi$ for synchrotron emission or radiation energy density u_r for Inverse Compton emission. Then the typical time scale such that the electron loss its internal energy is,

$$\tau_r \simeq \frac{3m_e c}{4\sigma_\mathrm{T} u}\frac{<\gamma>}{<\gamma^2\beta^2>} \simeq \frac{3m_e c}{4\sigma_\mathrm{T} u}\frac{1}{<\gamma>} = \frac{3m_e c}{4\sigma_\mathrm{T} u(\xi-\Theta)} \tag{7.12}$$

We will call this time scale as typical cooling time scale. Indeed the electrons loss their internal energy. We can compare this cooling time scale with the dynamical time scale of cooling due to transfer between internal energy and Kinetic energy. This time scale could be define as,

$$\frac{1}{\tau_d} \simeq h\mathbf{V}\cdot\mathbf{D}\ln e \simeq \frac{c}{r_s}\frac{\mu^{3/2}}{\nu}\frac{h_z^2}{h_\star^2}\frac{\mathrm{M}^2}{\mathrm{G}^2}\frac{d\ln e}{d\mathrm{R}} \tag{7.13}$$

From bolometric luminosity L we are able to estimate radiation energy density,

$$u_r = \frac{\mathrm{L}}{4\pi r_s^2 c}\frac{\mu^2}{\mathrm{R}c} \tag{7.14}$$

For the bolometric luminosity we will use the value for M87 $\mathrm{L} = 2{,}7\times10^{42}\mathrm{erg.s}^{-1}$ mention by Prieto et al. [2016]. For the magnetic energy density we get

$$u_\mathrm{B} = \frac{\mathrm{B}_{10r_s}^2}{8\pi}\frac{\mathrm{G}^4(10\mathrm{R}_s)}{\mathrm{G}^4(\mathrm{R})} \tag{7.15}$$

where we use the value at ten Schwarzschild radius $\mathrm{B}_{10r_s} \simeq 1-15\mathrm{G}$ of M87 supermassive black hole mention in Kino et al. [2014]. Combining the different previous equation we are able to calculate the ratio of the different time scale,

$$\begin{cases} \dfrac{\tau_c}{\tau_d} = \dfrac{3\pi m_e c^3 r_s}{\sigma_\mathrm{T}\mathrm{L}}\dfrac{\frac{h_z^2}{h_\star^2}\frac{\mathrm{M}^2}{\mathrm{G}^2}\frac{de/c^2}{d\mathrm{R}}}{\nu\sqrt{\mu}\left(1+\frac{e}{c^2}\right)\frac{e}{c^2}} \\ \dfrac{\tau_s}{\tau_d} = \dfrac{6\pi m_e c^2}{\sigma_\mathrm{T} r_s \mathrm{B}_{10r_r}^2}\dfrac{\frac{\mu^{3/2}}{\nu}\frac{h_z^2}{h_\star^2}\frac{\mathrm{G}^2\mathrm{M}^2}{\mathrm{G}^4(10\mathrm{R}_s)}\frac{de/c^2}{d\mathrm{R}}}{\left(1+\frac{e}{c^2}\right)\frac{e}{c^2}} \end{cases} \tag{7.16}$$

Using for luminosity the bolometric luminosity of M87 mentioned in Prieto et al. [2016] we obtain, $\frac{\sigma_T L}{3\pi m_e c^3 r_s} \simeq 0.11634$ and $\frac{\sigma_T r_s B_{10r_r}^2}{6\pi m_e c^2} \simeq 7,7\times10^{-5} - 1.7\times10^{-2}$. We also are able to plot this ratio of time scale,

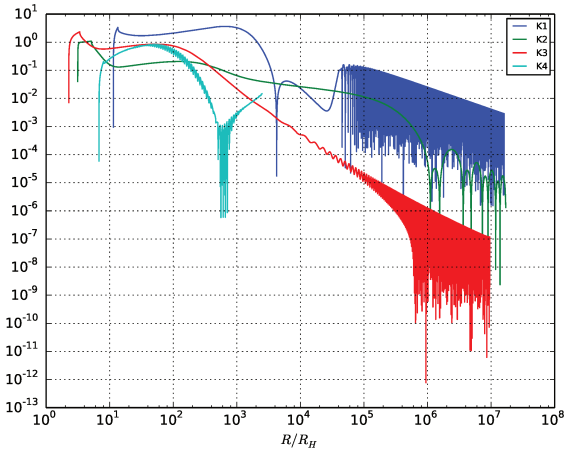

Figure 7.29 – Evolution for the different solution of the ratio between the Compton cooling time scale and the dynamical time scale τ_c/τ_d along the axis in function of distance $R/R_{\mathscr{H}}$

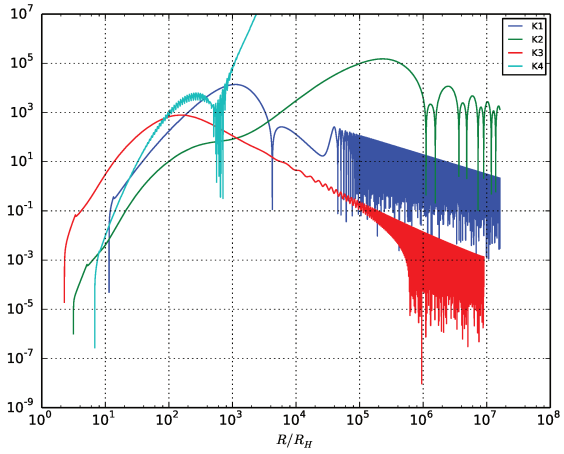

Figure 7.30 – Evolution for the different solution of the ratio between the synchrotron cooling time scale and the dynamical time scale τ_s/τ_d along the axis in function of distance $R/R_{\mathscr{H}}$

On Fig.(7.29) we observe that cooling time scale due to Compton cooling is quite small in comparison of dynamical cooling time scale in large part of the jet, nevertheless it became really small for all solution behind dynamical time scale at large distance, we deduce that this phenomena need to be include to describe the jet dynamics and especially at large distance.

On Fig.(7.30), we observe that for all solution the synchrotron time scale became small behind the dynamical time scale for each solution at the base of the jet, it imply that the dynamics of the base of the jet must be impact by the synchrotron cooling. In the conical solution **K4** the ration between synchrotron emission dynamical cooling time explode at large distance, it is due to a faster decreasing of the magnetic field. In collimated solution, the magnetic field reach a non-null value, which imply more or less strong magnetic energy density at large distance, More the expansion factor G_∞ is large more small is this energy density and more long is the cooling time due to synchrotron emission. It explain why **K2** and **K3** solution also have $\tau_s/\tau_d \ll 1$ for $R/R_{\mathscr{H}} \geq 10^5$. Final cooling time ratio is also determine by the final value of internal energy.

7.5.3 Deviation from thermodynamical equilibrium

It is also interesting to see if it is possible to estimate the deviation from thermodynamical equilibrium needed to produce the additional total enthalpy and effective temperature. Here we use the main results of Sec.(3.3.3) in order to estimate the κ value of relativistic κ-distribution function required on the axis (not the deviation of pressure sphericity κ). So we propose to look at the extra-energy and the effective temperature for solutions **K2** and **K3**.

On Fig.(7.31, 7.32), we present the evolution on the axis of the effective temperature $\Theta = \frac{P}{\rho_0 c^2}$ as a function of the radius. On Fig.(7.33, 7.34) is plotted the evolution along the axis of the internal energy component $\xi = \xi_{eq} + \frac{\delta e}{c^2}$ for solutions **K2** and **K3**. First of all, we note that the curves are similar for the two solutions. Most of the extra-internal energy is localized at the base of the flow during the acceleration phase. The effective temperature decreases at the beginning then increase and reaches a maximum before it happens a new decrease towards a limiting value. The specific dimensionless enthalpy ξ decreases during the whole acceleration phase of the flow. Indeed, $h\gamma\xi$ remains constant along the axis. This enthalpy constitutes a kind of energy reservoir.

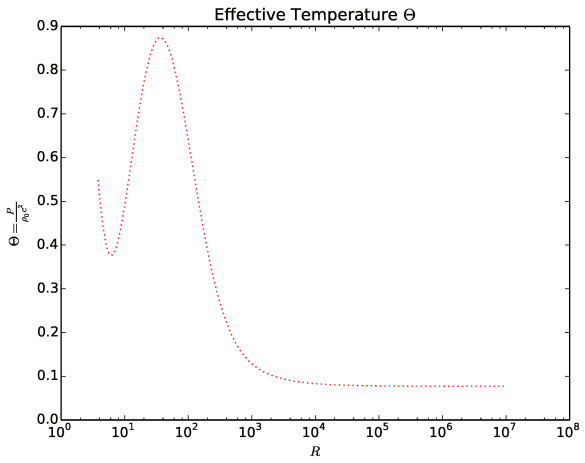

Figure 7.31 – Temperature for **K3** solution on the axis

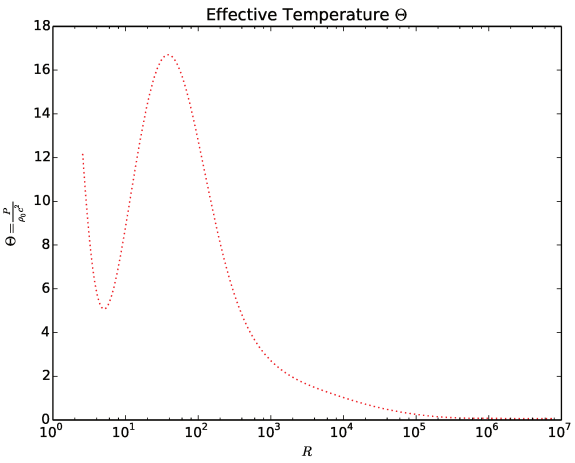

Figure 7.32 – Temperature for **K2** solution on the axis

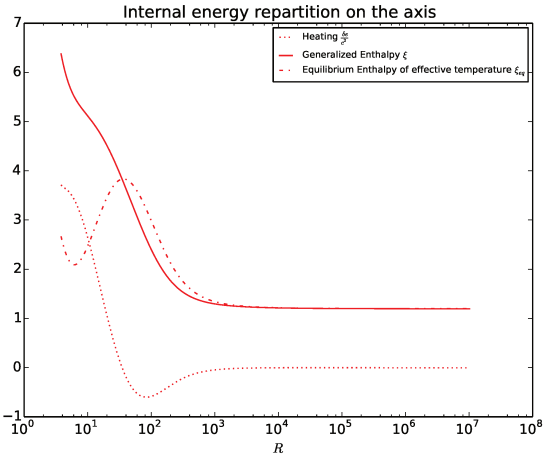

Figure 7.33 – Distribution of the two components of the enthalpy for **K3** solution on the axis

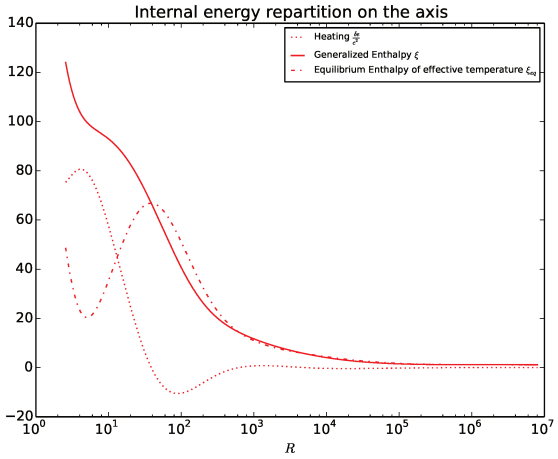

Figure 7.34 – Distribution of the two components of the enthalpy for **K2** solution on the axis

Part of the total enthalpy is transformed into kinetic energy when moving away from the central black hole.

Nevertheless, the value of $(\delta e/c^2, \Theta) \sim (40-80, 6-18)$ of **K2** requires that the distribution function is far from equilibrium. It cannot be modeled by a κ-distribution function because, in this case the extra-internal energy is two large. Thus other types of non-equilibrium distribution functions or other mechanisms should be explored to explaining the acceleration phase of the **K2** solution. For **K3** we have values of $\delta e \sim 0.5-4$, with values of $\Theta \sim 0.5-1$ at the base of the flow. Part of this area could therefore be explained by using the κ-distribution function with values in range $\kappa \sim 3-3.5$.

7.6 Conclusion

We have presented several solutions with flow accelerations and different geometries.

We have explored the effect of introducing the deviation from sphericity of the Alfvén Mach number, to take into account the previously neglected effect of the light cylinder. The effect

is similar to an increase in the transverse pressure gradient. It increases the collimation, which results in a lower terminal velocity. Other modifications due to the introduction of this deviation include an effect of the increased gravity force, which results in a stronger initial acceleration.

The outflow solutions can be divided into two main categories, cylindrical and conical solutions. For cylindrical solution, collimation may be insured by transverse pressure gradient , e.g. **K1** or by toroidal magnetic field e.g. **K2** and **K3**. On the axis, all solutions are accelerated by the total enthalpy, which contains the gas enthalpy for the effective temperature P/ρ_0 plus an extra-internal energy. It seems difficult with this model to increase the role of the electromagnetic forces for the gas acceleration out of the axis. However, the solutions were not obtained taking this goal into account. The Poynting flux of **K2** can reach 20% of the total energy flux at the edge of the jet. High Lorentz factors can be obtained at the infinity $\gamma_{\mathrm{K3}} \sim 5.5$ or $\gamma_{\mathrm{K2}} \sim 100$ by adapting the solution parameters.

We obtained a solution **K3** for modeling the extragalactic jet of M87. It has Lorentz factors, a width and a launching base of the jet close to those evaluated by Mertens et al. [2016].

The plot the magnetization map of the solution, and we see that even if the model is an expand near the axis where magnetization is zero, the magnetization can grow quickly and reach non negligible value especially at the base of the flow and for collimated solution. We also observe a transfer from Poynting to Kinetic energy on the non axial field line, even if ithe gas is mainly pressure driven.

We also studied the role of the new parameters introduced in this model, namely the spin of the black hole l and the variation e_1 of the energy integral $\mathscr{E}$ with the magnetic flux α.

- About the l parameter, it is not obvious that the different parameters of the model depend on the l parameter. Thus, from this parametric study on l, no single structural parameter appears, which is only a function of l/μ (or strongly dependent on l/μ) allowing an indirect measurement of the spin of the central black holes through the measurable physical characteristics of the jet. Nevertheless, by fixing all the other parameters, it seems that the increase of the black hole spin leads to an increase of the magnetic collimation parameter for collimated jets. For conical jets, this increase is produced regardless of the direction of rotation of the black hole. The maximal value of the Lorentz factor decreases with l.

- Concerning e_1, this parameter allows to distribute the energy flow in the jet. If it is positive then the energy available for the flow increases as one moves away from the axis. Thus the stratification of the velocity in the jet decreases less fast for positive values of e_1 and faster for negative values of e_1. The final velocity of the flow increases with e_1 while the collimation decreases with the increase of e_1. It plays a role similar to δ.

The efficiency of cylindrical jets is calculated admitting the scaling relation between magnetic flux and accretion rate given in Zamaninasab et al. [2014]. We obtain an efficiency of $\eta_{\mathrm{jet}} \simeq 0.52$ for **K2** and $\eta_{\mathrm{jet}} \simeq 0.40$ for **K3**.

The comparison between the effective temperature $\Theta = \mathrm{P}/\rho_0 c^2$ of the solutions and the brightness temperature observed by Homan et al. [2006] leads to conclude that the matter in the hottest jet zone is composed mostly of leptons rather than baryons. However our analysis is limited by the interpretation of the effective temperature. Indeed, it depends if the temperature includes supplementary amounts to the thermal temperature. The baryon proportion should a priori increase as one moves away from the axis of the jet.

Such high temperature potentially increase the synchrotron and the Compton emission. We estimated the typical cooling time of these process we compare these cooling time with a dynamical cooling time. We observe a potentially strong influence on dynamics of Compton emission particularly at large distance, when the synchrotron emission need to be taken account at the base of the flow. Conical solution are less dynamically influence by synchrotron at large distance. Others model need to be construct to taken these process account in order to get physically relevant description of such flow.

The internal energy supplement $\delta e/c^2$ of the solution **K2** is too large for a κ-distribution function. For **K3** only part of the jet can be interpreted as having a κ-distribution function. This does not mean that the internal energy supplement cannot be explained by means of a velocity distribution out of thermal equilibrium. Yet this out-of-equilibrium distribution cannot be explained only by a κ-distribution function.

7.7 References

Jeffrey M. Anderson, Zhi-Yun Li, Ruben Krasnopolsky, and Roger D. Blandford. Locating the launching region of t tauri winds: The case of dg tauri. *The Astrophysical Journal Letters*, 590 (2):L107, 2003. URL http://stacks.iop.org/1538-4357/590/i=2/a=L107. 121

R. D. Blandford and D. G. Payne. Hydromagnetic flows from accretion discs and the production of radio jets. *Monthly Notices of the Royal Astronomical Society*, 199(4):883–903, 1982. doi: 10.1093/mnras/199.4.883. URL http://dx.doi.org/10.1093/mnras/199.4.883. 122

L. Chantry, V. Cayatte, C. Sauty, N. Vlahakis, and K. Tsinganos. Nonradial and nonpolytropic astrophysical outflows. X. Relativistic MHD rotating spine jets in Kerr metric. aap, 612:A63, April 2018. doi: 10.1051/0004-6361/201731793. 114

A. Ferrari, S. R. Habbal, R. Rosner, and K. Tsinganos. A wind-type model for the generation of astrophysical jets. apjl, 277:L35–L39, February 1984. doi: 10.1086/184197. 130

A. Ferrari, E. Trussoni, R. Rosner, and K. Tsinganos. On wind-type flows in astrophysical jets. I - The initial relativistic acceleration. apj, 294:397–418, July 1985. doi: 10.1086/163307. 130

A. Ferrari, E. Trussoni, R. Rosner, and K. Tsinganos. On wind-type flows in astrophysical jets. II - Propagation outside the nucleus and the case of M87. apj, 300:577–590, January 1986. doi: 10.1086/163835. 130

S. R. Habbal and K. Tsinganos. Multiple transonic solutions with a new class of shock transitions in steady isothermal solar and stellar winds. jgr, 88:1965–1975, March 1983. doi: 10.1029/JA088iA03p01965. 130

O Hervet, Z Meliani, A Zech, C Boisson, V Cayatte, C Sauty, and H Sol. Shocks in relativistic transverse stratified jets-a new paradigm for radio-loud agn. *Astronomy & Astrophysics*, 606: A103, 2017. 121, 123

D. C. Homan, Y. Y. Kovalev, M. L. Lister, E. Ros, K. I. Kellermann, M. H. Cohen, R. C. Vermeulen, J. A. Zensus, and M. Kadler. Intrinsic Brightness Temperatures of AGN Jets. apjl, 642:L115–L118, May 2006. doi: 10.1086/504715. 134, 135, 139

J.-Y. Kim, R.-S. Lu, T. Krichbaum, M. Bremer, J. Zensus, and R. Walker. Resolving the Base of the Relativistic Jet in M87 at 6Rsch Resolution with Global mm-VLBI. *Galaxies*, 4:39, September 2016. doi: 10.3390/galaxies4040039. 135

M Kino, F Takahara, K Hada, and A Doi. Relativistic electrons and magnetic fields of the m87 jet on the 10 schwarzschild radii scale. *The Astrophysical Journal*, 786(1):5, 2014. 136

Yan-Rong Li, Ye-Fei Yuan, Jian-Min Wang, Jian-Cheng Wang, and Shu Zhang. Spins of supermassive black holes in m87. ii. fully general relativistic calculations. *The Astrophysical Journal*, 699(1):513, 2009. URL http://stacks.iop.org/0004-637X/699/i=1/a=513. 116

Ivan Martí-Vidal, Sébastien Muller, Wouter Vlemmings, Cathy Horellou, and Susanne Aalto. A strong magnetic field in the jet base of a supermassive black hole. *Science*, 348(6232):311–314, 2015. ISSN 0036-8075. doi: 10.1126/science.aaa1784. URL http://science.sciencemag.org/content/348/6232/311. 129

Jonathan C. McKinney. Total and jet blandford-znajek power in the presence of an accretion disk. *The Astrophysical Journal Letters*, 630(1):L5, 2005. URL http://stacks.iop.org/1538-4357/630/i=1/a=L5. 129, 130, 131

Jonathan C. McKinney, Alexander Tchekhovskoy, and Roger D. Blandford. General relativistic magnetohydrodynamic simulations of magnetically choked accretion flows around black holes. *Monthly Notices of the Royal Astronomical Society*, 423(4):3083–3117, 2012. doi: 10.1111/j.1365-2966.2012.21074.x. URL http://dx.doi.org/10.1111/j.1365-2966.2012.21074.x. 129, 130, 131

Z. Meliani and R. Keppens. Dynamics and stability of relativistic gamma-ray-bursts blast waves. a&a, 520:L3, September 2010. doi: 10.1051/0004-6361/201015423. 124

Z. Meliani, C. Sauty, N. Vlahakis, K. Tsinganos, and E. Trussoni. Nonradial and nonpolytropic astrophysical outflows. VIII. A GRMHD generalization for relativistic jets. aap, 447:797–812, March 2006. doi: 10.1051/0004-6361:20053915. 114

Z. Meliani, C. Sauty, K. Tsinganos, E. Trussoni, and V. Cayatte. Relativistic spine jets from Schwarzschild black holes. Application to AGN radio-loud sources. aap, 521:A67, October 2010. doi: 10.1051/0004-6361/200912920. 116

F. Mertens, A. P. Lobanov, R. C. Walker, and P. E. Hardee. Kinematics of the jet in M 87 on scales of 100-1000 Schwarzschild radii. a&a, 595:A54, October 2016. doi: 10.1051/0004-6361/201628829. 116, 120, 121, 122, 123, 139

D. Millas, R. Keppens, and Z. Meliani. Rotation and toroidal magnetic field effects on the stability of two-component jets. mnras, 470:592–605, September 2017. doi: 10.1093/mnras/stx1288. 132

Ramesh Narayan, Igor V. Igumenshchev, and Marek A. Abramowicz. Magnetically arrested disk: an energetically efficient accretion flow. *Publications of the Astronomical Society of Japan*, 55 (6):L69–L72, 2003. doi: 10.1093/pasj/55.6.L69. URL http://dx.doi.org/10.1093/pasj/55.6.L69. 129

A. Nathanail and I. Contopoulos. Black Hole Magnetospheres. apj, 788:186, June 2014. doi: 10.1088/0004-637X/788/2/186. 123

E. N. Parker. *Interplanetary dynamical processes*. 1963. 130

M. A. Prieto, J. A. Fernández-Ontiveros, S. Markoff, D. Espada, and O. González-Martín. The central parsecs of M87: jet emission and an elusive accretion disc. mnras, 457:3801–3816, April 2016. doi: 10.1093/mnras/stw166. 136, 137

C. Sauty and K. Tsinganos. Nonradial and nonpolytropic astrophysical outflows III. A criterion for the transition from jets to winds. aap, 287:893–926, July 1994. 115, 118, 130, 131

C. Sauty, E. Trussoni, and K. Tsinganos. Nonradial and nonpolytropic astrophysical outflows. V. Acceleration and collimation of self-similar winds. aap, 389:1068–1085, July 2002. doi: 10.1051/0004-6361:20020684. 116

C. Sauty, E. Trussoni, and K. Tsinganos. Nonradial and nonpolytropic astrophysical outflows. VI. Overpressured winds and jets. aap, 421:797–809, July 2004. doi: 10.1051/0004-6361:20035790. 115

C. Sauty, J. J. G. Lima, N. Iro, and K. Tsinganos. Nonradial and nonpolytropic astrophysical outflows. VII. Fitting ULYSSES solar wind data during minimum. aap, 432:687–698, March 2005. doi: 10.1051/0004-6361:20041606. 125

G. Silvestro, A. Ferrari, R. Rosner, E. Trussoni, and K. Tsinganos. A model for collimated outflows in molecular clouds and the case of HH 7-11. nat, 325:228–230, January 1987. doi: 10.1038/325228a0. 130

Alexander Tchekhovskoy. *Launching of Active Galactic Nuclei Jets*, pages 45–82. Springer International Publishing, Cham, 2015. ISBN 978-3-319-10356-3. doi: 10.1007/978-3-319-10356-3_3. URL https://doi.org/10.1007/978-3-319-10356-3_3. 123

Alexander Tchekhovskoy and Jonathan C. McKinney. Prograde and retrograde black holes: whose jet is more powerful? *Monthly Notices of the Royal Astronomical Society: Letters*, 423(1): L55–L59, 2012. doi: 10.1111/j.1745-3933.2012.01256.x. URL http://dx.doi.org/10.1111/j.1745-3933.2012.01256.x. 129

Alexander Tchekhovskoy, Ramesh Narayan, and Jonathan C. McKinney. Efficient generation of jets from magnetically arrested accretion on a rapidly spinning black hole. *Monthly Notices of the Royal Astronomical Society: Letters*, 418(1):L79–L83, 2011. doi: 10.1111/j.1745-3933.2011.01147.x. URL http://dx.doi.org/10.1111/j.1745-3933.2011.01147.x. 129, 130, 131

K. Tsinganos and C. Sauty. Nonradial and nonpolytropic astrophysical outflows. I - Hydrodynamic solutions with flaring streamlines. aap, 255:405–419, February 1992. 115

H. J. van Eerten, Z. Meliani, R. A. M. J. Wijers, and R. Keppens. Jet simulations and gamma-ray burst afterglow jet breaks. *Monthly Notices of the Royal Astronomical Society*, 410(3):2016–2024, 2011. doi: 10.1111/j.1365-2966.2010.17582.x. URL http://dx.doi.org/10.1111/j.1365-2966.2010.17582.x. 124

N. Vlahakis and A. Königl. Relativistic Magnetohydrodynamics with Application to Gamma-Ray Burst Outflows. II. Semianalytic Super-Alfvénic Solutions. apj, 596:1104–1112, October 2003a. doi: 10.1086/378227. 118

N. Vlahakis and A. Königl. Relativistic Magnetohydrodynamics with Application to Gamma-Ray Burst Outflows. I. Theory and Semianalytic Trans-Alfvénic Solutions. apj, 596:1080–1103, October 2003b. doi: 10.1086/378226. 118

N. Vlahakis and K. Tsinganos. Systematic construction of exact magnetohydrodynamic models for astrophysical winds and jets. *Monthly Notices of the Royal Astronomical Society*, 298(3): 777–789, 1998. doi: 10.1046/j.1365-8711.1998.01660.x. URL http://dx.doi.org/10.1046/j.1365-8711.1998.01660.x. 130

M. Zamaninasab, E. Clausen-Brown, T. Savolainen, and A. Tchekhovskoy. Dynamically important magnetic fields near accreting supermassive black holes. nat, 510:126–128, June 2014. doi: 10.1038/nature13399. 129, 130, 139

Andrzej A. Zdziarski, Marek Sikora, Patryk Pjanka, and Alexander Tchekhovskoy. Core shifts, magnetic fields and magnetization of extragalactic jets. *Monthly Notices of the Royal Astronomical Society*, 451(1):927–935, 2015. doi: 10.1093/mnras/stv986. URL http://dx.doi.org/10.1093/mnras/stv986. 130

Chapter 8

Inflow/outflow solutions and source terms

Contents

8.1 Introduction

The study of magnetized flows around massive rotating black holes is an extremely active research domain. Considering, the strong gravitational field, the reservoir of rotational energy of the black hole and the presence of an accretion disks may induce high energy phenomena as creation of pair mechanism, Compton and Inverse/Compton. These mechanisms need to be included in the General Relativistic Magneto-Hydrodynamic (GRMHD) the dynamical treatment of the flow. Indeed the X-rays and γ-ray emission could be explained taking into account Compton/ Inverse Compton scattering and pair formation mechanismes inside the jet dynamics Blandford and Levinson [1995]; Levinson and Blandford [1995].

The rotational energy extraction of the black hole leads to a lot of investigations. In this research on the extraction of rotational energy by the Poynting flux, the final calculation of Blandford and Znajek [1977] assumes an expansion, in the force-free assumption, with the black hole spin, from a solution where the magnetic flux is radial or parabolic. Nathanail and Contopoulos [2014] obtain solutions of the force-free Grad-Shafranov equation for black hole magnetosphere. They explore three kind of solutions, with high value of spin, where the infinite geometry of poloidal magnetic flux field lines is one of a split-monopole, the paraboloidal and vertical. They use a method which allows them to cross smoothly the two light cylinders (critical surfaces of the free-force problem), for the two configuration where the lines cross these surfaces. They also conclude as Komissarov and McKinney [2007] that no Meissner effect will ever occur in force-free magnetosphere. About Blanford-Znajek extraction process, they insist on the role for studying magnetic flux accumulation on black-hole horizon. To explore a wider set of configurations as different geometries and to include matter density, it is useful to solve the equations of GRMHD up to the black hole horizon in order to calculate the energy and angular momentum flux exchange with the black hole. Takahashi et al. [1990] and Hirotani et al. [1992] started to include full Magneto-Hydrodynamic (MHD) analysis for calculation of energy fluxes on the horizon. Globus and Levinson [2013, 2014] explored the role of the amount of pairs (and their energy) in the energy exchange with the black hole. Their solutions are calculated in the radial geometry without force free assumption. They obtained a decrease of the energy flux extracted from the black hole with the increase of created pairs. They obtained also limiting mass flux flowing into the black hole for getting an active extraction process. In the first paper Globus and Levinson [2013], the loading of the flow is done at stationarity surface. In the second paper Globus and Levinson [2014] build a model with a volumic loading of mass and energy adapted to neutrino annihilation in Gamma Ray Burst (GRB). Pu et al. [2015] built magnetized solutions by matching the inflow and the outflow solutions in a parabolic geometry. Nevertheless, they imposed a continuity for the current distribution I at the stagnation radius, where pairs are created. Thus there is no Poynting flux creation by the injection in the flow. This is not be the case here in this chapter; it could be an extra-assumption. Broderick and Tchekhovskoy [2015] argued about the region close to the stagnation surface as a natural site of formation and acceleration of pairs. More and more simulations McKinney [2005a,b] explored the role of the loading of pairs in the behavior of astrophysical flows.

The purpose of this chapter is to present some properties of inflows from the self-similar model presented in Ch.(5). We also explore the variety of possible exchanges between these inflows and the black hole. Then we talk about the geometry we obtain for these inflows. Finally, we propose different solutions matching the inflow with the outflow where we evaluate the source terms required to produce this matching. We also study the different surface currents produced by different source terms.

8.2 Inflow model

The model of meridional self-similar General Relativistic Axi-symmetric Stationary Ideal Magneto-Hydrodynamic (GRASIMHD) flows develloped in Ch.(5) can be used to produce inflow solutions. We present here the main properties of the inflow solutions. Then we present three kind of inflows characterized by the type of exchange they have with the black hole. Finally, we discuss the geometry of the inflowsolutions.

8.2.1 Properties of inflow solutions

Following the construction of the model, we can notice that the modelisation of $\Psi_{\rm A}$ Eq.(5.56) could be written without loss of generality, using Eq.(5.37) and Eq.(5.40),

$$\Psi_{\rm A}(\alpha) = \frac{{\rm B}_\star h_\star^2 c\nu}{h_\star \xi_\star \gamma_\star c^2 \sqrt{\mu}} \sqrt{1+\delta\alpha} \tag{8.1}$$

Indeed for infalling material flowing into the system at the $\star$ point ${\rm V}_\star \leq 0$ then $\nu \leq 0$ and $\Psi_{\rm A} \leq 0$, which is equivalent to say that material is falling. Thus inflow solutions need to be searched in the range of parameter where $\nu \leq 0$. The whole thread of model development can be followed as for the construction of the outflow. Then the system of equation, Eqs.(5.107) with $\nu \leq 0$, is also valid to build Inflow solutions. Using Eq.(4.29), this equation taken at the zero-th order allows us to find a relation, similar to the one presented in McKinney [2005]; Tchekhovskoy and McKinney [2012]; Tchekhovskoy et al. [2011], or McKinney et al. [2012]. It is also experimentally presented by Zamaninasab et al. [2014]. They link the accretion mass rate falling into the black hole with the magnetic flux crossing the black hole horizon.
From our model, we find,

$$\boxed{\Phi_{\rm BH}^2 \approx \frac{\sqrt{\mu}\xi_\star\gamma_\star\left(1+\sqrt{1-\left(\frac{2l}{\mu}\right)^2}\right)}{|\nu| h_\star {\rm G}_{\mathscr{H}}^2} \dot{\rm M}_{\rm inf} c \left(\frac{r_s}{2}\right)^2} \tag{8.2}$$

where the infall mass rate $\dot{\rm M}_{\rm inf}$ is calculated with Eq.(4.29) and we neglect the source term along the infall fieldlines ($k_m = 0$). The magnetic flux of the black hole is simply the value of magnetic flux on equator horizon, $\Phi_{\rm BH} \hat{=} {\rm A}(r = r_{\mathscr{H}}, \pi/2)$. It should be emphasized that here the mass rate $\dot{\rm M}_{\rm inf}$ is the one of the produced pairs falling on the black hole horizon and not the accretion mass rate. The value of the proportionality factor between $\Phi_{\rm BH}$ and $\sqrt{\dot{\rm M}_{\rm inf} c \left(\frac{r_s}{2}\right)^2}$ is a function of the parameters of the model. If we can constrain by the observations this proportionality factor we can deduce the value of $\xi_\star$. In a first step we could take the value of this factor equals to 50 as in the work of Zamaninasab et al. [2014]. The Eq.(8.2) could concern only a fraction of the accreted mass since we do not take into account the matter accreted by the black hole in the equatorial plane.

Note that for $l = 0$, the system of equations, Eqs.(5.107), is invariant by the transformation $\nu \leftrightarrow -\nu$. This property implies that the GRMHD system around a Schwarzschild black hole is unchanged under the transformation $\mathbf{V} \leftrightarrow -\mathbf{V}$, which is not the case for a rotating black hole. Indeed the rotation and the induced Lense-thirring forces break the symmetry of the system. In the Kerr case, the GRASIMHD system, Eqs.(4.17), is invariant under these transformations,

$$\begin{cases} \mathbf{V} \leftrightarrow -\mathbf{V} \\ a \leftrightarrow -a \end{cases} \Longrightarrow \begin{cases} \nu \leftrightarrow -\nu \\ l \leftrightarrow -l \end{cases} \quad \text{or} \quad \{\mathbf{V}_p \leftrightarrow -\mathbf{V}_p \Longrightarrow \begin{cases} \nu \leftrightarrow -\nu \\ \lambda \leftrightarrow -\lambda \end{cases}, \tag{8.3}$$

It explains why in all case the transformation keeping the absolute value of all parameters $\nu \leftrightarrow -\nu$ needs to be accompanied with the transformation $\nu \leftrightarrow -\nu$ and $\lambda l \leftrightarrow -\lambda l$. Indeed, the Lense-Thirring force is proportionnal to $\omega {\rm V}^{\hat{\phi}}$. Using Eq.(4.44), the first expansion term in α of $\omega {\rm V}^{\hat{\phi}}$

(which is of the order required to build the model) is proportional to $\Psi_{\rm A}{\rm L}\omega/\Psi_{\rm A}\propto\frac{\lambda l}{\nu}$. The Noether energy flux of solution is,

$$\Psi_{\rm A}\mathscr{E}=\frac{h_\star^2{\rm B}_\star\nu c}{\sqrt{\mu}}\sqrt{1+\delta\alpha}\,(1+e_1\alpha) \tag{8.4}$$

Then for an inflow solution ($\nu\leq 0$), the energy flux is flowing into the black hole along the axis. The only possibility to have some energy extraction from the black hole, is to have negative values of the e_1 parameter and sufficient magnetic flux which crosses the black hole horizon.

The null energy condition Eq.(4.89) implies that for finding solutions which extract energy from rotational energy of the black hole, we need to have the angular momentum extracted from the black hole. Then we need to seek solution with $\lambda\geq 0$. The first integrals Eq.(8.4) and Eq.(5.58) insure that the zero energy condition $\Psi_{\rm A}\mathscr{E}\leq\Psi_{\rm A}\mathscr{L}\omega_{\mathscr{H}}$ is automatically satisfied on the axis. However for $e_1\leq 0$ exists an α value for which the zero energy condition no longer holds. We shall focus on solutions where the zero energy condition is satisfied everywhere into the horizon.

The equation Eq.(5.68) implies that toroidal velocity is null on the horizon. Equivalently Eq.(5.69) implies that the toroidal magnetic field becomes infinite on the horizon. Nevertheless, the charge current I, which is an invariant quantity remains finite on the horizon.

In inflow solutions, the critical points of the system are crossed when R decreases from the stagnation surface up to the horizon. On the horizon the Lorentz factor of fluid measured by Zero Angular Momentum Observer (ZAMO) becomes infinite to avoid the divergence of effective enthalpy ξ. Going upstream, the field lines reach the Alfvén point then the slow-magnetic point and finally the point of stagnation.

We need to analyze now how, our differential system of equations reacts when the integration point gets closer and closer to the horizon. Indeed using the Boyer-Lindquist coordinates system it is possible to meet some discontinuity arriving from the coordinate singularity on this hypersurface. The horizon surface is defined for the radius $\mathrm{R}_{\mathscr{H}}=\frac{\mu}{2}\left(1+\sqrt{1-\left(\frac{2l}{\mu}\right)}\right)$. Note that just outside of the horizon for $\mathrm{R}=\mathrm{R}_{\mathscr{H}}+d\mathrm{R}$, we have $\mathrm{X}_+\underset{\mathrm{R}\to\mathrm{R}_{\mathscr{H}}}{\sim}\mu\mathrm{R}_{\mathscr{H}}+2\mathrm{R}_{\mathscr{H}}d\mathrm{R}$ and $h_z^2\underset{\mathrm{R}\to\mathrm{R}_{\mathscr{H}}}{\sim}\frac{2}{\mu}\frac{\sqrt{1-a^2}}{1+\sqrt{1-a^2}}d\mathrm{R}$. First of all, note that ϵ being constant, Eq.(5.90), is equivalent to,

$$\epsilon\underset{\mathrm{R}\to\mathrm{R}_{\mathscr{H}}}{\sim}\frac{1}{h_z^2}\left[-\frac{\mathrm{M}^4}{\mathrm{G}^2h_\star^4\mathrm{X}_+}\left(1+(\kappa-2m_1)\frac{\mathrm{X}_+}{\mathrm{G}^2}-\frac{l^2}{\mathrm{X}_+}\right)-\frac{\nu^2}{\mu}\left(2e^1-2m^1+\delta-\kappa\right)-\frac{\nu^2l^2\mathrm{G}^2}{\mu^3\mathrm{R}_{\mathscr{H}}^2}+2\lambda^2\left(\frac{\Lambda^2\mathrm{N}_{\rm B}}{\mathrm{D}}+\frac{\bar{\omega_z}}{\lambda}\right)\right]$$
$$+\lambda^2\left(\frac{\Lambda\mathrm{N}_{\rm V}}{h_\star\mathrm{GD}}\right)^2 \tag{8.5}$$

Since ϵ is constant, it implies that there is a constant ϵ' such that,

$$-\frac{\mathrm{M}^4}{\mathrm{G}^2h_\star^4\mathrm{X}_+}\left(1+(\kappa-2m_1)\frac{\mathrm{X}_+}{\mathrm{G}^2}-\frac{l^2}{\mathrm{X}_+}\right)-\frac{\nu^2}{\mu}\left(2e^1-2m^1+\delta-\kappa\right)-\frac{\nu^2l^2\mathrm{G}^2}{\mu^3\mathrm{R}_{\mathscr{H}}^2}+2\lambda^2\left(\frac{\Lambda^2\mathrm{N}_{\rm B}}{\mathrm{D}}+\frac{\bar{\omega_z}}{\lambda}\right)\underset{\mathrm{R}\to\mathrm{R}_{\mathscr{H}}}{\sim}\epsilon' h_z^2 \tag{8.6}$$

To see if our system Eqs.(5.107) contains a singularity when the solution approaches to the black hole horizon. We need to verify the continuity of $\mathscr{N}_{\mathrm{M}^2}$ and $\mathscr{N}_{\rm F}$ near the horizon. Using Eq.(5.110), and grouping terms proportional to $1/h_z^2$ we get,

$$\mathscr{N}_{\mathrm{M}^2}=\mathrm{R}_{\mathscr{H}}\frac{d\mathrm{M}^2}{d\mathrm{R}}\mathscr{D}_{\mathscr{H}}\underset{\mathrm{R}\to\mathrm{R}_{\mathscr{H}}}{\sim}\frac{\mu h_\star^4\mathrm{DRG}^2}{2h_z^2\mathrm{X}_+\mathrm{M}^2}\left[-\frac{\mathrm{M}^4}{\mathrm{G}^2h_\star^4\mathrm{X}_+}\left(1+(\kappa-2m_1)\frac{\mathrm{X}_+}{\mathrm{G}^2}-\frac{l^2}{\mathrm{X}_+}\right)-\frac{\nu^2}{\mu}\left(2e^1-2m^1+\delta-\kappa\right)\right.$$
$$\left.-\frac{\nu^2l^2\mathrm{G}^2}{\mu^3\mathrm{R}_{\mathscr{H}}^2}+2\lambda^2\left(\frac{\Lambda^2\mathrm{N}_{\rm B}}{\mathrm{D}}+\frac{\bar{\omega_z}}{\lambda}\right)\right]+\mathrm{R}_{\mathrm{M}^2} \tag{8.7}$$

The first term is proportional to the term of Eq.(8.6), then

$$\mathscr{N}_{\mathrm{M}^2} \underset{\mathrm{R}\to\mathrm{R}_{\mathscr{H}}}{\sim} \frac{\mu h_\star^4 \mathrm{D}\mathrm{R}\mathrm{G}^2\epsilon'}{2\mathrm{X}_+\mathrm{M}^2} + \mathrm{R}_{\mathrm{M}^2} \tag{8.8}$$

Thus $\mathscr{N}_{\mathrm{M}^2}$ is continuous. $\mathscr{D}$ given in Eq.(5.108), remains continuous on the horizon. Then $\frac{d\mathrm{M}^2}{d\mathrm{R}}$ remains continuous when we approach to the black hole horizon. Nevertheless $\mathscr{N}_{\mathrm{F}} \underset{\mathrm{R}\to\mathrm{R}_{\mathscr{H}}}{\sim} \mathrm{Cst}/h_z^2$ is not continuous when we reach the horizon. Some dependance implies that $\mathrm{F} \underset{\mathrm{R}\to\mathrm{R}_{\mathscr{H}}}{\sim} \ln(\mathrm{R}-\mathrm{R}_{\mathscr{H}})$, then the opening angle factor in Eq.(5.52) $h_z\mathrm{F} \underset{\mathrm{R}\to\mathrm{R}_{\mathscr{H}}}{\sim} \sqrt{\mathrm{R}-\mathrm{R}_{\mathscr{H}}}\ln(\mathrm{R}-\mathrm{R}_{\mathscr{H}}) \underset{\mathrm{R}\to\mathrm{R}_{\mathscr{H}}}{\longrightarrow} 0$. The field line enters radially into the black hole horizon, and we have $\mathrm{B}^{\hat{\theta}} = \mathrm{V}^{\hat{\theta}} = 0$ on the horizon. The function $\mathrm{G}^2 \underset{\mathrm{R}\to\mathrm{R}_{\mathscr{H}}}{\sim} \mathrm{G}^2_{\mathscr{H}}$ has a limit on the horizon. Let us have a look to the differential equation Eq.(5.111). The function representing the pressure Π can be smoothier on the black hole horizon, only if the velocity on the axis reaches c in the ZAMO frame at the horizon. To keep finite enthalpy ξ on the horizon, the convergence of this velocity has to be such as $1-\beta^2_{\mathrm{ax}} \underset{\mathrm{R}\to\mathrm{R}_{\mathscr{H}}}{\sim} h_z^2$. Thus for a finite value of enthalpy at the horizon, the factor $\nu^2 h_\star^4 - \frac{\mu\mathrm{M}^4}{\mathrm{G}^4} \underset{\mathrm{R}\to\mathrm{R}_{\mathscr{H}}}{\sim} h_z^2$, and the derivative $\frac{d\Pi}{d\mathrm{R}} \underset{\mathrm{R}\to\mathrm{R}_{\mathscr{H}}}{\sim} \frac{1}{h_z^2}$. Then the pressure function Π evolves with a logarithmic dependance $\Pi \underset{\mathrm{R}\to\mathrm{R}_{\mathscr{H}}}{\sim} \ln(\mathrm{R}-\mathrm{R}_{\mathscr{H}})$. The parameters shall be adapted to obtain such a solution. The property of Eqs.(5.107) allows to integrate as close as we want of the horizon. The solution can get as close as we ask from the horizon.

An another way to avoid the horizon "singularity" without changing fundamentally the model is to change coordinates. Keeping the time coordinate, for example using $\zeta(\mathrm{R})$ such that $d\zeta = \frac{d\mathrm{R}}{h_z^4}$. It may help us to transform and smooth the system of Eqs.(5.107).

8.2.2 Energetic exchange on the black hole horizon

We present now three solutions, for which the exchange of energy of the black hole differs in the nature of energetic flux decomposition Eqs.(4.88). First solution is a solution in which there is no extraction. The exchange is dominated by Φ_{M}, the matter falling everywhere on the black hole. The second contains some zone with out flowing of Noether energy (extraction). This extraction is dominated by the Lense-Thirring energy flux Φ_{LT}. The last presented solution gets also some zone where the Noether energy flux flows out of the horizon, but is dominated by the Poynting flux Φ_{EM}.

I1 : A solution dominated with negative energy flux on the horizon

First, we look at a physically solution. This means that the stress-energy tensor respects the null energy condition everywhere. We also ask a positive value of the isorotation function. We find the following set of parameters for solution **I1**,

	λ	κ	δ	ν	ℓ	μ	$\Pi_\star$	e_1
I1	0.036	0.468	0.075	-1.79	0.12	0.442	1.4	-0.21

Table 8.1 – Parameter values (with 10^{-3} accuracy) for solution **I1**

First of all, we present the evolution along the inflow of the four radial function $\mathrm{M}^2, \mathrm{G}^2, \mathrm{F}, \Pi$ which characterize the solution.

On Fig.(8.2) note that, as expected, the expansion factor $h_z\mathrm{F}$ reaches 0 on the black hole horizon. This confirms that the poloidal field lines are radial when they enter the horizon. The stagnation radius is around $3.17\mathrm{R}_{\mathscr{H}}$. The flux tube in Fig.(8.1), is in expansion ($\mathrm{R} \to \mathrm{G}^2$ is

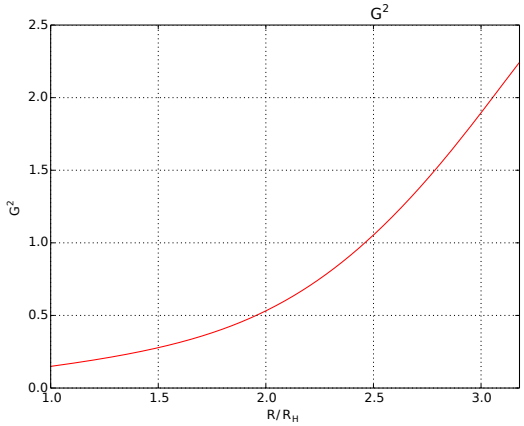

Figure 8.1 – Value of the flux tube radius function G^2 as function of the radius for the solution **I1**

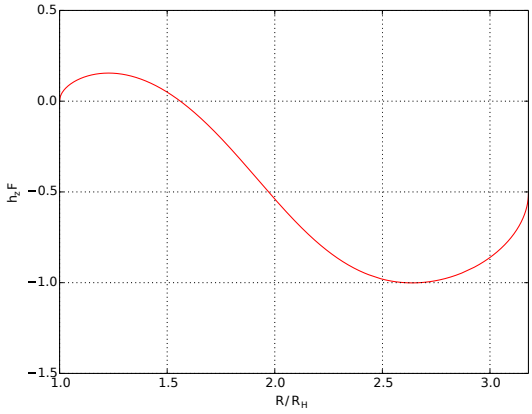

Figure 8.2 – Plot of the expansion factor function $h_z\mathrm{F}$ as a function of the radius for the solution **I1**

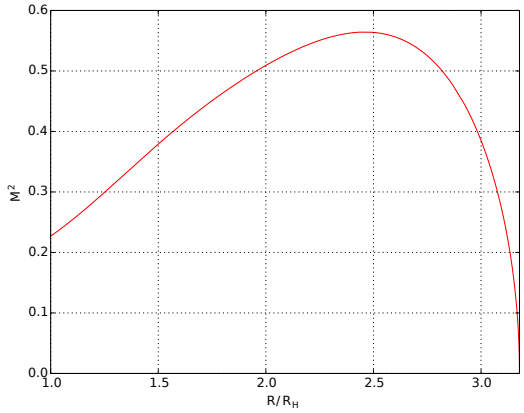

Figure 8.3 – Plot of the Alfvén polar Mach number M^2 as a function of the radius for the solution **I1**

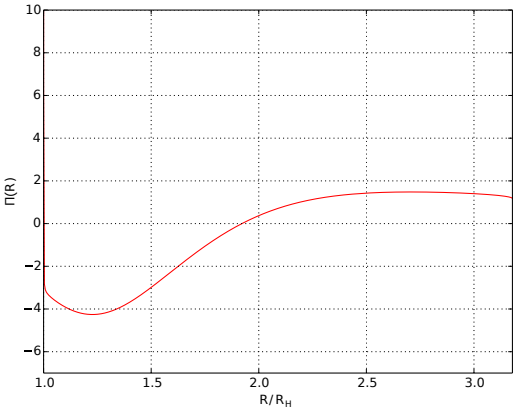

Figure 8.4 – Plot of the polar Mach number Π as function of the radius for the solution **I1**

increasing with) in the whole flow. Near the horizon the expansion factor varies between 0 and $0{,}2$, which corresponds, Eq.(5.52), to positive opening angles. The expansion is weaker than the radial expansion of the tube. For $\mathrm{R} \geq 1.6\mathrm{R}_{\mathscr{H}}$ the expansion factor becomes negative. The expansion of the tube is stronger than the radial expansion. This strong expansion leads to the formation of a magnetosphere.

The Alfvénic Mach number M^2, see Fig.(8.3), is 0 on the axis for the stagnation radius and starts to increase, following the flow ($\mathrm{R}\searrow$). Then at $\mathrm{R} \sim 2.5\mathrm{R}_{\mathscr{H}}$ it decreases to reach a finite value on the horizon. The evolution of M^2 and G^2 is such that the velocity of the plasma reaches almost the speed of light ($\gamma \sim 20$) on the axis when it enters the horizon. See Fig.(8.4). From the horizon going upstream ($\mathrm{R}\nearrow$) along the axis, the pressure Π decreases. The pressure slows down the accelerating of the flow. Then from $\mathrm{R} \sim 1.25\mathrm{R}_{\mathscr{H}}$ the pressure increases. The pressure is driving and accelerates the flow. Finally for $\mathrm{R} \sim 2.75\mathrm{R}_{\mathscr{H}}$, the pressure decreases again.

Now let us analyze the role of the different forces in the flow. As for the dynamical analysis of the Outflow Sec.(7.2), we project the forces parallel (longitudinal forces) or orthogonally (transverse forces) to the flow. We choose the projection vector aligned with the flow. So a longitudinal force accelerating the flow is positive in the following graphs. For transverse forces, we choose as projection vector the unit vector perpendicular to the flow tube directed inside it. Thus any transverse forces pushing the matter towards the axis (collimation) is positive in the following

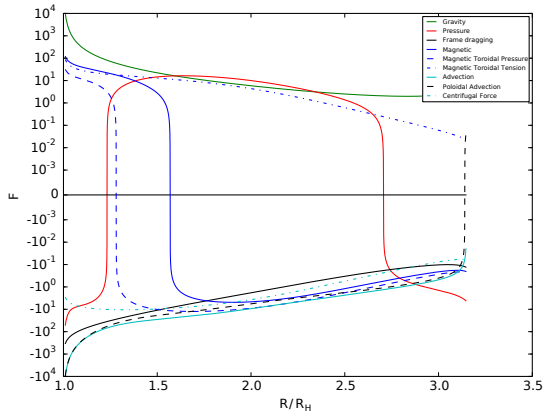

Figure 8.5 – Longitudinal Forces on a poloidal field line plotted in orange in Fig.(8.25) for the solution **I1**

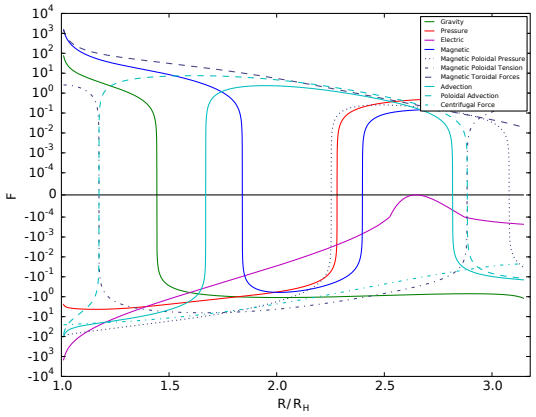

Figure 8.6 – Transversal Forces on a poloidal field line represented in orange in Fig.(8.25) for solution **I1**

graphs.

We see in Fig.(8.5) the evolution of the different forces on a field line. Positive values correspond to forces which accelerate the flow falling down into the horizon. The force driving the fall is mainly gravity, not surprisingly. There is also the pressure forces in the phase where the Π function decreases. The decrease of the pressure is probably due to the acceleration in the fall. The toroidal magnetic tension is also a driving force as the flow tubes are tightened. Surprisingly the toroidal magnetic pressure, mainly a braking force in the flow, becomes at some radius a driving force. Indeed the variation of the effective toroidal magnetic pressure, i.e. $h\mathrm{B}^{\hat{\Phi}}$, starts to decrease around $1.25\mathrm{R}_{\mathscr{H}}$. This decrease is probably due to the change of the opening angle factor which becomes weaker than the radial expansion in this region.

The main force that slows down the gas is its own inertia. Lense-Thirring forces is one order lower close the black hole. Weaker, in the middle of the flow, the magnetic forces start acting against the fall, mainly because of the toroidal pressure. Then there is a decreasing of the toroidal pressure $h\mathrm{B}^{\hat{\Phi}}$ along the flow. This decrease involves a change in the regime of the magnetic forces that opposes the acceleration of the flow. It becomes a driving force close to the black hole.

We see on Fig.(8.6) the evolution of the different transversal forces along a given field line. In the transverse equilibrium, the main force opening the tube is the force of gravity, when the flaring of the lines is greater than radial. The second forces opening the tube is the electric force, mainly in the environment of the horizon, where it becomes the main force. The electrical force is cancelled at the radius where the isorotation frequency is equal to that of the coordinate shift. The cancellation of the electric field also leads to the cancellation of the charge density measured by the ZAMO. This property of the electric field motivates some work on the gap solutions (Levinson and Segev [2017] and Ford et al. [2017]). Indeed as discussed in the introduction of Sec.(3.1.8), a gap region could exist since the pairs production rate is not strong enough to obtain the Goldreich-Julian density. This density is the one obtained by the electric field for an ideal conductor medium. Then the ideal conductivity assumption couldn't be kept in this region and we obtain an electric field component parallel to the flow. This kind of situation could occur where the Goldreich-Julian density is cancelled and this surface is called the null surface. The electric field cancellation in our model is equivalent to this null surface. Levinson and Segev [2017] showed that the existence of this gap couldn't stay steady. The poloidal magnetic tension acts as a force bringing the poloidal field lines back to their radial situation, so this force opens the tube when it widens faster than a radial tube and vice versa. Centrifugal force is, as usual, a force that pushes to open the tube where infall occurs.

The force pushing the inflow towards the axis of rotation is mainly the strength of the toroidal magnetic field. Then comes the poloidal advection force in the part of the flow where the tube

opening rate is faster than the radial tube opening rate (flaring tubes). The transverse pressure force changes sign. Indeed, while at the top of the flow, close to the stagnation point, the pressure is lower on the axis, it pushes the material into the axis. The drop and then the change of sign from Π eventually reverses this situation. The pressure becomes greater on the axis and contributes to the opening of the tubes close to the black hole.

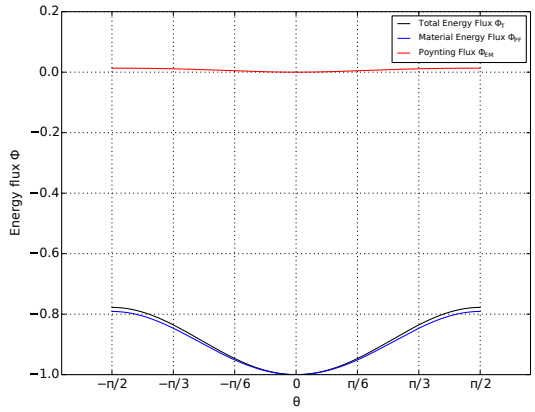

Figure 8.7 – Plot of the perfect fluid $\Phi_{\rm PF}$, the electro-magnetic $\Phi_{\rm EM}$ and the total flux $\Phi_{\rm T}$ normalized energy fluxes by unit of magnetic flux on the black hole horizon as a function of the latitude angle θ for solution **I1**. All the flux are normalized by the total flux on the polar axis $\frac{\Phi_{(A)}}{|\Phi_{\rm T}(0)|}$

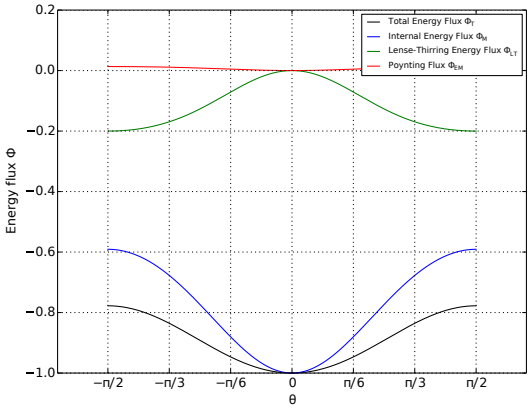

Figure 8.8 – Plot of the inertial $\Phi_{\rm M}$, Lense-Thirring $\Phi_{\rm LT}$, electro-magnetic $\Phi_{\rm EM}$ and the total flux $\Phi_{\rm T}$ normalized energy fluxes by unit of magnetic flux on the black hole horizon as a function of the latitude angle θ for solution **I1**. All the flux are normalized by the total flux on the polar axis $\frac{\Phi_{(A)}}{|\Phi_{\rm T}(0)|}$

In Fig. (8.7), we see that the energy fluxes of this solution on the horizon of the black hole are dominated by the matter. In comparison, the Poynting flux remains extremely low. This is not surprising considering that this flow has an isorotation of $\Omega \sim 6.2\%\omega_{\mathscr{H}}$. The flow also falls into the black hole in the direction of its rotation axis, so the Lense-Thirring flux is also negative. This type of solution, therefore, gives energy to the black hole. The mass of the black hole grows. Nevertheless, $\lambda \geq 0$ so the black hole gives angular momentum to the MHD field, its own angular momentum decreases Eq.(4.85). We are in a configuration such that anywhere on the horizon $\Psi_{\rm A}\mathscr{E} \leq 0 \leq \Psi_{\rm A} {\rm L}\omega_{\mathscr{H}}$.

I2 : A solution dominated by fluid type extraction

From the solution **I1**, we search, using the tools developed in Sec.(6.4) to move in the parameter space, to obtain a solution with $V^{\hat{\Phi}}$ positive on the equator of the horizon. We also seek an energy flux dominated by $\Phi_{\rm LT}$, while keeping the null energy condition. We have obtained the following parameter set for solution **I2**,

	λ	κ	δ	ν	ℓ	μ	$\Pi_\star$	e_1
I2	0.392	1.341	0.355	-1.562	0.17	0.807	0.859	-0.349

Table 8.2 – Parmameter values (with 10^{-3} accuracy) for solution **I2**

The stagnation point of this inflow is closer to the horizon ${\rm R} \approx 1.503{\rm R}_{\mathscr{H}}$. We see in Fig.(8.9), as for the solution **I1**, the cylindrical section of the flow tubes ${\rm G}^2$ is growing monotonously as we move upstream (${\rm R}\nearrow$). Nevertheless, Fig.(8.10) unlike **I1** this solution, does not have a region

in the black hole environment where the opening angle factor $h_z\mathrm{F}$ is positive. This implies that everywhere in the flow, the expansion of the tubes is faster than the radial expansion.

The Figs.(8.11, 8.12) for the Alfvénic Mach number on the axis M^2 and the pressure factor Π have quite similar evolution as for the solution **I1**.

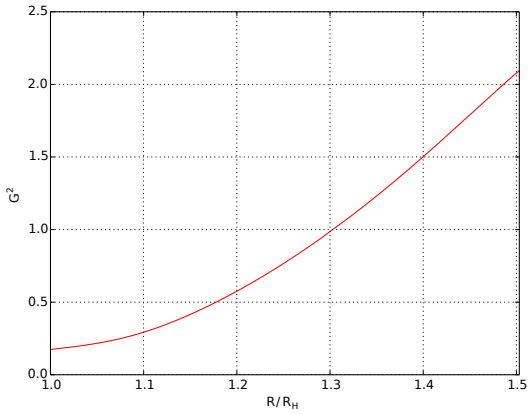

Figure 8.9 – Value of the flux tube radius function G^2 as function of the radius for the solution **I2**

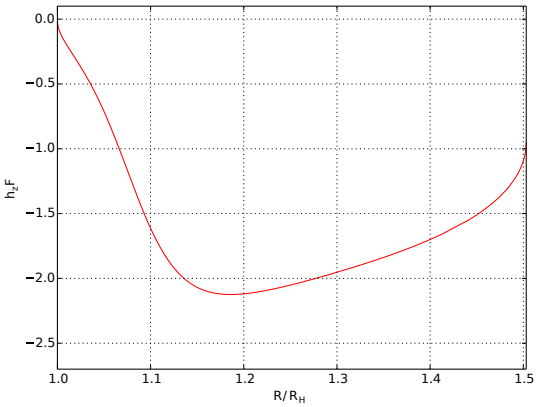

Figure 8.10 – Plot of the expansion factor function $h_z\mathrm{F}$ as a function of the radius for the solution **I2**

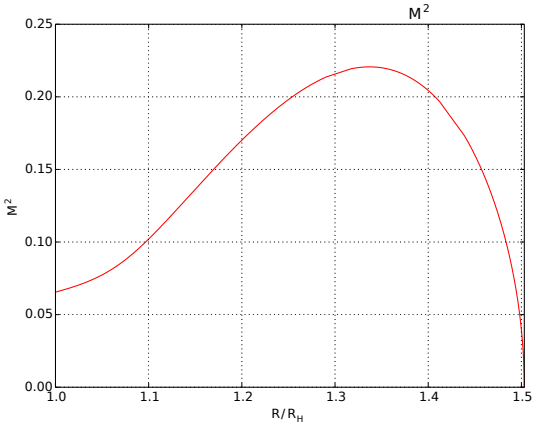

Figure 8.11 – Plot of the Alfvén polar Mach number M^2 as a function of the radius for the solution **I2**

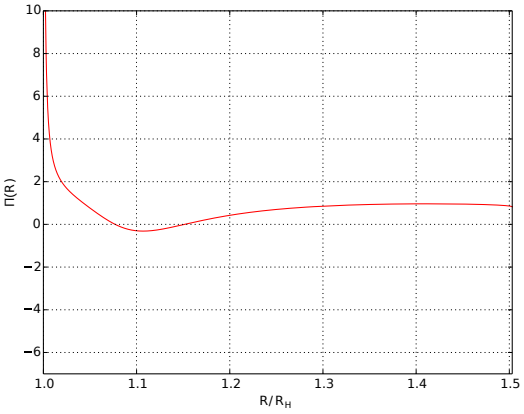

Figure 8.12 – Plot of the polar Mach number Π as function of the radius for the solution **I2**

About flow dynamics, let us first examine the forces along the flow, see Fig. (8.13). These are quite similar to those of the solution **I1**, but it is interesting to note the change in sign of the toroidal velocity along the flow. Cayatte et al. [2014] gave a criterion of counter rotation in GRASIMHD outflows, that can be extended to inflow solutions. This reversal of the toroidal velocity cancels the centrifugal force and is associated with a reversal of the frame dragging force. Remember that this graph concerns the longitudinal forces along the lines, shown in orange in Fig. (8.26).

The transverse forces are very different due to the very fast expansion in this **I2** solution of the flow tubes. Indeed, such an opening angle factor $h_z\mathrm{F}$ maintains the gravitational force as a force contributing to the opening of the tubes. The electric force does not cancel out, in fact, this flow is so close to the black hole that the isorotation frequency is constantly lower than the pulsation of coordinate shift. In this case, the cancellation of the electric field must be above the stagnation point. The pressure changes sign twice due to the faster increase of Π at the entry into

the horizon Fig.(8.12). Since the tube opening rate is constantly faster than the radial opening, the poloidal magnetic tension does not change sign and contributes to the opening of the tubes.

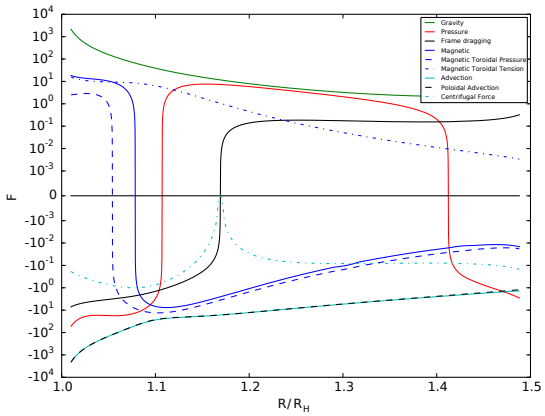

Figure 8.13 – Longitudinal Forces on a poloidal field line plotted in orange in Fig.(8.26) for the solution **I2**

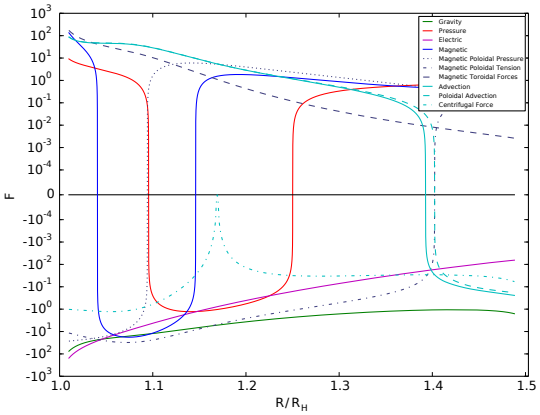

Figure 8.14 – Transversal Forces on a poloidal field line represented in orange in Fig.(8.26) for solution **I2**

Concerning the distribution of energy flux between the fluid and the electromagnetic fields on the horizon of the black hole, see Fig. (8.15), the solution is, as before, clearly dominated by the flux of the fluid. Indeed, the isorotation is relatively low, $\Omega = 9.6\%\omega_{\mathscr{H}}$. Nevertheless, we note that the flux $\Phi_{\rm PF}$ changes sign around $\pi/3$. The decomposition of the flux $\Phi_{\rm PF} = \Phi_{\rm M} + \Phi_{\rm LT}$ Fig.(8.16) shows that the Lense-Thirring flux changes sign and becomes quite dominant near the equator.

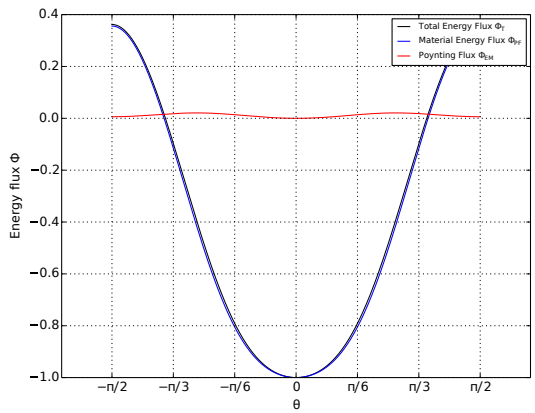

Figure 8.15 – Plot of the perfect fluid $\Phi_{\rm PF}$ and the electro-magnetic $\Phi_{\rm EM}$ and the total flux $\Phi_{\rm T}$ normalized energy fluxes by unit of magnetic flux on the black hole horizon as a function of the latitude angle θ for solution **I2**. All the flux are normalized by the total flux on the polar axis $\frac{\Phi(\rm A)}{|\Phi_{\rm T}(0)|}$

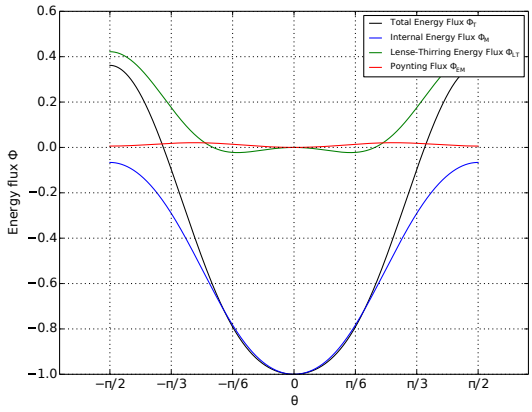

Figure 8.16 – Plot of the inertial $\Phi_{\rm M}$, Lense-Thirring $\Phi_{\rm LT}$ and electro-magnetic $\Phi_{\rm EM}$ and the total flux $\Phi_{\rm T}$ normalized energy fluxes by unit of magnetic flux on the black hole horizon as a function of the latitude angle θ for solution **I2**. All the flux are normalized by the total flux on the polar axis $\frac{\Phi(\rm A)}{|\Phi_{\rm T}(0)|}$

This kind of solution is therefore dominated by the Lense-Thirring flux $\Phi_{\rm LT}$ near the equator plane. It respects the zero energy condition everywhere. Nevertheless, it should not be forgotten that the model is the result of a two-order expansion in latitude close to the axis. So the solution is restricted to small angles among the axis. Nevertheless, it seem possible under specific conditions that the inflow into the black hole activates the Penrose process.

I3 : A solution dominated by Poynting type extraction

The goal to find the last inflow solution is to increase the extraction of Poynting flux. We move in the parameter space by increasing $\Omega/\omega_{\mathscr{H}}$ while keeping the angle of the extraction nearly constant, but also by keeping the zero energy condition. We also tried to keep the stagnation radius as high as possible during this parametric exploration. Indeed, the stagnation radius tends to decrease sharply as we increase $\Omega/\omega_{\mathscr{H}}$. In practice, other constraints need to be added, but this is a purely technical issue that we will not discuss here. Finally, the set of parameters for solution **I3** is,

	λ	κ	δ	ν	ℓ	μ	$\Pi_\star$	e_1
I3	0.388	5.898	0.259	-1.443	0.25	0.978	0.275	-0.555

Table 8.3 – Parmameter values (with 10^{-3} accuracy) for solution **I3**

The main functions which characterize the solution **I3** are represented in Fig.(8.17, 8.18, 8.19, 8.20). They have the same kind of evolution as the one for the solution I2. The stagnation radius is really close to the black hole, $\mathrm{R_{st}} \approx 1.175\mathrm{R}_{\mathscr{H}}$ horizon. Thus, the expansion angle factor is lower ($h_z\mathrm{F}$ reaches -2.5) than for the solution **I2**. Then the poloidal fieldlines open themselves faster. Also note that the pressure function Π stays positive. It implies that the pressure remains a force which pushes the material towards the axis, everywhere in the flow.

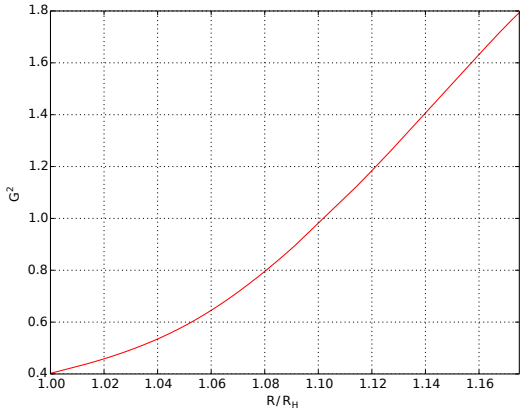

Figure 8.17 – Value of the flux tube radius function G^2 as function of the radius for the solution **I3**

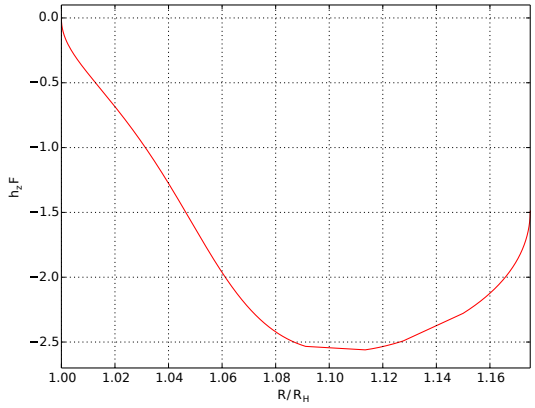

Figure 8.18 – Plot of the expansion factor function $h_z\mathrm{F}$ as a function of the radius for the solution **I3**

We look at the evolution of the longitudinal equilibrium of the forces along the field lines, Fig.(8.21). As for the previous solutions, gravity is the main force accelerating the flow. We can see that unlike the previous flow, the pressure at the top of the flow is already a force that accelerates the flow. Then the pressure variation reverses from the middle of the fall and counteracts the acceleration of the flow towards the horizon. As for **I2**, we observe a change in the sign of the toroidal velocity.

Regarding the transverse forces Fig.(8.22), we have a situation where the opening forces of the tubes are dominated, as in the other solutions, by the gravity and the electric force. Conversely the forces pushing the mater on the axis are dominated by the poloidal advection and the pressure, which is not the case for the solution **I2** and **I3**.

By obtaining **I3**, where $\Omega \approx 0.5\omega_{\mathscr{H}}$, we increase the values of the Poynting flux Eq.(4.88) with respect to isorotation. We can continue to improve this value by working on the Mach number values on the horizon, or increasing α_{BH}. We obtain, Fig.(8.23), a solution where the Poynting

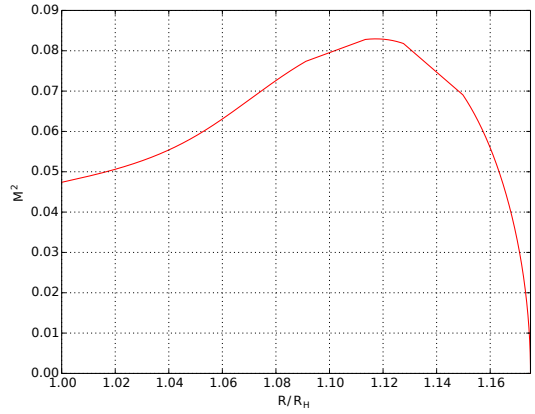

Figure 8.19 – Plot of the Alfvén polar Mach number M^2 as a function of the radius for the solution **I3**

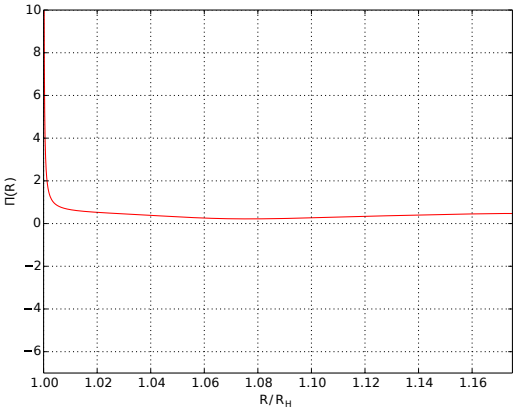

Figure 8.20 – Plot of the polar Mach number Π as function of the radius for the solution **I3**

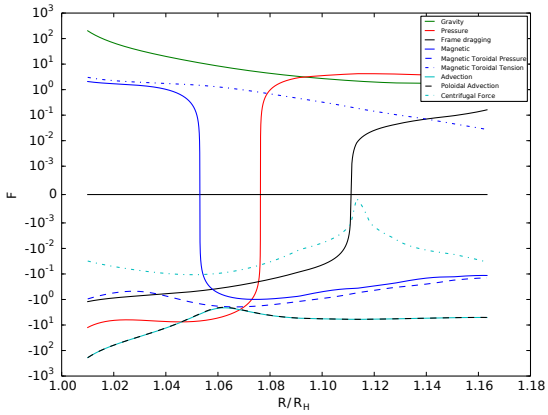

Figure 8.21 – Longitudinal Forces on a poloidal field line plotted in orange in Fig.(8.27) for the solution **I3**

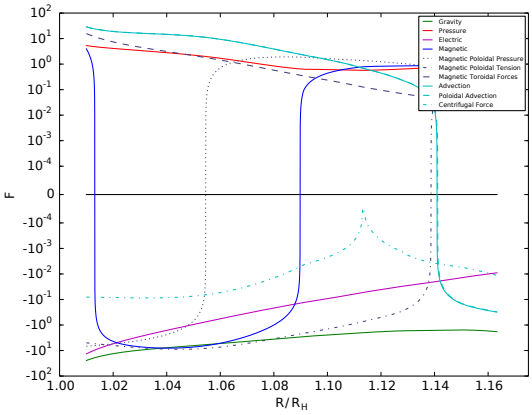

Figure 8.22 – Transversal Forces on a poloidal field line represented in orange in Fig.(8.27) for solution **I3**

flux exceeds the matter flux for latitudes on the horizon around $\pi/4 - \pi/3$. The material flux increases on the upper hand over the poles and the on equator at the horizon.

The decomposition of the perfect fluide flux Fig. (8.24) shows that, in this solution the Lense-Thirring flux is absolutely not negligible. And it remains as in solution **I2** dominating at the equator while it is the internal energy flux that dominates on the poles.

We see that our model is able to produce solutions where the Poynting flux becomes the main component of the energy exchanges with the black hole. The rotational energy of this solution, can feed energy to the GRMHD fields via either the Lense-Thirring flux (Solution I2), or via the Poynting flux (Solution I3). This supply of energy flux can be turned into another type of energy flux along the flow.

8.2.3 Geometry of inflow solutions

During our description of the three inflow solutions characterized by a different types of energy exchange with the black hole, we have shown that the flow geometry is related to the the dynamical behavior.

It seems that in our model, all inflow solutions are characterized by a high expansion rate of the magnetic flux tubes, $h_z \mathrm{F} \leq 2$, between the black hole horizon and the stagnation radius.

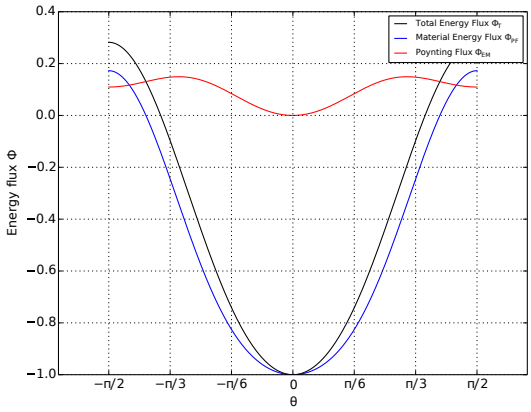

Figure 8.23 – Plot of the perfect fluid $\Phi_{\rm PF}$ and the electro-magnetic $\Phi_{\rm EM}$ and the total flux $\Phi_{\rm T}$ normalized energy fluxes by unit of magnetic flux on the black hole horizon as a function of the latitude angle θ for solution **I3**. All the flux are normalized by the total flux on the polar axis $\frac{\Phi_{(\rm A)}}{|\Phi_{\rm T}(0)|}$

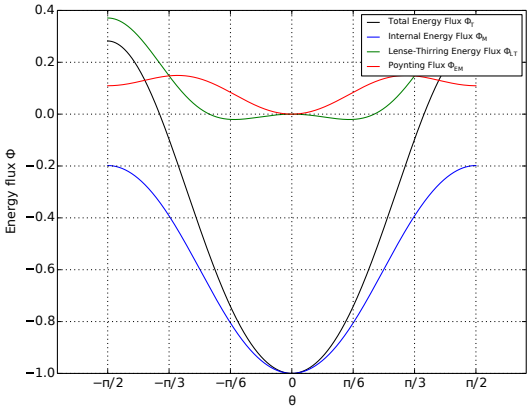

Figure 8.24 – Plot of the inertial $\Phi_{\rm M}$, Lense-Thirring $\Phi_{\rm LT}$ and electro-magnetic $\Phi_{\rm EM}$ and the total flux $\Phi_{\rm T}$ normalized energy fluxes by unit of magnetic flux on the black hole horizon as a function of the latitude angle θ for solution **I3**. All the flux are normalized by the total flux on the polar axis $\frac{\Phi_{(\rm A)}}{|\Phi_{\rm T}(0)|}$

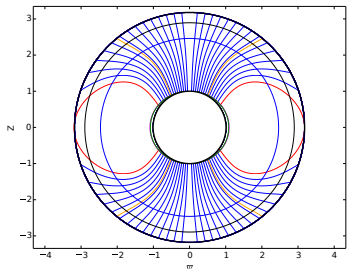

Figure 8.25 – Geometry of poloidal field line of solution **I1**

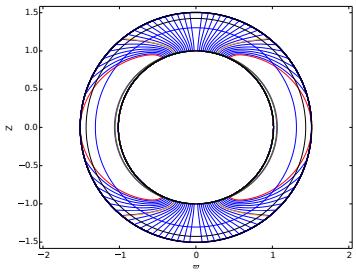

Figure 8.26 – Geometry of poloidal field line of solution **I2**

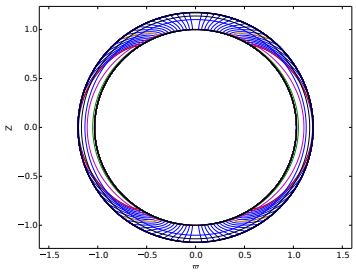

Figure 8.27 – Geometry of poloidal field line of solution **I3**

Nevertheless regarding the geometry, we can put aside the solution **I1** where the region close to the horizon has a slower flux tube expansion than the radial expansion $h_z{\rm F} \geq 0$. And on the other hand for the solutions **I2** and **I3**, in any position in the flow the opening of the tubes is faster than the radial expansion, $h_z{\rm F} \leq 0$.

In the case of solution **I1**, we see that the change in the tube opening regime results in a change in the role of gravity, as we increase or decrease the cross-sectional area of the flow tubes. The force of gravity is mainly radial Eq.(5.101), although the non radial gravity $\mathcal{Z}_{\rm G}$ due to the rotation of the black hole pushes the tubes to open. Gravity tends to align the flow with the direction of its field, $\mathbf{a} = \mathbf{D}\ln h$, which is the case for our tube at the horizon since $h_z{\rm F}|_{\mathscr{H}} = 0$. When the flow is pushed outwards by the other transverse forces, it pushes the tubes inwards and vice versa. Gravity tends to stabilize the geometry. While the electric force is still trying to push the tubes out, the toroidal magnetic forces have the opposite action. They always push the tubes inwards. From a dynamical point of view, the essential change between inflow **I1**, on the one hand, and inflows **I2** and **I3**, on the other hand seems to be the absence of the cancellation of the electric field. It implies for solution **I2** and **I3** a reinforcement of the work of the forces pushing the flow tubes towards the outside which could explain the differences of the $h_z{\rm F}$ regime between the two groups.

From a kinetic point of view, the positivity of $h_z{\rm F}$ near the horizon for solution **I1** implies the

formation of a torus represented in red (8.25) on the field line. The material inside the torus is trapped or accreted. Nevertheless, it should not be forgotten that the results of this model are questionable at high latitudes near the equatorial plane. Especially when the quantification of the stationarity brought by the expansion in latitude is not done. Indeed, for all solutions, the lines connecting the equator to the horizon can only be physically explained by an accretion from the disk or by a source term in the equatorial plane. In figures Figs.(8.26, 8.27) the red line represents the last line that could be fed by the plasma from the stagnation point. The mater inside the red field line of this inflowing "magnetosphere" may be matter coming from an accretion disk surronding the black hole in the equatorial plane.

8.3 Conditions for matching inflow/ouflow

Now, we build a "complete" solutions, including both the inflow (falling flow) and the outflow from the system (spine jet). Such solutions are very interesting because some lines of the magnetic field possibly connect the horizon from the black hole to infinity. Thus the energy exchanges between the black hole and the GRMHD fields can explain a fraction of the energy transported in these lines to infinity.

The easiest way, to build a "complete" solution is to match an inflow solution with an outflow solution in the frame of our model. These solutions have the same stagnation radius. We therefore consider two solutions of the model built from the GRASIMHD, without sources in their flow except on the stagnation radius. The matching between these two solutions is only possible with the presence of a source term at the interface. We calculate here the minimum necessary conditions allowing the matching between these solutions.

8.3.1 The continuity relation and the surface current

In order to describe the MHD field, from the horizon to infinity we need to use a matter source. Indeed this means that the loading terms k_n and $\mathbf{k}$ are null except at the stagnation radius of the solution. In fact, the shape of these loading terms are adapted to the mechanism of pair creation/annihilation from neutral particles. The way they are included in the basic equations, Eq. (4.17) does not directly disturb Maxwell's equations. The electro-magnetic field is only due to the charge four-current. Nevertheless the loading term on this thin layer, acting directly on others fields can be at the origin of surface charge four current of our gas in the layer which will imply some continuity-discontinuity of the electromagnetic fields.

First let us consider some thin layer at stagnation radius $r \in \left[r_{\rm sta} - \frac{\Delta_r}{2}; r_{\rm sta} + \frac{\Delta_r}{2} \right]$ where loading term $k_m, \mathbf{k}$ aren't null. The Maxwell equations without source (Maxwell-Flux) and (Maxwell-Faraday) ensures the continuity of the magnetic flux, Eq.(4.18), and the continuity of the isorotation function, Eqs.(4.24, 4.17,), along each magnetic field line,

$$\begin{cases} \mathbf{B}_p \cdot \mathbf{D}\mathrm{A} = & 0 \\ \mathbf{B}_p \cdot \mathbf{D}\Omega = & 0 \end{cases} \quad \underset{\Delta_r \to 0}{\Rightarrow} \quad \begin{cases} \mathrm{A}_{\rm out}(\mathrm{R}_{\rm exo}, \theta) = \mathrm{A}_{\rm in}(\mathrm{R}_{\rm exo}, \theta) \\ \Omega_{\rm out}(\mathrm{R}_{\rm exo}, \theta) = \Omega_{\rm in}(\mathrm{R}_{\rm exo}, \theta) \end{cases} \tag{8.9}$$

The surface current is included in the stagnation sphere. Then using Maxwell-Ampere equation, it implies that the magnetic field component $\mathrm{B}^{\hat{r}}$ normal to the layer (here a sphere) needs to be continuous, and that,

$$\partial_\theta \mathrm{A}_{\rm out}(\mathrm{R}_{\rm exo}, \theta) = \partial_\theta \mathrm{A}_{\rm in}(\mathrm{R}_{\rm exo}, \theta) \tag{8.10}$$

Thus, using Maxwell-Gauss, the meridional electric field $\mathrm{E}^{\hat{\theta}}$ is also continuous across the layer surface with loading terms. We may have discontinuity of $\partial_r \mathrm{A}$ at the sheet layer. This

discontinuity is source of toroidal surface flux current $\mathrm{J}_\sigma^{\hat{\phi}}$ and surface density of charge σ_e. From some integration of Maxwell-Gauss and Maxwell-Ampere Eq.(4.17), we get,

$$\left\{\begin{array}{rl} -\dfrac{\Omega-\omega}{hh_r c}\left(\partial_r \mathrm{A}_{\mathrm{out}}(\mathrm{R}_{\mathrm{exo}},\theta)-\partial_r \mathrm{A}_{\mathrm{in}}(\mathrm{R}_{\mathrm{exo}},\theta)\right)= & 4\pi\sigma_e \\ \dfrac{1}{\varpi h_r}\left(\partial_r \mathrm{A}_{\mathrm{out}}(\mathrm{R}_{\mathrm{exo}},\theta)-\partial_r \mathrm{A}_{\mathrm{in}}(\mathrm{R}_{\mathrm{exo}},\theta)\right)= & \dfrac{4\pi}{c}\mathrm{J}_\sigma^{\hat{\phi}} \end{array}\right. \tag{8.11}$$

where the surface current is generally defined by $\mathrm{J}_\sigma^{\hat{k}}=\lim\limits_{\Delta r\to 0}\int_{r_{\mathrm{sta}}-\Delta r/2}^{r_{\mathrm{sta}}+\Delta r/2}\mathrm{J}^{\hat{k}}\mathrm{d}r$, with $k=\theta$ or ϕ. Note that $\sigma_e c=-\mathrm{J}_\sigma^{\hat{\phi}}x$.

Using the inversion of first integrals, Eqs.(4.44), the toroidal magnetic field is also linked to the charge current, Eq.(4.22) which crosses the surface inside the circle $\mathscr{C}_{r,\theta}=\{\mathrm{M}\in\Sigma\,|\,\theta(\mathrm{M})=\theta, r(\mathrm{M})=r\}$. In the axi-symmetric and stationarity assumption, the toroidal magnetic field contains information on the poloidal Poynting flux $\Pi_p=-\frac{h\varpi\Omega \mathrm{B}^{\hat{\phi}}}{hc}\mathbf{B}_p=-\frac{2\mathrm{I}\Omega}{hc}\mathbf{B}_p$.

This current function, which is also proportional to the Poynting flux, $\Phi_{\mathrm{EM}}=-2\Omega\mathrm{I}$ is not constant along the line,

$$2\mathrm{I}=-\Psi_{\mathrm{A}}\mathrm{L}\left[1-\frac{\mathrm{M}_{\mathrm{Alf}}^2+\frac{\varpi^2\Omega(\Omega-\omega)}{c^2}}{\mathrm{M}_{\mathrm{Alf}}^2-h^2\left(1-x^2\right)}\right]-\Psi_{\mathrm{A}}\mathscr{E}\frac{\frac{\varpi^2(\Omega-\omega)}{c^2}}{\mathrm{M}_{\mathrm{Alf}}^2-h^2\left(1-x^2\right)} \tag{8.12}$$

Eqs.(4.26, 4.35, 4.39) imply the discontinuity of Ψ_{A}, $\Psi_{\mathrm{A}}\mathrm{L}$ and $\Psi_{\mathrm{A}}\mathscr{E}$ on the sheet layer. Thus looking at Eq.(8.12), we also get some discontinuity for the current function I. Which is equivalent to some discontinuity of $\mathrm{B}^{\hat{\phi}}$. Then we also have a discontinuity of the Poynting flux, which implies the presence of a meridional $\mathrm{J}_\sigma^{\hat{\theta}}$ surface current.

An apparent paradox appears because charges seem to accumulate somewhere on the sheet layer due to the existence of a non null $\mathrm{J}_\sigma^{\hat{\theta}}$. Looking at the following sketch on Fig.(8.28) of the iso contours of current intensity I in the poloidal plane, we see that in reality there is no accumulation of charges.

In our model $\Delta r\to 0$ and we get a discontinuity of the current intensity, which implies a discontinuity of $h\mathrm{J}^{\hat{r}}$. This is linked to the variation with θ of the surface current $\mathrm{J}_\sigma^{\hat{\theta}}$. After some calculations, using the equation of charge conservation, we obtain for the radial current discontinuity at each latitude,

$$h\mathrm{J}_{\mathrm{in}}^{\hat{r}}(\mathrm{R}_{\mathrm{sta}})=h\mathrm{J}_{\mathrm{out}}^{\hat{r}}(\mathrm{R}_{\mathrm{sta}})+\frac{1}{\Sigma\sin\theta}\frac{\partial}{\partial\theta}\left(\rho\sin\theta\mathrm{J}_\sigma^{\hat{\theta}}\right) \tag{8.13}$$

Keeping fixed the black hole mass and the angular momentum values for both flows and the stagnation radius, we finally obtain,

$$\left\{\begin{array}{r} r_{\star,\mathrm{in}}\mathrm{R}_{\mathrm{in,sta}}=r_{\star,\mathrm{out}}\mathrm{R}_{\mathrm{out,sta}} \\ r_{\star,\mathrm{in}}\mu_{\mathrm{in}}=r_{\star,\mathrm{out}}\mu_{\mathrm{out}} \\ \dfrac{\ell_{\mathrm{in}}}{\mu_{\mathrm{in}}}=\dfrac{\ell_{\mathrm{out}}}{\mu_{\mathrm{out}}} \end{array}\right\}\quad \frac{\mathrm{R}_{\mathrm{in,sta}}}{\mu_{\mathrm{in}}}=\frac{\mathrm{R}_{\mathrm{out,sta}}}{\mu_{\mathrm{out}}} \tag{8.14}$$

To summarize all the conditions we get for matching an inflow to an outflow in term of the

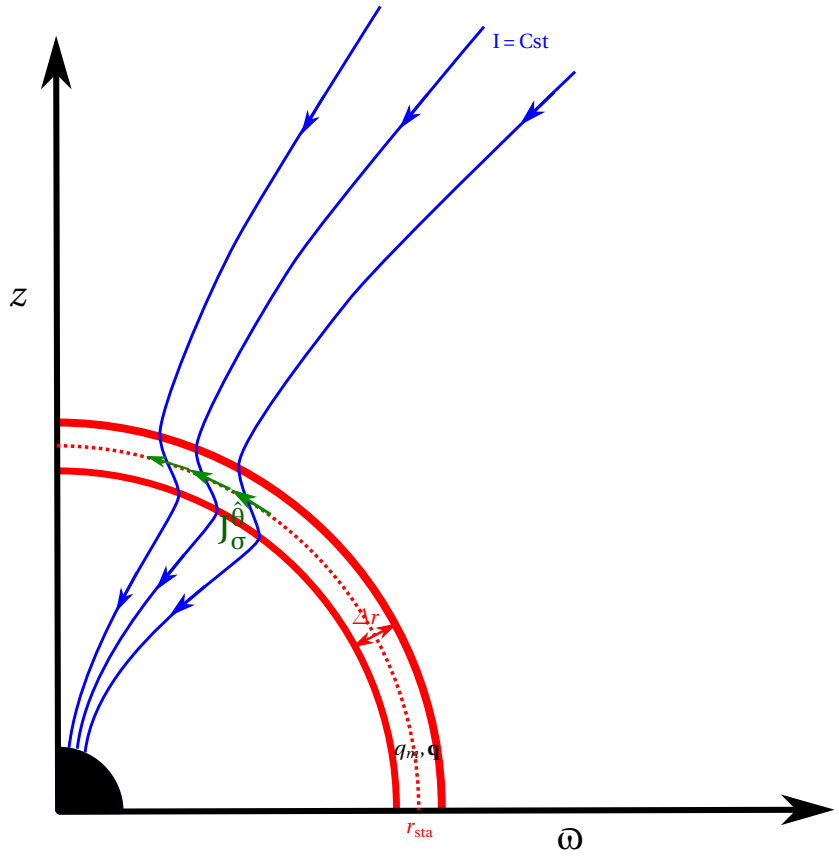

Figure 8.28 – Sketch representing the current intensity isocontour I in the layer of Δr thickness. Blue lines are iso contour of I. Red lines represent the boundary of the thin layer. The dotted red line is the surface of stagnation.

parameters of the model presented in Ch.(5). We get,

$$\begin{cases} \dfrac{\mathrm{R}_{\mathrm{sta,in}}}{\mu_{\mathrm{in}}} = \dfrac{\mathrm{R}_{\mathrm{sta,out}}}{\mu_{\mathrm{out}}} \\ \dfrac{\ell_{\mathrm{in}}}{\mu_{\mathrm{in}}} = \dfrac{\ell_{\mathrm{out}}}{\mu_{\mathrm{out}}} \\ \dfrac{\mathrm{B}_{\star,\mathrm{in}} f_{\mathrm{in}}\left(\mathrm{R}_{\mathrm{sta,in}}\right)}{\mu_{\mathrm{in}}^2} = \dfrac{\mathrm{B}_{\star,\mathrm{out}} f_{\mathrm{out}}\left(\mathrm{R}_{\mathrm{sta,out}}\right)}{\mu_{\mathrm{out}}^2} \\ \dfrac{l_{\mathrm{in}}\mu_{\mathrm{in}}^2}{\left(1+\ell_{\mathrm{in}}^2\right)^2} + \dfrac{\lambda_{\mathrm{in}}\mu_{\mathrm{in}}^{3/2} h_{\star,\mathrm{in}}}{\nu_{\mathrm{in}}} = \dfrac{l_{\mathrm{out}}\mu_{\mathrm{out}}^2}{\left(1+\ell_{\mathrm{out}}^2\right)^2} + \dfrac{\lambda_{\mathrm{out}}\mu_{\mathrm{out}}^{3/2} h_{\star,\mathrm{out}}}{\nu_{\mathrm{out}}} \end{cases} \tag{8.15}$$

8.3.2 Energetic balance at stagnation radius

The mass, angular momentum and energy exchanges with the Kerr black hole on the horizon are explicitly given by the equations Eqs.(4.85). In order to describe the MHD fields from the black hole horizon up to the infinity, we build two types of flows, calculated from our semi-analytical model. A matching between the inflow and outflow solutions has to be done, taken into account the loading terms. Thus the loading term of plasma pairs, k_m, and the recoiling force on pairs fluid $\mathbf{k}$ is proportional to a Dirac distribution function,

$$k_m = k_{m,\mathrm{sta}}(\theta)\,\delta\left(r - r_{\mathrm{sta}}\right)\,, \tag{8.16}$$

$$\mathbf{k} = \mathbf{k}_{\mathrm{sta}}(\theta)\,\delta\left(r - r_{\mathrm{sta}}\right)\,. \tag{8.17}$$

The integration at the stagnation radius of Eqs.(4.26,4.35,4.39) gives the variation of mass, angular momentum and energy fluxes at the stagnation radius. We get,

$$\Psi_{\rm A}^{\rm out}({\rm A}) = \Psi_{\rm A}^{\rm in}({\rm A}) + \frac{4\pi ch}{{\rm B}^{\hat{r}}} k_{m,{\rm sta}}(\theta_{\rm sta}({\rm A})) \ , \tag{8.18}$$

$$(\Psi_{\rm A}{\rm L})^{\rm out}({\rm A}) = (\Psi_{\rm A}{\rm L})^{\rm in}({\rm A}) + \frac{4\pi h}{{\rm B}^{\hat{r}}} \boldsymbol{\xi}\cdot\mathbf{k}_{\rm sta}(\theta_{\rm sta}({\rm A})) \quad , \tag{8.19}$$

$$(\Psi_{\rm A}\mathscr{E})^{\rm out}({\rm A}) = (\Psi_{\rm A}\mathscr{E})^{\rm in}({\rm A}) - \frac{4\pi ch}{{\rm B}^{\hat{r}}} \boldsymbol{\eta}\cdot\mathbf{k}_{\rm sta}(\theta_{\rm sta}({\rm A})) \ . \tag{8.20}$$

In the outflow, the mass flux is positive, whereas in the inflow, it is negative. Applying the first condition to Eq.(8.18) implies that for each colatitude $\frac{4\pi ch}{{\rm B}^{\hat{r}}} k_{m,{\rm sta}}(\theta({\rm A})) \geq \left(-\Psi_{\rm A}^{\rm in}({\rm A})\right)$. It means that the rate of pair creation needs to be sufficient to reverse the mass flux and allows to produce inflow and outflow.

These fluxes are conserved in the inflow. Let us consider a magnetic flux line, which crosses the horizon of the hole, using Eqs.(4.85). It is interesting to link these fluxes to the exchange of these quantities with the black hole:

$$\Psi_{\rm A}^{\rm out}({\rm A}) = -\frac{d^2{\rm M}_{\mathscr{H}}}{dtd{\rm A}}(\theta_{\mathscr{H}}({\rm A})) + \frac{4\pi ch}{{\rm B}^{\hat{r}}} k_{m,{\rm sta}}(\theta_{\rm sta}({\rm A})) \ , \tag{8.21}$$

$$(\Psi_{\rm A}{\rm L})^{\rm out}({\rm A}) = -\frac{d^2{\rm J}_{\mathscr{H}}}{dtd{\rm A}}(\theta_{\mathscr{H}}({\rm A})) + \frac{4\pi h}{{\rm B}^{\hat{r}}} \boldsymbol{\xi}\cdot\mathbf{k}_{\rm sta}(\theta_{\rm sta}({\rm A})) \ , \tag{8.22}$$

$$(\Psi_{\rm A}\mathscr{E})^{\rm out}({\rm A}) = -\frac{d^2{\rm E}_{\mathscr{H}}}{dtd{\rm A}}(\theta_{\mathscr{H}}({\rm A})) - \frac{4\pi ch}{{\rm B}^{\hat{r}}} \boldsymbol{\eta}\cdot\mathbf{k}_{\rm sta}(\theta_{\rm sta}({\rm A})) \ . \tag{8.23}$$

Thus for a line which cross the black hole horizon the flux at infinity is constituted of the flux given by the black hole and the flux given by the source terms. For creating leptonic pairs via photon annihilation, the photons which are transformed in pairs transfer to the pair fluid their energy and their angular momentum.

8.4 Inflow/ouflow solutions

We now use the minimal condition of matching Eqs.(8.15) to find for each of the inflows, a corresponding outflow. This one is not unique. We call "matching" the combination of these two flows. This "matching" allows to describe the fields from the horizon of the black hole to infinity. Eqs.(8.18, 8.23), allow to calculate the contribution of the source term in function of mass creation rate, angular momentum and energy to match the two flows. Then we compare these rates with the exchange of the same quantities associated between the fields MHD and the Kerr black hole. We also examine the surface density and the current surface, Eqs.(8.11, 8.13), at the stagnation radius.

8.4.1 Parameters and main characteristics of matched outflow solution

In what follows, we refer to the "matched" solutions as **M1**, **M2** or **M3**. They contain one of the inflows **I1**, **I2** or **I3** presented above and a corresponding outflow **O1**, **O2** or **O3** presenting the minimal conditions of matching Eqs.(8.15). We start by giving the parameters of the different outflow solutions,

The minimal conditions of matching Eqs.(8.15) are almost satisfied using the tools developed in Sec.(6.4).

The minimal condition of matching Eqs.(8.15) are tuned to precision of 10^{-3} Tab.(8.5). For a given inflow solution the outflow solution, satisfies the minimal conditions of matching. With the minimization of $\Pi_\star$ Sec. (6.3), an outflow solution is characterized by 7 parameters. Thus, since the minimal conditions of matching, Eqs.(8.15), impose 3 effectives conditions on the outflow solution parameters, all outflow solutions corresponding to a given inflow must be a sub-variety of dimension $7-3=4$ in the outflow parameter space. The set of solutions (Inflow+Outflow+Minimum

	λ	κ	δ	ν	ℓ	μ	e_1
O1	0,985	0,230	1,328	0,386	$1{,}016.10^{-2}$	$3{,}758.10^{-2}$	$6{,}892.10^{-3}$
O2	0,998	0,280	1,296	0,234	$6{,}502.10^{-3}$	$3{,}012.10^{-2}$	$6{,}892.10^{-3}$
O3	1.171	0.291	1.319	0.600	$4{,}767.10^{-2}$	0.184	$-6{,}268.10^{-2}$

Table 8.4 – Set of parameter of matched outflow solution

		a	$\Omega/\omega_{\mathscr{H}}$	$R_{sta}/R_{\mathscr{H}}$	$\gamma_{max,axe}$	$\xi_\star$
M1	**I1**	0,5429	$6{,}2167{,}10^{-2}$	3,1777	15	253
	O1	0,5410	$6{,}2047.10^{-2}$	3,1771	1,47	1.42
M2	**I2**	0,4316	$9{,}6912.10^{-2}$	1,5031	11	136
	O2	0,4316	$9{,}6912.10^{-2}$	1,5031	4	1,5
M3	**I3**	0,5189	0.5022	1,1755	12	162
	O3	0,5189	0.5022	1,1750	10	7,8

Table 8.5 – Values for minimal conditions of matching function for each inflow solution

conditions of continuity) is therefore characterized by a variety of dimension $4+8=12$. This implies a large variety of solutions.

Some interesting subsets can be searched by imposing other conditions of continuity. For example, we can, as Pu et al. [2015], impose the continuity of the Poynting flux. This is equivalent to the continuity of the current and thus at the absence of poloidal surface current j^θ_σ Eq.(8.13, 8.12) on the stagnation surface. One can also impose the $\mathscr{C}^1$ continuity of the magnetic flux which implies the absence of any toroidal surface current and charge density, Eq.(8.11), on the stagnation surface.Finally, other types of requirements such as the final Lorentz factor value can be used as a constraint. The value of $\xi_{\star,\mathrm{in}}$ is calculated in order to have in Eq.(8.2) the proportionality factor equals to 50 as in Zamaninasab et al. [2014]. The value of $\xi_{\star,\mathrm{out}}$ is chosen as in Sec.(7.2).

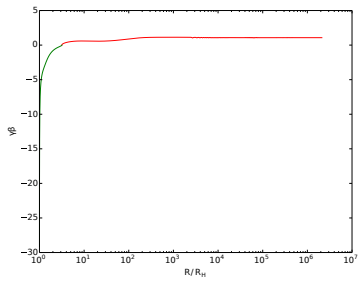

Figure 8.29 – Celerity on the axis $\gamma\beta$ for the **M1** matched solution in green the inflow part and in red the outflow part

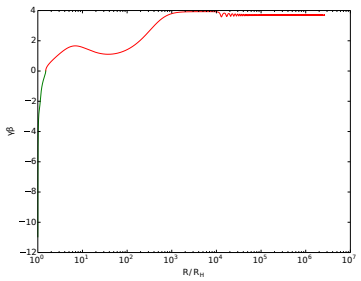

Figure 8.30 – Celerity on the axis $\gamma\beta$ for the **M2** matched solution in green the inflow part and in red the outflow part

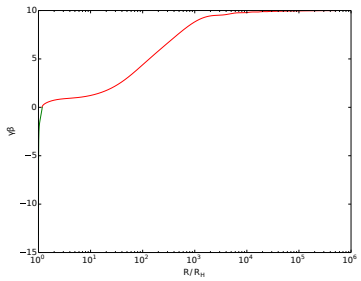

Figure 8.31 – Celerity on the axis $\gamma\beta$ for the **M3** matched solution in green the inflow part and in red the outflow part

Start by briefly presenting the curve Figs.(8.29, 8.30, 8.30). We plot the celerity $\gamma\beta$ on the axis of the three matching **M1**, **M2** and **M3**. In green we plot the curve corresponding to the inflow and in red the curve corresponding to the outflow. We see that the outflow of the matching solutions **M2** and **M3** reaches relatively high Lorentz factor values $\gamma \sim 4-10$,

8.4.2 Geometry

Let us have a look at the geometry of the first **M1** matching. We have plotted on Figs.(8.32, 8.33) the poloidal field lines of **M1**. In red, we have the stagnation surface separating the inflow and the outflow. In blue the Alfvén surfaces and in green the slow magnetosonic surfaces. We also represent the ergosphere in magenta. The outer light cylinder is in orange and the inner light cylinder in brown.

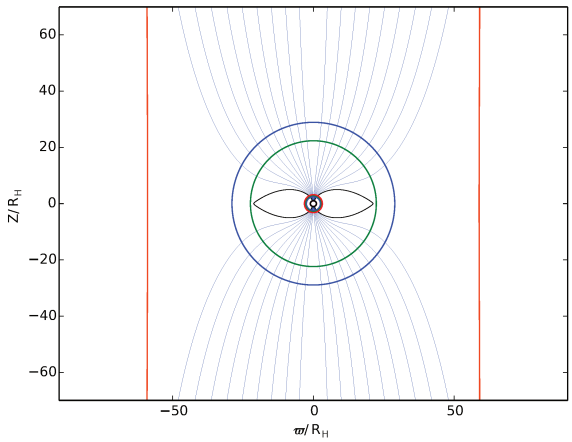

Figure 8.32 – Geometry of the poloidal field lines for the **M1** matched solution, in orange the external light-cylinder, in red the stagnation radius, in green the slow-magnetosonic surface.

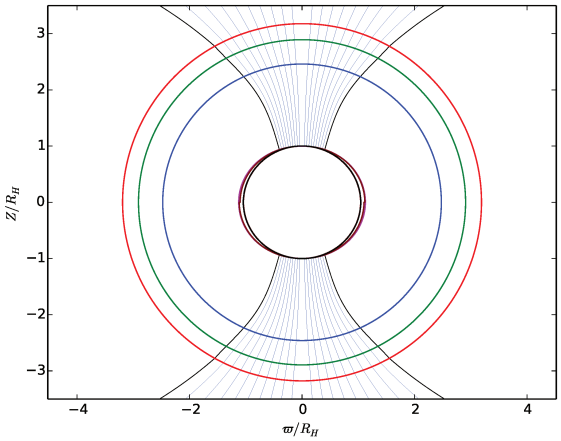

Figure 8.33 – Geometry of poloidal field lines for the **M1** matched solution, in brown the internal light cylinder, in magenta the ergosphere.

Although continuous field lines are not $\mathscr{C}^1$ at the stagnation surface, they are more open at the beginning of the outflow than at the beginning of the inflow, $\mathrm{F_{sta,out}} \leq \mathrm{F_{sta,in}}$. This implies that there are toroidal surface currents twisting the poloidal magnetic field lines at the stagnation surface, but also the surface charge density, Eq.(8.11). For **M1**, about 14% of the magnetic flux that crosses the horizon of the black hole reaches infinity. The rest of this magnetic flux crosses the horizon in the magnetosphere outside the torus for solution **M1**.

For **M2** matching geometry, in Figs.(8.34, 8.35), the same convention of colors is adopted for the different lines.

For **M2**, we observe a more open outflow than the inflow at the stagnation radius, $\mathrm{F_{sta,out}} \leq \mathrm{F_{sta,in}}$. The magnetosphere of this matching is extremely large. The fraction of the magnetic flux going through the black hole contained in the open lines is less than 1% of the magnetic flux through the black hole. Here the strong opening of the inflow and outflow is combined and reduces this fraction. The inner light cylinder is very close to the ergosphere but within the ergoregion.

Contrary to the two previous matched solutions, the solution **M3** has less open field lines than the inflow at the stagnation radius $\mathrm{F_{sta,out}} \geq \mathrm{F_{sta,in}}$. The size of magnetosphere is then smaller than in **M2**. The fraction of magnetic flux contained in the open line is around 8.8% of the magnetic flux which crosses the horizon. The ergosphere is larger and the stagnation radius approaches the Alfvén surface. The outer light cylinder is closer to the black hole horizon than the previous solutions. The internal light cylinder is contained within the ergosphere quite close to the horizon.

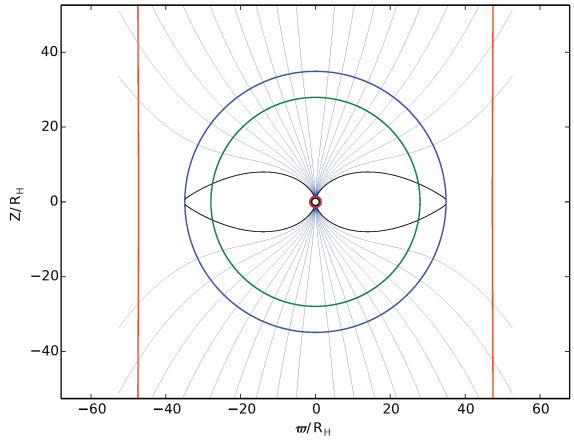

Figure 8.34 – Geometry of the poloidal field lines for the **M2** matched solution, in orange the external light-cylinder, in red the stagnation radius, in green the slow-magnetosonic surface.

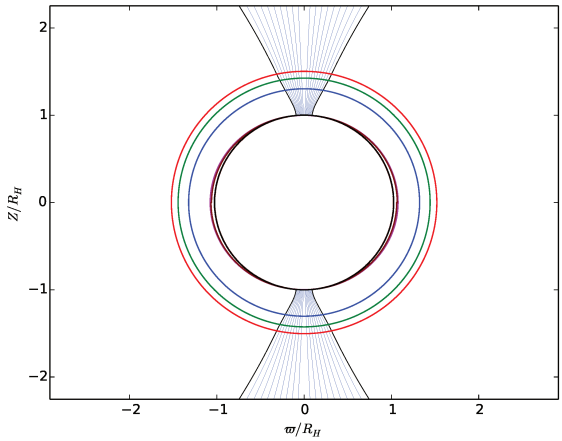

Figure 8.35 – Geometry of poloidal field lines for the **M2** matched solution, in brown the internal light cylinder, in magenta the ergosphere.

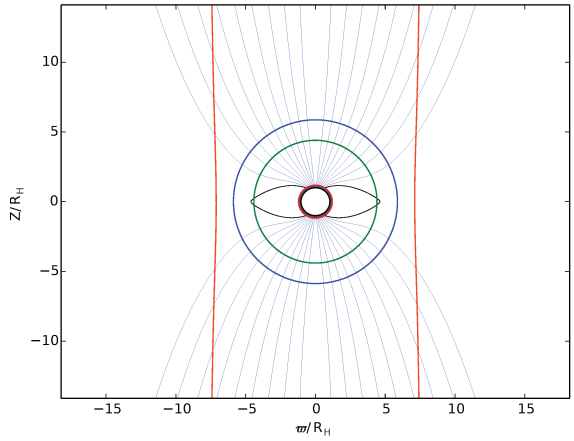

Figure 8.36 – Geometry of the poloidal field lines for the **M3** matched solution, in orange the external light-cylinder, in red the stagnation radius, in green the slow-magnetosonic surface.

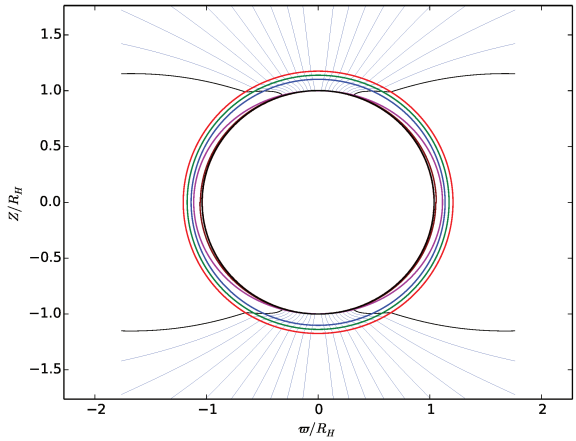

Figure 8.37 – Geometry of poloidal field lines for the **M3** matched solution, in brown the internal light cylinder, in magenta the ergosphere.

8.4.3 Source terms

We are now able to compare the fluxes of mass, angular momentum, and energy supplied/absorbed by the black hole and those supplied by the loading terms. Do not forget that these terms are calculated in order to make the connection between inflow and outflow. We stil have to justify this physically. The formulas given in Eqs.(3.48, 3.56, 3.78) can be used in a later analysis to see if the loading terms can be explained by the creation of pairs or in some other ways.

For simplicity, we present the different mass, angular momentum and energy fluxes by unit of solid angle. We also present them in a dimensionless way. Indeed in our models the mass fluxes by unit of solid angles are easily calculated in units of $\mathrm{B}^2_{\star,\mathrm{in}} r_s^2/c$. The angular momentum flux will be dimensioned by $\mathrm{B}^2_{\star,\mathrm{in}} r_s^3$ and the energy flux by $\mathrm{B}^2_{\star,\mathrm{in}} r_s^2 c$. In order to obtain orders of magnitude, the values of these quantities are given in the following tables for a black hole mass $\mathrm{M}_{\mathscr{H}} \approx (6,6 \pm 0.4) \times 10^9 \mathrm{M}_\odot = \mathrm{M}_9 \times 10^9 \mathrm{M}_\odot$ close to those of the M87 supermassive black hole

mentioned in Gebhardt et al. [2011] and for the same object a magnetic field $\approx 5 \pm 4$G Kino et al. [2014] at $10r_s$. It corresponds well to the magnetic field of the outflow at some smaller radius. Then we get $B_{\star,\rm out}$ using $B_{\star,\rm out}/G^2(10r_s) \approx 1$G. Using Eq.(8.15) we can get $B_{\star,\rm in}$ from $B_{\star,\rm out}$, then we obtain:

	$B^2_{\star,\rm in} r_s^2/c$ (g.s^{-1})	$B^2_{\star,\rm in} r_s^3$ (g.cm^2.s^{-2})	$B^2_{\star,\rm in} r_s^2 c$ (erg.s^{-1})
M1	1.09×10^{24}	6.39×10^{49}	9.84×10^{44}
M2	2.17×10^{26}	1.24×10^{52}	1.91×10^{47}
M3	1.62×10^{25}	9.47×10^{50}	1.45×10^{46}

Table 8.6 – Value of the dimensionnless parameters for a black hole of $M_{\mathscr{H}} = 6,6 \times 10^9 M_\odot$ and $B_{\star,\rm out} = 1$G

Try to estimate realistic total mass injection rate of M87. Using the calculation of pairs creation/annihilation total cross section presented in Svensson [1982] with mildly relativistic speed $\beta_m \sim 1/\sqrt{2}$, we get $\sigma_{\gamma\gamma} \sim 1.56 \times 10^{-25} cm^2$. Then the volume injection rate is $\simeq \sigma_{\gamma\gamma} c n_\gamma^2$. The typical size of material injection from photon is some Schwarzschild radius. The highly energetic photon are originate from the disk, then a model of disk emission is needed to estimate the photon density in the environment of the black hole. In his work, Levinson and Rieger [2011] estimate sufficiently energetic photon able to produce pairs emitted by the disk and its Radiative inefficient accretion flow (RIAF). They use cooling function for electron-ion and electron-electron bremsstrahlung from Narayan and Yi [1995] and choosing typically middly relativistic temperature for electron they are able to estimate the energy flux escaping from the accretion flow and the disk. Then using typical scale of the disk they are able to determine sufficiently energetic photon density in the system, $n_\gamma \simeq 7 \times 10^1 1 (r_s/r)^2 \ln(r/r_s) \dot{m} M_9$ where $\dot{m}$ is the the accretion rate is measured in units of the Eddington rate. Di Matteo et al. [2003] mention a value of $\dot{m} \simeq 6 \times 10^{-4}$. Compiling these result we are able to estimate mass injection rate for M87 system.

$$\dot{M}_{\rm th,M87} \simeq 2,3 \times 10^{26} \ln\left(\frac{r}{r_s}\right)\left(\frac{r_s}{r}\right) \dot{m}^4 M_9 g.s^{-1} \tag{8.24}$$

Because of the factor $\dot{m}^4$, for $\dot{m} \leq \dot{m}_{\rm lim}$, the scale value of injected mass from model Tab.(8.6) could be bigger than a realistic value estimated by Eq.(8.24). Nevertheless these value depend of the choose of $\xi_{\star \rm in}$ and $\xi_{\star \rm out}$ which as been chosen with a discutable method. Secondly even considering the solution only on the non-connected to equatorial plane field line the effective injection reduce the injection of models solution, using $M_9 \simeq 6,6 \pm 0.4$ and keeping the value adopted for $\xi_\star$ we get a limiting value of $\dot{m}_{\rm lim} \simeq 9.10^{-2}$ for **M1**, $\dot{m}_{\rm lim} \simeq 2.10^{-1}$ for **M2** and $\dot{m}_{\rm lim} \simeq 1,5.10^{-1}$ for **M3**, these value are still some order of magnitude more than those mentioned in Di Matteo et al. [2003] for M87. It is a typical problem also meet with force free model where Goldreich-Julian value of electric density is biggest than the density allowed by mass injection. Hirotani and Pu [2016] try to solves this difficulty introducing steady state gap solution of MHD. Nevertheless Levinson and Segev [2017] argue that such kind of models could not apply to concrete astrophysical system and propose to break down steady state assumption. In our case, we still can adapt the value of $\xi_\star$.

The power values for **M1** and **M2** are quite high in comparison with the value $\approx 10^{44}$erg.s^{-1} mentioned in Prieto et al. [2016] for M87 jets. Nevertheless to obtain the final value of the jet power of modelized jet you need to multiply these powers, with the integrals on the solide angle of the sphere of curves presented below in Figs.(8.40, 8.41). Furthermore, these solutions were not obtained in order to match with some observational constraints but just to present the ability of the model. Nevertheless, VLT/SINFONI imaging spectroscopy Nesvadba et al. [2017] mention stronger jet powers for different sources.

First we plot the mass fluxes. On the left Fig.(8.38), shows the accreted mass by the black hole and on the right Fig.(8.39) shows the mass rate from the loading terms, for the matching solution **M1**. It appears that the accreted mass rate is two orders of magnitude lower than the

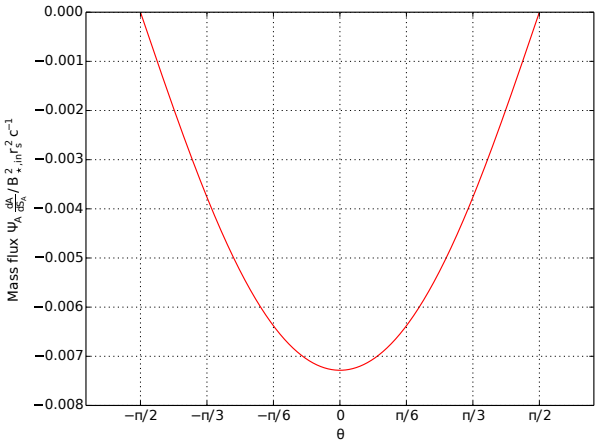

Figure 8.38 – Mass flux by unit of solid angle absorbed by the black hole for the matching solution **M1**

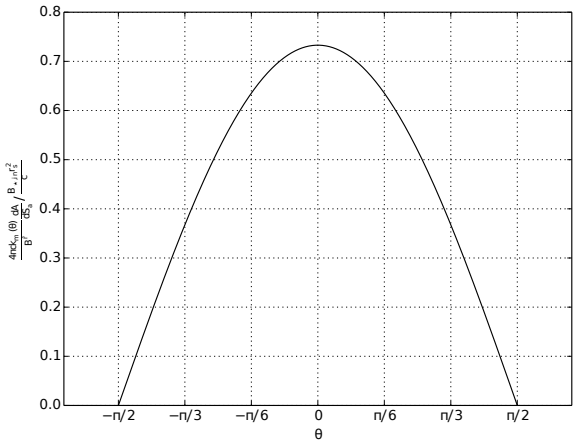

Figure 8.39 – Normalized material apparition rate by unit of solid angle for the matching solution **M1**

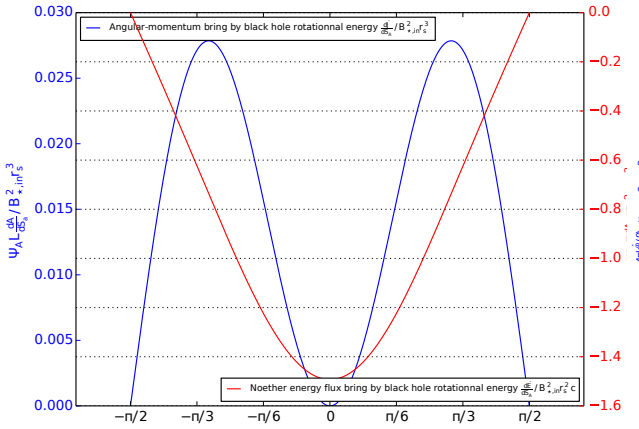

Figure 8.40 – Noether energy and angular momentum flux by unit of solid angle absorbed by the black hole for the matching solution **M1**

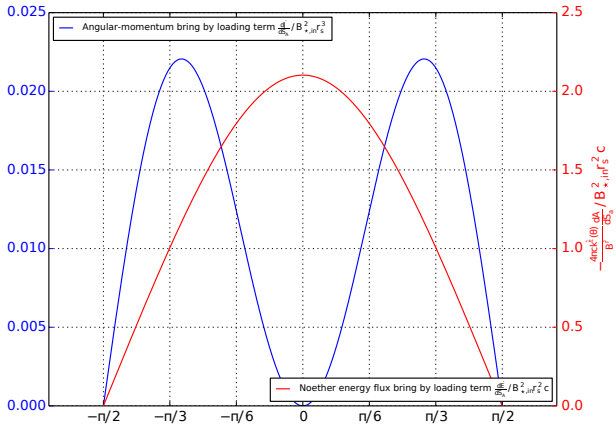

Figure 8.41 – Noether energy and angular momentum flux from loading terms by unit of solid angle for the matching solution **M1**

mass rate created. The created mass rate depends of the choice of the value $\xi_\star$ for the inflow and the outflow.

The flux and angular momentum are more interesting. We plot in Fig.(8.40), the flux of energy (red) and angular momentum (blue) at the horizon of the black hole. The black hole absorbs the energy of the field, but transmits angular momentum to the flow. In Fig.(8.41), we plot the same flux from the loading terms. The loading terms bring more energy than the black hole absorbs; it also brings an additional angular momentum to the flow, which is quite of the same order than the angular momentum given by the black hole. Because of the general opening of the inflow magnetic field lines, all the available flux on the horizon does not reach the stagnation surface. **M1** solution is dominated by the loading term of mass flux compared to mass flux on the horizon. But the energy and angular momentum fluxes of pairs have the same orders of magnitude between the amount extracted from the hole and the amount bring by the loading term.

For **M2** solution, we have,
We have in Figs.(8.42, 8.43) the accreted mass rate (left) and the mass rate produced by

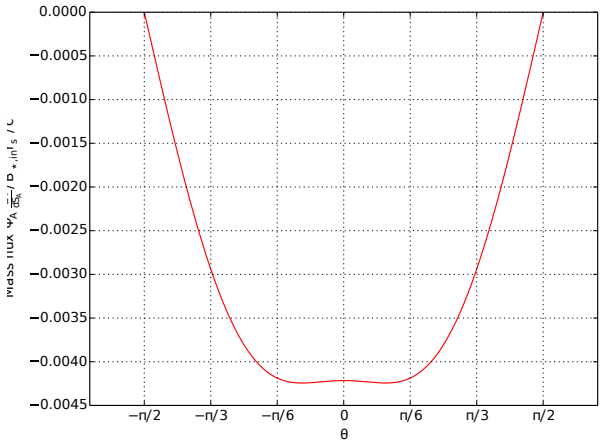

Figure 8.42 – Mass flux by unit of solid angles absorbed by the black hole for the matching solution **M2**

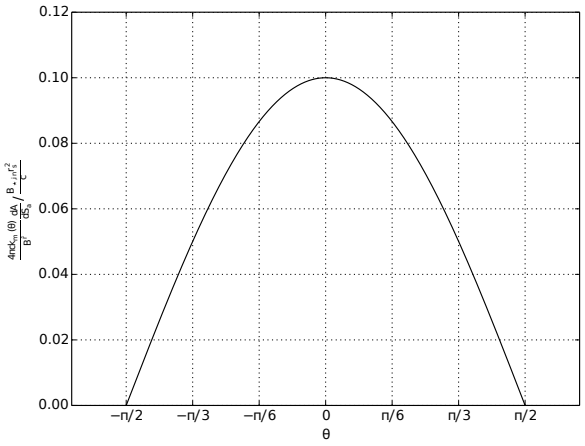

Figure 8.43 – Normalized material apparition rate by unit of solid angles for the matching solution **M2**

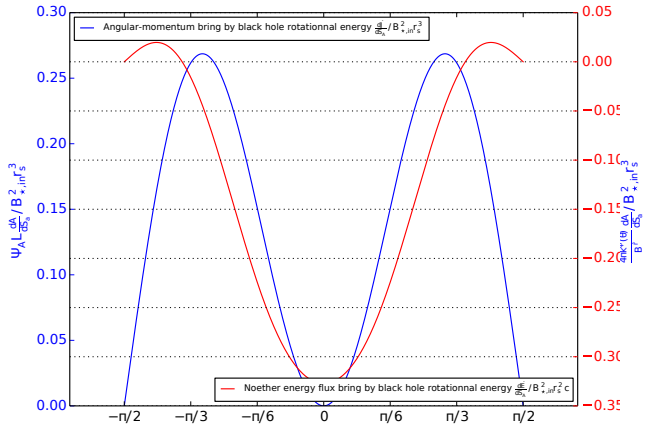

Figure 8.44 – Noether energy and angular momentum flux by unit of solid angles absorbed by the black hole for the matching solution **M2**

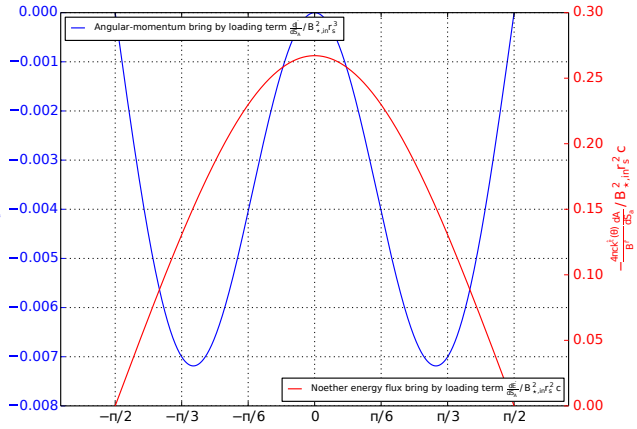

Figure 8.45 – Noether energy and angular momentum flux from loading terms by unit of solid angles for the matching solution **M2**

the loading terms (right). As before, we have a solution where most of the mass created by the loading term is found in the outgoing flow, with a bit less than two orders of magnitude difference between the 2 mass fluxes.

For the energy and angular momentum in Figs.(8.44, 8.45), it should be noted first that the loading terms bring a negative angular momentum to the flow. Nevertheless, this contribution is negligible compared to the angular momentum provided by the black hole. The energy fluxes have the same order of magnitude. It does not seem strange that the absolute value of energy flux of the loading term is lower on the axis the one that absorbed by the black hole. This is due to the high expansion rate of the field lines. In fact, the energy flux by unit of solid angle of the inflow is diluted with the opening of the tubes, increasing the solid angle between two flux tubes. As before, **M2** is dominated by loading terms because of the mass flux, but the energy and angular momentum flux of pairs have quite same orders of magnitude.

For **M3** solution, we have, the same quantities plotted in Figs.(8.46,,8.47, 8.48, 8.49)
The accreted mass rates (left) and the one produced by the loading terms (right). The mass

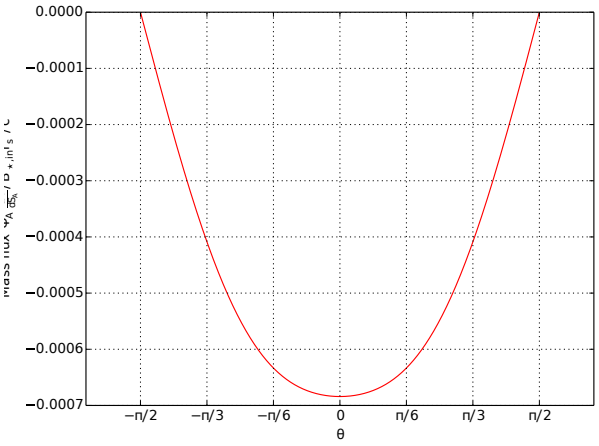

Figure 8.46 – Mass flux by unit of solid angles absorbed by the black hole for the matching solution **M3**

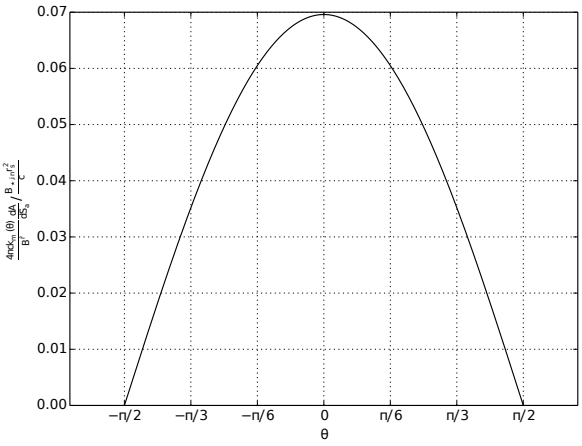

Figure 8.47 – Normalized material apparition rate by unit of solid angles for the matching solution **M3**

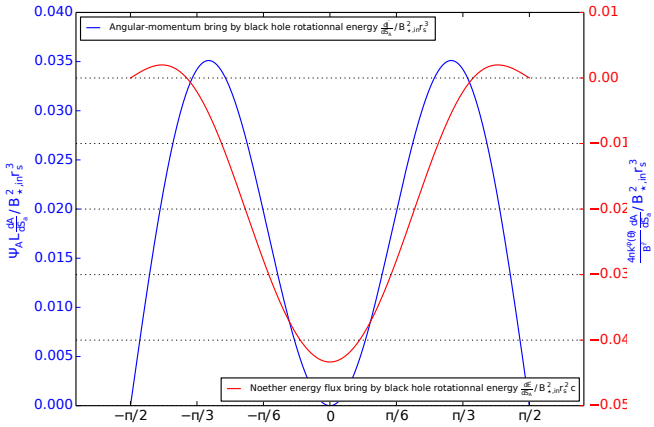

Figure 8.48 – Noether energy and angular momentum flux by unit of solid angles absorbed by the black hole for the matching solution **M3**

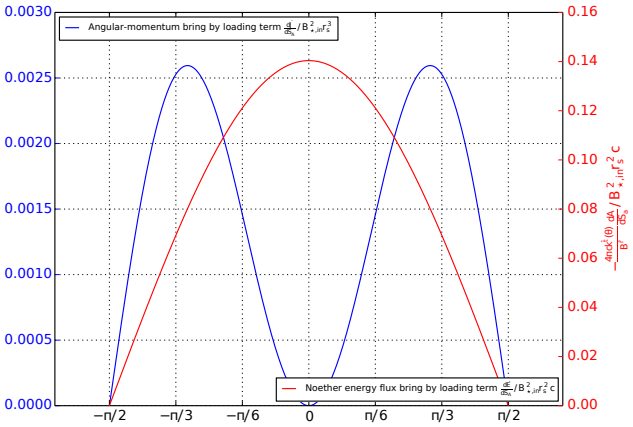

Figure 8.49 – Noether energy and angular momentum flux from loading terms by unit of solid angles for the matching solution **M3**

flow is again dominated by the loading terms (with 2 orders of magnitude difference).

The energy and the angular momentum of the solution **M3**, are plotted in Figs.(8.48, 8.49). We observe that the energy provided by the loading term is greater than the one provided by the black hole. The black hole loss of angular momentum is higher (one order of magnitude difference) than the one provided by the loading terms.

8.4.4 Surface current

Using Eqs.(8.11, 8.13), we are able to draw for our matched solutions the value of charge surface density, and the value of poloidal surface current.

The first result is the change in the sign of the surface density. Indeed, the Eq. (8.11) shows that the sign of surface density current depends on $(\Omega-\omega)\left(\mathrm{F}_{\mathrm{sta,out}}-\mathrm{F}_{\mathrm{sta,in}}\right)$. Thus since the cancellation of $\Omega-\omega$ occurs in the inflow for the **M1** solution and in the ouflow for **M2** and **M3**, and we have $\mathrm{F}_{\mathrm{sta,out}} \leq \mathrm{F}_{\mathrm{sta,in}}$ for **M1** and **M2**, and the opposite for **M3**. Indeed the sign change of σ_e

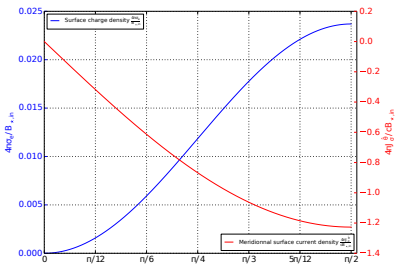

Figure 8.50 – Surface density and current of charge for **M1** solution

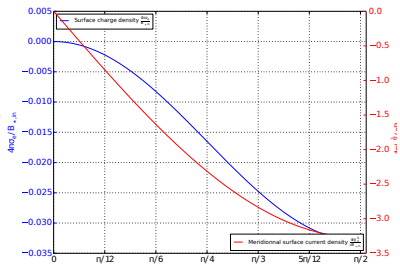

Figure 8.51 – Surface density and current of charge for **M2** solution

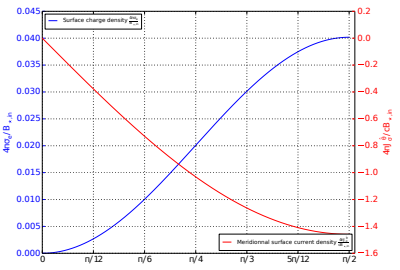

Figure 8.52 – Surface density and current of charge for **M3** solution

between **M1** and **M2** is explained by the change in the sign difference of $\Omega - \omega$ on the stagnation surface of the two matching solution. The second sign change between **M2** and **M3** is explained by the sign change of $\mathrm{F_{sta,out}} - \mathrm{F_{sta,in}}$ between the two solutions.

The current values are generally negative in the axis environment for inflow or outflow. Nevertheless, for the 3 solutions **M1**, **M2** and **M3**, the surface charge current is in the opposite direction $\boldsymbol{\epsilon}_\theta$. This further reduces the current values at the outflow level. (See in Figs.8.28)

8.5 Conclusion

In this chapter we have just explored the main properties of the inflows of our meridional self-similar model.

First of all, we shown that the model verifies, a scaling law between the magnetic flux through the black hole horizon and the infall mass rate. This equivalent to the scaling law observed in the simulations of McKinney [2005] or Tchekhovskoy et al. [2011] and experimentally by Zamaninasab et al. [2014], excepte the used the mass infall rate. The magnetic flux through the black hole horizon is proportional to the square root of the accretion rate. We also verified the ability of the model equations to be integrated up to the black hole horizon.

In our model, we have also shown with 3 inflow solutions, that different energy exchanges with the rotating black hole can occur. Three main categories are presented in Sec.(8.2). The first solution shows a dominating material energy flux everywhere on the horizon and then no extraction. The second solution where the Lense-Thirring flux dominates above a given angle allowing an extraction for some flux tubes. Finally in the third solution, the Poynting flux could become the most important flux, also allowing the extraction of the energy from the black hole. This variability in the behavior of energy fluxes is interesting, but it seems possible to obtain solutions with less open poloidal lines and flow tubes starting extraction closer to the black hole axis.

About geometry of field line, the resulting inflow solution has a magnetosphere. This means that expansion factor of flus tube is mostly negative. Nevertheless solution **I1** is different because in this solution the flux tube have positive expansion factor nearest to the black hole horizon. For all these inflow, the principal driving force is mostly gravity, the magnetic tension could also participate to the acceleration. The slowing down force is principally the inertial forces, but pressure and toroidal magnetic pressure could also play a role. The solution **I2** and **I3** present a change of rotational speed along the flow. The fluid first turns in the opposite direction of the black hole, then changes direction as it approaches the horizon. This being the case for field lines sufficiently close to the axis, this change of direction is not done for lines of sufficiently high

magnetic flux, which allows the Penrose process to be triggered for these lines. The pressure and the toroidal magnetic are the mainly force wich push matter toward the axis, therefore electric force and gravity are the main force pushing it on the equatorial plane.

Then we introduced the minimum conditions to make the matching between an inflow and an outflow minimally physically acceptable. This allows us to search and find 3 outflow solutions **O1**, **O2** and **O3** matching the **I1**, **I2** and solution **I3**. We finally discussed the main physical properties of the 3 matching solutions. Although there are still degrees of freedom regarding the construction of the outflow, most energy fluxes are dominated by the energy flux of the loading terms. Comparing our result to those of Globus and Levinson [2013, 2014] it seems that our loading terms are bigger than the upper limit of pairs production allowing for extracting energy from the black hole.

8.6 References

R. D. Blandford and A. Levinson. Pair cascades in extragalactic jets. 1: Gamma rays. apj, 441: 79–95, March 1995. doi: 10.1086/175338. 146

R. D. Blandford and R. L. Znajek. Electromagnetic extraction of energy from Kerr black holes. mnras, 179:433–456, May 1977. doi: 10.1093/mnras/179.3.433. 146

Avery E. Broderick and Alexander Tchekhovskoy. Horizon-scale lepton acceleration in jets: Explaining the compact radio emission in m87. *The Astrophysical Journal*, 809(1):97, 2015. URL http://stacks.iop.org/0004-637X/809/i=1/a=97. 146

V. Cayatte, N. Vlahakis, T. Matsakos, J. J. G. Lima, K. Tsinganos, and C. Sauty. Counter-rotation in Relativistic Magnetohydrodynamic Jets. *Apjl*, 788:L19, June 2014. doi: 10.1088/2041-8205/788/1/L19. 153

T. Di Matteo, S. W. Allen, A. C. Fabian, A. S. Wilson, and A. J. Young. Accretion onto the Supermassive Black Hole in M87. apj, 582:133–140, January 2003. doi: 10.1086/344504. 165

A. L. Ford, B. D. Keenan, and M. V. Medvedev. Electron-Positron Cascade in Magnetospheres of Spinning Black Holes. *ArXiv e-prints*, June 2017. 151

Karl Gebhardt, Joshua Adams, Douglas Richstone, Tod R. Lauer, S. M. Faber, Kayhan Gltekin, Jeremy Murphy, and Scott Tremaine. The black hole mass in m87 from gemini/nifs adaptive optics observations. *The Astrophysical Journal*, 729(2):119, 2011. URL http://stacks.iop.org/0004-637X/729/i=2/a=119. 165

N. Globus and A. Levinson. Loaded magnetohydrodynamic flows in Kerr spacetime. prd, 88(8): 084046, October 2013. doi: 10.1103/PhysRevD.88.084046. 146, 170

N. Globus and A. Levinson. Jet Formation in GRBs: A Semi-analytic Model of MHD Flow in Kerr Geometry with Realistic Plasma Injection. apj, 796:26, November 2014. doi: 10.1088/0004-637X/796/1/26. 146, 170

K. Hirotani and H.-Y. Pu. Energetic Gamma Radiation from Rapidly Rotating Black Holes. apj, 818:50, February 2016. doi: 10.3847/0004-637X/818/1/50. 165

K. Hirotani, M. Takahashi, S.-Y. Nitta, and A. Tomimatsu. Accretion in a Kerr black hole magnetosphere - Energy and angular momentum transport between the magnetic field and the matter. apj, 386:455–463, February 1992. doi: 10.1086/171031. 146

M Kino, F Takahara, K Hada, and A Doi. Relativistic electrons and magnetic fields of the m87 jet on the 10 schwarzschild radii scale. *The Astrophysical Journal*, 786(1):5, 2014. 165

S. S. Komissarov and J. C. McKinney. The 'Meissner effect' and the Blandford-Znajek mechanism in conductive black hole magnetospheres. mnras, 377:L49–L53, May 2007. doi: 10.1111/j.1745-3933.2007.00301.x. 146

A. Levinson and R. Blandford. Pair Cascades in Extragalactic Jets. II. The Beamed X-Ray Spectrum. apj, 449:86, August 1995. doi: 10.1086/176034. 146

A. Levinson and F. Rieger. Variable TeV Emission as a Manifestation of Jet Formation in M87? apj, 730:123, April 2011. doi: 10.1088/0004-637X/730/2/123. 165

Amir Levinson and Noam Segev. Existence of steady gap solutions in rotating black hole magnetospheres. *Phys. Rev. D*, 96:123006, Dec 2017. doi: 10.1103/PhysRevD.96.123006. URL https://link.aps.org/doi/10.1103/PhysRevD.96.123006. 151, 165

J. C. McKinney. Jet Formation in Black Hole Accretion Systems I: Theoretical Unification Model. *ArXiv Astrophysics e-prints*, June 2005a. 146

J. C. McKinney. Jet Formation in Black Hole Accretion Systems II: Numerical Models. *ArXiv Astrophysics e-prints*, June 2005b. 146

Jonathan C. McKinney. Total and jet blandford-znajek power in the presence of an accretion disk. *The Astrophysical Journal Letters*, 630(1):L5, 2005. URL http://stacks.iop.org/1538-4357/630/i=1/a=L5. 147, 169

Jonathan C. McKinney, Alexander Tchekhovskoy, and Roger D. Blandford. General relativistic magnetohydrodynamic simulations of magnetically choked accretion flows around black holes. *Monthly Notices of the Royal Astronomical Society*, 423(4):3083–3117, 2012. doi: 10.1111/j.1365-2966.2012.21074.x. URL http://dx.doi.org/10.1111/j.1365-2966.2012.21074.x. 147

R. Narayan and I. Yi. Advection-dominated Accretion: Underfed Black Holes and Neutron Stars. apj, 452:710, October 1995. doi: 10.1086/176343. 165

A. Nathanail and I. Contopoulos. Black Hole Magnetospheres. apj, 788:186, June 2014. doi: 10.1088/0004-637X/788/2/186. 146

N. P. H. Nesvadba, C. De Breuck, M. D. Lehnert, P. N. Best, and C. Collet. The SINFONI survey of powerful radio galaxies at z 2: Jet-driven AGN feedback during the Quasar Era. aap, 599:A123, March 2017. doi: 10.1051/0004-6361/201528040. 165

M. A. Prieto, J. A. Fernández-Ontiveros, S. Markoff, D. Espada, and O. González-Martín. The central parsecs of M87: jet emission and an elusive accretion disc. mnras, 457:3801–3816, April 2016. doi: 10.1093/mnras/stw166. 165

Hung-Yi Pu, Masanori Nakamura, Kouichi Hirotani, Yosuke Mizuno, Kinwah Wu, and Keiichi Asada. Steady general relativistic magnetohydrodynamic inflow/outflow solution along large-scale magnetic fields that thread a rotating black hole. *The Astrophysical Journal*, 801(1):56, 2015. URL http://stacks.iop.org/0004-637X/801/i=1/a=56. 146, 162

R. Svensson. The pair annihilation process in relativistic plasmas. apj, 258:321–334, July 1982. doi: 10.1086/160081. 165

M. Takahashi, S. Nitta, Y. Tatematsu, and A. Tomimatsu. Magnetohydrodynamic flows in Kerr geometry - Energy extraction from black holes. apj, 363:206–217, November 1990. doi: 10.1086/169331. 146

Alexander Tchekhovskoy and Jonathan C. McKinney. Prograde and retrograde black holes: whose jet is more powerful? *Monthly Notices of the Royal Astronomical Society: Letters*, 423(1): L55–L59, 2012. doi: 10.1111/j.1745-3933.2012.01256.x. URL http://dx.doi.org/10.1111/j.1745-3933.2012.01256.x. 147

Alexander Tchekhovskoy, Ramesh Narayan, and Jonathan C. McKinney. Efficient generation of jets from magnetically arrested accretion on a rapidly spinning black hole. *Monthly Notices of the Royal Astronomical Society: Letters*, 418(1):L79–L83, 2011. doi: 10.1111/j.1745-3933.2011.01147.x. URL http://dx.doi.org/10.1111/j.1745-3933.2011.01147.x. 147, 169

M. Zamaninasab, E. Clausen-Brown, T. Savolainen, and A. Tchekhovskoy. Dynamically important magnetic fields near accreting supermassive black holes. nat, 510:126–128, June 2014. doi: 10.1038/nature13399. 147, 162, 169

Chapter 9

Conclusion

Contents

9.1 Conclusion

The underlying motivation for this work is the study of the infall and ejection mechanism of magnetized flows from the environment near the super massive black holes of Active Galaxy Nuclei (AGN). On the one hand, we focus mainly on the launching, acceleration and collimation of extragalactic jets. On the other hand, we study the interaction of pair inflow with the central black hole and in particular the possibility for the black hole to provide energy to the Magneto-Hydrodynamic (MHD) field. Finally, we try to combine these two types of flows in order to describe in a relatively consistant way the flow in the environment of the rotation axis from the horizon of the black hole to infinity. The power involved in these phenomena makes them a real challenge for our community. Nevertheless, in addition to the pure astronomical and astrophysical interests in measuring and understanding the objects and material formation outside our atmosphere. The study of these flows presents an obvious interest for high-energy physics and theoretical research on strong field gravitation. These objects are real laboratories for using and testing these theories. It is also relevant to the behavior and understanding of black holes. In addition, the study of these phenomena contains an interest for studying the composition of intergalactic medium in which AGN are immersed O'Sullivan et al. [2011].

In this goal we have constructed a meridional self-similar model, presented in Ch.(4, 5), of the General Relativistic Axi-symmetric Stationary Ideal Magneto-Hydrodynamic (GRASIMHD) in Kerr metric. This model integrates the effects of the light cylinder, neglected until now in previous models of this type. These solutions describe the flow in the environment of the symmetry axis. The MHD equations in the Kerr geometry were formulated using the tools of 3+1 formalism presented in Ch.(2). First, we did not take into account, in the construction of the model, the possible source terms that could come from, or take into account phenomena such as the pair production or the material injection in field lines at the base of the jet by the turbulent flow of the corona around the central object. The solutions of the model are calculated from the solution of an ordinary differential system of four equations. This system itself is characterized by seven parameters. Among these parameters, four of them $\lambda, \kappa, \delta, e_1$ are related to the variation of the first integrals or pressure with the magnetic flux. The next two μ, l, are characteristic of the gravitational field and the position of the Alfvén surface. The last parameter ν is linked to the launching velocity. The parameter e_1 is an additional parameter taking into account the variation of the Bernoulli integral with the magnetic flux. The effects of the light cylinder were integrated in the model by assuming a non-spherical Alfvénic Mach number. The new dependence of this quantity with the magnetic flux is determined by the regularity conditions at the Alfvén surface. We have also generalized the expression of the magnetic collimation efficiency integral ϵ characteristic of the differential system for the self-similar models. We have also proposed a new expression, allowing it to be linked to the balance between (a) logaritmic variation with the magnetic flux of the effective enthalpy per unit volume and (b) logaritmic variation with the magnetic flux of the pressure. The integration of the differential system was performed using an RK4 algorithm presented in Ch.(6). We have also developed within the code the possibility to automatically find the solutions of these equations crossing all the singular points (Sec.6.2.3) or choosing the most appropriate pressure value at the Alfvén point (Sec.6.3). A dedicated subroutine that allows us to continuously exploring the parameter space under certain constraints (Sec.6.4).

We started by using the model to produce outflow solutions. As in previous meridional self-similar models, the model contains two large classes of outflows according to the regime reached at some distance from the black hole. Indeed, the geometry of the poloidal field lines tends to those of a radial or cylindrical geometry at infinity. This says nothing about the geometry of the lines at the base or inside the flow, for which the behavior mays vary according to the solutions. As presented in Ch.(7), our solutions results in a wide variety of flow velocities on the polar axis. Close to the axis, all our solutions are enthalpy driven. Collimation is mainly ensured by the

toroidal magnetic field. By taking into account or not the Alfvénic Mach number dependency with magnetic flux, we are able to calculate solutions that takes into account the light cylinder radius effect x. When we include the effect of the light cylinder, we observed an increase in the final collimation, but also a decrease in the final velocity of the jet. We explored the effect of the l parameter by varying it, and thus the rotation of the black hole, keeping the other parameters constant, and exploring all possible rotation values. This study was done around a parameter set of a cylindrical solution and around a parameter set of a conical solution and it seems to show that conical solutions are more collimated to infinity when the absolute value of rotation increases, while the collimation of cylindrical solutions to infinity increases with l. We also did the same type of analysis around a cylindrical solution for the e_1 parameter. The increase of e_1 corresponds to more energy to be distributed in the poloidal field-lines flow outside of the axis. Thus the transverse stratification of velocities shows a decrease for higher values of e_1. Collimation decreases with e_1 increases. We can link the effect of e_1 on the solutions to the effect of δ. Using a scaling law from numerical simulations of McKinney [2005]; Tchekhovskoy and McKinney [2012]; Tchekhovskoy et al. [2011], or McKinney et al. [2012] but also comparing to observations (Zamaninasab et al. [2014]), we were also able to calculate, the efficiency of our jets. We measure by calculating the fraction of rest mass power accretion which leaves the central system with the part of the of the rest mass energy power of the accretion. We obtain efficiency values similar to those of the simulations. The magnetization define by the ratio of Poynting flux with internal energy flux is null by construction on the axis, but could reach $0.2-0.4$ on region quite close from the axis. The magnetization decrease with distance on a field line, it imply that even if this effect is quite small, their is an acceleration due to the toroidal magnetic field. Assuming that our fluid contains leptons and baryons with the same effective temperature and fluid velocity, the effective pressure accelerating our flow can be interpreted as the sum of the pressure of the leptons and those of the baryons. This allows, by comparing the effective temperature of a solution with the brightness temperature from the observations (Homan et al. [2006]), to calculate the leptonic and baryonic fractions inside the jet. This analysis seems to indicate a leptonic composition at the core of the jet that decreases in favor of the baryonic fraction as we move away from the axis. The effective temperature require to accelerate the flow in the models allow us to estimate the ratio between typical cooling time due to Compton, synchrotron process and dynamical cooling time. We see that is we interpret this effective temperature as thermal temperature the synchrotron process need to be taken account at the base of the jet and the Compton process qui everywhere in the jet. We have also tried to quantify, using the κ-relativistic distribution function (Sec.3.3.3), the deviation from the thermodynamical equilibrium required to produce the additional internal energy necessary for the enthalpy driven acceleration of our solutions. This analysis can be satisfactory for some solutions. For our solutions, the deviation from the thermodynamic equilibrium increases at the base of the flow.

The outflow solutions of the model are able to describe the flow outside a stagnation radius. We call this sphere the stagnation surface. In order to know if the energy contained in the magnetic field lines of the outflow comes from the disk or from the black hole, we have solved the MHD equations up to the horizon of the black hole. How to use the model to calculate flow solutions entering the black hole horizon is presented in Ch.(8). Indeed, although suffering from a discontinuity on the horizon due to the choice of coordinates, we showed, (Sec.8.2.1), that the equations of the model could be integrated upstream to the horizon. We also mentioned that the inflow model obeys the same type of scaling law as the one extracted from the numerical simulations of McKinney et al. [2012] and Tchekhovskoy et al. [2011] and those confirmed by Zamaninasab et al. [2014]. This scaling law connects the magnetic flux passing through the horizon and the infalling mass rate (not the accretion mass rate as in the previous mentioned work) as a function of the model parameters. We have started to calculate different inflow solutions (Sec.8.2). The dynamical analysis shows that at the base of the inflow, close to the stagnation radius, the pressure pushes the flow away from the equator to fall into the horizon. The acceleration

of the flow is dominated by gravity forces. We also observed in some of these flows a cancellation of the electrical force when the isorotation frequency Ω is equal to the frequency of the shift of the coordinates ω. This cancellation of the electric field has motivated various studies such as those of Levinson and Segev [2017] and Ford et al. [2017] concerning an electric gap. This property occurs relatively close to the black hole and may be above or below the stagnation radius. In Sec.(4.3), we detailed the calculations of the different energy fluxes at the black hole horizon. The different fields outside the horizon can benefit from the rotational energy of the black hole in two ways that can be combined in the case of the MHD, through the Poynting flux (Blandford-Znajek) or through the Lense-Thirring flux (Penrose). Using the numerical tools presented in Sec.(6.4), to cleverly explore our parameter space, we were able to find three solutions exposing with different compositions of the energy exchange with the black hole. All the calculated solutions slowed down the rotation of the black hole. The first solution was such that the black hole absorbed positive energy. In the second solution, for high latitude values we obtain lines with negative energies, the extraction process being dominated by the Lense-Thirring flux. The last solution also has negative energy lines dominated by the Poynting flux. In all three solutions, the Poynting flux comes out of the black hole.

Without source term, the mass flow remains constant over a field line of poloidal magnetic fields. It is therefore necessary to use the equations of the MHD with source terms, (Eqs.4.3, 4.4) to develop inflow/outflow solutions. The equation shape was calculated in case this filling was done using the pair creation mechanism in Sec.(3.1.8) with explicit expression of the source terms. This analysis can also be used to calculate the force of Compton and Inverse Compton effects on the fluid. The effects of these source terms on the first integrals of the GRASIMHD is studied in particular in Sec.(4.2.2). Nevertheless, the solutions of our model did not include these terms in their development, so we follow a similar approach to the one presented in Globus and Levinson [2013] and especially in Pu et al. [2015]. It consists to apply the minimal matching condition between an inflow solution and an outflow solution. A thin layer at the stagnation radius includes the necessary source terms to the two solutions. Electrical current and charge density are derived from the matching condition in Sec.(8.3.1). The minimum conditions of continuity at the stagnation radius do not fully constrain the outflow. We have calculated three outflow solutions which can match the inflow solutions presented previously using an injection of mass term. We calculated the solution of the MHD equations with poloidal field-lines connecting the black hole to infinity. We are able to calculate, for the lines reaching infinity, the source of the energy whether it comes from the source terms or from the black hole energy extraction. In our solutions, most of the mass loaded by source terms goes in the outflow. Nevertheless, we observe that the typical values of the energy fluxes and angular momentum fluxes are within one order variation between black hole and loading term contributions. We also discussed the values obtained for charge density and electric current per unit area.

9.2 Prospects

Indeed, it is necessary to explore in more details the different mechanisms which can explain the origin of the additional energy in the model solutions. This work was initiated by proposing an explanation based on a gas that would not be in thermodynamical equilibrium. The high energy tail of relativistic κ-distribution functions are not sufficient to explain the effective internal energy of some model solutions. Indeed, it is necessary to explore in more details the different mechanisms that can explain the origin of the additional energy of the model solutions. Other distribution functions could probably solve this problem. Nevertheless the processes leading to the formation of such distribution functions must also be explained (turbulence, magnetic reconnection, electrical gap...). Various explorations must also be pursued, such as questioning the energy of a radiative component, turbulence or the presence of MHD waves in the flow. It would also be interesting

to develop an emission model, or even a semi-analytical MHD model associated with a simplified radiative component. Indeed, an optically thick assumption for the gas (even if it is not the case for jets) could allow a mathematical treatment of the radiation in terms of additional pressure and internal energy for plasma. This treatment is really important to take account properly the effect on the flow dynamics of Compton and Synchrotron emission.

For matched solutions, we will search to obtain some where the extraction process is even more efficient. Indeed we need to adjust our parameters to decrease the spherical deviation $-e_1\alpha_{\mathcal{H}}$ for the Bernoulli energy, in order to increase the accreted magnetic flux. Doing that we will increase the energy release by the black hole. Finally, it would be useful to build a model that includes a more realistic injection term than the one included here. Other processes such as the Compton and Inverse Compton process could also be included. We also want to build a code to automatize the search for matching solutions presented in Sec.(8.4). We also need to investigate deeper on the role of electric field cancellation when the isorotation frequency is included in the range $0 \leq \Omega \leq \omega_{\mathcal{H}}$. We want to explore the implication of the position of this cancellation relatively to the stagnation surface.

It will also be crucial to test, using simulations, the stability of these solutions resulting from a latitudinal expansion of the Euler equations. First, we plan to work on the stability of our flows away from the source using the PLUTO code. Finally, it will be interesting to carry out some simulations with the AMR-VAC code, combining the two components of the flow, the spine jet using this model and the disk wind using a radial self-similar solution in order to study their interaction.

Finally, the model being the result of a expansion of Euler equations, we still have to calculate and quantify more precisely the non stationarity deviation of the model solutions. It would also be very interesting to search for exact self-similar models in Kerr metric. This type of work requires an accurate modeling of the MHD functions in order to obtain a successful variable separation.

9.3 References

A. L. Ford, B. D. Keenan, and M. V. Medvedev. Electron-Positron Cascade in Magnetospheres of Spinning Black Holes. *ArXiv e-prints*, June 2017. 176

N. Globus and A. Levinson. Loaded magnetohydrodynamic flows in Kerr spacetime. prd, 88(8): 084046, October 2013. doi: 10.1103/PhysRevD.88.084046. 176

D. C. Homan, Y. Y. Kovalev, M. L. Lister, E. Ros, K. I. Kellermann, M. H. Cohen, R. C. Vermeulen, J. A. Zensus, and M. Kadler. Intrinsic Brightness Temperatures of AGN Jets. apjl, 642:L115–L118, May 2006. doi: 10.1086/504715. 175

Amir Levinson and Noam Segev. Existence of steady gap solutions in rotating black hole magnetospheres. *Phys. Rev. D*, 96:123006, Dec 2017. doi: 10.1103/PhysRevD.96.123006. URL https://link.aps.org/doi/10.1103/PhysRevD.96.123006. 176

Jonathan C. McKinney. Total and jet blandford-znajek power in the presence of an accretion disk. *The Astrophysical Journal Letters*, 630(1):L5, 2005. URL http://stacks.iop.org/1538-4357/630/i=1/a=L5. 175

Jonathan C. McKinney, Alexander Tchekhovskoy, and Roger D. Blandford. General relativistic magnetohydrodynamic simulations of magnetically choked accretion flows around black holes. *Monthly Notices of the Royal Astronomical Society*, 423(4):3083–3117, 2012. doi: 10.1111/j.

1365-2966.2012.21074.x. URL http://dx.doi.org/10.1111/j.1365-2966.2012.21074.x. 175

E. O'Sullivan, D. M. Worrall, M. Birkinshaw, G. Trinchieri, A. Wolter, A. Zezas, and S. Giacintucci. Interaction between the intergalactic medium and central radio source in the NGC 4261 group of galaxies. mnras, 416:2916–2931, October 2011. doi: 10.1111/j.1365-2966.2011.19239.x. 174

Hung-Yi Pu, Masanori Nakamura, Kouichi Hirotani, Yosuke Mizuno, Kinwah Wu, and Keiichi Asada. Steady general relativistic magnetohydrodynamic inflow/outflow solution along large-scale magnetic fields that thread a rotating black hole. *The Astrophysical Journal*, 801(1):56, 2015. URL http://stacks.iop.org/0004-637X/801/i=1/a=56. 176

Alexander Tchekhovskoy and Jonathan C. McKinney. Prograde and retrograde black holes: whose jet is more powerful? *Monthly Notices of the Royal Astronomical Society: Letters*, 423(1): L55–L59, 2012. doi: 10.1111/j.1745-3933.2012.01256.x. URL http://dx.doi.org/10.1111/j.1745-3933.2012.01256.x. 175

Alexander Tchekhovskoy, Ramesh Narayan, and Jonathan C. McKinney. Efficient generation of jets from magnetically arrested accretion on a rapidly spinning black hole. *Monthly Notices of the Royal Astronomical Society: Letters*, 418(1):L79–L83, 2011. doi: 10.1111/j.1745-3933.2011.01147.x. URL http://dx.doi.org/10.1111/j.1745-3933.2011.01147.x. 175

M. Zamaninasab, E. Clausen-Brown, T. Savolainen, and A. Tchekhovskoy. Dynamically important magnetic fields near accreting supermassive black holes. nat, 510:126–128, June 2014. doi: 10.1038/nature13399. 175

Appendix A

Algebra

A.1 Parallel gradient

Took two n-variable function, A and Φ and for each point of the space their exist a scalar λ such that $\mathbf{D}\Phi = \lambda(\mathrm{M})\mathbf{D}\mathrm{A}$. Noting $(x^i)_{i=1..n}$ the system of coordinate, if A is not constant then we do not loss generality saying that $(\mathrm{A}(x^1,...x^n), x^2, ..., x^n)$ is also a coordinate system (changing of privilegied coordinate if we need). Then noting $\tilde{\Phi}(\mathrm{A}, x^2, ..., x^n) = \Phi(x^1, x^2, ..., x^n)$, we can differentiate this equation after few calculation and use of the main property we get,

$$\left(\frac{\partial\tilde{\Phi}}{\partial\mathrm{A}} - \lambda(\mathrm{M})\right) d\mathrm{A} + \frac{\partial\tilde{\Phi}}{\partial x^k} dx^k = 0 \tag{A.1}$$

This imply that $\Phi = \tilde{\Phi}(\mathrm{A}, x^2, ..., x^n) = \tilde{\Phi}(\mathrm{A})$.

A.2 Covariant derivative usual property

$$\Gamma^{\alpha}_{\beta\gamma} = \frac{1}{2} g^{\alpha\sigma} \left(\partial_\alpha g_{\beta\sigma} + \partial_\beta g_{\sigma\alpha} - \partial_\sigma g_{\alpha\beta}\right) \tag{A.2}$$

$$\Gamma^{\mu}_{\mu\alpha} = \partial_\alpha \ln\sqrt{-g} \tag{A.3}$$

This implies a common expression of the divergence vector,

$$\nabla\cdot\mathbf{v} = \frac{1}{\sqrt{-g}} \frac{\partial}{\partial x^\mu} \left(\sqrt{-g}\, v^\mu\right) \tag{A.4}$$

$$\mathrm{R}^{\alpha}_{\beta\gamma\delta} = \partial_\gamma \Gamma^{\alpha}_{\beta\delta} - \partial_\delta \Gamma^{\alpha}_{\beta\gamma} + \Gamma^{\alpha}_{\gamma\lambda}\Gamma^{\lambda}_{\beta\delta} - \Gamma^{\alpha}_{\delta\lambda}\Gamma^{\lambda}_{\beta\gamma} \tag{A.5}$$

A.3 Lie derivative

The Lie derivative of a field vector $\mathbf{v}$ along a field vector $\mathbf{u}$ expresses as,

$$\mathscr{L}_{\mathbf{u}}\mathbf{v} = \left[u^\mu \partial_\mu v^\nu - v^\mu \partial_\mu u^\nu\right] \mathbf{e}_\nu \tag{A.6}$$

For a form $\boldsymbol{\omega} = \omega_\mu \mathbf{d}x^\mu$,

$$\mathscr{L}_{\mathbf{u}}\boldsymbol{\omega} = \left(u^\mu \partial_\mu \omega_\alpha + \omega_\sigma \partial_\alpha u^\sigma\right) \mathbf{d}x^\alpha \tag{A.7}$$

Instead of the partial derivative ∂, we can use any connection without torsion as ∇. Indeed, for any tensor we get,

$$\mathscr{L}_{\mathbf{u}} \mathrm{T}^{\alpha_1...\alpha_k}_{\beta_1...\beta_l} = u^\mu \nabla_\mu \mathrm{T}^{\alpha_1...\alpha_k}_{\beta_1...\beta_l} - \sum_{i=1}^{k} \mathrm{T}^{\alpha_1...\overbrace{\sigma}^{i}...\alpha_k}_{\beta_1...\beta_l} \nabla_\sigma u^{\alpha_i} + \sum_{i=1}^{l} \mathrm{T}^{\alpha_1...\alpha_k}_{\beta_1...\underbrace{\sigma}_{i}...\beta_l} \nabla_{\beta_i} u^\sigma \tag{A.8}$$

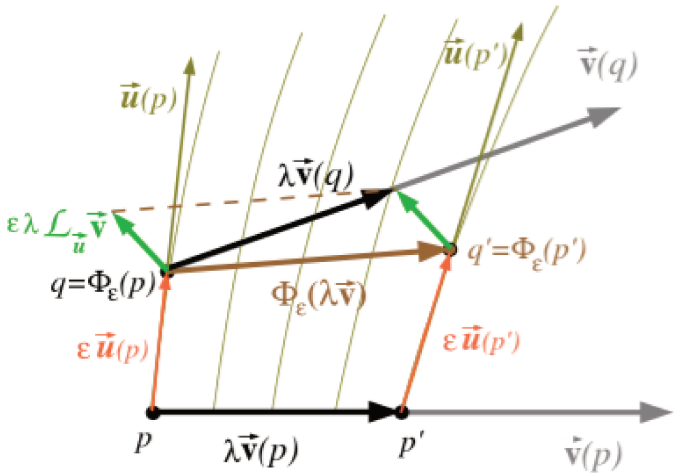

Figure A.1 – The construction of Lie derivation of a vector field (Credits : Gourgoulhon [2007])

A.4 Exterior derivative

If we call $\boldsymbol{\epsilon}$ the volume form, $\mathbf{d}$ the external derivative and $\mathbf{v}$ a vector field, we get the property,

$$\mathbf{d}(\mathbf{v}\cdot\boldsymbol{\epsilon}) = (\nabla\cdot\mathbf{v})\boldsymbol{\epsilon} \tag{A.9}$$

For a p-form $\boldsymbol{\omega}$, we get,

$$\mathscr{L}_{\mathbf{v}}\boldsymbol{\omega} = \mathbf{v}\cdot\mathbf{d}\boldsymbol{\omega} + \mathbf{d}(\mathbf{v}\cdot\boldsymbol{\omega}) \tag{A.10}$$

Stokes theorem,

$$\int_{\mathscr{U}} \mathbf{d}\boldsymbol{\omega} = \int_{\partial\mathscr{U}} \omega \tag{A.11}$$

A.5 Modified Bessel function

$$\frac{1}{x}\frac{d}{dx}\left(\frac{\mathrm{K}_n(x)}{x^n}\right) = -\frac{\mathrm{K}_{n+1}(x)}{x^{n+1}} \tag{A.12}$$

$$\mathrm{K}_{p+1}(x) - \mathrm{K}_{p-1}(x) = \frac{2p}{x}\mathrm{K}_p(x) \tag{A.13}$$

A.6 Hodge Dual

The hodge dual of a p-form wich act on vector space of dimension n is a (n-p)-form. The dual is proportional to its total contraction with the levi-civita tensor $\boldsymbol{\epsilon}$. Then

$$\star\omega = \boldsymbol{\epsilon} \underbrace{\cdot\ldots\cdot}_{\text{p times}} \omega \tag{A.14}$$

Thus for form on 4-dimensional spacetime

$$(\star\mathbf{v})_{\alpha\beta\gamma} = {}^4\epsilon^{\mu}{}_{\alpha\beta\gamma}\,v_\mu \tag{A.15}$$

For a two form we have

$$(\star\mathbf{F})_{\alpha\beta} = \frac{1}{2}{}^4\epsilon^{\mu\nu}{}_{\alpha\beta}\mathrm{F}_{\mu\nu} \tag{A.16}$$

A.7 Circular spacetime

Let introduce $(\mathscr{M},\mathbf{g})$ an axi-symmetric $(\boldsymbol{\xi})$ and stationnary $(\boldsymbol{\eta})$ four dimensionnal space-time. Then Carter [1970] show that no generality is lost considering that these Killing vector commute. This property imply that the curve parameter of these two Killing vector can be chosen as coordinate, then we have $\boldsymbol{\xi}=\boldsymbol{\partial}_\phi$ and $c\boldsymbol{\eta}=\boldsymbol{\partial}_t$. For each point $\mathrm{P}\in\mathscr{M}$, noting $\Pi_\mathrm{P}=\mathrm{Span}\left(\boldsymbol{\eta},\boldsymbol{\xi}\right)\subset\mathscr{T}_\mathrm{P}(\mathscr{M})$ the two plan subset of tangant space. Then we can decompose our tangent space,

$$\boxed{\mathscr{T}_\mathrm{P}(\mathscr{M})=\Pi\overset{\perp}{\bigoplus}\Pi^\perp} \tag{A.17}$$

If there is a family $\mathscr{P}_{t,\phi}\subset\mathscr{M}$ of two dimensional sub-manifold, which cover our spacetime $\bigcup_{t,\phi}\mathscr{P}_{t,\phi}=\mathscr{M}$ such that $\forall\mathrm{P}\in\mathscr{M}$ we have $\mathscr{T}_\mathrm{P}\left(\mathscr{P}_{t(\mathrm{P}),\phi(\mathrm{P})}\right)=\Pi^\perp$. Then we say that $\mathscr{M}$ is a circular space-time. In this case $\boldsymbol{\eta},\boldsymbol{\xi}$ are perpendicular to the poloidal sub manifold $\mathscr{P}_{t,\phi}\subset\mathscr{M}$. According to Frobenius theorem the necessary and sufficient conditions to be circular are.

$$\begin{aligned}\mathrm{C}_{\boldsymbol{\eta}}&\hat{=}\star\left(\boldsymbol{\eta}\wedge\boldsymbol{\xi}\wedge\mathbf{d}\boldsymbol{\eta}\right)=0\\ \mathrm{C}_{\boldsymbol{\xi}}&\hat{=}\star\left(\boldsymbol{\eta}\wedge\boldsymbol{\xi}\wedge\mathbf{d}\boldsymbol{\xi}\right)=0\end{aligned} \tag{A.18}$$

Introducing a coordinate (r,θ) system for the familly of poloidal sub-manifold. Then the natural basis associated to these coordinate $(\boldsymbol{\partial}_r,\boldsymbol{\partial}_\theta)$ are tangent to the poloidal sub-manifold. Which imply, using (eq.A.17) $\boldsymbol{\partial}_t\cdot\boldsymbol{\partial}_r=\boldsymbol{\partial}_t\cdot\boldsymbol{\partial}_\theta=\boldsymbol{\partial}_\phi\cdot\boldsymbol{\partial}_r=\boldsymbol{\partial}_\phi\cdot\boldsymbol{\partial}_\theta=0$. Using the fact that the coordinate r,θ,ϕ are adapted to the 3+1 decomposition, then the vector normal $\mathbf{n}$ is also perpendicular to $\boldsymbol{\partial}_r,\boldsymbol{\partial}_\theta,\boldsymbol{\partial}_\phi$, we can proove that the shift vector is only directed along $\boldsymbol{\xi}$, then we have

$$h\mathbf{n}=\boldsymbol{\eta}+\frac{\omega}{c}\boldsymbol{\xi}\qquad\text{with}\qquad\frac{\omega}{c}=-\frac{\boldsymbol{\eta}\cdot\boldsymbol{\xi}}{\boldsymbol{\xi}^2} \tag{A.19}$$

The metrics took the form,

$$\mathrm{d}s^2=-h^2c^2\mathrm{d}t^2+\varpi^2\left(\mathrm{d}\phi-\omega\mathrm{d}t\right)^2+h_r^2\mathrm{d}r^2+2h_{r,\theta}^2\mathrm{d}r\mathrm{d}\theta+h_\theta^2\mathrm{d}\theta^2 \tag{A.20}$$

Where the function h^2, ϖ^2, ω, h_r^2, $h_{r,\theta}^2$ and h_θ^2 are only function of r,θ because of stationarity and axi-symmetry.

Appendix B

Chapter 1 - 3+1 Methods

B.1 3+1 Decomposition of Einstein equations

Using the main tools of the 3+1 formalism, we propose here to detail the main steps to develop the chrono-geometric point of view of general relativity. As in Sec. (2.3) assume that the spacetime, $\mathscr{M}$, can be foliated with a spatial hyper-surface Σ_t of orthogonal unit vector $\mathbf{n}$.

Gauss and Codazzi relation

To get a chrono-geometric point of view on relativity, we need to be able to make a 3+1 decomposition of Einstein Equations. It means we need to be able to express all 3+1 components of the Ricci tensor, as presented here 2.2.1 for the energy-momentum tensor. First, let us begin with the **Codazzi** relations. We start projecting along $\mathbf{n}$ of Riemann tensor. To do so, we use the definition of Riemann tensor on the normal vector,

$$\left(\nabla_\alpha\nabla_\beta - \nabla_\beta\nabla_\alpha\right) n^\gamma = \mathrm{Riem}^\gamma_{\mu\alpha\beta}\, n^\mu\,, \tag{B.1}$$

Projecting this relation, we get,

$$p^\mu_\alpha p^\nu_\beta p^\gamma_\rho \left(\nabla_\mu\nabla_\nu - \nabla_\nu\nabla_\mu\right) n^\rho = p^\mu_\alpha p^\nu_\beta p^\gamma_\rho \mathrm{Riem}^\rho_{\sigma\mu\nu}\, n^\sigma\,, \tag{B.2}$$

To go further, remark that,

$$\begin{aligned} p^\mu_\alpha p^\nu_\beta p^\gamma_\rho \nabla_\mu\nabla_\nu n^\rho &= -p^\mu_\alpha p^\nu_\beta p^\gamma_\rho \nabla_\mu \left[\mathrm{K}^\rho_\nu + a^\rho n_\nu\right] \\ &= -p^\mu_\alpha p^\nu_\beta p^\gamma_\rho \left[\nabla_\mu \mathrm{K}^\rho_\nu + \nabla_\mu a^\rho n_\nu + a^\rho \nabla_\mu n_\nu\right] \\ &= p^\mu_\alpha p^\nu_\beta p^\gamma_\rho \left[-\nabla_\mu \mathrm{K}^\rho_\nu + a^\rho\left(\mathrm{K}_{\nu\mu} + a_\nu n_\mu\right)\right] \\ &= -\mathrm{D}_\alpha \mathrm{K}^\gamma_\beta + a^\gamma \mathrm{K}_{\alpha\beta} \end{aligned}$$

Because of the symmetry of the extrinsic curvature, we get the **Codazzi-Mainardi relation**,

$$\boxed{p^\mu_\alpha p^\nu_\beta p^\gamma_\rho \mathrm{Riem}^\rho_{\sigma\mu\nu}\, n^\sigma = \mathrm{D}_\beta \mathrm{K}^\gamma_\alpha - \mathrm{D}_\alpha \mathrm{K}^\gamma_\beta}\,. \tag{B.3}$$

To get the component of the Ricci tensor, contract this relation. Using the anti-symmetry of the Riemann tensor we get,

$$\boxed{p^\nu_\beta \mathrm{R}_{\sigma\nu} n^\sigma = \mathrm{D}_\beta \mathrm{K} - \mathrm{D}_\mu \mathrm{K}^\mu_\beta}\,. \tag{B.4}$$

Which is the **contracted Codazzi relation**. It gives the mixed component of the Ricci tensor. Now, we find a way to get the spatial component. Let us start from the first term of the intrinsic

curvature definition (eq.2.8),

$$\begin{aligned}
D_\alpha\left(D_\beta v^\gamma\right) &= p^\mu_\alpha p^\nu_\beta p^\gamma_\rho \nabla_\mu \left(D_\nu v^\rho\right) \\
&= p^\mu_\alpha p^\nu_\beta p^\gamma_\rho \nabla_\mu \left(p^\sigma_\nu p^\rho_\lambda \nabla_\sigma v^\lambda\right) \\
&= p^\mu_\alpha p^\nu_\beta p^\gamma_\rho \left[\nabla_\sigma v^\lambda \left\{p^\rho_\lambda \left((\nabla_\mu n_\nu) n^\sigma + n_\nu (\nabla_\mu n^\sigma)\right) + p^\sigma_\nu \left((\nabla_\mu n^\rho) n_\lambda + (\nabla_\mu n_\lambda) n^\rho\right)\right\} + p^\sigma_\nu p^\rho_\lambda \nabla_\mu \nabla_\sigma v^\lambda\right] \\
&= p^\mu_\alpha p^\nu_\beta p^\gamma_\lambda (\nabla_\mu n_\nu) n^\sigma \nabla_\sigma v^\lambda - p^\mu_\alpha p^\sigma_\beta p^\gamma_\rho (\nabla_\mu n^\rho) v^\lambda \nabla_\sigma n_\lambda + p^\mu_\alpha p^\sigma_\beta p^\gamma_\lambda \nabla_\mu \nabla_\sigma v^\lambda \\
&= -p^\mu_\alpha p^\nu_\beta p^\gamma_\lambda K_{\nu\mu} n^\sigma \nabla_\sigma v^\lambda - p^\mu_\alpha p^\sigma_\beta p^\gamma_\rho K^\rho_\mu K_{\lambda\sigma} v^\lambda + p^\mu_\alpha p^\sigma_\beta p^\gamma_\lambda \nabla_\mu \nabla_\sigma v^\lambda \\
&= -p^\gamma_\lambda n\sigma(\nabla_\sigma v^\lambda) K_{\beta\alpha} - K^\gamma_\alpha K_{\lambda\beta} v^\lambda + p^\mu_\alpha p^\sigma_\beta p^\gamma_\lambda \nabla_\mu \nabla_\sigma v^\lambda,
\end{aligned}$$

Which writes,

$$^{\Sigma}R^\gamma_{\mu\alpha\beta} v^\mu = (K^\gamma_\beta K_{\mu\alpha} - K^\gamma_\alpha K_{\mu\alpha}) v^\mu + p^\rho_\alpha p^\sigma_\beta p^\gamma_\lambda R^\lambda_{\mu\rho\sigma} v^\mu,$$

Because it is valid for each $\mathbf{v} \in \mathcal{T}(\mathcal{M})$, we obtain,

$$\boxed{p^\mu_\alpha p^\nu_\beta p^\gamma_\rho p^\sigma_\delta \mathrm{Riem}^\rho_{\sigma\mu\nu} = {}^{\Sigma}\mathrm{Riem}^\gamma_{\mu\alpha\beta} + \left(K^\gamma_\alpha K_{\delta\beta} - K^\gamma_\beta K_{\alpha\delta}\right)}. \tag{B.5}$$

This is the equation called **gauss relation**. It can be interesting to calculate the contraction to show up the Ricci tensor,

$$\boxed{p^\mu_\alpha p^\nu_\beta \left(R_{\mu\nu} + n^\lambda n^\rho \mathrm{Riem}_{\mu\rho\lambda\nu}\right) = {}^{\Sigma}R_{\alpha\beta} + K K_{\alpha\beta} - K_{\alpha\mu} K^\mu_\beta}. \tag{B.6}$$

This is the **contracted gauss relation**. Contract again to express the scalar curvature,

$$\boxed{R + 2\mathbf{R}(\mathbf{n},\mathbf{n}) = {}^{\Sigma}R + K^2 - K_{\mu\nu} K^{\mu\nu}}. \tag{B.7}$$

Indeed, using the symmetry of the Riemann tensor, we can show that $n^\lambda n^\rho p^{\mu\nu} \mathrm{Riem}_{\mu\rho\lambda\nu} = \mathbf{R}(\mathbf{n},\mathbf{n})$. This equation is called the **scalar Gauss relation**. It is a remarkable theorem because it links the intrinsic curvature ${}^{\Sigma}R$ to the extrinsic curvature $K^2 - K_{\mu\nu} K^{\mu\nu}$ and of the curvature of the manifold which contains the sub-manifold.

B.1.1 Lie derivative along m

There are some other important results to present in order to get the 3+1 decomposition of Einstein equations. First of all, let show that for for each vector field, $\forall \mathbf{v} \in \mathcal{T}(\Sigma_t)$, we have $\mathscr{L}_{\mathbf{m}} \mathbf{v} \in \mathcal{T}(\Sigma_t)$. There is a geometrical demonstration coming from the definition of Lie's derivative. Instead, we prefer to present here an analytical method using Eq. (A.6),

$$\begin{aligned}
\mathscr{L}_{\mathbf{m}} \mathbf{v} \cdot \mathbf{n} &= m^\mu (\partial_\mu v^\nu) n_\nu - v^\mu (\partial_\mu m^\nu) n_\nu \\
&= m^\mu v^\nu \partial_\mu (h \partial_\nu t) - v^\mu (\partial_\mu h n^\nu) n_\nu \\
&= -m^\mu (\partial_\mu \ln h) \underbrace{\mathbf{v} \cdot \mathbf{n}}_{0} + h m^\mu v^\nu \partial_\mu \partial_\nu t + v^\mu \partial_\mu h + \underbrace{h v^\mu (\partial_\mu \mathbf{n}) \cdot \mathbf{n}}_{0} \\
&= h m^\mu v^\nu \partial_\nu \partial_\mu t + v^\mu \partial_\mu h \\
&= -h m^\mu v^\nu \partial_\nu \frac{n_\mu}{h} + v^\mu \partial_\mu h \\
&= -h v^\nu \underbrace{n^\mu \partial_\nu n_\mu}_{0} + h^2 v^\nu \partial_\nu \frac{1}{h} + v^\mu \partial_\mu h = 0,
\end{aligned}$$

This property of Lie's derivative along $\mathbf{m}$ can be extended to any kind of tensor $\mathcal{T}(\Sigma_t)$, using Eq.(A.8). We can calculate the Lie derivative along $\mathbf{m}$ of the projector $p^\alpha_\beta = g^\alpha_\beta + n_\beta n^\alpha$

$$\begin{aligned}
\mathscr{L}_{\mathbf{m}} p^\alpha_\beta &= m^\mu \nabla_\mu \left(n^\alpha n_\mu\right) + p^\mu_\beta \nabla_\mu m^\alpha + p^\alpha_\mu \nabla_\beta m^\mu \\
&= m^\mu \nabla_\mu \left(n \alpha n_\mu\right) + p^\mu_\beta \left[h K^\alpha_\beta + D^\alpha h n_\mu - n^\alpha \nabla_\mu h\right] - p^\alpha_\mu \left[h K^\mu_\beta + D^\mu h n_\beta - n^\mu \nabla_\beta h\right] \\
&= D^\alpha h n_\beta + n^\alpha D_\beta h + h K^\alpha_\beta + 0 - n^\alpha D_\beta h - h K^\alpha_\beta - D^\alpha n_\beta + 0 = 0,
\end{aligned}$$

This implies that for any tensor tangent to the spatial hyper surface,

$$\boxed{\forall \mathbf{T} \in \mathcal{T}(\Sigma_t) \qquad \Rightarrow \qquad \mathscr{L}_{\mathbf{m}}\mathbf{T} \in \mathcal{T}(\Sigma_t)}. \tag{B.8}$$

We also need Lie's derivation along $\mathbf{m}$ of the spatial metrics. A similar calculation gives,

$$\boxed{\mathscr{L}_{\mathbf{m}}\gamma_{\alpha\beta} = -2hK_{\alpha\beta} \qquad \& \qquad \mathscr{L}_{\mathbf{m}}\gamma^{\alpha\beta} = 2hK^{\alpha\beta}}. \tag{B.9}$$

In the following we need to calculate Lie's derivative of the extrinsic curvature, using the property B.8,

$$\begin{aligned}
\mathscr{L}_{\mathbf{m}}K_{\alpha\beta} &= p^{\mu}_{\alpha}p^{\nu}_{\beta}\mathscr{L}_{\mathbf{m}}K_{\mu\nu} \\
&= p^{\mu}_{\alpha}p^{\nu}_{\beta}\left[m^{\sigma}\nabla_{\sigma}K_{\mu\nu} + K_{\sigma\nu}\nabla_{\mu}m^{\sigma} + K_{\mu\sigma}\nabla_{\nu}m^{\sigma}\right] \\
&= p^{\mu}_{\alpha}p^{\nu}_{\beta}\left[hn^{\sigma}\nabla_{\sigma}K_{\mu\nu} - 2hK_{\mu\sigma}K^{\sigma}_{\nu} - K_{\mu\sigma}D^{\sigma}hn_{\nu} - K_{\nu\sigma}D^{\sigma}hn_{\mu}\right],
\end{aligned}$$

So we get,

$$\mathscr{L}_{\mathbf{m}}K_{\alpha\beta} = hp^{\mu}_{\alpha}p^{\nu}_{\beta}n^{\sigma}\nabla_{\sigma}K_{\mu\nu} - 2hK_{\alpha\sigma}K^{\sigma}_{\beta}. \tag{B.10}$$

B.1.2 3+1 Decomposition of Ricci tensor

The decomposion of the Ricci tensor is the basis of the 3+1 decomposition of Einstein's equations. In sec.B.1 we start establishing some useful relations to decompose the Ricci tensor. From contracted Gauss relation (eq.B.6), in order to calculate the spatial part of the Ricci tensor we need to express the mixed Riemman tensor $p^{\mu}_{\alpha}p^{\nu}_{\beta}n^{\lambda}n_{\rho}R^{\rho}_{\mu\lambda\nu}$ in term of the 3+1 quantities.

$$\begin{aligned}
p^{\nu}_{\beta}p_{\mu\alpha}n^{\sigma}\mathrm{Riem}^{\mu}_{\rho\nu\sigma}n^{\rho} &= p^{\nu}_{\beta}p_{\mu\alpha}n^{\sigma}\left(\nabla_{\nu}\nabla_{\sigma} - \nabla_{\sigma}\nabla_{\nu}\right)n^{\mu} \\
&= p^{\nu}_{\beta}p_{\mu\alpha}n^{\sigma}\left[\nabla_{\nu}\left\{-K^{\mu}_{\sigma} - D^{\mu}\ln hn_{\sigma}\right\} + \nabla_{\sigma}\left\{K^{\mu}_{\nu} + D^{\mu}\ln hn_{\nu}\right\}\right] \\
&= p^{\nu}_{\beta}p_{\mu\alpha}n^{\sigma}\left[\nabla_{\sigma}K^{\mu}_{\sigma} - \nabla_{\nu}K^{\mu}_{\sigma} + \nabla_{\sigma}\left(D^{\mu}\ln h\right)n_{\nu} + D^{\mu}\ln h\nabla_{\sigma}n_{\nu} - \nabla_{\nu}\left(D^{\mu}\ln h\right)n_{\sigma} - D^{\mu}\ln h\nabla_{\nu}n_{\sigma}\right] \\
&= p^{\nu}_{\beta}p_{\mu\alpha}n^{\sigma}\nabla_{\sigma}K^{\mu}_{\sigma} - p^{\nu}_{\beta}p_{\mu\alpha}K^{\mu}_{\sigma}\left(K^{\sigma}_{\nu} + D^{\sigma}\ln hn_{\nu}\right) + p^{\nu}_{\beta}p_{\mu\alpha}D^{\mu}\ln ha_{\nu} + p^{\nu}_{\beta}p_{\mu\alpha}\nabla_{\nu}\left(D^{\mu}\ln h\right) \\
&= p^{\nu}_{\beta}p_{\mu\alpha}n^{\sigma}\nabla_{\sigma}K^{\mu}_{\sigma} - K_{\alpha\sigma}K^{\sigma}_{\beta} + \frac{D_{\beta}D_{\alpha}h}{h},
\end{aligned}$$

Using Eq. (B.10), we end up with,

$$p^{\nu}_{\beta}p_{\mu\alpha}n^{\sigma}\mathrm{Riem}^{\mu}_{\rho\nu\sigma}n^{\rho} = \frac{1}{h}\mathscr{L}_{\mathbf{m}}K_{\alpha\beta} + \frac{D_{\beta}D_{\alpha}h}{h} + K_{\alpha\sigma}K^{\sigma}_{\beta}, \tag{B.11}$$

So, using the contracted Gauss relation (eq.B.6) and Eq. (B.11), we are able to express the spatial component of the Ricci tensor, called **Ricci equation**,

$$\boxed{\mathbf{p}^{\star}\mathbf{R} = -\frac{1}{h}\mathscr{L}_{\mathbf{m}}\mathbf{K} - \frac{\mathbf{D}\mathbf{D}h}{h} + {}^{\Sigma}\mathbf{R} + \mathrm{K}\mathbf{K} - 2\mathbf{K}\cdot\mathbf{K}}. \tag{B.12}$$

The mixed component of the Ricci tensor is given by the contracted Codazzi relation (eq.B.4), that we write in a different form,

$$\boxed{\mathbf{R}\left(\mathbf{p}(.),\mathbf{n}\right) = \mathbf{D}\mathrm{K} - \mathbf{D}\cdot\mathbf{K}}. \tag{B.13}$$

Take the spatial trace of Eq. (B.12), using also Eq. (B.9) to get the temporal part,

$$\begin{aligned}
\gamma^{\sigma\lambda}p^{\mu}_{\sigma}p^{\nu}_{\lambda}R_{\mu\nu} &= -\frac{\gamma^{\mu\nu}}{h}\mathscr{L}_{\mathbf{m}}K_{\mu\nu} - \frac{\mathbf{D}^2h}{h} + {}^{\Sigma}R_{\sigma\lambda}\gamma^{\sigma\lambda} + K_{\sigma\lambda}\gamma^{\sigma\lambda} - 2K_{\mu\nu}K^{\mu\nu} \\
\gamma^{\mu\nu}R_{\mu\nu} &= -\frac{1}{h}\mathscr{L}_{\mathbf{m}}K + \frac{K_{\mu\nu}}{h}\mathscr{L}_{\mathbf{m}}\gamma^{\mu\nu} - \frac{\mathbf{D}^2h}{h} + {}^{\Sigma}R + K^2 - 2K_{\mu\nu}K^{\mu\nu} \\
R + \mathbf{R}(\mathbf{n},\mathbf{n}) &= -\frac{1}{h}\mathscr{L}_{\mathbf{m}}K + 2K_{\mu\nu}K^{\mu\nu} - \frac{\mathbf{D}^2h}{h} + {}^{\Sigma}R + K^2 - 2K_{\mu\nu}K^{\mu\nu},
\end{aligned}$$

Thus we have,

$$\mathrm{R}+\mathbf{R}(\mathbf{n},\mathbf{n})=-\frac{1}{h}\mathscr{L}_{\mathbf{m}}\mathrm{K}-\frac{\mathbf{D}^2h}{h}+{}^{\Sigma}\mathrm{R}+\mathrm{K}^2, \tag{B.14}$$

Which combined with (eq.B.7) gives,

$$\boxed{\mathbf{R}(\mathbf{n},\mathbf{n})=\frac{1}{h}\mathscr{L}_{\mathbf{m}}\mathrm{K}+\frac{\mathbf{D}^2h}{h}+\mathrm{K}_{\mu\nu}\mathrm{K}^{\mu\nu}}. \tag{B.15}$$

B.1.3 Decomposition of Stress-Energy tensor

In order to decompose Einstein's equations, the second step is to decompose the stress-energy tensor. Let introduce the **energy density** measured by the Zero Angular Momentum Observer (ZAMO).

$$\mathrm{E}=\mathbf{T}(\mathbf{n},\mathbf{n}) \tag{B.16}$$

In a similar way we can introduce the **momentum density flux** measured by the ZAMO,

$$\boxed{\mathbf{p}=-\mathbf{T}\left(\mathbf{n},\mathbf{p}(.)\right)} \tag{B.17}$$

Finally, the spatial part, which can be interpreted as a **stress tensor** measured by ZAMO, is,

$$\mathbf{S}=-\mathbf{T}\left(\mathbf{p}(.),\mathbf{p}(.)\right) \tag{B.18}$$

The introduction of these quantities allows us to decompose the stress energy tensor with respect to the ZAMO observer,

$$\boxed{\mathbf{T}=\mathrm{E}\mathbf{n}\otimes\mathbf{n}+\mathbf{n}\otimes\mathbf{p}+\mathbf{p}\otimes\mathbf{n}+\mathbf{S}} \tag{B.19}$$

This relation is fully general and can satisfy different kind of physical situations. Indeed, one just need to add the different kind of stress-energy tensors which compose the different physical components of the studied problem. Thus the trace of the stress-energy tensor is

$$\mathrm{T}=\mathrm{S}-\mathrm{E} \tag{B.20}$$

B.1.4 Decomposition of Einstein equations

After the work done before the decomposition of Einstein equation will be easy. Indeed from Einstein equation:

$$\boxed{\mathbf{R}-\frac{1}{2}\mathrm{R}\mathbf{g}=\frac{8\pi\mathscr{G}}{c^4}\mathbf{T}\qquad\text{or}\qquad\mathbf{R}=\frac{8\pi\mathscr{G}}{c^4}\left(\mathbf{T}-\frac{1}{2}\mathrm{T}\mathbf{g}\right)} \tag{B.21}$$

we can easily took the full spatial projection of the second way of writing the Einstein equation (eq.B.21), of these equations, using (eq.B.12) for the geometric left hand side, and (eq.B.20&B.18) for the physical right hand side. We obtain:

$$\boxed{\mathscr{L}_{\mathbf{m}}\mathrm{K}=-\mathbf{D}^2h+h\left\{{}^{\Sigma}\mathbf{R}+\mathrm{K}\mathbf{K}-2\mathbf{K}\cdot\mathbf{K}+\frac{8\pi\mathscr{G}}{c^4}\left((\mathrm{S}-\mathrm{E})\boldsymbol{\gamma}-2\mathbf{S}\right)\right\}}. \tag{B.22}$$

Where each term belongs to $\mathscr{T}_{\mathrm{P}}(\Sigma_t)$. We called this equation **full spatial projection of Einstein equation**. It gives you the time evolution of the second fundamental form. For the full temporal projection, using the first way of writing the Einstein equation (eq.B.21), after replace the left-hand side in using the contracted Gauss relation (eq.B.7) and for the left hand side the definition of energy density (eq.B.16) and the calculus of the trace of stress-energy tensor (eq.B.20), we obtain,

$$\boxed{{}^{\Sigma}\mathrm{R}+\mathrm{K}^2-\mathrm{K}_{\mu\nu}\mathrm{K}^{\mu}\nu=\frac{16\pi\mathscr{G}}{c^4}\mathrm{E}}. \tag{B.23}$$

This equation is also called the **Hamiltonian constraint**. It represented the link between the sum of intrisic and extrinsic scalar curvature and the density of energy of stress-tensor. Finally let's calculate the mixed projection. Using the first way of writing the Einstein equation (eq.B.21), after for the left hand side using the mixed projection of Ricci tensor (eq.B.13) and the definition of the momentum density flux (eq.B.17), we finally obtain:

$$\boxed{\mathbf{D}\cdot\mathbf{K}-\mathbf{D}\mathrm{K}=\frac{8\pi\mathscr{G}}{c^4}\mathbf{p}}. \tag{B.24}$$

That we called **mixed projection of Einstein equation**. The Einstein equation is equivalent to the system of equation (eqs.B.22 &B.24 &B.23). The full spatial projection of Einstein equation (eq.B.22) is a symetric and second tensorial order equations of $\mathscr{T}_{\mathrm{P}}(\Sigma_t)$, so it contains 6 scalars equations. For the mixed projection (eq.B.24) of Einstein equation it is a vectorial equation of $\mathscr{T}_{\mathrm{P}}\Sigma_t$ so it gives 3 scalars equations. And finally the Hamiltonian constrain (eq.B.23) gives one equation. So finally we get the 10 usual scalar Einstein equations. In fact the system is a second order system in term of the space-time metrics }. Adding the equation (eq.B.9), and re-ordering terms, we get a second order partial differential system ruling the evolution of $(\boldsymbol{\gamma},\mathbf{K},h,\boldsymbol{\beta})$, with the two constrain equation (eq.B.24&B.23).

The system constitutes by (eqs.B.9 &B.22 &B.24 &B.23) only imply quantity's define in $\mathscr{T}(\Sigma)$ and their time derivative thus it implies that we can consider only a manifold Σ_t which evolves during time, this is the chronogeometrics point of view on general relativity developed by Wheeler [1964]. The considered system do not contain any time derivative of the lapse function of shift vector, they are not dynamical variable. Which is not surprising if we remember us that they are function of the choice of the slicing (or temporal coordinate). In fact the gauge freedom for the system of coordinate in general relativity implies that we can impose a condition on the shift vector and the lapse function without change the physical solution. After integrating the equation an thus the knowledge of a volume of the spacetime we always can coming back to a different system of coordinate. The choose of the constraint need to be done in order to avoid singularity on coordinate.

B.2 General definition, property and composition of spatial operators

Using the definition of spatial covariant derivative $\mathbf{D}$ we are able, to construct the usual operators. The gradient is simply the application of spatial covariant derivative on a scalar function Φ. The co-variant component are the same but we need to be careful about the contra-variant one:

$$\begin{cases}\mathrm{D}_i\Psi=\partial_i\Psi\\ \mathrm{D}^i\Psi=\partial^i\Psi+n^{\mu}\partial_{\mu}\Psi n^i\end{cases} \tag{B.25}$$

The expression (eq.A.4) is also valid for space manifold, where the determinant of the metric is the determinant of spatial induced metrics. The link between spatial and space-time divergence is already calculate in (eq.2.23). Using the definition (eq.B.31) we are able to introduce the curl product,

$$\mathbf{A}\times\mathbf{B}=^3\epsilon^k{}_{ij}\mathrm{A}^i\mathrm{B}^j\mathbf{e}_k \tag{B.26}$$

Introduce also the property of permutativity of mixed product, wich came from permutativity of Levi-Civita tensor,

$$(\mathbf{A}\times\mathbf{B})\cdot\mathbf{C}=(\mathbf{C}\times\mathbf{A})\cdot\mathbf{B} \tag{B.27}$$

And thus, the curl operator:

$$\mathbf{D}\times\mathbf{V}=\star\mathbf{D}\mathbf{V}=^3\epsilon^i{}_j{}^k\partial_i(\mathrm{V}^j)\vec{e}_k \tag{B.28}$$

We also introduce the non symmetric advection operator,

$$(\mathbf{A}\cdot\mathbf{D})\mathbf{B} = \mathrm{A}^{\alpha}\mathrm{D}_{\alpha}\mathrm{B}^{\beta}\vec{e}_{\beta}$$

For the Laplacian operator,

$$\begin{aligned}\Delta\Psi &= \mathbf{D}\cdot(\mathbf{D}\Psi)\\ \Delta\Psi &= \mathbf{D}\,(\mathbf{D}\cdot\mathbf{A})\end{aligned} \tag{B.29}$$

These definition allow us to calculate some product based on Leibniz rule,

$$\begin{aligned}&\mathbf{D}\cdot(\alpha\mathbf{A}) = \alpha\mathbf{D}\cdot(\mathbf{A}) + \mathbf{D}\alpha\cdot\mathbf{A}\\ &\mathbf{D}\times(\alpha\mathbf{A}) = \alpha\mathbf{D}\times(\mathbf{A}) + \mathbf{D}\alpha\times\mathbf{A}\\ &\mathbf{D}\,(\mathbf{A}\cdot\mathbf{B}) = (\mathbf{A}\cdot\mathbf{D})\mathbf{B} + (\mathbf{B}\cdot\mathbf{D})\mathbf{A} + \mathbf{A}\times(\mathbf{D}\times\mathbf{B}) + \mathbf{B}\times(\mathbf{D}\times\mathbf{A})\\ &\mathbf{D}\times(\mathbf{A}\times\mathbf{B}) = (\mathbf{B}\cdot\mathbf{D})\mathbf{A} - (\mathbf{A}\cdot\mathbf{D})\mathbf{B} + (\mathbf{D}\cdot\mathbf{B})\mathbf{A} - (\mathbf{D}\cdot\mathbf{A})\mathbf{B}\\ &\mathbf{D}\cdot(\mathbf{A}\times\mathbf{B}) = -\mathbf{A}\cdot(\mathbf{D}\times\mathbf{B}) + \mathbf{B}\cdot(\mathbf{D}\times\mathbf{A})\\ &\mathbf{D}\alpha\beta = \beta\mathbf{D}\alpha + \alpha\mathbf{D}\beta\end{aligned} \tag{B.30}$$

B.3 Integration on hypersurfaces

As in 2.1 used a three dimensional plunged sub-manifold Σ, and note $\mathbf{n}$ his normal vector field. Then the induced Levi-Civita tensor on this hyper surface is

$${}^{3}\boldsymbol{\epsilon} = {}^{4}\boldsymbol{\epsilon}\,(\mathbf{n},.,.,.) \tag{B.31}$$

Apply the Stocks theorem on the Hodge dual of a one form $\boldsymbol{\omega}$ on a 3-dimensional subset $\mathcal{V}\subset\Sigma$, we have

$$\iiint_{\mathcal{V}}\mathbf{d}\,(\star\boldsymbol{\omega}) = \iint_{\partial\mathcal{V}}\star\boldsymbol{\omega}$$

Using (eq.A.9) and (eq.A.14) we obtain,

$$\iiint_{\mathcal{V}}\mathbf{D}\cdot\boldsymbol{\omega}^{3}\boldsymbol{\epsilon} = \iint_{\partial\mathcal{V}}\boldsymbol{\omega}\cdot{}^{3}\boldsymbol{\epsilon}$$

This is the **Green-Ostrogradskii** theorem, often written in the form:

$$\boxed{\iiint_{\mathbf{V}}\mathbf{D}\cdot\mathbf{B}dV = \iint_{\mathscr{S}}\mathbf{B}\cdot\mathbf{dS}} \tag{B.32}$$

Took an hypersurface $\mathscr{S}$ of Σ, then $\mathscr{S}$ is a 2-dimensionnal manifold. We can apply the Stocks theorem for a one form $\boldsymbol{\omega}$ and using the definition of curl operator (eq.B.28) and the fact that the composition of Hodge dual is identity, we get,

$$\begin{aligned}\int_{\partial\mathscr{S}}\boldsymbol{\omega} &= \iint_{\mathbf{S}}\mathbf{d}\boldsymbol{\omega}\\ &= \iint_{\mathscr{S}}\partial_{\alpha}\omega_{\beta}\mathbf{dx}^{\beta}\wedge\mathbf{dx}^{\alpha}\\ &= \iint_{\mathscr{S}}\star(\mathbf{D}\times\boldsymbol{\omega})\\ &= \iint_{\mathscr{S}}(\mathbf{D}\times\boldsymbol{\omega})\cdot{}^{3}\boldsymbol{\epsilon}\end{aligned}$$

This is the **Kelvin-Stokes** theorem, often written in the form:

$$\boxed{\iint_{\mathscr{S}}(\mathbf{D}\times\mathbf{A})\cdot\mathbf{dS} = \int_{\mathscr{C}}\mathbf{A}\cdot\mathbf{d}\ell} \tag{B.33}$$

Appendix C

Chapter 2 - Magneto-Hydrodynamics in curved spacetime

C.1 Conservation of volume form of phase space

Find here the detail of calculus which lead to the conservation of the volume form of space phase along geodesic movement (eq.3.20), for the a and b term we get:

$$\begin{aligned} a &= \frac{\partial u^\mu}{\partial x^\mu} = \frac{\partial u^0}{\partial x^0} \\ &= -\frac{1}{2u_0}\frac{\partial g_{\mu\nu}}{\partial x^0}u^\mu u^\nu \end{aligned} \qquad \begin{aligned} b &= u^\mu\left[\frac{\partial \ln g}{\partial x^\mu} - \frac{1}{u_0}\frac{\partial u_0}{\partial x^\mu}\right] \\ &= 2u^\mu \Gamma^\lambda_{\lambda\mu} - \frac{\partial g_{0\nu}}{\partial x^\mu}\frac{u^\mu u^\nu}{u_0} + \frac{g_{00}}{2u_0^2}\frac{\partial g_{\sigma\nu}}{\partial x^\mu}u^\sigma u^\nu u^\mu \end{aligned} \tag{C.1}$$

For c and d term we get:

$$\begin{aligned} c &= \Gamma^i_{\mu\nu}u^\mu u^\nu \frac{\partial}{\partial u^i}\ln u_0 = \frac{u^\mu u^\nu}{u_0^2}\Gamma^i_{\mu\nu}\left(g_{0i}u_0 - g_{00}u_i\right) \\ &= \frac{u^\mu u^\nu}{u_0^2}\left[\Gamma^i_{\mu\nu}\left(g_{0i}u_0 - g_{00}u_i\right) + \Gamma^0_{\mu\nu}\left(g_{00}u_0 - g_{00}u_0\right)\right] \\ &= \frac{u^\mu u^\nu}{u_0^2}\Gamma^\lambda_{\mu\nu}\left(g_{0\lambda}u_0 - g_{00}u_\lambda\right) \\ &= \frac{u^\mu u^\nu}{u_0^2}\left(2\frac{\partial g_{\nu\sigma}}{\partial x^\mu} - \frac{\partial g_{\nu\nu}}{\partial x^\sigma}\right)\left(\delta^\sigma_0 u_0 - g_{00}u^\sigma\right) \\ &= \frac{u^\mu u^\nu}{u_0^2}\frac{\partial g_{0\nu}}{\partial x^\mu} + \frac{u^\mu u^\nu}{2u_0}\frac{\partial g_{\mu\nu}}{\partial x^0} - \frac{g_{00}u^\mu u^\nu u^\sigma}{2u_0^2}\frac{\partial g_{\sigma\nu}}{\partial x^\mu} \end{aligned}$$

$$\begin{aligned} d &= \Gamma^i_{\mu\nu}\frac{\partial}{\partial u^i}\left(u^\mu u^\nu\right) = -2\Gamma^i_{\mu\nu}u^\mu\frac{\partial u^\nu}{\partial u^i} \\ &= -2\left(\Gamma^i_{0\mu}u^\mu\frac{\partial u^0}{\partial u^i} + \Gamma^i_{k\mu}u^\mu\frac{\partial u^k}{\partial u^i}\right) \\ &= 2\Gamma^i_{0\mu}u^\mu\frac{u_i}{u_0} - 2\Gamma^i_{i\mu}u^\mu \\ &= 2\frac{u^\mu}{u_0}\left(\Gamma^0_{0\mu}u_0 + \Gamma^i_{0\mu}u_i\right) - 2\Gamma^\lambda_{\lambda\mu}u^\mu \\ &= 2\frac{u^\mu}{u_0}\Gamma^\lambda_{0\mu}u_\lambda - 2\Gamma^\lambda_{\lambda\mu}u^\mu \\ &= 2\frac{u^\mu u^\nu}{u_0}\frac{\partial g_{\mu\nu}}{\partial x^0} - 2\Gamma^\lambda_{\lambda\mu}u^\mu \end{aligned} \tag{C.2}$$

About the movement due to electro-magnetism forces, using the relation (eq.3.5) and the anti-symmetry of electro-magnetic tensor, the t term gives:

$$\begin{aligned} t &= \mathrm{F}^i{}_\mu\frac{\partial}{\partial u^i}\left(\frac{u^\mu}{u_0}\right) \\ &= \mathrm{F}^i{}_\mu\left[-\frac{u^\mu}{u_0}\frac{\partial u_0}{\partial u^i} + \frac{\partial u^\mu}{\partial u^i}\right] \\ &= -\frac{\mathrm{F}^i{}_\mu u^\mu}{u_0^2}\left(g_{0i}u_0 - g_{00}u_i\right) + \mathrm{F}^i{}_k\frac{\partial u^k}{\partial u^i} - \mathrm{F}^i{}_0\frac{\partial u^0}{\partial u^i} \\ &= -\frac{\mathrm{F}^\nu{}_\mu u^\mu}{u_0^2}\left(g_{0\nu}u_0 - g_{00}u_\nu\right) + \mathrm{F}^i{}_i - \mathrm{F}^i{}_0\frac{u_i}{u_0} \\ &= -\frac{\mathrm{F}_0{}^\mu u_\mu}{u_0} + \frac{g_{00}\mathrm{F}_{\mu\nu}u^\mu u^\nu}{u_0^2} + +\mathrm{F}^i{}_i - \mathrm{F}^i{}_0\frac{u_i}{u_0} = 0 \end{aligned} \tag{C.3}$$

C.2 Flux of Feynmann four current of phase space

Took one particle denote $\star$, wich are plunged into our space-time manifold and obeys to (eq.3.18) so, get a trajectory in space phase: $z_\star^{\tilde{\mu}} : s \to z_\star(s)^{\tilde{\mu}} \in \mu$. Using one spatial hyper-surface Σ_{t_0} of our foliation, we note $\sigma_t = \Sigma_t \times \Omega$ a foliation of the space phase. Using the fact that $\mathbf{N} = \mathbf{n} \otimes \mathbf{0}$ is normal to σ_t and that $\mathbf{N} \cdot \frac{\mathbf{dz}}{\mathrm{ds}} = -hu^0 = -h\frac{\mathrm{dx}^0}{\mathrm{ds}}$ and the fact that elematary volume element of σ_t is $\delta^6\sigma = \frac{g}{hu_0}\mathrm{dx}^1\mathrm{dx}^2\mathrm{dx}^3\mathrm{du}^1\mathrm{du}^2\mathrm{du}^3$, if particles aren't being created or annihilated we can write:

$$
\begin{aligned}
1 &= \int_{\sigma_{t_0}} \delta^{(3)}\left(x^i - x_\star^i(s(t_0))\right)\delta^{(3)}\left(u^j - u_\star^j(s(t_0))\right)\mathrm{dx}^1\mathrm{dx}^2\mathrm{dx}^3\mathrm{du}^1\mathrm{du}^2\mathrm{du}^3 \\
&= \int_{\sigma_{t_0}} \delta^{(3)}\left(x^i - x_\star^i(s(t_0))\right)\delta^{(3)}\left(u^j - u_\star^j(s(t_0))\right)\left[\int_{t\in\mathbb{R}} \delta\left(x^0 - x_\star^0(s(t_0))\right)\mathrm{dx}^0\right]\mathrm{dx}^1\mathrm{dx}^2\mathrm{dx}^3\mathrm{du}^1\mathrm{du}^2\mathrm{du}^3 \\
&= \int_{\sigma_{t_0}}\int_{t\in\mathbb{R}} \delta^{(3)}\left(x^i - x_\star^i\left(s(x^0)\right)\right)\delta^{(3)}\left(u^j - u_\star^j\left(s(x^0)\right)\right)\delta\left(x^0 - x_\star^0(s(t_0))\right)\mathrm{dx}^0\mathrm{dx}^1\mathrm{dx}^2\mathrm{dx}^3\mathrm{du}^1\mathrm{du}^2\mathrm{du}^3 \\
&= \int_{\sigma_{t_0}}\int_{t\in\mathbb{R}} \delta^{(3)}\left(x^i - x_\star^i\left(s(x^0)\right)\right)\delta^{(3)}\left(u^j - u_\star^j\left(s(x^0)\right)\right)\delta\left(x^0 - x_\star^0(s(t_0))\right)\frac{\mathrm{dx}^0}{\mathrm{ds}}\mathrm{ds}\,\mathrm{dx}^1\mathrm{dx}^2\mathrm{dx}^3\mathrm{du}^1\mathrm{du}^2\mathrm{du}^3 \\
&= \int_{\sigma_{t_0}}\left[\int_{s\in\mathbb{R}} \delta^{(7)}\left(z^{\tilde{\mu}} - z_\star^{\tilde{\mu}}(s)\right)\frac{\mathrm{dx}^0}{\mathrm{ds}}\mathrm{ds}\right]\mathrm{dx}^1\mathrm{dx}^2\mathrm{dx}^3\mathrm{du}^1\mathrm{du}^2\mathrm{du}^3 \\
&= \int_{\sigma_{t_0}}\left[\int_{s\in\mathbb{R}} \delta^{(7)}\left(z^{\tilde{\mu}} - z_\star^{\tilde{\mu}}(s)\right)\frac{1}{h}\left(\mathbf{N}\cdot\frac{\mathbf{dz}}{\mathrm{ds}}\right)\mathrm{ds}\right]\mathrm{dx}^1\mathrm{dx}^2\mathrm{dx}^3\mathrm{du}^1\mathrm{du}^2\mathrm{du}^3 \\
&= \int_{\sigma_{t_0}}\int_{s\in\mathbb{R}} \frac{u_0}{g}\delta^{(7)}\left(z^{\tilde{\mu}} - z_\star^{\tilde{\mu}}(s)\right)\mathrm{ds}\frac{\mathbf{dz}}{\mathrm{ds}}\cdot\mathbf{N}\frac{g}{hu_0}\mathrm{dx}^1\mathrm{dx}^2\mathrm{dx}^3\mathrm{du}^1\mathrm{du}^2\mathrm{du}^3 \\
&= \int_{\sigma_{t_0}}\left[\left(\int_{s\in\mathbb{R}} \delta_{\mu}^{(7)}\left(z^{\tilde{\mu}} - z_\star^{\tilde{\lambda}}(s)\right)\mathrm{ds}\right)\frac{\mathbf{dz}}{\mathrm{ds}}\right]\cdot\mathbf{N}\delta^6\sigma
\end{aligned}
\tag{C.4}
$$

C.3 Equation of transfer

Consider $\mathscr{U} \subset \mathscr{M}$ any subsets of spacetime. Note $\mathscr{W} = \mathscr{U} \times \Omega \subset \mu$ a subset of space phase, let calculate the integrals,

$$
\begin{aligned}
\mathrm{I} &= \int_{\mathscr{W}} \hat{\mathscr{L}}\left[f\left(\mathrm{M}, u^i\right) t^{\alpha_1,\ldots,\alpha_i}_{\beta_1,\ldots,\beta_j}(\mathrm{M},\mathbf{u})\right]\frac{g}{u_0}d^4x d^3u \\
&= \int_{\partial\mathscr{W}} f\left(\mathrm{M}, u^i\right) t^{\alpha_1,\ldots,\alpha_i}_{\beta_1,\ldots,\beta_j}(\mathrm{M},\mathbf{u})\mathrm{Z}^{\tilde{\mu}}\mathrm{N}_{\tilde{\mu}}\delta^6\sigma
\end{aligned}
\tag{C.5}
$$

Indeed the Liouville operator is the composition of th multiplication by the speed in space phase with the divergence in this space phase. The border of the considered pieces of space phase can be decomposed $\partial\mathscr{W} = \partial\mathscr{U}\times\Omega + \mathscr{U}\times\partial\Omega$. Noticed that $f\left(\mathrm{M}, u^i\right) t^{\alpha_1,\ldots,\alpha_i}_{\beta_1,\ldots,\beta_j}(\mathrm{M},\mathbf{u})\mathrm{Z}^{\tilde{\mu}}\delta^6\sigma\, u^i \overrightarrow{\to} \partial\Omega\, 0$. Remark that if we note $\mathbf{n}_{\mathscr{T}}(\partial\mathscr{U})^\perp$ the normal unit vector of $\partial\mathscr{U}$ then $\mathbf{N} = \mathbf{n}\mathbf{n}\otimes\mathbf{0}_{\mathscr{T}}\mathscr{T}(\partial\mathscr{W})^\perp$ is the normal unit vector of $\partial\mathscr{W}$. So we get,

$$
\mathrm{I} = \int_{\partial\mathscr{U}}\int_{\Omega} f\left(\mathrm{M}, u^i\right) t^{\alpha_1,\ldots,\alpha_i}_{\beta_1,\ldots,\beta_j}(\mathrm{M},\mathbf{u})\, u^\mu n_\mu \delta^6\sigma
$$

Further more $\delta^6\sigma = \delta^3 x\delta^3 u$ where $\delta^3 x$ is the volume element of $\partial\mathscr{U}$ and $\delta^3 u$ is the volume element of Ω. So using the definition of (eq.3.45), we get:

$$
\begin{aligned}
\mathrm{I} &= \int_{\partial\mathscr{U}}\left[\int_\Omega f\left(\mathrm{M}, u^i\right) t^{\alpha_1,\ldots,\alpha_i}_{\beta_1,\ldots,\beta_j}(\mathrm{M},\mathbf{u})\, u^\mu\delta^3 u\right] n_\mu\delta^3 x \\
&= \int_{\partial\mathscr{U}} \bar{t}^{\mu\alpha_1,\ldots,\alpha_i}_{\beta_1,\ldots,\beta_j} n_\mu\delta^3 x \\
&= \int_{\mathscr{U}} \frac{1}{\sqrt{-g}}\frac{\partial}{\partial x^\mu}\left(\sqrt{-g}\,\bar{t}^{\mu\alpha_1,\ldots,\alpha_i}_{\beta_1,\ldots,\beta_j}\right)\sqrt{-g}\,d^4x
\end{aligned}
\tag{C.6}
$$

Restart from (eq.C.5), cause Liouville operator is order 1 linear differential operator and so respect the Leibniz rule. Using (eq.3.31), we get,

$$\mathrm{I} = \int_{\mathscr{W}} \left\{ \mathrm{I}(\mathrm{M},\mathbf{u})\, t^{\alpha_1,\ldots,\alpha_i}_{\beta_1,\ldots,\beta_j}(\mathrm{M},\mathbf{u}) + f(\mathrm{M},\mathbf{u})\, \hat{\mathscr{L}}\left[t^{\alpha_1,\ldots,\alpha_i}_{\beta_1,\ldots,\beta_j} \right] \right\} \frac{g}{u_0} d^4x d^3u \tag{C.7}$$

Because it is true for each subset $\mathscr{U}$ of spacetime, it achieve the demonstration.

C.4 Particles number conservation

From the transfer equation (eq.3.46) apply to $t = 1$, immediately gives,

$$\nabla \cdot \mathbf{J} = \int_{u^i \in \mathbb{R}^3} \frac{-\sqrt{-g}}{u_0} \left\{ \mathrm{I}(\mathrm{M},\mathbf{u}) + f(\mathrm{M},\mathbf{u})\, \hat{\mathscr{L}}[1] \right\} d^3u \tag{C.8}$$

However $\hat{\mathscr{L}}[1] = 0$, so all that remains is calculated the contribution of all the collisions. Note $k, l = -, +, \gamma$, we get for elastic collision,

$$\begin{aligned}
&\int_{\frac{\mathbf{p}}{m_e}\in\Omega}\int_{\frac{\mathbf{q}}{m_e}\in\Omega}\int_{\mathbf{n}\in\mathscr{S}_{\mathbf{p}+\mathbf{q}^\perp}} \left\{ f_k\left(\frac{\mathbf{p}'}{m_e}\right) f_l\left(\frac{\mathbf{q}'}{m_e}\right) - f_k\left(\frac{\mathbf{p}'}{m_e}\right) f_l\left(\frac{\mathbf{q}}{m_e}\right) \right\} \mathrm{A}^{kl}_{kl}(\mathbf{p},\mathbf{q},\mathbf{n})\, \delta^2 n \times \delta^3 p \times \delta^3 q \\
&= \int_{\frac{\mathbf{p}}{m_e}\in\Omega}\int_{\frac{\mathbf{q}}{m_e}\in\Omega}\int_{\mathbf{n}\in\mathscr{S}_{\mathbf{p}+\mathbf{q}^\perp}} f_k\left(\frac{\mathbf{p}'}{m_e}\right) f_l\left(\frac{\mathbf{q}'}{m_e}\right) \mathrm{A}^{kl}_{kl}(\mathbf{p},\mathbf{q},\mathbf{n})\, \delta^2 n \times \delta^3 p \times \delta^3 q \\
&\qquad - \int_{\frac{\mathbf{p}}{m_e}\in\Omega}\int_{\frac{\mathbf{q}}{m_e}\in\Omega}\int_{\mathbf{n}\in\mathscr{S}_{\mathbf{p}+\mathbf{q}^\perp}} f_k\left(\frac{\mathbf{p}'}{m_e}\right) f_l\left(\frac{\mathbf{q}}{m_e}\right) \mathrm{A}^{kl}_{kl}(\mathbf{p},\mathbf{q},\mathbf{n})\, \delta^2 n \times \delta^3 p \times \delta^3 q \\
&= \int_{\frac{\mathbf{p}'}{m_e}\in\Omega}\int_{\frac{\mathbf{q}'}{m_e}\in\Omega}\int_{\mathbf{n}'\in\mathscr{S}_{\mathbf{p}+\mathbf{q}^\perp}} f_k\left(\frac{\mathbf{p}'}{m_e}\right) f_l\left(\frac{\mathbf{q}'}{m_e}\right) \mathrm{A}^{kl}_{kl}(\mathbf{p}',\mathbf{q}',\mathbf{n}')\, \delta^2 n' \times \delta^3 p' \times \delta^3 q' \\
&\qquad - \int_{\frac{\mathbf{p}}{m_e}\in\Omega}\int_{\frac{\mathbf{q}}{m_e}\in\Omega}\int_{\mathbf{n}\in\mathscr{S}_{\mathbf{p}+\mathbf{q}^\perp}} f_k\left(\frac{\mathbf{p}'}{m_e}\right) f_l\left(\frac{\mathbf{q}}{m_e}\right) \mathrm{A}^{kl}_{kl}(\mathbf{p},\mathbf{q},\mathbf{n})\, \delta^2 n \times \delta^3 p \times \delta^3 q \\
&= 0
\end{aligned}$$

Where we used between the second and the third line the fact that the symmetry wich correspond to elastic collision (eq.3.34) conserve the volum. We also used the property of equality of differential section of inverse collision $\mathrm{A}^{kl}_{kl}(\mathbf{p}',\mathbf{q}',\mathbf{n}') = \mathrm{A}^{kl}_{kl}(\mathbf{p},\mathbf{q},\mathbf{n})$. Thus the only term wich brings creation of number of particles is the term due to inelastic collision due to creation or annihilation of pairs.

C.5 Conservation of impulsion

Use the transfer equation with $\mathbf{t} = mc^2\mathbf{u}$, we get,

$$\frac{1}{\sqrt{-g}} \frac{\partial}{\partial x^\mu} \left(\sqrt{-g}\, \mathrm{T}^{\mu\alpha} \right) = \int_{u^i \in \mathbb{R}^3} \delta^3 u \left\{ \mathrm{I}\left(x^\mu, u^i\right) mc^2 u^\alpha \left(x^\mu, u^i\right) + f\left(x^\mu, u^i\right) \hat{\mathscr{L}}\left[mc^2 u^\alpha \right] \right\}, \tag{C.9}$$

First of all let concentrate our effort to the Liouville operators of the second term in left hand

side,

$$\hat{\mathscr{L}}\left[u^\alpha\right] = \overbrace{-\Gamma^i_{\nu\sigma}u^\nu u\sigma\frac{\partial u^\alpha}{\partial u^i}}^{1} + \overbrace{\frac{q}{m}\mathrm{F}^i_\nu u^\nu\frac{\partial u^\alpha}{\partial u^i}}^{2} \qquad \Rightarrow \qquad \frac{\partial u^\alpha}{\partial u^i} = -\frac{1}{u_0}\left(\frac{\partial u^0}{\partial u^i}\delta^\alpha_0 + \frac{\partial u^j}{\partial u^i}\delta^\alpha_j\right) = -\frac{1}{u_0}\left(u_i\delta^\alpha_0 - u_0\delta^\alpha_i\right)$$

$$\begin{aligned}
1 &= \frac{\Gamma^i_{\nu\sigma}u^\nu u^\sigma}{u_0}\left(u_i\delta^\alpha_0 - u_0\delta^\alpha_i\right) = \frac{u^\nu u^\sigma}{u_0}\left(\Gamma^\mu_{\nu\sigma}u_\mu\delta^\alpha_0 - \Gamma^0_{\nu\sigma}u_0\delta^\alpha_0 - \Gamma^i_{\nu\sigma}u_0\delta^\alpha_i\right)\\
&= \frac{u^\nu u^\sigma}{u_0}\left(\Gamma^\mu_{\nu\sigma}u_\mu\delta^\alpha_0 - \Gamma^\mu_{\nu\sigma}u_0\delta^\alpha_\mu\right) = -\Gamma^\alpha_{\nu\sigma}u^\nu u^\sigma + \frac{\delta^\alpha_0}{u_0}\underbrace{u^\lambda u^\nu u^\sigma\partial_\nu g_{\lambda\sigma}}_{=0} = -\Gamma^\alpha_{\nu\sigma}u^\nu u^\sigma\\
2 &= \frac{q}{m}\mathrm{F}^i_\nu u^\nu\frac{\partial u^\alpha}{\partial u^i} = -\frac{q}{m}\mathrm{F}^i_\nu\frac{u^\nu}{u_0}\left(u_i\delta^\alpha_0 - u_0\delta^\alpha_i\right) = -\frac{q}{m}\frac{u^\nu}{u_0}\left(\mathrm{F}^i_\nu u_i\delta^\alpha_0 - \mathrm{F}^i_\nu u_0\delta^\alpha_i\right) = -\frac{q}{m}\frac{u^\nu}{u_0}\left(\mathrm{F}^\mu_\nu u_\mu\delta^\alpha_0 - \mathrm{F}^\mu_\nu u_0\delta^\alpha_\mu\right)\\
&= \frac{q}{m}\mathrm{F}^\alpha_\nu u^\nu
\end{aligned}$$

Thus we finally get,

$$\nabla_\mu \mathrm{T}^{\mu\alpha} + \mathrm{F}^\alpha_\mu j^\mu = mc^2\int_{u^i\in\mathbb{R}^3}\delta^3 u\left\{\mathrm{I}\left(x^\mu,u^i\right)u^\alpha\left(x^\mu,u^i\right)\right\}, \tag{C.10}$$

The term due to collision is composed of each kind of collision between each species of the gas. But for collision between particles of one species, using symmetry of the general expression and the differential cross section to do some change of variable we are able to rewrite,

$$\begin{aligned}
&\int_{\frac{\mathbf{p}}{m_e}\in\Omega}\int_{\frac{\mathbf{q}}{m_e}\in\Omega}\int_{\mathbf{n}\in\mathscr{S}_{\mathbf{p}+\mathbf{q}^\perp}}\mathbf{p}\left\{f_k\left(\frac{\mathbf{p}'}{m_e}\right)f_k\left(\frac{\mathbf{q}'}{m_e}\right) - f_k\left(\frac{\mathbf{p}'}{m_e}\right)f_k\left(\frac{\mathbf{q}}{m_e}\right)\right\}\mathrm{A}^{kk}_{kk}(\mathbf{p},\mathbf{q},\mathbf{n})\,\delta^2 n\times\delta^3 p\times\delta^3 q\\
&= \frac{1}{4}\int_{\frac{\mathbf{p}}{m_e}\in\Omega}\int_{\frac{\mathbf{q}}{m_e}\in\Omega}\int_{\mathbf{n}\in\mathscr{S}_{\mathbf{p}+\mathbf{q}^\perp}}(\mathbf{p}+\mathbf{q}-\mathbf{p}'-\mathbf{q}')\left\{f_k\left(\frac{\mathbf{p}'}{m_e}\right)f_k\left(\frac{\mathbf{q}'}{m_e}\right) - f_k\left(\frac{\mathbf{p}'}{m_e}\right)f_k\left(\frac{\mathbf{q}}{m_e}\right)\right\}\mathrm{A}^{kk}_{kk}(\mathbf{p},\mathbf{q},\mathbf{n})\,\delta^2 n\times\delta^3 p\times\delta^3 q = 0
\end{aligned} \tag{C.11}$$

Thus the only forces due to collision for the $k-$th species is due to its unelastic collision or collision with others species.

C.6 H-theorem

To established properly the H theorem the first step consisted as before to calculus the second term of right hand side of transfer equation. In this case using the Boltzmann system (eq.3.31) we get,

$$\hat{\mathscr{L}}\left[\ln\left(\frac{f_i}{e}\right)\right] = \frac{\hat{\mathscr{L}}\left[f_i\right]}{f_i\left(x^\mu,u^i\right)} = \frac{\mathrm{I}_i\left(x^\mu,u^i\right)}{f_i\left(x^\mu,u^i\right)} \tag{C.12}$$

From there we easily get (eq.3.58). Now for the sum of term due to, we used the same kind of calculation trick,

$$\begin{aligned}
&\sum_{i,j,k,l}\int_{\frac{\mathbf{p}}{m_e}\in\Omega}\int_{\frac{\mathbf{q}}{m_e}\in\Omega}\int_{\mathbf{n}\in\mathscr{S}_{\mathbf{p}+\mathbf{q}^\perp}}\ln\left(f_i(\mathbf{p})\right)\left\{f_i\left(\frac{\mathbf{p}'}{m_e}\right)f_j\left(\frac{\mathbf{q}'}{m_e}\right) - f_k\left(\frac{\mathbf{p}'}{m_e}\right)f_l\left(\frac{\mathbf{q}}{m_e}\right)\right\}\mathrm{A}^{kl}_{ij}(\mathbf{p},\mathbf{q},\mathbf{n})\,\delta^2 n\times\delta^3 p\times\delta^3 q\\
&= \frac{1}{2}\left[\sum_{i,j,k,l}\int_{\frac{\mathbf{p}}{m_e}\in\Omega}\int_{\frac{\mathbf{q}}{m_e}\in\Omega}\int_{\mathbf{n}\in\mathscr{S}_{\mathbf{p}+\mathbf{q}^\perp}}\ln\left(f_i(\mathbf{p})\right)\left\{f_i\left(\frac{\mathbf{p}'}{m_e}\right)f_j\left(\frac{\mathbf{q}'}{m_e}\right) - f_k\left(\frac{\mathbf{p}'}{m_e}\right)f_l\left(\frac{\mathbf{q}}{m_e}\right)\right\}\mathrm{A}^{kl}_{ij}(\mathbf{p},\mathbf{q},\mathbf{n})\,\delta^2 n\times\delta^3 p\times\delta^3 q\right.\\
&\left.+\sum_{i,j,k,l}\int_{\frac{\mathbf{p}}{m_e}\in\Omega}\int_{\frac{\mathbf{q}}{m_e}\in\Omega}\int_{\mathbf{n}\in\mathscr{S}_{\mathbf{p}+\mathbf{q}^\perp}}\ln\left(f_i(\mathbf{q})\right)\left\{f_i\left(\frac{\mathbf{q}'}{m_e}\right)f_j\left(\frac{\mathbf{p}'}{m_e}\right) - f_k\left(\frac{\mathbf{q}'}{m_e}\right)f_l\left(\frac{\mathbf{p}}{m_e}\right)\right\}\mathrm{A}^{kl}_{ij}(\mathbf{p},\mathbf{q},\mathbf{n})\,\delta^2 n\times\delta^3 p\times\delta^3 q\right]\\
&= \frac{1}{2}\sum_{i,j,k,l}\int_{\frac{\mathbf{p}}{m_e}\in\Omega}\int_{\frac{\mathbf{q}}{m_e}\in\Omega}\int_{\mathbf{n}\in\mathscr{S}_{\mathbf{p}+\mathbf{q}^\perp}}\ln\left(f_i(\mathbf{p})f_j(\mathbf{q})\right)\left\{f_i\left(\frac{\mathbf{p}'}{m_e}\right)f_j\left(\frac{\mathbf{q}'}{m_e}\right) - f_k\left(\frac{\mathbf{p}'}{m_e}\right)f_l\left(\frac{\mathbf{q}}{m_e}\right)\right\}\mathrm{A}^{kl}_{ij}(\mathbf{p},\mathbf{q},\mathbf{n})\,\delta^2 n\times\delta^3 p\times\delta^3 q\\
&= \frac{1}{4}\sum_{i,j,k,l}\int_{\frac{\mathbf{p}}{m_e}\in\Omega}\int_{\frac{\mathbf{q}}{m_e}\in\Omega}\int_{\mathbf{n}\in\mathscr{S}_{\mathbf{p}+\mathbf{q}^\perp}}\ln\left(\frac{f_i(\mathbf{p})f_j(\mathbf{q})}{f_k(\mathbf{p}')f_l(\mathbf{q}')}\right)\left\{f_i\left(\frac{\mathbf{p}'}{m_e}\right)f_j\left(\frac{\mathbf{q}'}{m_e}\right) - f_k\left(\frac{\mathbf{p}'}{m_e}\right)f_l\left(\frac{\mathbf{q}}{m_e}\right)\right\}\mathrm{A}^{kl}_{ij}(\mathbf{p},\mathbf{q},\mathbf{n})\,\delta^2 n\times\delta^3 p\times\delta^3 q
\end{aligned} \tag{C.13}$$

Between the first and the second equality we exchange $\mathbf{p} \leftrightarrow \mathbf{q}$ on the second integral term. For the next line we exchange the index on species $i \leftrightarrow j$ and $k \leftrightarrow l$. For the next line we re-separate in two our expression and make the following change of variables on the second term $\mathbf{p} \leftrightarrow \mathbf{p}'$ and $\mathbf{q} \leftrightarrow \mathbf{q}'$, after that a new change of index $i \leftrightarrow k$ and $j \leftrightarrow l$, using symetry of differential cross section we obtain the last line.

C.7 Notion of thermodynamics equilibrium

We will demonstrate the shape of the distribution function to the thermodynamic equilibrium Eq. (3.63). Let us consider a gas composed of a kind of particle, in thermodynamic equilibrium. That is to say,

$$s_c = \frac{k_B}{4} \int_{\frac{\mathbf{p}}{m} \in \Omega} \int_{\frac{\mathbf{q}}{m} \in \Omega} \int_{\mathbf{n} \in \mathscr{S}_{\mathbf{p}+\mathbf{q}^\perp}} f(\mathbf{p}') f(\mathbf{q}') \ln\left(\frac{f(\mathbf{p}) f(\mathbf{q})}{f(\mathbf{p}') f(\mathbf{q}')}\right) \left[1 - \frac{f(\mathbf{p}) f(\mathbf{q})}{f(\mathbf{p}') f(\mathbf{q}')}\right] \mathrm{A}(\mathbf{p}, \mathbf{q}, \mathbf{n}) = 0 \delta^2 n \times \delta^3 p \times \delta^3 q \tag{C.14}$$

However, $x \longrightarrow \ln(x)(1-x)$ is strictly positive on $\mathbb{R}_{++,\star}$. In addition, $\mathbf{p} \longrightarrow f(\mathbf{p})$ and $(\mathbf{p}, \mathbf{q}, \mathbf{n}) \longrightarrow \mathrm{A}(\mathbf{p}, \mathbf{q}, \mathbf{n})$ are also positive. So $s_c = 0$ implies that $\forall (\mathbf{p}, \mathbf{q}, \mathbf{p}', \mathbf{q}') \in m\Omega$ such that $\mathbf{p} + \mathbf{q} = \mathbf{p}' + \mathbf{q}$ we have,

$$f(\mathbf{p}) f(\mathbf{q}) = f(\mathbf{p}') f(\mathbf{q}') \tag{C.15}$$

We admit that this property is also valid for $\forall (\mathbf{p}, \mathbf{q}, \mathbf{p}', \mathbf{q}') \in \mathscr{T}(\mathscr{M})$, see Marle [1969] to have more details. Let's introduce $\mathrm{F} = \ln\left(\frac{f(\mathbf{p})}{f(\mathbf{0})}\right)$. It is then easy to show that F is checking,

$$\forall (\mathbf{p}, \mathbf{q}) \qquad \mathrm{F}(\mathbf{p}+\mathbf{q}) = \ln\left(\frac{f(\mathbf{p}+\mathbf{q})}{f(\mathbf{0})}\right) = \ln\left(\frac{f(\mathbf{p}+\mathbf{q}) f(\mathbf{0})}{f(\mathbf{0})^2}\right) = \ln\left(\frac{f(\mathbf{p}) f(\mathbf{q})}{f(\mathbf{0})^2}\right) = \mathrm{F}(\mathbf{p}) + \mathrm{F}(\mathbf{q}) \tag{C.16}$$

Which is sufficient adding the continuity of f to the fact that F is a linear form which imply that there exist $\boldsymbol{\lambda}$ such that $\mathrm{F}(\mathbf{p}) = \boldsymbol{\lambda} \cdot \mathbf{p}$. Then we have $f(\mathbf{p}) = f((\mathbf{0})) \exp(\boldsymbol{\lambda} \cdot \mathbf{p})$. We finally prove that $\boldsymbol{\lambda}$ is a future time oriented vector, using the definition of number four current. Indeed the number four-current Eq.(3.29) by definition is a future oriented vector. Then using calculation Eq.(3.67), you easily prove that $\boldsymbol{\lambda} = \beta \mathbf{u}_{\mathrm{fl}}$. Which achieve the demonstration. The case of a gas with several species can be reduced to the case of a gas with one species.

C.8 Energy momentum tensor

$$\mathrm{Z} = \mathrm{Z}(b^\mu) = \mathrm{Z}(\beta) = \mathrm{Z}(\sqrt{-\mathbf{b}^2}) \quad \Rightarrow \quad \frac{\partial \mathrm{Z}}{\partial b^\alpha} = \frac{\partial \mathrm{Z}}{\partial \beta} \frac{\partial \sqrt{-\mathbf{b}^2}}{\partial b^\alpha} = -\frac{\partial \mathrm{Z}}{\partial \beta} \frac{b_\alpha}{\beta} \tag{C.17}$$

$$\frac{\partial}{\partial b^\beta}\left(\frac{\partial \mathrm{Z}}{\partial b^\alpha}\right) = \frac{\partial}{\partial \beta}\left(\frac{1}{\beta}\frac{\partial \mathrm{Z}}{\partial \beta}\right) \beta \frac{b_\alpha b_\beta}{\beta} - \frac{1}{\beta}\frac{\partial \mathrm{Z}}{\partial \beta} g_{\alpha\beta} \tag{C.18}$$

Appendix D

Magneto-Hydrodynamics in curved spacetime

D.1 3+1 Decomposition of GRMHD

D.1.1 3+1 Decomposition of Maxwell equation

Using (eq.4.1&4.9) for the divergence of the exterior product,

$$\begin{aligned}
&\nabla\cdot(\mathbf{n}\wedge\mathbf{B})^{\alpha} = \nabla_{\mu}\left(n^{\alpha}\mathrm{B}^{\mu} - \mathrm{B}^{\alpha}n^{\mu}\right)\\
&= -\left[n^{\mu}\nabla_{\mu}\mathrm{B}^{\nu} - \mathrm{B}^{\mu}\nabla_{\mu}n^{\alpha} - n^{\alpha}\nabla_{\mu}\mathrm{B}^{\mu} - \mathrm{K}\mathrm{B}^{\alpha}\right]\\
&= -\left[\frac{1}{h}\left(m^{\mu}\nabla_{\mu}\mathrm{B}^{\nu} - \mathrm{B}^{\mu}\nabla_{\mu}m^{\alpha} + \mathrm{B}^{\mu}n^{\alpha}\nabla_{\mu}h\right) - n^{\alpha}\mathrm{D}_{\mu}\mathrm{B}^{\mu} - n^{\alpha}\mathrm{B}^{\mu}\nabla_{\mu}\ln h - \mathrm{K}\mathrm{B}^{\alpha}\right]\\
&= -\frac{1}{h}\left(\mathscr{L}_{\mathbf{m}}\mathbf{B}\right)^{\alpha} + (\mathbf{D}\cdot\mathbf{B})\,n^{\alpha} + \mathrm{K}\mathrm{B}^{\alpha}\\
&\Rightarrow \qquad \nabla\cdot(\mathbf{n}\wedge\mathbf{B}) = -\frac{1}{h}\mathscr{L}_{\mathbf{m}}\mathbf{B} + (\mathbf{D}\cdot\mathbf{B})\,\mathbf{n} + \mathrm{K}\mathbf{B}
\end{aligned} \tag{D.1}$$

Where we used between the second and the third line the definition of $\mathbf{m}$ the normal evolution vector (eq.2.13), but also the trace of extrinsic curvature. For the third line we also used the link between the divergence (eq.2.23) and the Lie derivative expression of a vector field (eq.A.6). For the second divergence we have

$$\begin{aligned}
&\nabla\cdot(\boldsymbol{\epsilon}(\mathbf{n},\mathbf{E},.,.))^{\alpha} = \nabla_{\mu}\left[{}^{4}\epsilon^{\rho\sigma\nu\mu}n_{\rho}\mathrm{E}_{\sigma}\right]\\
&=^{4}\epsilon^{\rho\sigma\nu\mu}\left[n_{\rho}\nabla_{\mu}\mathrm{E}_{\sigma} + \mathrm{E}_{\sigma}\nabla_{\mu}n_{\rho}\right]\\
&=^{4}\epsilon^{\rho\sigma\nu\mu}\left[n_{\rho}\nabla_{\mu}\mathrm{E}_{\sigma} - \mathrm{E}_{\sigma}\left(\mathrm{K}_{\mu\rho} + n_{\mu}\mathrm{D}_{\mu}\ln h\right)\right]\\
&=^{4}\epsilon^{\rho\sigma\nu\mu}\left[n_{\rho}\nabla_{\mu}\mathrm{E}_{\sigma} - \mathrm{E}_{\sigma}n_{\mu}\mathrm{D}_{\mu}\ln h\right]\\
&=^{3}\epsilon^{\sigma\nu\mu}\left[\partial_{\mu}\mathrm{E}_{\sigma} - \mathrm{E}_{\sigma}\partial_{\mu}\ln h\right]\\
&= \frac{1}{h}{}^{3}\epsilon^{\sigma\nu\mu}\partial_{\mu}(h\mathrm{E}_{\sigma})\\
&\Rightarrow \qquad \nabla\cdot(\boldsymbol{\epsilon}(\mathbf{n},\mathbf{E},.,.)) = \frac{1}{h}\mathbf{D}\times(h\mathbf{E})
\end{aligned} \tag{D.2}$$

D.1.2 The 3+1 form of Continuity equation

$$\begin{aligned}
\nabla\cdot\left(\rho_{0}\mathbf{u}\right) &= \nabla\cdot\left(\rho_{0}\gamma\mathbf{n}\right) + \frac{1}{c}\nabla\cdot\left(\rho_{0}\gamma\mathbf{V}\right)\\
&= \nabla_{\mathbf{n}}\rho_{0}\gamma - \rho_{0}\gamma\mathrm{K} + \frac{\mathbf{D}\cdot\left(\rho_{0}\gamma h\mathbf{V}\right)}{hc}
\end{aligned} \tag{D.3}$$

D.1.3 Spatial part of stress energy tensor conservation

For the divergence of the fluid stress-energy tensor,

$$\begin{aligned}
&\nabla_\mu\left(\rho_0\xi c^2 u^\mu u_\alpha\right) = \xi k_m c^2 u_\alpha + \rho_0 c^2 u^\mu \nabla_\mu\left(\xi u_\alpha\right)\\
&= \xi k_m c^2 u_\alpha + \rho_0 c^2 u^\mu \nabla_\mu\left(\xi\gamma n_\alpha\right) + \rho_0 c^2\gamma\left(n^\mu + \frac{V^\mu}{c}\right)\nabla_\mu\left(\frac{\gamma\xi V_\alpha}{c}\right)\\
&= \xi k_m c^2 u_\alpha + \rho_0 c^2 u^\mu \nabla_\mu\left(\xi\gamma\right) n_\alpha - \rho_0\xi\gamma c^2 u^\mu\left(K_{\mu\alpha} + D_\alpha \ln h n_\mu\right) + \frac{\rho_0 c\gamma}{h}\left[m^\mu\nabla_\mu\left(\gamma\xi V_\alpha\right) + \gamma\xi V_\mu\nabla_\alpha m^\mu - \gamma\xi V_\mu\nabla_\alpha m^\mu\right]\\
&\qquad + \rho_0\gamma V^\mu\left[D_\mu\left(\gamma\xi V_\alpha\right) + K_{\mu\nu}V^\nu n_\alpha\right]\\
&= \xi k_m c^2 u_\alpha + \left[\nabla_{\mathbf{n}}\ln\gamma\xi + \frac{1}{c}\nabla_{\mathbf{V}}\ln h\gamma\xi + \frac{1}{c^2}\mathbf{K}(\mathbf{V},\mathbf{V})\right] n_\alpha + \rho_0\gamma^2\xi c^2 D_\alpha \ln h + \frac{\rho_0\gamma c}{h}\left(\mathscr{L}_{\mathbf{m}}\gamma\xi\mathbf{V}\right)_\alpha + \rho_0\gamma\left(\mathbf{V}\cdot\mathbf{D}\right)\gamma\xi V_\alpha
\end{aligned} \tag{D.4}$$

Where we used a lot of time (eq.2.10), but also the definition of lie derivative of a 1-form (eq.A.7) and the continuity equation (eq.4.3)

This can be rewrote

$$\nabla\cdot\left(\rho_0\xi c^2\mathbf{u}\otimes\mathbf{u}\right) = \xi k_m c^2\mathbf{u} + \rho\xi\gamma^2 c^2\left[\nabla_{\mathbf{n}}\ln\gamma\xi + \frac{1}{c}\nabla_{\mathbf{V}}\ln h\gamma\xi + \frac{1}{c^2}\mathbf{K}(\mathbf{V},\mathbf{V})\right]\mathbf{n} + \rho_0\gamma^2\xi c^2\mathbf{D}\ln h + \frac{\rho_0\gamma c}{h}\mathscr{L}_{\mathbf{m}}\gamma\xi\mathbf{V} + \rho_0\gamma\left(\mathbf{V}\cdot\mathbf{D}\right)\gamma\xi\mathbf{V} \tag{D.5}$$

The pressure term gives immediately

$$\nabla\cdot\left(P\mathbf{g}\right) = \nabla P \tag{D.6}$$

The electro-magnetic term

$$\mathbf{F}\left(\frac{\mathbf{j}}{c},.\right) = -\rho_e\mathbf{E} - \frac{\mathbf{J}\times\mathbf{B}}{c} - \frac{\mathbf{J}\cdot\mathbf{E}}{c}\mathbf{n} \tag{D.7}$$

D.2 General results on GRASIMHD in Kerr geometry

D.2.1 The volumic poloidal forces

Decomposition-reorganization: prelude for Graad-Shafranov

For the poloidal advection using the link between poloidal magnetic fied and poloidal speed (eq.4.26) and the definition of Alfvenic Mach number (eq.4.42) we quickly obtain

$$\begin{aligned}
\mathscr{F}_{A_p} &= -\rho_0\gamma\left(\mathbf{V}\cdot\mathbf{D}\right)\gamma\xi\mathbf{V}\,|_p\\
&= -\frac{\Psi_A}{4\pi h}\left(\mathbf{B}_p\cdot\mathbf{D}\right)\frac{\xi\Psi_A}{4\pi\rho_0 h}\mathbf{B}_p\\
&= -\frac{1}{4\pi M_A^2}\left(\frac{M_A^2\mathbf{B}_p}{h}\cdot\mathbf{D}\right)\frac{M_A^2\mathbf{B}_p}{h} + \xi\gamma c k_m\mathbf{V}_p
\end{aligned} \tag{D.8}$$

The second term is destroyed with the second term of the loading forces. Le continue our work with the second term. Using the composition operation (eq.B.30) with the gradient of a scalar product:

$$-\frac{1}{M_A^2}\left(\frac{M_A^2\mathbf{B}_p}{h}\cdot\mathbf{D}\right)\frac{M_A^2\mathbf{B}_p}{h} = -\frac{1}{M_A^2}\left[\mathbf{D}\left(\frac{M_A^4\mathbf{B}_p^2}{2h^2}\right) - \frac{M_A^2}{h}\mathbf{B}_p\times\left\{\mathbf{D}\times\left(\frac{M_A^2\mathbf{B_p}}{h}\right)\right\}\right] = 4\pi\left[\mathscr{F}_{A_p}1 + \mathscr{F}_{A_p}2\right] \tag{D.9}$$

For calculation of $\mathscr{F}_{\mathrm{A}_p 2}$, let use the composition (eq.B.30) for a curl of a vectorial product. We obtain,

$$\begin{aligned}
\mathscr{F}_{\mathrm{A}_p 2} &= -\frac{1}{h}\left[\mathbf{D}\times\left\{\frac{\mathrm{M}_\mathrm{A}^2\mathbf{D}\mathrm{A}}{h}\times\frac{\boldsymbol{\epsilon}_\phi}{\varpi}\right\}\right]\times\mathbf{B}_p \\
&= -\frac{1}{h}\left[\left(\frac{\boldsymbol{\epsilon}_\phi}{\varpi}\cdot\mathbf{D}\right)\frac{\mathrm{M}_\mathrm{A}^2\mathbf{D}\mathrm{A}}{h} - \left(\frac{\mathrm{M}_\mathrm{A}^2\mathbf{D}\mathrm{A}}{h}\cdot\mathbf{D}\right)\frac{\boldsymbol{\epsilon}_\phi}{\varpi} + \cancel{\left\{\mathbf{D}\cdot\left(\frac{\boldsymbol{\epsilon}_\phi}{\varpi}\right)\right\}\frac{\mathrm{M}_\mathrm{A}^2\mathbf{D}\mathrm{A}}{h}} - \left\{\mathbf{D}\cdot\left(\frac{\mathrm{M}_\mathrm{A}^2\mathbf{D}\mathrm{A}}{h}\right)\right\}\frac{\boldsymbol{\epsilon}_\phi}{\varpi}\right]\times\mathbf{B}_p \\
&= -\frac{1}{h}\left[\frac{1}{\varpi}\left(\frac{\boldsymbol{\epsilon}_\phi}{\varpi}\cdot\mathbf{D}\ln\varpi\right)\boldsymbol{\epsilon}_\phi - \left(\frac{\mathrm{M}_\mathrm{A}^2\mathbf{D}\mathrm{A}}{h}\cdot\mathbf{D}\frac{1}{\varpi}\right)\boldsymbol{\epsilon}_\phi - \left\{\mathbf{D}\cdot\left(\frac{\mathrm{M}_\mathrm{A}^2\mathbf{D}\mathrm{A}}{h}\right)\right\}\frac{\boldsymbol{\epsilon}_\phi}{\varpi}\right]\times\frac{\mathbf{D}\mathrm{A}\times\boldsymbol{\epsilon}_\phi}{\varpi} \\
&= \frac{1}{h}\left[\frac{1}{\varpi^2}\mathbf{D}\cdot\left(\frac{\mathrm{M}_\mathrm{A}^2\mathbf{D}\mathrm{A}}{h}\right) + \frac{\mathrm{M}_\mathrm{A}^2\mathbf{D}\mathrm{A}}{h}\cdot\mathbf{D}\frac{1}{\varpi^2}\right]\boldsymbol{\epsilon}_\phi\times\left(\mathbf{D}\mathrm{A}\times\boldsymbol{\epsilon}_\phi\right) \\
&= \left[\mathbf{D}\cdot\left(\frac{\mathrm{M}_\mathrm{A}^2\mathbf{D}\mathrm{A}}{h\varpi^2}\right)\right]\frac{\mathbf{D}\mathrm{A}}{h}
\end{aligned} \tag{D.10}$$

The third term at the second line is null because of axisymmetry. For the first and the second term of this second line use the expression mixed advection (eq.2.43), a lot of term are simplify because $\frac{\mathrm{M}_\mathrm{A}^2\mathbf{D}\mathrm{A}}{h}$ is poloidal and $\frac{\boldsymbol{\epsilon}_\phi}{\varpi}$ is a toroidal field.

D.2.2 Grad-Shafranov approach

Introducing $f_1\left(\mathrm{M}_\mathrm{A}^2,\xi,h^2,\varpi^2,\omega,\Psi_\mathrm{A},\Psi_\mathrm{A}\mathrm{L},\Psi_\mathrm{A}\mathscr{E},\Omega\right)$ and $f_2\left(\mathrm{M}_\mathrm{A}^2,\xi,h^2,\varpi^2,\omega,\Psi_\mathrm{A},\Psi_\mathrm{A}\mathrm{L},\Psi_\mathrm{A}\mathscr{E},\Omega\right)$,

$$\begin{aligned}
f_1 &= \Psi_\mathrm{A}^2 h^2\xi^2c^2 + \left[\frac{\Psi_\mathrm{A}(\mathscr{E}-\mathrm{L}\omega)}{c}\right]^2\frac{\mathscr{N}_\mathrm{V}^2 - x^2\mathscr{N}_\mathscr{E}^2}{x^2\mathscr{D}^2} \\
f_2 &= \left[\frac{\Psi_\mathrm{A}(\mathscr{E}-\mathrm{L}\omega)}{c}\right]^2\frac{\varpi^2c^2\mathscr{N}_\mathrm{I}^2}{4h^2x^2\mathscr{D}^2}
\end{aligned} \tag{D.11}$$

$$\begin{aligned}
\mathscr{F} &= -\frac{1}{2h^2\mathrm{M}_\mathrm{A}^2}\mathbf{D}\left(\frac{\mathrm{M}_\mathrm{A}^4\mathbf{D}\mathrm{A}^2}{\varpi^2}\right) - \frac{2}{h^2c^2\varpi^2}\mathbf{D}\mathrm{I}^2 = \frac{1}{2h^2\mathrm{M}_\mathrm{A}^2}\mathbf{D}f_1 - \frac{2}{h^2c^2\varpi^2}f2 \\
&= \left[\frac{1}{2h^2\mathrm{M}_\mathrm{A}^2}\frac{\partial f_1}{\partial\mathrm{M}_\mathrm{A}^2} - \frac{2}{h^2c^2\varpi^2}\frac{\partial f_2}{\partial\mathrm{M}_\mathrm{A}^2}\right]\mathbf{D}\mathrm{M}_\mathrm{A}^2 + \left[\frac{1}{2h^2\mathrm{M}_\mathrm{A}^2}\frac{\partial f_1}{\partial\xi} - \frac{2}{h^2c^2\varpi^2}\frac{\partial f_2}{\partial\xi}\right]\mathbf{D}\xi + \left[\frac{1}{2h^2\mathrm{M}_\mathrm{A}^2}\frac{\partial f_1}{\partial h^2} - \frac{2}{h^2c^2\varpi^2}\frac{\partial f_2}{\partial h^2}\right]\mathbf{D}h^2 \\
&+ \left[\frac{1}{2h^2\mathrm{M}_\mathrm{A}^2}\frac{\partial f_1}{\partial\varpi^2} - \frac{2}{h^2c^2\varpi^2}\frac{\partial f_2}{\partial\varpi^2}\right]\mathbf{D}\varpi^2 + \left[\frac{1}{2h^2\mathrm{M}_\mathrm{A}^2}\frac{\partial f_1}{\partial\omega} - \frac{2}{h^2c^2\omega}\frac{\partial f_2}{\partial\omega}\right]\mathbf{D}\omega + \left[\frac{1}{2h^2\mathrm{M}_\mathrm{A}^2}\frac{\partial f_1}{\partial\Psi_\mathrm{A}} - \frac{2}{h^2c^2\varpi^2}\frac{\partial f_2}{\partial\Psi_\mathrm{A}}\right]\mathbf{D}\Psi_\mathrm{A} \\
&+ \left[\frac{1}{2h^2\mathrm{M}_\mathrm{A}^2}\frac{\partial f_1}{\partial\Psi_\mathrm{A}\mathrm{L}} - \frac{2}{h^2c^2\varpi^2}\frac{\partial f_2}{\partial\Psi_\mathrm{A}\mathrm{L}}\right]\mathbf{D}\Psi_\mathrm{A}\mathrm{L} + \left[\frac{1}{2h^2\mathrm{M}_\mathrm{A}^2}\frac{\partial f_1}{\partial\Psi_\mathrm{A}\mathscr{E}} - \frac{2}{h^2c^2\varpi^2}\frac{\partial f_2}{\partial\Psi_\mathrm{A}\mathscr{E}}\right]\mathbf{D}\Psi_\mathrm{A}\mathscr{E} \\
&+ \left[\frac{1}{2h^2\mathrm{M}_\mathrm{A}^2}\frac{\partial f_1}{\partial\Omega} - \frac{2}{h^2c^2\omega}\frac{\partial f_2}{\partial\Omega}\right]\frac{d\Omega}{d\mathrm{A}}\mathbf{D}\mathrm{A} \\
&= \left[\frac{\partial}{\partial\mathrm{M}_\mathrm{A}^2}\left(\frac{f_1}{2h^2\mathrm{M}_\mathrm{A}^2} - \frac{2f_2}{h^2c^2\varpi^2}\right) + \frac{f_1}{2h^2\mathrm{M}_\mathrm{A}^2}\right]\mathbf{D}\mathrm{M}_\mathrm{A}^2 + \left[\frac{1}{2h^2\mathrm{M}_\mathrm{A}^2}\frac{\partial f_1}{\partial\xi}\right]\mathbf{D}\xi + \frac{1}{h^2}\frac{\partial}{\partial h^2}\left[h^2\left(\frac{f_1}{2h^2\mathrm{M}_\mathrm{A}^2} - \frac{2f_2}{h^2c^2\varpi^2}\right)\right]\mathbf{D}h^2 \\
&+ \left[\frac{\partial}{\partial\varpi^2}\left(\frac{f_1}{2h^2\mathrm{M}_\mathrm{A}^2} - \frac{2f_2}{h^2c^2\varpi^2}\right) - \frac{2f_2}{h^2c^2\varpi^2}\right]\mathbf{D}\varpi^2 + \left[\frac{\partial}{\partial\omega}\left(\frac{f_1}{2h^2\mathrm{M}_\mathrm{A}^2} - \frac{2f_2}{h^2c^2\varpi^2}\right)\right]\mathbf{D}\omega + \frac{\partial}{\partial\Psi_\mathrm{A}}\left(\frac{f_1}{2h^2\mathrm{M}_\mathrm{A}^2} - \frac{2f_2}{h^2c^2\varpi^2}\right)\mathbf{D}\Psi_\mathrm{A} \\
&+ \frac{\partial}{\partial\Psi_\mathrm{A}\mathrm{L}}\left(\frac{f_1}{2h^2\mathrm{M}_\mathrm{A}^2} - \frac{2f_2}{h^2c^2\varpi^2}\right)\mathbf{D}\Psi_\mathrm{A}\mathrm{L} + \frac{\partial}{\partial\Psi_\mathrm{A}\mathscr{E}}\left(\frac{f_1}{2h^2\mathrm{M}_\mathrm{A}^2} - \frac{2f_2}{h^2c^2\varpi^2}\right)\mathbf{D}\Psi_\mathrm{A}\mathscr{E} + \frac{\partial}{\partial\Omega}\left(\frac{f_1}{2h^2\mathrm{M}_\mathrm{A}^2} - \frac{2f_2}{h^2c^2\varpi^2}\right)\frac{d\Omega}{d\mathrm{A}}\mathbf{D}\mathrm{A}
\end{aligned} \tag{D.12}$$

So it is useful to do the calculus of the different term to remark that we can simplify the

expression,

$$\frac{f_1}{2h^2\mathrm{M}_\mathrm{A}^2}-\frac{2f_2}{h^2c^2\varpi^2}=\frac{\Psi_\mathrm{A}^2\xi^2c^2}{2\mathrm{M}_\mathrm{A}^2}+\left[\frac{\Psi_\mathrm{A}(\mathscr{E}-\mathrm{L}\omega)}{c}\right]^2\frac{\mathscr{N}_0}{2h^2\mathrm{M}_\mathrm{A}^2x^2\mathscr{D}}=g_1+g_2\quad\text{with}\quad\mathscr{N}_0=\left[\mathrm{M}_\mathrm{A}^2\left(x_\mathrm{MR}^4-x^2\right)+h^2x^2\left(1-x_\mathrm{MR}^2\right)^2\right] \tag{D.13}$$

In the last equality of (eq.D.12), a fastidious calculs imply that the first term ($\propto \mathbf{D}\mathrm{M}_\mathrm{A}^2$) is identically null. The second term is equal to $4\pi\rho_0\xi c^2\mathbf{D}\xi$ and will be recombine with the pressure. In the same kind of calculs as the first term, the third term of the last equality of (eq.D.12) is exactly the opposite term of the term $\propto \mathbf{D}\ln h$ in (eq.4.61). The same simplification happens for the two following term, they are simplify with the term $\propto \mathbf{D}\ln\varpi^2$ and $\propto \mathbf{D}\ln\omega$ in (eq.4.61).

Then using all the development the Euler equation becomes,

$$\left[\mathbf{D}\cdot\left(\frac{\mathscr{D}\mathbf{D}\mathrm{A}}{h\varpi^2}\right)\right]\frac{\mathbf{D}\mathrm{A}}{h}+\left[\frac{\partial g_2}{\partial\Omega}-\frac{\Omega-\omega}{h^2c^2}\mathbf{D}\mathrm{A}^2\right]\frac{d\Omega}{d\mathrm{A}}\mathbf{D}\mathrm{A}+\left[4\pi\left(\rho_0\xi c^2\mathbf{D}\xi-\mathbf{D}\mathrm{P}+\mathbf{k}_p\right)+\frac{\partial g_1}{\partial\Psi_\mathrm{A}}\mathbf{D}\Psi_\mathrm{A}+\frac{\partial g_2}{\partial\Psi_\mathrm{A}\mathrm{L}}\mathbf{D}\Psi_\mathrm{A}\mathrm{L}+\frac{\partial g_2}{\partial\Psi_\mathrm{A}\mathscr{E}}\mathbf{D}\Psi_\mathrm{A}\mathscr{E}\right]=\mathbf{0} \tag{D.14}$$

The calculus of the term derivative of g_1 and g_2 leads to,

$$\begin{aligned}\frac{\partial g_2}{\partial\Omega}&=\frac{4\pi\rho_0}{\Psi_\mathrm{A}}\frac{2\mathrm{I}}{c} & \frac{\partial g_1}{\partial\Psi_\mathrm{A}}&=\frac{4\pi\rho_0\xi c^2}{\Psi_\mathrm{A}}\\ \frac{\partial g_2}{\partial\Psi_\mathrm{A}\mathrm{L}}&=\frac{4\pi\rho_0\gamma}{\Psi_\mathrm{A}\varpi}\left[\mathrm{V}^{\hat{\phi}}+\frac{\varpi\omega}{h}\right] & \frac{\partial g_2}{\partial\Psi_\mathrm{A}\mathscr{E}}&=-\frac{4\pi\rho_0\gamma}{\Psi_\mathrm{A}h}\end{aligned} \tag{D.15}$$

Indeed decompose $4\pi\left(\rho_0\xi c^2\mathbf{D}\xi-\mathbf{D}\mathrm{P}-\mathbf{k}_p\right)$ in a part along and a part transversal to the flow. It allows us to use the last equation of (eq.4.17) to replace term along the flow with something with the loading term. The rest of the term could also be simplify using the 3+1 decomposition of four-speed (eq.4.5), and the 3+1 decomposition of time killing vector $\boldsymbol{\xi}$ (eq.2.36).

$$\begin{aligned}4\pi\left(\rho_0\xi c^2\mathbf{D}\xi-\mathbf{D}\mathrm{P}-\mathbf{k}_p\right)&=\frac{4\pi}{\mathbf{D}\mathrm{A}^2}\left\{\left(\rho_0\xi c^2\mathbf{D}\xi-\mathbf{D}\mathrm{P}\right)\cdot\mathbf{D}\mathrm{A}\right\}\mathbf{D}\mathrm{A}-\frac{4\pi c}{\gamma\mathrm{V}_p^2}\left[\mathbf{u}\cdot\mathbf{k}+\xi c^2k_m\right]\mathbf{V}_p+4\pi\mathbf{k}_p\\&=\frac{4\pi}{\mathbf{D}\mathrm{A}^2}\left\{\left(\rho_0\xi c^2\mathbf{D}\xi-\mathbf{D}\mathrm{P}+\mathbf{k}_p\right)\cdot\mathbf{D}\mathrm{A}\right\}\mathbf{D}\mathrm{A}-\frac{4\pi c}{\gamma\mathrm{V}_p^2}\left[\frac{\gamma}{h}\left\{\boldsymbol{\eta}\cdot\mathbf{k}+\frac{h}{\varpi c}\left(\mathrm{V}^{\hat{\phi}}+\frac{\varpi\omega}{h}\right)\right\}\boldsymbol{\xi}\cdot\mathbf{k}+\xi c^2k_m\right]\mathbf{V}_p\end{aligned} \tag{D.16}$$

These term will be combine with the term $\propto \mathbf{D}\Psi_\mathrm{A}$, $\propto \mathbf{D}\Psi_\mathrm{A}\mathrm{L}$ and $\propto \mathbf{D}\Psi_\mathrm{A}\mathscr{E}$ in (eq.D.12). Indeed decompose these gradient term in their component along the flow and their component normal to the flow and using (eqs.4.26&4.35&4.39). We are able to reorganize, recombine the term in parenthesis in (eq.D.14), we obtain,

$$\begin{aligned}&\left[4\pi\left(\rho_0\xi c^2\mathbf{D}\xi-\mathbf{D}\mathrm{P}+\mathbf{k}_p\right)+\frac{\partial g_1}{\partial\Psi_\mathrm{A}}\mathbf{D}\Psi_\mathrm{A}+\frac{\partial g_2}{\partial\Psi_\mathrm{A}\mathrm{L}}\mathbf{D}\Psi_\mathrm{A}\mathrm{L}+\frac{\partial g_2}{\partial\Psi_\mathrm{A}\mathscr{E}}\mathbf{D}\Psi_\mathrm{A}\mathscr{E}\right]\\&=\frac{4\pi}{\mathbf{D}\mathrm{A}^2}\left\{\left(\rho_0\xi c^2\mathbf{D}\xi-\mathbf{D}\mathrm{P}+\mathbf{k}_p\right)\cdot\mathbf{D}\mathrm{A}\right\}\mathbf{D}\mathrm{A}+\frac{4\pi\rho_0\xi c^2}{\Psi_\mathrm{A}}\frac{\mathbf{D}\Psi_\mathrm{A}\cdot\mathbf{D}\mathrm{A}}{\mathbf{D}\mathrm{A}^2}\mathbf{D}\mathrm{A}+\frac{4\pi\rho_0\gamma}{\Psi_\mathrm{A}\varpi}\left[\mathrm{V}^{\hat{\phi}}+\frac{\varpi\omega}{h}\right]\frac{\mathbf{D}\Psi_\mathrm{A}\mathrm{L}\cdot\mathbf{D}\mathrm{A}}{\mathbf{D}\mathrm{A}^2}\mathbf{D}\mathrm{A}\\&+\frac{4\pi\rho_0\gamma c^2}{\Psi_\mathrm{A}h}\frac{\mathbf{D}\Psi_\mathrm{A}\mathscr{E}\cdot\mathbf{D}\mathrm{A}}{\mathbf{D}\mathrm{A}^2}\mathbf{D}\mathrm{A}\end{aligned} \tag{D.17}$$

Let present the details which leads to (eqs.4.68&4.69), rewrote again Bernoulli,

$$\frac{||\,\mathbf{D}\mathrm{A}\,||^2}{2}=-\frac{1}{2\mathrm{M}_\mathrm{A}^2}\left(h^2\varpi^2\Psi_\mathrm{A}^2\xi^2c^2+\frac{\mathrm{K}}{\mathscr{D}^2}\right)=-\frac{\mathrm{F}(\mathrm{M}_\mathrm{A}^2,\xi,h,\varpi,\omega,\Psi_\mathrm{A},\Omega,\Psi_\mathrm{A}\mathrm{L},\Psi_\mathrm{A}\mathscr{E})}{2}\quad\text{with}\quad\mathrm{K}=\frac{\Psi_\mathrm{A}^2(\mathscr{E}-\mathrm{L}\omega)^2}{c^2}\frac{\mathscr{N}_\mathrm{V}^2-x^2\mathscr{N}_\mathscr{E}^2}{x^2} \tag{D.18}$$

Then, using (eq.4.65) we have,

$$\begin{aligned}-2(\mathbf{D}\mathrm{A}\cdot\mathbf{D})\mathbf{D}\mathrm{A}=&\left[\frac{\partial\mathrm{F}}{\partial\mathrm{M}_\mathrm{A}^2}-\frac{2\xi^2}{\mathrm{M}_\mathrm{A}^2}\frac{\partial\mathrm{F}}{\partial\xi^2}\frac{c_s^2/c^2}{1-c_s^2/c^2}\right]\mathbf{D}\mathrm{M}_\mathrm{A}^2+\frac{\partial\mathrm{F}}{\partial h^2}\mathbf{D}h^2+\frac{\partial\mathrm{F}}{\partial\varpi^2}\mathbf{D}\varpi^2+\frac{\partial\mathrm{F}}{\partial\omega}\mathbf{D}\omega+\left[\frac{\partial\mathrm{F}}{\partial\Psi_\mathrm{A}^2}-\frac{2\xi^2}{\Psi_\mathrm{A}^2}\frac{\partial\mathrm{F}}{\partial\xi^2}\frac{c_s^2/c^2}{1-c_s^2/c^2}\right]\mathbf{D}\Psi_\mathrm{A}^2\\&+\frac{\partial\mathrm{F}}{\partial\Psi_\mathrm{A}\mathrm{L}}\mathbf{D}\Psi_\mathrm{A}\mathrm{L}+\frac{\partial\mathrm{F}}{\partial\Psi_\mathrm{A}\mathscr{E}}\mathbf{D}\Psi_\mathrm{A}\mathscr{E}\end{aligned} \tag{D.19}$$

Then we have

$$\mathscr{D}_{\rm SF} = -\frac{\mathscr{D}}{2}\left[\frac{\partial \mathrm{F}}{\partial \mathrm{M}_\mathrm{A}^2} - \frac{2\xi^2}{\mathrm{M}_\mathrm{A}^2}\frac{\partial \mathrm{F}}{\partial \xi^2}\frac{c_s^2/c^2}{1-c_s^2/c^2}\right] \tag{D.20}$$

So let calculate $\frac{\partial \mathrm{F}}{\partial \mathrm{M}_\mathrm{A}^2}$,

$$\begin{aligned}
\frac{\partial \mathrm{F}}{\partial \mathrm{M}_\mathrm{A}^2} &= -\frac{2}{\mathrm{M}_\mathrm{A}^6}\left(h^2\varpi^2\Psi_\mathrm{A}^2\xi^2c^2 + \frac{\mathrm{K}}{\mathscr{D}^2}\right) + \frac{1}{\mathrm{M}_\mathrm{A}^4}\frac{\partial \mathrm{K}/\mathscr{D}^\epsilon}{\partial \mathrm{M}_\mathrm{A}^2} \\
&= -\frac{2\mathrm{F}}{\mathrm{M}_\mathrm{A}^2} + \frac{2\Psi_\mathrm{A}^2}{c^2\mathrm{M}_\mathrm{A}^4\mathscr{D}^4}\left[\mathscr{D}^2\left\{\mathrm{M}_\mathrm{A}^2\left(\mathrm{L}^2h^2c^2 - \varpi^2(\mathscr{E}-\mathrm{L}\omega)^2\right) + h^2\varpi^2(\mathscr{E}-\mathrm{L}\omega)\right\} - \mathscr{D}\left\{\mathrm{M}_\mathrm{A}^2\left(\mathrm{L}^2h^2c^2 - \varpi^2(\mathscr{E}-\mathrm{L}\omega)^2\right) + h^2\varpi^2(\mathscr{E}\right.\right. \\
&= -\frac{2\mathrm{F}}{\mathrm{M}_\mathrm{A}^2} + \frac{2\Psi_\mathrm{A}^2}{c^2\mathrm{M}_\mathrm{A}^4\mathscr{D}^3}\left[-h^2(1-x^2)\mathrm{M}_\mathrm{A}^2\left(\mathrm{L}^2h^2c^2 - \varpi^2(\mathscr{E}-\mathrm{L}\omega)^2\right) - \varpi^2h^4(1-x^2)(\mathscr{E}-\mathrm{L}\omega)^2 - h^2\varpi^2(\mathscr{E}-\mathrm{L}\Omega)^2\mathscr{D}\right] \\
&= -\frac{2\mathrm{F}}{\mathrm{M}_\mathrm{A}^2} - \frac{2\Psi_\mathrm{A}^2(\mathscr{E}-\mathrm{L}\omega)^2h^4}{\mathrm{M}_\mathrm{A}^4\mathscr{D}^3(\Omega-\omega)^2}\left[(1-x^2)\mathrm{M}_\mathrm{A}^2\left(x_{\rm MR}^4 - x^2\right) + x^2h^2(1-x^2)(1-x_{\rm MR}^2)^2 + x^2(1-x_{\rm MR}^2)^2\mathrm{M}_\mathrm{A}^2\right. \\
&\left.-x^2h^2(1-x_{\rm MR}^2)^2(1-x^2)\right] \\
&= -\frac{2\mathrm{F}}{\mathrm{M}_\mathrm{A}^2} - \frac{2\Psi_\mathrm{A}^2(\mathscr{E}-\mathrm{L}\omega)^2h^4}{\mathrm{M}_\mathrm{A}^2\mathscr{D}^3(\Omega-\omega)^2}\left[x_{\rm MR}^2 - x^2\right]^2 \\
&= \frac{2\mathbf{D}\mathrm{A}^2}{\mathrm{M}_\mathrm{A}^2}\left(1 - \frac{h^2\mathrm{B}\hat{\phi}^2}{\mathscr{D}\mathrm{B}_p^2}\right)
\end{aligned} \tag{D.21}$$

For the last term $\frac{2\xi^2}{\mathrm{M}_\mathrm{A}^2}\frac{\partial \mathrm{F}}{\partial \xi^2}\frac{c_s^2/c^2}{1-c_s^2/c^2}$, we immediately get get

$$\frac{2\xi^2}{\mathrm{M}_\mathrm{A}^2}\frac{\partial \mathrm{F}}{\partial \xi^2}\frac{c_s^2/c^2}{1-c_s^2/c^2} = \frac{2\mathbf{D}\mathrm{A}^2}{\mathrm{M}_\mathrm{A}^2}\left(-\frac{c^2}{\gamma^2\mathbf{V}_p^2}\frac{c_s^2/c^2}{1-c_s^2/c^2}\right) \tag{D.22}$$

D.3 Flux on the horizon of event for a Kerr hole

Let demonstrate and precise the form of the integrals Eqs.(4.80). Start to integrate on $\mathscr{U}$, the conservation equation Eq.(4.37) (without loading term), using Stokes theorem we get,

$$\int_{\partial\mathscr{U}} \boldsymbol{\epsilon}\left(\mathbf{P}, \mathbf{dx_1}, \mathbf{dx_2}, \mathbf{dx_3}\right) \tag{D.23}$$

Where if (x^1, x^2, x^3) is a system of coordinate on $\partial\mathscr{U}$, the vector $\mathbf{dx_i} = dx^i\boldsymbol{\partial}_i$. Then we decompose $\partial\mathscr{U} = \mathscr{V}_{t+dt} \cup \mathscr{V}_t \cup \left(\bigcup_{t\in[t,t+\Delta_t]}\Delta\mathscr{S}_t\right) \cup \left(\bigcup_{t\in[t,t+\Delta_t]}\sigma_{\rm ext}\right)$, which allow us to decompose the integrals. Use a coordinate system on $\mathscr{M}$, t, u^1, u^2, u^3 adapted to the 3+1 foliation, and note $(\boldsymbol{\partial}_{u,i})$ the natural associated basis. Started with the easiest one,

$$\begin{aligned}
\int_{\mathscr{V}_{t+dt}} \boldsymbol{\epsilon}\left(\mathbf{P}, \boldsymbol{\partial}_{u,1}, \boldsymbol{\partial}_{u,2}, \boldsymbol{\partial}_{u,3}\right) du^1du^2du^3 &= -\int_{\mathscr{V}_{t+dt}} (\mathbf{P}\cdot\mathbf{n})\,\boldsymbol{\epsilon}\left(\mathbf{n}, \boldsymbol{\partial}_{u,1}, \boldsymbol{\partial}_{u,2}, \boldsymbol{\partial}_{u,3}\right) du^1du^2du^3 \\
&= -\int_{\mathscr{V}_{t+dt}} (\mathbf{P}\cdot\mathbf{n})\,\boldsymbol{\epsilon}\left(\mathbf{n}, \boldsymbol{\partial}_{u,1}, \boldsymbol{\partial}_{u,2}, \boldsymbol{\partial}_{u,3}\right) du^1du^2du^3 \\
&= -\int_{\mathscr{V}_{t+dt}} (\mathbf{P}\cdot\mathbf{n})\,\sqrt{\gamma}du^1du^2du^3
\end{aligned} \tag{D.24}$$

Continue with the integrals on $\left(\bigcup_{t\in[t,t+\Delta_t]}\sigma_{\rm ext}\right)$. Suppose we get a system of coordinate x^2, x^3 on $\sigma_{\rm ext}$, such that t, x^1, x^2 is a system of coordinate on $\left(\bigcup_{t\in[t,t+\Delta_t]}\sigma_{\rm ext}\right)$, then the natural basis associated to this system of coordinate is $\boldsymbol{\eta} = \boldsymbol{\partial}_t$, $\boldsymbol{\partial}_{x,2}, \boldsymbol{\partial}_{x,3} \in \mathscr{T}(\Sigma)$. Took the normal $\mathbf{s}$ to $\sigma_{\rm ext}$ is

include inside $\mathscr{T}(\Sigma)$. This vector allow us to make a decomposition of $\mathbf{P}$. Then we obtain,

$$\begin{aligned}\int_{\left(\bigcup_{t\in[t,t+\Delta_t]}\sigma_{\text{ext}}\right)}\boldsymbol{\epsilon}\left(\mathbf{P},\boldsymbol{\partial}_t,\boldsymbol{\partial}_{x,2},\boldsymbol{\partial}_{x,3}\right)cdtdx^2dx^3 &= \int_{\left(\bigcup_{t\in[t,t+\Delta_t]}\sigma_{\text{ext}}\right)}(\mathbf{P}\cdot\mathbf{s})\,\boldsymbol{\epsilon}\left(\mathbf{s},\mathbf{n},\boldsymbol{\partial}_{x,2},\boldsymbol{\partial}_{x,3}\right)hcdtdx^2dx^3\\ &= \int_{\left(\bigcup_{t\in[t,t+\Delta_t]}\sigma_{\text{ext}}\right)}(\mathbf{P}\cdot\mathbf{s})\,d^2\mathrm{S}hcdt\&\\ &= \int_t^{t+\Delta t}\left(\int_{\sigma_{\text{ext}}}h\mathbf{P}\cdot\mathbf{d^2S}\right)cdt\end{aligned} \tag{D.25}$$

Where $d^2\mathrm{S}=\boldsymbol{\epsilon}\left(\mathbf{s},\mathbf{n},\boldsymbol{\partial}_{x,2},\boldsymbol{\partial}_{x,3}\right)dx^2dx^3$. Let finish with the integrals on the horizon of the black hole, $\left(\bigcup_{t\in[t,t+\Delta t]}\Delta\mathscr{S}_t\right)=\Delta\mathscr{H}$ is a null hypersurface. Its normal vector is $\boldsymbol{\ell}=\boldsymbol{\eta}+\frac{\omega_{\mathscr{H}}}{c}\boldsymbol{\xi}$, it is also tengant to the horizon. As in Sec.(2.2.1), we can build the vector $\mathbf{k}$ in order to get the projector Eq.(2.4). Introducing y^1,y^2 a coordinate system on $\mathscr{S}_t$ then,

$$\begin{aligned}\int_{\left(\bigcup_{t\in[t,t+\Delta_t]}\Delta\mathscr{S}_t\right)}\boldsymbol{\epsilon}\left(\mathbf{P},\boldsymbol{\partial}_t,\boldsymbol{\partial}_{y,2},\boldsymbol{\partial}_{y,3}\right)cdtdy^2dy^3 &= -\int_{\left(\bigcup_{t\in[t,t+\Delta_t]}\Delta\mathscr{S}_t\right)}(\mathbf{P}\cdot\boldsymbol{\ell})\,\boldsymbol{\epsilon}\left(\mathbf{k},\boldsymbol{\partial}_t,\boldsymbol{\partial}_{y,2},\boldsymbol{\partial}_{y,3}\right)cdtdy^2dy^3\\ &= -\int_{\left(\bigcup_{t\in[t,t+\Delta_t]}\Delta\mathscr{S}_t\right)}(\mathbf{P}\cdot\boldsymbol{\ell})\,\boldsymbol{\epsilon}\left(\mathbf{k},\boldsymbol{\ell},\boldsymbol{\partial}_{y,2},\boldsymbol{\partial}_{y,3}\right)cdtdy^2dy^3\\ &= -\int_t^{t+\Delta t}\left(\int_{\Delta\mathscr{S}_t}\mathbf{P}\cdot\boldsymbol{\ell}\,d^2q\right)cdt\end{aligned} \tag{D.26}$$

Where $d^2q=\boldsymbol{\epsilon}\left(\mathbf{k},\boldsymbol{\ell},\boldsymbol{\partial}_{y,2},\boldsymbol{\partial}_{y,3}\right)dy^2dy^3$

Appendix E

Resolution of the system and numerical work

Let prove the property used in Subsec.(6.4.2). $\forall \mathbf{u} \in \mathbb{R}^{\mathrm{N}}_{\star}$ using the definition of projector orthogonal to $\mathbf{u}$,

$$\begin{array}{rl} \mathbf{p}_1(.;\mathbf{u}): & \mathbb{R}^{\mathrm{N}} \longrightarrow \mathbb{R}^{\mathrm{N}} \\ & \mathbf{x} \longrightarrow \mathbf{x} - \frac{\mathbf{x}\cdot\mathbf{u}}{\mathbf{u}^2}\mathbf{u} \end{array} \tag{E.1}$$

Introduce the proposal, for $\mathrm{N} \geq n \geq 2$

$$\mathscr{P}_n : \begin{cases} \forall \mathbf{u}_{i\in[1;n]} \in \mathbb{R}^{\mathrm{N}} \quad \mathbf{R}^{\mathrm{N}} = \mathrm{Span}\left(\mathbf{u}_{i\in[1;n]}\right) \overset{\perp}{\oplus} \mathrm{Span}\left(\mathbf{u}_{i\in[1;n]}\right)^{\perp} \\ \text{then} \quad \begin{array}{rl} \mathbf{p}_n(.;\mathbf{u}_1,....,\mathbf{u}_n): & \mathbb{R}^{\mathrm{N}} \longrightarrow \mathbb{R}^{\mathrm{N}} \\ & \mathbf{x} \longrightarrow \mathbf{p}_{n-1}\left(\mathbf{p}_1(\mathbf{x};\mathbf{u}_n);\mathbf{p}_1(\mathbf{u}_1;\mathbf{u}_n),....,\mathbf{p}_1(\mathbf{u}_{n-1};\mathbf{u}_n)\right) \end{array} \\ \text{is the orthogonal projector adapted to the decomposition} \end{cases} \tag{E.2}$$

Base case.The first step consist to prove $\mathscr{P}_2$. The calculation of $\mathbf{p}_2(\mathbf{x};\mathbf{u},\mathbf{v})$ gives,

$$\mathbf{p}_2(\mathbf{x};\mathbf{u},\mathbf{v}) = \mathbf{x} - \frac{(\mathbf{x}\cdot\mathbf{u})\mathbf{v}^2 - (\mathbf{u}\cdot\mathbf{v})(\mathbf{x}\cdot\mathbf{v})}{\mathbf{u}^2\mathbf{v}^2 - (\mathbf{u}\cdot\mathbf{v})^2}\mathbf{u} - \frac{(\mathbf{x}\cdot\mathbf{v})\mathbf{u}^2 - (\mathbf{u}\cdot\mathbf{v})(\mathbf{x}\cdot\mathbf{u})}{\mathbf{u}^2\mathbf{v}^2 - (\mathbf{u}\cdot\mathbf{v})^2}\mathbf{v} \tag{E.3}$$

Which easily allows us to prove that $\mathbf{p}_2(\mathbf{x};\mathbf{u},\mathbf{v}) \in \mathrm{Span}(\mathbf{u},\mathbf{v})^{\perp}$ and $\mathbf{x} - \mathbf{p}_2(\mathbf{x};\mathbf{u},\mathbf{v}) \in \mathrm{Span}(\mathbf{u},\mathbf{v})$ which prove that $\mathbf{p}_2(.;\mathbf{u},\mathbf{v})$ is the orthogonal projector associated to the orthogonal decomposition $\mathbf{R}^{\mathrm{N}} = \mathrm{Span}(\mathbf{u},\mathbf{v}) \overset{\perp}{\oplus} \mathrm{Span}(\mathbf{u},\mathbf{v})^{\perp}$.

Induction step. Let's assume $\mathscr{P}_{n-1}$ true, let's try to prove $\mathscr{P}_n$. $\mathscr{P}_{n-1}$ is true, then$\forall \mathbf{x}$, $\mathbf{p}_{n-1}\left(\mathbf{p}_1(\mathbf{x};\mathbf{u}_n);\mathbf{p}_1(\mathbf{u}_1;\mathbf{u}_n),....,\mathbf{p}_1(\mathbf{u}_{n-1};\mathbf{u}_n)\right) \in \mathrm{Span}\left(\left(\mathbf{p}_1(\mathbf{u}_i;\mathbf{u}_n)\right)_{i\in[1;n-1]}\right)^{\perp}$, then,

$$\forall i \in [1;n-1] \quad \mathbf{p}_{n-1}\left(\mathbf{p}_1(\mathbf{x};\mathbf{u}_n);\mathbf{p}_1(\mathbf{u}_1;\mathbf{u}_n),....,\mathbf{p}_1(\mathbf{u}_{n-1};\mathbf{u}_n)\right)\cdot\left(\mathbf{u}_i - \frac{\mathbf{u}_i\cdot\mathbf{u}_n}{\mathbf{u}_n^2}\mathbf{u}_n\right) = 0 \tag{E.4}$$

$\mathscr{P}_{n-1}$ is true, then $\mathbf{p}_{n-1}\left(\mathbf{p}_1(\mathbf{x};\mathbf{u}_n);\mathbf{p}_1(\mathbf{u}_1;\mathbf{u}_n),....,\mathbf{p}_1(\mathbf{u}_{n-1};\mathbf{u}_n)\right) - \mathbf{p}_1(\mathbf{x};\mathbf{u}_n) \in \mathrm{Span}\left(\left(\mathbf{p}_1(\mathbf{u}_i;\mathbf{u}_n)\right)_{i\in[1;n-1]}\right)$ which implies $\exists(\lambda_i)_{i\in[1;n-1]}$ such that,

$$\begin{cases} \mathbf{p}_{n-1}\left(\mathbf{p}_1(\mathbf{x};\mathbf{u}_n);\mathbf{p}_1(\mathbf{u}_1;\mathbf{u}_n),....,\mathbf{p}_1(\mathbf{u}_{n-1};\mathbf{u}_n)\right) - \mathbf{p}_1(\mathbf{x};\mathbf{u}_n) = \sum_{i=1}^{n-1}\lambda_i\mathbf{p}_1(\mathbf{u}_i;\mathbf{u}_n) \\ \Rightarrow \mathbf{p}_{n-1}\left(\mathbf{p}_1(\mathbf{x};\mathbf{u}_n);\mathbf{p}_1(\mathbf{u}_1;\mathbf{u}_n),....,\mathbf{p}_1(\mathbf{u}_{n-1};\mathbf{u}_n)\right)\cdot\mathbf{u}_n = 0 \end{cases} \tag{E.5}$$

It implies that $\forall \mathbf{x}$, $\mathbf{p}_n(\mathbf{x};\mathbf{u}_1,....,\mathbf{u}_n) \in \mathrm{Span}\left((\mathbf{u}_i)_{i\in[1;n]}\right)^{\perp}$ but also $\mathbf{x} - \mathbf{p}_n(\mathbf{x};\mathbf{u}_1,....,\mathbf{u}_n) \in \mathrm{Span}\left((\mathbf{u}_i)_{i\in[1;n]}\right)$, which completes the demonstration. ■

E.1 References

Brandon Carter. The commutation property of a stationary, axisymmetric system. *Communications in Mathematical Physics*, 17(3):233–238, Sep 1970. ISSN 1432-0916. doi: 10.1007/BF01647092. URL https://doi.org/10.1007/BF01647092. 181

E. Gourgoulhon. 3+1 Formalism and Bases of Numerical Relativity. *ArXiv General Relativity and Quantum Cosmology e-prints*, March 2007. xvi, 180

C. Marle. Sur l'établissement des équations de l'hydrodynamique des fluides relativistes dissipatifs. i. - l'équation de boltzmann relativiste. *Annales de l'I.H.P. Physique théorique*, (1):67–126, 1969. 193

J.A. Wheeler. *Geometrodynamics and the issue of the final state, in Relativity*. August 1964. 187

Appendix F

List of acronyms

AGN Active Galaxy Nuclei. xvii, 2–4, 26, 38, 174

ASIMHD Axi-symmetric Stationary Ideal Magneto-Hydrodynamic. 80

EOS Equation of state. 43, 44, 48, 50

FIDO Fiducials Observers. xi, 9, 16–18, 27, 55–57

GR General Relativity. 80

GRASIMHD General Relativistic Axi-symmetric Stationary Ideal Magneto-Hydrodynamic. vii, ix, 5, 53, 58, 59, 67, 68, 70, 73–76, 98, 147, 153, 158, 174, 176, 196

GRB Gamma Ray Burst. 1, 26, 38, 146

GRMHD General Relativistic Magneto-Hydrodynamic. vii, 3, 23, 25, 26, 38, 53–55, 57, 58, 64, 70, 76, 146, 147, 156, 158

GU Gaussian Unit. 37, 54, 56

MHD Magneto-Hydrodynamic. 2–5, 26, 38, 50, 54, 73, 146, 152, 160, 161, 165, 174–177

RIAF Radiative inefficient accretion flow. 165

SR Special Relativity. 80

SRMHD Special Relativistic Magneto-Hydrodynamic. 3

ZAMO Zero Angular Momentum Observer. 16, 20, 23, 58–64, 71, 72, 80, 148, 149, 151, 186

RÉSUMÉ

Les jets sont des phénomènes d'éjection collimatée de plasma magnétisé. Ces phénomènes liés à l'accrétion d'un disque sur un objet central, sont relativement répandus dans l'univers : les environnements des étoiles jeunes (objets Herbig-Haro, étoiles T Tauri), des binaires X, des sursauts gamma et les noyaux actifs de galaxies... Les jets extra-galactiques sont issus des trous noirs super-massifs au centre de galaxies telles que les quasars ou les radiogalaxies. Ils sont caractérisés par leur taille, leur puissance et la vitesse du plasma.

Les jets extragalactiques sont étudiés dans de ce travail de thèse, même si les outils et méthodes développés peuvent être utilisés pour les binaires X et les microquasars. Nous poserons en particulier les questions des mécanismes de lancement, d'accélération et de collimation de ces écoulements. Nous traiterons également de la source énergétique à l'origine de l'écoulement qui peut atteindre une puissance de l'ordre de 10^{47} erg.s^{-1}.

Le liens avec l'accrétion, la proximité de la base des jets avec le trou noir central, les vitesses d'écoulement observées dans certains jets, montrent que le traitement de ces questions doit inclure les effet de la relativité générale. Nous étudierons donc des solutions de la décomposition 3+1 des équations de la magnéto-hydrodynamique en métrique de Kerr. Nous nous appliquerons au développement d'un modèle d'écoulement auto-similaire meridional avec un traitement consistant du cylindre de lumière. Ce modèle pouvant s'appliquer à la fois au jet et à l'accrétion. Nous explorons les mécanismes d'accélération et de collimation des solutions produites. Nous calculerons des solutions de l'écoulement entrant dans l'horizon et de l'écoulement sortant à l'infini incluant des termes d'injection de paires. Le rôle du mécanisme de création de paires et des processus d'extraction de l'énergie du trou noir sera exploré.

MOTS CLÉS

Jets relativistes - Magnétohydrodynamique en relativité général - Auto-similarité - Jets extra-galactique - Physique des trous noirs

ABSTRACT

Jets are collimated ejection phenomena of magnetized plasma. These phenomena related to the accretion of a disk on a central object, are relatively common in the universe: the environment of young stars (Herbig-Haro Objects, T Tauri stars...), X-ray binaries, Gamma-ray-bursts, and active galactic nuclei... Extragalactic jets come from super-massive black holes in the center of galaxies such as quasars or radiogalaxies. They are characterized by their size, their power and speed of the plasma.

Extragalactic jets will be the subject of studies in this thesis work, although the tools and methods developed can be used for X-ray binaries and microquasars. In particular, we will ask questions about the mechanisms of launching, accelerating and collimating these flows, but also about the energy source at the origin of the flow that can reach a power in the order of 10^{47}erg.s^{-1}.

The links with the accretion, the proximity of the jet base to the central black hole, flow velocities observed in some jets, show that the treatment of these issues must include the effects of general relativity. We will therefore study solutions of the 3+1 decomposition of magneto-hydrodynamic equations in Kerr metric. We will apply ourselves the development of a meridional self-similar magnetized flow model with a consistent treatment of the light cylinder effect. This model can be applied to both spine jet and inflow onto the black hole. We explore the mechanisms of acceleration and collimation of the obtained solutions. We will calculate solutions of the incoming flow on the horizon and the outgoing flow reaching infinity including injection terms. The role of the pair creation mechanism and the processes of extracting energy from the black hole are explored.

KEYWORDS

Relativistic jets - General relativistic magnetohydrodynamics - Self-similarity - Extragalactic jets - Black hole physics